

Imaging nuclear motion during the photofragmentation of halomethane molecules triggered by ultraviolet light.

by

Farzaneh Ziaee

B.S., Kharazmi University, Iran, 2011

M.S., Laser, and Plasma Research Institute, Shahid Beheshti University, Iran, 2013

AN ABSTRACT OF A DISSERTATION

submitted in partial fulfillment of the requirements for the degree

DOCTOR OF PHILOSOPHY

Department of Physics  
College of Arts and Sciences

KANSAS STATE UNIVERSITY  
Manhattan, Kansas

2022

## Abstract

Understanding the photoexcitation of molecules and visualizing the ensuing dynamics on their natural time scale is essential for our ability to describe and exploit many fundamental processes in different areas of science and technology. Prominent examples of such processes include, among many others, the adverse impacts of different classes of molecules on the ozone layer in atmospheric chemistry, light conversion into electricity through photovoltaics, photocatalysis, and some essential biological processes like vision and photosynthesis. Studies of molecular dynamics triggered by photon-molecule interaction underpin our understanding of many of these phenomena by adding the intermediate state to the “before-and-after” view of such photochemical or photobiological reactions. While identifying the initial molecular structure at equilibrium and determining the final products are crucial steps for the reaction characterization, understanding the dynamics connecting these initial and final states is essential for comprehending how the reaction really happens and potentially controlling its outcome. In other words, besides the “static” view of photo-induced reactions, identifying all intermediate states involved and mapping their spatio-temporal evolution are of great interest and importance. Since photoexcitation often induces coupled electron and nuclear motion on Angström spatial and femtosecond time scales, resolving such dynamics in space and time represents a significant scientific and technological challenge. Experimental tools to address this challenge have recently become available with the development of femtosecond lasers and imaging techniques capable of visualizing the evolving molecular structure.

The present thesis aims to investigate the photodissociation dynamics of halomethane molecules triggered by ultraviolet (UV) light using coincidence ion momentum imaging as a primary structural characterization tool. Halomethanes are often considered as prototypical systems for molecular photodissociation in the UV domain. Due to the complicated excited-state structure driving the photochemistry of these molecules, they exhibit rich dynamics while being small enough to still allow for a detailed theoretical treatment. The primary goal of this work is to disentangle the photo-induced reaction channels, including direct and indirect dissociation pathways, and to visualize the motion of the individual molecular fragments in each of these channels. The photofragmentation reactions considered here include two- and three-body dissociation, transient isomerization and molecular halogen formation. The experiments are

carried out at two different excitation wavelengths, 263 nm and 198 nm, which enables varying the dominant reaction pathways. To carry out these measurements, the 3<sup>rd</sup> and 4<sup>th</sup> harmonics of a 790 nm Ti: Sa femtosecond laser are used to initiate the dynamics of interest, which are then probed by multiple ionization and Coulomb explosion induced by an intense 790 nm pulse arriving after a variable time delay. The ions created in such pump-probe experiments are detected employing COLd Target Recoil Ion Momentum Spectroscopy (COLTRIMS). To facilitate interpreting the experimental results, they are compared to an extensive set of Coulomb explosion simulations.

More specifically, this thesis describes three major studies. The first one is a set of time-resolved measurements on iodomethane (CH<sub>3</sub>I) photodissociation in the A-band, one of the best-studied reactions in ultrafast photochemistry. Here, the focus is on a detailed characterization of direct dissociation dynamics by Coulomb explosion imaging (CEI) and disentangling the competing reaction pathways involving single- and multi-photon excitations. The coincident measurement mode and an improved time resolution of 40-45 fs allowed us to observe a new feature in the two-body CEI pattern of this well-studied reaction, which was predicted theoretically but not yet observed experimentally, and to identify signatures of two- and three-photon processes populating Rydberg and ionic states.

The second part of this work focuses on time-resolved studies of bromiodomethane (CH<sub>2</sub>BrI) and chloriodomethane (CH<sub>2</sub>ICl) photofragmentation in the A-band at 263 nm and, in particular, on imaging the co-fragment rotation. Here, the main objectives are to evaluate the effects of halogen-atom substitution on molecular dynamics and map the time evolution of individual photodissociation pathways. For these molecules, photoabsorption in the A-band predominantly breaks the C-I bond, with weaker but non-negligible contribution from the C-Br (or C-Cl) bond cleavage. Coincident two-body CEI analysis is used to map both of these channels, as well as a minor contribution from molecular halogen (IBr or ICl) formation. Three-body CEI patterns offer a deeper insight into the dynamics of these reactions and, in addition, reveal clear signatures of the three-body dissociation, which – at this wavelength – is most likely driven by the two-photon absorption. The three-body analysis also suggests that some fragmentation pathways pass through a transient linearized configuration, which is reached within ~100 fs from the initial photoabsorption and decays on a comparably fast time scale.

One of the interesting aspects of dihalomethanes photodissociation in the A-band is that, unlike CH<sub>3</sub>I, where the excess energy is primarily channeled into translational motion, a significant

portion of the available energy is partitioned into rotational excitation. Carbon-halogen bond cleavage results in the rotation of the molecular co-fragment, which can be unambiguously traced in the coincident three-body CEI maps for the corresponding dissociation channel. In this work, such rotational motion is directly imaged for the dissociation of either halogen atom, resulting in a “molecular movie” of the dissociating and rotating molecule.

The third group of experiments described in this thesis includes time-resolved studies of bromiodomethane and diiodomethane ( $\text{CH}_2\text{I}_2$ ) photofragmentation in the B-band at 198 nm. In this part, the main goal is to trace the wavelength dependence of the photochemical reaction pathways. For  $\text{CH}_2\text{BrI}$ , we observe a reversal of the branching ratio of C-I and C-Br bond cleavage compared to the 263 nm data, in agreement with earlier spectroscopic and theoretical studies. However, at 198 nm, three-body dissociation and molecular halogen formation become dominant photofragmentation channels for both molecules.

Finally, the  $\text{CH}_3\text{I}$  photodissociation is also studied in the B-band at 198 nm, where the excitation of the lowest-lying Rydberg states is expected to trigger pre-dissociation dynamics. Although no in-depth data analysis and modeling for this reaction have been carried out, the two-body CEI results clearly demonstrate the pre-dissociation nature of  $\text{CH}_3\text{I}$  fragmentation at this wavelength, reflected in a broad, diffuse dissociation band, which is very different from distinct dissociation features observed for direct dissociation processes. Moreover, the data exhibit a pronounced oscillatory structure with a periodicity of 130-140 fs, which is visible only within the pre-dissociation lifetime of the excited state ( $\sim 1.5$  ps). While the exact origin of this structure remains unclear and will be a subject of further analysis and theoretical work, it most likely reflects the bound-state vibrational motion, which lasts until it pre-dissociates.

The work presented in this thesis represents a significant step towards a better understanding of the UV-driven photochemistry of halomethanes and contains several examples of direct visualization of the atomic motion during these photochemical reactions. Our experimental approach enabled us to identify and disentangle different dissociation pathways and track their time evolution. The experimental methodology described here can be directly applied to investigate the light-driven nuclear motion in other molecular systems with different light sources.

Imaging Nuclear Motion during the Photofragmentation of Halomethane Molecules Triggered by  
Ultraviolet Light

by

Farzaneh Ziaee

B.S., Kharazmi University, Iran, 2011

M.S., Laser, and Plasma Research Institute, Shahid Beheshti University, Iran, 2013

A DISSERTATION

submitted in partial fulfillment of the requirements for the degree

DOCTOR OF PHILOSOPHY

Department of Physics  
College of Arts and Sciences

KANSAS STATE UNIVERSITY  
Manhattan, Kansas

2022

Approved by:

Co-Major Professor  
Daniel Rolles

Approved by:

Co-Major Professor  
Artem Rudenko

# Copyright

© Farzaneh Ziaee 2022.

## Abstract

Understanding the photoexcitation of molecules and visualizing the ensuing dynamics on their natural time scale is essential for our ability to describe and exploit many fundamental processes in different areas of science and technology. Prominent examples of such processes include, among many others, the adverse impacts of different classes of molecules on the ozone layer in atmospheric chemistry, light conversion into electricity through photovoltaics, photocatalysis, and some essential biological processes like vision and photosynthesis. Studies of molecular dynamics triggered by photon-molecule interaction underpin our understanding of many of these phenomena by adding the intermediate state to the “before-and-after” view of such photochemical or photobiological reactions. While identifying the initial molecular structure at equilibrium and determining the final products are crucial steps for the reaction characterization, understanding the dynamics connecting these initial and final states is essential for comprehending how the reaction really happens and potentially controlling its outcome. In other words, besides the “static” view of photo-induced reactions, identifying all intermediate states involved and mapping their spatio-temporal evolution are of great interest and importance. Since photoexcitation often induces coupled electron and nuclear motion on Angström spatial and femtosecond time scales, resolving such dynamics in space and time represents a significant scientific and technological challenge. Experimental tools to address this challenge have recently become available with the development of femtosecond lasers and imaging techniques capable of visualizing the evolving molecular structure.

The present thesis aims to investigate the photodissociation dynamics of halomethane molecules triggered by ultraviolet (UV) light using coincidence ion momentum imaging as a primary structural characterization tool. Halomethanes are often considered as prototypical systems for molecular photodissociation in the UV domain. Due to the complicated excited-state structure driving the photochemistry of these molecules, they exhibit rich dynamics while being small enough to still allow for a detailed theoretical treatment. The primary goal of this work is to disentangle the photo-induced reaction channels, including direct and indirect dissociation pathways, and to visualize the motion of the individual molecular fragments in each of these channels. The photofragmentation reactions considered here include two- and three-body dissociation, transient isomerization and molecular halogen formation. The experiments are

carried out at two different excitation wavelengths, 263 nm and 198 nm, which enables varying the dominant reaction pathways. To carry out these measurements, the 3<sup>rd</sup> and 4<sup>th</sup> harmonics of a 790 nm Ti: Sa femtosecond laser are used to initiate the dynamics of interest, which are then probed by multiple ionization and Coulomb explosion induced by an intense 790 nm pulse arriving after a variable time delay. The ions created in such pump-probe experiments are detected employing COLd Target Recoil Ion Momentum Spectroscopy (COLTRIMS). To facilitate interpreting the experimental results, they are compared to an extensive set of Coulomb explosion simulations.

More specifically, this thesis describes three major studies. The first one is a set of time-resolved measurements on iodomethane ( $\text{CH}_3\text{I}$ ) photodissociation in the A-band, one of the best-studied reactions in ultrafast photochemistry. Here, the focus is on a detailed characterization of direct dissociation dynamics by Coulomb explosion imaging (CEI) and disentangling the competing reaction pathways involving single- and multi-photon excitations. The coincident measurement mode and an improved time resolution of 40-45 fs allowed us to observe a new feature in the two-body CEI pattern of this well-studied reaction, which was predicted theoretically but not yet observed experimentally, and to identify signatures of two- and three-photon processes populating Rydberg and ionic states.

The second part of this work focuses on time-resolved studies of bromiodomethane ( $\text{CH}_2\text{BrI}$ ) and chloriodomethane ( $\text{CH}_2\text{ICl}$ ) photofragmentation in the A-band at 263 nm and, in particular, on imaging the co-fragment rotation. Here, the main objectives are to evaluate the effects of halogen-atom substitution on molecular dynamics and map the time evolution of individual photodissociation pathways. For these molecules, photoabsorption in the A-band predominantly breaks the C-I bond, with weaker but non-negligible contribution from the C-Br (or C-Cl) bond cleavage. Coincident two-body CEI analysis is used to map both of these channels, as well as a minor contribution from molecular halogen (IBr or ICl) formation. Three-body CEI patterns offer a deeper insight into the dynamics of these reactions and, in addition, reveal clear signatures of the three-body dissociation, which – at this wavelength – is most likely driven by the two-photon absorption. The three-body analysis also suggests that some fragmentation pathways pass through a transient linearized configuration, which is reached within ~100 fs from the initial photoabsorption and decays on a comparably fast time scale.

One of the interesting aspects of dihalomethanes photodissociation in the A-band is that, unlike  $\text{CH}_3\text{I}$ , where the excess energy is primarily channeled into translational motion, a significant

portion of the available energy is partitioned into rotational excitation. Carbon-halogen bond cleavage results in the rotation of the molecular co-fragment, which can be unambiguously traced in the coincident three-body CEI maps for the corresponding dissociation channel. In this work, such rotational motion is directly imaged for the dissociation of either halogen atom, resulting in a “molecular movie” of the dissociating and rotating molecule.

The third group of experiments described in this thesis includes time-resolved studies of bromiodomethane and diiodomethane ( $\text{CH}_2\text{I}_2$ ) photofragmentation in the B-band at 198 nm. In this part, the main goal is to trace the wavelength dependence of the photochemical reaction pathways. For  $\text{CH}_2\text{BrI}$ , we observe a reversal of the branching ratio of C-I and C-Br bond cleavage compared to the 263 nm data, in agreement with earlier spectroscopic and theoretical studies. However, at 198 nm, three-body dissociation and molecular halogen formation become dominant photofragmentation channels for both molecules.

Finally, the  $\text{CH}_3\text{I}$  photodissociation is also studied in the B-band at 198 nm, where the excitation of the lowest-lying Rydberg states is expected to trigger pre-dissociation dynamics. Although no in-depth data analysis and modeling for this reaction have been carried out, the two-body CEI results clearly demonstrate the pre-dissociation nature of  $\text{CH}_3\text{I}$  fragmentation at this wavelength, reflected in a broad, diffuse dissociation band, which is very different from distinct dissociation features observed for direct dissociation processes. Moreover, the data exhibit a pronounced oscillatory structure with a periodicity of 130-140 fs, which is visible only within the pre-dissociation lifetime of the excited state ( $\sim 1.5$  ps). While the exact origin of this structure remains unclear and will be a subject of further analysis and theoretical work, it most likely reflects the bound-state vibrational motion, which lasts until it pre-dissociates.

The work presented in this thesis represents a significant step towards a better understanding of the UV-driven photochemistry of halomethanes and contains several examples of direct visualization of the atomic motion during these photochemical reactions. Our experimental approach enabled us to identify and disentangle different dissociation pathways and track their time evolution. The experimental methodology described here can be directly applied to investigate the light-driven nuclear motion in other molecular systems with different light sources.

# Table of Contents

List of Figures .....	xiii
List of Tables .....	xxii
Acknowledgments.....	xxiii
Dedication .....	xxvi
Chapter 1 - Introduction.....	1
Chapter 2 - Introduction to the UV-driven photochemistry of halomethanes .....	10
2.1 Photodissociation .....	10
2.1.1 Transition probability and Franck-Condon principle.....	14
2.1.2 Types of photodissociation reactions.....	15
2.1.3 Conical intersections .....	18
2.2 Photoionization .....	19
2.2.1 Dissociative photoionization:.....	20
2.3 Introduction to the photochemistry of halomethanes .....	20
2.3.1 Photodissociation dynamics of a halomethane; iodomethane (CH <sub>3</sub> I).....	20
2.3.1.1. Dynamics upon A-band photoexcitation .....	21
2.3.1.2. Dynamics upon B- and C-bands photoexcitation .....	26
2.3.2 Photodissociation dynamics of dihalomethanes .....	31
2.4 Principles of Coulomb explosion imaging (CEI) .....	37
Chapter 3 - Experimental methods .....	46
3.1 Ultrafast laser system; chirped pulse amplification .....	46
3.2 Ultrafast pulse characterization .....	48
3.2.1 Frequency-resolved optical gating (FROG).....	49
3.2.2 Cross-correlation frequency-resolved optical gating (XFROG).....	51
3.3 New frequency component generations using intense femtosecond laser.....	52
3.3.1 Introduction to nonlinear optics .....	52
3.3.2 New frequency generation .....	57
3.3.3 Pulse compression: the effect of pulse dispersion on ultrashort pulses .....	62
3.3.4 Pulse characterization .....	70
3.4 COLd Target Recoil Ion Momentum Spectrometer (COLTRIMS) .....	75

3.5 Experimental setup for pump-probe experiments with COLTRIMS .....	80
3.6 Data processing; 3D momentum imaging principles.....	81
3.7 Peak intensity calibration.....	81
Chapter 4 - Single- and multi-photon-induced ultraviolet excitation and photodissociation of CH <sub>3</sub> I probed by strong-field ionization.....	84
4.1 Measurements with single UV pulses.....	84
4.2 Ionization, dissociative ionization and Coulomb explosion of CH <sub>3</sub> I with NIR pulses.....	88
4.3 UV-induced photodissociation of CH <sub>3</sub> I with time-resolved ion momentum imaging .....	94
4.3.1 Channel identification by comparison of coincident and non-coincident data.....	97
4.3.2 Pathways contributing to the low-energy region of non-coincident CH <sub>3</sub> <sup>+</sup> and I <sup>+</sup> .....	100
4.3.2.1. Non-coincident spectra in the “overlap” region and the role of light-induced conical intersection .....	101
4.3.3 Probing UV-induced dissociation dynamics with coincident CE imaging.....	105
4.4 Coulomb explosion simulation.....	109
4.4.1 Modelling the dissociation process .....	109
4.4.2 Simulations with a purely Coulombic di-cationic states.....	112
4.4.3 Simulations with calculated di-cationic PEC.....	113
4.4.4 Modelling dissociative ionization .....	115
4.5 CH <sub>3</sub> <sup>+</sup> + I <sup>2+</sup> channel and enhanced ionization of the dissociating molecule .....	116
4.6 Two-photon Rydberg states excitation .....	121
4.7 Summary.....	125
Chapter 5 - Imaging UV-driven dynamics in dihalomethanes at 263 and 198 nm.....	127
5.1 CH <sub>2</sub> BrI molecule under a single NIR pulse.....	129
5.1.1 Non-coincident spectra .....	129
5.1.2 Two-body coincident analysis .....	131
5.1.3 Three-body breakup and triple-coincidence data.....	133
5.2 CH <sub>2</sub> BrI molecule under a single UV pulse.....	143
5.3 Time-resolved Coulomb explosion of UV-induced photodissociation of CH <sub>2</sub> BrI with two-body breakup coincident channels.....	145
5.4 Time-resolved analysis of UV-driven photodissociation dynamics in CH <sub>2</sub> BrI probed via three-body coincident channels .....	150

5.4.1 Overview of the delay-dependent data for $\text{CH}_2^+ + \text{Br}^+ + \text{I}^+$ coincident channel .....	151
5.4.2 Identification of different pump-induced dissociation channels.....	157
5.4.3 Analysis of $\text{CH}_2^+ + \text{Br}^{2+} + \text{I}^{2+}$ three-body coincident channel: search for transient isomerization signal .....	164
5.5 Time-resolved analysis of UV-driven photodissociation dynamics in $\text{CH}_2\text{ClI}$ probed via three-body coincident channels .....	175
5.6 Photodissociation of the $\text{CH}_2\text{BrI}$ molecule at 198 nm probed by strong-field ionization and Coulomb explosion.....	180
5.6.1 The $\text{CH}_2\text{BrI}$ molecule under single UV pulse at 198 nm.....	181
5.6.2 Pump probe results for $\text{CH}_2\text{BrI}$ at 198 nm.....	181
5.6.3 Pump probe results for $\text{CH}_2\text{I}_2$ at 198 nm.....	186
5.7 Summary.....	187
Chapter 6 - Direct imaging of the UV-driven rotational motion of the radical co-fragments in the photodissociation of dihalomethanes.....	189
6.1 Partitioning of excess energy into rotational degrees of freedom .....	189
6.2 Mapping the rotational motion of radical co-fragments .....	191
6.3 Molecular dynamics and Coulomb explosion simulations.....	205
6.4 Imaging the rotational motion in $\text{CH}_2\text{ClI}$ triggered by ultraviolet light .....	210
6.5 Summary.....	213
Chapter 7 - Pre-dissociation dynamics of $\text{CH}_3\text{I}$ in its B-band .....	215
7.1 Ionization by the 198-nm UV pulse.....	216
7.2 Ionization and fragmentation by a single NIR pulse at relatively high intensity .....	218
7.3 Time-resolved dissociation dynamics observed via two-body breakup channels .....	219
7.4 Summary.....	224
Chapter 8 - Conclusion .....	225
Bibliography .....	229
Appendix A - Native-frame analysis .....	256

## List of Figures

Figure 1.1. Schematics of a time-resolved CEI experiment .....	6
Figure 1.2. The photoabsorption spectrum of CH <sub>3</sub> I.....	7
Figure 2.1. Photodissociation of a molecule AB along the internuclear distance .....	11
Figure 2.2. Schematic representation of photodissociation of a molecule AB along the internuclear distance into dissociation products A+ B.....	15
Figure 2.3. Schematic representation of indirect photodissociation processes of a molecule AB along the internuclear distance into dissociation products A+ B.....	17
Figure 2.4. Illustration of a conical intersection between two potential energy surfaces opening up non-adiabatic processes in the excited state dynamics .....	18
Figure 2.5. Schematic representation of potential energy curves of molecule AB and AB <sup>+</sup> .....	19
Figure 2.6. Correlation diagram of CH <sub>3</sub> I n → σ* transitions in the A-band .....	21
Figure 2.7. A-band absorption cross-section and the related potential energy curves .....	23
Figure 2.8. Time-evolution of the nuclear wave packet on the PECs involved in the A-band dissociation and simulated wave packet distributions along the C-I bond distance at different times after excitation to the <sup>3</sup> Q <sub>0</sub> and the <sup>1</sup> Q <sub>1</sub> states. ....	25
Figure 2.9. A- and B-band potential energy curves of CH <sub>3</sub> I .....	27
Figure 2.10. Absorption spectrum of CH <sub>3</sub> I in the B-band absorption region with assignments to vibronic transitions .....	29
Figure 2.11. UV absorption spectra of CH <sub>2</sub> BrI, CH <sub>2</sub> ICl and CH <sub>2</sub> I <sub>2</sub> at 298 K in the gas phase from nearly 200 to 380 nm .....	31
Figure 2.12. Dihalomethanes potential energy curves.....	32
Figure 2.13. Snapshots of CH <sub>3</sub> I, CH <sub>2</sub> ICl and CH <sub>2</sub> BrI dissociation .....	34
Figure 2.14. Schematic diagrams depicting the equilibrium geometries of the ground state of iso-CH <sub>2</sub> Br-I and the ground state of iso-CH <sub>2</sub> I-Br.....	36
Figure 2.15. Computed PECs for CH <sub>2</sub> BrI as a function of the C–Br distance .....	37
Figure 2.16. Classical Coulomb explosion simulation of CH <sub>2</sub> BrI.....	39
Figure 2.17. CES for the two equilibrium and linear isomer geometries .....	42
Figure 2.18. Schematic of Newton diagram displaying the fragments' momenta and angles.....	43
Figure 2.19. Simulated momentum correlation obtained from a classical Coulomb simulation.	44

Figure 2.20. Simulated momentum energy obtained from a classical Coulomb simulation for the concerted breakup starting from equilibrium and isomer geometry in the Dalitz plot representation.....	44
Figure 3.1. A schematic view of pulse duration and intensity evolution during chirped-pulse amplification (CPA).....	47
Figure 3.2. Typical PULSAR output spectrum after the second amplification stage.....	48
Figure 3.3. Schematic layout for a FROG apparatus.....	50
Figure 3.4. Nonlinear frequency mixing with a $\chi^2$ nonlinear crystal.....	53
Figure 3.5. Time delay between the fundamental and second harmonic for a BBO crystal with 150 $\mu\text{m}$ thickness and 29.2° cut angle.....	58
Figure 3.6. Schematic setup for a collinear third harmonic generation.....	59
Figure 3.7. The typical measured SHG and THG spectra. ....	60
Figure 3.8. A typical measured spectrum of the FHG. ....	60
Figure 3.9. Photo of the fourth harmonic generation (FHG) setup.....	61
Figure 3.10. Frequency chirping in the laser pulse.....	63
Figure 3.11. A dispersion compensation device: chirped mirror.....	65
Figure 3.12. Sketch of a diffraction grating-pair compressor.....	66
Figure 3.13. Schematic of the conventional four-prism pulse-compressor.....	67
Figure 3.14. Schematic of a prism-pair compressor in a folded geometry.....	68
Figure 3.15. Cross-correlation between UV (263 nm) and NIR (790 nm) pulses.....	69
Figure 3.16. Scanning the XFROG traces by changing the separation of the two prisms.....	71
Figure 3.17. Cross-correlation between UV (263 nm) and NIR (790 nm) pulses.....	72
Figure 3.18. High-intensity laser filamentation experimental setup.....	73
Figure 3.19. Measured signal of the transmitted UV pulse as a function of the delay between the UV and NIR pulses.....	74
Figure 3.20. Schematic of the COLTRIMS apparatus with exemplary ions and electrons trajectories.....	76
Figure 3.21. Schematic of microchannel plate (MCP) and working principle of a delay-line anode (DLA).....	77
Figure 3.22. Sketch of the experimental setup for UV - NIR pump-probe experiments.....	79

Figure 3.23. Measured cross-correlation between 790-nm and 263-nm pulses from PULSAR using two-color ionization of Ar from our COLTRIMS .....	80
Figure 4.1. Ion TOF spectrum from the ionization of CH <sub>3</sub> I by a single UV pulse and 2-D TOF vs. position maps for CH <sub>x</sub> <sup>+</sup> , I <sup>+</sup> and CH <sub>3</sub> I <sup>+</sup> .....	85
Figure 4.2. Kinetic energy (KE) distribution of CH <sub>3</sub> <sup>+</sup> , I <sup>+</sup> , and CH <sub>3</sub> I <sup>+</sup> fragments after CH <sub>3</sub> I ionization by a single UV pulse .....	86
Figure 4.3. Time-of-Flight (TOF) of the generated ions upon irradiation of the CH <sub>3</sub> I molecule with the single UV pulse at 263 nm and different UV intensities and the yield of the major ionic fragments as a function of UV intensities.....	87
Figure 4.4. Time-of-flight spectrum of the generated ions upon irradiation of the CH <sub>3</sub> I molecule with the single NIR pulse and 2-D TOF vs. position maps for CH <sub>x</sub> <sup>+</sup> , I <sup>+</sup> and CH <sub>3</sub> I <sup>+</sup> .....	88
Figure 4.5. CH <sub>3</sub> <sup>+</sup> TOF distribution as a function of ion hit position on the detector after ionization of the molecule by a single NIR pulse .....	89
Figure 4.6. KE distributions of CH <sub>3</sub> <sup>+</sup> and I <sup>+</sup> .....	90
Figure 4.7. Photoion-photoion coincidence (PIPICO) spectrum for the fragmentation of CH <sub>3</sub> I molecule by a single NIR pulse .....	91
Figure 4.8. Kinetic energy distributions of CH <sub>3</sub> <sup>+</sup> and I <sup>+</sup> detected in coincidence after the single NIR pulse .....	92
Figure 4.9. Potential energy curves along the C-I bond for the di-cation CH <sub>3</sub> I <sup>2+</sup> .....	93
Figure 4.10. A-band dissociation.....	95
Figure 4.11. Excitation to higher-lying Rydberg states .....	96
Figure 4.12. Excitation schemes and relevant electronic states for UV multi-photon dissociative ionization.....	97
Figure 4.13. Delay-dependent kinetic energy distribution of CH <sub>3</sub> <sup>+</sup> and I <sup>+</sup> ions.....	98
Figure 4.14. Delay-dependent KER distribution of the two-body coincident channel CH <sub>3</sub> <sup>+</sup> + I <sup>+</sup> .....	99
Figure 4.15. Schematics of the LICI formation .....	102
Figure 4.16. Schematic of relevant energy levels for neutral and ionic states involved in one- and two-photon excitations in the Franck-Condon region and the asymptotic regime .....	104
Figure 4.17. Delay-dependent KER distribution for the CH <sub>3</sub> <sup>+</sup> + I <sup>+</sup> coincidence channel at different UV intensities.....	107

Figure 4.18. The projections of the KER distributions of Fig. 4.17 onto the KER axis for three UV-intensities .....	109
Figure 4.19. Time-dependent velocity and internuclear distance using the actual shape of the dissociative PECs of $^3Q_0$ and $^1Q_1$ states. Comparison between time-dependent velocity and internuclear distance using different dissociation velocity distributions.....	111
Figure 4.20. Comparison of CES based on different dissociation velocities for the $^3Q_0$ state with the experimental delay-dependent KER distribution for $CH_3^+ + I^+$ coincidence channel ....	112
Figure 4.21. Comparison of the experimental delay-dependent KER distribution for $CH_3^+ + I^+$ coincidence channel.....	114
Figure 4.22. Enlarged view of the experimental data at small delays compared with the simulation assuming dissociation along $^3Q_0$ and $^1Q_1$ neutral PEC probed by the transition to the lowest di-cationic PEC.....	114
Figure 4.23. The kinetic energy gained in dissociation along the neutral $^3Q_0$ state compared to the depth of the potential barrier for the lowest di-cationic state .....	115
Figure 4.24. CES of dissociative ionization channel using exponential rise dissociation velocity function and the simulated curve of I and I* channels with the actual shape of the dissociative states.....	116
Figure 4.25. Delay-dependent KER distribution of the coincident channel $CH_3^+ + I^{2+}$ .....	117
Figure 4.26. Enlarged view of the delay-dependent KER distribution for $CH_3^+ + I^{2+}$ channel.	118
Figure 4.27. Schematic illustration of the electronic potentials of a diatomic molecule for three different internuclear separations illustrating the concept of “enhanced ionization”. .....	119
Figure 4.28. Delay-dependent KER distribution for the two-body coincidence channel $CH_3^+ + I^{2+}$ at three different probe pulse intensities .....	121
Figure 4.29. Delay-dependent yields of the singly-charged parent ion for different UV intensities and schematic of one-and two-photon excitation by the pump pulse followed by the ionization with a delayed NIR pulse.....	123
Figure 5.1. TOF spectrum of the ions generated upon irradiation of $CH_2BrI$ molecule with the single NIR pulse.....	130
Figure 5.2. Kinetic energy (KE) distributions of ionic fragments of $CH_2BrI$ molecule after a single NIR pulse .....	131

Figure 5.3. PhotoIon-PhotoIon COincidence (PIPICO) map for the fragmentation of CH <sub>2</sub> BrI molecule after a single NIR pulse .....	132
Figure 5.4. KE distributions of the two-body fragmentation of CH <sub>2</sub> BrI into CH <sub>2</sub> Br <sup>+</sup> + I <sup>+</sup> and CH <sub>2</sub> I <sup>+</sup> + Br <sup>+</sup> coincident channels.....	133
Figure 5.5. TRIPICO map of the three-body breakup into CH <sub>2</sub> <sup>+</sup> + Br <sup>+</sup> + I <sup>+</sup> coincident channel after the single NIR pulse, KE distributions of the individual fragments and the total KER distributions of this three-body breakup .....	134
Figure 5.6. KER-θ <sub>23</sub> map for CH <sub>2</sub> <sup>+</sup> + Br <sup>+</sup> + I <sup>+</sup> channel .....	135
Figure 5.7. Newton diagrams for three-body fragmentation channel CH <sub>2</sub> <sup>+</sup> + Br <sup>+</sup> + I <sup>+</sup> .....	136
Figure 5.8. Dalitz plots for three-body fragmentation channel CH <sub>2</sub> <sup>+</sup> + Br <sup>+</sup> + I <sup>+</sup> .....	137
Figure 5.9. Iodine-bromine energy correlation map for three-body fragmentation channel CH <sub>2</sub> <sup>+</sup> + Br <sup>+</sup> + I <sup>+</sup> .....	138
Figure 5.10. Native-frame analysis .....	140
Figure 5.11. KER-θ <sub>23</sub> plot for the three-body fragmentation of CH <sub>2</sub> BrI into CH <sub>2</sub> <sup>+</sup> + Br <sup>2+</sup> + I <sup>2+</sup> after a single NIR pulse .....	141
Figure 5.12. Newton diagrams for the three-body fragmentation of CH <sub>2</sub> BrI into CH <sub>2</sub> <sup>+</sup> + Br <sup>2+</sup> + I <sup>2+</sup> after the single NIR pulse, Dalitz and energy-sharing plots. ....	142
Figure 5.13. Time-of-Flight of the generated ions after a single UV pulse.....	144
Figure 5.14. KE distributions of the ionic fragments of CH <sub>2</sub> BrI produced by single UV pulse	145
Figure 5.15. Delay-dependent KER distribution for the two-body CH <sub>2</sub> Br <sup>+</sup> + I <sup>+</sup> coincident channel after UV pump and NIR probe pulses.....	146
Figure 5.16. KE distribution of the two-body CH <sub>2</sub> Br <sup>+</sup> + I <sup>+</sup> coincident channel after UV pump and NIR probe pulse at 2.5 and 20 ps .....	147
Figure 5.17. KER distribution for the two-body CH <sub>2</sub> Br <sup>+</sup> + I <sup>+</sup> coincident channel after UV pump and NIR probe pulse obtained at different UV intensities .....	148
Figure 5.18. Delay-dependent KER distribution for CH <sub>2</sub> I <sup>+</sup> + Br <sup>+</sup> channel and CH <sub>2</sub> <sup>+</sup> + BrI <sup>+</sup> channel after UV pump and NIR probe pulses.....	149
Figure 5.19. Delay-dependent KER distribution for CH <sub>2</sub> BrI fragmentation into CH <sub>2</sub> <sup>+</sup> + Br <sup>+</sup> + I <sup>+</sup> after UV pump and NIR probe pulses.....	151
Figure 5.20. KER-θ <sub>23</sub> plot for CH <sub>2</sub> <sup>+</sup> + Br <sup>+</sup> + I <sup>+</sup> coincident channel .....	153

Figure 5.21. Different representations of the $\text{CH}_2^+ + \text{Br}^+ + \text{I}^+$ coincident events in regions (1) and (2) of the KER- $\theta_{23}$ plot integrated over all delays: Newton diagrams, Dalitz plots, and halogen energy correlation diagram. ....	154
Figure 5.22. KER- $\theta_{23}$ snapshots for the three-body coincident $\text{CH}_2^+ + \text{Br}^+ + \text{I}^+$ channel at different UV-NIR delays .....	155
Figure 5.23. KER- $\theta_{23}$ snapshots for the three-body coincident $\text{CH}_2^+ + \text{Br}^+ + \text{I}^+$ channel at 0 fs, 2.5 ps, 10 ps, and 20 ps .....	156
Figure 5.24. Simulated KER- $\theta_{23}$ for $\text{CH}_2^+ + \text{Br}^+ + \text{I}^+$ final state assuming different dissociation pathways: $\text{CH}_2\text{Br} + \text{I}$ , $\text{CH}_2\text{I} + \text{Br}$ , and $\text{CH}_2 + \text{BrI}$ .....	158
Figure 5.25. Different representations of the $\text{CH}_2^+ + \text{Br}^+ + \text{I}^+$ coincident events in regions (3) and (4) of the KER- $\theta_{23}$ plot at 20 ps .....	160
Figure 5.26. Simulated energy correlation map and KER- $\theta_{23}$ plot for $\text{CH}_2\text{Br} + \text{I}$ and $\text{CH}_2\text{I} + \text{Br}$ dissociating pathways probed at 20 ps delay via coincident $\text{CH}_2^+ + \text{Br}^+ + \text{I}^+$ final state....	162
Figure 5.27. Delay-integrated KER- $\theta_{23}$ plots for the $\text{CH}_2^+ + \text{Br}^+ + \text{I}^+$ coincident channel with different conditions on the sum KE of the two halogen ions.....	163
Figure 5.28. Different representations of the $\text{CH}_2^+ + \text{Br}^+ + \text{I}^+$ coincident events in the region (5) of the KER- $\theta_{23}$ plot at 20 ps .....	164
Figure 5.29. Delay-dependent KER distribution for $\text{CH}_2\text{BrI}$ fragmentation into $\text{CH}_2^+ + \text{Br}^{2+} + \text{I}^{2+}$ ions after UV pump and NIR probe pulse. ....	165
Figure 5.30. KER- $\theta_{23}$ snapshots for the $\text{CH}_2^+ + \text{Br}^{2+} + \text{I}^{2+}$ three-body coincident channel at different delays from 0 to 2.5 ps .....	166
Figure 5.31. KER- $\theta_{23}$ plot for the three-body $\text{CH}_2^+ + \text{Br}^{2+} + \text{I}^{2+}$ coincident channel at 20 ps....	168
Figure 5.32. Different representations of the $\text{CH}_2^+ + \text{Br}^{2+} + \text{I}^{2+}$ coincident events in regions (1) and (2) of the KER- $\theta_{23}$ plot at 20 ps .....	168
Figure 5.33. Different representations of the $\text{CH}_2^+ + \text{Br}^{2+} + \text{I}^{2+}$ coincident events in regions (4) and (5) of the KER- $\theta_{23}$ plot at 20 ps .....	169
Figure 5.34. Newton diagram, Dalitz plot and (Br, I) energy correlation map for the events in region (6) of the KER- $\theta_{23}$ plot at 20 ps.....	171
Figure 5.35. Delay-dependent yield of $\text{CH}_2^+ + \text{Br}^{2+} + \text{I}^{2+}$ coincident events in region (3) of the KER- $\theta_{23}$ maps .....	172

Figure 5.36. Newton diagram, Dalitz Plot, and halogen energy correlation map for $\text{CH}_2^+ + \text{Br}^{2+} + \text{I}^{2+}$ coincident events in region (3) of the KER- $\theta_{23}$ plot at 100 fs.....	172
Figure 5.37. Delay-dependent KE of the $\text{CH}_2^+$ ions from the $\text{CH}_2^+ + \text{Br}^{2+} + \text{I}^{2+}$ channel in the region (3) of the KER- $\theta_{23}$ plot .....	174
Figure 5.38. KER- $\theta_{23}$ for the three-body fragmentation of $\text{CH}_2\text{ClI}$ into $\text{CH}_2^+ + \text{Cl}^+ + \text{I}^+$ and $\text{CH}_2^+ + \text{Cl}^{2+} + \text{I}^{2+}$ after a single NIR pulse .....	176
Figure 5.39. Delay-dependent KER distribution of $\text{CH}_2\text{ClI}$ fragmentation into $\text{CH}_2^+ + \text{Cl}^+ + \text{I}^+$ after UV pump and NIR probe pulses. ....	176
Figure 5.40. KER- $\theta_{23}$ maps for the three-body coincident $\text{CH}_2^+ + \text{Cl}^+ + \text{I}^+$ channel at different delays from 0 to 2.5 ps .....	177
Figure 5.41. KER- $\theta_{23}$ snapshots for three-body coincident channels $\text{CH}_2^+ + \text{Cl}^+ + \text{I}^+$ and $\text{CH}_2^+ + \text{Cl}^{2+} + \text{I}^{2+}$ channels at 20 ps .....	178
Figure 5.42. KER- $\theta_{23}$ snapshots for the three-body coincident $\text{CH}_2^+ + \text{Cl}^{2+} + \text{I}^{2+}$ channel at different delays from 0 to 2.5 ps .....	179
Figure 5.43. Time-of-Flight (TOF) of the generated ions after a single UV pulse of $5 \times 10^{12} \text{ W/cm}^2$ intensity.....	181
Figure 5.44. Delay-dependent KER distribution for the two-body $\text{CH}_2\text{Br}^+ + \text{I}^+$ , $\text{CH}_2\text{I}^+ + \text{Br}^+$ and $\text{CH}_2^+ + \text{BrI}^+$ coincident channels.....	182
Figure 5.45. Delay-dependent KER distribution of fragmentation of $\text{CH}_2\text{BrI}$ into $\text{CH}_2^+ + \text{Br}^+ + \text{I}^+$ after UV pump at 198 nm and NIR probe pulse .....	183
Figure 5.46. KER- $\theta_{23}$ snapshots for the three-body coincident $\text{CH}_2^+ + \text{Br}^+ + \text{I}^+$ channel at 0 fs, and 2.5 ps .....	184
Figure 5.47. KER- $\theta_{23}$ snapshots for the three-body coincident $\text{CH}_2^+ + \text{Br}^+ + \text{I}^+$ and $\text{CH}_2^+ + \text{Br}^{2+} + \text{I}^{2+}$ channels at 20 ps .....	185
Figure 5.48. Delay-dependent KER distribution of fragmentation of $\text{CH}_2\text{I}_2$ into $\text{CH}_2^+ + \text{I}^+ + \text{I}^+$ after UV pump at 198 nm and NIR probe pulse .....	186
Figure 5.49. KER- $\theta_{23}$ snapshots for the three-body coincident $\text{CH}_2^+ + \text{I}^+ + \text{I}^+$ and $\text{CH}_2^+ + \text{I}^{2+} + \text{I}^{2+}$ channels at 20 ps .....	187
Figure 6.1. Mechanistic picture of $\text{CH}_2\text{BrI}$ photodissociation.....	189
Figure 6.2. Schematic diagrams of the potential energy curves and cartoon snapshots of the propagating wave packet for different dissociation pathways.....	190

Figure 6.3. Delay-dependent KE distributions of the individual fragment ions $\text{CH}_2^+$ , $\text{Br}^+$ , and $\text{I}^+$ from the $\text{CH}_2^+ + \text{Br}^+ + \text{I}^+$ coincident channel .....	192
Figure 6.4. Same delay-dependent KE distributions of the individual fragment ions with the additional requirement that the total KER of the $\text{CH}_2^+ + \text{Br}^+ + \text{I}^+$ coincident channel is below 11eV .....	193
Figure 6.5. Delay-dependent KE distributions for $\text{Br}^+$ and $\text{I}^+$ in $\text{CH}_2^+ + \text{Br}^+ + \text{I}^+$ coincident channel with the conditions $\text{KER} < 11\text{eV}$ and $\text{KE}(\text{CH}_2^+) > 4.3\text{ eV}$ .....	194
Figure 6.6. Delay-dependence of the $\text{CH}_2^+$ and $\text{Br}^+$ ion yields in the regions corresponding to the maxima of the respective oscillatory structures .....	195
Figure 6.7. Delay-dependence of the $\text{Br}^+$ ion yields .....	196
Figure 6.8. Gated $\text{Br}^+$ and $\text{I}^+$ maps .....	197
Figure 6.9. Delay-dependent kinetic energy distributions of $\text{Br}^+$ with all the events satisfying the triple gates including $\text{KER} < 11\text{eV}$ , $\text{KE}(\text{CH}_2^+) > 4.3\text{ eV}$ and $\text{KE}(\text{I}^+) < 0.2\text{ eV}$ .....	198
Figure 6.10. Delay-dependence of the $\text{I}^+$ in the energy range of 0-0.2 eV .....	199
Figure 6.11. Delay-dependent angle between the measured momentum vectors of the two ions for $\text{CH}_2\text{-I}$ , $\text{CH}_2\text{-Br}$ , and $\text{Br-I}$ .....	200
Figure 6.12. Time evolution of Newton diagrams with $\text{I}^+$ momentum vector along +X.....	201
Figure 6.13. Time evolution of Newton diagrams with $\text{CH}_2^+$ momentum vector along +X. ....	203
Figure 6.14. A set of gated Newton diagrams showing the $\text{CH}_2^+$ and $\text{Br}^+$ relative momenta with respect to the $\text{I}^+$ flying to the right .....	204
Figure 6.15. Simulated delay-dependent KER distributions of the $\text{CH}_2^+ + \text{Br}^+ + \text{I}^+$ coincident channel and the KE distributions of the individual ions .....	206
Figure 6.16. Time-dependent molecular bond angle, defined by C-I and C-Br bonds, in different carbon-halogen bond dissociation.....	207
Figure 6.17. Simulated momentum angles for the C-I and C-Br bond dissociation.....	208
Figure 6.18. Cartoon snapshots of the molecular structure generated from simulations at different delays are stacked.....	208
Figure 6.19. Comparison of the outcome of CES with experimental results .....	209
Figure 6.20. Delay-dependent kinetic energy distributions of $\text{CH}_2^+$ , $\text{Cl}^+$ , and $\text{I}^+$ in the three-body coincidence channel $\text{CH}_2^+ + \text{Cl}^+ + \text{I}^+$ .....	210

Figure 6.21. Delay-dependent kinetic energy distributions of $\text{CH}_2^+$ , $\text{Cl}^+$ , and $\text{I}^+$ in the three-body coincidence channel $\text{CH}_2^+ + \text{Cl}^+ + \text{I}^+$ with $\text{KER} < 12 \text{ eV}$ .....	211
Figure 6.22. Delay-dependent kinetic energy distributions of $\text{Br}^+$ and (b) $\text{I}^+$ in $\text{CH}_2^+ + \text{Cl}^+ + \text{I}^+$ coincident channel; all coincident events with $\text{KER} < 12 \text{ eV}$ and $\text{KE}(\text{CH}_2^+) > 4 \text{ eV}$ . .....	212
Figure 6.23. Delay dependence of $\text{CH}_2^+$ and $\text{Cl}^+$ ion yields and an FFT of modulating yields. ....	213
Figure 7.1. Time-of-Flight (TOF) spectrum of the ions generated upon irradiation of the $\text{CH}_3\text{I}$ molecule with a single UV pulse at 198 nm .....	216
Figure 7.2. Time-of-flight (TOF) spectrum of the ions generated upon irradiation of the $\text{CH}_3\text{I}$ molecule with a single NIR pulse and TOF-position maps of selected ions .....	217
Figure 7.3. PIPICO map for fragmentation of $\text{CH}_3\text{I}$ after a single NIR pulse.....	218
Figure 7.4. Delay-dependent KER distribution of the two-body coincident channel $\text{CH}_3^+ + \text{I}^+$ after UV and NIR pulses .....	220
Figure 7.5. KE distribution of the two-body $\text{CH}_3^+ + \text{I}^+$ coincident channel after UV pump and NIR probe pulse at 2.4 and 20 ps.....	220
Figure 7.6. Delay-dependent KE distribution of the $\text{I}^+$ originating from $\text{CH}_3^+ + \text{I}^+$ after UV and NIR pulses.....	221
Figure 7.7. Delay-dependent KE distribution of the $\text{I}^+$ originating from $\text{CH}_3^+ + \text{I}^+$ after UV and NIR pulses in different KE ranges .....	222
Figure 7.8. Projection of the bound and dissociating in the delay-dependent KE distribution of the $\text{I}^+$ originating from $\text{CH}_3^+ + \text{I}^+$ after UV and NIR pulses .....	223
Figure A.1. Schematic definition of the Jacobi coordinates, the two-step sequential fragmentation through $\text{CH}_2\text{Br}^{2+}$ and the definition of the $\theta_{\text{CH}_2\text{Br}, \text{I}}$ angle. ....	257
Figure A.2. Yield of the $\text{CH}_2^+ + \text{Br}^+ + \text{I}^+$ coincidence channel as a function of the $\text{KER}_{\text{CH}_2\text{Br}}$ and $\theta_{\text{CH}_2\text{Br}, \text{I}}$ , and different representation of the corresponding events.....	258

## List of Tables

Table 4-1. Parameters extracted from fitting the time-dependent parent ion signal of Fig. 4.30 as a function of UV-intensity .....	124
--	-----

## Acknowledgments

*“Thankfulness brings you to the place where the beloved lives. ~ Rumi*

I owe a debt of gratitude to many people for helping me reach this stage. First and foremost, I would like to thank my dissertation advisors, Artem Rudenko and Daniel Rolles. I have been fortunate to have them as my academic advisors and work in their joint groups in the past few years. I am grateful for the many things they taught me. They showed me what it means to be dedicated, each in their own unique way. Artem and Daniel, each of you have given of your time, energy and expertise and were very patient with me, for which I am eternally grateful. What I have learned from your approach to problem-solving and scientific reasoning is one of the most valuable skills I learned during graduate school. You taught me to be critical and, at the same time, optimistic with the experimental findings and become more efficient in presenting them to others.

I want to thank Artem Rudenko, Daniel Rolles, Christine Aikens, Loren Greenman, and Vinod Kumarrappan for serving on my committee and devoting their precious time to help in maintaining the quality and rigor of my work. Their critical insights on my projects which they transferred to me through comments, suggestions and questions, were a significant source of help.

Artem and Daniel's prolific joint groups have also given me inspiration and motivation, and the chance to work with many bright students and postdocs who have made the long hours in the lab so much more enjoyable, and I feel incredibly fortunate to have worked with them. A substantial piece of my gratitude is for Kurtis Borne, with whom I spent most of my lab time. Kurtis, your dedication and willingness to work in the lab was always a source of inspiration. Thanks for always being there for me. I also appreciate working with wonderfully knowledgeable post-docs such as Kanaka Raju Pandiri, Surjendu Bhattacharyya and Enliang Wang. They made significant contributions to the work in this dissertation, and I was always inspired by how they loved their work in the lab. I am also grateful to other group members; Seyyed Javad Robotjazi, Xiang Li, Shashank Pathak, Anbu Venkatachalam, Keyu Chen, Nathan Marshalls, Balram Kaderiya, and Yubaraj Malakar, for their help, friendship and companionship inside and outside of the lab.

I would also like to thank Itzik Ben-Itzhak's group members, Travis Severt, Bethany Jochim and Peyman Feizollah, for fruitful collaborations on COLTRIMS experiments. Help and

support from Huynh Lam and Tomthin Nganba Wangjam from Vinod Kumarappan's group is also appreciated.

I was fortunate to have been a part of the Macdonald Lab, and I am grateful to all of the people who made working there so great. I would like to sincerely thank the former and current lab directors, Itzik Ben-Itzhak and Brett Esry, for the high standard working policies and providing guidance and support over the last few years. I want to thank all AMO faculty members for their knowledge, inspiration and encouragement. Brett, I greatly appreciate your compassionate effort to teach us quantum mechanics and AMO physics. However, that is not the only reason for my heartfelt thanks to you. I am eternally grateful for your guidance and your belief in me. I always felt comfortable coming to your office with my questions, knowing that your office door is always open to students desperately looking for advice. Itzik, thanks for your critical insights on various projects and for helping me in one form and another over the last few years. Vinod, thanks for enthusiastically answering the questions we dealt with multiple times and being a very knowledgeable point of reference. Kevin, I am beyond grateful for your countless hours of educating us and troubleshooting the data acquisition system. You always made my life easier by patiently helping with SpecTcl, especially for our frequent needs on Friday afternoons.

The outstanding support staff facilitates the quality research done at the J.R. Macdonald Laboratory, and I am grateful to several members for their time and dedication to helping make my projects possible. Thanks to Charles Fehrenbach for his assistance with the laser, Chris Aikens, Justin Millette, and Al Rankin for helping me solve technical problems and Scott Chainey for his help with all electronics issues. Thanks to Vince Needham and PCSC crews for helping with computers and software.

During my Ph.D., I had a support person from thousands of miles away, Ruaridh Forbes, who always helped me with his comments and suggestions. In addition, I would like to thank Aleksy Aleyev, Luis Banares and Maria Corrales for sharing the calculated potential energy curves of  $\text{CH}_3\text{I}$  that I need for my simulations.

During my time at KSU, I have made many friendships that made my life more enjoyable. I want to thank them for helping us make unforgettable memories and having wonderful times together. There are too many names, but I want to remember a friend with a beautiful heart who is no longer with us in this world. Sahar jan, we all have missed you so much.

Last but absolutely not least, I would like to offer my sincerest thanks to the lovely ones in my life. My parents have worked so hard for my well-being and comfort so that I would experience less of the hardships they endured in their lives. Daddy and mommy, Look! Here is my name on this thesis. I made it as you wished for me. It was not easy to be 7000 miles away from home, but it was worth it! I would also like to thank my husband, Jalal. He is the kindest, most loving, and most caring partner one could ever wish for. He has been on this journey with me through my successes and failures. I have been extremely fortunate to have him by my side to believe in me, give me the courage to do the right thing, and truly empower me to succeed. His encouragement and vision have been great companions in my Ph.D. I truly love him and thank him very much for loving me with all of my flaws and weaknesses. Jalal, I will never forget all those midnights you were patiently waiting for me in JRML hall, all those moments that I was finding you fall asleep but smiling, and then forgetting the challenges I had in the lab, we were heading to our lovely tiny house. I am excited for what is to come with our next careers.

## **Dedication**

To my parents and the best friend ever, Jalal!

## Chapter 1 - Introduction

Making “molecular movies” or, in other words, imaging the nuclear motion during a molecular transformation with atomic-scale spatial and temporal resolution has been a prolonged ambition in molecular dynamic studies [1]–[7]. Nowadays, molecular dynamics is a flourishing field of research that often focuses on processes triggered by photon–molecule interaction. Such light-induced molecular dynamics are of great interest for different sub-fields of physics, chemistry, and biology and underpin our understanding of many fundamental processes in nature. For instance, they are of critical importance to a broad range of photobiological processes in our daily lives, such as photosynthesis [8], [9], DNA photo-protection [10], DNA mutation and damage under ultraviolet (UV) radiation [11]–[13], isomerization reaction in the retina of the human eye [14]–[18] and formation of vitamin D [19].

The development of X-ray crystallography resulted in a breakthrough in determining the three-dimensional (3D) structure of macromolecules, acknowledged by the Nobel Prize in Chemistry awarded to John Kendrew and Max Perutz [20]. Since then, there has been an ongoing effort to go beyond static structure determination and combine it with advanced tools for studying dynamics. These efforts link back to the critical lesson of the historic “Horse in Motion” study by Eadweard Muybridge [21]. This first example of “chronophotography” proved the contested hypothesis that there are moments during a horse’s stride when all four hooves are off the ground. This earliest example of a successful time-resolved experiment demonstrated the importance of a direct observation of the object in motion, which can yield information not accessible by static measurement. Such dynamical, time-resolved studies are needed to comprehend the behavior of ever-changing molecular systems. In other words, even the atomic-scale resolution of the static molecular structure is often not enough to understand how the system “functions” or how a chemical reaction proceeds. Thus, understanding the underlying dynamics is essential. In a broader sense, molecular dynamics studies add the intermediate state to the “before-and-after” view of chemical reactions and identify different quantum paths during the interactions. In contrast to static measurements, they also often deal with far-off-equilibrium molecular configurations.

The photoexcited molecule could be a starting point for a variety of chemical reactions, such as dissociation (involving the cleavage of one or more molecular bonds) [22]–[27], bond rearrangement, different types of isomerization processes [28]–[34], etc. Following the absorption

of one or several photons, a molecule can undergo rather complex structural transformations, often accompanied by a complicated electronic and nuclear energy redistribution. Many of the most interesting (and also hardest to study) photo-induced dynamics occur when different potential energy surfaces (PES) of the molecule cross each other. Such regions of the potential energy landscape are frequently referred to as conical intersections [35]. These crossings enable population exchange between multiple states on femtosecond time scales [36], and the molecule can undergo various non-radiative relaxation processes such as intramolecular vibrational redistribution, where the energy is redistributed between different vibrational states [37]–[39], internal conversion [40]–[43], or intersystem crossing [44]–[46] when the transition happens between the electronic states of the same and different spin multiplicities, respectively. In the vicinity of conical intersections, the strong coupling of the electronic and nuclear degrees of freedom breaks down the Born-Oppenheimer approximation, making dealing with these nonadiabatic processes experimentally and theoretically challenging. In particular, complex molecular vibrational dynamics often limit spectroscopic methods: because of the large density of vibrational states, the nonadiabatic coupling results in broadened spectral features in the energy/frequency domain. This limitation highlights the importance of complementary time-dependent methods with adequate temporal resolution.

Over the last few decades, time-resolved measurements enabled by advances in ultrafast laser technology have offered an opportunity to observe a molecular system in the continuous process of its evolution from reactants to products and paved the way towards following certain dynamical processes in real-time [47]–[49]. The development of femtosecond laser systems and the progress in time-resolved techniques laid the first stone of the field of femtochemistry, which resulted in a Nobel Prize in chemistry for its pioneer, Ahmed Zewail, in 1999 [5], [6]. Subsequent progress in developing ultrashort pulses in a broad range of wavelengths, from infrared to vacuum ultraviolet (VUV) and X-ray regions of the spectrum, brought tremendous advances in time-resolved molecular dynamics. Combined with theoretical analysis, these experiments provided detailed information about various photo-induced dynamics in molecular systems.

Practically, time-resolved measurements are usually performed within pump-probe configurations, where processes of interest are triggered by a first “pump” pulse, followed by a second, time-delayed “probe” pulse that monitors the ensuing dynamics. The achievable temporal

resolution is then limited by the duration of both pulses and the temporal jitter (delay) between them.

Initially, pump-probe measurements were developed for optical pump and optical probe pulses. Here, typical probe schemes include, among others, fluorescence and absorption measurements, as well as a variety of ionization-based methods, like time-resolved photoelectron spectroscopy or ion mass-spectrometry. Subsequently, the pump-probe technique was generalized by replacing the optical probe pulse with different probing schemes. Prominent examples here are transient absorption with femtosecond or attosecond XUV pulses produced by high harmonics generation (HHG) [50]–[52], ultrafast electron diffraction (UED) driven by the development of the relativistic electrons pulses [53], [54], [63], [64], [55]–[62] and ultrafast x-ray diffraction (UXRD) at x-ray free-electron laser (FEL) [65]–[73]. The ultrashort laser, electron- or X-ray pulse duration allows one to accurately define the initiation time and track the temporal changes to build a dynamical picture of photo-induced reactions.

The selection of a particular probing scheme largely depends on the specific goals of a pump-probe experiment since each method has its strengths and weaknesses. For example, in a pump-probe configuration, spectroscopic methods like absorption, fluorescence, or photoelectron spectroscopy, which, in combination with theory, provide a lot of structural information from static measurements, are typically used to characterize the evolution of the electronic structure. Ion mass spectrometry can be sensitive to electronic and nuclear components but yield only indirect information. In contrast, diffraction-based techniques provide direct information on the (evolving) molecular geometry but are less sensitive to its electronic structure. In addition, since the diffraction signal depends on the atomic mass, diffraction experiments have different sensitivity for light and heavy atoms. While UXRD can provide superior temporal resolution, limited only by the duration of XFEL pulses, its main limitation stems from relatively small X-ray scattering cross-sections, which makes experiments on gas-phase small molecules consisting of light atoms rather challenging. UED approach benefits from much larger electron scattering cross sections but currently cannot access time scales shorter than  $\sim 100$  fs for pulses charges compatible with gas-phase experiments. Therefore, despite tremendous advances in UED, UXRD and time-resolved techniques employing spectroscopic probes, there is still serious motivation to develop further experimental schemes to address some of the above-mentioned limitations. For example, there is an ongoing effort to combine the advantages of UED and UXRD approaches by illuminating the

molecule “from within,” exploiting its own photoelectrons, either in laser-induced electron diffraction [74]–[80] or inner-shell electron diffraction [81], [82] experiments.

The main focus of this thesis is the development of an alternative technique for mapping nuclear motion in molecular reactions based on the so-called Coulomb explosion imaging (CEI) concept [83], [84]. This imaging technique produces a highly charged unstable molecular ion by rapidly removing multiple electrons from a stable neutral or ionic species. The repulsive forces between multiple charges then result in the molecule’s Coulomb explosion (CE). CEI is a powerful and conceptually simple tool, which is sensitive to the original molecular geometry, especially in the idealized limit where the ionization process is fast compared to the time scale of molecular dynamics of interest, and the molecule is ionized high enough such that the final-state PESs can be considered to be purely Coulombic. In that case, this technique provides information about the molecular structure without prior knowledge about the molecule itself. For example, in diatomic molecules, for which the so-called “axial recoil approximation” [85] is valid, the molecule’s bond length and its orientation in space are imprinted in the kinetic energies and emission angles of the generated ions, respectively. A conceptually similar approach can be applied to larger and more complicated molecules that have an abundance of different forms of vibration motions [86], [87].

Methods for inducing multiple ionization processes include collisions of accelerated molecular ions with several MeV energy with a thin foil [88], collisions with highly-charged ion beams [89] or using the intense electric field of a femtosecond laser (or XFEL) pulse to ionize the molecule [90–104]. The most important advantage of laser-based CEI is its compatibility with pump-probe experiments. Thus, time-resolved imaging of dynamical processes with CEI is achieved by combining a pump pulse initiating the reaction of interest with ultrafast and intense probe pulse that induces rapid ionization and Coulomb explosion of the molecule into its constituent fragments. The information on the instantaneous molecular structure is then obtained by detecting some or all of the ejected ionic fragments. The most elaborate version of this technique involves measuring the 3D momentum vectors of these ions in coincidence, revealing the correlated momenta of the reaction products. In general, even such coincident CEI data do not allow one to resolve the so-called “inverse problem”, i.e., to uniquely retrieve the molecular geometry from the experimental results, although some progress towards this ambitious goal has been reported recently [105]. However, these data provide an extensive set of stringent constraints for possible molecular configurations at each pump-probe delay, which—in many cases—is

sufficient to adequately characterize a time-dependent dynamical process and to distinguish between different reaction pathways [106]–[108].

Although CEI has been mainly used for small molecules so far, it can also be extended towards larger polyatomic systems. It was recently demonstrated [109] that CEI can visualize the position of each atom in a ring molecule with 10-12 atoms if a high level of ionization and complete fragmentation of the molecule can be achieved. There, it was shown that it is enough to detect only three or four ionic fragments in coincidence under such conditions, which is critical since a larger number of coincident fragments significantly increases the required acquisition times of the measurement since the ion detection efficiency is typically well below unity. For lower levels of ionization, the interpretation of the CEI data for polyatomic molecules can be less straightforward since molecular PECs for lower charge states can be non-Coulombic, and since the fragmentation processes become more complicated due to channels involving stepwise fragmentation [110]–[112].

Because of its inferior spatial resolution, CEI cannot compete with electron or x-ray diffraction as a static structure determination technique. However, for time-resolved experiments, where the spatial resolution of diffraction-based techniques is often limited by the properties of the short electron or x-ray pulses which significantly reduce the signal-to-noise ratio compared to the static measurements, the situation is often different. Moreover, there are a few decisive advantages of the CEI approach. First, its sensitivity for light and heavy elements remains the same. Second, CEI in its coincidence mode is by definition a “molecular frame” technique, where the spatial orientation of each molecule is, within the limits of the axial recoil approximation, retrieved from the experimental data. This allows one to avoid averaging over different spatial orientations of the molecules, which is crucial for many photo-induced processes, without using laser-alignment techniques. Finally, due to the availability of the complete final-state momentum correlation pattern of the fragments for each individual molecule, CEI is very efficient in separating contributions from different molecular configurations. This is crucial for situations where initial photoexcitation triggers several reaction pathways and enables detailed investigations of minor reaction channels that are difficult to access with other time-resolved techniques.

Prominent recent examples of using CEI to study time-resolved dynamics include tracking photodissociation [94], [100]–[103], and photoisomerization [29], [104], [108], [113], [114] dynamics or imaging of rotational [115] and vibrational [116], [117] molecular wave packets. A

basic concept of the laser pump-probe experiment employing CEI as a probe is illustrated in Fig. 1.1. The pump pulse initiates the process of interest, such as photodissociation, launching a bound or dissociating wave packet in the excited state, as shown schematically in Fig. 1.1 (a). While the wave packet propagates and evolves on the potential energy curve, the probe pulse arrives at a certain delay with respect to the pump pulse, interacts with the excited system, and projects the wave packet on excited multiply charged state, producing a set of delay-dependent observables that can be calculated from the measured 3D momentum vectors of the detected ions. Since the wave packet generated by the pump pulse is located in different spatial regions at different times, the signal generally depends on the delay time.

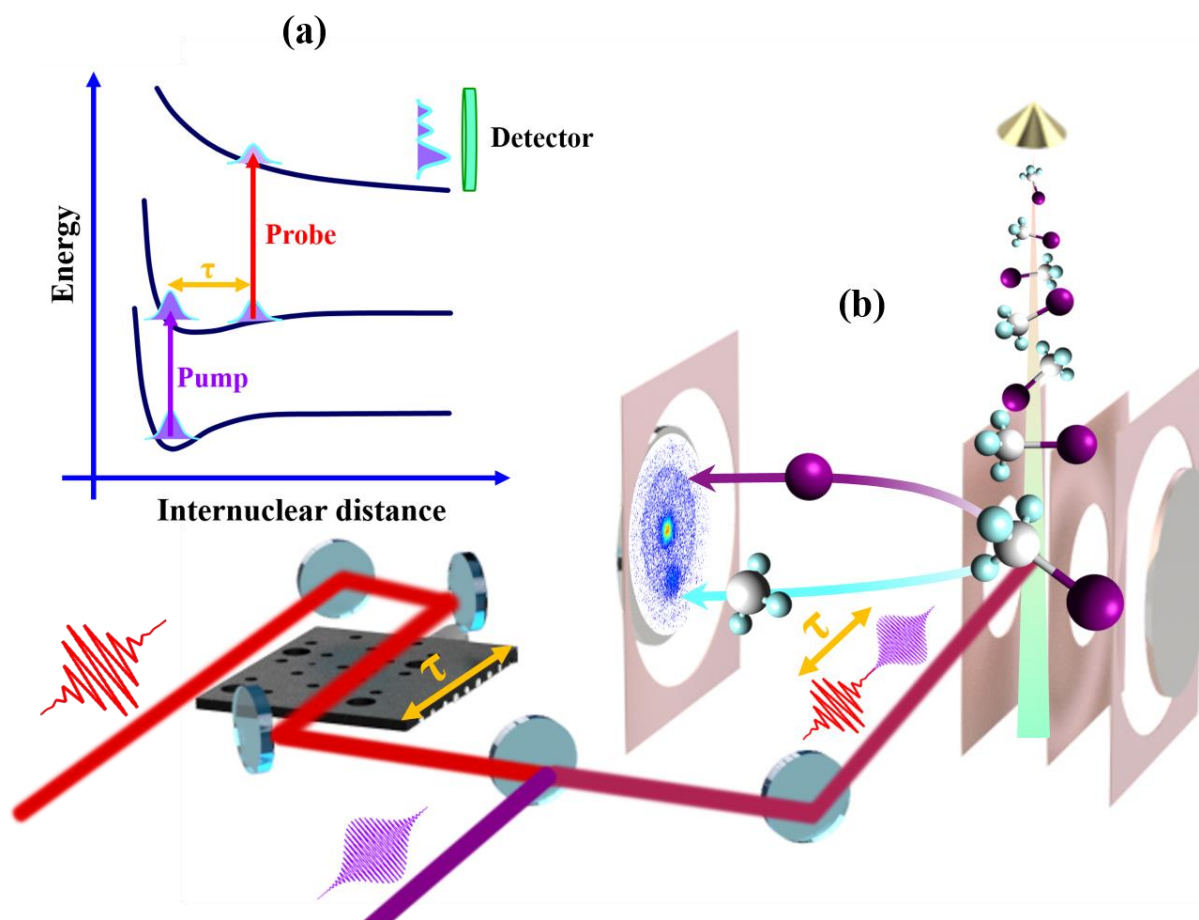


**Figure 1.1.** Schematics of a time-resolved CEI experiment. **(a)** The pump pulse launches a wave packet on an excited state; the delayed probe pulse ionizes the molecule. **(b)** A sketch of the corresponding experimental setup. The colinear pulses are focused into the reaction chamber, where the laser pulses intersect a molecular beam, and the resulting ions hit the detector. The momenta of generated ions are measured as a function of pump-probe delay,  $\tau$ .

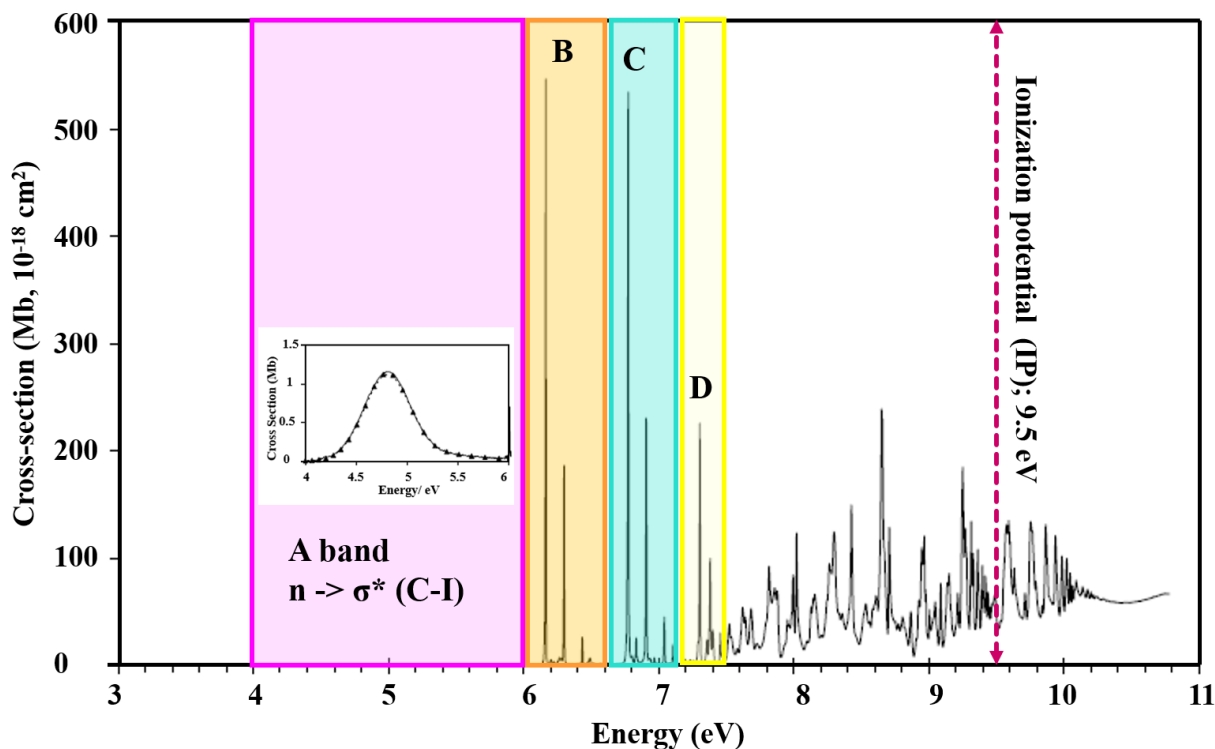


**Figure 1.2.** The photoabsorption spectrum of CH<sub>3</sub>I. It includes a broad featureless absorption continuum between 4 to 6 eV known as A-band and followed by excitation into Rydberg states at higher energies showing vibrational structure known as B, C and D bands at different peak energies. The position of the ionization potential (IP) at 9.5 eV has been indicated by a dashed vertical arrow. The figure is adapted from Ref. [118].

The work presented in this thesis primarily focuses on applying the time-resolved CEI technique to study UV-induced photodissociation dynamics of halomethanes in the gas phase. Halomethanes are often considered as prototypical systems for molecular photodissociation in the UV domain. Due to the complicated excited-state structure driving the photochemistry of these molecules, they exhibit rich dynamics while being small enough to still allow for a detailed theoretical treatment. The specific goal of this work is to disentangle the photo-induced reaction channels, including direct and indirect dissociation pathways, and to visualize the motion of the individual molecular fragments in each of these channels. The photofragmentation reactions considered here include two- and three-body dissociation, transient isomerization, and molecular halogen formation. The experiments are carried out at two different excitation wavelengths, 263

nm and 198 nm, enabling varying the dominant reaction pathways to investigate the wavelength dependence of photochemical dynamics triggered by single-photon absorption in the ultraviolet range.

The ultraviolet absorption spectrum of molecules belonging to the halomethane family lies between approximately 170 and 350 nm [118]. For example, Fig. 1.2 shows the absorption spectrum of CH<sub>3</sub>I, which exhibits multiple distinct absorption bands assigned to different transitions from the ground to the excited states through promotion into different molecular orbitals. The assignments are based on high-level *ab initio* calculations [119]–[121]. These transitions predominantly reflect the single excitation from the HOMO orbitals corresponding to the lone pairs on the halogen atoms into the carbon-halogen molecular orbitals. Therefore, excitation at different UV wavelengths generally results in different molecular dynamics. We employ multiple ionization by intense 790 nm NIR pulses and the CEI technique as a probe for all processes studied here. The experiments were performed using a 10 kHz Ti: sapphire laser system, known as PULSAR, at the James R. Macdonald Laboratory (JRML) at Kansas State University and its 3<sup>rd</sup> and 4th harmonics.

The dissertation is organized as follows:

Chapter 2 begins with an introduction and the conceptual prerequisite to understanding the basic principles of the UV-induced excited states molecular dynamics in halomethanes. This chapter includes a brief literature review and specific discussion on CH<sub>3</sub>I and the two dihalomethanes, CH<sub>2</sub>BrI and CH<sub>2</sub>ClI. Chapter 3 presents an overview of the experimental tools used in these experiments, including a short description of the laser system used to generate femtosecond NIR pulses and the nonlinear processes involved in generating the third and fourth harmonics of the fundamental NIR pulse. The details of the home-built prism compressor and the characterization of the pulses are also described in this chapter. The experimental results and discussions are presented in the following four chapters.

Chapter 4 describes experiments on time-resolved photodissociation dynamics of iodomethane (CH<sub>3</sub>I) in its A-band, focusing on the characterization of direct dissociation dynamics by Coulomb explosion imaging (CEI) and on disentangling the competing reaction pathways involving single- and multi-photon excitations. We investigated the dynamics triggered by a single-photon absorption and two-photon excitation to Rydberg states and three-photon dissociative ionization.

Chapter 5 describes time-resolved studies of bromiodomethane ( $\text{CH}_2\text{BrI}$ ) and chloriodomethane ( $\text{CH}_2\text{ICl}$ ) photofragmentation at 263 and 198 nm, aiming to identify and disentangle individual photodissociation pathways and track them in time and the effects of halogen-atom substitution on the molecular dynamics. We identified two-body dissociation pathways with different branching ratios of the carbon-halogen bond and molecular halogen formation at these two wavelengths. Our experimental results suggest that upon 263 nm photoexcitation, some of the photodissociation trajectories involve a formation of a transient linearized configuration of the molecule that quickly forms and decays within less than 200 fs after the initial photoabsorption. In addition, we disentangled and identified three-body dissociation pathways resulting from two-photon absorption.

Chapter 6 focuses on one of the specific channels discussed in Chapter 5, the two-body dissociation triggered by the 263 nm pump. Here, we directly map the rotational motion of the radical co-fragments in UV-excited dihalomethanes during the dissociation process, which is a direct consequence of the energy storage in the internal degrees of freedom. The rotational motion shows up as oscillatory structures in the delay-dependent observables, e.g., kinetic energies and the relative momentum angles of the detected ions. Chapter 7 presents preliminary results on pre-dissociation dynamics of  $\text{CH}_3\text{I}$  at 198 nm excitation. This dissociation is known to occur via the surface crossing of the low-lying Rydberg excited states (dubbed the B-band) with some of the components of the dissociative A-band manifold. Although further data analysis and modeling are still required to fully interpret the observed experimental results in this section, they clearly show the signatures of pre-dissociation dynamics, very different from direct dissociation discussed in previous chapters. In addition, the data exhibit a pronounced oscillatory structure, which exists only within the pre-dissociation lifetime. The exact origin of this structure remains unclear and will be a subject of further work.

Finally, conclusions and outlook are presented in Chapter 8.

## Chapter 2 - Introduction to the UV-driven photochemistry of halomethanes

The interaction of electromagnetic radiation with matter is the subject of spectroscopy. As a result of the interaction of the oscillating electromagnetic field with the charged particles of matter, different light-induced processes such as absorption, emission, and ionization are observed. Depending on the radiation wavelength, these processes result in electronic, vibrational, and rotational transitions for molecules. Quantum mechanically, spectroscopy is treated as an induced perturbation by the light that couples the charged particles' quantum states. In other words, the interaction of the field with the charged particle causes a time-dependent perturbation resulting in a transition between the quantum states of the system.

The transition probability can be calculated by solving the time-dependent Schrödinger equation. For convenience, this interaction is often treated semi-classically, which describes the matter quantum mechanically, and the light is described classically. The transitions are governed by the so-called electric dipole approximation ( $e^{i\vec{k}\cdot\vec{r}} \rightarrow 1$ ) which simplifies the computation of the matrix elements based on the resulting selection rules [122]. First-order time-dependent perturbation theory can be used to calculate the probability of an electric dipole transition. When there is a resonance between the radiation and the quantum states and the selection rules are fulfilled, the transition probability is maximum. In numerous cases, this approach is good enough to predict the behavior of molecules in light-matter interactions, and the obtained results match those of a complete quantum mechanics approach.

The work presented in this thesis deals with a specific instance of the light-matter interaction: the photodissociation of halomethane molecules upon UV photon absorption. The ultimate purpose of this chapter is to outline the basics needed for understanding the dynamics of the UV-photodissociated halomethanes in the gas phase.

### 2.1 Photodissociation

Conceptually, photodissociation is a process of molecular bond cleavage upon absorption of one or multiple photons and a transition to excited electronic states. This transition is possible if the energy obtained from the photon absorption provides enough energy to overcome the binding energy of the chemical bond. The required energy to cleave the bond is known as the dissociation

energy and denoted as  $D_0$  or  $D_e$  when accounted with reference to the lowest vibrational state or the equilibrium potential depth. Any photon with sufficient energy can, in principle, cause photodissociation, and electromagnetic radiation ranging from visible light to more energetic photons like UV light can dissociate the molecule. In general, photodissociation depends on molecular geometry and hence on the shape of molecular PES. The photodissociation typically happens along a particular internuclear axis; the reaction coordinate along which the bond is cleaved. Hence, even for polyatomic systems, molecular dissociation can sometimes be represented in terms of 1-D potential energy curves (PEC), for which the potential energy depends only on the internuclear distance between the two fragments and the other degrees of freedom are treated as being frozen. A brief overview of general molecular photodissociation mechanisms is presented in this section, primarily based on the material presented in [123]–[128].

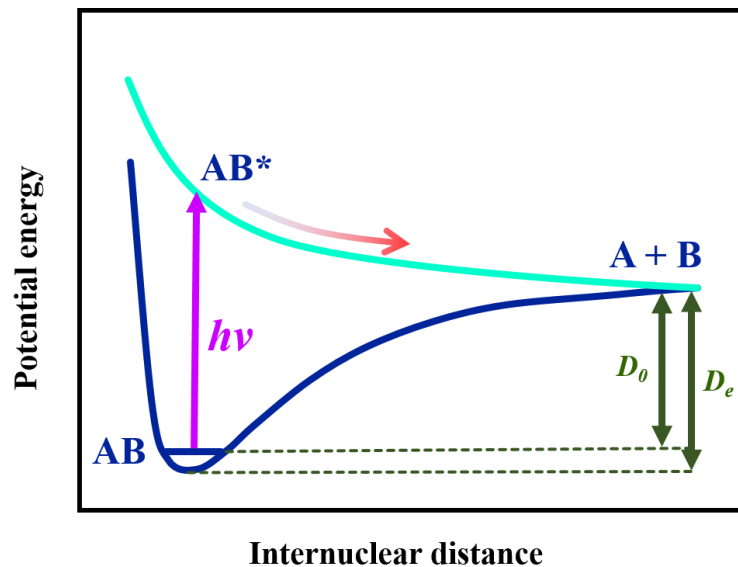
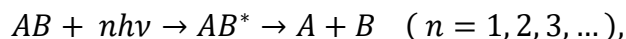


**Figure 2.1.** Photodissociation of a molecule AB along the internuclear distance. Photoexcitation of the molecule in its ground state results in a transition to a repulsive excited state  $AB^*$  followed by an increase in the bond distance until the photodissociation finally occurs, leading to two neutral fragments A and B. The dissociation energy of the molecular bond is denoted as  $D_0$  or  $D_e$  relative to the ground vibrational state and the potential depth at the equilibrium distance.

Fig. 2.1 shows exemplary PECs for the molecule AB. When the molecule in its ground state absorbs one or more photons with photon energy  $h\nu$  and undergoes a transition to an excited state ( $AB^*$ ), which is repulsive for the internuclear distance and related to an antibonding

molecular orbital, this results in the two-body dissociation of the molecule into the neutral fragments A and B:



where  $n$  is the number of photons of frequency  $\nu$ . The photon(s) provide the energy to overcome the dissociation barrier, and the excess energy ( $E_{\text{excess}}$ ) partitions into translational ( $E_{\text{trns}}$ ) and internal ( $E_{\text{int}}$ ) energy, which can be shared between electronic, vibrational and rotational degrees of freedom. According to energy conservation, we have

$$\begin{aligned} nh\nu &= D_0 + E_{\text{excess}}, \\ &= D_0 + E_{\text{int}} + E_{\text{trans}}, \end{aligned} \tag{2.1}$$

where  $D_0$  is the dissociation energy.

Studies of photodissociation dynamics provide valuable information on the bond cleavage processes, including the lifetime of the dissociation and the energy redistribution among different degrees of freedom. On the other hand, depending on the specific goal of the investigation, to appropriately characterize the process, one might rely on some pre-acquired knowledge such as the dissociation energy, symmetry of the states involved, absorption cross-section for different excited states, the quantum yield of each dissociation channel, etc.

Assuming an internally cold molecular target and evaluating the dissociation in the coordinate system with the origin placed at the center of mass of the parent molecule, we can simplify this expression like the following:

$$\begin{aligned} E_{\text{excess}} &= nh\nu - D_0, \\ E_{\text{excess}} &= E_{\text{int}}(A) + E_{\text{int}}(B) + E_{\text{trans}}(A) + E_{\text{trans}}(B), \end{aligned} \tag{2.2}$$

where the translational energy of each photofragment with the mass  $m$  and the velocity  $V$  is defined as:

$$E_{\text{trans}} = \frac{1}{2}mV^2. \tag{2.3}$$

The conservation of the energy and momentum for the fragments flying back-to-back along the dissociation bond axis is given as:

$$\frac{1}{2}m_A V_A^2 + \frac{1}{2}m_B V_B^2 = KER, \tag{2.4}$$

$$mV_A + mV_B = 0, \tag{2.5}$$

where KER stands for kinetic energy release. This gives the translational kinetic energy of each fragment:

$$KE_A = \frac{m_B}{m_A + m_B} KER, \quad 2.6$$

$$KE_B = \frac{m_A}{m_A + m_B} KER. \quad 2.7$$

In addition, if the molecule dissociates through multiple dissociation channels, the quantum yield of each channel is defined as the relative ratio of the yield of that channel to the total yield of the photodissociation process. For two excited states with yields a and b:

$$\Phi = \frac{[a]}{[a] + [b]}, \quad 2.8$$

$$\Phi^* = \frac{[b]}{[a] + [b]},$$

where  $\Phi$  and  $\Phi^*$  are the quantum yields of the two photoproducts.

Another observable which gives us precious information about the photodissociation dynamics is the angular distribution of the photoproducts. In the case of linearly polarized light, the transition preferentially happens when the transition dipole moment  $\vec{\mu}$  is parallel to the polarization direction. As mentioned earlier in this chapter, the transition probability depends on the selection rules and the symmetry of the states. When the dipole moment is parallel to the molecular axis, the transition is called parallel. On the other hand, when the transition dipole moment is perpendicular to the molecular axis, the transition is perpendicular. In the case of a prompt photodissociation (more specifically, within the limits of the axial recoil approximation), the angular distribution of the fragments resulting from either parallel or perpendicular transitions would be anisotropic.

For a one-photon dissociation, the angular distribution  $I(\theta)$  is given by [\[129\]](#)

$$I(\theta) = \frac{\sigma}{4\pi} (1 + \beta_2 P_2(\cos(\theta))), \quad 2.9$$

where  $\theta$  is the angle between the polarization direction and the molecular axis (technically equivalent to the photoproducts velocity direction),  $\sigma$  is the total absorption cross-section,  $\beta$  is the anisotropy parameter,  $P_2(\cos(\theta))$  is the second-order Legendre polynomial, and  $4\pi$  is accounting for the normalization factor for a full solid angle. When the molecule breaks into two pieces, the anisotropy parameter for pure parallel and perpendicular transitions is equal to  $\beta_2 = 2$  and  $\beta_2 = -1$ , respectively. This parameter can generally lie between these two limits and can be written as a

linear combination that determines the percentage of the parallel or perpendicular character of the transition. For an isotropic distribution,  $\beta_2=0$ . Thus, the angular distribution reflects the electronic transition and the symmetries of the excited states.

The situation could be different for the dissociation mechanisms with a long time scale. For instance, when the dissociation occurs on a time scale that is of the same order as the rotational period of the molecule, the alignment with respect to the molecular axis would be lost during the time, resulting in a more isotropic angular distribution, and the rotation plays a key role.

### 2.1.1 Transition probability and Franck-Condon principle

The interaction of atoms and molecules with electromagnetic waves induces an oscillating electric and magnetic moment. For an electron transition between two involved states in photodissociation, the frequency of the induced moment must be the same as the energy difference between the states; in other words, the photons must be resonantly absorbed. The amplitude of this moment is called transition moment and is defined as the transition probability from one state with an eigenstate  $\psi_1$  to the other state with  $\psi_2$ .

$$M_{21} = \int \psi_2 \mu \psi_1 d\tau, \quad 2.10$$

where  $\mu$  is the transition dipole moment operator. Based on the BO approximation, the electronic wavefunction can be separated into electronic  $\psi_e(R)$ , vibrational  $\psi_v(R)$  and rotational  $\psi_r(R)$  parts:

$$\psi(r, R) = \psi_e(r, R_e) \psi_v(R) \psi_r(R). \quad 2.11$$

In this approximation, the electronic wavefunction is approximated at the equilibrium distance, and since the electrons are significantly lighter than the nuclei, the rotational and vibrational wavefunctions are defined by the nuclear geometry. Neglecting the rotational wavefunction and exploiting the fact that the electronic wavefunctions are orthogonal, the transition dipole moment can be simplified as [130]

$$\int \psi_e'(r, R_e) \mu_e \psi_e''(r, R_e) dr \int \psi_v'(R) \psi_v''(R) dR, \quad 2.12$$

where the prime and double prime represent the upper and lower states, respectively. The first integral is the basis of the selection rules for electronic transitions. The second one defines the vibrational selection rules and is the basis of the Franck-Condon principle. As the electronic transitions happen fast compared to the nuclear motion, the vibrational transition happens when

the vibrational states of both electronic levels have a significant overlap. It explains why specific vibrational peaks in a spectrum are strong while others are weak or even not observed in absorption spectroscopy. Under this condition, the transition can be considered instantaneous and represented by a vertical line in the potential energy diagram.

### 2.1.2 Types of photodissociation reactions

The photodissociation could be either direct or indirect, depending on the shape of the excited-state PECs. In the case of a direct dissociation, the dissociation occurs through a repulsive excited state in the absence of barriers and crossings with other surfaces. Consequently, the lifetime of the repulsive excited state is very short and often less than one vibrational period. This process, represented with a set of PECs for the molecule AB, is schematically shown in Fig. 2.2 (a). Direct dissociation can also happen through an excited state with a bound character; if the obtained energy exceeds the dissociation limit, it dissociates into the neutral photoproducts. This scheme is shown in Fig. 2.2 (b).

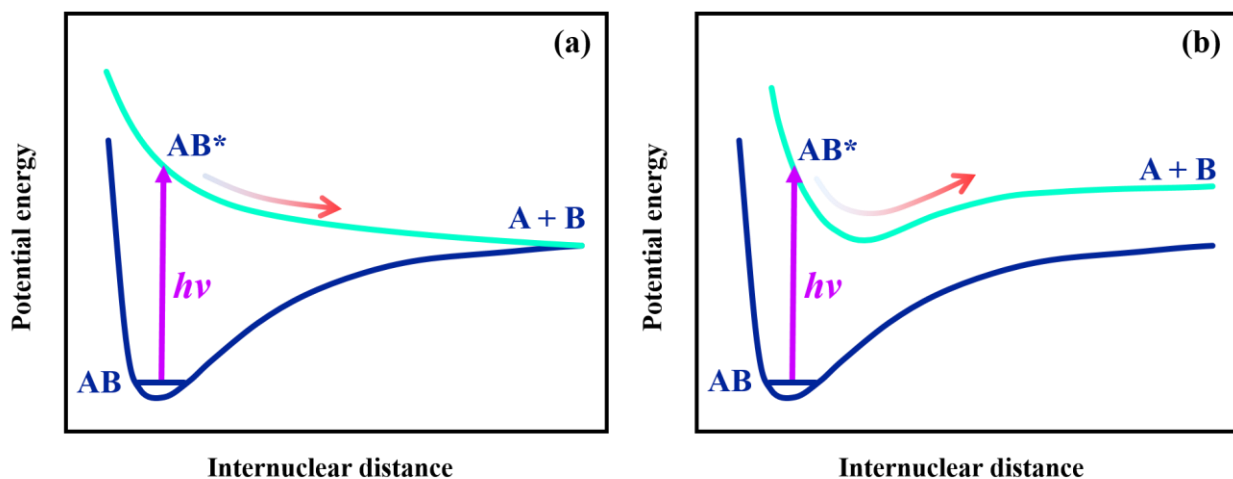


**Figure 2.2.** Schematic representation of photodissociation of a molecule AB along the internuclear distance into dissociation products A+B. The ground-state molecules absorb a photon into various shapes of the excited states. (a) Transition to a repulsive state ( $AB^*$ ), where it dissociates by propagating on that state. (b) Transition to a bound state with the dissociation limit lower than the excess energy, which results in a direct dissociation.

The other type of photodissociation process is indirect dissociation, or pre-dissociation, classified into three categories presented in Fig. 2.3 and discussed in the following. Upon photoabsorption and transition to an excited state, the molecule faces potential barriers or other types of dynamic impediments that must be overcome to let the molecule dissociate. Hence, the dissociation is delayed, taking place over many vibrational periods, and the molecule undergoes transition states and finally enters the exit channel and dissociates. Therefore, the molecular bond is not promptly cleaved, and the lifetime of the excited state often increases to the order of a few ps or more.

**Electronic pre-dissociation:** In this dissociation, the initially excited state is not dissociative at the given energy, and the molecule must undergo a non-adiabatic transition into a second dissociative excited state coupled to the first excited state. This coupling involves nuclear and electronic motion, often leading to the Born–Oppenheimer (BO) approximation breakdown. There are two primary types of electronic pre-dissociation. In the first one, as shown in Fig. 2.3 (a), the transition between the electronic states happens due to the strong coupling either in the form of vibronic (vibrational-electronic) or purely electronic nature, as in the case of the conical intersections [126]. Second, when there is no actual crossing between two different electronic states, the transition is driven by the very high density of vibrational states on a second electronic state through non-radiative transitions, as shown in Fig 2.3 (b). This mechanism is called internal conversion for spin-allowed processes and intersystem crossing for spin-forbidden processes.

**Vibrational pre-dissociation:** In this type of photodissociation, photodissociation occurs through excitation to a quasi-bound state. The molecule is transferred to the PES with a particular vibrational state that is non-dissociative or has a barrier that hinders the dissociation channel. Therefore, to dissociate, the excited molecule must undergo a non-adiabatic transition to a lower vibrational state, transferring energy from a vibrational degree of freedom to the dissociative mode. In other words, it is accompanied by intramolecular redistributions of vibrational energy between different nuclear degrees of freedom. This energy exchange process is called intramolecular redistribution of vibrational energy (IVR). Its time scale ranges from a few to thousands of vibrational oscillation periods. This dissociation scheme is illustrated in Fig. 2.3(c).

**Rotational pre-dissociation:** In this case known as Herzberg type-III, the excited molecule is transferred to a non-dissociative PES with a particular rotational state. Therefore, similar to vibrational pre-dissociation, if it is to dissociate, it must undergo a non-adiabatic

transition to a lower rotational state, transferring energy from rotational degrees of freedom to the dissociative mode or tunnel through the barrier as shown in Fig. 2.3 (d)

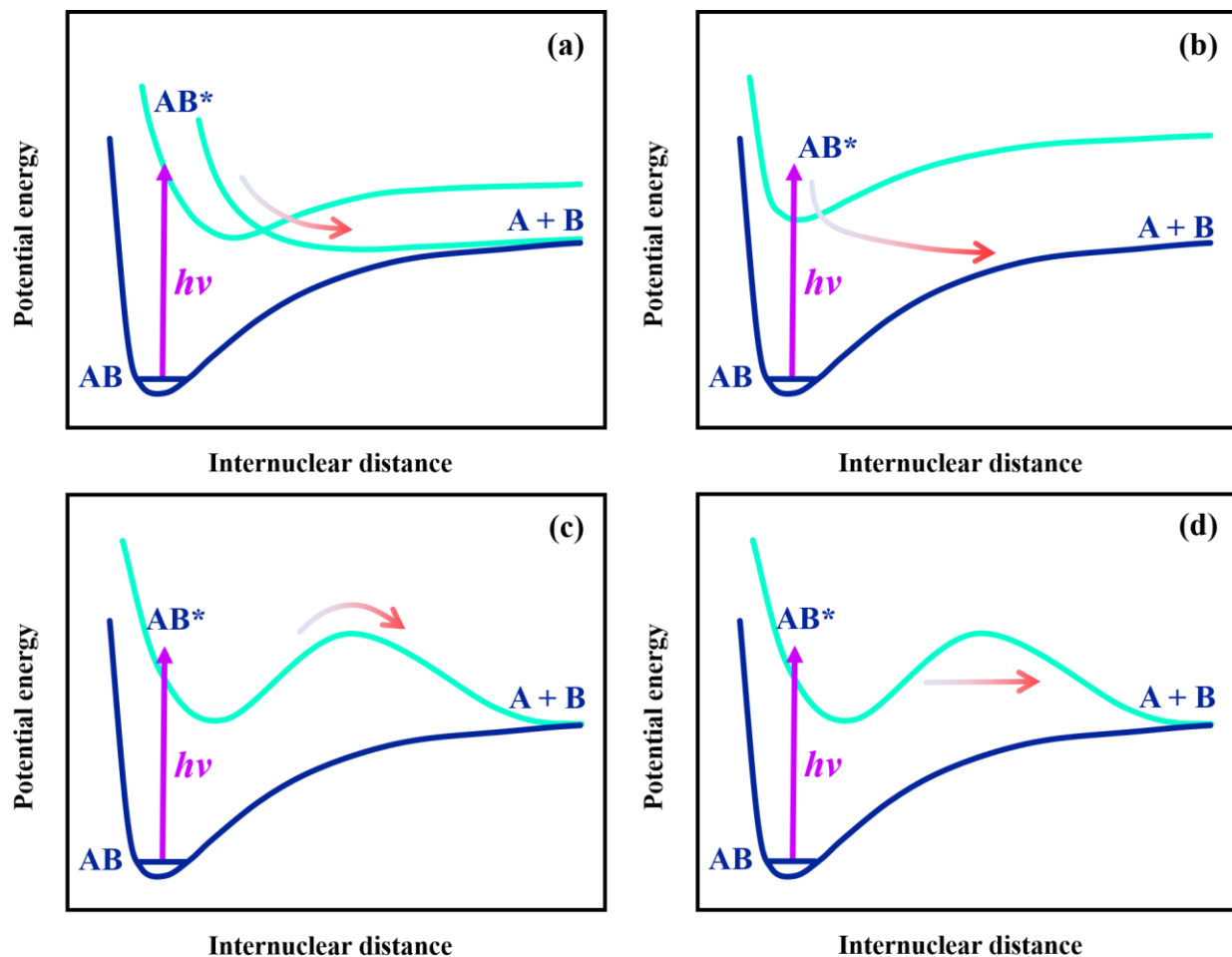


**Figure 2.3.** Schematic representation of indirect photodissociation processes of a molecule AB along the internuclear distance into dissociation products A+ B. **(a)** Electronic pre-dissociation through excitation into a bound excited state and the photodissociation occurs through coupling to a dissociative excited state. **(b)** Electronic pre-dissociation through internal conversion from an excited bound state; the molecule dissociates on the ground electronic state to which it transitions by a non-radiative transition. **(c)** Vibrational and **(d)** rotational pre-dissociation due to absorption into a quasi-bound state with a barrier. Figure adapted from Ref. [124].

Different photodissociation mechanisms can co-exist depending on the characteristics of the various excited electronic states of the molecule and the excitation energy. In this situation, the resultant dynamics are determined by a combination of several competing dissociation processes.

### 2.1.3 Conical intersections

As discussed above, molecular photodissociation does not necessarily occur exclusively along the initially excited state. It is often driven by the presence of non-adiabatic crossing, e.g., the conical intersection between potential energy surfaces that allows population transfer from one state to the other. Conical intersections play a critical role in the excited-state dynamics of polyatomic molecules, particularly at ultrashort timescales [22], [131]. They significantly influence and often define the reaction pathways of many non-adiabatic processes. The resulting dynamics generally cannot be described within the BO approximation framework. The electronic and nuclear wave functions are separable due to the distinct time scale of the electronic and nuclear motions.

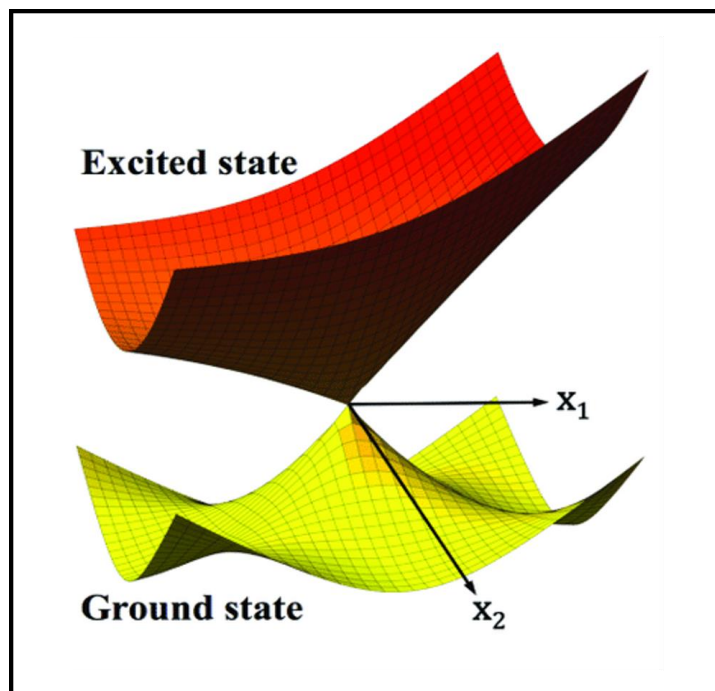


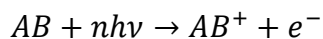
**Figure 2.4.** Illustration of a conical intersection between two potential energy surfaces opening up non-adiabatic processes in the excited state dynamics. Figure adapted from Ref. [132].

In the vicinity of conical intersections, adiabatic potential surfaces come close in energy. At the crossing points, the nuclear motion induces coupling between two adjacent adiabatic surfaces through non-adiabatic transitions, and the degeneracy is canceled out along at least two internal degrees of freedom resulting in radiationless transitions between electronic states. The crossing allows the wavefunction to funnel through the conical intersection back to the highly

excited ground state's vibrational levels, from which it dissociates. The energy representation of the conical intersection between two potential states is shown in Fig. 2.4, illustrating a double funnel [132].

## 2.2 Photoionization

Besides molecular photodissociation, other light-induced reactions relevant to this work include photoionization and dissociative ionization. Their presence is mainly defined by the wavelength and the intensity of the employed light. In case of photoionization, upon absorption of one or multiple photons, if the total absorbed energy is above the ionization threshold, i.e., ionization potential ( $I_p$ ), the molecule ( $AB$ ) turns into a cation ( $AB^+$ ):



2-13

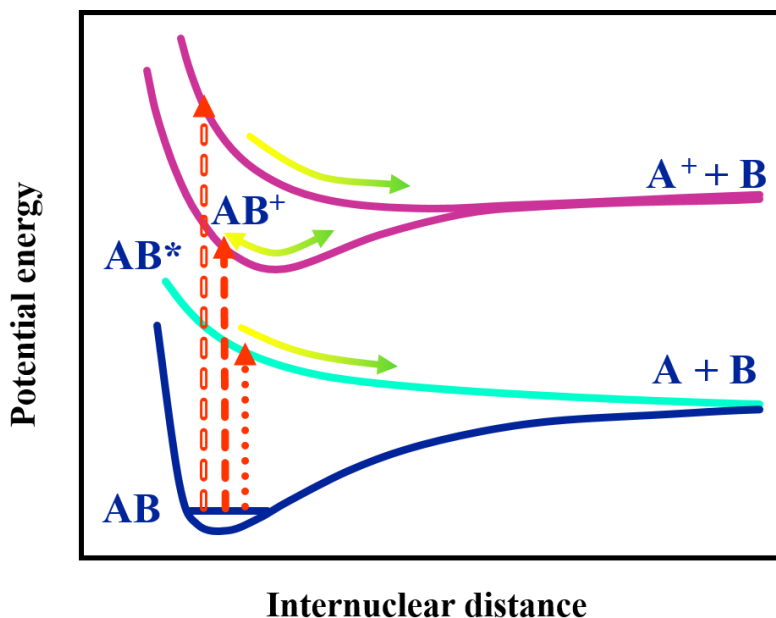


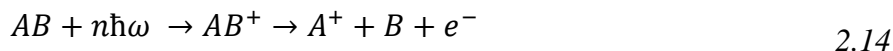
**Figure 2.5.** Schematic representation of potential energy curves of molecule  $AB$  and its cation ( $AB^+$ ). Various light-induced processes are displayed: photodissociation of the excited state (dotted arrow), photoionization to a bound ionic state (dashed arrow), and dissociative photoionization to a repulsive ionic state (open-dashed arrow).

The multi-photon ionization process can be direct in which the molecular cation is formed directly in the ionic state with rapid electron ejection. It can also be indirect when the molecule is excited to one of the high-lying states above the ionization threshold with subsequent relaxation

to the ionic state and electron ejection, a process known as autoionization. Alternatively, multi-photon ionization can proceed via intermediate resonant states, accessed either via single-photon resonance or via multi-photon resonance with Stark-shifted states [133].

### 2.2.1 Dissociative photoionization:

In dissociative ionization, the ionization process is followed up by photodissociation. Conceptually, this process can be grasped as a combination of photodissociation and photoionization. In this process, the ionized molecule is promoted to the repulsive cationic excited states, where it dissociates and produces ionic fragments, neutral fragments, and an ejected photoelectron.



The dissociative ionization can also happen directly through ionization to the repulsive excited states. We will discuss these various processes within the multi-photon process in UV-excitation of the iodomethane ( $\text{CH}_3\text{I}$ ) in chapter 4. To track these processes, one of the observables could be the energy and angular distribution of the photoproducts, which can be directly measured for ionic fragments. Depending on a particular light-induced process, the kinetic energy distribution could be pathway-specific. Fig. 2.5. illustrates several different processes and the involved potential energy curves of the ground and ionic states for exemplary molecule AB.

## 2.3 Introduction to the photochemistry of halomethanes

### 2.3.1 Photodissociation dynamics of a halomethane; iodomethane ( $\text{CH}_3\text{I}$ )

The photochemistry of halomethanes has attracted a great deal of attention due to their considerable impact on atmospheric and environmental science and, most prominently, their role in ozone layer depletion [134], [135]. Additionally, the complicated excited-state structure involved in the photochemistry of these molecules causes additional academic interest and makes them popular targets for quantum control studies. In particular, photochemistry of various halomethanes such as  $\text{CH}_3\text{I}$ ,  $\text{CH}_2\text{I}_2$ ,  $\text{CHBr}_3$ , and more has been comprehensively investigated, with the goal of understanding plausible fragmentation patterns and the ensuing dynamics using different experimental and theoretical techniques.

Among numerous halomethanes, iodomethane ( $\text{CH}_3\text{I}$ ) is one of the most studied molecules in photochemistry [103],[118],[119],[134]–[158] and has received massive attention in the last few years two decades because of its well-studied electronic and vibrational energy states.  $\text{CH}_3\text{I}$  is often considered a prototype molecule for studying photofragmentation and photodissociation dynamics of polyatomic molecules. In addition,  $C_{3v}$  point group symmetry provides a great deal of information about its quantum states and simplifies the interpretation of the electronic, vibrational and rotational dynamics [158]. Depending on the character of the excited states, it shows distinctly different dissociation dynamics [140]. In particular, photodissociation via excitation in the first absorption band, referred to as the *A*-band, has been extensively studied by various researchers. In addition to the *A*-band, dissociation and vibrational structure of higher excited states (i.e., Rydberg states known as *B*- and *C*-bands) of  $\text{CH}_3\text{I}$  molecule have been studied to understand the impact of vibronic interactions in the photodissociation of the molecule. [151].

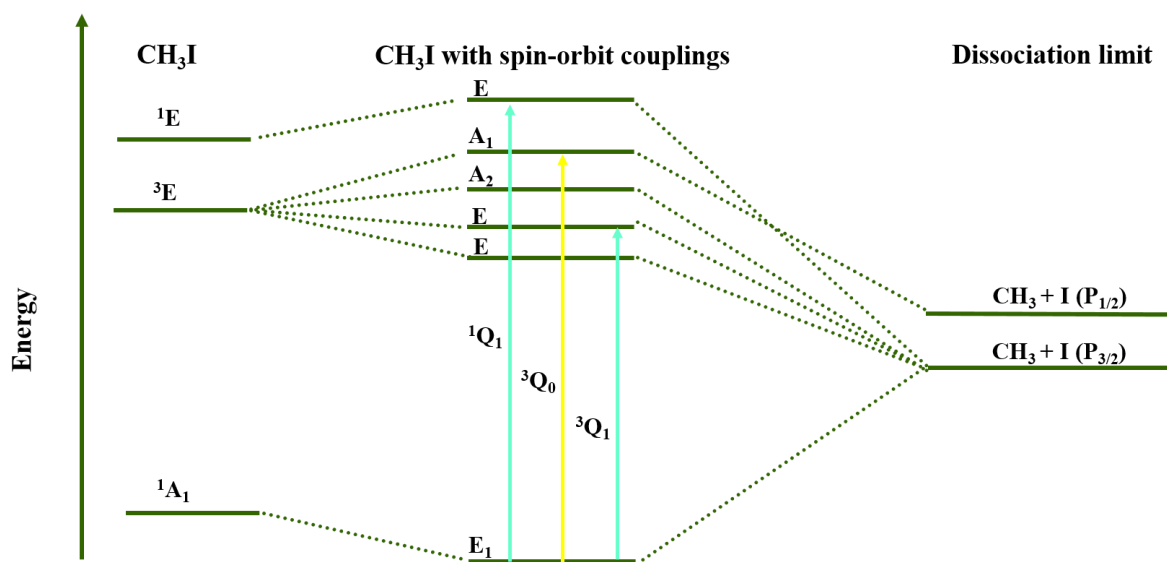


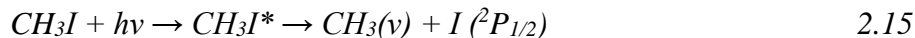
**Figure 2.6.** Correlation diagram of  $\text{CH}_3\text{I}$   $n \rightarrow \sigma^*$  transitions in the *A*-band. The states with and without spin-orbit coupling are indicated along with the dissociation limits. The arrows indicate electric-dipole allowed transitions:  $^3Q_1$  arrow corresponding to a parallel transition, and  $^3Q_0$  and  $^1Q_1$  arrows corresponding to perpendicular transitions. The figure is adapted from Ref. [140].

### 2.3.1.1. Dynamics upon *A*-band photoexcitation

Spectroscopically, the *A*-band is a structureless absorption band in the ultraviolet region between 220 and 350 nm with a maximum of around 260 nm, as shown in Fig. 1.2. It results from

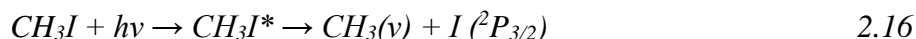
an  $n(I) \rightarrow \sigma^*(C-I)$  transition, where a non-bonding p electron of iodine is promoted to the lowest-energy antibonding molecular orbital [158]. This band includes transitions to five electronically excited states denoted as  $E$ ,  $E$ ,  $A_1$ ,  $A_2$ , and  $E$  within the symmetry group, resulting from SO couplings induced by the unpaired electron remaining on the heavy iodine atom [119], [120], [145]. In Mulliken notation [160], these states are labeled as  ${}^3Q_2$ ,  ${}^3Q_1$ ,  ${}^3Q_{0+}$ ,  ${}^3Q_{0-}$ , and  ${}^1Q_1$ . Transitions from the ground state to  ${}^3Q_1$ ,  ${}^3Q_{0+}$ , and  ${}^1Q_1$  states are dipole allowed and optically accessible. The electronic configurations are depicted in Fig. 2.6 [140] in the absence and presence of the SO interactions, and the allowed transitions are shown as the vertical arrows.

Potential energy curves along the C-I bond distance and the decomposed absorption cross-section for these three excited electronic states are shown in Fig. 2.7 [120], [161]–[164]. It is worth mentioning that there is some uncertainty in the relative contribution of these states to the total cross-section. The experimental measurement of the angular distributions of the dissociation products by Eppink and Parker [146] showed that the A-band dissociation is dominated by a parallel transition to the  ${}^3Q_0$  state. The Franck-Condon region for the population of the excited states is spread between the C-I separation of 2 - 2.25 Å. This internuclear distance is the range accessible for the wave packet in the ground vibrational state, i.e.,  $v=0$ . The transitions to  ${}^1Q_1$  and  ${}^3Q_1$  states within the A-band absorption cross-section are perpendicular and weaker. These states contribute less than a few percent to this spectrum [120], [146]. For the parallel transition to  ${}^3Q_0$ , the transition dipole points along with the C–I bond. Therefore, molecules with a bond axis parallel to the direction of the electric field of the linearly polarized light are mainly excited and dissociated along the laser polarization direction. These excited states are all dissociative along the C–I bond, which results in a rapid dissociation into separate iodine and methyl fragments. Thus, the A-band dissociation is dominated by a parallel transition to the  ${}^3Q_0$  state through a resonant one-photon excitation, resulting in the C-I bond cleavage and neutrally dissociating the molecule into  $CH_3$  radical and ground state or SO excited iodine atom  $I({}^2P_{1/2})$  (henceforth denoted  $I^*$ ).



Light-induced molecular excited-state dynamics are often governed by the interplay between different electronic excited states connected by non-adiabatic crossings, which result in population transfer and lead to other asymptotic reaction products. In  $CH_3I$ , while the molecule dissociates, a portion of the excited state population is transferred to the  ${}^1Q_1$  state due to a non-adiabatic crossing between  ${}^3Q_0$  and  ${}^1Q_1$ . There is a conical intersection at 2.37 Å where the

population leaks to the other dissociation pathway. This dissociation pathway correlates with the  $\text{CH}_3$  radical in its ground state and the iodine atom  $\text{I} (^2\text{P}_{3/2})$  (henceforth denoted  $\text{I}$ ).



Hence, upon excitation to the A-band, the molecule promptly dissociates via these two resonant excited electronic states. The branching ratio between  $\text{I}^*$  and  $\text{I}$  depends on the exact excitation wavelength and has been reported to lie between 0.70–0.81 for 266 and 248 nm [140].

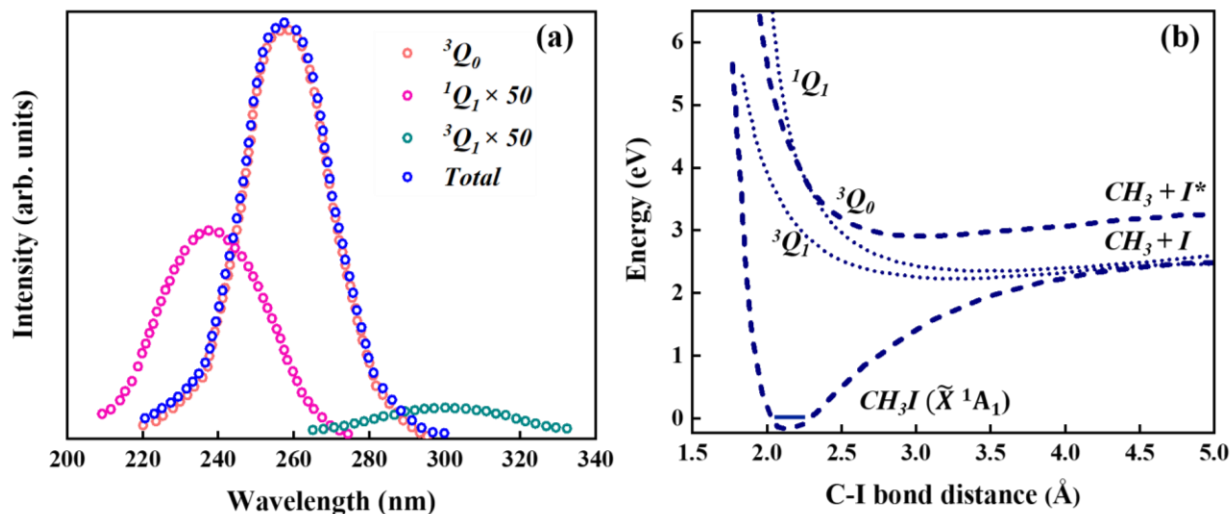


**Figure 2.7.** A-band absorption cross-section and the related potential energy curves. (a) Total absorption spectrum of  $\text{CH}_3\text{I}$  and spectral decomposition corresponding to the  $^3\text{Q}_0$ ,  $^1\text{Q}_1$  and  $^3\text{Q}_1$  excited states. (b) Potential energy curves in the A-band dissociation. Excitation is primarily to the  $^3\text{Q}_0$  state, which is dissociative and correlates to methyl and  $\text{I} (^2\text{P}_{1/2})$  radicals. Methyl radicals paired with a ground state  $\text{I} (^2\text{P}_{3/2})$  are produced following a non-adiabatic curve crossing to the  $^1\text{Q}_1$  state. Adapted from Ref. [146].

The dynamics following excitation to the A-band depend on the excited state. Several experimental measurements and theoretical calculations investigated the wavelength-dependent excitation fraction into different Q-states. Gadenken et al. [165] performed some magnetic circular dichroism measurements to determine these excitation fractions and evidenced significant contributions from the  $^1\text{Q}_1$  state on the order of 14% of the total absorption cross-section at 255 nm. On the other hand, their measurements at 269 nm showed that the wave packet will predominantly be excited into the  $^3\text{Q}_0$  state, and there is little or no excitation into the  $^1\text{Q}_1$  and  $^3\text{Q}_1$  states. Although Eppink and Parker [146] obtained these fractions from the angular distribution of

the products observed a similar trend at these wavelengths, but the fractions are drastically different on the order of a few percentages. The calculations by Alekseyev et al. [120] and Bañares et al. [161], [162] suggested a combined fraction of excitation of about 20% into these states at these wavelengths with a significant increase excitation into  $^3Q_1$  at longer wavelengths.

Recently, to investigate these dependences, Minns and coworkers [141]–[143] observed quite different dynamics at blue and red edges of the A-band (255 and 269 nm, respectively), with notable differences in the measured lifetime and structural dynamics. They rationalized the observed differences in the context of changes in excitation cross-sections of the accessible excited states and the ensuing dynamics on the individual state. Their measurements in the first level were in line with the other studies and showed fast rapid dynamics for the longer wavelength, which is dominated by the dynamics along with the  $^3Q_0$  state. Second, they observed more complicated dynamics with significantly increased lifetimes along the  $^1Q_1$  state at the shorter wavelength besides the well-known dynamics along the  $^3Q_0$  state.

On another note, Bañares and coworkers [162] used a pump-probe experiment to investigate the reverse non-adiabatic crossing ( $^1Q_1 \rightarrow ^3Q_0$ ) in the blue edge of the A-band (217-230 nm). They observed dominant excitation to the  $^1Q_1$  state at the bluest excitation wavelength. They observed that the quasi-parallel angular distributions of both channels at 230 nm become highly perpendicular at 217 nm. These observations are explained in terms of an increasing contribution of the  $^1Q_1$  state, through direct adiabatic dissociation in the  $\text{CH}_3 + \text{I} (^2P_{3/2})$  channel and through “reverse” non-adiabatic curve-crossing  $^3Q_0 \leftarrow ^1Q_1$  for the  $\text{CH}_3 + \text{I}^*$  channel.

In addition, Eppink and Parker investigated the energy partitioning between translational and internal degrees of freedom by tracking the dissociated iodine and methyl photofragments [146]. They found that the kinetic energy distributions of the dissociated fragments exhibit vibrational structure resulting from vibrationally hot photodissociated  $\text{CH}_3\text{I}$ . Also, the Bañares group observed vibrational structure in the kinetic energy distribution of the methyl photofragment after photodissociation at longer wavelengths up to about 330 nm with less contribution from the vibrational ground state ( $v=0$ ) and higher initial vibrational excitation [161].

Besides the vibrational and angular distributions of the dissociation products, numerous time-resolved studies of the  $\text{CH}_3\text{I}$  photodissociation have been performed by several groups. De Nalda *et al.* [166] determined the time-evolution of the excited-state wave packet in the  $^3Q_0$  and  $^1Q_1$  states at 266 nm. This experiment is sketched in Fig. 2.8, which illustrates the spread of the

wave packets initially localized in the Franck-Condon region toward the longer internuclear distances after  $\sim 50$  fs. Later, Corrales *et al.* [137] measured the appearance times of the  $I^*$  and  $I$  products to be 84 and 94 fs, respectively. In a different study, the same group probed the dissociated dynamics with a strong field and with the help of quantum calculation, they showed the existence of a potential well in the PEC of the  $CH_3I^{2+}$  [136]. Later on, they tried to visualize the conical intersection directly employing the non-coincidence CEI technique and compared their experimental results to trajectory surface hopping calculations [138]. Although the results were promising, achieving this goal needed better temporal and energy resolutions. Eventually, Leone and coworkers [149] used attosecond XUV absorption spectroscopy to directly map the conical intersection dynamics and visualize the bifurcation of the wave packets. They used UV pump and XUV probe pulses to track  $I$  (4d) core-to-valence absorption transitions for the real-time mapping of  $CH_3I$  dissociation through the  ${}^3Q_0 \rightarrow {}^1Q_1$  conical intersection in the A-band identified through signatures of multi-photon states in the experimental transients.

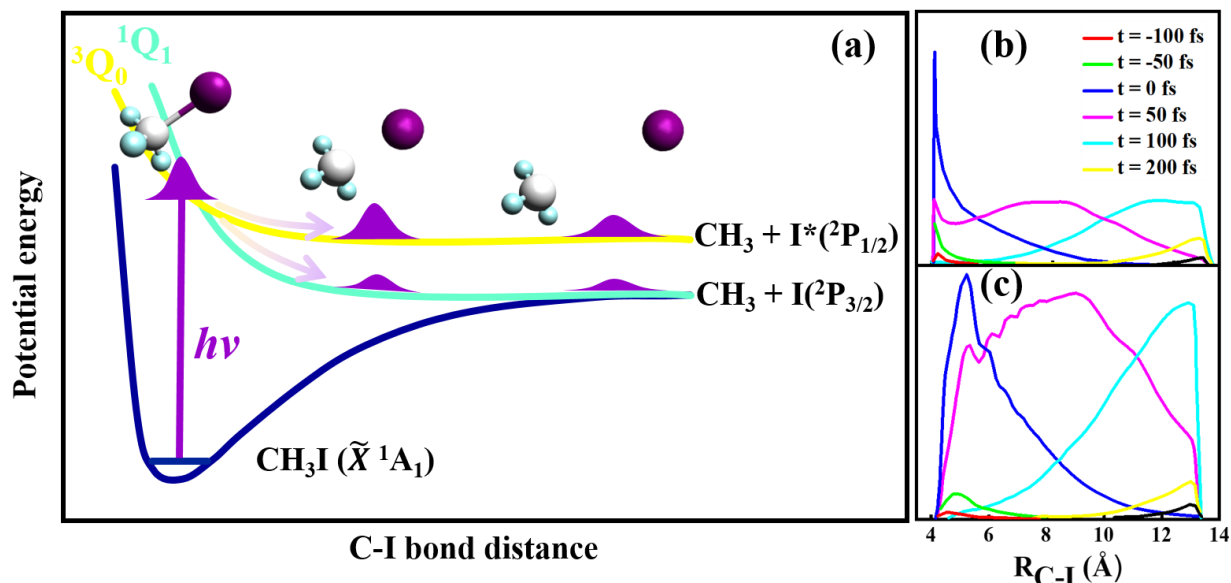


**Figure 2.8.** (a) Time-evolution of the nuclear wave packet on the PECs involved in the A-band dissociation. A nuclear wave packet is launched in the  ${}^3Q_0$  potential energy and propagates, yielding  $CH_3 + I({}^2P_{1/2})$ . A small portion of the initial wave packet leaks nonadiabatically to the  ${}^1Q_1$  surface, which correlates with  $CH_3 + I({}^2P_{3/2})$ . Simulated wave packet distributions along the C-I bond distance at different times after excitation to the  ${}^3Q_0$  (b) and the  ${}^1Q_1$  states (c). The figures are adapted from [166].

### 2.3.1.2. Dynamics upon B- and C-bands photoexcitation

In addition to A-band excitation with one UV-photon absorption at 250-270 nm, CH<sub>3</sub>I can excite many higher-lying intermediate Rydberg states. A deeper UV or vacuum ultraviolet spectral (VUV) range enables this manifold of Rydberg states to be accessible, triggering ultrafast reaction dynamics and opening up more reaction pathways.

The pre-dissociation of CH<sub>3</sub>I occurs through excitation of the vibrational state of the lower-lying bound Rydberg states (previously mentioned as B-band) to a repulsive excited state. The B-band originates from promoting a non-bonding 5p $\pi$  electron of the iodine atom to the lowest energy Rydberg molecular orbital of s, p, and d [167]. This excitation generates the <sup>3,1</sup>E states, and the remaining three iodine electrons experience strong SO coupling; therefore, the triplet state is strongly separated. In this case, this interaction is stronger than the exchange interaction, leading to the formation of the two doublets E(<sup>3</sup> $\Pi_2$ ), E(<sup>3</sup> $\Pi_1$ ) and A1(<sup>3</sup> $\Pi_0$ ), E(<sup>1</sup> $\Pi$ ), instead of the conventional triplet-singlet states for the case of the weak SO coupling. Excitations to these four states are split into two bands, B and C, where transitions to the two lower states (<sup>3</sup>R<sub>2</sub> and <sup>3</sup>R<sub>1</sub>) covering the spectral range from 190 to 205 nm corresponding to 6s (<sup>2</sup>E<sub>3/2</sub>) molecular orbital in 6.2 - 6.7 eV energy are conventionally considered the B-band excitation. The transitions to the upper two (<sup>3</sup>R<sub>0+,0-</sub> and <sup>1</sup>R) make the higher-lying C-band in the range of 170–185 nm corresponding to the 6s (<sup>2</sup>E<sub>1/2</sub>) molecular orbital in 6.7 - 7.2 eV energy [168]. The ground state transition to the <sup>3</sup>R<sub>1</sub> state is dominated, with a weak transition to the <sup>3</sup>R<sub>2</sub> state at slightly lower energies. It is worth mentioning that the transitions are perpendicular due to the E character of the states in C<sub>3v</sub> symmetry. The CH<sub>3</sub>I absorption in the B- and C-band is dominated by transitions to bound Rydberg states, followed by their prompt pre-dissociation into CH<sub>3</sub> (<sup>2</sup>A<sub>2</sub>'') + I(<sup>2</sup>P<sub>1/2</sub>) and CH<sub>3</sub> (<sup>2</sup>A<sub>2</sub>'') + I(<sup>2</sup>P<sub>3/2</sub>). These transitions characterize the excitation of lower-lying bound Rydberg states followed by pre-dissociation. Higher Rydberg states result from promotion to higher energy orbitals of 6p and 7s with energies in the range of 8 eV [154], [169], and higher-lying Rydberg states result from excitation to higher energy orbitals. Excitation to the manifold's higher-lying states, right below the ionization threshold, yields atomic iodine Rydberg states [152] and ground state methyl fragments, which could be ionized to ionic states. The importance of different reaction pathways involving intermediate Rydberg states has been investigated experimentally [152], [157], [170]–[177] and theoretically [121], [178].

The first theoretical calculations on the pre-dissociation dynamics of the lower Rydberg states were performed by Donaldson [179] based on a combination of theoretical and experimental data of dissociative surfaces and a series of hypotheses for the coupling of the surface. Their results suggested that the symmetry of at least two dissociative potentials of  $A_1$  and  $A_2$  play a prominent role in the pre-dissociation of the  $B$ -band states. Tadjeddine [180] and Alekseyev [121] performed *ab initio* calculations to compute the lowest valence and Rydberg states as a function of the internuclear distance of the C-I coordinate. The computed PECs are shown in Fig. 2.9, where the states belonging to the  $A$ ,  $B$  and  $C$ -bands have been pinpointed. In this figure, the states have been calculated, including the SO interaction and the  $\Lambda - S$  notation is used ( $^3Q$ ,  $^3A_1$ , etc.). In addition, for the lowest Rydberg states, the  $^{1,3}R$  notation is used, an extension of Mulliken's  $^{1,3}Q$  notations used for the  $A$ -band states.

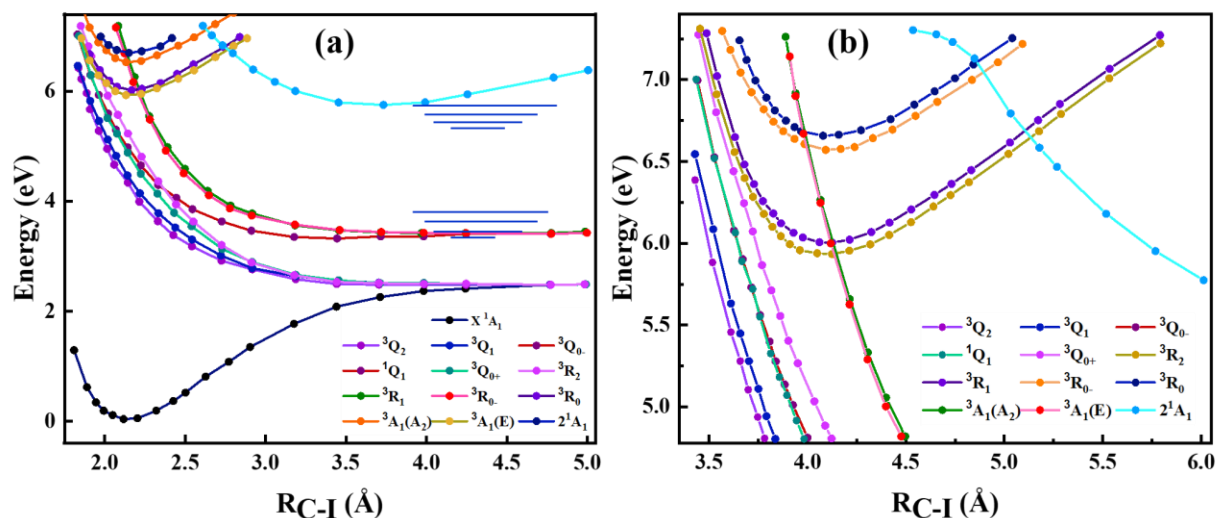


**Figure 2.9.** A- and B-band potential energy curves of CH<sub>3</sub>I. (a) Potential energy curves calculated along the C–I coordinate for the low-lying states of CH<sub>3</sub>I. The states corresponding to A, B and C-bands are identified. (b) The excited states' potential energy curves of CH<sub>3</sub>I relevant to the B- and C-band and pre-dissociation by crossing between the bound state and the repulsive  $^3Q_0$  state. The lowest vibrational levels are shown for the bound  $^3R_1$  and  $^1R_0$  states. Adapted from Ref. [121].

The computed transition dipole moment (TDM) by Alekseyev shows that TDM for perpendicular transition to the  $^3R_1$  and  $^1R_1$  states is relatively strong. The main contributions to both transitions are coming from the allowed transition from the ground state to the  $^1R(1E)$ . The parallel transition moment to the  $^3R_{0+}(A_1)$  is significantly weaker than those for the perpendicular

transitions. This spin-forbidden transition becomes allowed due to the SO coupling with the  $\tilde{X}^1A_1$  and  $2^1A_1$  singlet states. However, at larger internuclear distances, the TDM for this transition increases when the two states are getting close to each other. Also, there is a weak excitation to the  $^3R_2$  state, although it is forbidden. Syage [159] interpreted their experimental results so that the  $^3A_1 (A_2)$  component of the repulsive  $^3Q_0$  state of the *A*-band has a significant role in the process of C–I bond cleavage after absorption of about 200-nm photon. In other words, in the excitation to the *B*-band, the coupling between the Rydberg state  $^3R_1$  and the dissociative states of the *A*-band  $^3Q_0$  have a substantial effect on the pre-dissociation process. Consequently, significant differences are observed in the dissociation dynamics depending on the vibronic level at which the molecule is initially excited.

One of the particular goals of the present thesis is to study the pre-dissociation dynamics of the lower bound states of the *B*-band. The repulsive  $E(^3A_1)$ , and  $A_2(^3A_1)$  states cross the *B*-band states near their minimum, resulting in the main pre-dissociation channel. However, from symmetry considerations, it is clear that the main decay channel for the  $^3R_2$ ,  $^3R_1$ ,  $^1R$  states of *E* symmetry is the transition to the  $^3A_1(E)$  state, and the SO coupling causes their pre-dissociation [121]. This decay channel results in the formation of the spin-excited I ( $^2P_{1/2}$ ) atoms. Gitzinger [172] argued that if the ground state I ( $^2P_{3/2}$ ) atoms could be obtained from the  $CH_3I$  photodissociation in the *B* band, and according to the computed PECs, this could be possible only through repulsive  $^1Q (E)$  state at relatively high excitation energies  $\geq 6.2$  eV. It should be noted that these excitation energies correspond to lower internuclear distances ( $\leq 3.6$  au), and hence we might be able to look for the ground state I ( $^2P_{3/2}$ ) atoms as photodissociation products at the lower excitation wavelength of about 180 nm. Nevertheless, it could still be problematic experimentally due to the strong absorption to the  $^1R (E)$  state, with the  $O_0^0$  band. In addition, it is known from the experiment [175] that all the vibrationally excited states have different lifetimes than that of the vibrationless level. Wang *et al.* found that the pre-dissociation of the  $^3R_1 (E)$  state is slower upon excitation of the  $\nu_3$  C–I stretching mode [176]. This finding was later confirmed by measuring the pre-dissociation lifetime, which increases three times from  $O_0^0$  to  $3_0^1$ . In the axial-recoil approximation, the C–I coordinate is the dissociation coordinate, so the excitation of the  $\nu_3$  mode should enhance dissociation and reduce the lifetime.

Fig. 2.10 shows the absorption spectrum of  $CH_3I$  in the *B*-band. Contrary to the broad structureless absorption spectrum of the *A*-band, this spectrum exhibits a clear vibrational structure

containing resonance lines with significant spectral broadening due to the finite lifetime associated with the pre-dissociation. In this nomenclature, in the assigned number  $X_Z^Y$ , X indicates the vibrational mode of the molecule, the Z subscript indicates the number of vibrational quanta in the X mode that the molecule has in the ground state, and the Y superscript represents the number of vibrational quanta in the Rydberg state. For instance,  $O_0^0$  refers to the transition from the vibrationless ground electronic state to the Rydberg state in the vibrational ground state;  $3_0^1$  represents the excitation of the molecule a vibrational quantum in the C-I stretching mode  $\nu_3$  from the ground state with  $\nu=0$  to the Rydberg state, and this can be generalized to the other assignments. Two intense absorption bands correspond to the  $O_0^0$  (at 201.2 nm) and  $2_0^1$  (at 196.7 nm) transitions from the ground state to the  $^3R_1$  Rydberg state, with ground vibration level ( $\nu_0=0$ ) and the level with a vibrational quantum in the umbrella mode ( $\nu_2=1$ ). The corresponding signals from the transitions to other vibration levels of CH<sub>3</sub>I in the B-band are very weak; inevitably, one needs to multiply the spectrum to make the weakest absorption bands visible. Here, it is multiplied by a factor of 25. All bands correspond to the  $^3R_1$  state absorption, except for  $[1]6_0^1$  which corresponds to the  $^3R_2$  state. In this transition, quantum states are mixed due to the different absorption present, and the probability of absorption at this level increases.

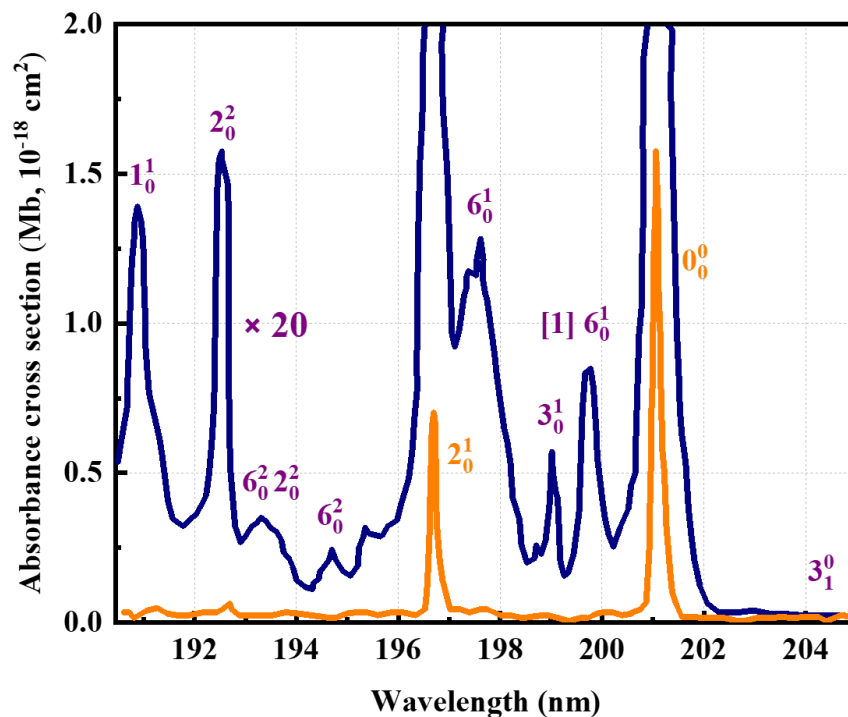


**Figure 2.10.** The absorption spectrum of CH<sub>3</sub>I in the B-band absorption region with assignments to vibronic transitions. The figure is adapted from Ref. [174].

Time-dependent studies of the pre-dissociation of Rydberg states [175] were performed by measuring the time-evolution of the parent ion signal produced by photoionization of the Rydberg states. In these measurements, the vibrationless level of the first optically active Rydberg state was found to have a picosecond lifetime, while higher vibrational levels of this state were found to have significantly shorter lifetimes. Gitzinger *et al.* [172] measured the pre-dissociation lifetimes of several vibronic levels using femtosecond Velocity Map Imaging (VMI) technique through resonant and non-resonant Multi-Photon Ionization (MPI). The decay of the parent ion was found to be  $1.52 \pm 0.10$  ps in the origin of the *B*-band ( $O_0^0$ ), while the vibrational states of  $2_0^1$  and  $3_0^1$  lifetimes were found to be  $0.85 \pm 0.04$  ps and  $4.34 \pm 0.13$  corresponding to the excitation of the umbrella mode ( $\nu_2$ ) and the C–I stretching mode ( $\nu_3$ ), respectively. Thiré *et al.* [170], [171] employed similar techniques and got similar results.

One of the most controversial discussions concerning the *B*-band dissociation is the determination of the  $I^*$  quantum yield. Following Alekseyev's [121] calculations, the pre-dissociation through the coupling between Rydberg state  $^3R_1$  and the repulsive  $^3A_1$  state leads to dissociating into  $CH_3 + I^*$ . His calculations predict a quantum yield of unity. However, in practice, a small amount of *I* is detected [181] in its ground spin-orbit state correlated with ro-vibrationally excited  $CH_3$ , assigned to a second curve crossing between  $^3R_1$  and the repulsive state  $^1Q_1$ . The branching ratio for this channel was not precisely determined, and there have been significant discrepancies. Subsequently, Hancock *et al.* [182] reproduced an identical experiment and attributed the value of less than 1 to an experimental artifact. Later on, Gitzinger *et al.* [173] measured the quantum yield between 0 in the  $O_0^0$  to 0.87 in the  $3_0^1$  vibronic band, suggesting the presence of  $I(^2P_{3/2})$  due to the competition between two decoupling paths, through the  $^3A_1$  state and throughout the  $^1Q_1$  state, due to the weak coupling between the  $^3R_1$  and the  $^3A_1$  state, even at lower excitation energies.

Forbes *et al.* [177] investigated the pre-dissociation dynamics of the 6s Rydberg state using time-resolved Coulomb explosion imaging. XUV pulses were used for site-specific probing by the inner-shell ionization at the *I* atomic site employing a VMI setup spectrometer coupled with the PImMS camera [183]. For the *B*-band excitation at 201.2 nm, similar results to Gitzinger [172] were obtained, revealing the discussed pre-dissociation mechanism. In addition, the quantum yield of  $I^*$  was measured to be unity. The angular distributions of photofragments were extracted out of slice images, revealing the perpendicular nature of the transition to the Rydberg state at short

pump-probe delays and a subsequent loss of anisotropy due to rotation of the parent molecule before dissociation.

### 2.3.2 Photodissociation dynamics of dihalomethanes

In this section, the discussion of photodissociation dynamics of halomethanes is extended to dihalomethanes to investigate the effect of the substituent halogen atom. In dihalomethanes, these dynamics are mainly characterized by the electronic nature of particular excited states involving the C-X (X = Br, Cl, I) bond cleavage, which influences the product channels by which the molecule dissociates. In general, and the energy distribution after photoabsorption and the reaction time scales depend on the size of the substituting halogen atom.

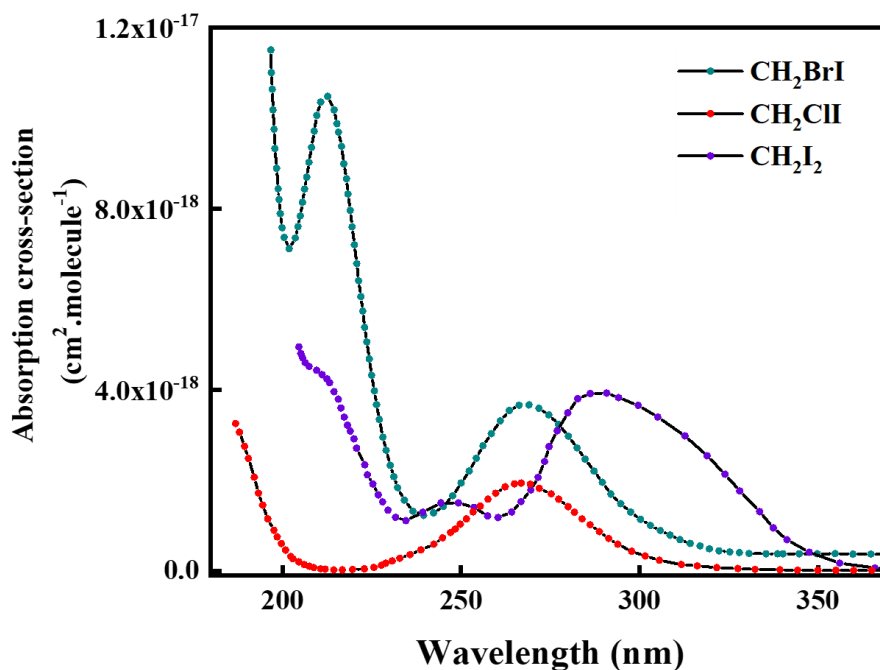


**Figure 2.11.** UV absorption spectra of CH<sub>2</sub>BrI (green), CH<sub>2</sub>ICl (red) and CH<sub>2</sub>I<sub>2</sub> (purple) at 298 K in the gas phase from nearly 200 to 380 nm adapted from Ref. [184].

Fig. 2.11 illustrates dihalomethanes' (CH<sub>2</sub>X I, X = Br, Cl, I) absorption spectra in the first and second absorption bands [184]. The spectrum for CH<sub>2</sub>BrI shows three noticeable peaks above 190 nm, including a broad peak near 270 nm assigned to the promotion of a non-bonding electron on the iodine to an antibonding orbital on the C-I bond, a broadband peak around 215 nm assigned to the promotion of a non-bonding electron on the Br atom to an antibonding orbital corresponding

to the C-Br bond, and sharp features around 190 nm correlated to Rydberg transitions on the I atom. These transition features are similar to the shape of the equivalent transitions observed in CH<sub>3</sub>I. The difference is that the broad bands are significantly more intense, with a slight red-shifted peak at lower wavelengths. This shift is attributed to the fact that the carbon atom has a more positive charge than it does in a CH<sub>3</sub>I (monohalomethane), stabilizing the antibonding orbitals [146]. This stabilization occurs because the electron transitions to an antibonding orbital have a more significant charge-transfer character. This transfer reduces the positive charge associated with the upper state, lowering its energy and producing a red shift [185]. CH<sub>2</sub>ClI spectrum shows an unstructured continuum peak at approximately 266 nm, assigned to the n(I) → σ\*(C-I) transition localized on the C-I bond similar to the CH<sub>2</sub>BrI molecule. The transition localized on the C-Cl bond peaks at 173 nm, corresponding to the B-band of CH<sub>2</sub>ClI. Another noteworthy point is that the more intense broad bands indicate a moderate coupling between the two chromophores.

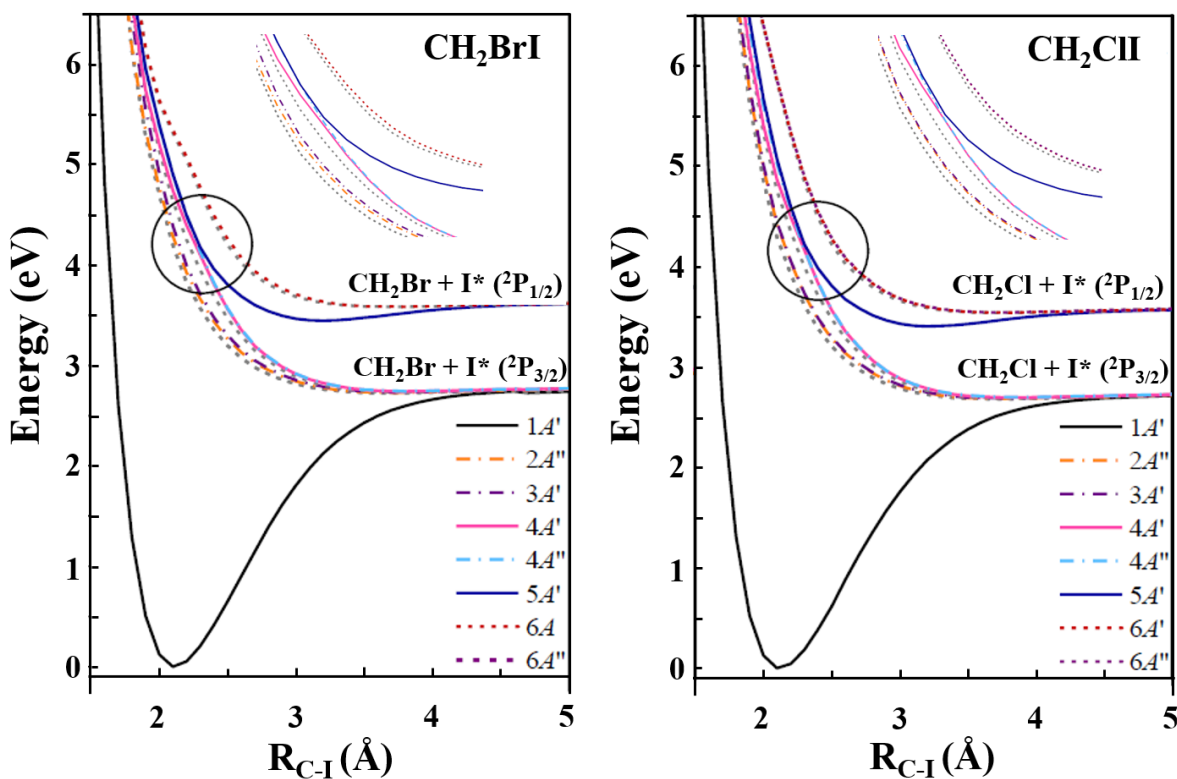


**Figure 2.12.** Dihalomethanes potential energy curves. The potential energy curves of the CH<sub>2</sub>BrI (left) and CH<sub>2</sub>ClI (right) molecules as a function of the C-I distance, considering the relaxed planar geometry of the CH<sub>2</sub>X co-fragment. The regions of the avoided crossing are marked by the black circles, are enlarged in the insets. The figures are taken from Ref. [186].

Bromiodomethane and chloriodomethane have two different carbon-halogen bonds, and the predominant cleavage of one stronger bond under a specific light wavelength is an excellent example for investigating bond selectivity upon electronic excitation. Therefore, these molecules can be considered prototypes for photochemistry bond-selective electronic excitation. Butler *et al.* [187] showed that the excitation of CH<sub>2</sub>BrI at wavelengths close to the peak of the A-band results predominantly in the C–I dissociation, with a lower contribution of the C–Br bond dissociation. In contrast, they observed that the scenario changes to a prevailing C–Br bond dissociation at 210 nm (known as A'-band), where the experimental results showed the C–Br bond's selective breaking and no C–I bond cleavage. Minor dissociation channels were observed at A'-band, leading to a concerted elimination of IBr and a three-body fragmentation CH<sub>2</sub> + Br + I at this excitation wavelength. Photoabsorption at 193 nm corresponds to the excitation to the B-band and IBr molecular halogen production by concerted elimination. The elimination channel is attributed to long-living molecular Rydberg states [187].

These dihalomethanes are categorized as C<sub>s</sub> symmetry molecules with less symmetry and more complex electronic structures than the C<sub>3v</sub> symmetry CH<sub>3</sub>I. These electronic structures and the spin-orbit interactions due to heavy halogen atoms give rise to fascinating dynamical properties. In this regard, the <sup>3</sup>Q<sub>0</sub> state in C<sub>3v</sub> symmetry transforms into the 4A' state in C<sub>s</sub> symmetry, while the doubly degenerated <sup>3</sup>Q<sub>1</sub> and <sup>1</sup>Q<sub>1</sub> states split into the 3A' and 2A'' and the 4A'' and 5A' states, respectively. In C<sub>s</sub> symmetry, A' electronic states are characterized by a transition dipole moment in the X–C–Y plane, while for A'' states, it is perpendicular to that plane [185], [186]. The conical intersection in this symmetry is turned into an avoided crossing. Like the CH<sub>3</sub>I molecule, the 4A' excited state correlates to the I\*(<sup>2</sup>P<sub>1/2</sub>) formation in a diabatic representation, while an avoided crossing between the 4A' and 5A' states may lead to I(<sup>2</sup>P<sub>1/2</sub>). The X–C–I plane (X=Cl or Br) is located in the X–Y plane and the Y-axis along the C–I bond. With the symmetry features, the 2A'' and 4A'' excited states are characterized by a TDM perpendicular to the X–C–I plane. In contrast, the 3A', 4A', 5A' excited states are attributed to TDMs in the plane at a certain angle with respect to the C–I bond, in contrast to CH<sub>3</sub>I, where electronic states are characterized by TDMs completely parallel or perpendicular to the C–I bond.

By increasing the mass of the halogen atom in the dihalomethanes, the contribution of the 4A' excited state decreases with the increase in the transitions to the [4A'', 5A'] states. As mentioned in the last section, in CH<sub>3</sub>I, the predominant absorption to the <sup>3</sup>Q<sub>0</sub> state is due to the coupling with

different singlet electronic states by the agency of the strong spin-orbit interaction. In the dihalomethanes discussed here, this coupling seems not as effective as in iodomethane and, consequently, leads to a lower excitation of the 4A' state. The heavier the second halogen, the lower excitation of the 4A' state. Fig. 2.12 [186] shows the computed adiabatic PECs of the two dihalomethanes as a function of the C–I bond distance. The I channel correlates with the excitation to the [2A'', 3A'], 4A'', and 4A', while the I\* dissociation limit is correlated with the 5A' and 6A' excited states. The insets show an avoided crossing between the 4A' and 5A' states close to the Franck-Condon region. In the non-adiabatic representation, the excitation to the 4A' state leads directly to the I\* channel, while the I formation via an avoided crossing competes with the direct dissociation through the 5A' or 4A'' states. The electronic structure is similar irrespective of the halogen-atom substitution.

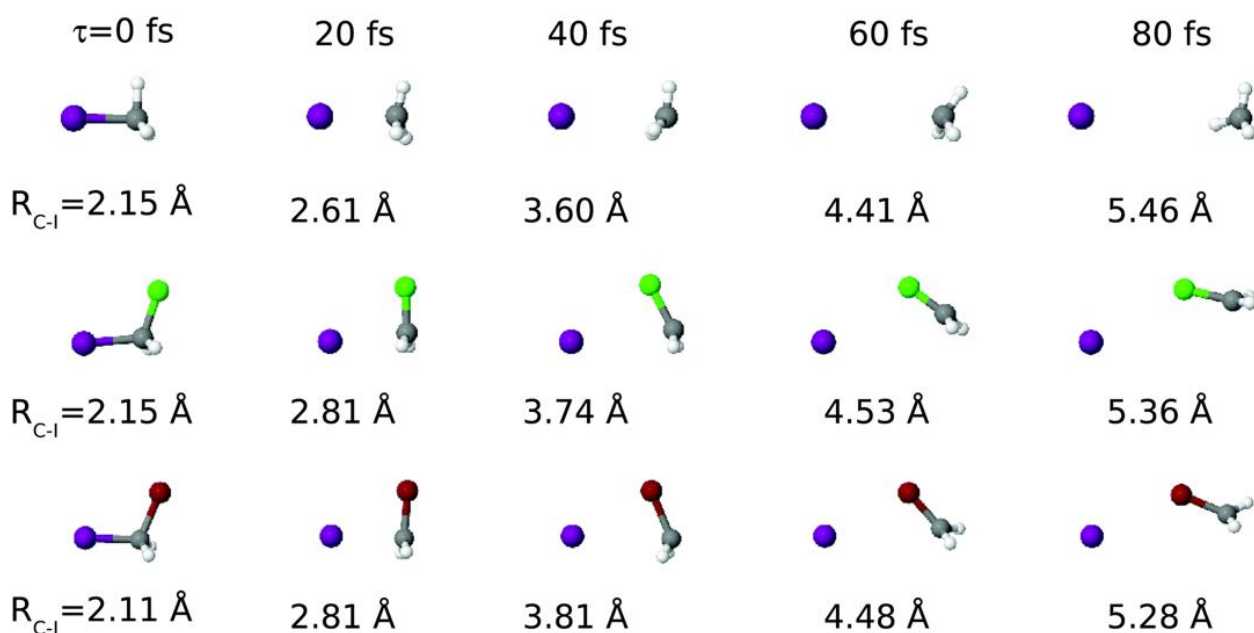


**Figure 2.13.** Snapshots of CH<sub>3</sub>I, CH<sub>2</sub>ICl and CH<sub>2</sub>BrI dissociation. The delay time  $\tau$  and the C–I distance are indicated in each frame. At time zero, the C–I distance is at the equilibrium distance of the molecule. The figure is adapted from Ref. [186]

With respect to C–I bond dissociation, CH<sub>3</sub>I, to a large extent, behaves as a quasi-diatomic molecule. After photoabsorption in the A-band, it promptly dissociates, and the majority of the excess energy turns into translational energy of the products. In contrast, the initial steps of the bond cleavage process for both dihalomethanes are dominated by a significant induced rotational

motion of the radical co-fragments due to an "anchor" effect of the halogen atom (Cl or Br). Since the dissociation does not occur along the axis connecting the centers-of-mass of both fragments, the radical co-fragment experiences a significant torque, and the energy partitioning into its rotation is very efficient, reducing the I fragment's translational energy. Murillo-Sanchez et al. [186] also did on-the-fly adiabatic full-dimension classical trajectory calculations, including surface hopping. The snapshots corresponding to selected trajectories are shown for  $\text{CH}_3\text{I}$ ,  $\text{CH}_2\text{BrI}$  and  $\text{CH}_2\text{ICI}$  in Fig. 2.12. The A-band photodissociation dynamics appear to be consistent with a qualitative description within an impulsive semi-rigid radical model with the  $\text{CH}_2\text{Br}$  radical changing to a more planar structure. A signature of the fragment rotation in the photodissociation of a dihalomethane ( $\text{CH}_2\text{I}_2$ ) has already been observed in earlier ultrafast electron diffraction (UED) measurements [53]. They started with reasonably well-defined geometry and observed rotational motion once it was aligned to the polarization direction set parallel to the detector plane.

The experimental results of Butler et al. [187] showed other interesting dynamical properties. Their results suggest that the C-Br bond cleavage is a minor channel at the A-band dissociation. They did not see any sign of channels where H is making new bonds with I or Br. So the channels of  $\text{CHI} + \text{HBr}$  and  $\text{CHBr} + \text{HI}$  were absent. More importantly, the molecular halogen elimination channel ( $\text{CH}_2 + \text{BrI}$ ) was extremely weak.

Moreover, the  $\text{CH}_2\text{Br}$  and  $\text{CH}_2\text{I}$  products after the C-I or C-Br bond dissociation in the A-band cannot have enough internal energy to dissociate spontaneously, such that its secondary dissociation can occur only via absorption of another photon. Overall, the energy threshold for the three-body breakup, direct or step-wise, was reported to be 5.66 eV [187], [188]. That means that for a three-body dissociation channel to happen, we need at least two-photon absorption to make this reaction possible at 263 nm. At shorter wavelengths, single-photon three-body dissociation becomes energetically accessible. Following the Butler et al. observations, depending on the photoexcitation wavelength, the weighting factor of each individual reaction channel could be different. The results show that while IBr elimination is negligible at the origin of the A-band, it becomes a minor channel 210 nm and going down in the wavelength to 193 nm, it turns out to be the dominant channel. Therefore, the photodissociation pathways of dihalomethanes were also found to be critically sensitive to the electronic nature of the initial excitation. The comparison of the photodissociation of dihalomethanes resulting in C-I and C-Br (or C-Cl) bond cleavage at 266 and 215 nm, and upon Rydberg states excitation at 193 nm highlight bond selectivity of

photodissociation. It is worth mentioning that identifying all the primary dissociation channels of  $\text{CH}_2\text{BrI}$  excited via absorption of a 193 nm photon is complicated because the photon energy is greater than the threshold energy of the three-body dissociation channel  $\text{CH}_2 + \text{Br} + \text{I}$ .

At certain wavelengths, there is also the possibility of forming a linear isomer [189], [190], as shown in Fig. 2.14, followed by either ejection of one halogen or  $\text{BrI}$  formation. There has been a long debate on how the halogen-halogen bonds are formed. A theoretical claim states that this process partly appears through a short-lived intermediate state with a linear geometry at first, which could be followed by either ejection of one halogen or molecular halogen formation, which confirms that this reaction could happen. Depending on the timescales for isomerization and the relative stabilities of the isomers, it may be possible to observe these structures shortly in time-resolved experiments. For  $\text{CH}_2\text{I}_2$ , the isomers may be stable for ~100-150 fs before dissociation [191]–[193].

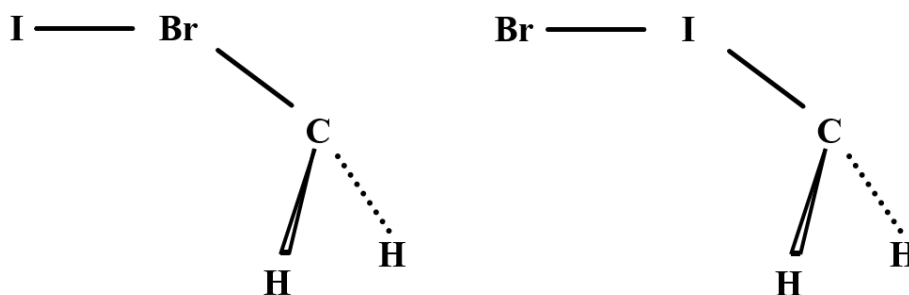


**Figure 2.14.** Schematic diagrams depicting the equilibrium geometries of (left) the ground state of iso- $\text{CH}_2\text{Br-I}$  and (right) the ground state of iso- $\text{CH}_2\text{I-Br}$ . Adapted from Ref. [189]

Several bound excited states correlating with an upper limit at around 6.2 eV are observed at higher energy excitation corresponding to the A'-band. In particular, transitions from the ground state to the  $8\text{A}''$ ,  $9\text{A}'$ , and  $10\text{A}''$  states indeed correspond to this band. Fig. 2.15 shows the potential energy curves as a function of the C–Br internuclear distance. Considering that the A-band is associated with the C–I bond cleavage, and the A'-band corresponds to the C–Br bond cleavage, the production of Br and  $\text{Br}^*$  atoms at 266 nm is explained if an avoided crossing is produced between the excited states corresponding to both bands [186]. In a diabatic representation, direct dissociation of the  $9\text{A}'$  excited state is expected to lead to the Br or  $\text{Br}^*$  channels.

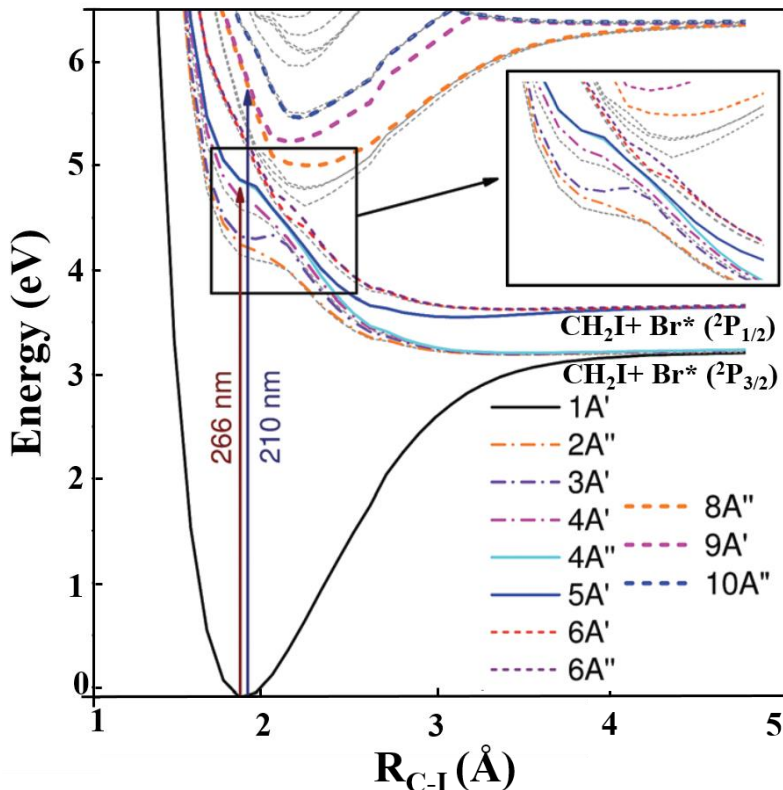


**Figure 2.15.** Computed PECs for  $\text{CH}_2\text{BrI}$  as a function of the C–Br distance. The inset shows the avoided crossing region. The figure is adapted from Ref. [186].

## 2.4 Principles of Coulomb explosion imaging (CEI)

In the experimental work presented in this thesis, we used CEI to directly probe the dissociation dynamics of halomethanes using multiple ionization by intense NIR laser pulses. As briefly mentioned in Chapter 1, typical laser interaction with a molecule strips off the least-bound valence electrons to form a collection of ionic fragments and neutral partners. The resulting process of rapid fragmentation and mutual separation between the charged fragments occurs due to the strong Coulomb repulsion. The ionic fragments can contain geometric and, if measured as a function of pump-probe delay in a time-resolved experiment, also dynamic information about the original system. To obtain the molecule's structural and dynamical properties using CEI, the ionization and the ensuing fragmentation must be swift so that it does not undergo a significant structural change from its equilibrium position. Suppose the ionization process occurs on a much smaller time scale than nuclear motion. In this case, the momenta of the fragment ions can be used to extract

geometrical information of the molecule prior to the Coulomb explosion. It is worth mentioning that both pulses interact with the molecule in a pump-probe experiment but fundamentally in different ways. We use a relatively low-intensity pump pulse to avoid ionization. In contrast, the NIR probe pulse is much more intense to induce multi-photon ionization.

The Coulombic repulsion between the ionized fragments overcomes the attractive force between them. For a diatomic molecule (or, more generally, for a two-body breakup), the Coulomb force depends on the mutual distance between the charges, and the Coulomb energy takes the form

$$E (r_{12}) = \frac{1}{4\pi\epsilon_0} \frac{q_1 q_2}{r_{12}}. \quad 2.17$$

Here,  $q_1$  and  $q_2$  are the charges on the fragments and  $r_{12}$  is the separation between the fragments. For three charged fragments, the energy depends on the relative positions of the three fragments. Accordingly, the total Coulombic energy can be expressed as a function of three distances.

$$E (r_{12}, r_{23}, r_{13}) = \frac{1}{4\pi\epsilon_0} \left[ \frac{q_1 q_2}{r_{12}} + \frac{q_2 q_3}{r_{23}} + \frac{q_1 q_3}{r_{13}} \right]. \quad 2.18$$

The measured KER is not unique to the initial geometry; hence, the energy cannot directly measure the structure. The momenta imparted on the atomic species provides information on the structure. In a coincident CEI experiment, the 3-D asymptotic momentum vectors  $\vec{p}_k$  for each ion are measured. Under the assumptions of instantaneous ionization and purely-Coulombic final-state PESs, the measured momenta and the Coulomb forces are related through the equations below, which connect the momentum measurements to the absolute geometries denoted by position vectors in the real space  $\{\vec{r}_k\}$ .

$$\vec{p}_{kl} = \sum_{k \neq l}^{n_{ions}} \int_0^\infty \vec{F}_{kl}(t) dt \quad 2.19$$

$$\vec{F}_{kl} = \frac{1}{4\pi\epsilon_0} \left( \frac{q_k q_l}{|\vec{r}_k(t) - \vec{r}_l(t)|^2} \right) \quad 2.20$$

It should be noted that the first equation is not invertible, and there could be degeneracies in such a way that two different sets of position vectors end up into the same momentum vectors. Consequently, for the CEI to explicitly measure the geometries, further information is required either with momentum simulations or geometry reconstruction.

The trajectories of the ion fragments could be modeled with a coupled set of nonlinear ordinary differential equations arising from their mutual Coulomb repulsion force. Newton's

equation of motion determines the motion of the ionic fragments, which gives the time-dependent position, velocity and acceleration vectors.

As mentioned above, to simulate a Coulomb explosion of the molecule, we use several simplifying assumptions that will allow us to make a simple picture of the fragmentation. First, we assume that the chemical bonds are broken instantaneously at  $t=0$ , and the motion of the ions is governed only by their mutual Coulomb repulsion. Therefore, the molecular bonds do not affect the ion trajectories, and that neutral fragments do not interact with any other fragment. Second, the constituents are considered localized point-charged particles charged at  $t=0$  without redistribution. Third, it is supposed that the molecule starts at equilibrium geometry, and the initial nuclear positions are determined from the ground-state geometry of the molecule. Altogether, with these assumptions, we neglect the rearrangement of the atoms under the influence of the intense electromagnetic field of the laser pulse and the inevitable momentum imparted on the atoms at the initial moment of this interaction. Under such assumptions, we can solve the classical equations of motion for each ion right after the explosion. Classical trajectory calculations are performed using well-defined routines such as the Runge-Kutta method, beginning with a set of known geometries. In this approach, the geometries are obtained by comparing the calculated and measured asymptotic momenta and evaluated to ascertain the uniqueness of the geometry. This approach minimizes the difference between calculated and measured momenta in geometry reconstruction.

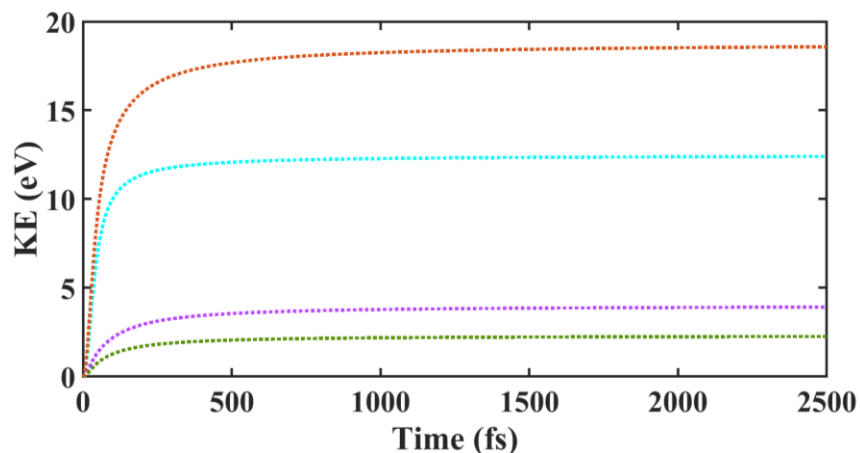


**Figure 2.16.** Classical Coulomb explosion simulation of  $\text{CH}_2\text{BrI}$ . The time evolution of the individual fragments KE and total KER distributions for a  $\text{CH}_2\text{BrI}$  molecule that fragments into singly-charged  $\text{CH}_2$ , Br, and I fragment starting from the equilibrium geometry of the neutral molecule.

We used this numerical algorithm provided by MATLAB to calculate the momentum vectors and kinetic energies of all fragments for a pure Coulombic interaction between the charges for the static case, to map the reaction pathways in a sense to track what the probe pulse exclusively does on the molecule. Coulomb explosion stimulation (CES) gives us all kinematic information, including nuclear position and velocity of the fragments from which we can extract their momenta and kinetic energies. In addition, the correlation angles can also be calculated between fragment momenta from the momentum vectors of those simulated fragments. One further step deals with the time evolution of the molecular structures connecting intermediate geometries, which will be introduced later in this chapter and presented for the  $\text{CH}_3\text{I}$  molecule in Chapter 4 and  $\text{CH}_2\text{BrI}$  in Chapter 5.

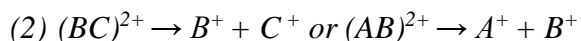
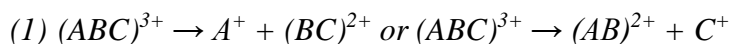
For static stimulations, we begin with two specific geometries; the neutral molecule's equilibrium geometry and the linearized geometry of the isomer. For both cases, we assume that the charges are localized on atomic fragments or on the center of masses of the molecular fragments detected in coincidence measurements. Then we numerically solve the coupled classical equations of motion using standard Runge-Kutta integration, where the positions and velocities are used to calculate the momentum vectors of the ionic fragments. These momentum vectors are then used to calculate different observables in different representations in the following chapters. As an illustration, Fig. 2.16 shows the three-body Coulomb explosion of the  $\text{CH}_2\text{BrI}$  molecule where the total kinetic energy release (KER) and the individual kinetic energies are obtained as a function of propagation time. Here, in this simulation, the ions are tracked in the propagation of 2.5 ps.

The fundamental assumptions used in CEI work better for the ionization of the dissociated molecules, where the atoms are far apart, and for the ionization to the higher-charged states that are essentially purely Coulombic. Thus, they are not necessarily rational assumptions for the ionization of a bound molecule to the doubly or triply-charged final state, where the PESs often deviate from the purely Coulombic and sometimes even have bound character. On the other hand, CEI has further shortcomings if ionization to highly-charged states with intense laser pulses is employed because of potential nuclear motion during ionization. For example, the leading edge of the pulse can singly ionize the molecule while further ionization might occur later, and during this time, the molecular geometry might have been changed. Nevertheless, despite these shortcomings,

CEI has been efficiently used to image the dynamics of many important reactions presented, e.g., in [68], [194], [195].

The CEI discussion above assumes that a multiply ionized molecule rapidly breaks up into the final fragments. This is often called a concerted fragmentation mechanism. There is an alternative scenario known as sequential fragmentation for breakup channels involving three or more particles. This term normally refers to two or more successive and independent dissociation reactions.

For an exemplary triatomic molecule, ABC in the triply-charged final state, the two dissociation steps could be defined as:



During the time between the cleavage of the two bonds, the intermediate metastable moiety  $(BC)^{2+}$  or  $(AB)^{2+}$  can rotate. This rotation represents a complete breakdown of the axial recoil approximation and, thus, is incompatible with the main concept of CEI since any information about the initial molecular structure is lost. At the same time, this rotation provides a signature allowing sequential fragmentation to be discerned from concerted fragmentation in the measured coincidence momentum patterns [110].

Identification of the sequential from concerted three-body fragmentation processes has been an objective of many studies [89], [111]. The coincident three-dimensional momentum imaging of the resulting fragments is practical to discern sequential from concerted fragmentation and disentangling different reaction paths. Recently, a novel method for such channel separation based on the so-called “Native Frames” analysis has been developed [110], [111]. A specific example of such separation for the  $\text{CH}_2\text{BrI}$  molecule will be discussed in Chapter 5.

For three-body CEI, there exist many possible representations of the coincident experimental data. In the following, we will present the results of the CES for some common representations, which will be used to present the results throughout this thesis. All of the simulations presented here assume the concerted breakup of the molecule.

Unlike the two-body breakup, in which the internuclear distance and the absolute orientation of the molecular axis in the laboratory frame are the only determining factors defining the outcome of the CEI experiment, and the two fragments always fly back to back because of the momentum conservation, in three-body fragmentation processes, the angle between the ejected

fragments is also essential. Therefore, an informative representation could be plotting the KER distribution versus the angle between the momentum vectors of the two detected fragments. For an example of the CH<sub>2</sub>BrI molecule, this could be the angle between the second (bromine) and third (iodine) detected ions:

$$\theta = \cos^{-1} \left[ \frac{\vec{P}_{(2)} \cdot \vec{P}_{(3)}}{|\vec{P}_{(2)}| |\vec{P}_{(3)}|} \right], \quad 2.21$$

where  $\vec{P}_{(i)}$  are the individual momentum vectors, and the numbering reflects the order in which the corresponding ions hit the detector.

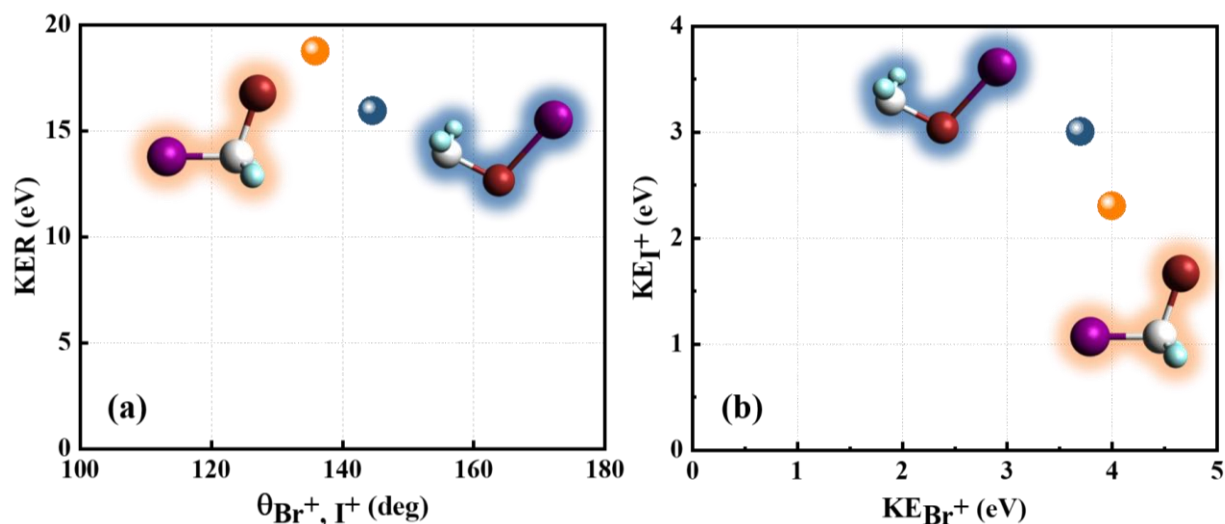


**Figure 2.17.** CES for the two equilibrium and linear isomer geometries. (a) KER- $\theta$  plot and (b) KE sharing between the Br and I fragments in the three-body breakup of CH<sub>2</sub><sup>+</sup> + Br<sup>+</sup> + I<sup>+</sup>. The orange and blue circles show the results of the CES for the equilibrium geometry and the isomer.

Results of a static CES for the equilibrium and the linearized isomer geometries for this molecule are shown in the form of three-body representations in Fig. 2.17. The simulated KEs and the KER and angles appear as data points that could be compared with the experimental results. The results for the isomer clearly differ from the primary geometry, manifesting somewhat smaller KER and a larger angle between the I and Br momenta (a). In addition, the simulation for the energy sharing between the two heavier fragments is shown in Fig. 2.17 (b), suggesting that in this three-body channel, Br takes the larger share of energy. These representations are helpful and complete a part of the puzzle but lack pieces of information necessary to make a uniform and

consistent picture of the photochemical reactions by generalizing the plots to include all pairwise energy and momentum correlations.

One of the conventional representations to illustrate the vector correlation of the dissociated fragments is the Newton diagram, which represents the momentum vectors of each fragment in the coordinate frame defined by the momenta of the two of them. Because of the momentum conservation, all three momentum vectors must lie in the same plane (defined as the x-y plane). We can assign the +Px to either of the fragments' momentum vectors in the Newton diagram. Then the second fragment defines the +Py half-plane, and eventually, the third fragment would be assigned to the -Py half-plane. Each momentum component is then converted as follows:

$$\begin{aligned}
 P_{1x} &= P_1 & P_{1y} &= 0 \\
 P_{2x} &= P_2 \cos \varphi_2 = m_2 \frac{\vec{v}_1 \cdot \vec{v}_2}{|\vec{v}_1|} & P_{2y} &= P_2 \sin \varphi_2 = \sqrt{P_2^2 - P_{2x}^2} \\
 P_{3x} &= P_3 \cos \varphi_3 = m_3 \frac{\vec{v}_1 \cdot \vec{v}_3}{|\vec{v}_1|} & P_{3y} &= P_3 \sin \varphi_3 = \sqrt{P_3^2 - P_{3x}^2}
 \end{aligned}$$

where  $\varphi_i$  is the angle of the individual momentum vectors with respect to +X direction. Consequently, the momentum distributions of all three fragments are contained in one diagram while one axis is fixed in space.

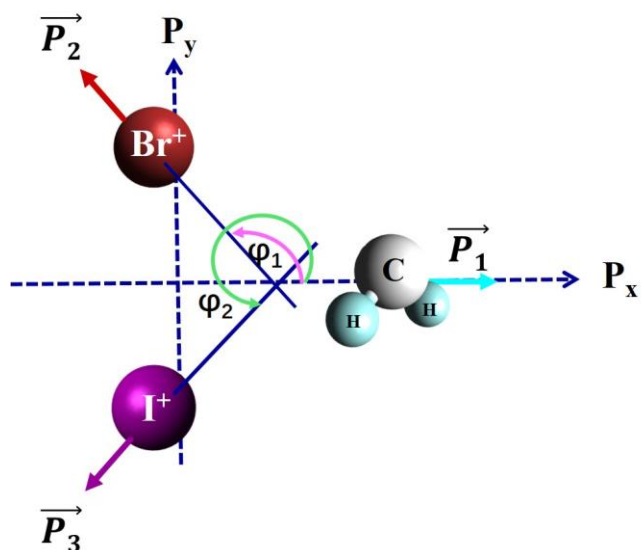


**Figure 2.18.** Schematic of Newton diagram displaying the fragments' momenta and angles.

The schematic of the fragment momenta and angles are shown in Fig. 2.18, and the procedure is illustrated in Fig. 2.19 for the  $\text{CH}_2\text{BrI}$  molecule, where the  $\text{CH}_2^+$  momentum pointing in the +X direction is taken as a reference. The relative momentum vectors of the second and third fragments

( $\text{Br}^+$  and  $\text{I}^+$ , respectively) are displayed with respect to that reference in the upper and lower half-planes. For example, the Newton diagrams calculated from the outcome of the CES for the equilibrium and isomer geometries of  $\text{CH}_2\text{BrI}$  are shown in Fig. 2.18. In this diagram, the momentum of the reference fragment has been normalized to one.

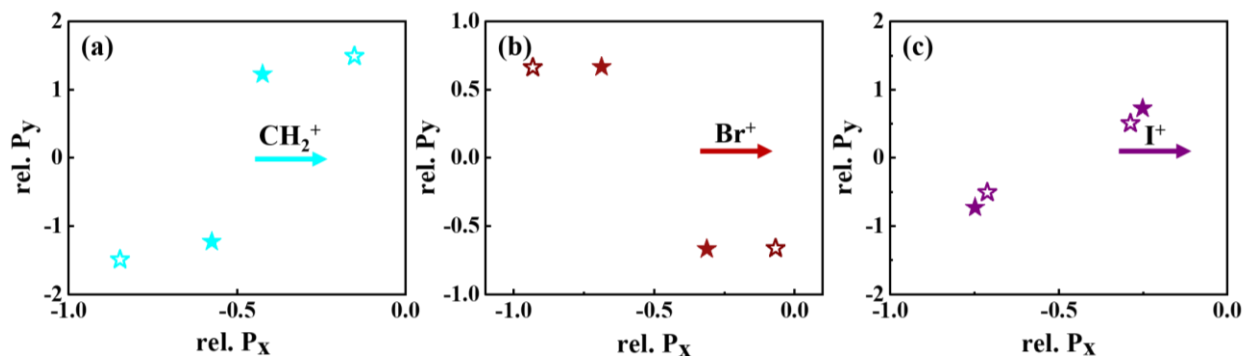


**Figure 2.19.** Simulated momentum correlation obtained from a classical Coulomb simulation. The results for the concerted breakup start from equilibrium (solid asterisk) and isomer geometry (open asterisk). (a) Newton diagrams with taking the  $\text{CH}_2^+$  fragment as reference ion, and the momenta of the  $\text{Br}^+$  and  $\text{I}^+$  fragment ions are plotted in the upper and lower half, respectively. (b) Same plot but with the  $\text{Br}^+$  fragment as a reference ion. (c) Same plot but with the  $\text{I}^+$  fragment as a reference ion.

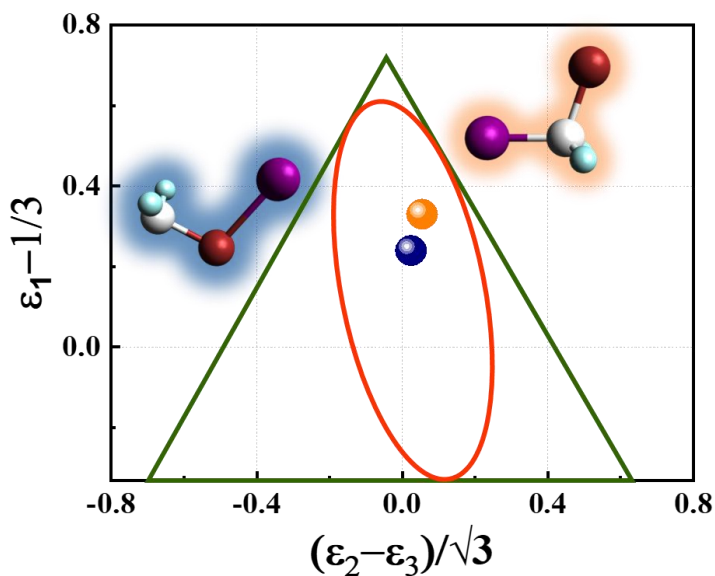


**Figure 2.20.** Simulated momentum energy obtained from a classical Coulomb simulation for the concerted breakup starting from equilibrium and isomer geometry in the Dalitz plot representation.

Another representation universally used in the three-body breakup analysis is the Dalitz plot, which shows the energy correlation of all three fragments. This representation is based on the reduced energy of fragments in the molecular frame defined as  $\varepsilon_i = E_i/\text{KER}$ , where  $\varepsilon_i$  is the energy of the individual fragments after the breakup, with the total reduced energy normalized to 1 ( $\sum \varepsilon_i = 1$ ). The axes of the Dalitz plots are defined by differences in the particles' reduced energies.

$$X = \frac{\varepsilon_2 - \varepsilon_3}{\sqrt{3}} \quad 2.22$$

$$Y = \varepsilon_1 - 1/3 \quad 2.23$$

The Dalitz plot constructs a triangle with an enclosed ellipse with this approach. All the events within the triangle satisfy the energy conservation, while from those only the events located in the ellipse satisfy the momentum conservation. The shape of the Dalitz plot depends on the fragments' masses. The triangle sides correspond to the dissociation reactions where the molecular geometry is getting a linear shape. Due to the momentum conservation between the fragments, the kinetic energy is distributed inside the ellipse. In this plot, regions with high incidence represent which fragment receives more kinetic energy after the fragmentation. The simulated momentum energy correlations are obtained from a classical Coulomb simulation for the concerted breakup starting from equilibrium and isomer geometry shown in Fig. 2.19.

## Chapter 3 - Experimental methods

The central focus of this thesis is to investigate the photo-induced dynamics in halomethanes triggered by photoexcitation in the UV domain at two different wavelengths corresponding to the third and fourth harmonics of the output of a NIR Ti: Sapphire laser with a central wavelength of 790 nm. We use a laser system known as PULSAR operated at the James R. Macdonald Laboratory, which is described in Ref. [196]. The primary technical development in this work involves the generation and compression of the UV pulses at these two wavelengths. These developments made the studies of the dissociation dynamics in halomethanes (discussed in detail in Chapter 2) with sufficiently high temporal resolution feasible. In our time-resolved experiments, the UV-induced photodissociation dynamics are probed via strong-field ionization and CEI (see Section 2.4). In order to get the 3D kinematic information of the fragmentation channels, the femtosecond pump-probe experiment is coupled to an ion momentum imaging apparatus, where the ion-ion coincidence events are recorded event by event. This is realized by utilizing a standard COLd Target Recoil Ion Momentum Spectrometer (COLTRIMS). This spectrometer is equipped with a supersonic gas jet to provide a cold target with time- and position-sensitive detectors to record the ions created by laser-molecule interactions. The following chapter describes in detail the optical setup and the ion imaging apparatus used in our experiments. The details of the laser pump-probe setup are discussed first, followed by the description of the COLTRIMS machine.

### 3.1 Ultrafast laser system; chirped pulse amplification

This section gives a brief overview of the primary laser system used for producing ultrashort laser pulses for the time-resolved experiments described in the present thesis. The laser system is located in the James R. Macdonald Laboratory (JRML) and is called PULSAR: Prairie Ultrafast Light Source for Attosecond Research. This laser is based on a Ti: sapphire oscillator and a Ti: Sapphire two-staged multi-pass amplifier [197]–[199] that produces linearly p-polarized 2 mJ pulses at 10 kHz and 23 fs (FWHM in intensity) pulse duration with a central wavelength around 790 nm. The coincidence experiments described here benefited from the relatively high repetition rate of PULSAR that allows experiments that would be unfeasible with lower rate laser systems. Further details of the laser system are described elsewhere [196].

The heart of the system is a Kerr-lens mode-locked Ti: Sapphire femtosecond oscillator [200]–[202] from KM Labs. A nonlinear titanium-doped sapphire lasing medium behaves as a lens for the laser beam with a Gaussian intensity profile. The crystal inside the laser cavity is optically pumped by a continuous-wave 532 nm diode-pumped solid-state, frequency-doubled Nd: Vanadate (Nd: YVO4) laser (Verdi laser). The mode-locking mechanism is the nonlinear optical Kerr effect, allowing high-intensity pulses to be supported in the cavity. While the gain bandwidth supports many cavity modes, ultrashort pulse generation is achieved through mode-locking. The otherwise random cavity modes are phase-locked to interfere constructively within a very short period, eventually producing ultrashort laser pulses with a repetition rate of 75.2 MHz and 300 mW power corresponding to 4 nJ pulse energy. A prism pair in the oscillator compensates for the group-velocity dispersion (GVD) and reduces the pulse duration to 14 fs in the oscillator.

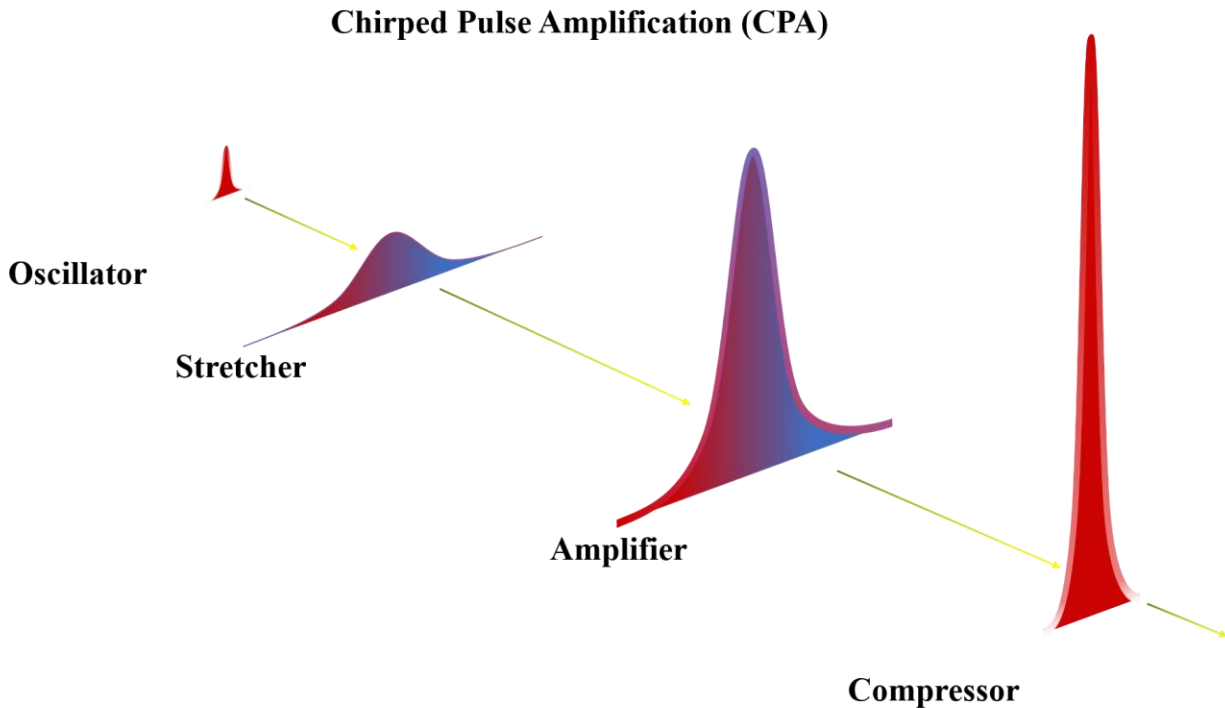


**Figure 3.1.** A schematic view of pulse duration and intensity evolution during chirped-pulse amplification (CPA). The figure is adapted from Ref. [203]

As a requisite for strong-field experiments, the pulse energy needs to be increased from nJ to a few mJ through multi-pass amplification. The chirped-pulse amplification (CPA) technique is employed to maintain the bandwidth and preclude damaging the amplifier [199], [204]. The

principle of CPA is illustrated in Fig 3.1. In the CPA technique, the oscillator's output is stretched to tens of picoseconds in a grating-based stretcher to avoid damage to the amplifier crystal. The repetition rate is reduced to 10 kHz following the stretcher using a Pockels cell [204], [205], and the multi-pass amplification system further amplifies only the reduced number of laser pulses. The oscillator's output is used to seed the multi-pass amplifier stage, pumped by a diode-pumped, intracavity frequency-doubled, Q-switched Nd: YLF laser. The first stage involves 14 passes through the Ti: Sapphire gain medium, after which the pulse energy is almost 1 mJ. The second amplification stage increases the pulse energy to about 2mJ in 5 passes through another Ti: Sapphire crystal. Finally, a grating-based compressor reverses the stretching process, resulting in about 23 fs (FWHM in intensity) pulses with high peak power. A typical spectrum of the output after the second amplification stage is shown in Fig. 3.2.

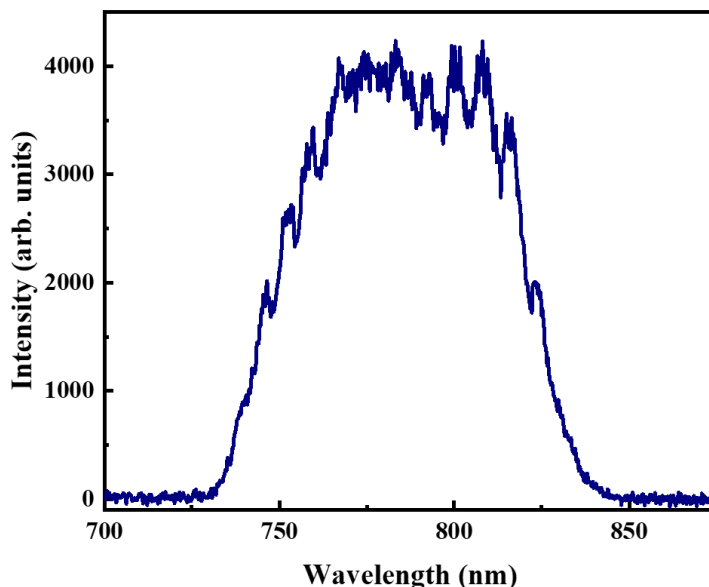


**Figure 3.2.** Typical PULSAR output spectrum after the second amplification stage.

### 3.2 Ultrafast pulse characterization

In order to follow ultrafast dynamics in photochemical reactions, we need to generate short pulses. The generation of the short-pulsed electric field is tied up with the control over the bandwidth and the phase. Laser parameters, i.e., pulse duration, phase, and chirp, can significantly impact the outcome of the experiments [206]. Therefore, the ultrashort pulses used in the experiments need to be characterized. Several techniques are employed to characterize

femtosecond pulses, where the basic principle is to reconstruct the laser's electric field. This section focuses on two methods used in our experiments: frequency-resolved optical gating (FROG) and cross-correlation frequency-resolved optical gating (XFROG) techniques.

Historically, ultrafast laser pulse measurements were made either in the time or frequency domains. The time-domain measurements were made using a technique called autocorrelation [207]. This method involves measuring the pulse by splitting it into two identical halves and delaying one of them. Both pulse replicas are focused on a rapidly responding nonlinear medium, resulting in a signal sent to the photodetector, which depends on the temporal overlap of the two pulses. This intensity of the signal denoted as  $I(\tau)$ , with  $\tau$  being the time-delay between the identical pulses, is given by equation

$$I(\tau) = \left| \int_{-\infty}^{+\infty} \varepsilon(t) \varepsilon(t-\tau) dt \right|^2. \quad 3.1$$

Here,  $\varepsilon(t)$  is the electric field of the pulse to be measured, and  $\varepsilon(t-\tau)$  is the time-delayed part of the pulse, also known as the “gate”. The bandwidth of the signal represents the pulse duration.

Typically, the intensity autocorrelation reveals very little information about the actual shape of the pulse. This ambiguity in the pulse shape arises because the autocorrelation is symmetric with respect to the delay, which could bring about unreliable measurements [208]. The spectrum analysis of the resulting signal provides preliminary information about the constituent frequencies of the pulse. However, this analysis lacks information on the chirp of the pulse and further details of its time-frequency structure. Therefore, a hybrid technique in the time-frequency domain is required to resolve this issue. In 1991, Trebino [206] showed that a spectrally resolved autocorrelation signal returns both the duration and phase of the ultrashort laser pulses developing a method called Frequency-Resolved Optical Gating (FROG) described below.

### 3.2.1 Frequency-resolved optical gating (FROG)

As mentioned above, information about the time-frequency profile of the electric field of the laser pulse can be obtained from a spectrally resolved autocorrelation signal. In other words, in this time-resolved measurement, one can measure the signal's spectrum resulting from the interaction of the two pulses in the nonlinear medium. This technique has the potential to fully determine the shape of an ultrafast laser pulse. There are various schemes of FROG for different particular applications, such as second harmonic generation (SHG-FROG) [209], polarization

gating (PG-FROG) [210], self-diffraction (SD-FROG) [211], and transient grating (TG-FROG) [212]. Here, we describe the SHG-FROG method, which was employed to characterize the PULSAR pulses and which uses the laser pulse to gate itself by splitting it into two identical copies and crossing them in an SHG BBO crystal. Therefore, the SHG-FROG setup resembles the intensity autocorrelation, except that the SHG signal is now frequency-resolved by a grating spectrometer. Consequently, equation 1 is adapted for the case where the signal is resolved in frequency, yielding the expression:

$$I^{SHG}(\omega, \tau) = \left| \int_{-\infty}^{+\infty} \varepsilon(t) \varepsilon(t-\tau) \exp(-i\omega t) dt \right|^2 \quad 3.2$$

$I^{SHG}(\omega, \tau)$  is called the FROG trace or the spectrogram of the autocorrelation; a 2D map of the pulse intensity as a function of time-delay and frequency, as shown in the inset of Fig. 3.3.

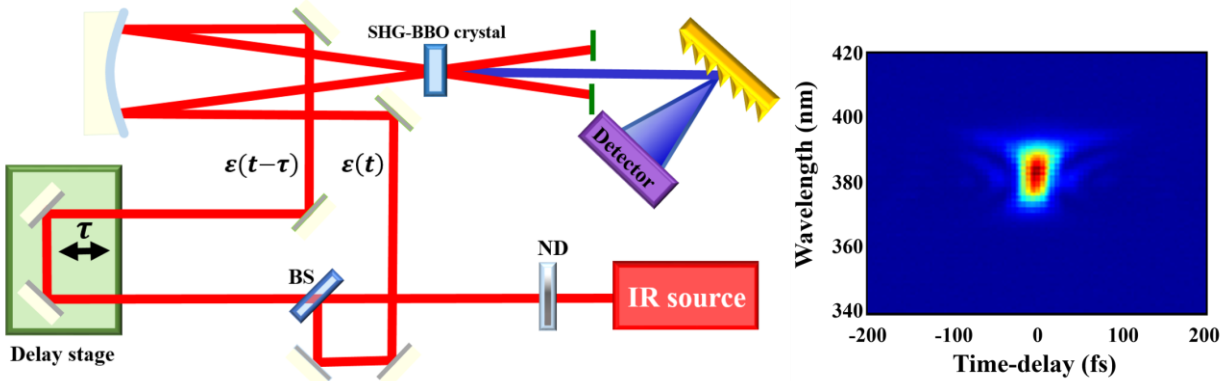


**Figure 3.3.** Schematic layout for a FROG apparatus. ND - neutral density filter, BS - beam splitter. The inset shows the measured signal.

Contrary to the intensity autocorrelation, which has a simple analytical method to analyze the measurement outcome, interpreting a FROG measurement requires an iterative deconvolution algorithm to reconstruct the electric field and to yield its magnitude and phase of the electric field [213], [214]. The reconstruction algorithm is initiated with a guessed electric field. The corresponding computed spectrogram is compared with the measured trace, and the electric field is iteratively changed until a spectrogram similar to the measured one is obtained. The optical layout of an SHG-FROG is shown in Fig. 3.3. The inset depicts a typical measured PULSAR FROG trace for a laser pulse with a central wavelength of 790 nm and a pulse duration of 23 fs FWHM in intensity.

A drawback of the SHG-FROG technique is that the algorithm does not give a unique solution. In addition, it cannot distinguish between a positively and negatively chirped-pulse; in other words, it is insensitive to the time inversion.

### 3.2.2 Cross-correlation frequency-resolved optical gating (XFROG)

In our experiments, we used an SHG-FROG to characterize the Ti: Sapphire laser pulse output. However, when the pulses are weak or the wavelengths lie in the ultraviolet region, the conventional FROG technique is inefficient. In order to address this issue, a method called the cross-correlation FROG (XFROG) technique was suggested, where a fully characterized intense laser pulse is used as the gate pulse, and the spectrogram is obtained through the nonlinear frequency conversion process in a nonlinear crystal [215]. It is worth mentioning that in pulse characterization methods based on the nonlinear process as in FROG and XFROG, due to the required nonlinear frequency mixing crystal, the minimum pulse duration that can be characterized is limited by the achievable phase-matched spectral bandwidth, the group velocity mismatch, the frequency conversion efficiency, the transparent spectral range of the crystal, and material dispersion-induced broadening of the pulses. These determining factors have severe effects in the deeper UV regions and hence play a more important role in the pulse duration measurement of the UV pulses than the NIP pulse.

XFROG technique gives the characterized electric field, and the gate pulse is no longer a half-split of the pulse to be measured. The gate pulse can be any known electric field, and with a difference-frequency generation (DFG) XFROG, even a weak ultrashort UV pulse can be characterized. Similar to eq. 3.2, the output signal in this method is therefore given by:

$$A^{XFROG}(\omega, \tau) = \left| \int_{-\infty}^{+\infty} \varepsilon(t) \varepsilon_g(t - \tau) \exp(-i\omega t) dt \right|^2, \quad 3.3$$

where  $\varepsilon_g$  is the gating field. Our experiment uses an SHG-FROG that gates the UV pulse with an intense NIR pulse that is already characterized by a FROG measurement, as explained in section 3.2.1. The resulting XFROG trace,  $A^{XFROG}$ , can be used with the known electric field of the gate pulse  $\varepsilon_g(t)$  to extract the UV pulse electric field  $\varepsilon(t)$  using a modified version of the retrieval algorithm we used for the SHG-FROG. In practice, we did not do this reconstruction and used the visual shape of the spectrogram to minimize the chirp and then obtained the UV pulse duration using the definition of the FWHM of the cross-correlation.

$$\tau_{uv} = \sqrt{\tau_{XC}^2 - \tau_{NIR}^2} \quad 3.4$$

where  $\tau_{UV}$ ,  $\tau_{NIR}$ , and  $\tau_{XC}$  are the FWHM of the UV, NIR and the cross-correlation of the two pulses.

### 3.3 New frequency component generations using intense femtosecond laser

We need both NIR and UV wavelengths for the time-resolved experiments described in this thesis. One of the most straightforward approaches to generating UV pulses is nonlinear frequency conversion. The fundamentals of these processes are described in this section.

#### 3.3.1 Introduction to nonlinear optics

Nonlinear optics deal with modifying the optical properties of a material system by the presence of light. Nonlinear optical phenomena are "nonlinear" in the sense that the response of a material system to an applied optical field depends on a nonlinear relation with the strength of the optical field. During the interaction of the laser field with the matter, the electric field  $\epsilon$  exerts Lorentz force  $F$  on the charged particles  $q$  in the medium. This force accelerates the charges, which leads to the radiation of the new field [216], [217].

$$F = q (\epsilon + V \times B) \quad 3.5$$

where  $B$  is the magnetic field. Given that the electrons are significantly less massive than the ions, they are accelerated more and therefore mainly responsible for the new fields generated in the medium. The ions move much slower than the speed of light, and hence the magnetic field component of the Lorentz force would be negligible [216], [217]. We simplify the math with the scalar quantities by assuming linearly polarized fields in the X-direction. The resulting force on the electrons is

$$F_x = -e\epsilon_x. \quad 3.6$$

As a consequence, the electron oscillates around the equilibrium position. An anharmonic potential, which binds the electron, is written as a Taylor series with respect to the equilibrium position  $x = 0$ :

$$U(x) = U(0) + x \left. \frac{\partial U}{\partial x} \right|_{x \rightarrow 0} + \frac{x^2}{2} \left. \frac{\partial^2 U}{\partial x^2} \right|_{x \rightarrow 0} + \frac{x^3}{3} \left. \frac{\partial^3 U}{\partial x^3} \right|_{x \rightarrow 0} + \dots \quad 3.7$$

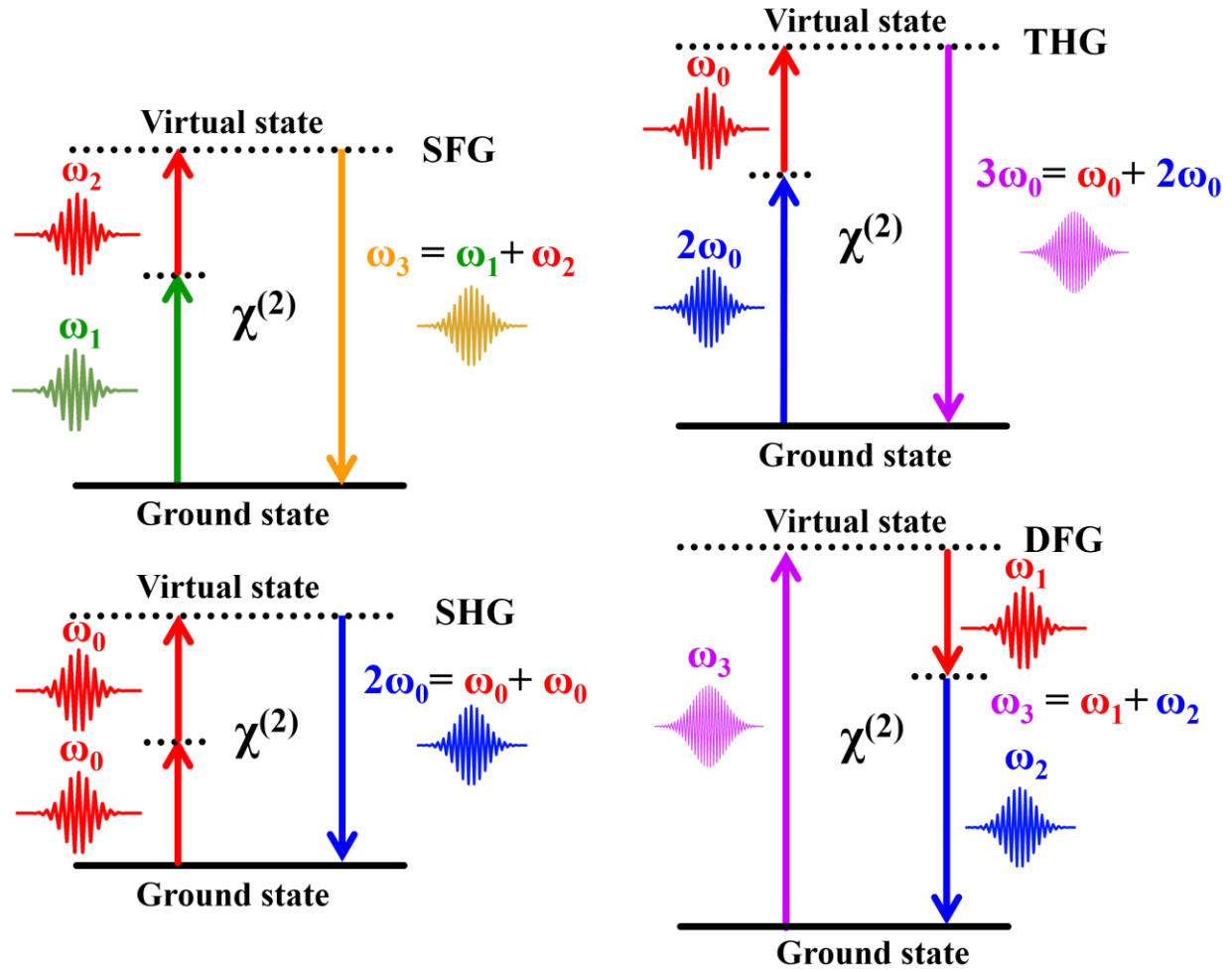


**Figure 3.4.** Nonlinear frequency mixing with a  $\chi^2$  nonlinear crystal. (a) Sum Frequency Generation (SFG). (b) Second Harmonic Generation (SHG), (c) Third Harmonic Generation (THG), and (d) Difference-Frequency Generation (DFG).

The first term in this equation is the linear contribution, and all following terms are nonlinear. The restoring force on the electrons in the potential given by

$$F = -\frac{\partial U}{\partial x}. \quad 3.8$$

Using this restoring force and force due to the electric field in the equation of motion for the electron, we can derive the displacement expression for the polarization. For such an oscillating dipole moment, we define the time-dependent polarization as the following

$$d(t) = -ex(t), \quad 3.9$$

where  $x(t)$  is the displacement of the electron. The polarization of a medium is a measure for the density of electric dipole moments:

$$P_x(t) = Nd(t) = -Nex(t), \quad 3.10$$

where  $N$  is the number density. Conventionally, the polarization is given as a function of the electric susceptibility of the medium [216]

$$P_x(t) = \varepsilon_0 \chi^{(1)} \varepsilon(t), \quad 3.11$$

Here,  $\varepsilon_0$  is the permittivity of the free space, and  $\chi^{(1)}$  is the material's susceptibility, which indicates the strength of the material's response to the applied electric field. Generally,  $\chi^{(1)}$  is a second-order tensor, but this coefficient is treated as a scalar here since we limit ourselves to the case of linear polarization. Once the electric field is applied, the electric charges oscillate and emit electromagnetic radiation. This polarization depends linearly on the field intensity at low intensities, and this linear relationship breaks down at high intensity. One can expand the polarization into higher orders of the electric field [217]

$$P_x(t) = \chi^{(1)}E + \chi^{(2)}E^2 + \chi^{(3)}E^3 + \dots \quad 3.12$$

where the first term corresponds to the linear polarization and the higher-order terms are the nonlinear parts of the polarization. The coefficients  $\chi^{(i)}$  are higher-order nonlinear optical susceptibilities. Maxwell's wave equation describes the propagation of the electric field in the medium [206]

$$\frac{\partial^2 \varepsilon_x}{\partial z^2} + \frac{1}{c^2} \frac{\partial^2 \varepsilon_x}{\partial t^2} = \mu_0 \frac{\partial^2 P_x}{\partial t^2} \quad 3.13$$

where  $\mu_0$  is the vacuum permeability. The source term on the right side of the equation describes the generation of new fields in the medium. Since the polarization is proportional to the electron displacement, its second partial derivative with respect to the time describes the electron acceleration. An oscillating term at a given frequency in polarization leads to a new field oscillating at this frequency. This property gives rise to sum- and difference-frequency generation explained in the following.

To study the implications of the wave equation, we consider circumstances in which the optical field in a second-order nonlinear medium has two frequency components in the form of [217]:

$$\varepsilon(t) = \varepsilon_1 e^{-i\omega_1 t} + \varepsilon_2 e^{-i\omega_2 t} + c.c \quad 3.14$$

where  $\varepsilon_1$  and  $\varepsilon_2$  are the amplitudes of the two frequency components of the electric fields with frequencies  $\omega_1$  and  $\omega_2$ , respectively. Inserting the electric field into the second-order contribution to the polarization expansion gives

$$P^{(2)}(t) = e_0\chi^{(2)}[\varepsilon_1^2 e^{-2i\omega_1 t} + \varepsilon_2^2 e^{-2i\omega_2 t} + 2\varepsilon_1\varepsilon_2 e^{-2i(\omega_1 + \omega_2)t} + 2\varepsilon_1\varepsilon_2^* e^{-2i(\omega_1 - \omega_2)t} + c.c.] + 2e_0\chi^{(2)}(\varepsilon_1\varepsilon_1^* + \varepsilon_2\varepsilon_2^*) \quad 3.15$$

This expression contains various frequency components of the polarization categorized as shown below:

$$P^{(2)}(t) \propto \varepsilon_1^2 + \varepsilon_2^2 + \varepsilon_1^2 e^{-2i\omega_1 t} + \varepsilon_2^2 e^{-2i\omega_2 t} + \varepsilon_1\varepsilon_2 e^{-2i(\omega_1 + \omega_2)t} + \varepsilon_1\varepsilon_2 e^{-2i(\omega_1 - \omega_2)t} \quad 3.16$$

The complex amplitudes of this expression represent various optical processes. The first two terms correspond to the optical rectification that consists of the generation of the DC polarization component. The third and fourth terms correspond to the second harmonic generation with twice the original frequency. The fifth is the sum-frequency generation (SFG), and the last is the difference-frequency generation (DFG). Several of these nonlinear processes that lead to a conversion of light frequencies are shown in Fig. 3.4.

An alternative approach to studying these nonlinear processes is using the laws of energy and momentum conservation and illustrating them with energy level diagrams in the photon picture. The photons can be mixed and split and eventually create new photons. For example, the SFG process involves mixing of two different frequencies of  $\omega_1$  and  $\omega_2$  and creating a new field with the sum frequency of  $\omega_1 + \omega_2$ . The energy and momentum conservation laws imply that

$$\hbar\omega_1 + \hbar\omega_2 = \hbar(\omega_1 + \omega_2) \quad 3.17$$

$$\hbar k_1 + \hbar k_2 = \hbar(k_1 + k_2) \quad 3.18$$

where  $k = \frac{n}{c}\omega$  is the wavenumber.

As we have seen so far, the SHG is a particular case of the SFG process where  $\omega_1 = \omega_2 = \omega_0$  and  $\varepsilon_1 + \varepsilon_2 = \varepsilon_0$  and the electric field and the polarization are

$$\varepsilon_x(t) = \varepsilon_0 e^{-i\omega_0 t} \quad 3.19$$

$$P^{(2)} = e_0\chi^{(2)}\varepsilon_x^2 = e_0\varepsilon_x^2\chi^{(2)} e^{-i2\omega_0 t} \quad 3.20$$

which shows that the new field oscillates with a frequency twice as large as the original one. The efficiency of this process depends on the phase matching and the value of the susceptibility. A significant aspect of frequency conversion is the efficiency of the process. The conversion

efficiency has been derived in [216], [217]. Plugging the electric field and polarization into Maxwell's wave equation for SHG results in the following coupled differential equations

$$\frac{\partial \varepsilon_{\omega_0}}{\partial z} = \frac{-i\omega\chi^{(2)}}{2cn(\omega_0)} \varepsilon_{\omega_0}^*(z) \varepsilon_{2\omega_0}(z) e^{-i\Delta kz} \quad 3.21$$

$$\frac{\partial \varepsilon_{2\omega_0}}{\partial z} = \frac{-i\omega\chi^{(2)}}{2cn(2\omega_0)} \varepsilon_{\omega_0}^2(z) e^{i\Delta kz} \quad 3.22$$

where  $\Delta k$  is the wavenumber mismatch. These two equations are typically solved numerically. With an assumption of the constant amplitude of the electric field and integrating the second equation over the crystal length, the SHG efficiency is obtained as

$$\eta_{SHG} = \frac{I_{2\omega_0}}{I_{\omega_0}} = \frac{2\pi^2(X^{(2)})^2 I_{\omega_0}(0)L^2 \text{sinc}^2\left(\frac{\Delta kL}{2}\right)}{\lambda^2 e_0 cn(\omega_0)^2 n(2\omega_0)} \quad 3.23$$

The efficiency is proportional to the pump intensity, implying that the efficiency is increased by increasing the laser power as far as the damage threshold of the crystal allows. In addition, the efficiency depends on the overlap of the fields across the medium. When  $\Delta k=0$ , the efficiency is maximum, known as the phase-matching condition. By propagation of the fundamental wave through the medium, its intensity drops, and the intensity of the generated wave drops as well. This conversion is efficient if the fundamental and the generated fields maintain the phase relation all the time through the length of the medium. However, the two waves generally travel at different velocities due to chromatic dispersion, resulting in a phase mismatch. One possible solution here is using birefringent crystals that ensure a constant refractive index and therefore a constant velocity for the frequencies. In these crystals, frequencies with different polarization experience different refractive indexes.

It is worth mentioning that for ultrashort laser pulses with significant bandwidth, the phase-matching condition is fully satisfied only for one wavelength. Therefore, a wide range of wavelengths must be phase-matched to make the conversion efficiency realistic and achieve proper mixing. This range of wavelengths is known as the phase-matching bandwidth. In nonlinear crystals, the laser pulses travel with the group velocity  $v_g$

$$v_g = \frac{\partial \omega}{\partial k} = \frac{\partial \omega}{\omega \partial n(\omega)} \quad 3.24$$

Even with the phase-matching condition and  $n(\omega) = n(2\omega)$ , since the derivatives are not identical, the pulses have different group velocities resulting in a velocity mismatch between them and a decrease in energy transfer. This time delay between the two pulses is obtained as

$$\Delta t = L \left| \frac{1}{v_g(2\omega)} - \frac{1}{v_g(\omega)} \right| \quad 3.25$$

Consequently, the phase-matching bandwidth of a Gaussian pulse is obtained using the time-bandwidth product [218]:

$$\Delta \nu = cL \frac{0.441\lambda_0^2}{\left| \frac{1}{v_g(2\omega)} - \frac{1}{v_g(\omega)} \right|} \quad 3.26$$

The phase-matching bandwidth and the conversion efficiency suggest that the crystal thickness compromises phase-matching bandwidth ( $\propto L^{-1}$ ) and the conversion efficiency ( $\propto L^2$ ).

### 3.3.2 New frequency generation

**Second Harmonic Generation (SHG):** SHG, like other nonlinear processes, requires a proper medium selection. As we saw, the second harmonic signal depends on the second-order susceptibility, which vanishes in a centrosymmetric medium. In this work, we used Barium Borate (BBO) for the sum-frequency generation process to generate the second, third, and fourth harmonic of the 790 nm Ti: Sapphire pulse. The basic principle of the new frequency generation is the phase-matching condition. Below, we will discuss each process separately.

The incident beam with a polarization perpendicular to the optical axis and the wavevector  $\vec{k}$  has an angle-dependent refractive index component  $n_o$ .  $n_o(\omega)$  is called the ordinary refractive index, and the beam propagating along this axis is called the ordinary. Any other polarization with an angle  $\theta$  with respect to the polarization direction experiences a different refractive index  $n_e(\omega, \theta)$ . Moreover, the beam along this axis is called extraordinary. There are two basic phase-matching schemes known as type 1 and type 2, depending on the polarization of the incident and the generated radiations. In our SHG, we use type 1 phase-matching, where the polarization of the incident beam is along the ordinary axis and experiences  $n_o(\omega)$ . Consequently, the generated second harmonic travels along the extraordinary axis in the plane containing the optical axis and the  $\vec{k}$  vector, and experience  $n_e(\omega, \theta)$ . Therefore, the phase-matching condition implies that:

$$\frac{n_{\omega_0}}{\lambda_{\omega_0}} + \frac{n_{\omega_0}}{\lambda_{\omega_0}} = \frac{n_{2\omega_0}}{\lambda_{2\omega_0}} \quad 3.27$$

This can be simplified to  $n(\omega_0) = n(2\omega_0)$ .

We used a type-I BBO crystal with a cut angle of  $29.2^\circ$  and a thickness of  $150 \mu\text{m}$ . To select the appropriate nonlinear crystals and model their performance with our pulse parameters, we used SNLO nonlinear optics software [219].

To achieve the phase-matching, we tuned the axis of the crystal to match the laser polarization direction. We achieved 35-42 % conversion efficiency in SHG.

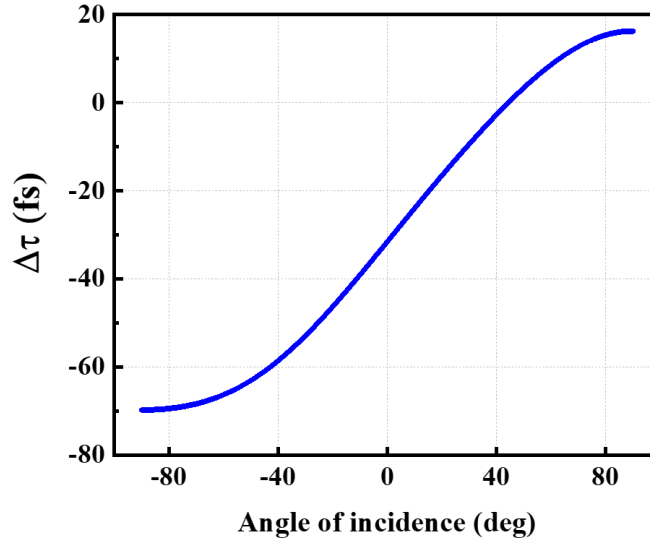


**Figure 3.5.** Time delay between the fundamental and second harmonic for a BBO crystal with  $150 \mu\text{m}$  thickness and  $29.2^\circ$  cut angle.

The time delay between the fundamental and the second harmonic pulses is calculated to be  $194 \text{ fs/mm}$  for a type-I BBO crystal with normal incidence [218]. We calculated the time delay for our [220] BBO crystal shown in Fig. 3.5 as a function of the incidence angle. For normal incidence, which is the case in our setup, the time delay is  $-30 \text{ fs}$ , and the negative sign indicates that the second harmonic falls behind the fundamental pulse. This time delay needs to be compensated for when generating a new frequency, such as third harmonic generation (THG).

**Third Harmonic Generation (THG):** To generate the third harmonic of the fundamental, we use a two-step process involving two sequential harmonic generation steps arranged in a collinear geometry, as shown in Fig. 3.6.

We combine the second harmonic generation produced in the first step with sum-frequency generation in a second type-I  $\beta$ -BBO crystal with a thickness of  $20\ \mu\text{m}$  and phase-matching angle of  $44^\circ$ . The fundamental and the second harmonic must have the minimum delay and have the same polarization to generate THG efficiently. Therefore, we need to compensate for the delay between the fundamental and the second harmonic and rotate the polarization of one of them to mix efficiently in the THG BBO crystal. We used a calcite crystal with  $2\ \text{mm}$  thickness to adjust the delay. A dual-half waveplate is used to rotate the fundamental polarization by  $90$  degrees with no change of the second harmonic orientation. The two overlapping pulses in the BBO crystal mix to generate the third harmonic with perpendicular polarization. To avoid an extra half-wave plate to rotate the third harmonic, which is more dispersive than the longer wavelengths, we adjusted the incoming polarization to end up with a p-polarized third harmonic beam required for the experiment. The resulting third harmonic is then separated from the fundamental and the second harmonic using multiple harmonic separators that reflect the third harmonic and transmit the other two pulses, which are finally dumped. With the thin BBO crystal, the conversion efficiency is about  $2\%$ . The second and third harmonic spectra are shown in Fig. 3.7.

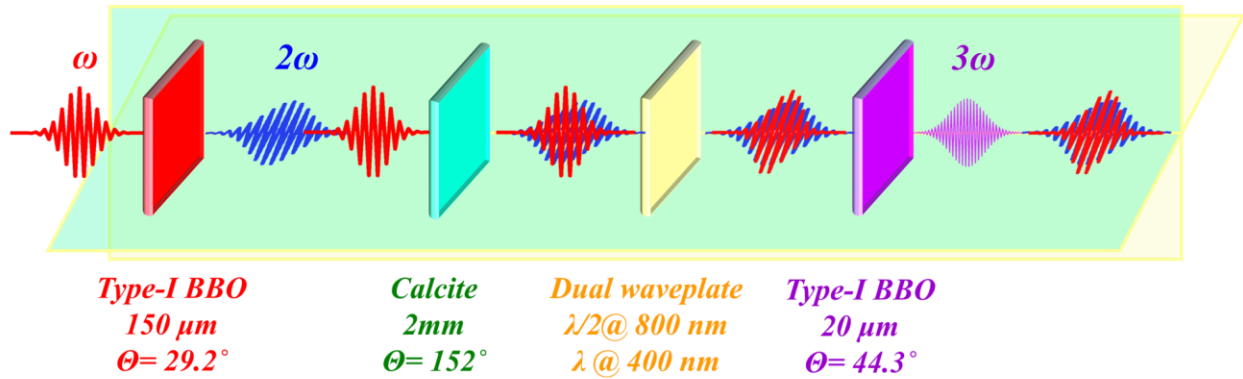


**Figure 3.6.** Schematic setup for a collinear third harmonic generation. A linearly p-polarized laser pulse generates s-polarized SHG and p-polarized THG.

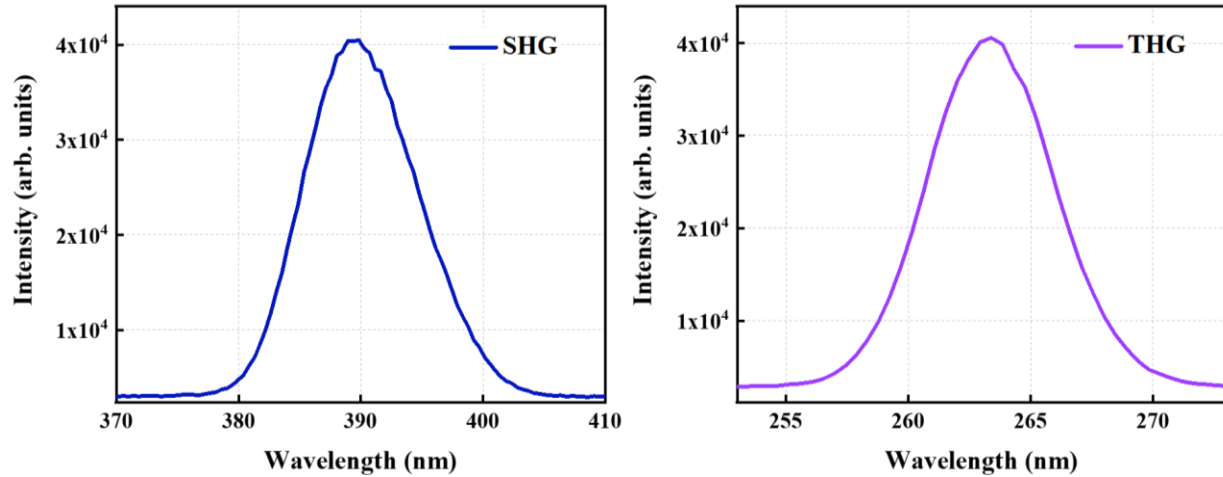


**Figure 3.7.** The typical measured (a) SHG and (b) THG spectra.

The obtained bandwidth was enough to support a short UV pulse. To give a feeling about how the thin crystal helps get a short pulse, we tested two BBO crystals with 100 and 20  $\mu\text{m}$  thickness and obtained about 70 and 40 fs UV pulse durations by increasing the bandwidth from 4 to 7 nm. With a central wavelength of 263 nm and a bandwidth of 7 nm, the UV pulse is directed through a home-built calcium fluoride double-pass prism compressor to compensate for the Group Velocity Dispersion (GVD) and minimize the UV pulse duration. The details of the pulse compression with the prism-pair compressor will be presented in section 3.3.3.

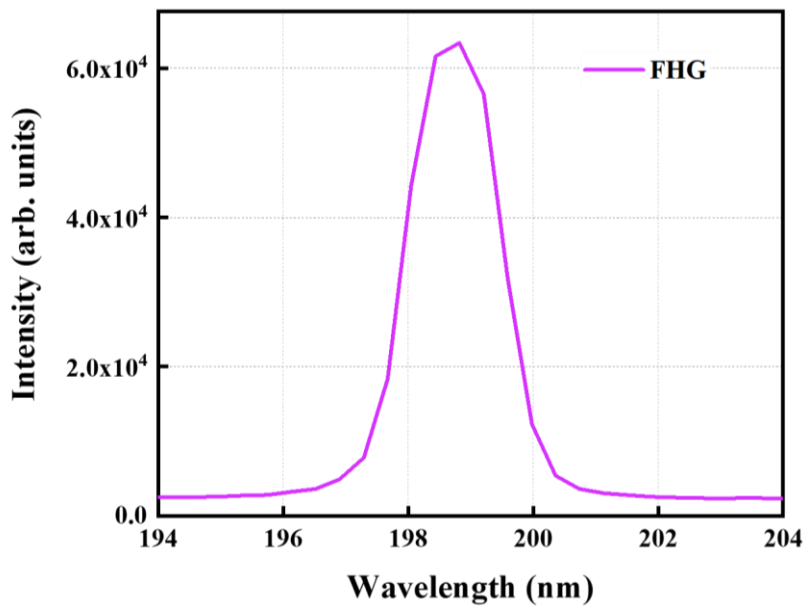


**Figure 3.8.** A typical measured spectrum of the FHG.

**Fourth harmonic generation (FHG):** To generate the fourth harmonic of the Ti: Sapphire beam, we could either mix the fundamental and the third harmonic in another nonlinear crystal or obtain it through an immediate doubling of the second harmonic using two separate second harmonic generation stages. Through the mixing of the fundamental wave and the TH, FHG is phase matchable in several commercially available crystals that are transparent near 200 nm, including BBO,  $\text{KB}_5\text{O}_8 - 4\text{H}_2\text{O}$  and LBO. With the central wavelength of our optical source, the last two crystals are not well-suited for our purpose. The  $\text{KB}_5\text{O}_8 - 4\text{H}_2\text{O}$  crystal has a nonlinearity 50 times smaller than the BBO, and the LBO does not have a phase-matching angle for mixing the fundamental and third harmonic pulses. Therefore, we used a 50  $\mu\text{m}$  type-I BBO crystal and a phase-matching angle of  $65^\circ$  to generate the fourth harmonic by mixing two s-polarized beams. The NIR pulse delay is adjusted to get the maximum FH signal. The fourth harmonic spectrum is shown in Fig. 3.8. We obtained  $\sim 0.35\%$  efficiency. Like the other generation steps, the crystal's thickness was chosen based on the SNLO simulation. The experimental setup is shown in Fig. 3.9 with the marked beam pathways and the harmonic generation stages.

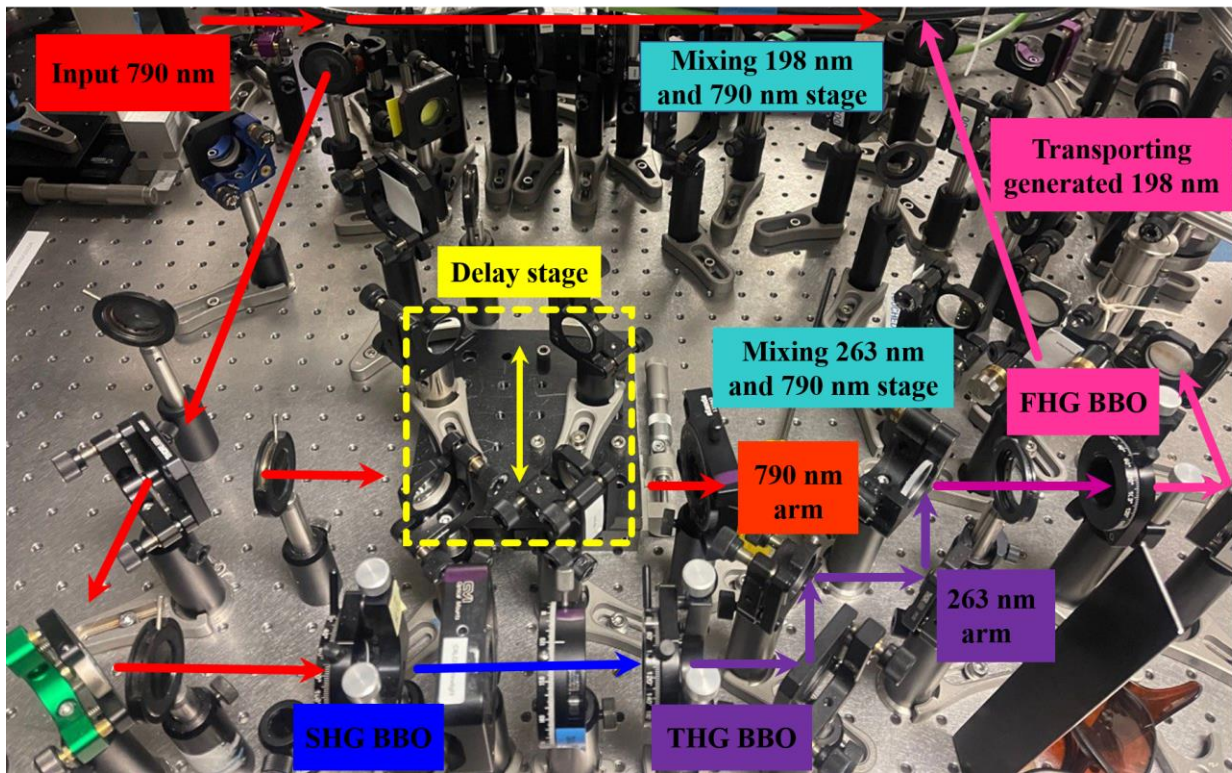


**Figure 3.9.** Photo of the fourth harmonic generation (FHG) setup.

### 3.3.3 Pulse compression: the effect of pulse dispersion on ultrashort pulses

Since ultrashort pulses have rather broad spectral bandwidths, and since different colors travel at different speeds in a dispersive medium, a short laser pulse spreads in time when traveling in a dispersive medium. Longer pulses lead to a lower peak intensity and lower temporal resolution. This section discusses several schemes to compensate dispersion, with particular emphasis on the methods used in our setup.

The electric field of an ultrashort pulse can be described entirely in the time domain by specifying the time-dependent intensity and phase of the pulse.

$$E(t) = \sqrt{I(t)}e^{-i\varphi(t)} \quad 3.28$$

The equivalent electric field in the frequency domain is obtained the Fourier-Transform of this expression as given below

$$\tilde{E}(\omega - \omega_0) = \sqrt{S(\omega - \omega_0)} e^{-i\varphi(\omega - \omega_0)} \quad 3.29$$

where  $S(\omega - \omega_0)$  is the spectral intensity,  $\varphi(\omega - \omega_0)$  is the spectral phase, and  $\omega_0$  is the carrier frequency. When the spectral phase is constant for all frequency components, the pulse width reaches the minimum permitted by the Fourier transform relation for the given spectral bandwidth. It is called Fourier-Transform Limited pulse (FTL). On the other hand, when the spectral phase is non-zero, it causes the pulse to spread in time. A Taylor series expansion of the spectral phase around the central frequency gives the essential terms used as pulse width control parameters:

$$\begin{aligned} \varphi(\omega) = \varphi_0 + \frac{d\varphi}{d\omega}(\omega - \omega_0) + \frac{1}{2} \frac{d^2\varphi}{d\omega^2}(\omega - \omega_0)^2 + \frac{1}{6} \frac{d^3\varphi}{d\omega^3}(\omega - \omega_0)^3 \\ + \frac{1}{9} \frac{d^4\varphi}{d\omega^4}(\omega - \omega_0)^4 + \dots \end{aligned} \quad 3.30$$

In this expression, the first term,  $\varphi_0$ , is the absolute phase which describes the exact phase of the carrier frequency. The first derivative of the spectral phase is group delay, referring to the arrival time of the different frequency components. This effect is known as dispersion. Dispersion is the wavelength dependence of the refractive index, which causes the different frequency components to face different speeds, and the resulting pulse would be broadened. Different colors will be separated when a short laser pulse passes through a medium. This is mainly because of the group velocity mismatch between different colors. Group velocity will increase by increasing the wavelength. Then the higher frequency components travel slower than the lower ones, and the

head of the pulse will fall into the red, and the tail of the pulse will be shifted to the blue shown. This description is related to the normal dispersion, and the reverse situation is called anomalous dispersion. These two types are shown in Fig. 3.10.

The quadratic term physically means that the delay varies linearly with frequency, known as the linear chirp. The coefficient of this term is the derivative of the group delay or the second derivative of the spectral phase,  $\frac{d^2\varphi}{d\omega^2}$  defined as the group delay dispersion (GDD). GDD is positive for all dispersive materials in the normal dispersion regime. Negative GDD must be added through some techniques (some of the are presented as the following) to cancel out the chirp. The third-order phase corresponds to the third-order dispersion (TOD) and has an additional effect on the pulses besides stretching them. TOD can manifest itself when the redder and the bluer colors both arrive before or after the green color. These components beat to cause ringing of the intensity envelope of the pulse, closer to the edges of the pulse. The sign of the TOD term specifies if the ringing occurs on the leading edge or the trailing edge of the pulse. Like the second-order dispersion, the positive TOD can be compensated by adding the negative TOD through a pulse compressor. The following terms are the higher-order dispersions.  $\varphi_0$  and  $\frac{d\varphi}{d\omega}$  do not affect the short pulse, but the higher-order terms have significant impacts on the behavior of the short pulse.

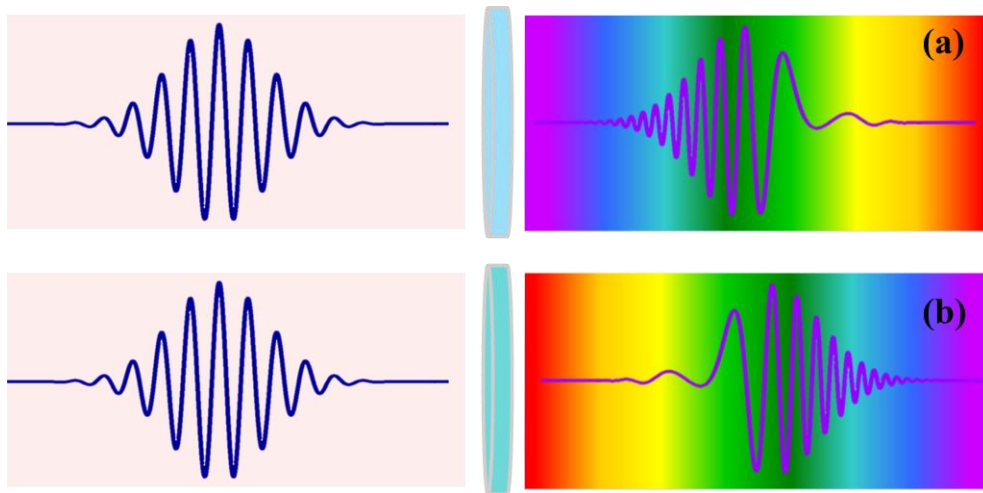


**Figure 3.10.** Frequency chirping in the laser pulse. **(a)** When a short laser pulse experiences positive chirping, the lower frequency components arrive faster than the higher frequency component. **(b)** When a short laser pulse experiences negative chirping, the higher frequency components precede the lower frequency components. The pulse duration is broadened by the positive or negative chirping. Adapted from Ref. [206].

It is worth mentioning that the shorter we go down in the pulse duration, the more the higher orders play a crucial role and need to be considered and compensated or avoided. For instance, dealing with a pulse as short as 30 fs, TOD is critical, and going down to 10 fs, fourth-order dispersion (FOD) needs to be considered. Following [199], the electric field for a Gaussian pulse is given by

$$E(t) = \sqrt{A_1} e^{-\ln 2 \left(\frac{-2t}{\Delta t}\right)^2} e^{-i(\omega_0 t + \varphi(t)) + c.c.} \quad 3.31$$

The phase  $\varphi(t)$  alters the pulse duration, plays a significant role in broadening the pulse in dispersive media, and adds a complex width to the Gaussian envelope. Similar to the general form above, in the frequency domain

$$E(\omega) = \sqrt{A_\omega} e^{-\ln 2 \left(\frac{2(\omega - \omega_0)}{\Delta \omega}\right)^2} e^{-i\varphi_{pulse}(\omega - \omega_0)}. \quad 3.32$$

When an input pulse travels through a dispersive medium, the added phase due to the material dispersion is given by an additional exponential term

$$E_{out} = \sqrt{A_\omega} e^{-\ln 2 \left(\frac{2(\omega - \omega_0)}{\Delta \omega}\right)^2} e^{-i(\varphi_{2,pulse} + \varphi_{2,material}) \frac{(\omega - \omega_0)^2}{2}}. \quad 3.33$$

Rewriting this expression in terms of the pulse parameters yields

$$E_{out} = \sqrt{A'_t} e^{\frac{4(\ln 2)t^2}{2[\Delta t^2 + i4(\ln 2)\varphi_2]}} \quad 3.34$$

where  $\varphi_2$  is the sum of the total group delay dispersion (both the material and the pulse). Therefore, the duration of the output pulse,  $\Delta t_{out}$

$$\Delta t_{out} = \frac{\sqrt{\Delta t^4 + 16(\ln 2)^2 \varphi_2^2}}{\Delta t}. \quad 3.35$$

And the GDD can be written as

$$\varphi_2 = \frac{1}{4(\ln(2))} \sqrt{\left(\frac{TB \Delta t_{out}}{\Delta \nu}\right)^2 - \left(\frac{TB}{\Delta \nu}\right)^4} \quad 3.36$$

where TB is the time-bandwidth product for various pulse profiles. In order to estimate the amount of GDD introduced by a material of length L, the wavelength-dependent index of refraction,  $n(\lambda)$ , is calculated with Sellmeier's equation, and the second derivative at the wavelength of interest is determined. Group velocity dispersion (GVD) is related to the second derivative of the refractive index with respect to wavelength. GVD is the GDD per length of the material.

Several nonlinear methods are used for pulse compression by exploiting nonlinear interactions like optical fibers [221] and electrooptic phase modulators with pulse shaping [222]. The detailed description of these methods falls beyond the scope of the present work. Instead, we limit ourselves to an introduction of chirped mirrors, diffraction grating-pairs, and finally, the prism-pair compressor that we used in this work.

**Chirped mirrors:** They are made of multiple layers of dielectric coatings which precisely reflect a specific wavelength at a particular depth of the mirror. The basic principle of this chirp compensation device is shown in Fig. 3.11. The reflected wavelength increases linearly with the axial position in the mirror. This feature makes the bluer wavelength arrive ahead of the redder wavelength. Consequently, it adds a negative chirp to the pulse. Generally, each bounce off the mirror adds several hundred  $\text{fs}^2$  of GDD, and several hundred reflections of the pulse are often required to compensate for significant dispersion. They also compensate for the higher-order dispersion, such as TOD and FOD [223]. In addition, as the operating bandwidths increase, the reflection efficiency drops significantly. However, once a mirror is manufactured, the ratio of the higher-order dispersion to GDD remains fixed. It cannot be altered, narrowing the scope of application to specific setups only, i.e., needing to be customized for specific goals.

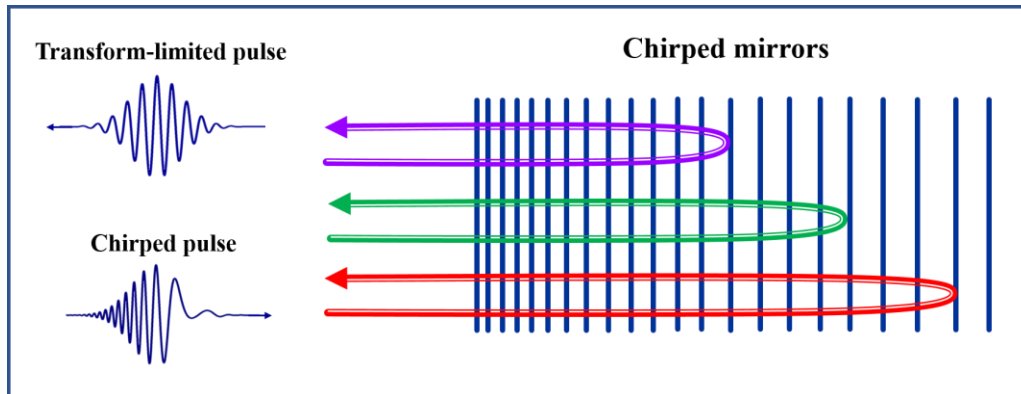


**Figure 3.11.** A dispersion compensation device: chirped mirror. Adapted from Ref. [224]

**Diffraction grating-pair compressor:** A grating pair introduces negative dispersion due to the varying wavelengths difference in the optical path or, in other words, due to the angular dispersion [225]–[228]. It is shown that angular dispersion always produces negative GDD, irrespective of its sign. Pulse compressors based on angular dispersion, illustrated in Fig. 3.12, are the most versatile and commonly used devices for dispersion compensation. The output is a

spatially incoherent beam which can be solved by retroreflecting the light back into the grating pair, generating double the negative dispersion. Diffraction gratings to generate negative dispersion introduce relatively significant losses and do not provide a dispersion easily adjustable through zero value. Similarly, a diffraction grating written on a prism, known as grism, can also be used to compress the pulse [229].

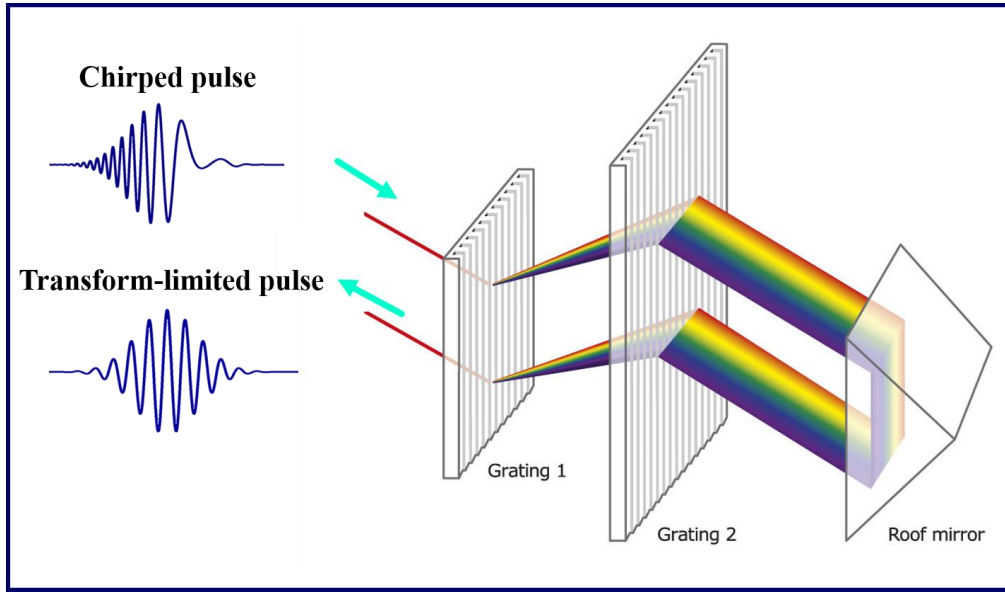


**Figure 3.12.** Sketch of a diffraction grating-pair compressor taken from Ref. [230].

**Prism-pair compressor:** Like gratings, prisms are used to introduce angular dispersion and are commonly used as a dispersion compensation technique [231]–[234]. Prism pairs have relatively low losses compared to gratings, making them an excellent option for compensating and controlling ultrafast pulses passing through various media. The main drawback is that they provide a limited window of angular dispersion. Therefore, one needs to control the GDD via longer separation between the prisms, which is impossible in some applications. Practically, even though angular dispersion is the basic principle of compression in the prism configuration, it also introduces spatial chirp and pulse front tilt, which are undesirable [235]. In principle, angular diffraction-based pulse compressors require four identical dispersive components; the first introduces angular and spatial dispersion, and the second eliminates the angular dispersion. Eliminating the angular and spatial dispersion requires propagation through an additional identical pair of prisms. The red colors travel a longer optical path than blue colors in this configuration. Therefore, the idea is that the redder colors pass through the thicker regions of the second and third

prisms, allowing the bluer colors to catch up with them. If this configuration is set correctly, negative GDD is provided without undesirable spatiotemporal distortions, such as the pulse-front tilt [234] which means that an ultrashort pulse's arrival time varies across the beam profile. In other words, there is an angle between the pulse front and the beam's propagation direction.

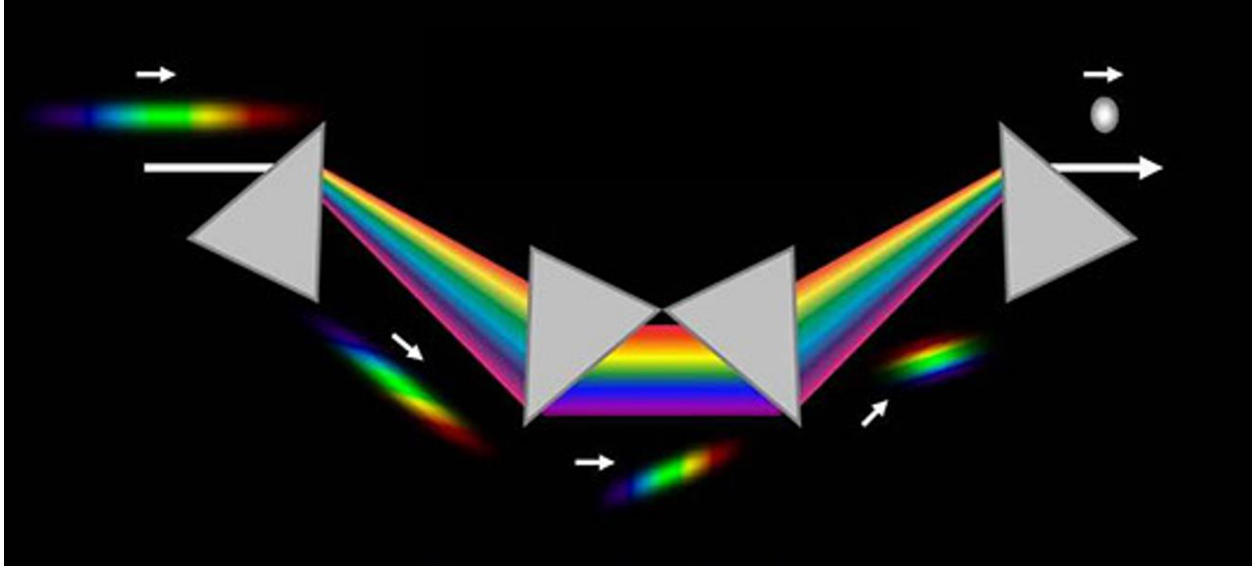


**Figure 3.13.** Schematic of the conventional four-prism pulse-compressor. Adapted from Ref. [231].

The golden question is how much GDD the compressor is supposed to produce to compensate for the chirp. We follow the approach presented in [235] to answer this question. We consider an unfolded geometry of four prisms, shown in Fig. 3.13, that generate negative GDD and correct the distortion. The prisms are at the minimum deviation angle (we consider the situation when the diffracted beam is parallel to the prism's base). Therefore, the beam path will be symmetric, and the incident and exit angles will be the same. This feature could be a positive point because by changing the separations between the two prisms, there would not be a change in the output beam angle, and by moving the prism perpendicular to the line connecting the two prisms, we can tune the dispersion coming from the prism material. Since the minimum deviation angle is a function of the apex angle, the incident and the exit angles satisfy Brewster's angle. Consequently, there is less reflection loss for the p-polarization.

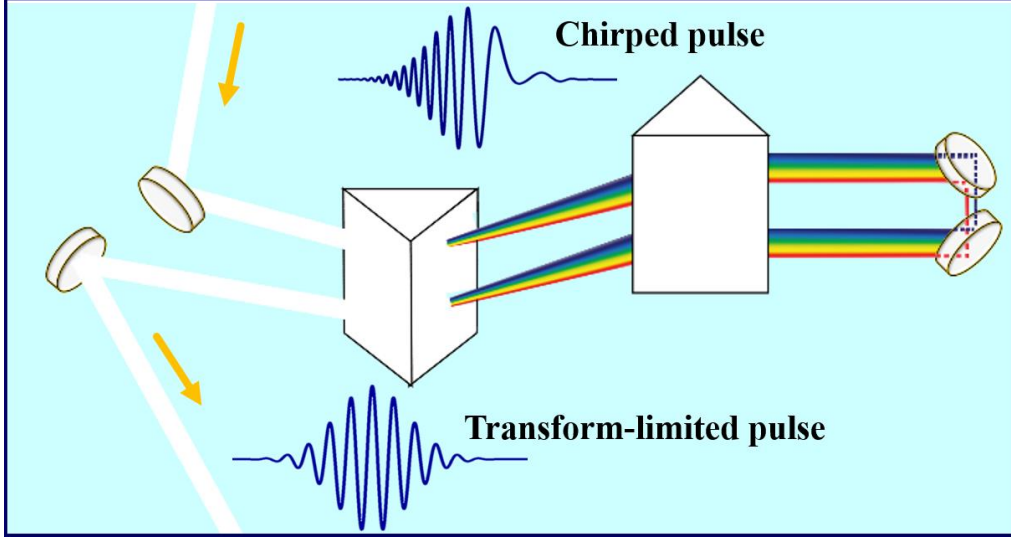


**Figure 3.14.** Schematic of a prism-pair compressor in a folded geometry. The figure is adapted from [235].

Gordon and Fork [231], [236] geometrically showed that the GDD is linked to the wavelength-dependent path length's second derivative,  $P(\lambda)$ :

$$GDD_{prism} = \frac{\lambda^3}{2\pi c^3} \frac{d^2 P}{d\lambda^2} \quad 3.37$$

The optical path length is given by

$$P = 2l \cos \beta \quad 3.38$$

where  $\beta$  is the angle of the dispersed beam after the first prism and  $l$  is the distance between the two apices of the prisms. Therefore, the calculation of the derivatives of the  $P$  results in the following expression with the approximation of a small  $\beta$  angle

$$GDD_{prism} \approx \frac{\lambda^3}{2\pi c^3} \left[ -4l \left\{ 2 \left[ \left( \frac{dn}{d\lambda} \right)^2 \right] + 4 \left( \frac{d^2 n}{d\lambda^2} \right) (r_0) \right\} \right] \quad 3.39$$

where  $r_0$  is the beam diameter. We ended up with two different terms: the first term depends on the distance between the two prisms and has a negative sign, and the other depends on the optical path length and has a positive sign. We can tune the amount of GDD produced in the setup by changing the distance between the two prisms. Using the Sellmeiers' equation and calculating the derivatives of the refractive index for the prism material, we can simplify this expression to a first-order inequality. To have negative GDD, one needs to determine the prism separation parameter  $l$  from  $GDD < 0$ . Therefore, the distance between the two apexes of the prisms is estimated by calculating the available dispersion in different dispersive optical elements within the setup. By

increasing the distance, we increase the amount of negative GVD experienced by the beam to compensate for the positive dispersion generated by the dispersive elements.

Trebino suggested several different prism configurations, including four-prism, double prism, and single prism setups. They have a standard building block, through which the beam must go through the setup four times to compensate the chirp and correct the spatial and angular chirp. With the details of these setups, they have their pros and cons. The four-prism setup requires ample space, and to vary GDD over an extensive range, the separations between the prisms must be varied and maintained precisely equal to each other. In addition, if the input wavelength changes, all four prisms must be rotated by precisely the same amount maintaining equal incidence angles for all the prisms. The unfolded setup could be simplified to two components by replacing the last two prisms with a periscope after the second prism and folding the beam back through the first two prisms. This design is more straightforward, and tuning and maintaining the setup is less burdensome. For the experiments presented in this thesis, we made a prism-pair compressor, as shown in Fig. 3.14. A single-prism compressor has solved the alignment technicalities by reducing the number of dispersive elements to one and tuning GDD using a corner cube. In our attempt to make a prism compressor, we did not go for this option due to the challenges of finding appropriate corner cubes with low dissipation.

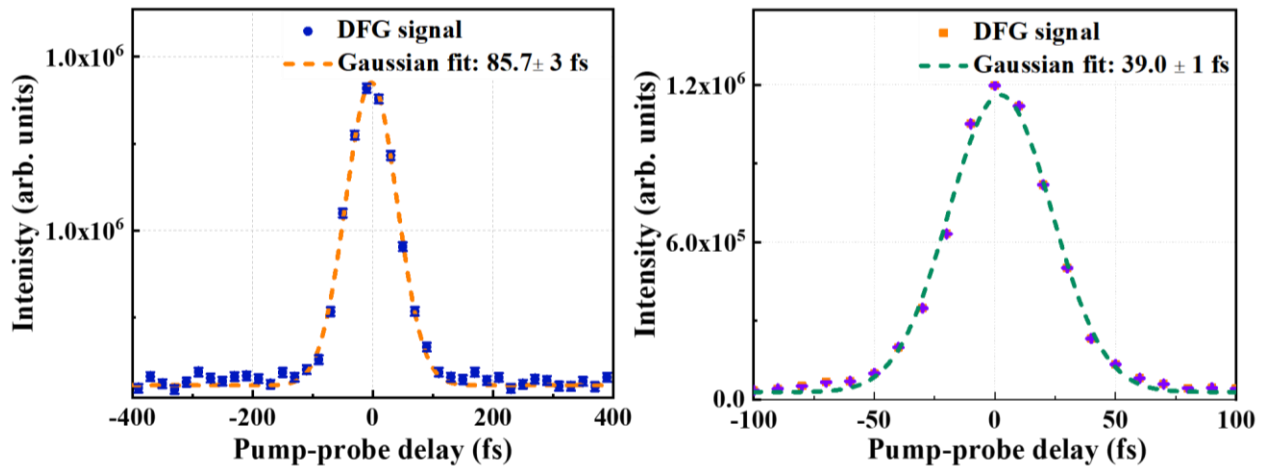


**Figure 3.15.** Cross-correlation between UV (263 nm) and NIR (790 nm) pulses. (a) uncompressed beam, (b) compressed beam.

### 3.3.4 Pulse characterization

**Characterization of the Third Harmonic Generation:** For the experiments discussed in this thesis, the prism compressor was built in a folded geometry using a pair of  $\text{CaF}_2$  prisms, cut at Brewster's angle for our third harmonic wavelength; the distance between the two prisms was determined using estimates of the dispersion in various transmitting optics within the setup.  $\text{CaF}_2$  was preferred over fused silica due to the less dispersive character at ultraviolet wavelengths, thus reducing in particular the amount of higher-order dispersion introduced by the prisms. Characterization of the uncompressed and compressed UV pulse duration was performed by an XFROG-type measurement in which the pulse characterization is based on the cross-correlation measurements of the NIR and UV pulses using difference frequency generation (DFG). The NIR arm's pulse duration was measured independently by a FROG and optimized to 23 fs. We mixed the fundamental and the third harmonic in a BBO crystal identical to the one we used in the third harmonic stage. A computer-controlled delay stage varied this NIR path length to provide a variable time delay between UV and NIR pulses. The resulting second harmonic signal representing the cross-correlation between the two pulses was measured as a function of the pump-probe delay using an Ocean Optics FLAME-S-XR1-ES spectrometer. Once the two pulses overlap in time, we obtain the maximum yield of the second harmonic signal. The resulting signal had two practical applications. First, the signal's peak position in time represents the temporal overlap of the two pulses that we could use for the real molecular time-resolved studies.

Second, this signal was used to characterize the prism-pair compressor and tune it to get the shortest possible third harmonic signal. The uncompressed beam was measured to about 85 fs with the careful selection of the nonlinear crystals, i.e., preferring thinner crystals for the sake of getting the shortest pulse duration over the higher efficiencies with thicker crystals. After tuning the prism compressor [237], we could bring the pulse duration down to about 32 fs, close to the transform limit (about 21 fs) calculated assuming a Gaussian pulse envelope for the available bandwidth shown in Fig.3.7 (b). The corresponding cross-correlation traces for uncompressed and compressed pulses are shown in Fig. 3.15.

To check the performance of the prism compressor, we scanned the delay stage around the optimal position, and in XFROG traces, we observed the change in the slope of the spectrogram by going in the two directions. The results are shown in Fig. 3.16.

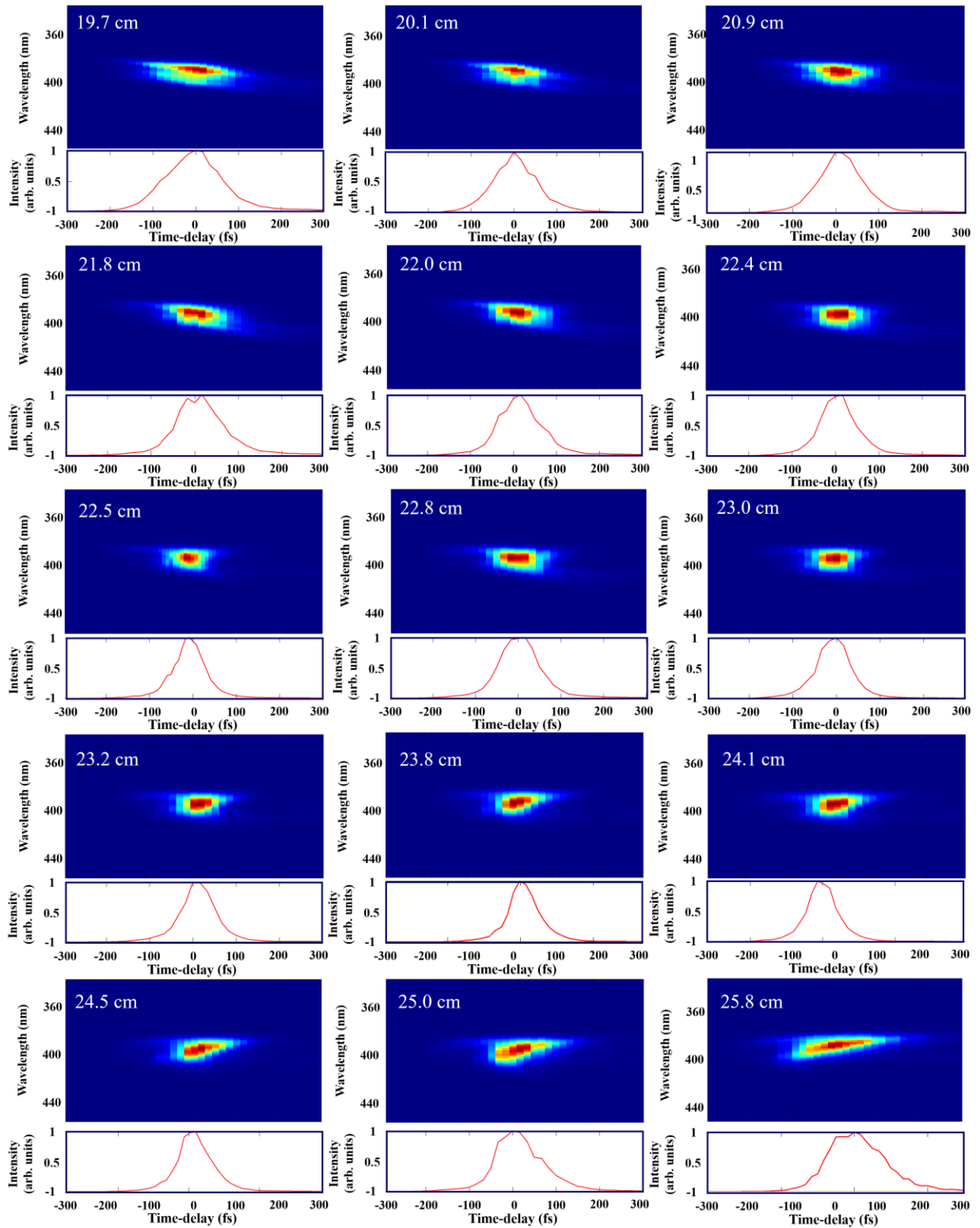


**Figure 3.16.** Scanning the XFROG traces by changing the separation of the two prisms. The projections onto the delay axis are shown on the bottom. Changing the sign of the chirp from positive to zero and continuing to the negative sign is evident in the graphs.

It was critical to do this measurement with a replica of the identical pulses that are focused into the chamber. Therefore, the measurement was performed after passing through the dispersive elements and right before the COLTRIMS entrance. Subsequently, the compressed UV pulse was combined with the NIR pulse from the delaying arm and routed to the COLTRIMS chamber.

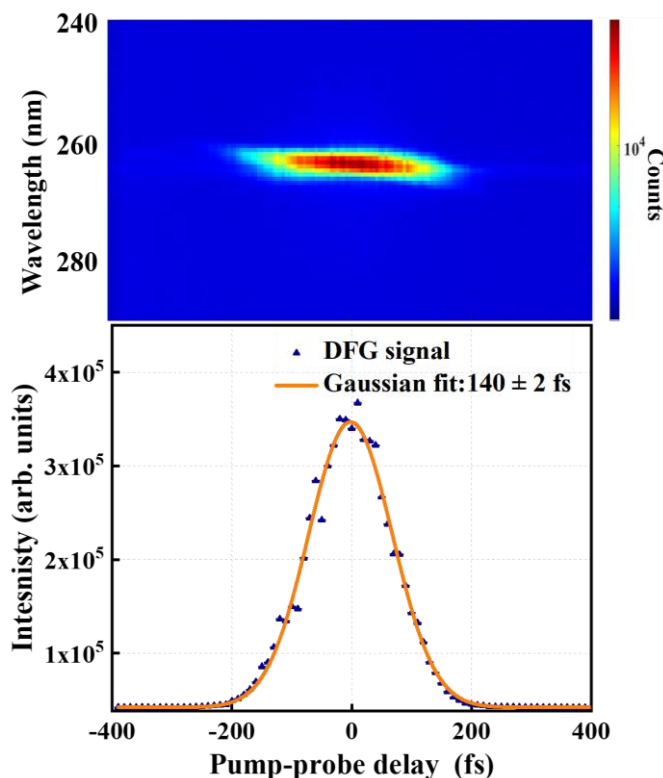


**Figure 3.17.** Cross-correlation between UV (263 nm) and NIR (790 nm) pulses used for the FHG.

**Characterization of the Fourth Harmonic Generation:** The generated fourth harmonic was combined with the delayed NIR pulse and co-linearly propagated through a 50  $\mu\text{m}$  BBO. In order to find the temporal overlap and characterize the fourth harmonic duration, the cross-correlation of the fundamental and the third harmonic signal was measured through the DFG process. The resulting signals were sent to the spectrometer and characterized similarly to the way we characterized THG. The measurements show a cross-correlation with FWHM of 140 fs depicted in Fig. 3.17.

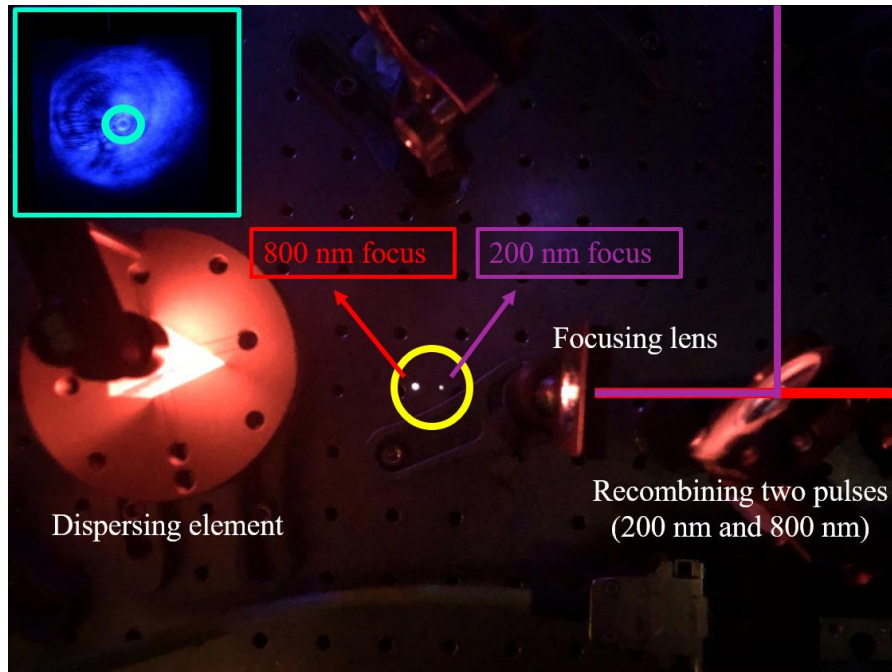


**Figure 3.18.** High-intensity laser filamentation experimental setup. Focusing of co-propagated UV (198 nm) and NIR (790 nm) pulses in the air decreases the transmission of the UV pulse passing through the plasma produced by the NIR pulse and thus causes the UV beam intensity drop, allowing us to find the temporal overlap. The imaged UV beam profile reveals a hole at NIR early in the inset.

In addition to the regular DFG process, we used an approach previously described by Dachraoui et al. [238] for finding the temporal overlap between FH and NIR pulse and confirm the pulse duration obtained from the DFG measurement. Nonlinear pulse propagation involves a self-induced, intensity-dependent refractive index variation across the mode profile, resulting in self-focusing that tends toward eventual collapse if the beam's power exceeds the critical power threshold for self-focusing. The beam ionizes the medium at high enough intensities, generating plasma and preventing collapse by defocusing the beam. A self-guided light structure known as a laser filament is formed when the self-focusing is balanced by the plasma-defocusing effect and diffraction. We focused the combined high-intensity beams in the air resulting in nonlinear effects such as Kerr-effect and free-electron formation, which decrease the fused silica transmission. The corresponding optical setup is shown in Fig. 3.18.

Delaying the NIR pulse to arrive earlier than FH causes the FH beam intensity drop, allowing us to find the temporal overlap and characterize the pulse duration. The intensity drop persists up to hundreds of picoseconds, corresponding to the long-lived free electrons inside the plasma channel [239]. We estimated 300-600 ps for the plasma lifetime (equivalent to 10-20 mm on the delay stage). Fig 3.18 shows the projected image of the diverged FH beam profile containing a hole due to the filamentation when UV arrives later than NIR. The resulting drop of the signal is shown in Fig. 3.19. To obtain transmitted UV signal, we used a dispersive element (here, a prism) to better separate the NIR pulse, which could make the image scrambled and challenging to find the hole. In the next step, the FH signal is sent to the spectrometer to be quantified. Deconvolution of the signal results in FWHM of about 143 fs, which corresponds to the pulse duration of the FH beam of about 140 fs, similar to the results obtained using the DFG technique.

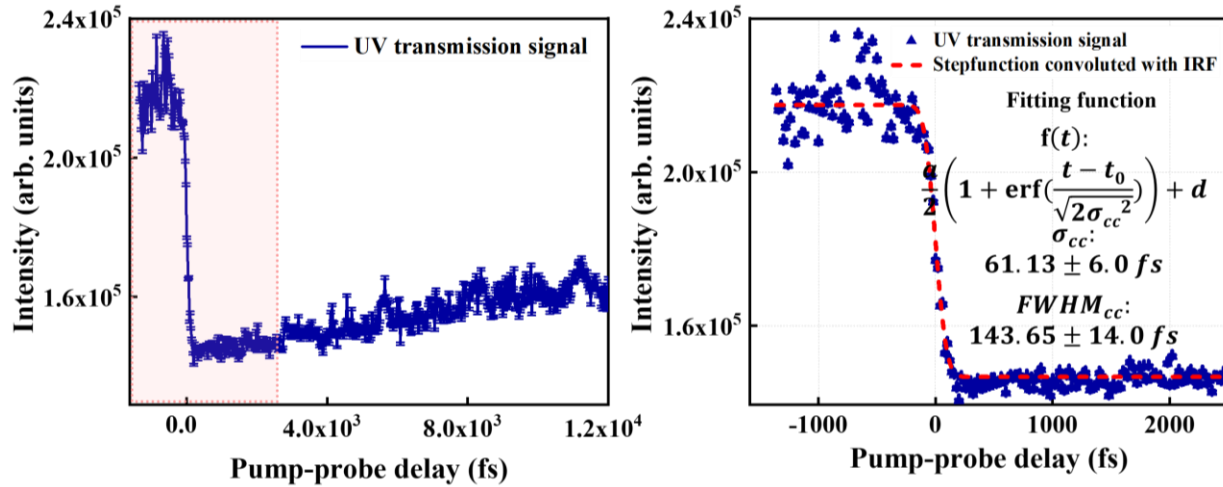


**Figure 3.19.** Measured signal of the transmitted UV pulse as a function of the delay between the UV and NIR pulses. The NIR-induced plasma results in a drop in the UV intensity when the NIR pulse precedes the UV pulse. Deconvolution of the drop results in full width at the half maximum of cross-correlation function (FWHM) of about 143 fs, which corresponds to a pulse duration of 198 nm beam of about 140 fs.

### 3.4 COLd Target Recoil Ion Momentum Spectrometer (COLTRIMS)

Spectroscopy is a probing approach used extensively in a broad range of disciplines, from astronomy to quantum physics. “Conventional” atomic and molecular spectroscopy focuses on investigating light-matter interactions as a function of wavelength, the composition, and the physical properties of molecules and atoms in different physical phases. Momentum spectroscopy is a spectroscopic technique relying on measuring momenta of the particles resulting from photo fragmentation or ionization processes., which often reveals complementary information compared to traditional methods. If this approach yields 2D or 3D momenta of the fragments, it is sometimes called “momentum imaging”. These “momentum imaging” or “momentum spectroscopy” techniques typically rely on the detection of charged reaction products, ions or/and electrons, although experimental techniques capable of detecting neutrals also exist [203], [240]–[242]. A momentum imaging apparatus can measure complete 3D momentum vectors of several ions and electrons in coincidence in its most complete realization. Such machines are often called reaction microscopes (REMI) [243], [244].

The momentum measurement technique employed in this thesis is called COLd Target Recoil-Ion Momentum Spectroscopy (COLTRIMS). As indicated by its name, this method relies on using internally cold (and well-localized) targets provided by collimated supersonic gas jets. This enables achieving ion momentum resolution well below the limit set by the room-temperature thermal motion of the target particles, which is sometimes even sufficient to resolve the electron-recoil contribution to the measured ion momentum. This technique enabled pioneering “kinematically complete” experiments on atomic and molecular fragmentation processes, where the complete 3D momenta of all created ions and electrons could be revealed [243]–[245]. Although the name explicitly refers to ion measurements, a typical COLTRIMS apparatus also includes an electron detection system. A sketch of the COLTRIMS setup used in this work is shown in Fig. 3.20. Even though, as shown in the figure, the electron detector was installed, the experiments described in this thesis did not involve any electron measurements.

As illustrated in Fig. 3.20, in a COLTRIMS apparatus, a collimated supersonic beam of cold atoms or molecules is crossed by a projectile beam (in our specific case, a laser beam) in the middle of an ultra-high vacuum chamber housing the spectrometer and the detectors. The cross-over between the two beams defines the interaction region. The spectrometer consists of a set of closely spaced electrodes that produce a homogeneous electric field in the interaction region. The

field guides the created ions and electrons towards two large-area time- and position-sensitive detectors located on each side of this acceleration region. The electrodes also screen the charged particles from external electric fields. The time of flight (TOF) and impact position on the detector are measured for each particle. From these data, each particle's full-dimensional momentum vectors are computed. The TOF must be measured with respect to a trigger signal that uniquely defines the interaction's timing, which is provided by a photodiode signal characterizing the arrival time of the laser pulse. The TOF spectrum includes two essential pieces of information. First, it allows one to sort all generated ions according to their mass to charge ratio, which in most cases results in different TOFs for different ion species. Second, the shapes of individual ion peaks contain information about the component of the initial ion momentum parallel to the spectrometer axis. The other two momentum components are obtained from the hit positions on the detector.

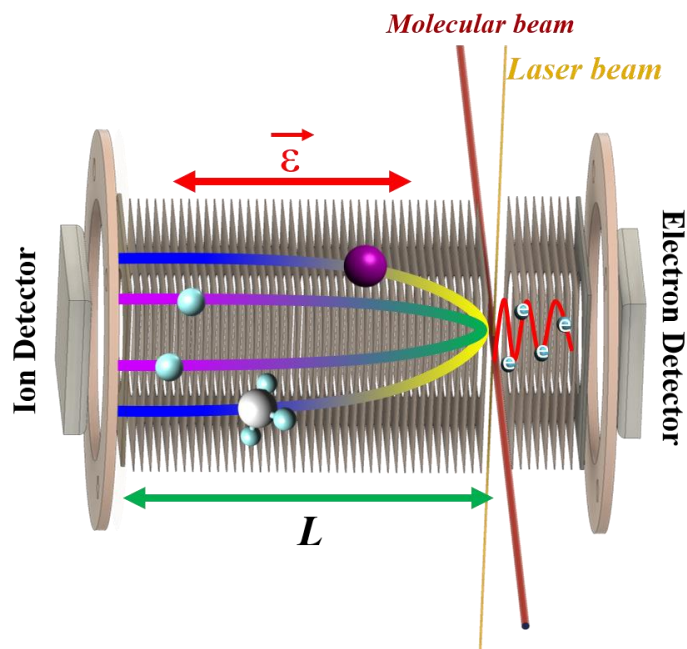


**Figure 3.20.** Schematic of the COLTRIMS apparatus with exemplary ions and electrons trajectories. The ions' flight distance is denoted as  $L$ .

**Supersonic gas jet:** COLTRIMS requires a well-localized and cold target to achieve excellent momentum resolution for the recoil ions. Atomic or molecular target is introduced to the interaction region by a supersonic beam expansion, where the target under high pressure is injected into a high vacuum chamber through a nozzle of  $30\ \mu\text{m}$  diameter. During the supersonic expansion,

the free enthalpy and the thermal kinetic energy of atoms or molecules of the target are transferred into their kinetic energy in the beam propagation, producing a fast and internally cold beam. The supersonic jet also creates a shock wave that compresses the residual gas in the vacuum chamber. Only before the first shock, in the so-called “zone of silence,” the gas can expand freely [246]. To preserve the cooled beam and to restrict the perpendicular velocity distribution, the beam passes through a 200  $\mu\text{m}$  skimmer, a reversed funnel made of copper, placed within the “zone of silence”, and is further collimated by two consequent downstream apertures of 1- and 2-mm diameter. The resulting beam has a narrow Boltzmann velocity distribution. The diameters of the openings and relative distances between the nozzle, skimmer, and slits have been adjusted to get the desired target density in the interaction region.

There must be a very good vacuum in the reaction chamber for COLTRIMS experiments. Otherwise, the single laser pulse would trigger many ionization and fragmentation events. In this case, one would obtain random coincidences between fragments originating from different ionization events. This would lead to a massive background in the recorded data. Correspondingly, the main chamber is kept at ultra-high vacuum (below  $10^{-10}$  mbar) using several differentially pumped stages between the jet nozzle and the interaction region and a differentially pumped “catcher”, where the molecular beam is dumped.

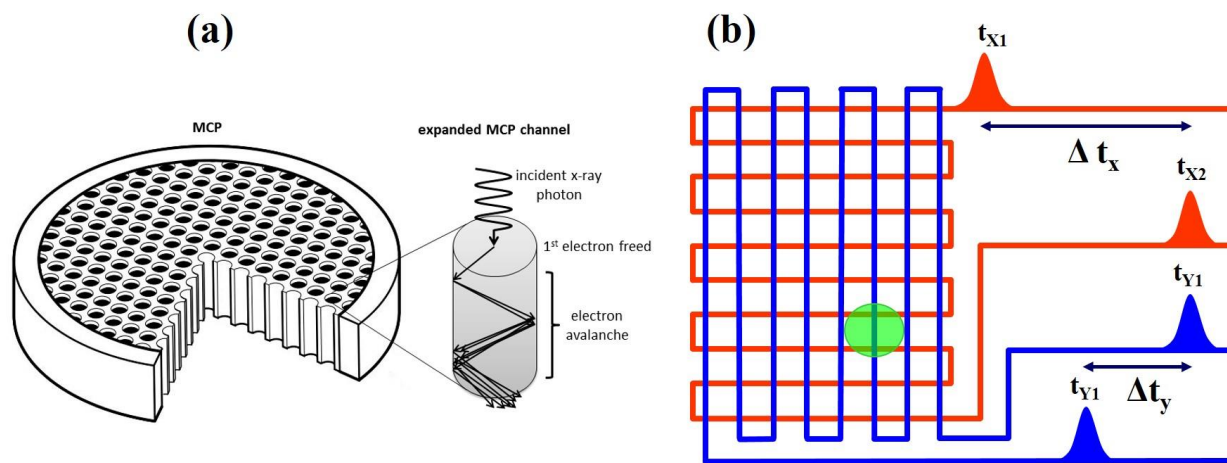


**Figure 3.21.** Microchannel plate (MCP). **(a)** Schematic of an MCP. Left: a cut-out of a lead glass plate with microchannels. Right: an expanded view of an individual channel. Figure adapted from Ref. [247]. **(b)** Working principle of a delay-line anode (DLA). The amplified electron signal from the MCP hits the DLA, creating two pairs of signals with run-times towards the corners  $t_{x1}$ ;  $t_{x2}$  and  $t_{y1}$ ;  $t_{y2}$ . The hit’s x,y position information is determined from these signals.

**Spectrometer:** The heart of the COLTRIMS machine is the spectrometer located in the main chamber. As illustrated in Fig. 3.20, a constant electric field is applied along the spectrometer through a stack of equally spaced electrodes connected by resistors. The spectrometer used in this work is not symmetric with respect to the interaction region. In the experiments described in this thesis, the ions are guided to the longer side of the spectrometer to increase the momentum resolution, and the electron side was not used.

**Detectors:** In COLTRIMS experiments, charged particles are typically detected using a combination of microchannel plates (MCPs) and a delay-line anode (DLA) [248]. Such detector arrangement is also used in this work. Since a single charged particle cannot produce a measurable electrical signal, it must be amplified. Here, it is done by a triple stack of MCPs. Each of those is an approximately 80 mm diameter and 1-1.5 mm thick porous glass plate with numerous miniature electron multipliers channels with a diameter of approximately 12  $\mu\text{m}$  (front plate) to 25  $\mu\text{m}$  (back pair). When a charged particle hits the MCP, secondary electrons are created. An applied electric field then accelerates these electrons along the channels, producing even more secondary electrons. Thus, the stack of MCPs converts the impacting charged particle into an avalanche of electrons, resulting in a measurable electrical pulse used for the TOF measurement.

The amplified electron bunch impacts a DLA, consisting of two layers of wires wound in the direction perpendicular to each other. Each layer has two wires, signal and reference, kept at slightly different voltages. The impact on the wire causes an electrical pulse. This pulse propagates toward the ends of wires. The time difference in traveling time between the pulses is used to compute the electron impact position. The position of the hit denoted by the coordinate  $(X_j; Y_j)$  is reconstructed from the time delay between signals arriving at the two ends of each wire.

$$X_j = g_x \Delta t_x = g_x (t_L - t_R) \quad 3.40$$

$$Y_j = g_y \Delta t_y = g_y (t_U - t_D), \quad 3.41$$

where  $t_L$ ,  $t_R$ ,  $t_U$ , and  $t_D$  are the timing signals from the ends of the X and Y wires. The proportional constants are  $g_x$  and  $g_y$ , determining the propagation speeds of the signals in each direction.

If we get the signal of both wires, the 2-D position of the events is obtained. For each wire, the total travel time towards both ends and, thus, the sum of the two timing signals must be constant. This restriction is used to eliminate false events by keeping only those events with a time sum within a small interval (determined by the length of the wire). In addition, the time of flight signal of the hit is picked up from the front side of the MPC. Therefore, as mentioned earlier, the

position and time of the events are obtained from the MCP and DLA signals. The position and time signals are amplified and sent to an electronic device called Constant-Fraction Discriminator (CFD) to generate a standardized NIM output signal independent of the height of the original pulse. These analog signals are then sent into a time-to-digital converter (TDC). The TDC used here allows for up to 16 hits per channel. TDC receives NIM pulse for amplified MCP signal and 4 position signals from the CFD and converts them to digital signals. The MCP pulse gives us the TOF signal. A photodiode irradiated by the laser pulse triggers the TDC and the DAQ with a 10 kHz repetition rate. The photodiode signal is treated as a reference signal, and all the time and position signals are measured with respect to this signal.

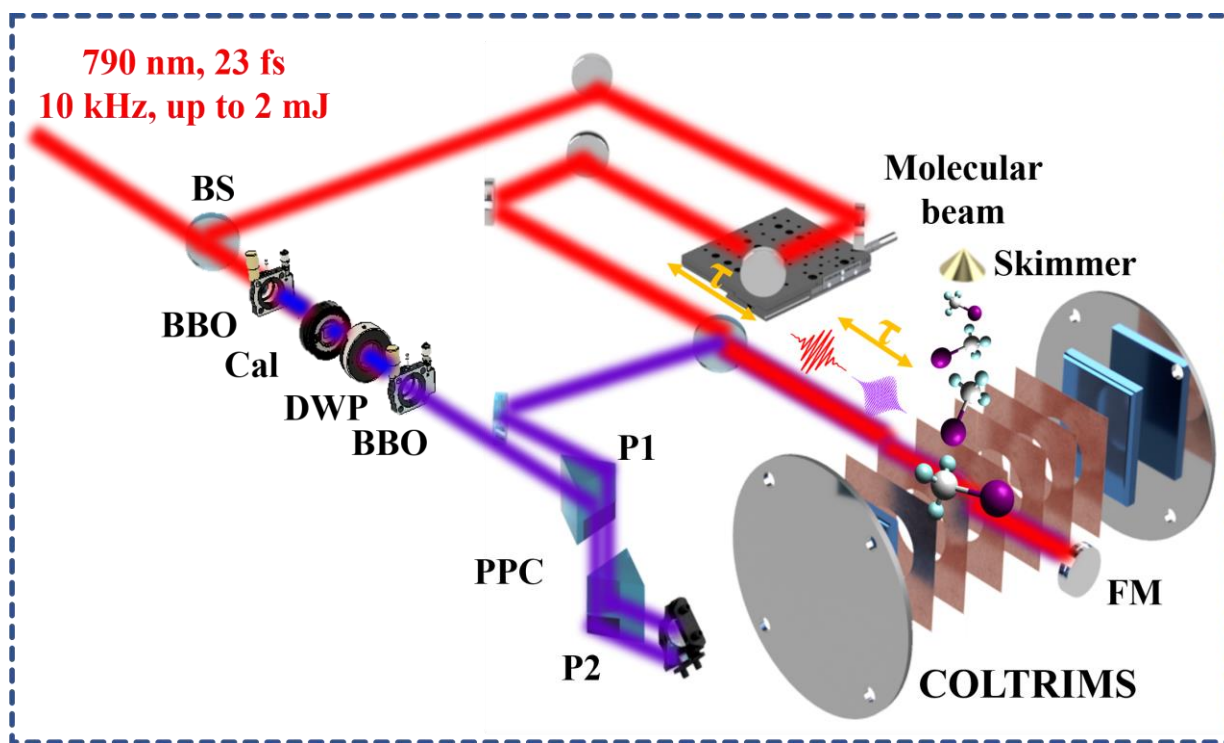


**Figure 3.22.** Sketch of the experimental setup for UV - NIR pump-probe experiments. The compressed 263-nm and the 790-nm laser beams are collinearly propagated and focused inside a supersonic target sample of methyl iodide molecules at the center of a COLd Target Recoil Ion Momentum Spectrometer (COLTRIMS). Ions were detected with time- and position-sensitive detectors. BS: Beam Splitter, BBO: Barium Borate, Cal: Calcite, DWP: Dual-Wave Plate, PPC: Prism-Pair Compressor, P1: Prism #1, P2: Prism #2, FM: Focusing Mirror.

### 3.5 Experimental setup for pump-probe experiments with COLTRIMS

In our femtosecond pump-probe experiments, the linearly polarized NIR laser pulse is split into two arms by an 80:20 beam splitter. The dominant split, transmitted through the beam splitter, generates the third harmonic of the fundamental with a two-step process involving two sequential higher-order harmonic generation steps arranged in a collinear geometry, as discussed in section 3.3. With a central wavelength of 263 nm and a bandwidth of 4 nm, the UV pulse is directed through a home-built calcium fluoride double-pass prism compressor to compensate for the Group Velocity Dispersion (GVD) and minimize the UV pulse duration. DFG measurements show that the UV pulse is compressed to approximately 39 fs (FWHM in intensity). The NIR arm’s pulse duration was measured independently by a frequency-resolved optical grating (FROG) and optimized to about 23 fs. A computer-controlled delay stage varies this weaker beam’s path length to provide a variable time delay between UV and NIR pulses. The two pulses are recombined outside the COLTRIMS chamber. They are then focused onto a supersonic molecular beam by an in-vacuum, on-axis spherical concave mirror with a 7.5 cm focal length.

The experimental setup for UV pump-NIR probe experiments using coincident ion momentum imaging is sketched in Fig. 3.22. The detector is calibrated using a well-known proton kinetic energy spectrum [249]. Moreover, to determine in-situ “time zero” for our pump-probe measurements, we used the cross-correlation signal resulting from two-color UV and NIR multi-photon ionization of argon as shown in Fig. 3.23.

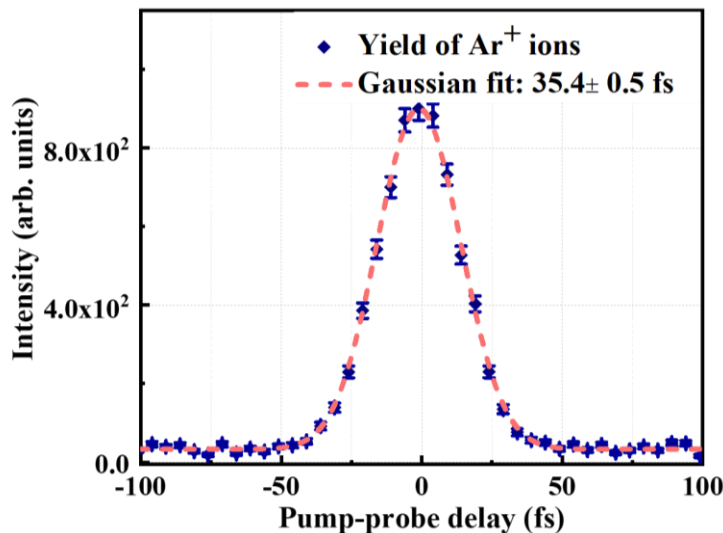


**Figure 3.23.** Measured cross-correlation between 790-nm and 263-nm pulses from PULSAR using two-color ionization of Ar from our COLTRIMS.

### 3.6 Data processing; 3D momentum imaging principles

The data obtained in this work were recorded shot-by-shot using the NSCL SpecTcl DAQ system [250]. The ion TOF values and hit positions recorded for each individual laser shot are used to reconstruct the initial 3D momenta for the related events. All further observables, like KER values, absolute or relative ion emission angles, etc., are determined from these 3D momentum values [251]. In our COLTRIMS design, the laser propagation direction is along the x-axis, the jet direction along the Y-axis, and finally, the spectrometer axis is along the Z-axis, along which we employ homogenous fields. The interaction point, where the laser crosses the ion beam, is defined as the origin of the Z-axis ( $z_0$ ). The center of the detector is the origin of the hit coordinate ( $x_0, y_0$ ). The ion imaging detector is parallel to the XY plane perpendicular to the spectrometer axis. Therefore, the motion of the ions in this plane is field-free. In addition, the motion of the ions along the Z-axis can be described as a constant acceleration motion. Using the Newton's equation of motion, the three components of momentum gained by an ion of mass  $m$  and charge  $q$  accelerated in z-direction flying the distance from interaction region to the ion detector  $l_i$  are calculated as:

$$P_x = \frac{m(x - x_0)}{t - t_0}$$
$$P_y = \frac{m(y - y_0)}{t - t_0}$$
$$P_z = \frac{ml_i}{t - t_0} - \frac{1}{2}qE(t - t_0)$$

where  $t_0$  is the interaction time offset due to laser molecule interaction in relative to the arrival time of photodiode signal to DAQ system to trigger data recording and also includes electronics delays. Now that we compute the momenta of the ion species generated in the light-molecule interaction we calculate the kinetic energy distributions of the ions and the total kinetic energy as well as the direction of the ejected ions. For the case of coincident analysis, the momentum vectors are linked through momentum conservation.

### 3.7 Peak intensity calibration

To interpret the experimental results, one needs to determine the intensity regime where the interaction happens. In the zeroth order of accuracy, the peak intensity of the ultrafast laser

pulse can be estimated from the laser parameters with an approximation of a Gaussian beam profile. Assuming the Gaussian intensity profile, this distribution is symmetric around the beam's center and decreases as the distance from the center of the beam perpendicular to the direction of propagation increases.

$$I(r) = I_0 \exp\left(\frac{-2r^2}{\omega_0^2}\right). \quad 3.52$$

Here,  $I_0$  is the peak intensity at the center of the beam,  $r$  is the radial distance from the center of the beam, and  $\omega_0$  is the Gaussian beam radius, the radius at which the intensity is  $e^{-2}$  of the peak intensity. By integrating the intensity from 0 to  $r$ , the power distribution is obtained as a Gaussian distribution.

The total power is within a radius of  $2\omega_0$ :

$$P(r) = P_0 [1 - \exp\left(\frac{-2r^2}{\omega_0^2}\right)], \quad 3.53$$

$$P_0 = I_0 \frac{\pi\omega_0^2}{\lambda}. \quad 3.54$$

The beam size on the transverse axis (perpendicular to the propagation direction) and the radius of curvature is obtained as

$$\omega^2(x) = \omega_0^2 \left[1 + \left(\frac{\lambda x}{\pi\omega_0^2}\right)^2\right], \quad 3.55$$

$$R^2(x) = x^2 \left[1 + \left(\frac{\pi\omega_0^2}{\lambda x}\right)^2\right]. \quad 3.56$$

Parameters containing  $\lambda$  and  $\omega_0$ , Rayleigh range  $X_R = \frac{\pi\omega_0^2}{\lambda}$  shows the minimum radius of curvature at  $X = X_R$ . From the spot size of the focus ( $\pi\omega_0^2$ ), the power ( $P$ ), and the repetition rate ( $f_{\text{rep}}$ ) of the laser and the pulse duration ( $\tau$ ), the peak intensity ( $I$ ) are estimated as:

$$I = \frac{P}{\pi\omega_0^2 f_{\text{rep}} \tau}, \quad 3.57$$

$$\omega^2(x) = \omega_0^2 \left[1 + \left(\frac{\lambda x}{\pi\omega_0^2}\right)^2\right] = \omega_0^2 \left[1 + \left(\frac{x}{X_R}\right)^2\right]. \quad 3.58$$

If the focusing mirror with focal length  $f$  is at  $x = f$ .

$$\omega^2(x) = \omega_0^2 \left[1 + \left(\frac{x}{f}\right)^2\right]. \quad 3.59$$

Since  $f \gg X_R$ , the radius of the beam at the mirror:

$$\omega(f) = \frac{\pi\omega_0^2}{\lambda} \quad 3. 60$$

Therefore, the radius of the focus can be written in terms of the focal length (f) of the mirror, size of beam ( $\omega$ ), and wavelength of light.

$$\omega_0 = \frac{f\lambda}{\pi\omega} \quad 3. 61$$

With our laser parameters, the estimated intensity of the UV beam at P= 4 mW is  $5 \times 10^{12}$  W/cm<sup>2</sup>.

Since the laser beam profile is not necessarily strictly Gaussian, and the exact focal volume profile in the COLTRIMS chamber is not known, alternative “in-situ” methods are often used for more accurate intensity calibration. To determine the absolute NIR pulse intensity, we used a procedure based on the measured recoil ion momentum distributions from the single ionization of Ne, as described in [249]. In this measurement, the ion momentum distribution directly reflects the momentum distribution of emitted electrons because of the momentum conservation. The intensity calibration is performed using a clear change of the slope of this momentum distribution, which corresponds to the transition between the directly emitted electrons and the so-called re-scattering plateau [252]. According to a semiclassical three-step model of laser ionization [253], this transition corresponds to the electron (and thus, recoil ion) momenta of  $2\sqrt{U_p}$  [249] where  $U_p$  is the cycle-averaged energy of a free electron in the oscillating laser field called the pondermotive energy. Since  $U_p$  is directly related to the pulse peak intensity (for radiation with frequency  $\omega$ ,  $U_p = I/4\omega$ , where all quantities are expressed in atomic units), the intensity can be readily calculated from the measured  $2\sqrt{U_p}$  value.

## **Chapter 4 - Single- and multi-photon-induced ultraviolet excitation and photodissociation of CH<sub>3</sub>I probed by strong-field ionization**

This chapter studies UV-induced photodissociation dynamics of CH<sub>3</sub>I after photoexcitation at 263 nm using time-resolved CEI. As discussed in detail in Section 2.3.1, at this wavelength, one-photon absorption results in the excitation to one of the repulsive states within the A-band and subsequent C-I bond cleavage, dissociating the molecule into two neutral fragments, the CH<sub>3</sub> radical and the iodine atom in its ground or excited spin-orbit state. Besides this most probable one-photon excitation process, if the UV pump pulse is intense enough, two- or three-photon absorption becomes non-negligible. While the absorption of two UV photons excites the neutral molecule to one of the Rydberg states slightly below the ionization threshold, three-photon absorption results in ionization or dissociative ionization (DI). In all cases, the intense NIR probe pulse results in single, double or multiple ionization of bound or dissociating molecules, and the dynamics are mapped by monitoring delay-dependent yields and kinetic energies of the created ions. Here we combine the analysis of coincident ion pairs and “non-coincident” data, i.e., individual ionic fragments or parent ions. This approach allows us to consider all pump-probe scenarios ending up in different final charge states, and in most of the cases, enables conclusive assignment of specific fragmentation pathways. Classical Coulomb explosion simulations are used to verify our assignments for the final states with two charged fragments.

This chapter starts with discussing the molecular response to individual UV or NIR pulses. Single-pulse measurements present initial information on different dissociation and ionization pathways and provide reference data for the time-dependent pump-probe studies, facilitating the identification of pump-induced dynamics. Then we discuss time-resolved measurements and Coulomb explosion simulations.

### **4.1 Measurements with single UV pulses**

Since the dominant UV-induced process considered in this chapter, the photodissociation of CH<sub>3</sub>I in the A-band, results in two neutral fragments, its signatures cannot be directly traced in the measurements with only UV pulses. However, since the absorption cross-section of the molecule is relatively low (approximately 1.4 MB at 263 nm), to have a meaningful signal-to-noise ratio of the pump-probe measurement, we need to use rather a high pump pulse intensity.

We employed UV intensities in the range of  $0.2 - 4 \times 10^{13} \text{ W/cm}^2$  (determined from the laser beam parameters presented in Section 3.7). Under these conditions, three-photon or higher-order processes resulting in ionization of the molecule are definitely possible and can be identified in UV-only measurements.

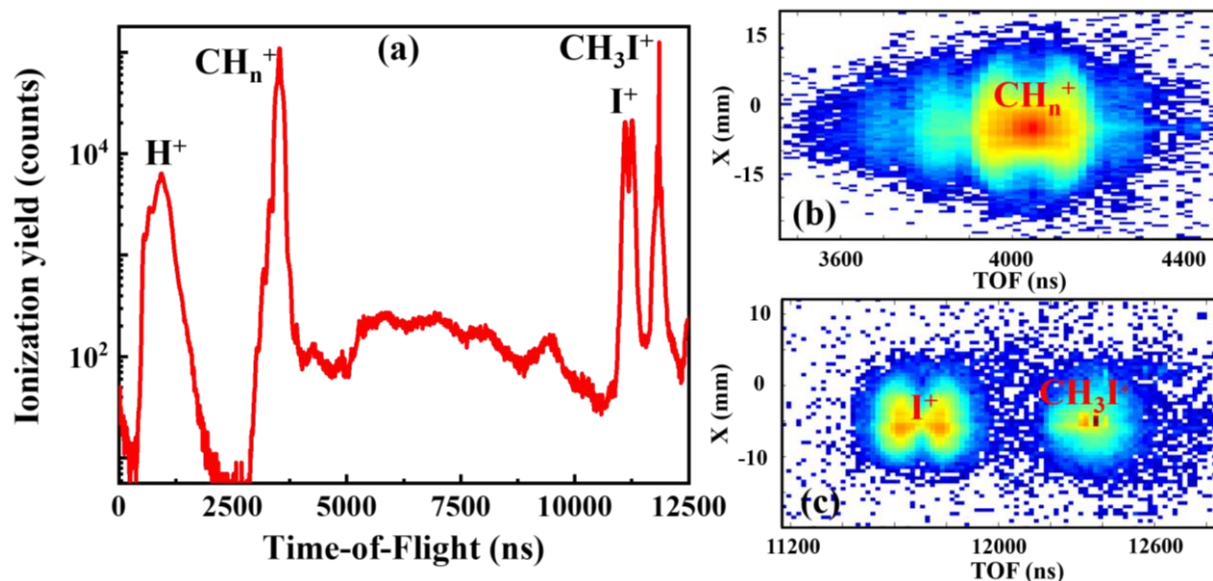


**Figure 4.1.** (a) Ion TOF spectrum from the ionization of  $\text{CH}_3\text{I}$  by a single UV pulse at the intensity of  $1.5 \times 10^{13} \text{ W/cm}^2$  intensity. 2-D TOF vs. position maps for two different TOF regions: (b)  $\text{CH}_n^+$  (c)  $\text{I}^+$  and  $\text{CH}_3\text{I}^+$ .

Fig. 4.1 shows the measured TOF spectrum of detected ions using a 263 nm pulse with a peak intensity of  $1.5 \times 10^{13} \text{ W/cm}^2$ . Vertical lines indicate the ion TOFs for different species calculated assuming zero momentum along the spectrometer axis. The figure shows that the primary species generated with UV are singly charged ions,  $\text{CH}_3\text{I}^+$ ,  $\text{CH}_3^+$ ,  $\text{I}^+$  and  $\text{H}^+$ , besides significantly lower contribution from the residual gas (broad features without labels). Since we do not consider channels involving deprotonation or hydrogen atom detachment in this work, we focus our further analysis on the heavier fragments. The spectrum clearly shows that the methyl ( $\text{CH}_3^+$ ) and iodine ions exhibit broad structures roughly symmetric around the zero-momentum lines. The left half corresponds to the ions flying towards the detector, and the right half corresponds to the ions initially flying in the opposite direction. The TOF vs. position maps are shown as 2-D maps in the insets of Fig. 4.1, representing scaled projections of the 3-D momentum sphere of specific species onto the x-y plane, determined by the TOF axis and the laser propagation

direction. These maps in insets manifest strong localized signals at the center of the images for  $\text{CH}_3^+$  and  $\text{I}^+$ , which could be attributed to the multi-photon DI resulting in low KE of the fragments.

The corresponding ion kinetic energy (KE) distributions shown in Fig 4.2 are dominated by low-energy fragments. The  $\text{CH}_3\text{I}^+$  parent ions appear with essentially zero KE because, due to momentum conservation, almost all access photon energy for this channel is carried by the emitted electron. For  $\text{CH}_3^+$ , besides the main peak very close to zero, we also observe a broad shoulder starting at  $\sim 0.5$  eV. The dominant zero-energy channel could be attributed to the ionization to higher vibrational states of the cationic  $\tilde{A}$  state, which dissociates via internal conversion to the  $\tilde{X}$  state, resulting in the  $\text{CH}_3^+ + \text{I}$  fragment pair [117]. The shoulder beyond 0.5 eV in  $\text{CH}_3^+$  spectrum as well as the events producing  $\text{I}^+$  ions most likely result from multi-photon ionization to one of the higher-lying repulsive states, which asymptotically generates either  $\text{CH}_3^+ + \text{I}^*$  or  $\text{CH}_3 + \text{I}^+$  products. We will discuss these DI scenarios later in this chapter (see section 4.3 below).

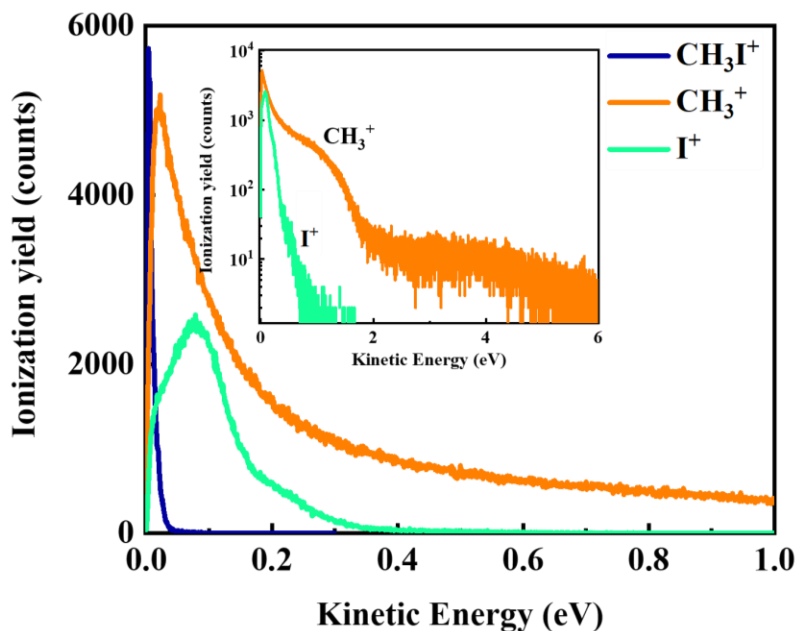


**Figure 4.2.** Kinetic energy (KE) distribution of  $\text{CH}_3^+$ ,  $\text{I}^+$ , and  $\text{CH}_3\text{I}^+$  fragments after  $\text{CH}_3\text{I}$  ionization by a single UV pulse at the intensity of  $1.5 \times 10^{13} \text{ W/cm}^2$  intensity. The inset shows the logged scale of the distribution over a larger KE range.

We did not observe any meaningful coincidence events from these measurements. Furthermore, we did not detect any doubly charged ions above the noise level. Both of these observations suggest that double ionization by the UV pulse alone can be neglected in our pump-probe measurements

Since ionization or DI of  $\text{CH}_3\text{I}$  by the UV light at 263 nm energetically requires at least three photons, the yields of these processes should depend non-linearly on the UV pulse intensity. In Fig. 4.3, we present the results obtained at several different UV intensities to verify this dependence. The TOF spectra normalized to the number of laser shots for multiple UV powers are shown in Fig. 4.3 (a), whereas the normalized yields of individual ions as a function of UV powers are plotted in Fig. 4.3 (b). The average UV power has been varied from  $2 \times 10^{12}$  to  $4 \times 10^{13}$   $\text{W}/\text{cm}^2$ . In the perturbative regime and in the absence of any saturation effects, the ionization yield resulting from the absorption of  $n$  photons is expected to be proportional to the  $n$ th power of the laser intensity as  $I^n$ . Subsequently, for fixed pulse duration and focusing parameters, it should have a similar dependence on the pulse power ( $P$ ), being proportional to  $P^n$ .

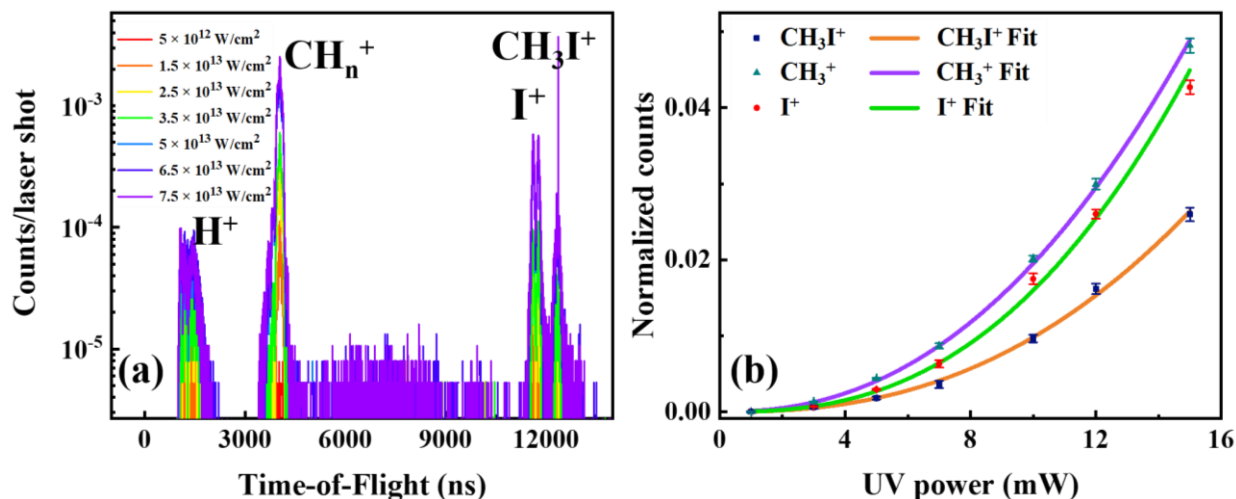


**Figure 4.3.** (a) Time-of-Flight (TOF) of the generated ions upon irradiation of the  $\text{CH}_3\text{I}$  molecule with the single UV pulse at 263 nm and different UV intensities in the range of 1- 15 mW power equivalent to  $5 - 7.5 \times 10^{13}$   $\text{W}/\text{cm}^2$  intensity. (b) The yield of the major ionic fragments as a function of UV intensities. The ion TOFs are labeled based on their mass-to-charge ratio, and solid lines show the power fits of the corresponding ion yield curves.

We fit the ionization yields of the individual ions in Fig. 4.3 (b) with a polynomial fit function of the form of  $\alpha P^n$ . We obtain the power dependence of  $n = 2.26 \pm 0.06$  for  $\text{CH}_3\text{I}^+$ ,  $2.69 \pm 0.14$  for  $\text{CH}_3^+$ , and  $2.76 \pm 0.07$  for  $\text{I}^+$ , which confirms the ionization rate of these ions scales nonlinearly with UV-intensity, proving the multi-photon nature of the process. However, the obtained values of  $n$  are lower than the value of 3 expected for a three-photon process. For the case of  $\text{CH}_3\text{I}^+$  with an ionization threshold of 9.54 eV, absorption of two photons in the blue edge of the

UV pulse spectrum (below 260 nm, see Fig. 3.7 (b)) can be sufficient for ionization, resulting in a possible mixture of two and three-photon processes. The production of  $\text{CH}_3^+$  and  $\text{I}^+$  ions, with energetic thresholds of 12.54 and 12.72 eV, respectively, needs at least three photons. The observed power dependence between two and three implies some degree of saturation for one of the absorption steps. Given the value of the absorption cross-section and our focal spot size, it is likely that the absorption of the first UV photon in the A band reaches a saturation regime above 5 mW. This is consistent with the results of our pump-probe experiments performed with different UV pump power discussed later in this chapter.

## 4.2 Ionization, dissociative ionization and Coulomb explosion of $\text{CH}_3\text{I}$ under intense NIR pulses

Fig 4.4 shows the TOF spectra and TOF-position maps for  $\text{CH}_3\text{I}$  molecule irradiated by NIR pulse with  $2.8 \times 10^{14} \text{ W/cm}^2$ . The same NIR intensity is used for all NIR-only data shown in this section.

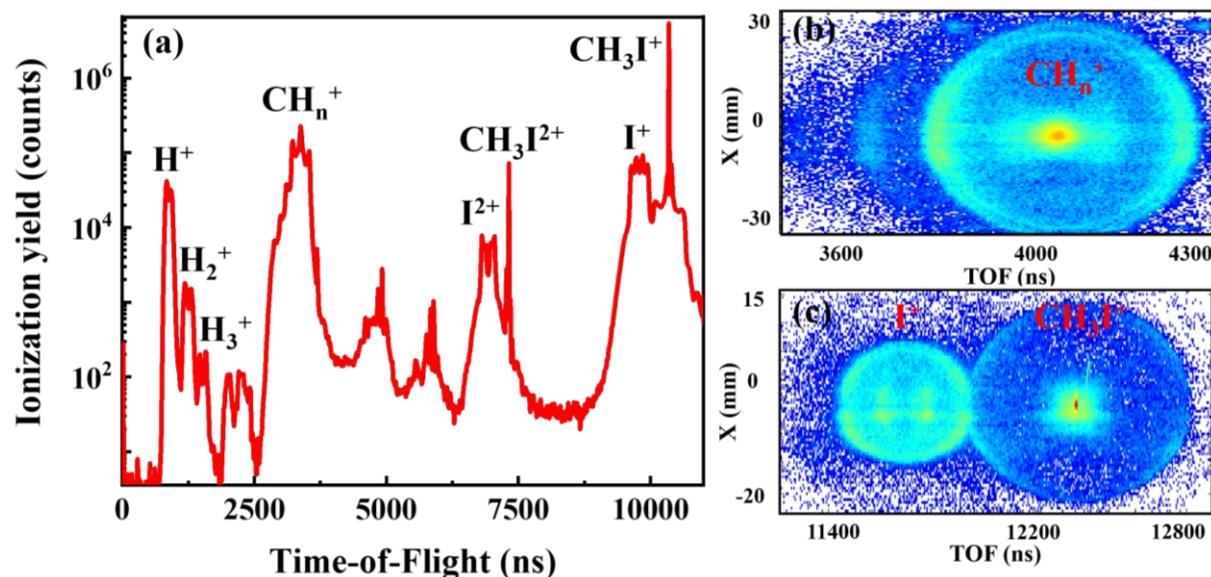


**Figure 4.4.** (a) Time-of-flight (TOF) spectrum of the generated ions upon irradiation of the  $\text{CH}_3\text{I}$  molecule with the single NIR pulse with  $2.8 \times 10^{14} \text{ W/cm}^2$  intensity. The TOF peaks are labeled based on the mass-to-charge ratios. 2-D TOF vs. position maps for two different TOF regions, (b)  $\text{CH}_n^+$  (c)  $\text{I}^+$  and  $\text{CH}_3\text{I}^+$  show the DI and CE channels.

Similar to the results for the UV pulse shown in Fig. 4.1, the spectrum is dominated by the bound parent ions ( $\text{CH}_3\text{I}^+$ ) and by  $\text{CH}_3^+$  and  $\text{I}^+$  fragments. However, in contrast to the UV spectrum of Fig. 4.1, non-negligible contributions from doubly charged ions are clearly distinguishable. In particular, the doubly charged parent ion could be seen as a localized narrow peak, reflecting the relatively small momentum sum of the two emitted electrons.

Fig. 4.4 shows that the NIR pulse alone causes both DI and CE of the molecule in the absence of the UV field. The signatures of these two processes can be clearly observed in the  $\text{CH}_3^+$  TOF vs. position image shown in Fig. 4.5. The central, low-kinetic-energy region corresponds to the DI process, where the second resulting fragment, iodine, remains neutral. More energetic features consisting of two outer ring-like structures can be assigned to CE. In agreement with earlier studies [117], [136], these data indicate that more than one channel contributes to the CE of the molecule. These rings show marked parallel anisotropy and are attributed to excitation to different electronic states of the  $\text{CH}_3\text{I}^{2+}$  di-cation, which we will discuss in the following.

The (non-coincident) KE distributions of the  $\text{CH}_3^+$  and  $\text{I}^+$  fragment ions are shown in Fig. 4.6. The spectra for both ion species show dominant peaks at nearly zero kinetic energy. These peaks, which correspond to the middle spot of the 2-D TOF vs. position maps, are due to the ions resulting from the DI of the molecule that have neutral partners.

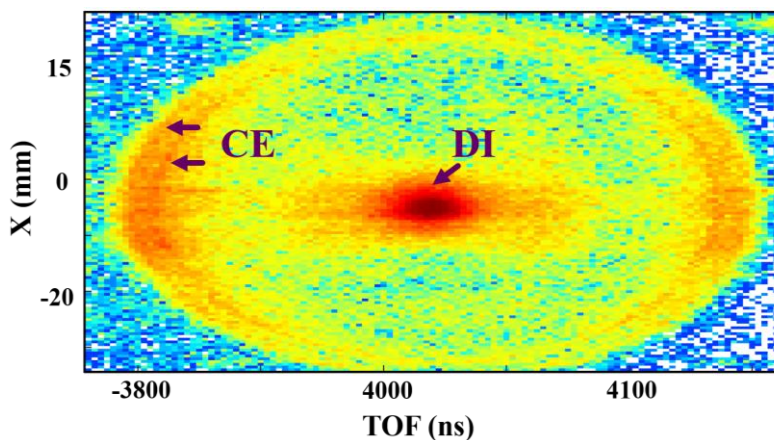


**Figure 4.5.**  $\text{CH}_3^+$  TOF distribution as a function of ion hit position on the detector after ionization of the molecule by a single NIR pulse. CE: Coulomb explosion; DI: dissociative ionization.

Two peaks centered around 3.82 and 4.44 eV are distinguished in the high kinetic energy regions for the  $\text{CH}_3^+$  ions, reflecting the two ring structures observed in Fig. 4.5. They correspond to the CE of the molecule and originate from the coincident channel  $\text{CH}_3^+ + \text{I}^+$ . The peak energy

values of these pathways agree with that reported by Liu. et al. [153] and in more recent studies [117], [136]. The values reported in the latter studies were 3.9 and 4.6 eV. These features are also present for  $I^+$ , but the limited energy resolution for smaller KE values does not allow to fully resolve them at the chosen settings for the spectrometer extraction fields. The  $CH_3^+$  energy distribution shows a weak feature at higher energies attributed to the CE with the higher-charged partner such as  $I^{2+}$ . These assignments are confirmed by coincidence data analysis discussed later in this section.

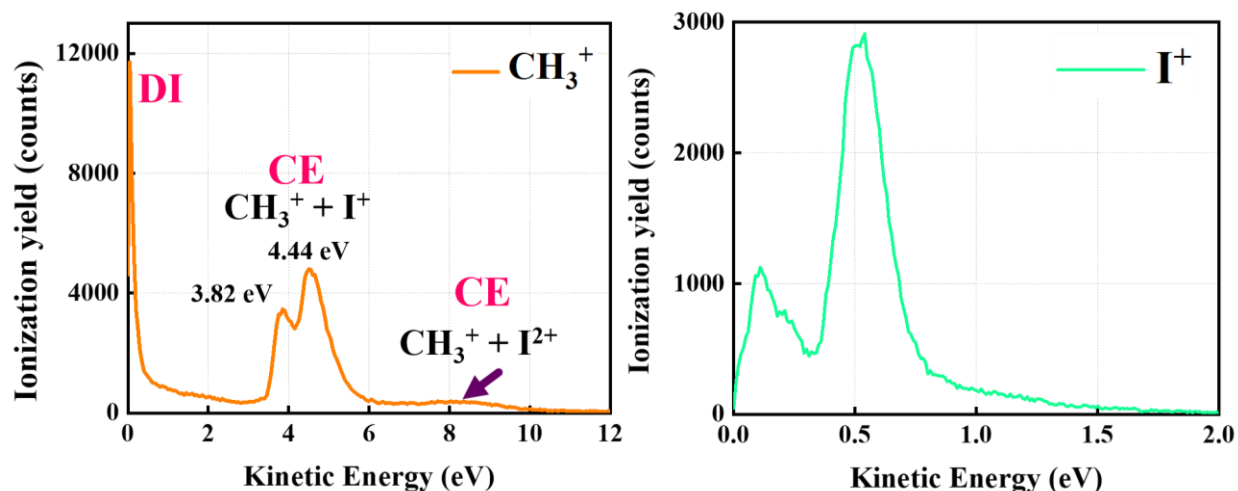


**Figure 4.6.** (a) KE distributions of  $CH_3^+$  (b) and  $I^+$ . The dominant peaks at nearly zero kinetic energy illustrate the molecule's DI. Two peaks centered around 3.82 and 4.44 eV correspond to the CE of the molecule and originate from the coincident channel  $CH_3^+ + I^+$ . The  $CH_3^+$  KE shows a weaker peak at higher energies due to the CE of the molecule with  $I^{2+}$  fragment.

In order to identify different two-body breakup channels more reliably, a PhotoIon-PhotoIon COincidence map (PIPICO) is commonly used. In the PIPICO spectrum shown in Fig. 4.7, the ionization yield is plotted as a function of the time of flight of the first hit ( $TOF_1$ ) and the time of flight of the second hit ( $TOF_2$ ). Due to the momentum conservation along the TOF direction, ions fragmented from a molecule end up in a diagonal coincidence stripe. These sharp lines represent two-body breakup channels, where both ionic fragments from the same parent molecule are detected in coincidence, satisfying the momentum conservation condition. It should be noted that if the parent molecule breaks up, the momenta of the nuclei are much higher than the momentum sum of absorbed photons and emitted electrons. Apart from the sharp lines, events resulting from false coincidences, where the two detected ions originate from different molecules,

or from many-body breakup processes, where one or more fragments are not detected, appear as broad structureless features.

After selecting the channel of interest, particular gates, as shown in Fig. 4.7, can be applied on that coincidence stripe, and only the events within the chosen coincidence channel are maintained for further analysis. Besides setting a gate on the PIPICO spectrum, which reflects momentum conservation condition for the momentum components parallel to the spectrometer axis, similar conditions are set on the other two momentum components, parallel to the laser beam and molecular beam propagation direction. Adding such 3D momentum conservation filter helps to isolate all those events originating from a particular channel. The comprehensive details of such a coincidence analysis procedure can be found in [89], [251], [254].

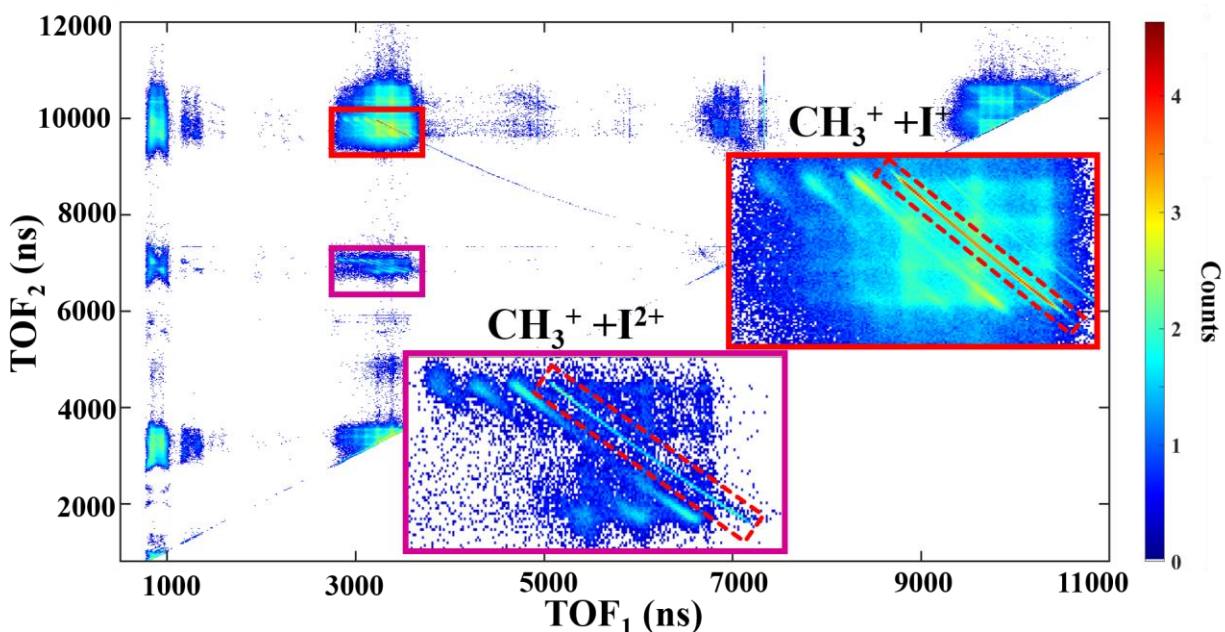


**Figure 4.7.** Photoion-photoion coincidence (PIPICO) spectrum for the fragmentation of  $\text{CH}_3\text{I}$  molecule by a single NIR pulse. The solid boxes indicate two selected coincident channels, and their zoomed-in maps are shown as insets. These maps also show a set of parallel lines reflecting the “incomplete” channels, where one or more hydrogens are detached.

The PIPICO spectrum shown in Fig. 4.7 specifically illustrates two coincident channels that will be discussed in more detail below: (i)  $\text{CH}_3^+ + \text{I}^+$  and (ii)  $\text{CH}_3^+ + \text{I}^{2+}$ . Besides these two structures, which are marked by the boxes and shown in the insets, there is also a long, tail-like feature in the main PIPICO spectrum, which originates from the line corresponding to channel (i) and goes towards the point corresponding to the TOF of doubly charged parent ions for both

detected ions. This line reflects the events where the doubly-charged parent ion is in a metastable state and decays into  $\text{CH}_3^+ + \text{I}^+$  ion pair on its way towards the detector. A detailed analysis of this feature can be found in [255]. The spectrum lacks any sharp lines associated with  $\text{H}^+$ ,  $\text{H}_2^+$  and  $\text{H}_3^+$  ions TOF positions, indicating that these ions either have neutral partners or result from the outcome of the fragmentation of the parent molecule into three or more fragments.

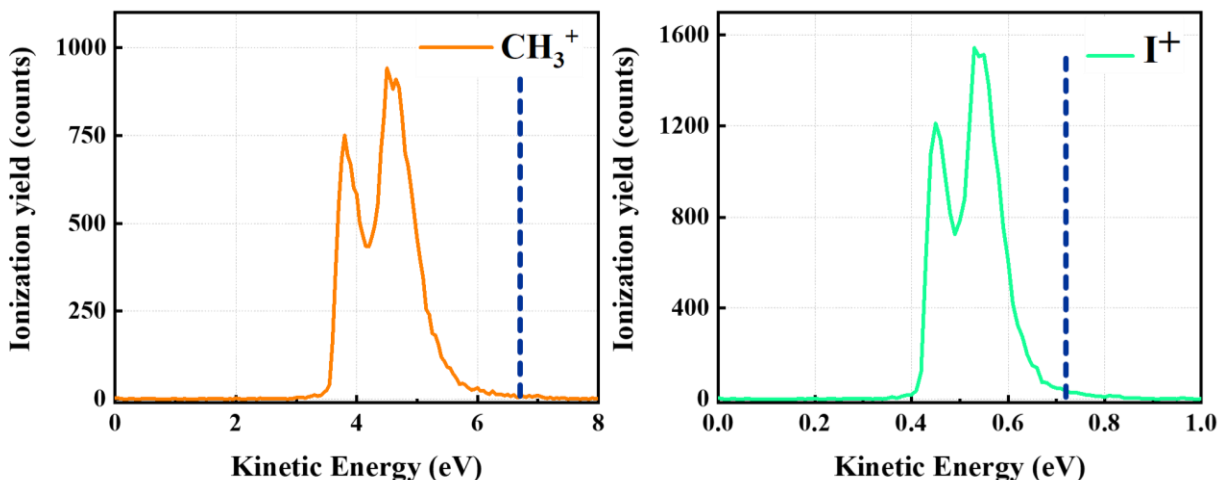


**Figure 4.8.** Kinetic energy distributions of (a)  $\text{CH}_3^+$  and (b)  $\text{I}^+$  detected in coincidence after the single NIR pulse. The solid lines represent the experimental data. The vertical dashed lines depict the CE simulation results obtained assuming that two point-like charges are instantaneously created at the position of the iodine atom and at the center-of-mass of the methyl group at the equilibrium geometry of the neutral  $\text{CH}_3\text{I}$  molecule.

Fig 4.8 illustrates KE distributions of  $\text{CH}_3^+$  and  $\text{I}^+$  for the two-body breakup of  $\text{CH}_3^+ + \text{I}^+$  under the coincidence condition. Compared to the KE distributions in the non-coincidence case, the events originating from the dissociative ionization of the singly charged fragments do not survive the momentum conservation filter, and the strong low-energy feature is thus absent in these distributions. Comparing these coincident spectra with the non-coincident results shown in Fig. 4.6, we can confirm the assignment of the main high-energy features in the non-coincident spectra to the  $\text{CH}_3^+ + \text{I}^+$  CE events. In this case, the energy sharing between the two fragments is determined by the inverse ratio of masses, with the lighter fragments taking most of the available KE. In this graph, the experimental data are compared with the prediction of a simple Coulomb explosion simulation (CES), which assumes instantaneous double ionization of the molecule at its equilibrium geometry and purely Coulombic final-state PEC, as described in section 2.6.

The measured individual KEs are significantly lower than the energies obtained from this simple CES. There are two major factors that could contribute to this discrepancy. First, because of the nuclear motion between the two ionization steps, the CE can take place at a distance larger than the equilibrium distance, reducing the resulting CE energy. Second, more importantly, the PECs of the doubly-charged states of CH<sub>3</sub>I are definitely non-Coulombic. The appearance of the bound CH<sub>3</sub>I<sup>2+</sup> di-cations in the TOF spectrum is shown in Fig. 4.4., as well as the signatures of metastable di-cations observed in the PIPICO spectrum of Fig. 4.7, indicate the existence of a potential minimum for CH<sub>3</sub>I<sup>2+</sup>. This is well-documented in the earlier work of Corrales et al. [136]

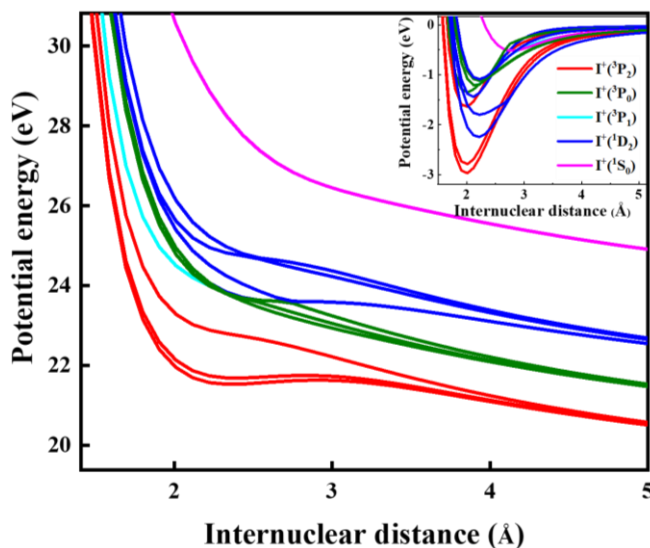


**Figure 4.9.** Potential energy curves along the C-I bond for the di-cation CH<sub>3</sub>I<sup>2+</sup>. The potential curves that correlate with the same electronic state of I<sup>+</sup> have been represented with the same color. The inset shows the potential energy curves after subtracting the purely Coulombic PEC and downward shifting in the energy axis to the zero-potential energy to better appreciate the bound character and its depth in the different electronic states of the di-cation denoted with different colors. PECs are adapted from Ref. [136].

Their *ab-initio* calculations revealed the existence of such bound minimum in low-lying CH<sub>3</sub>I<sup>2+</sup> PECs, as illustrated in Fig. 4.9. While the higher di-cationic PECs show a purely repulsive character, for the lower PECs, particularly those correlated with I<sup>+</sup> (<sup>3</sup>P<sub>2</sub>) fragments, the attractive covalence forces in the Franck-Condon region are comparable with the Coulomb force. This results in the formation of metastable states and in the reduction of the fragment energies. The kinetic energy of the fragments for each di-cation fragmentation channel can be obtained from the

depth of the well after the Coulomb energy subtraction. Based on their calculated PECs, they assigned the experimental peak at 4.41 eV to the channel yielding the ground state  $\text{CH}_3^+$  and  $\text{I}^+$  ( $^1\text{D}_2$ ), whereas the peak at 5.23 eV was assigned to several contributing channels, including  $^3\text{P}_{2,1,0}$ , and  $^1\text{D}_2$ .

### 4.3 UV-induced photodissociation of $\text{CH}_3\text{I}$ studied with time-resolved ion momentum imaging

This section presents the results of UV-NIR pump-probe experiments on  $\text{CH}_3\text{I}$  photodissociation dynamics, which employ time-resolved CEI as a probing scheme. Here, the observables discussed in the previous sections, such as yields and KE distributions of coincident and non-coincident ionic fragments, are analyzed as a function of UV-NIR delay. For most of the experiments discussed here, we used the UV pump pulse intensity of  $\sim 1.5 \times 10^{13} \text{ W/cm}^2$  and NIR probe pulse intensity of  $2.8 \times 10^{14} \text{ W/cm}^2$ , corresponding to the values used in single-pulse experiments illustrated in Figs. 4.1 - 4.2 and Figs. 4.4 - 4.8, respectively. The pump-probe data below are shown for this combination of intensities unless explicitly stated otherwise. In addition, for several studies, we scanned either the pump or the probe intensity. Since this section mainly focuses on two-body dynamics involving C-I bond cleavage, the events resulting in the breakup of the methyl group (e.g., the detachment of one or more hydrogen atoms or protons) are not considered here.

As briefly mentioned at the beginning of this chapter, even though the central goal of this work is to study the dynamics following the absorption of a single UV photon, at the pump pulse intensities used here, contributions from the competing processes resulting from the absorption of two or three UV photons cannot be neglected. Figs. 4.10 - 4.12 illustrate three basic scenarios for probing the dynamics induced by one-, two- or three-photon absorption in a pump-probe experiment with an intense NIR probe. These scenarios are discussed employing a set of PECs for neutral and cationic states of  $\text{CH}_3\text{I}$  obtained as a 1D cut of molecular PESs along the C-I internuclear distance coordinate. The curves are adapted from Ref. [119], [136].

**1. A-band dissociation:** After the absorption of a single UV photon, resonant single-photon excitation results in a rapid C-I bond cleavage and breaks the molecule into neutral  $\text{CH}_3$  and  $\text{I}$  fragments. A subsequent delayed NIR probe pulse can singly, doubly, or triply ionize the dissociating molecule. Correspondingly, the photodissociation dynamics can be mapped by

analyzing delay-dependent yields and KE distributions of  $\text{CH}_3^+$  and  $\text{I}^+$  ions resulting from the interaction of the molecule with pump and probe pulses. This scheme is shown in Fig 4.10.

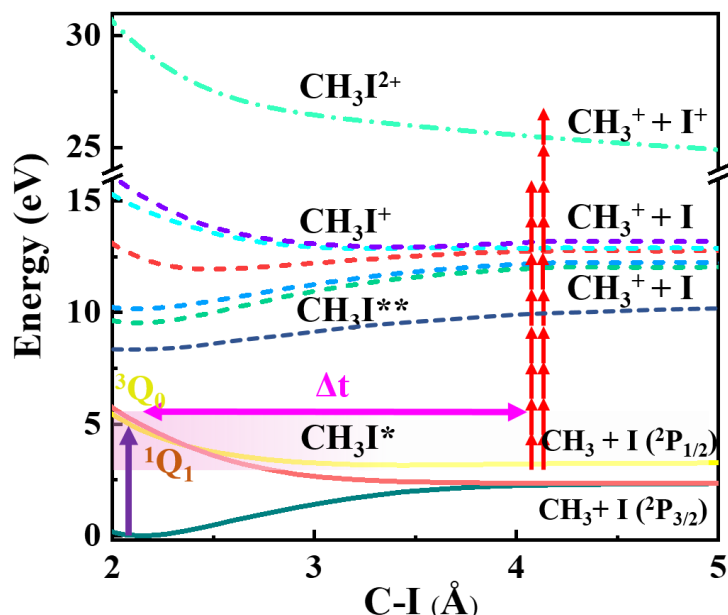
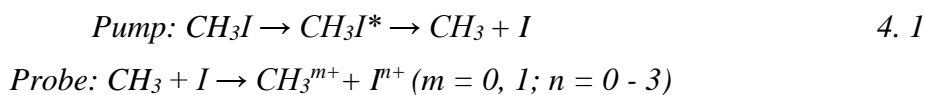


**Figure 4.10.** A-band dissociation. Excitation schemes and relevant electronic states in UV-photodissociation of  $\text{CH}_3\text{I}$  followed by strong-field ionization to cationic or di-cationic states by the probe pulse. Potential energy curves (PECs) are adapted from [119], [136].

- Rydberg excitation:** Absorption of an additional pump photon can transfer the population to higher-lying Rydberg states of the molecule. Although the absorption of two UV photons from the high-energy tail of our UV spectrum (below 260 nm) can result in ionization, for our central wavelength of 263 nm, two-photon absorption populates the states just slightly below the ionization threshold, which can be ionized by a single NIR photon from the probe pulse. As sketched in Fig. 4.11, two-photon excitation to Rydberg states can proceed directly via quasi-instantaneous absorption of both UV photons or involve a non-negligible time delay between the two absorption steps within the duration of the UV pulse. In the latter case, the first photon excites the molecule to the dissociative A-band manifold and, while dissociating, it can absorb a second photon, resulting in the population of somewhat lower Rydberg states at larger C-I

distances. Under this scenario, a delay-dependent yield of bound parent ions is a useful pump-probe observable, in addition to methyl or iodine fragments.



4. 2

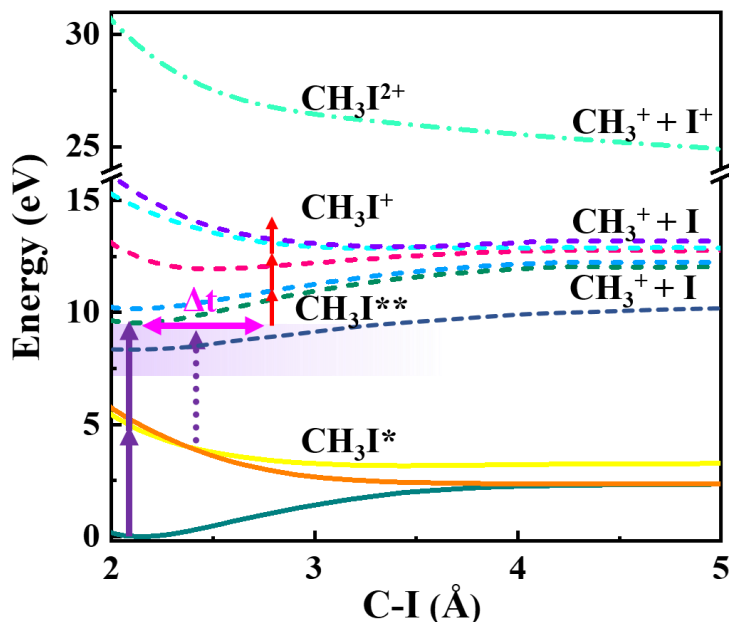
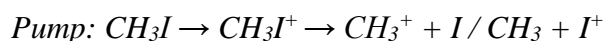
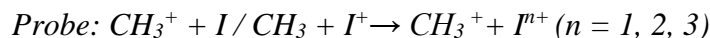


**Figure 4.11.** Excitation to higher-lying Rydberg states by either a direct transition or through intermediate neutral excited states. Excitation schemes and relevant electronic states in UV-photodissociation of  $\text{CH}_3\text{I}$  followed by multi-photon ionization, probing to cation, and di-cation states. Potential energy curves (PECs) are adapted from [119], [136].

**3. Dissociative multi-photon ionization:** At high UV intensities, another possible scenario is multi-photon dissociative ionization (DI) by the pump pulse. As discussed in Section 4.1, this scenario requires the absorption of at least three UV photons, and its relevance can be monitored by the appearance of low-energy  $\text{CH}_3^+$  and  $\text{I}^+$  ions in the UV-only data, as well as by their dependence on the UV pulse intensity. This excitation scheme is illustrated in Fig. 4.12.



4. 3



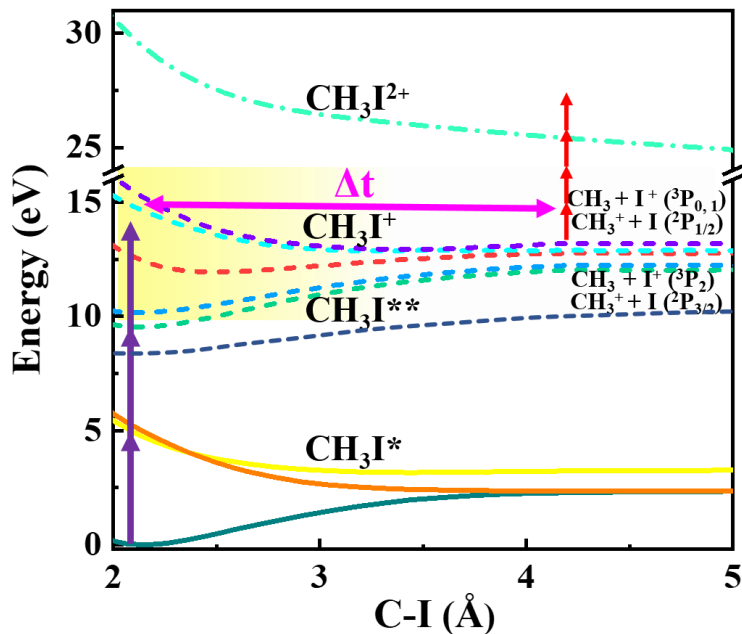


**Figure 4.12.** Excitation schemes and relevant electronic states for UV multi-photon dissociative ionization. Potential energy curves (PECs) are adapted from [119], [136].

### 4.3.1 Channel identification by comparison of coincident and non-coincident data

We start our presentation of the pump-probe results with the non-coincident data for  $\text{CH}_3^+$  and  $\text{I}^+$  fragments. Fig. 4.13 shows the delay-dependent KE distribution for all detected  $\text{CH}_3^+$  (a) and  $\text{I}^+$  (b) ions. These maps include contributions from all possible final states resulting in the production of at least one of those singly charged ions, which might have either neutral or charged partners. To complement these data, in Fig. 4.14, we show a similar spectrum but for  $\text{CH}_3^+$  and  $\text{I}^+$  ions detected in coincidence with each other in the same measurement. Here, the kinetic energy release (KER) for this channel, which is calculated as a sum of individual KE of  $\text{CH}_3^+$  and  $\text{I}^+$ , is plotted as a function of UV-NIR pump-probe delay. While all the events plotted in Fig. 4.14 are included in Fig. 4.13 (a) and (b), these two graphs also contain additional events, where the corresponding  $\text{CH}_3^+$  (4.13 (a)) and  $\text{I}^+$  (4.13(b)) ions appear with either neutral partner, or with some other charged fragment.

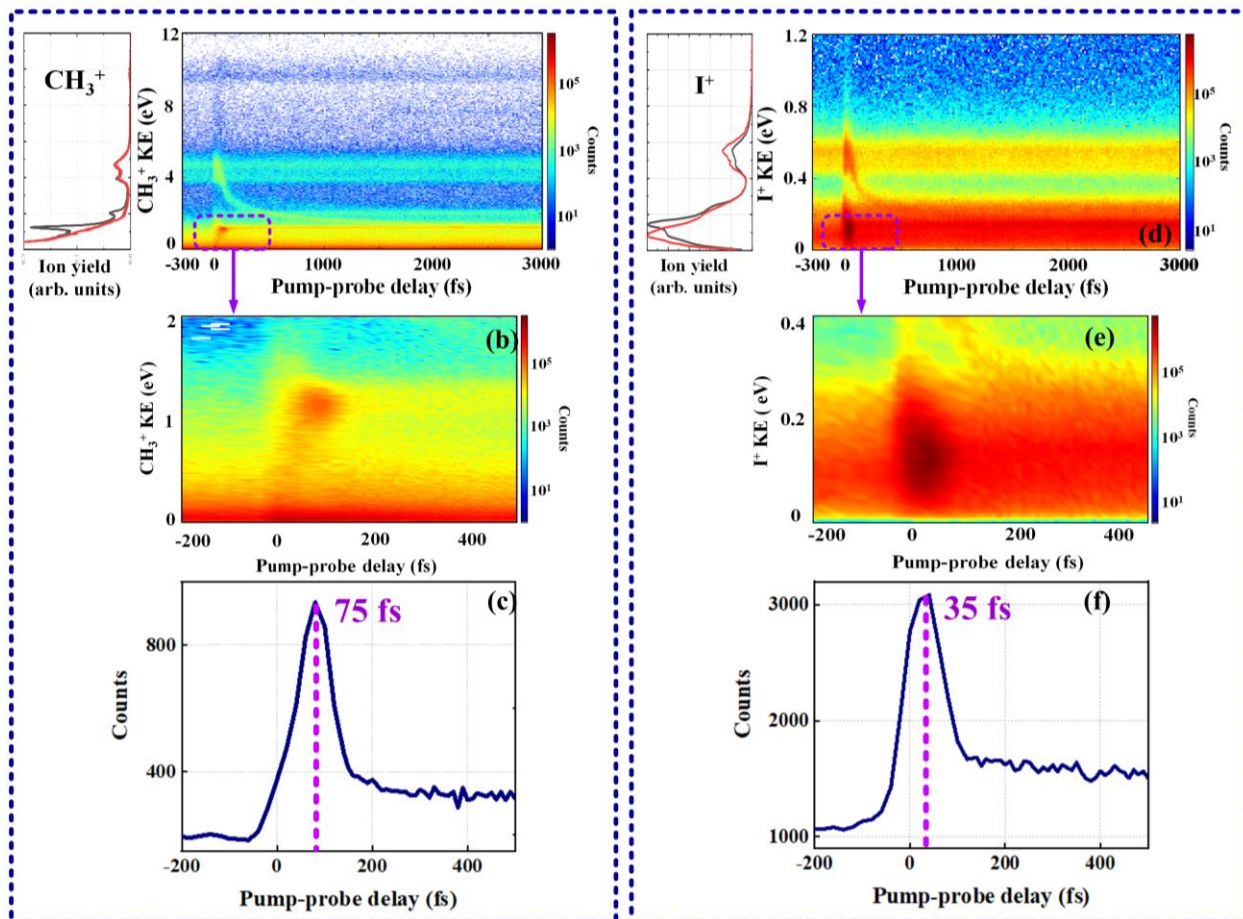


**Figure 4.13.** Delay-dependent kinetic energy distribution of (a)  $\text{CH}_3^+$  and (b)  $\text{I}^+$  ions. Here, as well as in all other delay-dependent graphs, negative and positive delays correspond to the NIR and UV pulses arriving first, respectively. The projections of these graphs onto the kinetic energy axis in the delay range of 2.5–3 ps (black) and -500–-100 fs (red) are shown on the left. (c), (d) The projections of the areas marked by dashed rectangles, centered at 1.25 eV in (a) and 0.1 eV in (b), onto the delay axis. The projections peak at the delay values of 75 fs for  $\text{CH}_3^+$  ions shown in (c) and at 35 fs for  $\text{I}^+$  ions in (d).

There are two structures that display a similar shape in Fig. 4.13 (a, b) and Fig. 4.14. First, in all three graphs, there is a horizontal high-energy band consisting of two lines, which appear to be essentially delay-independent except for the small region around zero delay. As can be seen from the projections on the KE axis, the KE distribution for this region is nearly identical to the corresponding region in the KE spectra obtained with the probe pulse alone (shown in Fig. 4.6 and 4.8 for the non-coincident and coincident data, respectively). Therefore, this two-peak structure

mainly reflects the events, where double ionization and subsequent CE occur in the NIR pulse without a pronounced effect from the UV pump. The molecules contributing to this band either did not absorb any UV photons or remained bound after their interaction with the UV pulse. This assignment is also consistent with the results of our earlier UV-NIR [98] and NIR-NIR [117] pump-probe experiments, where a very similar structure has been observed. The origin of the two peaks within this feature and its washed-out appearance in non-coincident  $I^+$  data have already been rationalized in section 4.2.

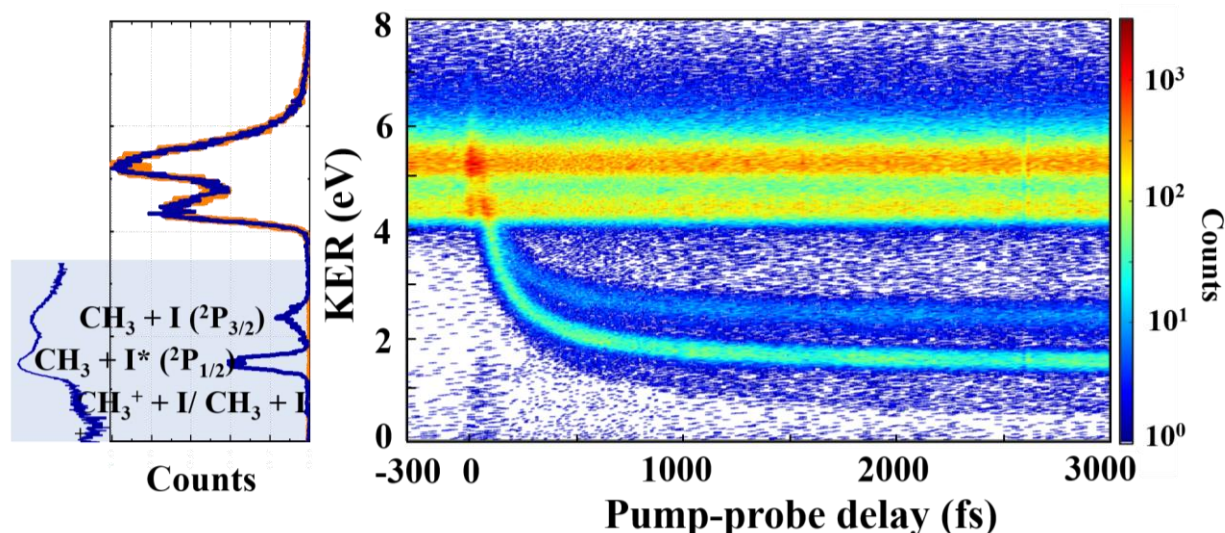


**Figure 4.14.** Delay-dependent KER distribution of the two-body coincidence channel  $CH_3^+ + I^+$ . The projections of KER distribution in the delay range of 2.5–3 ps (navy) and -500–-100 fs (orange) are shown on the left. For the former projection, the shaded area is also shown in log scale as an inset to illustrate the shape of the low-KER part.

Second, a descending band, which appears as a triangular-shaped structure overlapping with the high-energy feature discussed above around zero delay and propagates towards lower KER values as the delay increases, can be observed in both non-coincident and coincident spectra of Figs. 4.13 (a, b) and Fig. 4.14. While in the coincident plot shown in Fig. 4.14, this band splits into two after a few hundred femtoseconds and can be clearly resolved at larger delays, in the non-coincident spectra of Fig. 4.13 (a, b), it merges with intense low-KE structures within less than 500 femtoseconds. This feature is due to the molecules dissociated by the pump pulse and then doubly ionized and Coulomb-exploded by the probe at increasing internuclear separations. This channel represents the main scenario that is used for studies of photodissociation dynamics in this

chapter and will be discussed in detail below. However, we first start with a discussion of the features that do not appear in the coincident graph of Fig. 4.14 but are present in single-ion data shown in Fig. 4.13.

In general, such events can be coarsely classified into three different groups. First, there could be  $\text{CH}_3^+$  or  $\text{I}^+$  ions from multiple ionization of the molecule that is produced with a charged partner but not with each other. For  $\text{CH}_3^+$  in Fig. 4.13 (a), signatures of such channel(s) can be traced at high KEs (above 6-7 eV). The corresponding  $\text{CH}_3^+$  ions result from the breakup of triply-ionized molecules or from even higher charge states and appear with doubly- or multiply-charged iodine partners. Most of those events can be identified in other two-body coincident spectra like the  $\text{CH}_3^+ + \text{I}^{2+}$  channel, which will be discussed below. For  $\text{I}^+$  ions in Fig. 4.13(b), such contributions from multiple ionization are more difficult to identify since the methyl group does not remain stable with two or more charges, resulting in a variety of several possible few-body breakup channels. Second, some of  $\text{CH}_3^+$  and  $\text{I}^+$  ions in Fig. 4.13 could originate from  $(\text{CH}_3\text{I})_2$  dimers, a small fraction of which is present in our molecular beam. Third, most importantly, the majority of the low-KE  $\text{CH}_3^+$  and  $\text{I}^+$  ions in Fig. 4.13, absent in the coincident data of Fig. 4.14, result from the events where only one ionization occurs after both pump and probe pulses.

### **4.3.2 Pathways contributing to the low-energy region of non-coincident $\text{CH}_3^+$ and $\text{I}^+$ spectra**

For both  $\text{CH}_3^+$  and  $\text{I}^+$ , the low-KE region contains a significant amount of events resulting from the DI of  $\text{CH}_3\text{I}$  induced by either UV or NIR pulses alone (quantitatively dominated by the latter). The KE distributions of the corresponding contributions are identical to those shown in Figs. 4.2 and 4.6, respectively. They are delay-independent and peak close to zero. In addition, the UV pulse often induces dissociation of the neutral molecule, producing methyl and iodine fragments which can be ionized by the NIR probe pulse. If the NIR pulse arrives before the molecule dissociates, this scenario could lead to the production of a singly-charged parent ion,  $\text{CH}_3\text{I}^+$ , which either remains bound or dissociates along one of the ionic repulsive PECs. In contrast, if the NIR pulse arrives when the neutral molecule is already fully dissociated, single ionization always generates one of the ionic fragments, either  $\text{CH}_3^+$  or  $\text{I}^+$ . This effect results in the enhancement of the low-KE  $\text{CH}_3^+$  and  $\text{I}^+$  ion yields at large positive delays (compared to negative

delays, where the NIR pulse arrives first), as can be clearly seen in the corresponding projections onto the delay axis shown in Fig. 4.13 (c) and (d), respectively.

The KE distribution of these fragments is determined by the shape of the repulsive PECs of neutral  $\text{CH}_3\text{I}$  (see Figs. 2.7-2.8 and 4.10) and, at large delays, manifests two peaks, which reflect the dissociation pathways producing ground-state  $\text{I}(^2\text{P}_{3/2})$  and spin-orbit-excited  $\text{I}(^2\text{P}_{1/2})$  state iodine atoms. For  $\text{CH}_3^+$  ions in Fig. 4.13 (a), these two channels appear as two horizontal bands at large delays, or as two peaks in the projection of the large-delay region onto the KE axis, both centered as  $\sim 1.3$  eV for  $\text{CH}_3 + \text{I}^*$  and at  $\sim 2$  eV for  $\text{CH}_3 + \text{I}$  channels (see the discussion in section 2.3.1.1). This interpretation is consistent with the results of earlier non-coincident pump-probe experiments [98], [138]. While the signatures of these two bands can also be traced in Fig 4.13 (b) for  $\text{I}^+$  ions, at much lower KE values determined by the 15:127 fragment mass ratio, they are much less distinct because of the limited KE resolution and very low absolute KEs. It should be noted that at the delays larger than a few hundred femtoseconds, the same dissociation events but probed via a doubly charged state (i.e., ending up in the  $\text{CH}_3^+ + \text{I}^+$  final state) produce  $\text{CH}_3^+$  or  $\text{I}^+$  ions with essentially the same kinetic energies, as can be seen from the comparison of Figs. 4.13 (a,b) and 4.14. This is because at large delays (and, thus, at large internuclear separations), the Coulomb repulsion between the final-state ions becomes negligible, and the KE of the ions is determined by the energy gained during the dissociation along the neutral PECs.

#### **4.3.2.1. Non-coincident spectra in the “overlap” region and the role of light-induced conical intersection**

While the contributions from the pathways discussed above can reasonably account for the formation of the non-coincident spectra of Fig. 4.13 at large delays, they cannot explain the behavior of the low-energy part of these spectra around zero delay, where the UV-pump and NIR-probe pulses fully or partially overlap. While an overall enhancement of ionization signal driven by the simultaneous presence of both pulses can be expected and is a common feature of such pump-probe experiments (see, e.g., [98], [99], [256]), the results of Fig. 4.13 for both ions manifest a pronounced maximum at a non-zero delay (75 fs for  $\text{CH}_3^+$  and 35 fs for  $\text{I}^+$ , see Fig. 4.13 (c) and (d), respectively) for the KE value approximately coinciding with the KE of the  $\text{CH}_3 + \text{I}^*$  band. Moreover, for  $\text{CH}_3^+$ , a titled band starting at zero KE at zero delay and reaching the region of

maximum enhancement at  $\sim 75$  fs can be observed in the spectrum, as highlighted in the inset of Fig. 4.13 (c), where the enlarged view of the corresponding region is shown. A similar tilted feature has been observed in earlier experiments [137], [138], where it was attributed to the creation of a light-induced conical intersection (LICI) in neutral  $\text{CH}_3\text{I}$  by moderately intense NIR pulse.

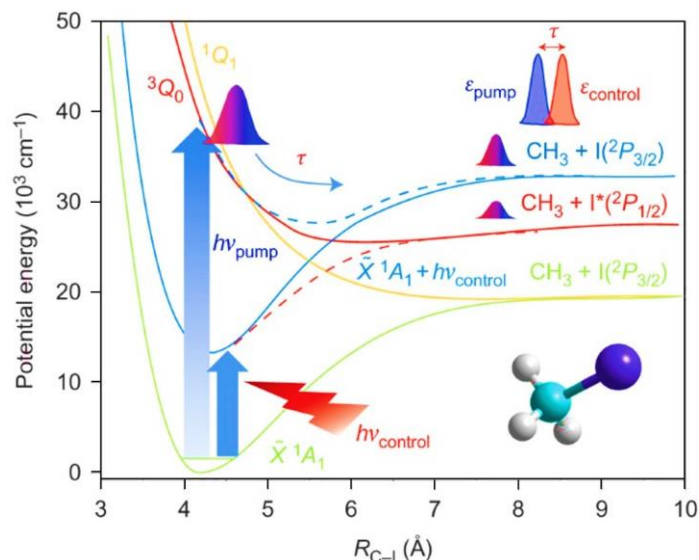


**Figure 4.15.** Schematics of the LICI formation. A UV pump pulse prepares a wave packet in the  ${}^3\text{Q}_0$  excited state, while the (time-delayed) NIR pulse creates the LICI, here shown as the crossing of  ${}^3\text{Q}_0$  and the ground  $\tilde{\text{X}}\text{ }^1\text{A}_1$  state shifted up in energy by one NIR photon. For sufficiently strong fields, the NIR pulse can also induce a strong modulation of the potentials around the LICI, as shown by dashed red and blue lines. Adapted from Ref. [137].

This scenario is schematically depicted in Fig. 4.15. In brief, with the UV pulse only, the molecule mainly dissociates via a repulsive excited state (in our specific case,  ${}^3\text{Q}_0$ ), with some part of the wave packet channeling to  ${}^1\text{Q}_1$  PEC via a conical intersection, as discussed in section 2.3.1.1. At some larger internuclear distance ( $\sim 5.4$ - $5.5$  a.u in Fig. 4.15, corresponding to  $\sim 2.9$ - $3$  Å), this excited state is separated from the ground state by one NIR photon, which in the presence of the NIR results in the creation of LICI. When crossing such LICI, part of the wave packet, for which the kinetic energy acquired while evolving in the excited state is enough to overcome the remaining bond energy, can proceed to dissociation via the (up-shifted) ground state. This results in the production of  $\text{CH}_3 + \text{I}({}^2\text{P}_{3/2})$  fragment pair; however, because of the potential well in the ground state, the KE energy of the fragments are lower than for both “regular” UV-induced dissociation channels. As detailed in Ref. [137], the exact value of the KE, location of the LICI as well as the

shape of the molecular PECs in its vicinity depend on the wavelength, intensity and duration of the NIR pulse, as well as on UV-NIR delay. However, qualitatively, the KER of the corresponding channel (and, thus, the KE of the resulting individual fragments) varies from zero, when the wave packet has just enough energy to overcome the bond energy, to the full energy of the excited-state channel when all parts of the excited-state wave packet dissociate without being disturbed by the NIR pulse. This is reflected in the tilted band highlighted in the inset of Fig. 4.13 (c).

The experiment in Ref. [137] employed a dedicated “control” NIR pulse with variable parameters to induce the LICI and a separate probe pulse at a very large delay. In contrast to our experiments, the NIR pulse has a dual role in forming the low-KE part of the spectrum. First, it reshapes the PES and creates the LICI. Second, it probes the photodissociated fragments via ionization. It should be noted that since the intensity of the NIR pulse is rather high ( $2.8 \times 10^{14}$  W/cm<sup>2</sup>), and the LICI formation is a one-photon process with respect to NIR light, the effective time window where it is possible can be much longer than the 23-25 fs FWHM duration of the pulse. For example, the UV-induced wave packet can pass through the LICI already in the leading edge of the NIR pulse, well before its maximum, where the ionization is likely to occur. Therefore, even though the delay of 75 fs corresponding to the maximum of the CH<sub>3</sub><sup>+</sup> signal in Fig. 4.13 (c) lies outside of the direct overlap between the UV and NIR pulses if it is considered in terms of FWHM of both pulses, it is still likely that at least up to this delay, the growth of the signal, which is also accompanied by the increase in the KE of the corresponding ions, is driven by the presence of the LICI created by the NIR pulse. We should also note that in the experiment in Ref. [138], where the configuration was similar to the present study, but both pulses were significantly longer, the tilted low-energy feature at small delays manifested a very similar shape.

While the interpretation based on the LICI picture gives a reasonable explanation for the KE and the temporal shape of the low-KE CH<sub>3</sub><sup>+</sup> signal, it cannot directly account for different positions of the maxima of the delay-dependent CH<sub>3</sub><sup>+</sup> and I<sup>+</sup> signals, which is clearly observed in Fig. 4.13 (c, d). The exact origin of this difference still remains unclear. A similar effect was also observed in an earlier experiment UV-NIR pump-probe experiment reported in Ref. [256]. There, the authors considered and ruled out pure ionic- or Rydberg-state dynamics as potential scenarios behind their observations and focused on the pathways involving initial one-photon excitation in the A-band, followed by the absorption of additional UV photon(s) later in the pump pulse. In this scenario, first UV-photon absorption initiates the A-band dissociation and launches a wave packet

on the repulsive excited states manifold. While the wave packet is accelerated on these PECs before the probe pulse arrives, it can absorb further UV photon(s), e.g., from the trailing edge of the pulse. As sketched in Fig. 4.11, the absorption of one additional UV photon results in the transition to one of the high-lying Rydberg states slightly below the ionization threshold, which can be coupled to the ground ( $\tilde{X}$ ) or to the first excited ( $\tilde{A}$ ) ionic states by simultaneous or subsequent absorption of one or a few NIR photons. If the wave packet moving down the neutral PECs has already gained enough energy, it can escape the corresponding ionic potential well and result in the production of  $\text{CH}_3^+$  or  $\text{I}^+$  ions. Since the asymptotic limit for the production of  $\text{I}^+$  is  $\sim 0.6$  eV higher than for  $\text{CH}_3^+$  (see Fig. 4.16), the range of internuclear separations where it remains accessible with two UV and three NIR photons is smaller than for  $\text{CH}_3^+$  generation, which can cause an earlier peak of the delay-dependent  $\text{I}^+$  signal in Fig. 4.13 (d). Alternatively, if, in total, three UV photons are absorbed from the pump pulse, the molecule can be directly ionized to the ionic  $\tilde{A}$  state. In this case, the transient  $\text{I}^+$  signal can be influenced by the position of one-photon NIR resonance with one of the higher-lying repulsive states converging to the  $\text{CH}_3 + \text{I}^+$  limit.

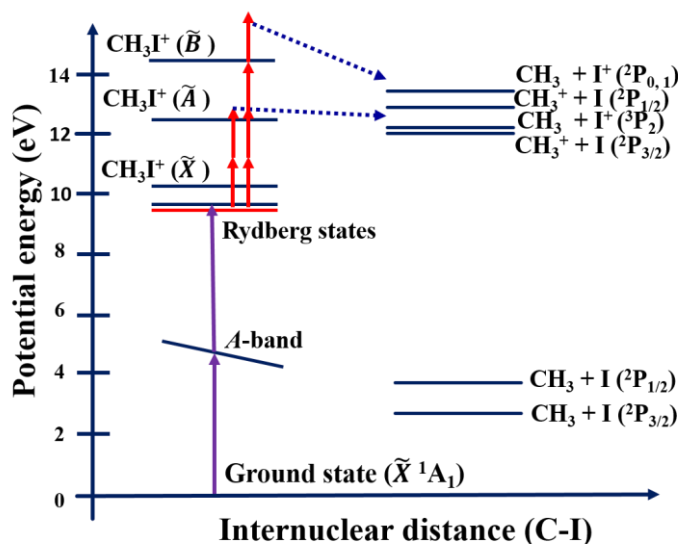


**Figure 4.16.** Schematic of relevant energy levels for neutral and ionic states involved in one- and two-photon excitations in the Franck-Condon region and the asymptotic regime. The values are obtained from Ref. [164]

We argue that potential contributions from one of the two mechanisms outlined above, which add up to the events originating from the formation of the LICl, are likely responsible for

different temporal behavior of the low-KE  $I^+$  and  $CH_3^+$  signals at small delays. Since both of these mechanisms are non-linear with respect to the UV photoabsorption, they should manifest a non-linear dependence on the UV pulse power. Although a dedicated experiment, where we measured the yields of the corresponding channels as a function of UV power, did not deliver conclusive results, we did observe certain deviation from linear dependence, which is consistent with potential contributions from two- or three-photon channels

### 4.3.3 Probing UV-induced dissociation dynamics with coincident CE imaging

As illustrated by the analysis presented in section 4.3.1, in a measurement exclusively relying on non-coincidence imaging mode, an ambiguity exists in the assignment of the counterpart fragment ion(s). This ambiguity can be resolved by employing a coincident momentum imaging approach (see, e.g., [86], [244], [257], [258]), where all the fragment ions generated from a single parent ion are detected in coincidence. Consequently, unambiguous identification of all ionic final-state products of a molecular breakup can be achieved for such coincident measurement, which often helps to identify and disentangle different fragmentation pathways. In this section, we employ two-body ion-ion coincident measurements to map UV-induced photodissociation dynamics in  $CH_3I$ .

#### 4.3.3.1. A-band dissociation dynamics triggered by a single-photon excitation

We start with analyzing the delay-dependent KER distribution map for the  $CH_3^+ + I^+$  coincident channel shown in Fig. 4.14. As discussed in section 4.3.1, this map mainly consists of two structures: the delay-independent two-fold band between 4 and 6 eV, which results from the CE of the molecules that remain bound after the pump pulse, and the delay-dependent bands, which propagate towards lower KER values at the large delay and reflect the CE of dissociating molecules. Since we extensively discussed the delay-independent high-KER feature in sections 4.2 and 4.3.1, we will now focus on the delay-dependent structure. In contrast to the non-coincident data of Fig. 4.13, its evolution can be clearly resolved at large delays where it splits into three channels. The two strongest channels, which separate from each other within the first 200 fs and become nearly flat at large delays, centered at KER values of  $\sim 2.3$  eV and  $\sim 1.5$  eV, can be assigned to double ionization and CE of the neutral molecule dissociating upon the absorption of a single UV photon. In accordance with the discussion in section 2.3.1.1 and earlier in this chapter, the

more intense of these two bands (converging to  $\sim 1.5$  eV) is due to the  $\text{CH}_3 + \text{I}^*$  channel dissociating along the  $^3\text{Q}_0$  PEC, whereas a somewhat weaker band at larger KER reflects a transition to the  $^1\text{Q}_1$  state and dissociation to  $\text{CH}_3 + \text{I}$  fragments. As detailed in section 4.3.1 above, in the non-coincident maps of Fig. 4.13, these bands merge with the horizontal structures reflecting the same dissociation dynamics but probed via single ionization at large delays, where the Coulomb repulsion between the ions in the final state becomes negligible.

The above channel assignment is consistent with the results of earlier experiments [98], [138] and is also confirmed by the results of our simulations, which will be discussed below. These simulations also shed light on the nature of a triangle-shaped structure, which can be observed close to zero delay, where both delay-dependent and delay-independent features in Fig. 4.14 overlap. However, before discussing this structure, we will consider the origin of the third channel, which can be observed within the dissociating band of Fig. 4.14 at lower KER.

#### 4.3.3.2. Dissociative ionization dynamics triggered by a three-photon excitation

In Fig. 4.14, a diffuse band below the most intense descending line can be observed starting from  $\sim 200$  fs, which reaches KER values between 0.5 eV and one eV at the largest positive delays. This band is significantly weaker than the two main features discussed above, such that in the projection onto the KER axis, it can be clearly distinguished only in a logarithmic-scale representation shown as an inset. We attribute this band to the events where the pump pulse triggers dissociative ionization (DI) via one of the cationic states, which is then further ionized and Coulomb-exploded by the NIR probe pulse. We make this assignment based on the following arguments. First, from the UV-only single pulse experiments described in section 4.1, we know that the pump pulse at the intensities used in our pump-probe experiments induces measurable DI signal, which includes both  $\text{CH}_3^+ + \text{I}$  and  $\text{CH}_3 + \text{I}^+$  channels. Second, the KER values and overall appearance of this band closely resemble the results obtained in the earlier NIR-NIR pump-probe experiment [117], which studied the dissociation dynamics in the cationic states of  $\text{CH}_3\text{I}$ . Third, most importantly, it is corroborated by the dependence on the intensity of the UV pump pulse.

As discussed in section 4.1 and at the beginning of section 4.3, and also highlighted in Fig. 4.12, the DI by the UV pulse at 263 nm requires the absorption of at least three UV photons. This should result in the non-linear dependence of the corresponding signal on the UV intensity (and power), which is illustrated in Fig. 4.3 (b) for the measurements with a single UV pulse. To study

such dependence of the low-KER band in our pump-probe experiment, in Fig. 4.17, we present a delay-dependent KER distribution for the  $\text{CH}_3^+ + \text{I}^+$  coincidence channel similar to that shown in Fig. 4.14 but measured with three different UV pump pulse intensities.

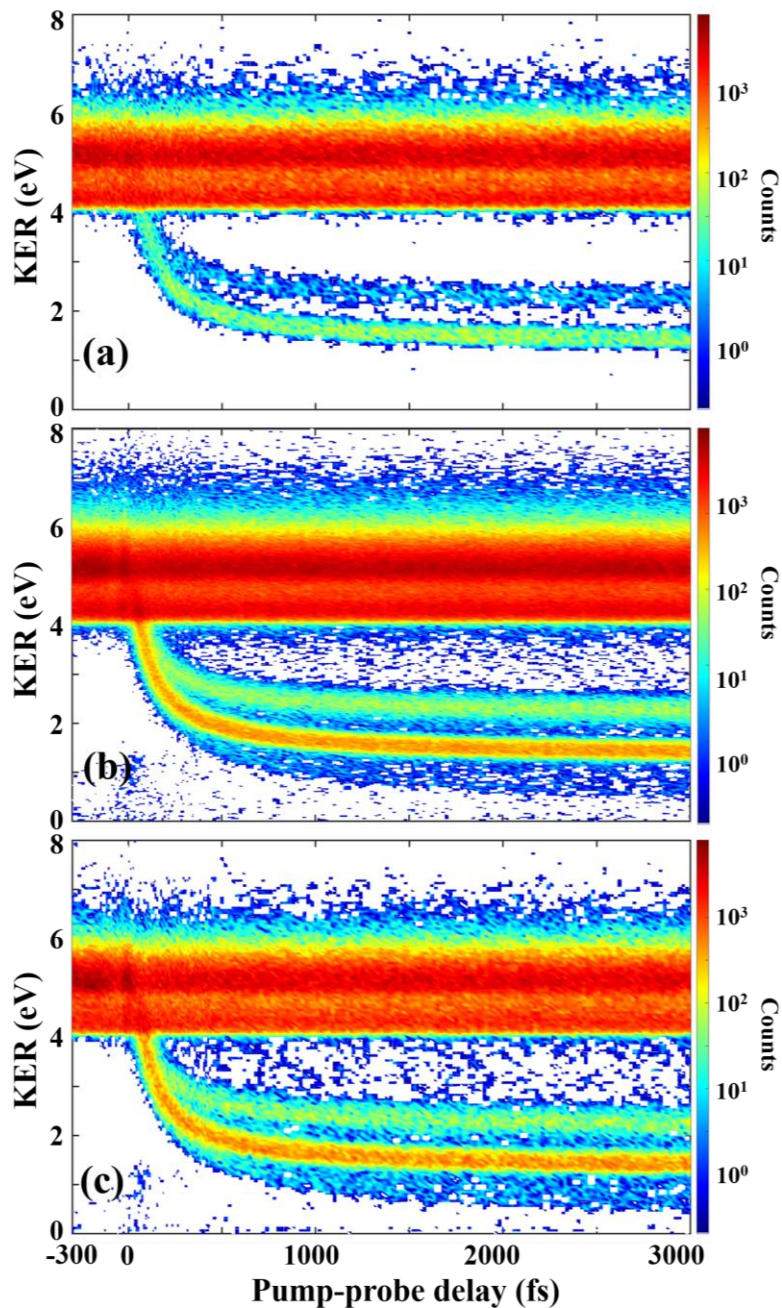


**Figure 4.17.** Delay-dependent KER distribution for the  $\text{CH}_3^+ + \text{I}^+$  coincidence channel at different UV intensities. (a)  $1 \times 10^{13} \text{ W/cm}^2$ ; (b)  $2 \times 10^{13} \text{ W/cm}^2$ ; (c)  $3 \times 10^{13} \text{ W/cm}^2$ . NIR peak intensity is kept at  $5 \times 10^{14} \text{ W/cm}^2$  for all three panels. The appearance of the extra third curve at higher UV-intensities is clearly distinguishable.

The intensity of the NIR probe pulse is kept constant. Qualitatively, the contribution from the low-KER dissociation channel is essentially absent at the lowest pump intensity, confirming that it originates from a non-linear process. To address this more quantitatively, in Fig. 4.18, the projections of the delay-dependent maps of Fig. 4.17 onto the KER axis are shown for the delay range between 2.5 and 3 ps. The data are normalized to the maximum of the displayed KER distributions at  $\sim 1.5$  eV, which results from single UV photoabsorption and, thus, is expected to scale linearly with UV intensity. As expected, the second single-photon channel at  $\sim 2.3$  eV manifests identical intensity dependence. At the same time, the low-KER feature between 0.5 and 1 eV clearly manifests a steeper, non-linear dependence on the UV pulse intensity, confirming that it originates from the multi-photon DI process.

At our central wavelength of 263 nm, three UV-photons absorption carry the total energy of 14.1 eV. As can be seen from Figs. 4.12 and 4.16, it is well above the asymptotic dissociation limits for all low-lying dissociating states (sketched in both figures). However, while this energy is sufficient to populate the high-lying vibrational levels of  $\tilde{A}$  state, it is not enough to directly reach any of the higher-lying repulsive ionic states in a vertical transition. Although it is known that the vibrational levels above  $v = 10$  for  $\text{CH}_3\text{I}^+$   $\tilde{A}$  state dissociate via internal conversion to the  $\tilde{X}$  cationic state, converging to the asymptotic limit of  $\text{CH}_3^+ + \text{I} (^2\text{P}_{3/2})$ , this process proceeds on a time scale much slower than the delay range of Figs. 4.14 and 4.17 [117], [150], [180]. It also does not produce  $\text{I}^+$  ions, which are certainly observed in our UV-only experiments (see Figs. 4.1–4.3). Therefore, our experimental observations suggest that the three-photon DI by the UV pump pulse at least partially proceeds via the direct population of one of the repulsive ionic states. In a “vertical ionization” scenario, this can be realized by absorbing more energetic photons from the blue spectral edge of the UV pulse. However, more likely, such transition can be facilitated by intermediate dynamics upon the absorption of the first one or two UV photons. Such dynamics can result in the stretching of the C-I bond in one of the intermediate states and, since the lowest ionic repulsive curve is rather steep (see Fig. 4.12), it can become accessible by the absorption of the last photon(s) at somewhat larger internuclear separations.

A broad KER distribution of the DI feature at large delays in Figs. 4.14 and 4.18 is consistent with the single-pulse kinetic energy spectra shown in Fig. 4.2. A Coulomb explosion simulation confirming the assignment of this feature in the delay-dependent KER maps will be presented at the end of the next section.

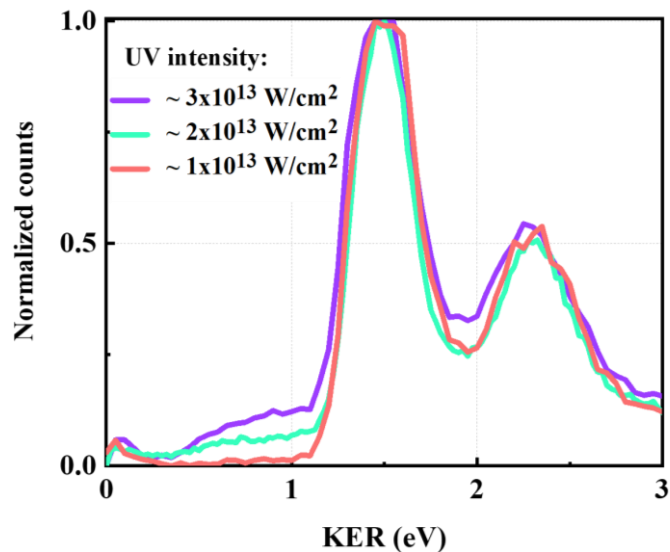


**Figure 4.18.** The projections of the KER distributions of Fig. 4.17 onto the KER axis for three UV-intensities. Only the events in the delay range of 2.5–3 ps are included. The small peak very close to zero results from false coincidences. The counts are normalized are normalized to the maximum of the KER distributions at ~1.5 eV.

## 4.4 Coulomb explosion simulation

To support the assignment of particular regions in the delay-dependent coincident ion spectra shown in Figs. 4.14 and 4.17 to particular photofragmentation pathways, and to understand the origin of a non-trivial “triangle-shaped” structure appearing in these spectra at small UV-NIR delays, in this section, we present a set of Coulomb explosion simulations (CES) and compare them with the experimental data. Since basic principles behind these simulations have been presented in section 2.4, only the specific details of the procedure used for two-body CES discussed in this section are given here.

### 4.4.1 Modelling the dissociation process

In CES of pump-probe experiments described here, the KER of a resulting fragment ion pairs at each time delay is calculated as a sum of the translational energy  $E_{trans}$  that both fragments have after the photodissociation and the energy of Coulomb repulsion  $E_{CE}$  between the two ions in the final state:

$$KER = E_{trans} + E_{CE} \quad 4.4$$

Assuming a purely Coulombic final-state PEC, the value of  $E_{CE}$  can be calculated using Eq. 2.17. To correctly approximate the dissociation of neutral  $\text{CH}_3\text{I}$  molecules along C-I internuclear distance, in this work, we use the real shape of the known dissociative  $^3\text{Q}_0$  and  $^1\text{Q}_1$  PECs taken from Ref. [119]. The time-dependent velocity is then computed using a classical 1-D model assuming initial zero velocity and acceleration resulting from moving on these dissociative PECs.

$$v(r) = \sqrt{2\left(\frac{U(r_0) - U(r)}{\mu}\right)} \quad 4.5$$

Time-dependent changes in C-I internuclear distance  $r$  during the dissociation can be obtained from the following equation:

$$t - t_0 = \int_{r_0}^r \frac{dr}{\sqrt{\frac{2}{\mu}(U(r) - U(r_0))}} \quad 4.6$$

Here  $r_0$  is the equilibrium distance,  $U(r_0)$  is the potential energy at the excitation point,  $\mu$  is the reduced mass in a two-body dissociation, and  $t-t_0$  is the pump-probe delay.

This modeling assumes that the initial photoexcitation exclusively populates the  $^3\text{Q}_0$  state by absorption of one 263 nm photon at time zero and equilibrium internuclear distance of 2.18 Å. To simulate the dynamics on the  $^1\text{Q}_1$  state, we calculated the delay time and the corresponding internuclear distance where the excited wave packet to the  $^3\text{Q}_0$  state reaches the conical intersection, and some excited molecules are depopulated and leaked to this state. This coordinate is determined to be about 9.17 fs and the C-I distance of 2.37 Å.

The calculated time-dependent velocity and internuclear distance are shown in Fig. 4.19 (a) and (b), respectively, for both  $^3\text{Q}_0$  and  $^1\text{Q}_1$  states. These graphs illustrate how the wave packet velocity increases from zero to its asymptotic values approximately at 50 fs and remains nearly constant afterward, and how the internuclear distance varies with time delay. Since the  $^1\text{Q}_1$  state is steeper, rolling down this surface results in a higher final velocity, depicted in Fig. 4.19 (a), and a larger slope in the corresponding time-distance curve in Fig. 4.19 (b). To test how sensitive the time-dependent dissociation velocity and internuclear distance are to the detailed shape of the PEC, in the following, we compare the results obtained using the realistic PEC for the  $^3\text{Q}_0$  state with the predictions of two simplified models often used in literature. These models either assume that the

dissociating fragments fly apart with constant velocities [98], [155], [259] or that the velocity rises exponentially towards its asymptotic value [99].

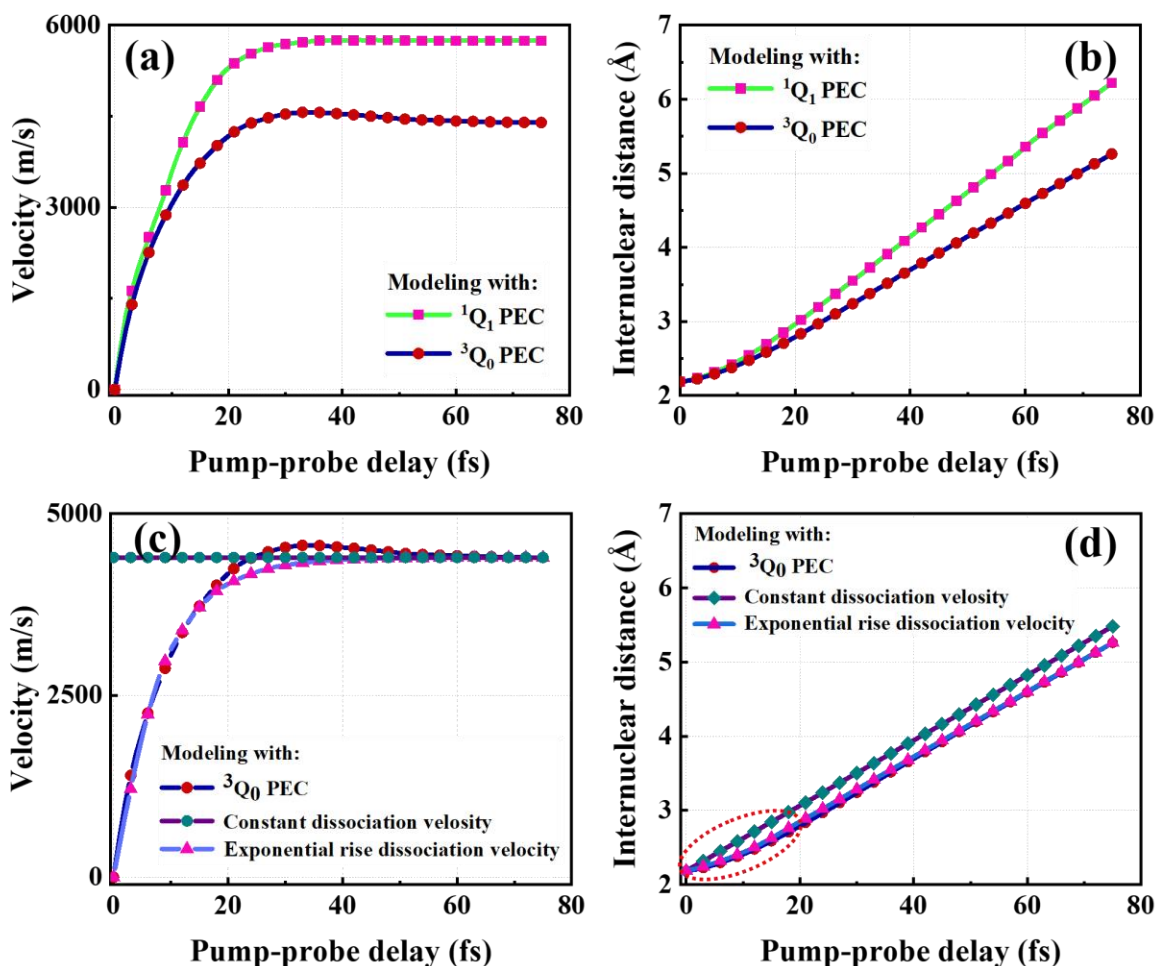


**Figure 4.19.** Time-dependent velocity (a) and internuclear distance (b) using the actual shape of the dissociative PECs of  $^3Q_0$  and  $^1Q_1$  states. The steeper slope of the  $^1Q_1$  state results in a more significant acceleration and final velocity. Comparison between time-dependent velocity (c) and internuclear distance (d) using different dissociation velocity distributions; the velocity of dissociation on  $^3Q_0$  surface, constant velocity distribution, and exponential rise velocity.

The results of this comparison are shown in Fig. 4.19 (c) and (d) for dissociation velocity and internuclear distance, respectively. While the constant velocity model clearly overestimates the internuclear separation at a given time, the exponential rise model resembles the PEC-based model much better, with only slight deviations in the velocity values at short delays. This deviation is attributed to the shape of the  $^3Q_0$  PEC, which a single exponential function cannot fully describe.

The calculations by Alekseyev et al. [119] showed that this state has a shallow minimum of about 0.1 eV, which lies outside of the Franck-Condon region and shifts toward larger internuclear distances.

#### 4.4.2 Simulations with a purely Coulombic di-cationic states

Modeling the dissociation process described above provides the necessary input for the CES, directly yielding the first term in Eq. 4.1 as well as the time-dependent internuclear separation, which is needed to calculate the second term in that equation,  $E_{CE}$ . Fig. 4.21 compares the CES results with the experimental data for three different dissociation models described above. In all cases, the final doubly-charged state is assumed to be purely Coulombic, such that the  $E_{CE}$  term is simply proportional to the inverse of internuclear separation, as given by Eq. 2.17.

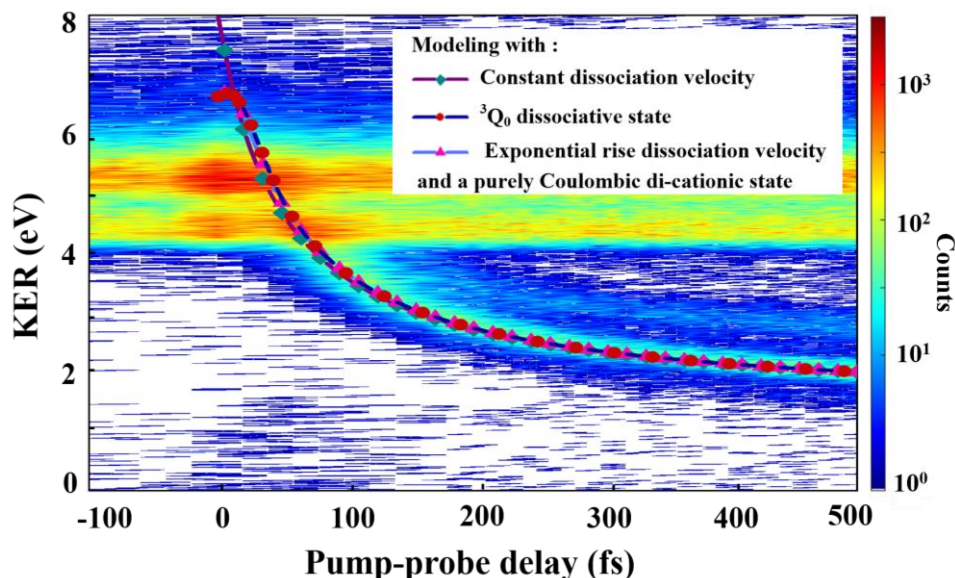


**Figure 4.20.** Comparison of CES based on different dissociation velocities for the  $^3Q_0$  state with the experimental delay-dependent KER distribution for  $\text{CH}_3^+ + \text{I}^+$  coincidence channel. For all three curves, the final state is assumed to be purely Coulombic.

Here, we only consider the wave packet propagating on the  $^3Q_0$  state. We used the known asymptotic KE for this dissociation channel to generate the curves for both constant velocity and exponential rise dissociation models. While all three CES curves match the experimental data well at large delays, all three models clearly overestimate the experimental KER at short delays, below  $\sim 50$  fs. Nevertheless, the dissociative PEC and the exponential rise velocity models yield the

results noticeably closer to the experiment than the constant velocity model. The latter model assumes that the asymptotic values of dissociation velocity and, thus, KE are reached instantaneously, which is not realistic at short delays and, thus, at small internuclear separations. Therefore, for modeling dissociation dynamics in the following discussion (both in this and subsequent chapters), we will use either the actual PEC or the exponential rise velocity model if the actual PEC is not readily accessible.

### 4.4.3 Simulations with calculated di-cationic PEC

Despite noticeably smaller deviation from the experiment observed for more realistic dissociation models, neither of the CES curves in Fig. 4.20 yields good agreement with the experimental data at small delays. The main reason for this is the assumption of the purely Coulombic final state, which is known to be too coarse an approximation for low-lying di-cationic states of CH<sub>3</sub>I, which have a shallow potential well in the Franck-Condon region [138], [173]. In Fig. 4.21, we compare the CES assuming (a) the purely Coulombic final state with the simulation employing (b) the actual shape of di-cationic PECs calculated in Ref. [173]. In both cases, the dissociation dynamics are modeled for each of the <sup>3</sup>Q<sub>0</sub> and <sup>1</sup>Q<sub>1</sub> states using the actual PECs, as discussed above. For the calculation using the actual shape of the di-cationic PECs, equation 4.1 is re-written as

$$KER(t) = \frac{1}{2}mv(t)^2 + \frac{kq_{CH_3}q_I}{r_{C-I}(t)} + E_{corr}, \quad 4.7$$

where  $v(t)$  is the time-dependent velocity,  $k$  is the Coulomb constant,  $q_{CH_3}$  and  $q_I$  are the charges on the methyl and iodine fragments, and  $r_{C-I}$  is the time-dependent distance.  $E_{corr}$  in this expression is the correction term accounting for the difference between the pure Coulombic interaction and the actual di-cationic PEC.

While the CES in Fig. 4.22 (a) still strongly deviate from the experimental results at small UV-NIR delays, the agreement with the simulations using the realistic di-cationic PECs in Fig. 4.22 (b) is much better. Interestingly, each of the simulated curves in Fig. 4.22 (b) initially manifests the KER increasing with increasing delay. This reflects the fact that the neutral dissociative curves are steeper than the di-cationic curves near the Franck-Condon region. Moreover, for the lowest few di-cationic states, which clearly manifest the potential minimum [173], dissociation and CE are classically allowed only if the KE of the wave packet gained on the

neutral dissociative PEC is greater than the potential barrier's depth; otherwise, it is classically forbidden. As shown in Fig. 4.24, the wave packet needs to propagate about 13 fs and 0.3 Å on the  $^3Q_0$  to gain the energy needed to overcome the potential barrier in the lowest di-cationic state. For each of the simulated curves shown in Fig. 4.22 (b), part of the simulation corresponding to the classically forbidden region is shown as open symbols.

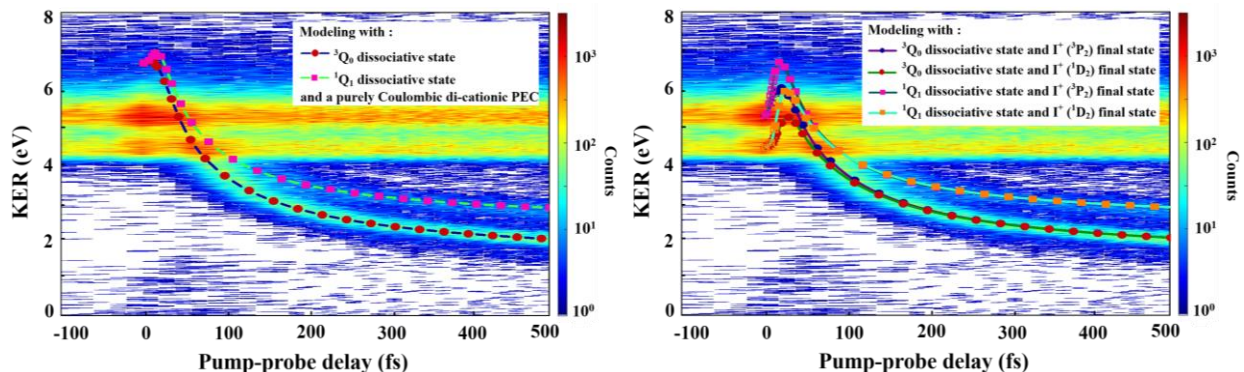


**Figure 4.21.** Comparison of the experimental delay-dependent KER distribution for  $CH_3^+ + I^+$  coincidence channel. The simulation assumes purely Coulombic di-cationic final state (a) or using the set of non-Coulombic di-cationic PECs from Ref. [173] (b). Specific di-cationic PEC correlated with different  $I^+$  states used for each simulation are indicated in the figure. In both (a) and (b), the dissociation dynamics are modeled for both  $^3Q_0$  and  $^1Q_1$  states using the PECs from Ref. [119], as discussed earlier in this section. Open symbols for all curves represent the classically forbidden region (see text).

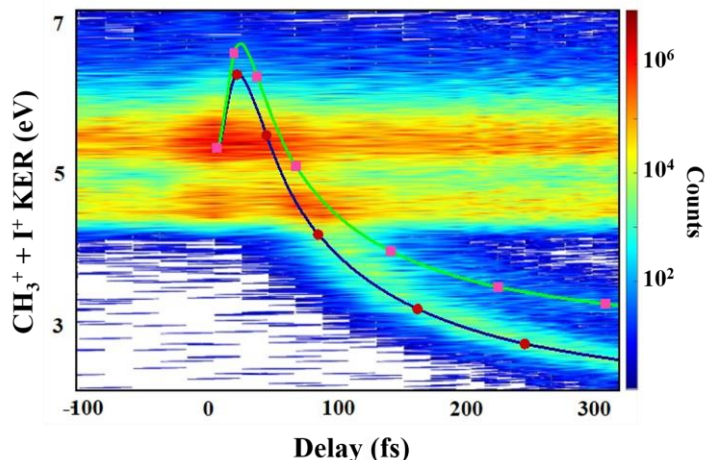


**Figure 4.22.** Enlarged view of the experimental data at small delays compared with the simulation assuming dissociation along  $^3Q_0$  and  $^1Q_1$  neutral PEC probed by the transition to the lowest di-cationic PEC.

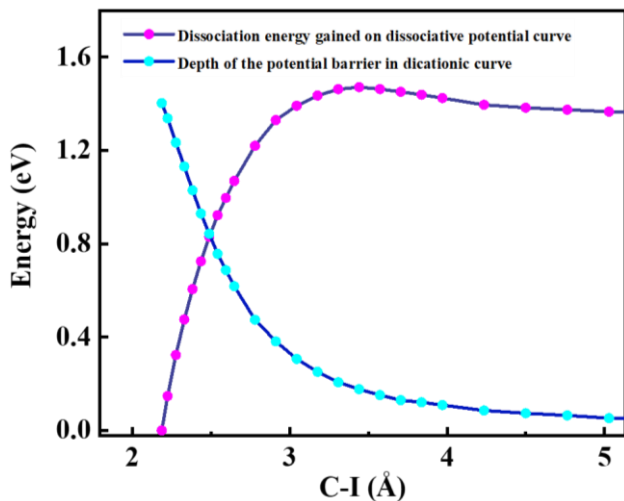


**Figure 4.23.** The kinetic energy gained in dissociation along the neutral  ${}^3Q_0$  state compared to the depth of the potential barrier for the lowest di-cationic state. The wave packet must propagate about 13 fs and  $\sim 0.3 \text{ \AA}$  to gain sufficient energy to overcome the barrier.

The initial increase and subsequent decrease of the measured delay-dependent KER is clearly visualized in Fig. 4.23, which depicts the enlarged view of the corresponding region of the spectrum. This characteristic trend can be traced in both experimental and theoretical results. It should be noted that such behavior of the CE signal has been theoretically predicted in earlier work [138]. However, because of the non-coincident mode and significantly longer UV and NIR pulses used in that work, corresponding signatures could not be resolved in the experimental data.

#### 4.4.4 Modelling dissociative ionization

Besides considering neutral dissociation dynamics, we also modeled the DI process that manifested itself as the lowest-KER channel in Figs. 4.14, 4.17 and 4.18. From comparing three different dissociation velocity models in section 4.4.1, we realized that besides a slight deviation at short delays, there is not much difference between the exponential rise velocity model and our other classical model using the actual shape of the dissociative PECs. Since, as discussed in section 4.3, the DI can involve several different ionic states, we employed the exponential rise velocity model to simulate it. The asymptotic KER value of 0.4 eV used for this simulation was obtained from the experimental data measured at large delays.

The results of this simulation, as well as the simulation for two major neutral dissociation channels, are compared with the experimental data in Fig. 4.25. The lowest di-cationic PEC

(correlated with  $I^+$  ( $^3P_2$ ) fragment) is used as a final state for all three simulations. As can be seen from the figure, the CES for the DI channel yields a decent agreement with the lowest descending band observed in the experiment. The broad and diffuse appearance of this structure between 0.4 and 1 eV at the largest delay of Fig. 4.25 is consistent with the KE distributions for  $I^+$  and  $CH_3^+$  ions obtained in the experiments with single UV pulses (see Fig. 4.2).

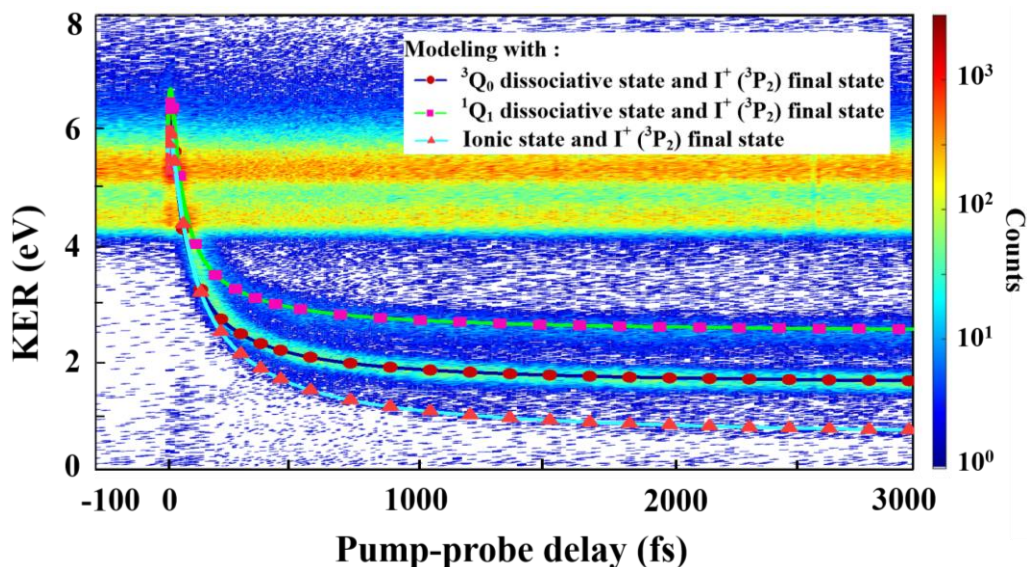


**Figure 4.24.** CES of dissociative ionization channel using exponential rise dissociation velocity function and the simulated curve of I and I\* channels with the actual shape of the dissociative states. The experimental data are the same as shown in Fig. 4.14.

#### 4.5 $CH_3^+ + I^{2+}$ channel and enhanced ionization of the dissociating molecule

With the pump and probe pulse intensities that we use in our experiments, the dominant coincidence channel result from the double ionization of the molecule by the probe pulse. Still, we also have considerable amounts of triple ionization events, as evidenced by the appearance of  $CH_3^+ + I^{2+}$  coincidence line in the PIPICO spectrum shown in Fig. 4.7. Probing photodissociating dynamics by CE of higher charge state has several advantages. First, it provides a complementary set of observables for mapping the same dynamics discussed in previous sections but using a different final state. Second, the deviation from the Coulombic form for the final-state PECs becomes less pronounced for higher charge states, even though they are still not purely Coulombic for triple ionization of  $CH_3I$  [173]. As a drawback, at moderate intensities, the statistics for coincident events resulting from the breakup of such higher charge states is typically rather limited.

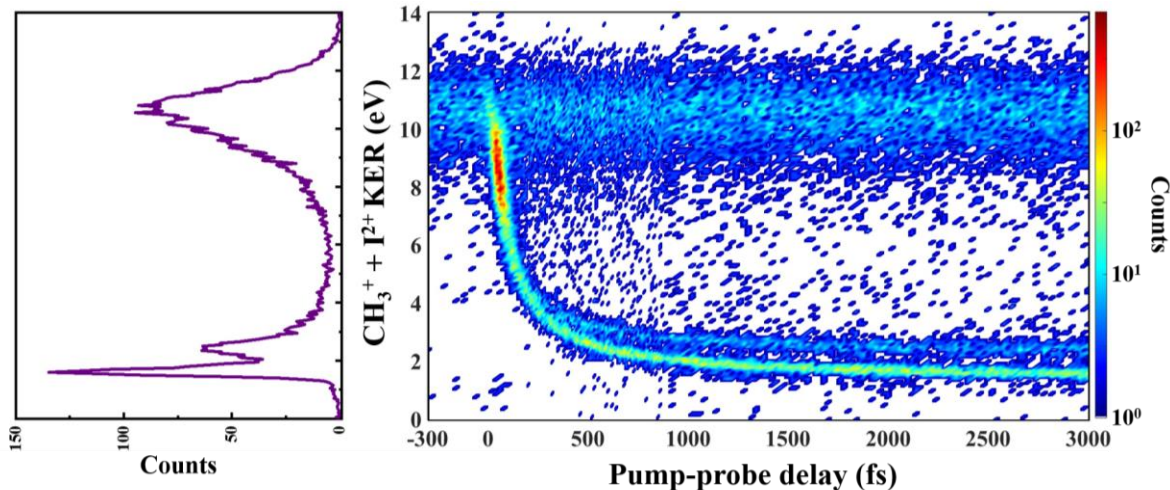


**Figure 4.25.** Delay-dependent KER distribution of the two-body coincidence channel  $\text{CH}_3^+ + \text{I}^{2+}$ . The projection onto the KER axis for the delay range of 2.5–3 ps is shown on the left.

In Fig. 4.26, we consider the delay-dependent KER distribution for the  $\text{CH}_3^+ + \text{I}^{2+}$  coincidence channel obtained in the same measurement as the data of Figs. 4.13 and 4.14. Despite rather low statistics, we can identify two main features similar to those discussed in section 4.3 for the  $\text{CH}_3^+ + \text{I}^+$  channel. First, there is again a delay-independent high-energy band, here located between 9 and 12 eV, which reflects triple ionization and CE of molecules that remained bound after the pump pulse. For the  $\text{CH}_3^+ + \text{I}^{2+}$  data in Fig. 4.26, this band does not split in two as for the  $\text{CH}_3^+ + \text{I}^+$  channel, since here the dynamics on the final-state PEC is not influenced by the existence of bound states. Nevertheless, the KER values observed in the experiment for this channel, as well as earlier theoretical analysis presented in Ref. [173], suggest that even for this channel, the final-state PECs are not purely Coulombic.

Second, there is a descending feature, which starts from the top of the horizontal high-KER band at zero delay and propagates towards lower KER as the delay increases. This feature originates the A-band dissociation triggered by the pump, which is probed via CE at increasing internuclear separation. Similar to the results for the  $\text{CH}_3^+ + \text{I}^+$  channel, this band splits in two after a few hundred femtoseconds, reflecting the wave packet propagation on  $^3\text{Q}_0$  and  $^1\text{Q}_1$  repulsive states, asymptotically resulting in  $\text{CH}_3 + \text{I}^*$  and  $\text{CH}_3 + \text{I}$  dissociation, respectively. A contribution from DI triggered by the pump, which is clearly distinguishable at low KERs in Figs. 4.14 and 4.17 for  $\text{CH}_3^+ + \text{I}^+$  channel, in Fig. 4.26 is hard to distinguish because of diffuse background from false coincidence events. Since repulsive tri-cationic PECs are steeper than the neutral dissociative

states, the triangular-shaped structure discussed in sections 4.3 and 4.4 does not appear for the  $\text{CH}_3^+ + \text{I}^{2+}$  channel.

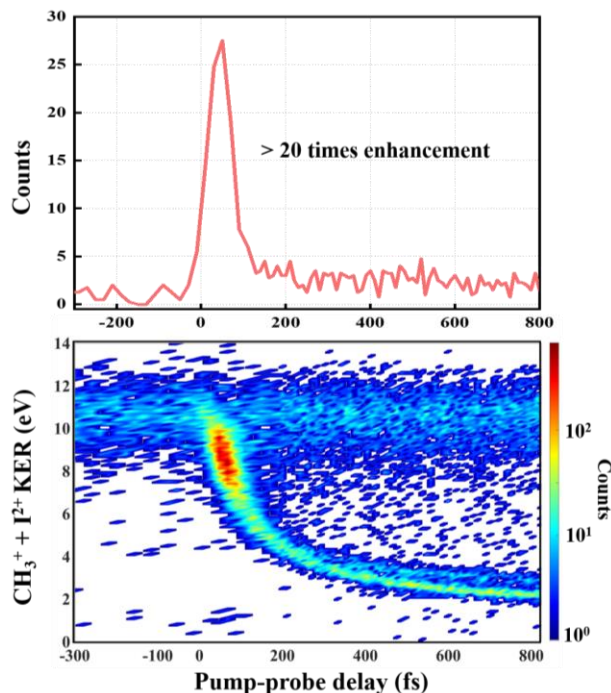


**Figure 4.26.** Enlarged view of the delay-dependent KER distribution for  $\text{CH}_3^+ + \text{I}^{2+}$  channel shown in Fig. 4.26 at small UV-NIR delays. The enhancement of the signal within the descending band around  $\sim 50$  fs delay is distinct in this map. The projection onto the delay axis over the entire energy range is shown on the top.

Another noticeable feature observed in the delay-dependent KER map of Fig. 4.26 is an enhancement of the signal in the descending CE channel at small positive delays. As shown in a zoomed-in view presented in Fig. 4.27, there is a pronounced maximum in the yield of this triply-charged, two-body coincident channel in the delay window centered at about 50 fs. Assuming that the wave packet propagates on the  $^3\text{Q}_0$  dissociative PEC, 50 fs time corresponds to the C-I distance of  $4.15 \text{ \AA}$  (see Fig. 4.19 (b)), which is approximately twice the equilibrium distance. This feature is clearly shifted to positive delays with respect to the position of the temporal overlap between the pump and the probe pulses, where overall enhancement of the ionization signal can be expected. As shown in the projection on the top of Fig. 4.27, the ionization signal starts to rise at about 20 fs, peaks around 50 fs and sharply decreases beyond 100 fs.

The shift of this feature with respect to time zero suggests that it is due to the so-called “enhanced ionization” of the molecular ion at certain internuclear separations. This phenomenon has been thoroughly investigated theoretically [260] and experimentally [101], [116], [145], [244], [256]–[262] for several diatomic and small polyatomic molecules. The basic idea of this enhancement mechanism, which is based on the electron tunneling picture, is illustrated in Fig. 4.28 for a two-center system. In brief, if a slowly-varying external laser field tilts the molecular potential, at certain internuclear separations (red curve in Fig. 4.28 (b)), an electron localized at the “upper” potential well (sketched on the left) can tunnel into the continuum through the relatively narrow “inner” potential barrier. While at smaller internuclear distances (green curves in Fig. 4.28), the intramolecular barrier is small, and the delocalized valence electron can only tunnel into the continuum through the outer barrier, at larger distances (blue curves) the inner barrier becomes large, and the ionization (tunneling) process is essentially atomic-like. Correspondingly, the ionization rate at the intermediate separations (shown by the red curves in Fig. 4.28) can be strongly enhanced. The corresponding internuclear separation is then called a “critical distance”,  $R_c$ .

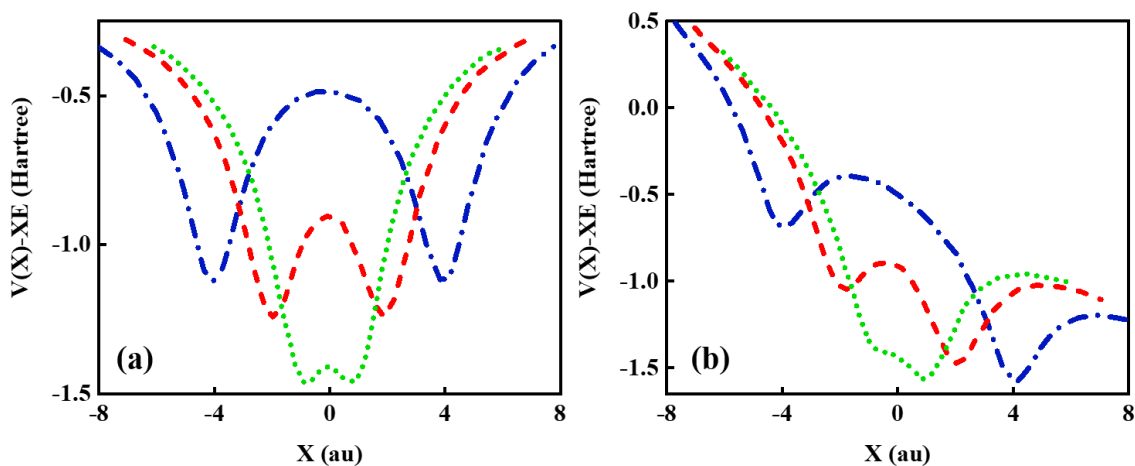


**Figure 4.27.** Schematic illustration of the electronic potentials of a diatomic molecule for three different internuclear separations illustrating the concept of “enhanced ionization”. The potentials are shown in the absence of field (a) and in the presence of a constant field (b). The red dashed curves correspond to the critical internuclear distance  $R_c$ . Adapted from Ref. [268].

While the scenario outlined above is often discussed as a reason for experimentally observed ionization enhancement at critical internuclear distances, which are typically about twice

the equilibrium distance, the enhancement mechanisms are not restricted to this scheme. For polyatomic molecules such as  $C_2H_2$ , Erattupuzha et al. [261] recently argued that the enhanced ionization occurs due to energy-upshift of lower valence energy orbitals as the bond length stretches, and the laser field couples multiple orbitals. As the valence states shift up, their binding energy is reduced, and, due to lower energy spacing, the coupling between the lower and higher states by NIR laser fields becomes more robust, leading to the enhancement in the ionization rate of the polyatomic molecules [261].

Detailed understanding of specific enhanced ionization mechanisms at work requires theoretical modeling beyond the scope of this work. However, the experiment can test whether the observed enhancement really originates from the distance-dependent ionization probability or it whether it can be due to some other factors like, for example, the dynamics triggered by the pump. In general, the signal enhancement observed in the delay-dependent KER distribution is shown in Figs. 4.27 and 4.28 appear to be rather similar to the results of other time-resolved experiments discussed in terms of enhanced ionization [116], [249], [264]. In order to test its origin, as shown in Fig. 4.29, we repeated this measurement for three different intensities of the probe pulse. The logic behind this attempt is that if the enhancement is due to a larger ionization probability at certain internuclear distances, it should either disappear or become less pronounced for high probe intensities, which results in ionization saturation. Comparing the results presented in Fig. 4.29 (a-c), we can conclude that this is indeed the case: for the highest probe intensity in panel (c), the enhancement of the signal in the descending band is hardly visible.

Since we do not observe similar enhanced ionization signatures in the delay-dependent KER spectra for the  $CH_3^+ + I^+$  channel, we assume that the enhancement observed in Figs. 4.26, 4.27, 4.29 reflects an enhancement of the ionization rate of the di-cation. Previously, Liu et al. [153] reported enhanced ionization signatures for the ionization of  $CH_3I^{2+}$ , resulting in further ionization to  $CH_3I^{3+}$  and its CE into the same  $CH_3^+ + I^{2+}$  channel we discussed here. In that work, a critical distance for enhanced ionization was determined to be  $\sim 3.7 \text{ \AA}$  based on the KE distributions of the fragments obtained with a single NIR pulse. Although it is somewhat lower than the distance we can assign to the enhancement we observe, it is not unreasonable, since in a single-pulse experiment, the accessible delay range between the individual ionization steps is limited by the effective pulse duration, and, thus, it is likely to weight contributions from smaller internuclear distances more favorably.

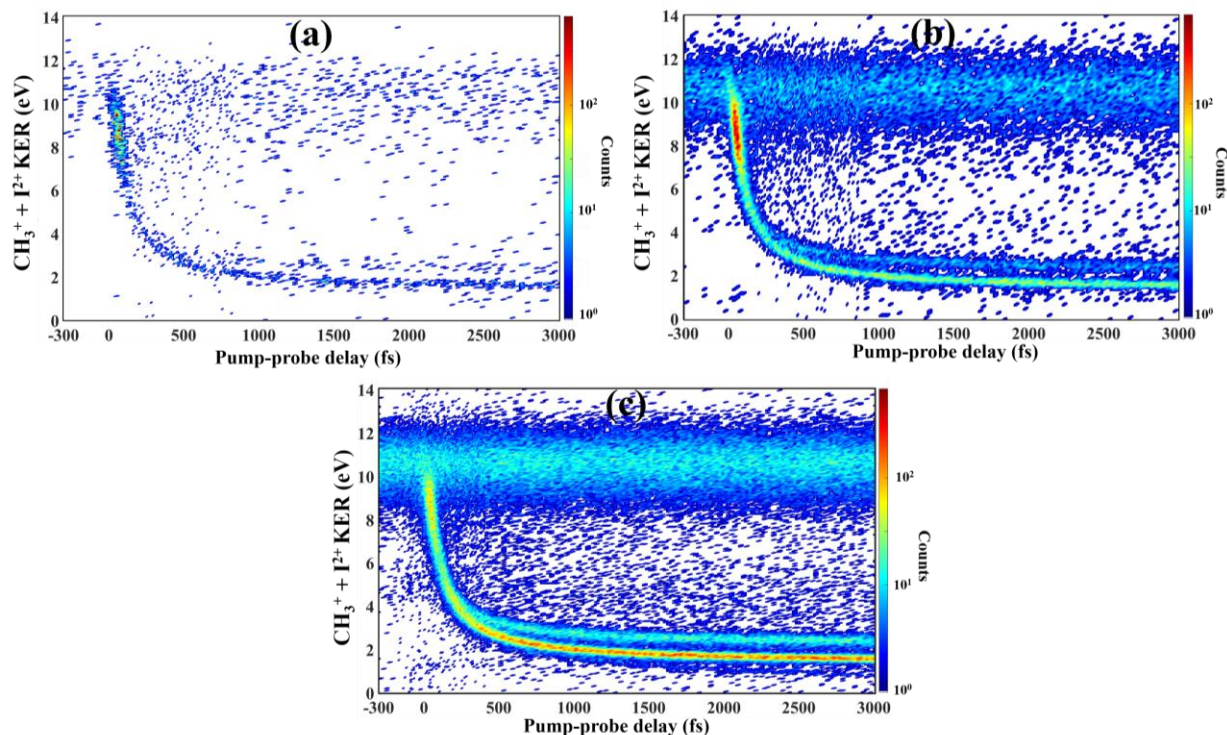


**Figure 4.28.** Delay-dependent KER distribution for the two-body coincidence channel  $\text{CH}_3^+ + \text{I}^{2+}$  at three different probe pulse intensities. **(a)**  $2.2 \times 10^{14}$ , **(b)**  $2.8 \times 10^{14} \text{ W/cm}^2$ , **(c)**  $5 \times 10^{14} \text{ W/cm}^2$ . The intensity of the pump pulse is kept constant at  $1.5 \times 10^{13}$ , same as for Figs. 4.26 and 4.27.

It should be noted that an enhancement very similar to the one discussed here was also observed in an earlier NIR-NIR pump-probe experiment [117] for the same coincident channel. The results of that study, which employed essentially the same NIR pump as this work, yield very similar estimate for the internuclear separation at which the enhancement occurs, supporting the argument that the distance-dependent change of the ionization probability of the di-cationic states of  $\text{CH}_3\text{I}$  by the NIR pulse is indeed the reason behind our observations.

## 4.6 Two-photon Rydberg states excitation

So far, we have analyzed delay-dependent yields and KE distributions of iodine or methyl ionic fragments resulting from the breakup of singly-, doubly- or triply-charged final states of the molecule. This analysis mainly focused on mapping the neutral molecule's photodissociation pathways upon single UV photon absorption, as well as on three-photon-induced cationic-state dynamics, and on some aspects of double and triple ionization of the molecule. However, as

discussed at the beginning of section 4.3, another likely process in CH<sub>3</sub>I excitation at 263 nm involves two-photon transitions to one of the high-lying Rydberg states. As sketched in Fig. 4.11, a broad range of Rydberg states, from directly below the ionization threshold to significantly lower-lying states, are accessible for such excitation, in particular, considering the rather broad spectrum of our UV pulse (see Fig. 3.7 (b)) and the possibility of intermediate dynamics on one of the dissociative states in the A-band. Although some implications of such processes have been discussed in relation to multi-photon DI in section 4.3.3.2, direct signatures of such two-photon excitation are hard to trace in the fragment ion spectra. To visualize these signatures, in this section, we examine the yields of CH<sub>3</sub>I<sup>+</sup> parent ions that remain bound after the interaction with pump and probe pulses.

In Fig. 4.30 (a-e), the delay-dependent yields of singly-charged parent ion are shown in a delay interval of up to 2 ps for five different UV pump pulse intensities. The intensity of the NIR probe pulse is kept constant at  $5 \times 10^{14}$  W/cm<sup>2</sup>. The resulting spectra are normalized to [0,1]. While at the lowest UV intensity in Fig. 4.30 (a), the signal exhibits a pronounced enhancement in the overlap region, which is symmetric with respect to zero delay, at higher intensities, the spectra become asymmetric, with pronounced decaying feature gradually developing at positive delays.

The symmetric spectrum at the lowest pump intensity is formed by direct two-color ionization of the molecule. Here, the dominant pump-induced process is one-photon excitation to the dissociative A-band. In the overlap region, this strongly facilitates ionization by the NIR pulse, resulting in pronounced signal enhancement. If the nuclear wave packet has enough time to propagate on the steep dissociative curve after the UV photoabsorption, subsequent ionization of the molecule results in fragment ions rather than the bound parent ion. Since the effective dissociation time is shorter than the UV pulse duration, the shape of the signal in Fig. 4.30 (a) is determined by the cross-correlation between UV and NIR pulses and not by the A-state dissociation dynamics.

However, at higher UV intensities, the contribution from two-photon absorption becomes non-negligible. Rydberg states populated by such a two-photon process can be readily ionized by a single NIR photon. Since the excited states reached by the two-photon absorption typically do not undergo rapid dissociation, the two-color signal in Fig. 4.30 (b-e) extends to larger delays. The contribution of this process becomes more pronounced as the pump pulse intensity grows, such that a clear signature of the exponential decay of the signal can be observed in these spectra.

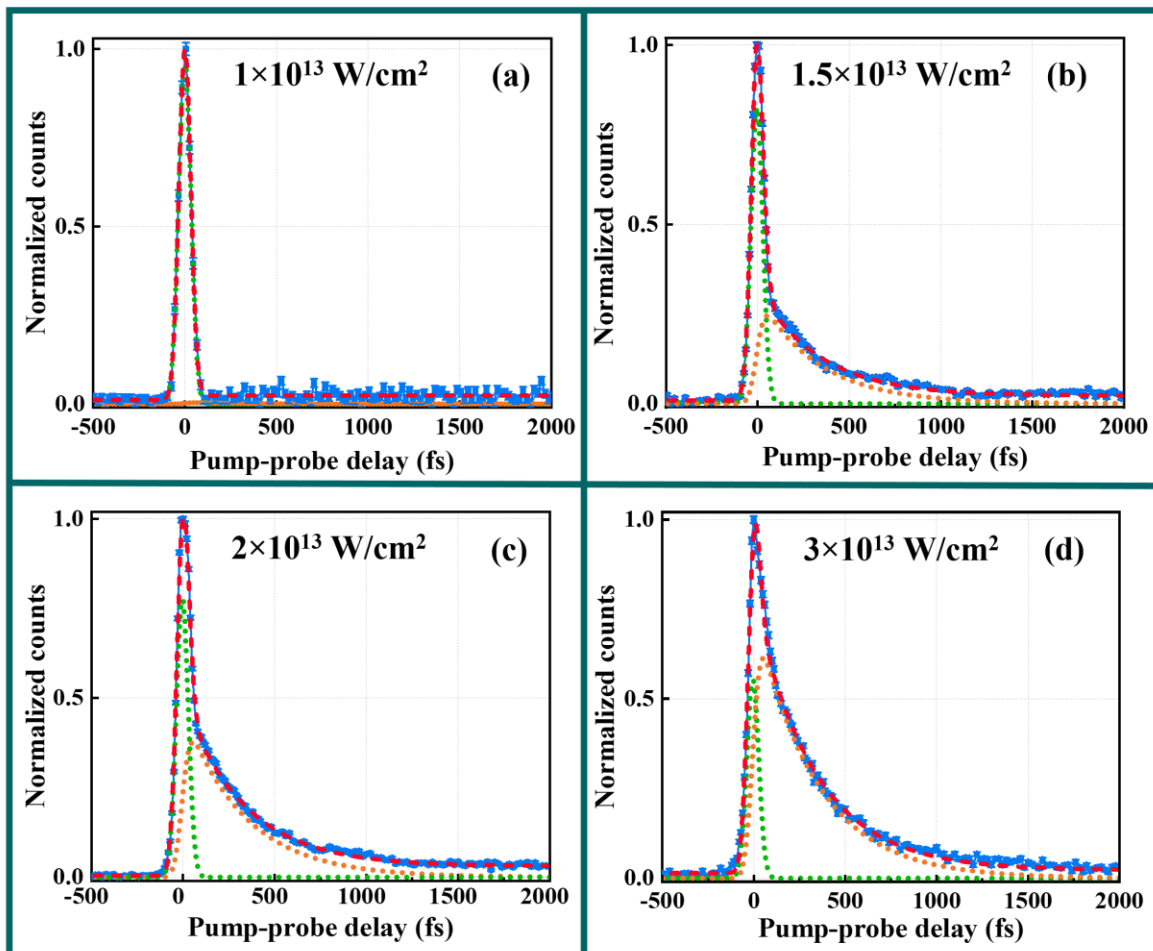


**Figure 4.29.** (a-d) Delay-dependent yields of the singly-charged parent ion for different UV intensities (indicated in the figure). The NIR probe pulse intensity is kept constant at  $5 \times 10^{14}$  W/cm<sup>2</sup>. The total fitted curves described by Eq. 4.8 are shown in red. The two components of the fit function are also plotted individually: the Gaussian distribution is shown in cyan, and the convolution function described in the text is shown in green. (f) Schematic of one- and two-photon excitation by the pump pulse followed by the ionization with a delayed NIR pulse.

The observed behavior suggests that the spectra presented in Fig. 4.30 are formed by two competing processes: (1) single UV photoabsorption followed by the NIR ionization in the Franck-Condon region, and (2) two-photon UV excitation of Rydberg state series with subsequent single-photon ionization by the NIR. The resulting transient two-color signal transforms from a quasi-

symmetric Gaussian in the lowest UV intensity to an exponentially modified Gaussian distribution extending towards positive delays at higher intensities.

To characterize the contributions from these two processes more quantitatively, the time-dependent parent ion signals of Fig. 4.30 (a-d) have been fitted using a superposition of two functions: A Gaussian function representing the cross-correlation of the two pulses, and an exponential decay function convolved with a Gaussian distribution of the same width, which is expected to account for the contribution from intermediate Rydberg states with a finite lifetime. This fitting is used to determine the weighting factors of each process constructing the time-dependent signal. The expression for fitting the signal is given by [269]

$$y(t) = y_0 + Ae^{-\left(\frac{t-t_0}{2\sigma}\right)^2} + B e^{\frac{1}{2}\left(\frac{\sigma}{\tau}\right)^2 - \frac{(t-t_0)}{\tau}} \left[ \frac{1}{2} \left( \operatorname{erf} \left( \frac{(t-t_0)/\sigma - \sigma/\tau}{\sqrt{2}} \right) + 1 \right) \right], \quad 4.8$$

where  $t_0$  corresponds to zero delay time,  $\sigma$  is the standard deviation of the Gaussian distribution, and  $\tau$  is the lifetime of the exponential decay. The coefficients A and B represent the weighting factors of one-photon excitation and two-photon excitation, respectively. The total fit function as well as individual fit components are plotted in Fig. 4.30 (a-d).

The results of the fits are summarized in Table 1, indicating the downward trend in the weighting factor of one-photon excitation accompanied by the growth of the two-photon contribution. As can be expected, the weighting coefficient reflecting the two-photon process gradually increases with increasing UV intensity. Remarkably, the extracted lifetime with respect to an exponential decay (330-340 fs) is very similar for all intensities where this contribution is non-negligible.

<b>Intensity (W/cm<sup>2</sup>)</b>	<b>Single Gaussian coefficient (A)</b>	<b>Convolution coefficient (B)</b>	<b>Life-time (fs)</b>
<b>1×10<sup>13</sup></b>	<b>0.98</b>	<b>~ 0.01</b>	<b>NA</b>
<b>1.5×10<sup>13</sup></b>	<b>0.82</b>	<b>0.30</b>	<b>339±2.91</b>
<b>2×10<sup>13</sup></b>	<b>0.78</b>	<b>0.47</b>	<b>336±3.47</b>
<b>3×10<sup>13</sup></b>	<b>0.55</b>	<b>0.76</b>	<b>330±1.018</b>

**Table 4-1.** Parameters extracted from fitting the time-dependent parent ion signal of Fig. 4.30 as a function of UV-intensity. The coefficients A and B of fitting components represent weighting factors for both physical processes.

More specifically, two-photon UV excitation at a central wavelength of 263 nm (sum photon energy of 9.4 eV) prepares the system in higher-lying Rydberg states of 10d, 11d, and 12d series converging to the first ionization potential  ${}^2E_{3/2}$  at 9.540 eV [118], [154], [168].

The extracted exponential decay time of 330-340 fs most likely reflects the lifetime of the corresponding Rydberg states with respect to their dissociation. It should be noted that, to the best of our knowledge, the lifetimes of the highly excited states of CH<sub>3</sub>I have only been reported for the lower-lying levels so far. While for the B-band, the characteristic predissociation time was found to be much longer than the value we obtained here (~ 1.5 ps at the band origin, see section 2.3.1.2 and references therein for details), for 6p and 7s, Rydberg states much shorter lifetimes, below 150 fs [154], [157] have been reported. Baumann et al. [157] have also discussed excitation of high-lying Rydberg states by the absorption of two 268 nm photons from a broadband 21 fs UV pulse, which was probed by a single VUV photoabsorption at 161 nm. They reported  $478 \pm 30$  fs decay time for the corresponding decay time, significantly longer than the values observed in the present work. It remains unclear whether this difference was caused by a slightly different central wavelength or by the use of a very different probing scheme. Overall, theoretical modeling of molecular PESs for these high-lying states and understanding of specific dissociation pathways responsible for their decay is required for a more quantitative understanding of the observed lifetimes.

## 4.7 Summary

In this chapter, we studied the photodissociation dynamics of iodomethane using UV pump - NIR probe measurements and employing ion momentum imaging as the probe scheme. Combining the analysis of coincident and non-coincident data, we disentangled signatures of one-, two- and three-photon processes and mapped major dissociation pathways using the Coulomb explosion imaging (CEI) approach. Since photoexcitation at our central UV wavelength of 263 nm triggers resonant single-photon dissociation into neutral fragments breaking the C-I bond, most of the observed dynamics involve stretching this bond along one of the PECs within the A-band manifold. The most important result presented in this chapter is the CEI of this prototypical photochemical reaction. By combining channel-specific experimental data obtained with high temporal resolution and theoretical modeling, we achieved a detailed understanding of CEI pattern formation mechanisms and disentangled effects due to pump-induced dynamics from specific

features induced by the chosen probing scheme. In particular, we visualized the initial increase of the time-dependent CE energy for doubly-charged final states and highlighted the role of actual di-cationic PECs. Although such an increase was already predicted theoretically, to the best of our knowledge, it was not yet resolved experimentally. These results are important for many CEI studies of molecular dynamics employing doubly- or triply-charged final states.

Besides that, several other important findings are presented here. First, we demonstrated that similar dynamics in the neutral molecule can be probed by higher charge states, which are less influenced by the non-Coulombic nature of the final-state PECs. At the same time, this study identified signatures of enhanced ionization of intermediate molecular ion, highlighting the importance of saturating the ionization step for laser-induced time-resolved CEI. Moreover, we analyzed two-color-induced dynamics reflected in non-coincident singly-charged ion spectra, which can be, to a large extent, interpreted using the concept of light-induced conical intersection introduced in earlier work [\[137\]](#). Finally, we visualized signatures of two-photon excitation to high-lying Rydberg states and determined their characteristic decay time. Together with several other studies of CH<sub>3</sub>I Rydberg state lifetimes, these results call for a more detailed analysis of Rydberg-state PESs for this prototypical system.

## Chapter 5 - Imaging UV-driven photochemical dynamics in dihalomethanes at 263 and 198 nm

Dihalomethanes have two carbon-halogen bonds, which makes them particularly interesting for investigating bond-selectivity in the photodissociation of molecules. As discussed in section 2.3.2, due to different broadband features in their UV absorption cross-section, which can result in different carbon-halogen bond cleavage, dihalomethanes exhibit rich dissociation and fragmentation dynamics (see Refs. [66], [187], [270]–[272] for some examples). Correspondingly, a range of probable photodissociation pathways upon UV photoabsorption goes far beyond the dynamics discussed in previous chapter for iodomethane, which mostly unfold along single C-I bond. In the following two chapters, we investigate some of these dynamics using the time-resolved CEI approach. The main general motivation here is to study the effects originating from the presence of two halogen atoms. Besides the possibility of breaking different carbon-halogen bonds, the presence of another heavy nucleus provides more possibilities for genuine few-body dynamics. Correspondingly, in this and the next chapter, we mainly rely on three-body CE as a probing tool, which enables a more direct view into the correlated motion of two halogens and the methylene group compared to the two-body analysis discussed in Chapter 4.

Here, we first discuss the dissociation dynamics of dihalomethanes upon absorption of a 263 nm photon in the *A*-band. The selected molecular targets for this study are bromiodomethane ( $\text{CH}_2\text{BrI}$ ) and chloriodomethane ( $\text{CH}_2\text{ClI}$ ). As discussed in Chapter 2, in both cases, the C-I bond cleavage is expected to be the dominant dissociation channel, with a minor but non-negligible contribution of the C-Br (or C-Cl) bond cleavage [187], [273]. For  $\text{CH}_2\text{BrI}$ , the energy of a single UV-photon at 263 nm (4.70 eV) is sufficient to overcome the dissociation thresholds of either C-I or C-Br bonds or induce molecular halogen (IBr) elimination (3.84 eV), but is still below the energetic threshold for the three-body breakup (5.66 eV) [187], [188]. Two-photon absorption at 263 nm or single-photon absorption at a shorter UV wavelength makes such three-body dissociation possible. For  $\text{CH}_2\text{ClI}$ , the thresholds [273] are comparable to  $\text{CH}_2\text{BrI}$ , and, therefore, qualitatively similar dynamics are expected. Therefore, we mainly focus on  $\text{CH}_2\text{BrI}$  discussion and only briefly present the  $\text{CH}_2\text{ClI}$  results for comparison.

As a next step, we discuss dissociation dynamics in  $\text{CH}_2\text{BrI}$  and  $\text{CH}_2\text{I}_2$  (diiodomethane) at 198 nm (in the *B*-band). We used identical probing schemes and NIR probe pulse intensities for

both UV wavelengths. As discussed in Chapter 2, since the dissociation pathways critically depend on the electronic excitation, branching ratios of different dissociation channels change at shorter wavelength. More specifically, at 198 nm, larger contributions from C-Br bond breaking, iodine monobromide (BrI) elimination and three-body dissociation ( $\text{CH}_2 + \text{Br} + \text{I}$ ) are expected compared to 263 nm results [187], [188]. Disentangling these fragmentation pathways and their comparative analysis for two different photoexcitation wavelengths is the central goal of this chapter. Methodologically, in doing this we—to a large extent—follow the three-body CEI data analysis procedures and channel identification scheme developed in earlier work [274] for  $\text{CH}_2\text{I}_2$  experiments at 800 nm and 266 nm, and extend them for the case of two distinguishable halogen atoms.

Then, in Chapter 6, we specifically focus on two-body dissociation channels involving carbon-halogen bond cleavage upon 263 nm excitation, and study rotational motion of  $\text{CH}_2\text{X}$  molecular reaction product ( $\text{X} = \text{Br}, \text{I}, \text{Cl}$ ). As discussed in section 2.3.2, in single-photon dissociation of dihalomethanes, a substantial fraction of the excess photon energy can be deposited into internal degrees of freedom, triggering rotation of the molecular fragment (see Fig. 2.13 and the corresponding discussion). This effect is less pronounced in monohalomethanes like  $\text{CH}_3\text{I}$  where the dissociation proceeds along the line connecting the center of masses of both reaction products. In contrast, it is expected to play much bigger role in dihalomethanes, where the photodissociation can exert significant torque on the molecular co-fragment [98], [99], [186]. We will present a detailed movie of this reaction in Chapter 6, while the main goal of Chapter 5 is to reliably identify and disentangle the contributing reaction pathways.

For all pump-probe experiments described here, the NIR laser peak intensity was kept to approximately  $8 \times 10^{14} \text{ W/cm}^2$ . From a technical point of view to have less than one event per laser shot, this turned out to be the highest intensity at which coincident measurements remained feasible. The intensity is set to such a high value in order to ensure significant rate in three-body coincident channels resulting from CE of triply- or multiply-charged states. As discussed in previous chapters, the CEI approach in general works better for higher level of ionization because the final-state PESs approach purely Coulombic ones. In addition, the use of higher probe intensity ensures that the probing efficiency is more uniform for all positions of the nuclear wave packet and less influenced by the dependence of ionization probability on molecular geometry. The intensity of the UV pump pulses was chosen in the range of  $1\text{-}3 \times 10^{13} \text{ W/cm}^2$ . Generally, one-

photon excitation is the dominant dissociation channel at low UV pulse intensity, whereas at higher intensities multi-photon processes will be triggered, often undesired. However, due to the moderate absorption cross-section of CH<sub>2</sub>BrI (~2.25 MB [184] for 263 nm), to ensure a high contrast pump-probe signal and a reasonable signal-to-noise ratio, we need to keep the pump pulse intensity relatively high, such that two- or three-photon absorption cannot be excluded.

Similar to the previous chapters, we first discuss molecular response to the individual UV and NIR pulses to identify dissociation and ionization pathways induced by the pump and the probe pulses alone. In the next step, we discuss the time-resolved measurements. Because the NIR probe pulse is the same for the experiments at both UV wavelengths discussed in this chapter, we begin the discussion with the results for single NIR pulse.

## 5.1 CH<sub>2</sub>BrI molecule under a single NIR pulse

### 5.1.1 Non-coincident spectra

Fig 5.1 shows the ion TOF spectrum obtained for the CH<sub>2</sub>BrI molecule irradiated by the NIR pulse with  $8 \times 10^{14}$  W/cm<sup>2</sup> intensity. Here, the spectrum is dominated by the singly-charged parent ion (CH<sub>2</sub>BrI<sup>+</sup>) and almost all plausible singly-charged ionic fragments. The spectrum reveals the formation of a significant amount of doubly-charged parent ion (CH<sub>2</sub>BrI<sup>2+</sup>) and higher charged iodine and bromine ions, as well as non-negligible amount of molecular halogen ions (BrI<sup>+</sup>). Despite the very high peak intensity, single ionization and dissociative ionization, where a singly-charged fragment with a neutral partner is produced in a two-body fragmentation channel, are the predominant fragmentation pathways contributing to the spectrum. This is because of the focal volume averaging of the collected ion data. Even though in the center of the laser focus single ionization can be completely saturated, and all molecules are further ionized, in the wings of the focus, in the regions of smaller peak intensity, single ionization still remains the dominant channel. In this non-coincident TOF spectrum, different charge states of I and Br show comparatively broad structures with outer wings (or rings in TOF vs position maps) shoulders representing CE events.

The measured KE distributions for the primary singly-charged photoproducts are shown in Fig. 5.2 without any coincidence conditions. All four spectra in Fig. 5.2 contain a strong DI peak at very low KE, and also noticeable CE contributions at higher energies, which are most pronounced in Br<sup>+</sup> data shown in Fig. 5.2 (d).

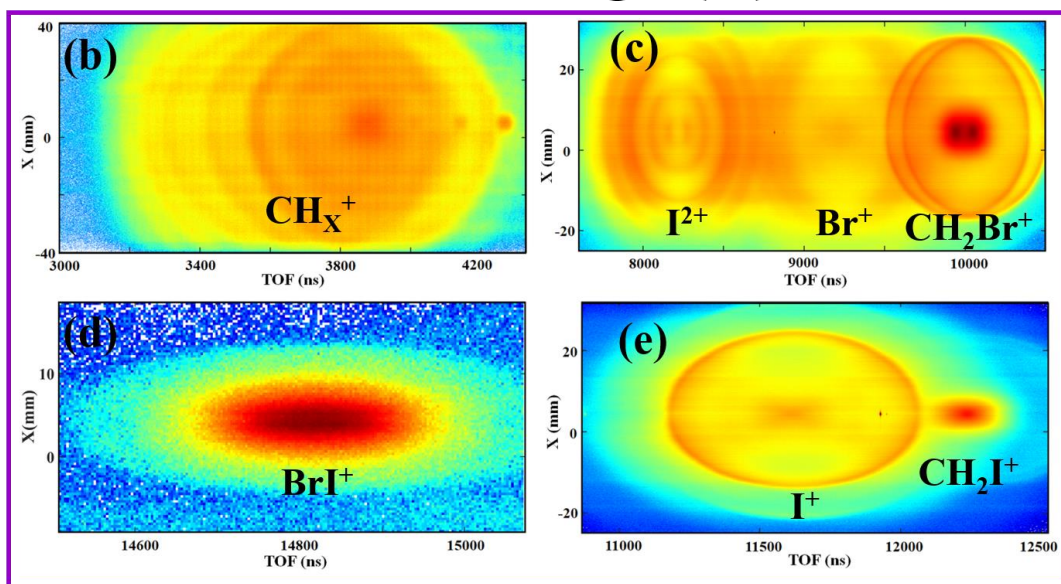
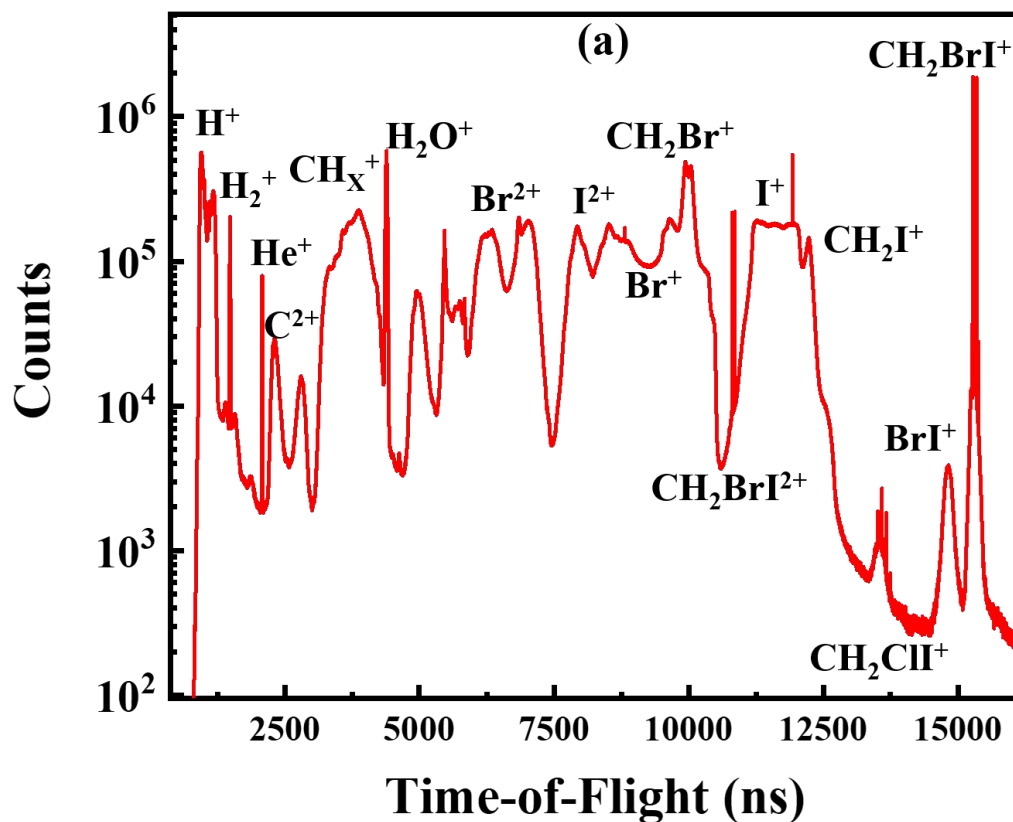


**Figure 5.1.** (a) TOF spectrum of the ions generated upon irradiation of  $\text{CH}_2\text{BrI}$  molecule with the single NIR pulse with  $8 \times 10^{14} \text{ W/cm}^2$  intensity. The TOF-position (specifically, TOF vs X coordinate, where X is the laser beam propagation direction) maps of selected ions (b-e) showing the DI and CE channels.

We analyze the corresponding two- and three-body coincident data to trace the contributions from various coincident channels to these spectra.

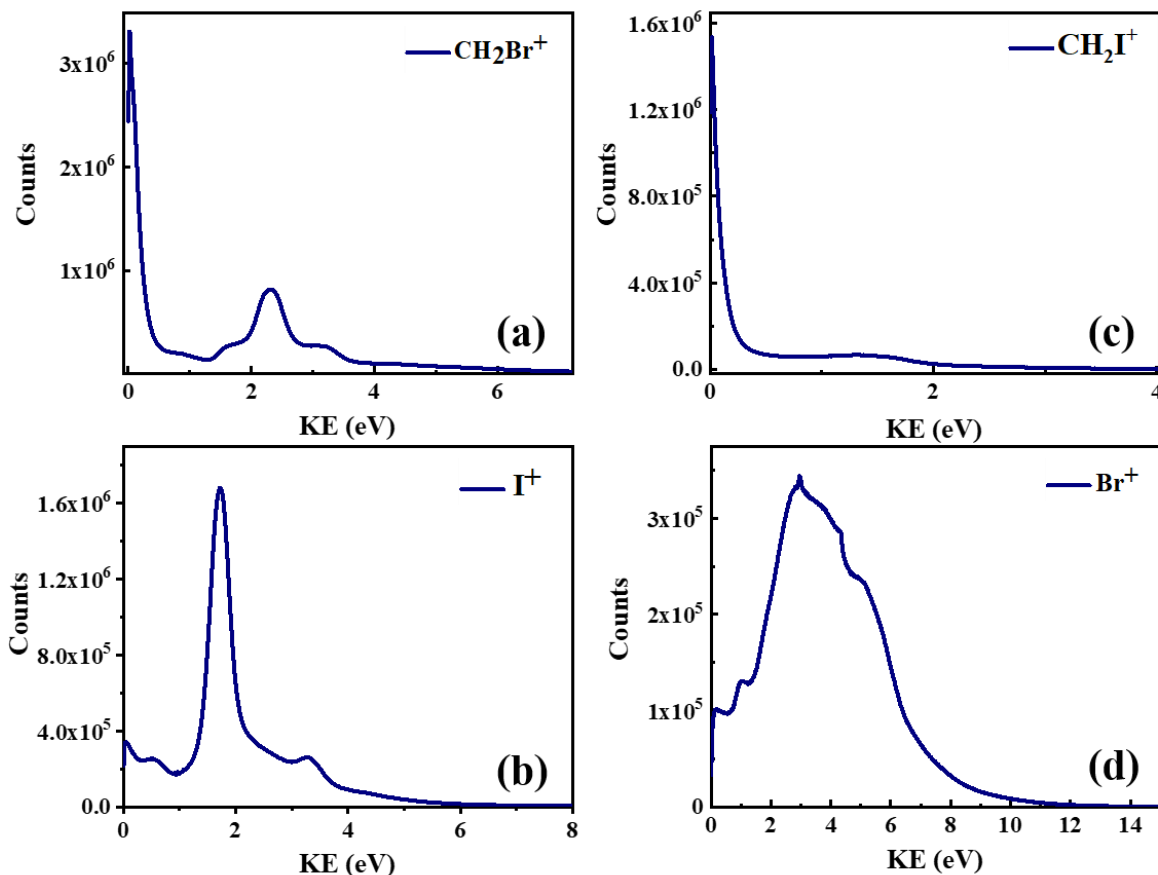


**Figure 5.2.** Kinetic energy (KE) distributions of ionic fragments of  $\text{CH}_2\text{BrI}$  molecule after a single NIR pulse with  $8 \times 10^{14} \text{ W/cm}^2$  intensity. The KE distributions are shown for the (a)  $\text{CH}_2\text{Br}^+$ , (b)  $\text{I}^+$ , (c)  $\text{CH}_2\text{I}^+$ , and (d)  $\text{Br}^+$  fragments, where the distributions are dominated by DI and CE peaks.

### 5.1.2 Two-body coincident analysis

The PIPICO spectrum at this NIR intensity is shown in Fig. 5.3. It illustrates several “complete” two-body fragmentation pathways resulting from double, triple and quadruple final charge states. More specifically, we can trace  $\text{CH}_2\text{Br}^+ + \text{I}^+$ ,  $\text{CH}_2\text{I}^+ + \text{Br}^+$ ,  $\text{CH}_2^+ + \text{BrI}^+$ ,  $\text{CH}_2\text{Br}^{2+} + \text{I}^+$ ,  $\text{CH}_2\text{Br}^{2+} + \text{I}^{2+}$ , and  $\text{I}^+ + \text{CH}_2\text{Br}^{2+}$  coincident ion pairs. Due to the nearly equal abundance of the two isotopes of Br,  $^{79}\text{Br}$  and  $^{81}\text{Br}$ , each of these coincident channels results in two sharp diagonal lines in the PIPICO spectrum. For our further analysis, we select the lines corresponding to the heavier  $^{81}\text{Br}$  isotope.

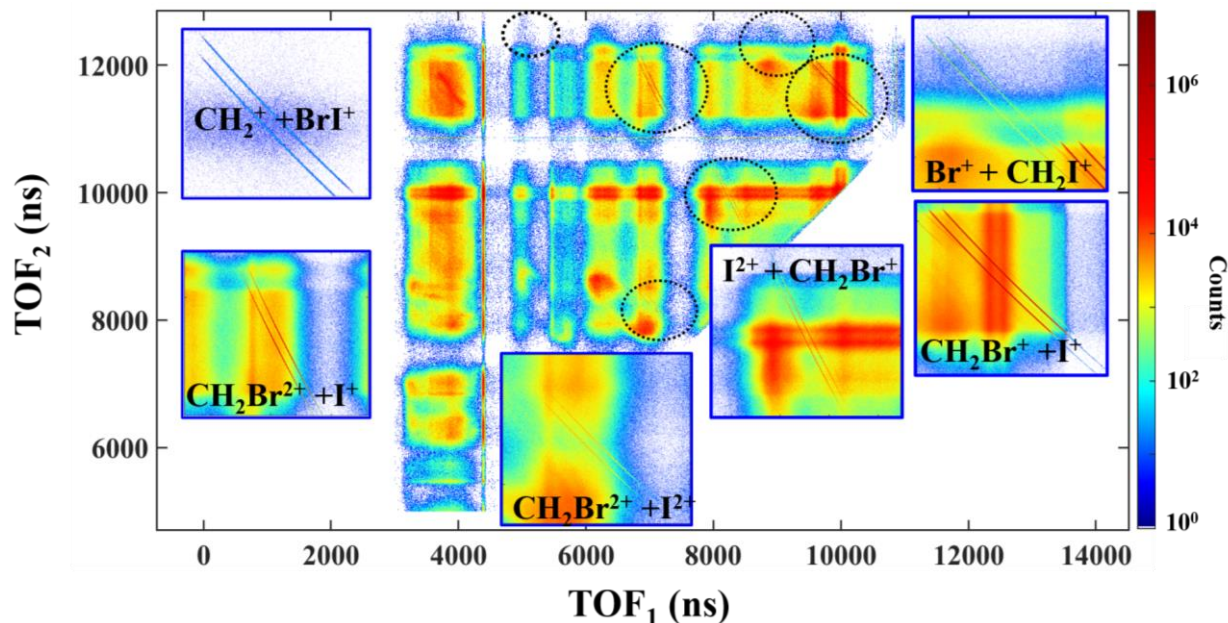


**Figure 5.3.** PhotoIon-PhotoIon COincidence (PIPICO) map for the fragmentation of  $\text{CH}_2\text{BrI}$  molecule after a single NIR pulse. Dashed circles indicate the coincident channels, and their zoomed-in pictures are shown surrounding the map. Each coincident channel produces two diagonal lines due to the two naturally occurring  $^{79}\text{Br}$  and  $^{81}\text{Br}$  isotopes, which are nearly equally abundant.

The KE distributions for two most abundant two-body CE channels,  $\text{CH}_2\text{Br}^+ + \text{I}^+$ , and  $\text{CH}_2\text{I}^+ + \text{Br}^+$ , are shown in Fig. 5.4. The available energy is shared between the co-fragments according to their masses, with the lighter species taking the larger share. While our main observable will be the sum of the energies of both fragments (or all three for later three-body analysis), here we also plot the individual fragment's KEs on order to facilitate identifying their contributions in the non-coincident KE distributions of Fig. 5.2. It can be clearly seen that the individual KE peaks in Fig. 5.4 coincide with the CE features in the corresponding panels of Fig. 5.2. The vertical dashed lines show the KE values expected from a simple CES, assuming that point-like charges are instantaneously created on the molecule that remains at equilibrium geometry. As shown in the figure, the simulated values fall into high-energy tails of the distributions and overestimate the experimental results. The main reason for this is the non-Coulombic shape of the doubly-charged PECs, which have a potential minimum in the Franck-Condon region, as discussed in detail for  $\text{CH}_3\text{I}$  in the previous chapter. The existence of such

potential wells for di-cationic PECs of  $\text{CH}_2\text{BrI}$  is also supported by the presence of bound doubly charged parent ion in the TOF spectrum in Fig. 5.1. We should also note that the stretching of the corresponding carbon-halogen bond between the two ionization steps can also reduce the experimental KE values compared to the CES, which assumes instantaneous “vertical” ionization.

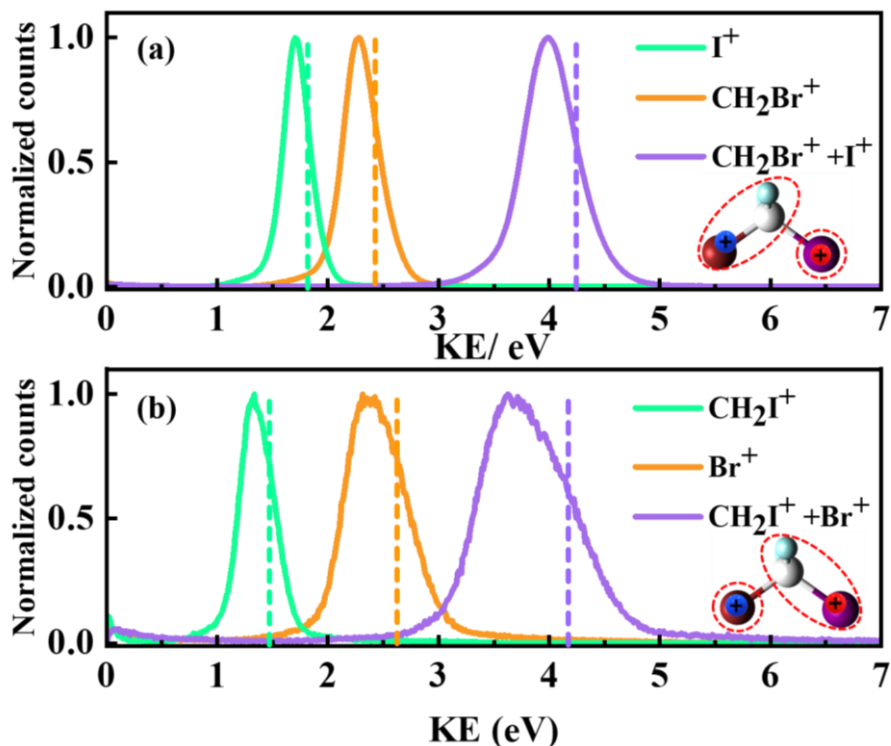


**Figure 5.4.** KE distributions of the two-body fragmentation of  $\text{CH}_2\text{BrI}$  into (a)  $\text{CH}_2\text{Br}^+ + \text{I}^+$  and (b)  $\text{CH}_2\text{I}^+ + \text{Br}^+$  coincident channels. The solid lines are the experimental data compared with the CES results shown with the vertical dashed lines. Each panel shows the assumed charge distributions and molecular geometries in these simulations.

### 5.1.3 Three-body breakup and triple-coincidence data

The analysis of the two-body coincident channels we have discussed thus far can be generalized to many-body fragmentation channels, for instance, a three-body breakup pattern. For this purpose, the three ionic photofragments are measured in coincidence and depicted in a coincidence map called TRIPLE PhotoIon COincidence (TRIPICO), where the yield of the three ions detected in coincidence is plotted with respect to the TOF of one fragment and the sum of the TOFs of the other two fragments. Similar to a PIPICO spectrum, due to the momentum conservation along the TOF direction, if a multiply ionized molecule breaks up into three ions and

all of them are detected, they end up in coincident diagonal stripes in TRIPICO. A TRIPICO spectrum zoomed in on a region corresponding to the three-body breakup into  $\text{CH}_2^+ + \text{Br}^+ + \text{I}^+$  is shown in Fig. 5.5 (a), where the TOF of the lighter fragment ( $\text{CH}_2^+$ ) is plotted versus the sum of the two heavier fragments' TOFs. This map also shows the incomplete channels where one or two hydrogens are missing. We ignore these channels in our current data analysis but they could be investigated in a similar manner. As for the two-body data in the previous section, in this figure we selected the three-body channel containing the heavier isotope,  $^{81}\text{Br}$ , surrounded by a blue box in our coincident channel selection.

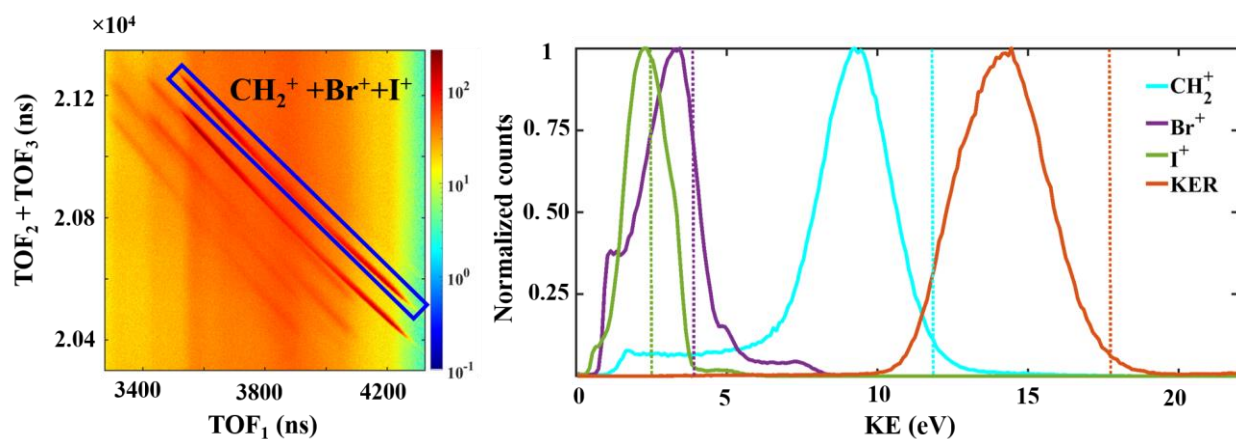


**Figure 5.5.** TRIPICO map of the three-body breakup into  $\text{CH}_2^+ + \text{Br}^+ + \text{I}^+$  coincident channel after the single NIR pulse. (a) The  $\text{CH}_2^+$  time-of-flight ( $\text{TOF}_1$ ) is plotted versus the sum of  $\text{Br}^+$  and  $\text{I}^+$  times-of-flight ( $\text{TOF}_2 + \text{TOF}_3$ ) with the blue box showing the coincident channel with  $^{81}\text{Br}$ . This map also contains incomplete channels with the  $\text{CH}^+$  and  $\text{C}^+$  fragments. (b) The corresponding KE distributions of the individual fragments and the total KER distributions of this three-body breakup. The yields of the fragments are normalized to 1 for the maximum count. The vertical dashed lines represent the simulated values assuming instantaneous CE from the equilibrium geometry.

The KER distribution and the KE of the individual fragments corresponding to this three-body breakup channel are shown in Fig. 5.5 (b). The predictions of the CE simulation assuming the molecular geometry at equilibrium geometry are compared with the experimental results. Here, again, the simulated values lie in the high-energy tail of the experimental energy distributions due to the non-Coulombic nature of the final-state PECs and potential elongation of molecular bonds between the individual ionization steps.

As discussed in Chapter 2, to map intermediate molecular geometries of the molecule that undergo dissociation and, thus, to identify different dissociation and fragmentation pathways, evaluation of different momentum correlation patterns of the three fragments can be very helpful. We start this analysis plotting the measured yield of the  $\text{CH}_2^+ + \text{Br}^+ + \text{I}^+$  three-body breakup channel as a function of its total KER and the angle between the momentum vectors of the two halogen ions. The schematic definition of the emission angle ( $\theta_{23}$ ) and the resulting 2D KER- $\theta_{23}$  map for this channel are shown in Fig. 5.6. Note that even though the angle  $\theta$  is related to the bond angle of the neutral molecule, the relation is not direct and the two angles should not be confused.

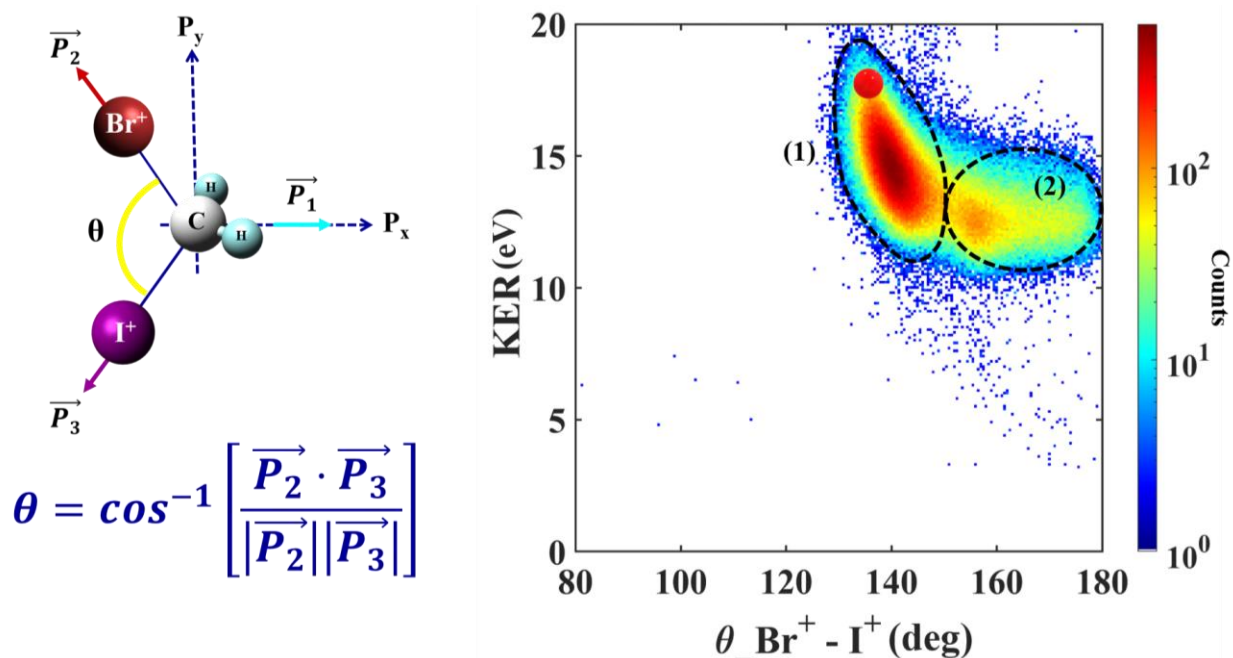


**Figure 5.6.** KER- $\theta_{23}$  map for  $\text{CH}_2^+ + \text{Br}^+ + \text{I}^+$  channel, where the measured yield of such three-body events is plotted as a function of their KER values and the measured angle between the  $\text{I}^+$  and  $\text{Br}^+$  momentum vectors. The dominant features of this map are marked with dashed circles. The red dot shows the  $(\text{KER}, \theta_{23})$  value obtained from the CES simulation assuming instantaneous CE at the equilibrium distance of the neutral molecule. Molecular geometry cartoon and the definition of the plotted angle are schematically depicted on the left.

Two distinct regions in this KER- $\theta_{23}$  map are marked: (1) a dominant feature centered at 14-15 eV KER and at an emission angle of about  $140^\circ$ , and (2) an adjacent weaker structure at about 12 eV covering the whole angular range up to  $180^\circ$ . A red circle within this structure shows the  $(\text{KER}, \theta_{23})$  value obtained from the CES assuming instantaneous CE at the equilibrium distance

of the neutral molecule. Overall, our CESs as well as an analogy with earlier results obtained for  $\text{CH}_2\text{I}_2$  [274] suggest that the events in region (1) mainly originate from the concerted breakup of the bound molecule. Moreover, based on the conclusions of previous work [112], [274], we can tentatively assign region (2) at lower KER and larger emission angles to the sequential breakup of the molecule. In the following, we will provide more information explaining and justifying these assignments.

Throughout this chapter, to identify and disentangle different reaction channels, and to prove claims on channel assignments, we use different three-body representations introduced in section 2.4. Besides the KER- $\theta$  map discussed above, these representations include Newton diagrams, Dalitz plots and energy correlation maps for two halogen ions.

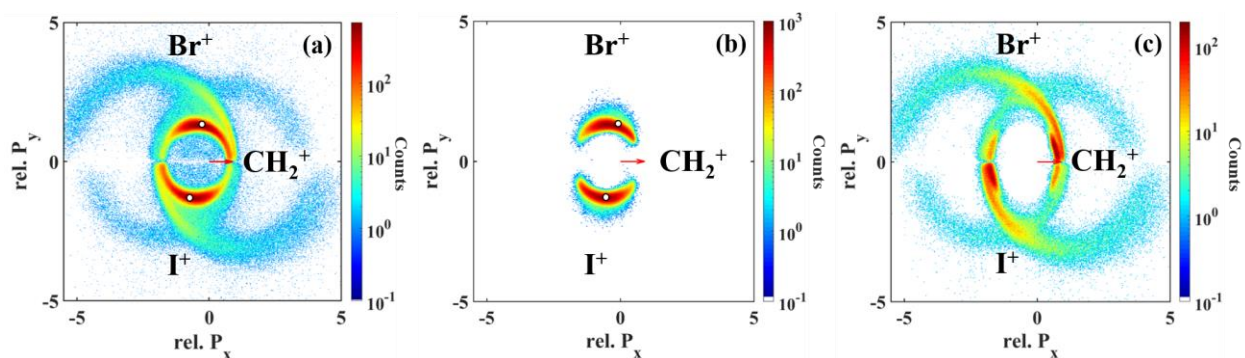


**Figure 5.7.** Newton diagrams for the three-body fragmentation of  $\text{CH}_2\text{BrI}$  into  $\text{CH}_2^+ + \text{Br}^+ + \text{I}^+$ . The momentum of the  $\text{CH}_2^+$  fragment is chosen to be along the x-axis. **(a)** All events for  $\text{CH}_2^+ + \text{Br}^+ + \text{I}^+$  channel. **(b)** Only the events from region (1) in the KER- $\theta$  map of Fig. 5.6. **(c)** Only the events from region (2) of Fig. 5.6. White dots in **(a)** and **(b)** depict the results of the CES simulation for concerted breakup.

First, different fragmentation channels can be visualized in Newton diagrams, which reflect the correlation between the momentum vectors of three detected particles. A Newton diagram for the  $\text{CH}_2^+ + \text{Br}^+ + \text{I}^+$  fragmentation channel, with the momentum vector of  $\text{CH}_2^+$  ion plotted along the positive x-axis, is shown in Fig. 5.7 (a). These diagrams manifest a rather complicated set of several distinct features, including “crescent-like” and, using the language of Refs. [110-112], “sprinkler” shapes overlapping with semi-circular structures. These structures reflect a mixture of concerted and sequential breakup channels. To identify the origin of individual structures, in Fig. 5.7 (b) we plot the same Newton diagram but including only the events from region (1) of the

KER- $\theta$  map shown in Fig. 5.6, whereas the Newton diagram for the events in region (2) of that figure is shown in Fig. 5.7 (c). The Newton diagram for region (1) in Fig. 5.7 (b) appears as a pair of separated crescent-like structures, nearly symmetric with respect to the horizontal axis. Each of these structures is centered around the relative momentum values expected from the CES (shown as white dots), which assumes concerted breakup scenario, i.e., instantaneous triple ionization and CE at equilibrium geometry (see also Fig. 2.18 and corresponding discussion). This channel can be schematically described as:

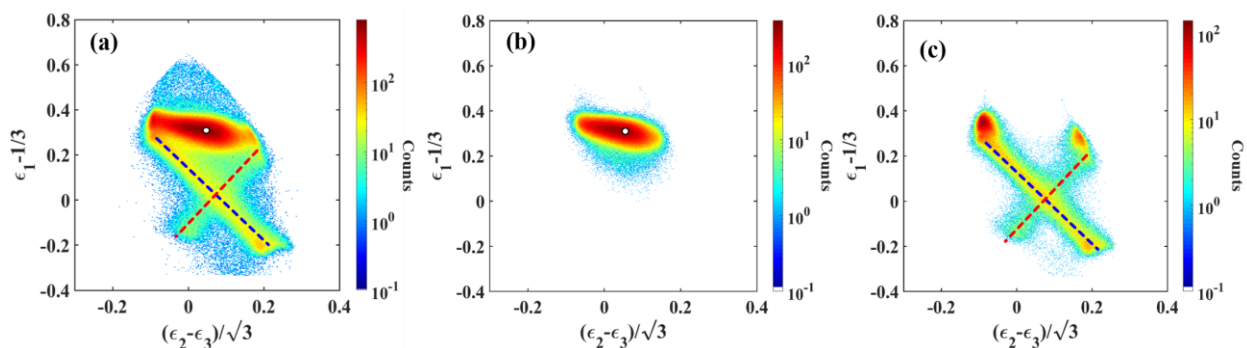


**Figure 5.8.** Dalitz plots for three-body fragmentation of  $\text{CH}_2\text{BrI}$  into  $\text{CH}_2^+ + \text{Br}^+ + \text{I}^+$ . **(a)** All events for  $\text{CH}_2^+ + \text{Br}^+ + \text{I}^+$  channel. **(b)** Only the events from region (1) in the KER- $\theta$  map of Fig. 5.6. **(c)** Only the events from region (2) of Fig. 5.6. White dots in **(a)** and **(b)** depict the results of the CES simulation for concerted breakup. Red and blue dashed lines mark the contributions from two different sequential channels (see text for details).

The Newton diagram for region (2) shown in Fig. 5.7 (c) manifests a more complicated structure, with two pairs of distinguishable “sprinkler-like” features. Based on the results presented in Refs. [110–112], we can interpret these features as signatures of different sequential fragmentation channels. As explained in section 2.4, such sequential channels for a triply charged molecule start with two-body breakup and a formation of a metastable intermediate di-cation that lives longer than its rotational period. When such metastable di-cation later decays into two singly charged fragments, any angular correlation with the ion emitted in the first step is lost. Typical signatures of such process in the Newton diagrams appear as the offset semi-circles or “sprinkler-like” structures, depending on whether the first- or the second-step ion is chosen for determining the x axis. These shapes reflect the loss of angular correlation between the fragments, with the offset being determined by the mass difference [110]–[112].

As discussed in section 2.4, another useful representation of molecular three-body breakup, which directly reflect the fraction of the total KER carried by each fragment, is given by the Dalitz plots. In Fig. 5.8, the Dalitz plots for the same breakup channel are shown for all events in panel (a), and for the events from regions (1) and (2) of Fig. 5.6 in panels (b) and (c), respectively. The plot in Fig. 5.8 (a) consists of a slightly tilted oval band mainly reflecting the events from region (1), and a cross-like pattern (marked by red and blue dashed lines), which is mainly due to the events from region (2). The oval feature encloses the result from the CES for concerted breakup (white dots in (a) and (b)), again suggesting that region (1) contains the events from this direct mechanism. The cross-like feature is yet another characteristic signature of sequential processes, reflecting the lack of direct energy correlation between the ions from the first and the second fragmentation steps [110]–[112], [275].

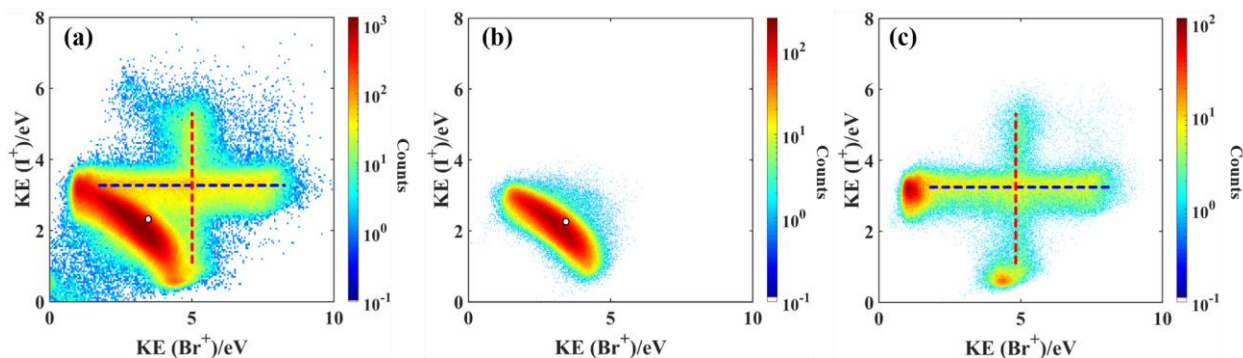
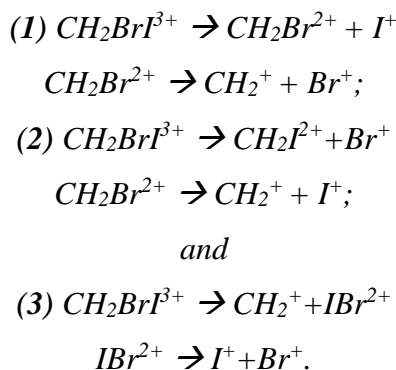


**Figure 5.9.** Iodine-bromine energy correlation map for three-body fragmentation of  $\text{CH}_2\text{BrI}$  into  $\text{CH}_2^+ + \text{Br}^+ + \text{I}^+$ . **(a)** All events for  $\text{CH}_2^+ + \text{Br}^+ + \text{I}^+$  channel. **(b)** Only the events from region (1) in the KER- $\theta$  map of Fig. 5.6. **(c)** Only the events from region (2) of Fig. 5.6. White dots in **(a)** and **(b)** depict the results of the CES simulation for concerted breakup. Red and blue dashed lines mark the contributions from the same two sequential channels as in Fig. 5.8 (see text).

Since the absolute KE of individual fragments are also often helpful for channel identification and disentanglement, we will also use the energy correlation diagrams between two fragments (i.e., two halogen ions) as introduced in Fig. 2.17 (b). Such maps for (a) all events in  $\text{CH}_2^+ + \text{Br}^+ + \text{I}^+$  channel, (b) events from region (1) and (c) from region (2) of Fig. 5.6 are plotted in Fig. 5.9. Again, the full map consists of an oval band (here slightly curved and oriented along the diagonal) reflecting region (1) and a cross-shaped pattern marked by dashed lines (here parallel to the axes), which originate from region (2). Similar to previous representations, the shape of Fig. 5.9 (c) suggests that this is mainly due to sequential channels, with vertical and horizontal lines

highlighting the lack of KE correlation between iodine and bromine ions, whereas the pattern in Fig. 5.9 (b) is consistent with concerted molecular breakup.

To reliably confirm these assignments of concerted and sequential channels, we have carried out Native Frames analysis, following the procedures described in Ref. [110]–[112], [275]. This analysis includes explicit assumptions about the steps involved in sequential fragmentation. For triply charged  $\text{CH}_2\text{BrI}^3+$ , there are three possible sequential pathways with different intermediate di-cations:



To illustrate the essence of the Native Frames method, here we focus only on the first of these three channels. The details of the analysis procedure are given in Appendix 1 (see also Refs. [110–112]). The results of this analysis are presented in Fig. 5.10. In brief, in Fig. 5.10 (a) the yield of all three-body events for  $\text{CH}_2^+ + \text{Br}^+ + \text{I}^+$  channel is plotted as a function of the KER of the second step of channel (1) listed above and the angle between the momentum of the first-step ion and the metastable di-cation axis. If the rotation of the metastable di-cation occurs in the fragmentation plane, one can expect a uniform distribution of this angle [110]–[112]. Finding the angle-independent vertical band in Fig. 5.10 (a) and gating on it, we can select events originating from this specific sequential channel. For the selected events, we plot KER- $\theta$  map (b), Dalitz plot (c) and the Newton diagram (d).

The results presented in Fig. 5.10 (b-d) clearly support the coarse assignment of concerted and sequential channels made above. The sequential events for the specific sequential channel (1) are clearly restricted to the region (2) of KER-  $\theta$  map of Fig 5.6, are responsible for one of the “sprinkler” structures in the corresponding Newton map (Fig. 5.7 (c)), and correspond to one of the tilted bands in the Dalitz plot of Fig. 5.8 (c), marked by the blue dashed line.

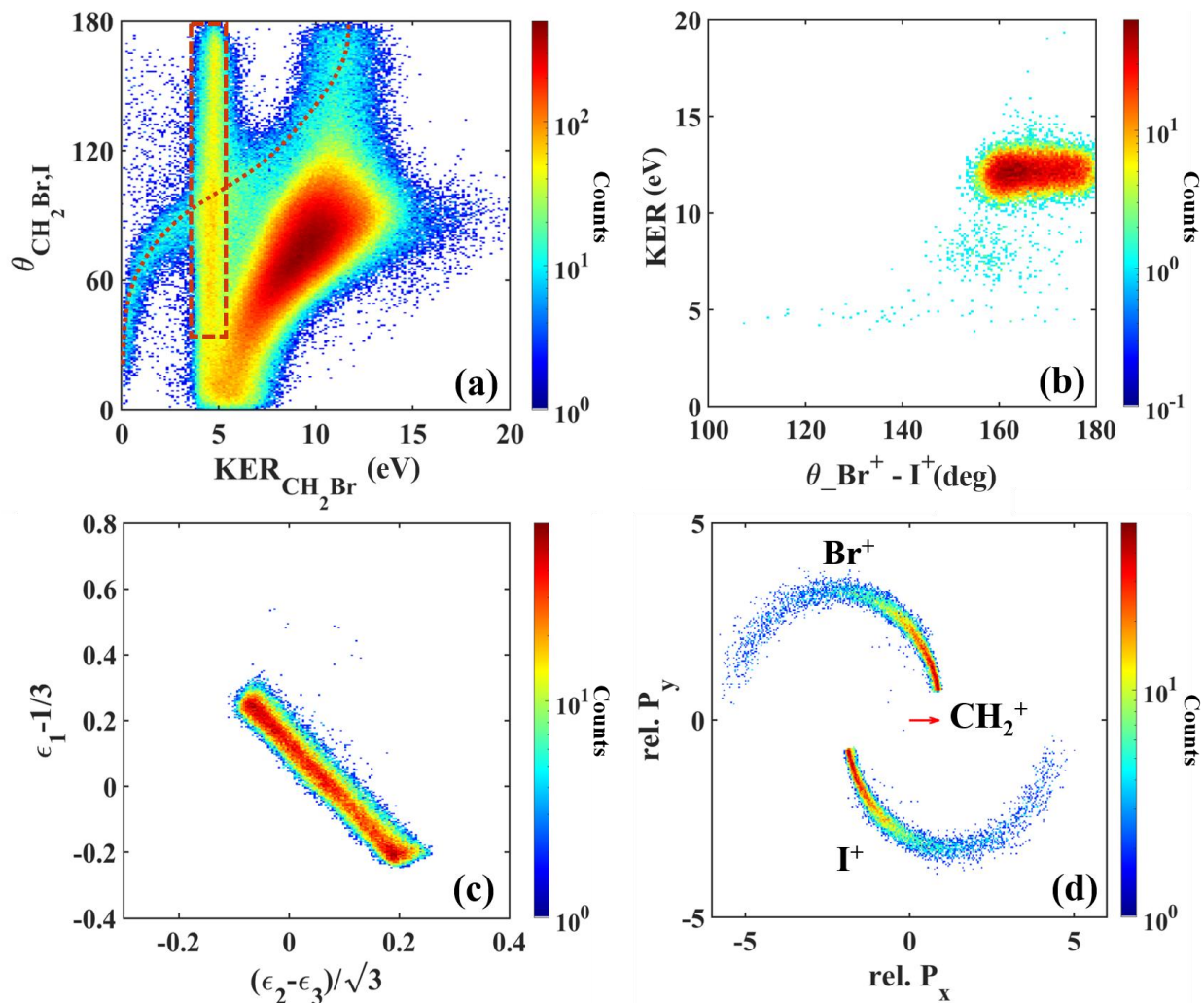


**Figure 5.10.** (a) Yield of  $\text{CH}_2^+ + \text{Br}^+ + \text{I}^+$  coincident channel as a function of the  $\text{KER}_{\text{CH}_2\text{Br}}$  and  $\theta_{\text{CH}_2\text{Br}, \text{I}}$  (see Appendix.A for details). (b) KER- $\theta_{23}$  map; (c) Dalitz plot; and (d) Newton diagram for the events confined to the rectangular box in panel (a). Dotted curve in (a) reflects the location of events corresponding to sequential channel (2) involving metastable  $\text{CH}_2\text{I}^{2+}$  di-cation.

These events are also responsible for the horizontal band in the energy correlation map of Fig. 5.9 (c), also marked blue. In each of the graphs in panels (c) of Figs. 5.7-5.9 a complementary, somewhat weaker feature can be found, flipped around the horizontal axis in the Newton map of Fig. 5 (c) or rotated by  $90^\circ$  counterclockwise and marked by red dashed lines in the Dalitz plot and energy correlation map of Figs. 5.8. (c) and 5.9 (c). This weaker feature denoted by the dotted curve on the Native Frame plot in Fig. 5.10 (a) reflects sequential channel (2) listed above, with  $\text{Br}^+$  being detached in the first step and forming metastable  $\text{CH}_2\text{I}^{2+}$  di-cation.

While we can clearly trace signatures of sequential channels (1) and (2) in Native Frames analysis, and in different three-body fragmentation patterns shown in Fig. 5.6-5.9, we cannot unambiguously identify the contributions from channel (3) involving intermediate  $\text{BrI}^{2+}$  formation. It does not produce a clear single-independent signature in the Native Frame plot like the one shown in Fig. 5.10 (a). However, some contributions from this channel are consistent with the appearance of Figs. 5.7-5.9. Based on our understanding of the process, we would expect this channel to produce a pair of slightly offset semi-circles in a Newton diagram, a horizontal band in a Dalitz plot, showing the lack of correlation with the  $\text{CH}_2^+$  KE, and a diagonal band in I-Br energy correlation map. Some hints of its presence can be observed in all three representations in Figs. 5.7-5.9, distributed between the contributions from regions (1) and (2) shown in panels (b) and (c) of these figures. We argue that this channel contributes at least to some extent to both regions (1) and (2) in Fig. 5.6. It is also likely responsible for the pair of localized spots visible in panels (c) of Figs. 5.7-5.9, and could also contribute to the broadening of the structures due to concerted breakup in panels (b) of the same figures. Nevertheless, our analysis strongly suggests that region (1) is dominated by the contributions from direct, concerted breakup of the molecule.

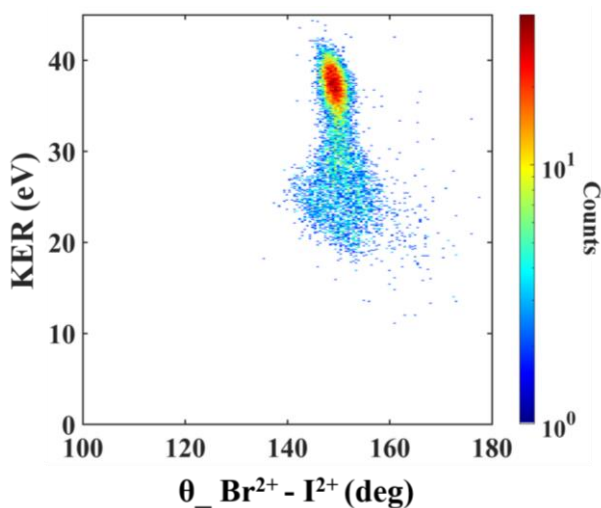


**Figure 5.11.** KER- $\theta_{23}$  plot for the three-body fragmentation of  $\text{CH}_2\text{BrI}$  into  $\text{CH}_2^+ + \text{Br}^{2+} + \text{I}^{2+}$  after a single NIR pulse with  $8 \times 10^{14} \text{ W/cm}^2$  intensity.

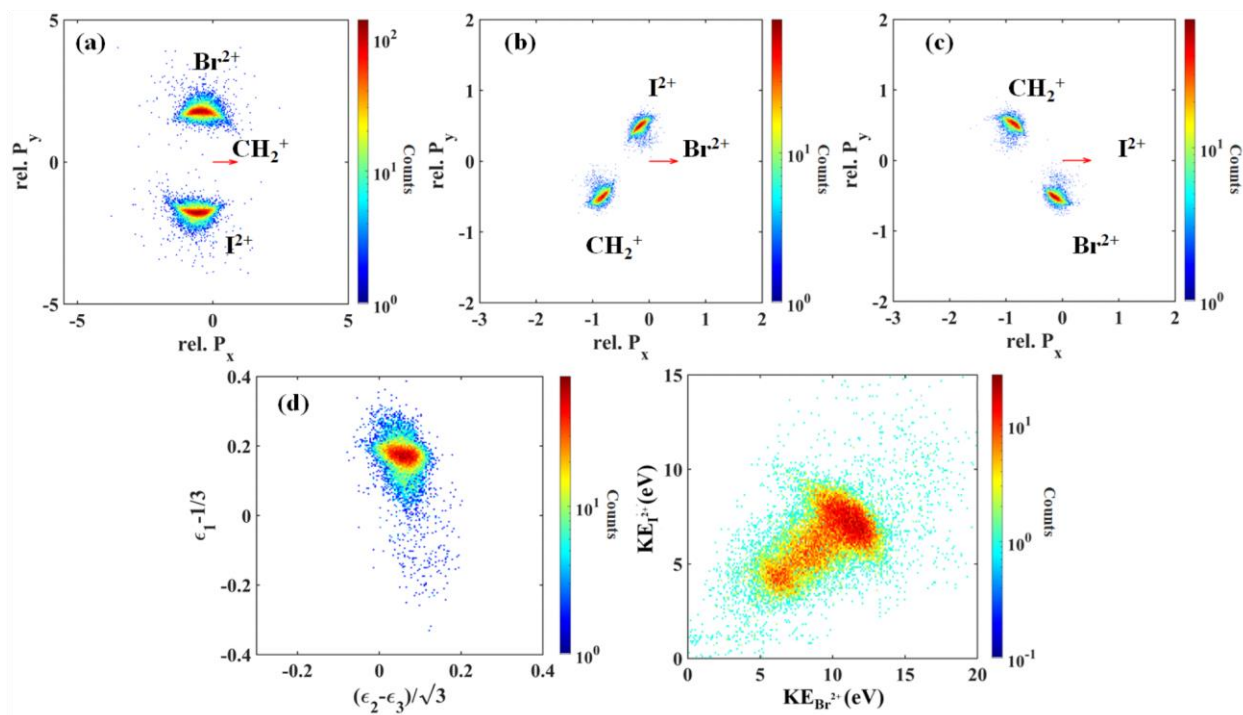


**Figure 5.12.** (a-c) Newton diagrams for the three-body fragmentation of  $\text{CH}_2\text{BrI}$  into  $\text{CH}_2^+ + \text{Br}^{2+} + \text{I}^{2+}$  after the single NIR pulse. (d) Dalitz and (e) energy-sharing plots for this coincident channel.

Sequential breakup processes wash out the relation between final-state momenta of the fragments and molecular geometry, and, thus, are unsuitable for CEI, which assumes of rapid fragmentation of the molecule. In earlier PhD work from our group on  $\text{CH}_2\text{I}_2$  [274], three-body coincident channels with higher final charge states provided the opportunity to track the dynamics whose signatures in the breakup of the triply charged molecules were covered by the contribution from sequential channels discussed above. In particular, this concerns region (2) of the KER- $\theta_{23}$  map shown in Fig. 5.6, where the signatures of the  $\text{CH}_2\text{Br-I}$  isomer contribution can be expected. Fig. 5.11 shows similar KER- $\theta_{23}$  but plotted for the ionization of the molecule to the five-fold charge state and breaking up into  $\text{CH}_2^+ + \text{Br}^{2+} + \text{I}^{2+}$  channel. The observed pattern does not include any events at large angles corresponding to region (2) in Fig. 5.6. However, besides the main localized spot, it shows a diffuse feature at somewhat lower KER values.

The analysis of this coincident channel demonstrates that the concerted fragmentation is the dominant process in the five-fold case where the Newton diagrams with each fragment as a reference axis do not show any of those sprinkler-shaped features representing the sequential

breakup and the localized maxima dominate them. As expected, we get similar impressions from the Dalitz and energy-sharing plots, as shown in Fig. 5.12.

The analysis of other three-body patterns for this coincident channel summarized in Fig. 5.12. strongly suggests that essentially all of the events in this three-body breakup channel with five charges result from concerted fragmentation of the molecule. Newton diagrams plotted with respect to the momentum of either fragment as a reference do not show any of the sprinkler-shaped or semi-circular features characteristic for sequential breakup. Instead, the plots are dominated by the localized maxima at positions close to expectations based on CES. Similar conclusions can be made from the Dalitz and energy-correlation plots, as shown in Fig. 5.12 (d) and (e). In the later map, a clear contribution at lower sum energy of both fragments can be seen, which corresponds to the lower-KER events in Fig. 5.11. Following the arguments presented in Ref. [274], we speculate that these events are due to the molecules, that undergo significant dynamics in one of the intermediate states (e.g. di-cationic) during the ionization process.

## 5.2 CH<sub>2</sub>BrI molecule under a single UV pulse

Given the ionization potential of the parent CH<sub>2</sub>BrI molecule of 9.7 eV [276], we require at least three 263 nm photons to generate ionic fragments. This could be satisfied at higher UV pulse intensities. Since the primary goal of this experiment is to study single-photon excitations, similar to the CH<sub>3</sub>I experiment, this contribution is unwanted. However, to ensure a reasonable pump-probe contrast, the intensity cannot be set too low. The absorption cross-section of CH<sub>2</sub>BrI at 263 nm is comparable to that of CH<sub>3</sub>I. Therefore, to limit contributions from higher-order processes, but, at the same time, to limit contributions from multiphoton processes, we set the intensity of the UV pulses to  $1.5 \times 10^{13}$  W/cm<sup>2</sup>, which is in the mid-range of intensities available in our experimental setup. This value is the same as what was used for most of CH<sub>3</sub>I experiments described in Chapter 4.

Fig. 5.13 shows the measured TOF spectrum of detected ions using a UV pulse with a peak intensity of  $1.5 \times 10^{13}$  W/cm<sup>2</sup>. At this intensity, the dominant photoion is the singly-charged parent ion (CH<sub>2</sub>BrI<sup>+</sup>), with certain amount of dissociative ionization (DI) products (CH<sub>2</sub>Br<sup>+</sup>, CH<sub>2</sub>I<sup>+</sup>, I<sup>+</sup>, Br<sup>+</sup>, and CH<sub>2</sub><sup>+</sup>) also present in the spectrum. This figure also includes 2D TOF vs. position maps for each of these ions, showing that they are predominantly produced at the center of the detector i.e., with low momenta or KE, and only rather small contributions from more energetic ions.

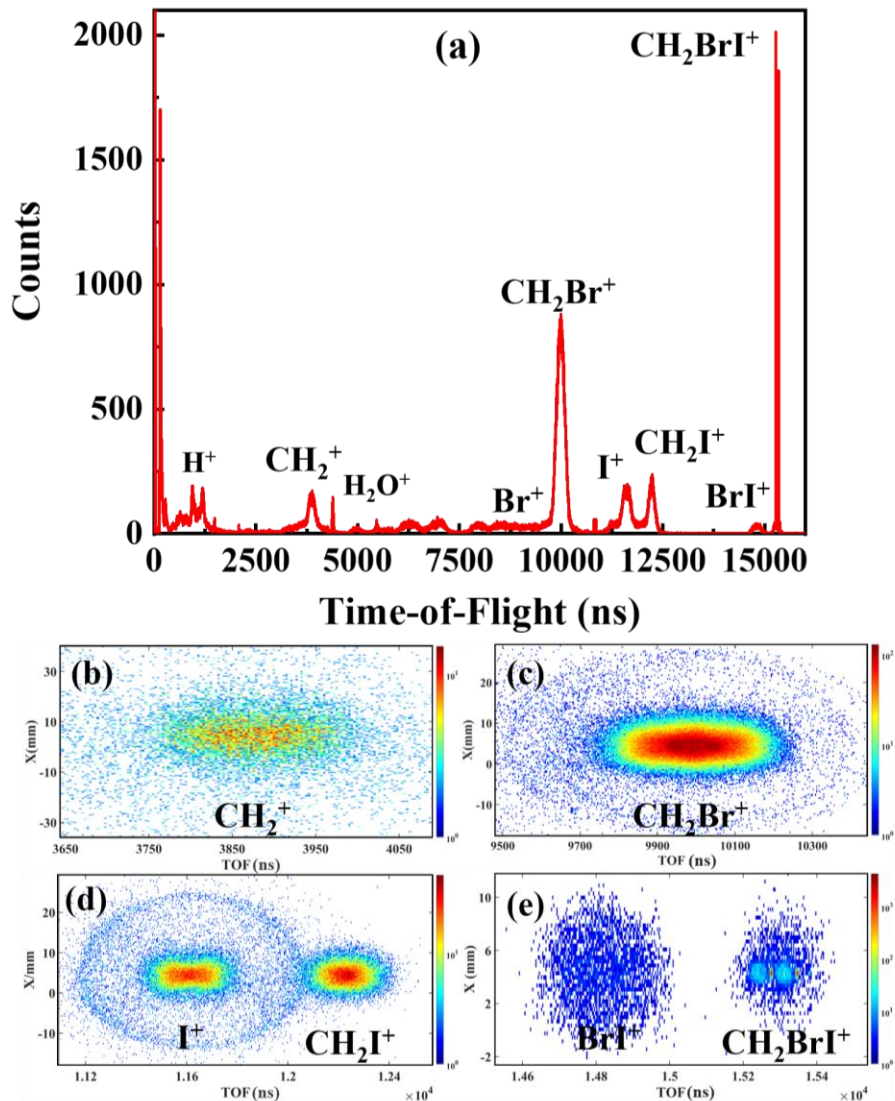


**Figure 5.13.** Time-of-Flight (TOF) of the generated ions after a single UV pulse of  $1.5 \times 10^{13}$  W/cm<sup>2</sup> intensity. The ion TOFs are labeled based on their mass-to-charge ratio with the associated 2-D TOF vs. position on top of each peak.

The non-coincident KE distributions of four major ionic fragments are shown in Fig. 5.14. All spectra display a dominant contribution at nearly zero KE, along with smaller peaks at higher energies. Our coincident analysis (not shown here) indicates that these high energy ions originate from the CE of doubly-ionized states. While the CE contributions appear only as a weak shoulder in Fig. 5.14 (a-c), for  $Br^+$  ions in panel (d) their total yield exceed the yield of low-KE product. Since the absolute yield of this channel in  $Br^+$  is comparable with the other CE products in Fig.

5.14 (a-c), this observation simply highlights that DI of  $\text{CH}_2\text{BrI}$ , which proceeds via singly-charged states, is unlikely to produce  $\text{Br}^+$  fragments.

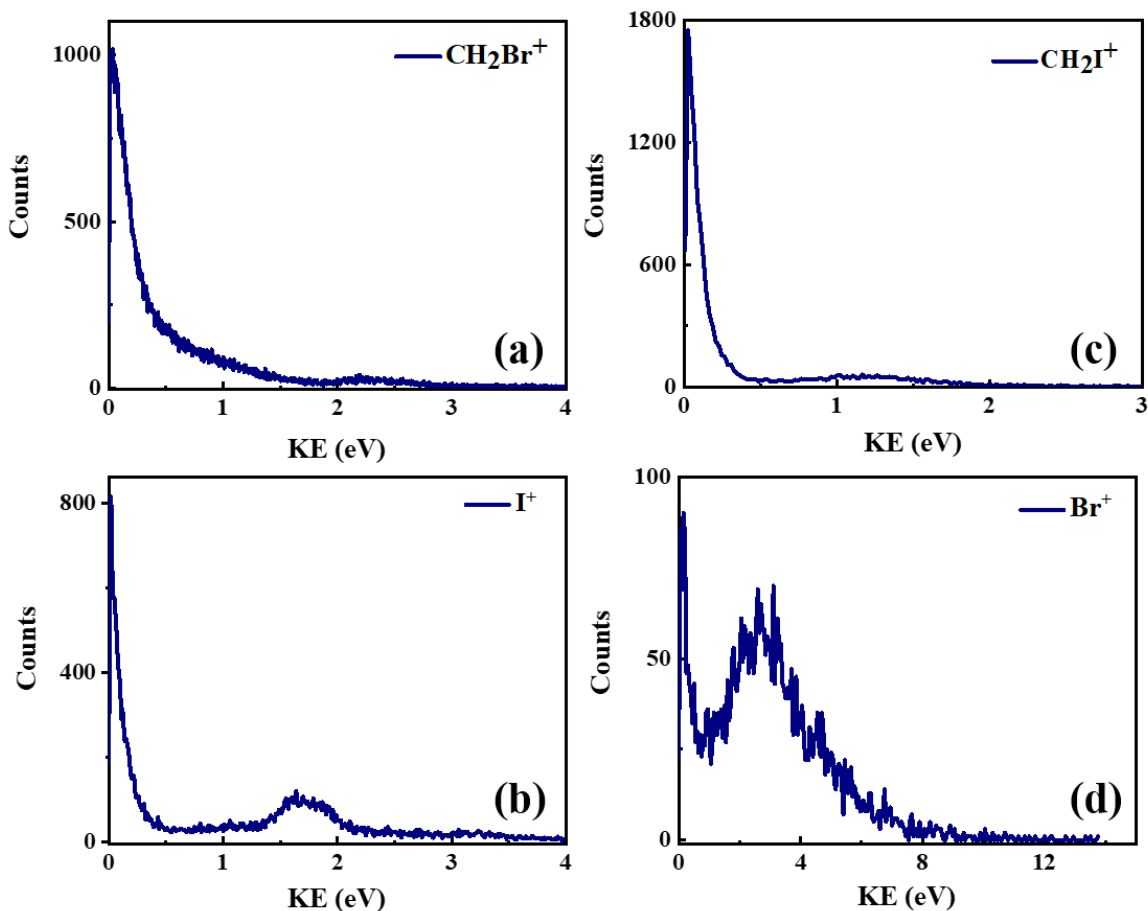


**Figure 5.14.** KE distributions of the ionic fragments of  $\text{CH}_2\text{BrI}$  molecule. (a)  $\text{CH}_2\text{Br}^+$ , (b)  $\text{I}^+$ , (c)  $\text{CH}_2\text{I}^+$ , and (d)  $\text{Br}^+$  produced by a single UV pulse at  $1.5 \times 10^{13} \text{ W/cm}^2$  intensity. In addition to the dominant low energy peak, the distributions show weak shoulders at higher energies mainly due to the CE of the molecule from doubly-charged states.

### 5.3 Time-resolved Coulomb explosion of UV-induced photodissociation of $\text{CH}_2\text{BrI}$ with two-body breakup coincident channels

The preceding sections identified primary dissociation and ionization pathways in the  $\text{CH}_2\text{BrI}$  molecule after interaction with individual NIR and UV (263 nm) pulses. This section concentrates on probing UV-induced dynamics via two-body coincident channels from the doubly-charged final states. Based on a PIPICO map similar to the one shown in Fig. 5.3, we identify several two-body coincident channels, with the  $\text{CH}_2\text{Br}^+ + \text{I}^+$  channel being the strongest one.

Fig. 5.15 displays the total KER distributions of this channel as a function of the delay between the two pulses. Similar to the time-resolved  $\text{CH}_3\text{I}$  maps shown in Chapter 4, there are two distinct features: a horizontal band centered at 4.0 eV corresponding to the CE of bound molecules, and a descending band corresponding to the CE of the molecule dissociating after the pump pulse. As in the case of  $\text{CH}_3\text{I}$ , the KER distribution of the horizontal high-energy band closely resembles the spectrum obtained for the same channel with the probe pulse alone (see Fig. 5.4 (a)).

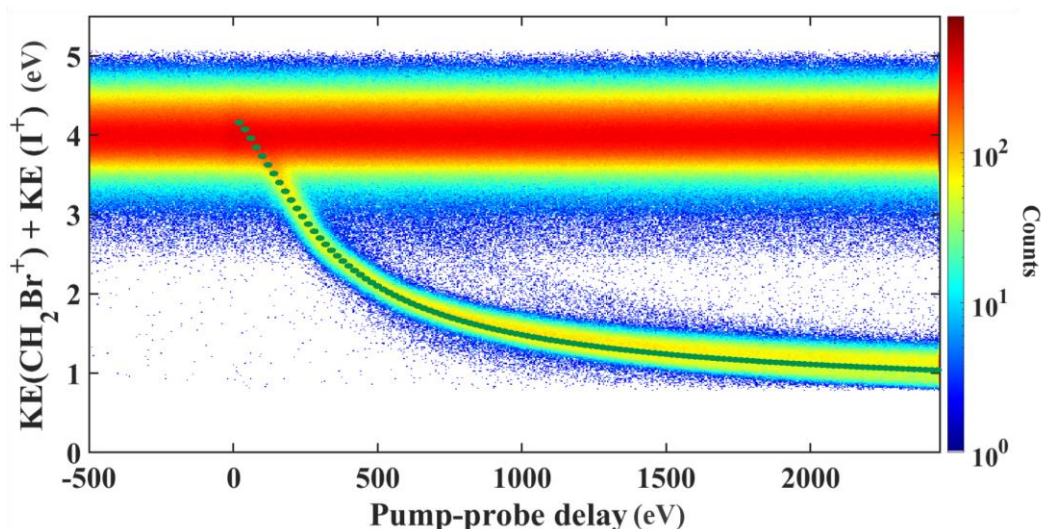


**Figure 5.15.** Delay-dependent KER distribution for the two-body  $\text{CH}_2\text{Br}^+ + \text{I}^+$  coincident channel after UV pump and NIR probe pulses. The dotted curve represents the simulated KER values as a function of the delay between the two pulses, assuming exponential rise of dissociation velocity of the dissociating fragments. Here, as well as in all other data presented in sections 5.3 and 5.4, the UV and NIR pulse intensities are kept at  $1.5 \times 10^{13}$  and  $8 \times 10^{14}$   $\text{W}/\text{cm}^2$ , unless stated otherwise.

As can be seen from Fig. 5.16, which depicts the KER distributions for the same channel measured at two fixed UV-NIR delays (2.5 ps and 20 ps), the descending band splits into two branches at longer delays, with the third, very-low KER feature becoming visible at 20 ps (green curve in Fig. 5.16). While the two higher-KER peaks reflect two dissociation pathways of a neutral molecule associated with spin-orbit-split ground- and excited-state iodine, the lowest-energy channel is due to DI events triggered by the pump pulse. More specifically, based on the earlier photochemistry data from Refs. [277], [278], the strongest peak of the low-KER band, centered at 0.8 eV, can be assigned to  $\text{CH}_2\text{Br}+\text{I}$  ( $^2\text{P}_{3/2}$ ) neutral dissociation channel, whereas its weaker shoulder at 0.53 eV is attributed to the  $\text{CH}_2\text{Br}+\text{I}$  ( $^2\text{P}_{1/2}$ ) channel. Based on the photochemistry of this molecule discussed in section 2.3.2 (see Fig. 2.12 (a) and the corresponding discussion), the

ratio of the I to I\* channels is expected to be 4:3 [277], [278] matching our experimental data reasonably well.

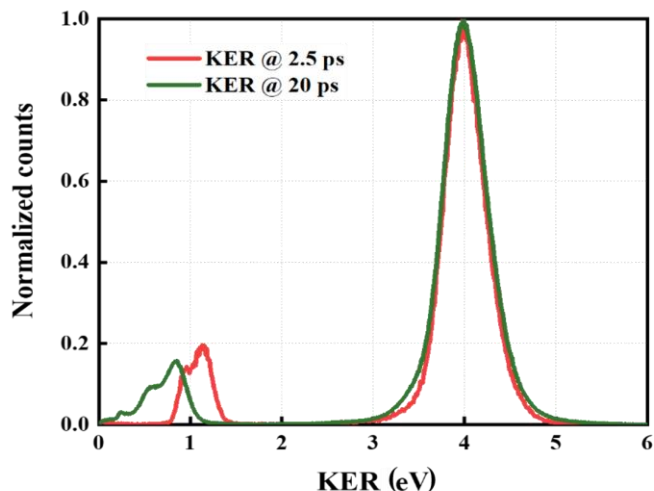


**Figure 5.16.** KE distribution of the two-body  $\text{CH}_2\text{Br}^+ + \text{I}^+$  coincident channel after UV pump and NIR probe pulse at 2.5 and 20 ps illustrates the time evolution of the dissociating molecules.

The delay-dependent KER distribution in Fig. 5.15 is compared with a classical CES assuming an exponential rise of dissociation velocity of the dissociated fragments (see section 4.4.1). In this simulation, the translational velocity of the fragments is determined from the “asymptotic” velocity of the dissociating fragments using the KER distribution at 20 ps delay between the two pulses. Specifically, for the CES plotted in Fig. 5.15, we used the value corresponding to the highest of the low-KER peaks measured at 20 ps (red curve in Fig. 5.16). At the equilibrium geometry of the neutral molecule, assuming that the two charges are located at the iodine atom and at the center of mass of the  $\text{CH}_2\text{Br}$ , the Coulomb repulsion is about 4.17 eV, slightly above the maximum of the horizontal, delay-independent band (see also magenta curve and vertical dashed line Fig. 5.4 (a)). Similar to the CES performed in Chapter 4 for the  $\text{CH}_3\text{I}$  molecule, there is a reasonable correspondence between the simulated and experimental results for the descending dissociation band over the entire delay range. However, the CES slightly overestimates the energy near the Franck-Condon region due to this molecule’s bound di-cation potential energy curves.

As discussed in section 2.3.2, the partitioning of excess photon energy upon the photoabsorption in the A-band in dihalomethanes like  $\text{CH}_2\text{BrI}$  is different from  $\text{CH}_3\text{I}$ . In these molecules, the two spin-orbit states of the iodine could not be well-resolved because the energy

release is now shared more equally by the two fragments, as opposed to the CH<sub>3</sub>I case, in which the methyl fragment carries most of the energy. In addition, due to the presence of the second halogen atom, there is a much larger degree of internal (in particular, rotational) excitation following the photodissociation, which reduces the kinetic energy differences between the two product channels and broadens the observed kinetic energy distributions. In mechanistic terms, there is a large torque on the CH<sub>2</sub>Br (or CH<sub>2</sub>I) co-fragment during photodissociation.

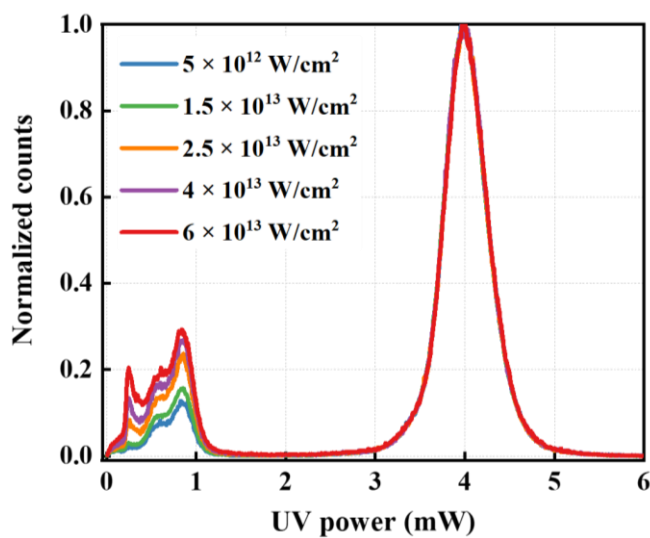


**Figure 5.17.** KER distribution for the two-body CH<sub>2</sub>Br<sup>+</sup> + I<sup>+</sup> coincident channel after UV pump and NIR probe pulse obtained at different UV intensities. UV-NIR delay was kept at 20 ps. The absolute yield of low-KER dissociation channels is linearly growing by increasing the UV intensity. The UV intensity was changed from  $5 \times 10^{12}$  to  $6 \times 10^{13}$  W/cm<sup>2</sup>, whereas the NIR intensity is kept at  $8 \times 10^{14}$  W/cm<sup>2</sup>.

Similar to the CH<sub>3</sub>I molecule discussed in Chapter 4, the photochemistry of CH<sub>2</sub>BrI at 263 nm is dominated by a single-photon resonant transitions to neutral dissociating PECs. Correspondingly, a linear dependence of dissociation yields on UV pulse intensity can be expected. To confirm this, we performed a series of measurements at different UV pulse powers keeping the pump-probe delay at 20 ps. The data suggest that the peak at lower KER (~0.23 eV) shows a steeper and non-linear dependence on the UV intensity. This behavior confirms the assignment of this low-energy peak to multiphoton DI by UV pulse. The very low KE of this channel at 20 ps delay, which has not necessarily reached its asymptotic value yet, is consistent with the dominance

of nearly zero-KE peaks in the KE distributions of  $I^+$  and  $CH_2Br^+$  ions obtained with the UV pulse alone observed in Fig. 5.14 (a, b).

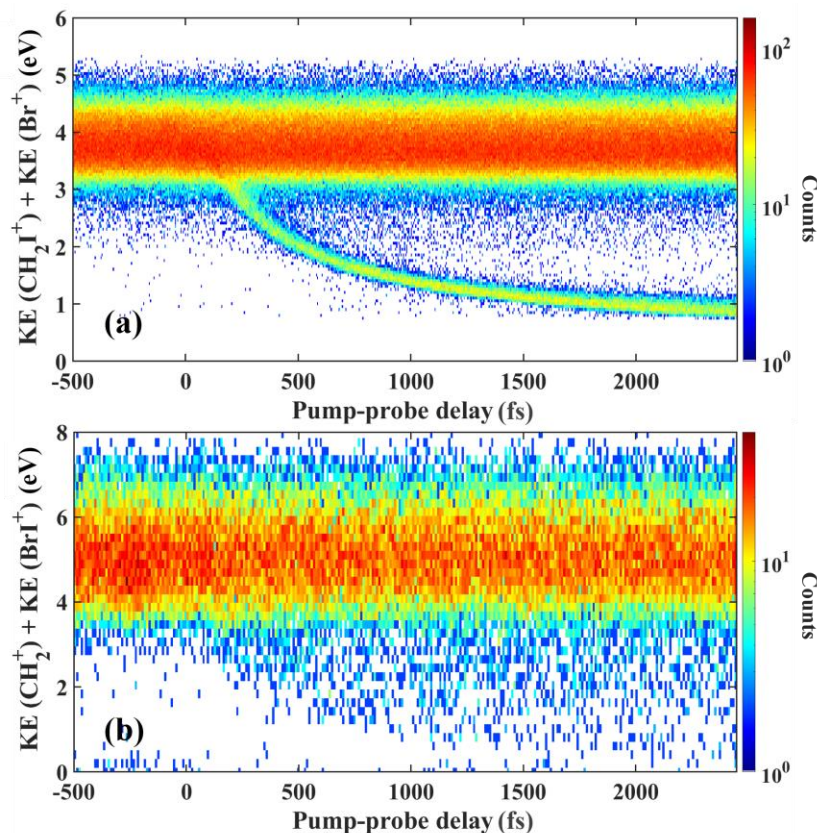


**Figure 5.18.** Delay-dependent KER distribution for two other two-body coincident channels after UV pump and NIR probe pulses. **(a)**  $CH_2I^+ + Br^+$  channel; **(b)**  $CH_2^+ + BrI^+$  channel.

The coincident measurements allow tracking the dynamics through other possible dissociation pathways. As discussed earlier, besides the main dissociation channel,  $CH_2BrI$  molecule can undergo a C-Br bond cleavage or dissociate into the  $CH_2 + BrI$  channel and molecular halogen ( $BrI$ ) formation [99], [279]. Our time-dependent coincident data confirm the existence of both of these pathways. The corresponding delay-dependent KER maps for  $CH_2I^+ + Br^+$  and  $CH_2^+ + BrI^+$  coincident channels are shown in Fig. 5.18 (a) and (b), respectively. The  $CH_2I^+ + Br^+$  channel manifest the same two major features as the  $CH_2Br^+ + I^+$  data in Fig. 4.15, reflecting the molecules that either remain bound or dissociate after the pump pulse. Comparing the absolute yields in the data of Figs. 5.15 and 5.18 (a), it is clear that the C-Br dissociation channel is significantly weaker than the C-I dissociation, confirming that the dominant dissociation mechanism at 263 nm is the C-I bond cleavage. The  $BrI$  formation channel in Fig. 5.18 (b) also

displays two similar structures, nearly delay-independent band at 4-6 eV, and a broad descending structure at lower KER. While the latter delay-dependent band is clearly distinguishable in the data, it is very diffuse and weak, in agreement with previous studies suggesting that this is a minor channel at this wavelength [187], [188]. Furthermore, the fact that the dissociating channel appears as such a diffuse structure suggests that BrI is not formed on a dissociative PEC with a well-defined start time for the dissociation but more likely via a pre-dissociative state, thus smearing out the descending structure in time. We should note that the delay-dependent feature in  $\text{CH}_2\text{I}^+ + \text{Br}^+$  final state can also include contributions from BrI or  $\text{BrI}^+$  formation on one of the cationic PES, or from two-photon Rydberg-state excitation. A  $\text{BrI}^+$  formation channel in the cationic states can be expected given weak but non-negligible signals of  $\text{BrI}^+$  ions in the UV-only data presented in Fig. 5.13.

#### **5.4 Time-resolved analysis of UV-driven photodissociation dynamics in $\text{CH}_2\text{BrI}$ probed via three-body coincident channels**

As demonstrated in Chapter 4 for  $\text{CH}_3\text{I}$  and in section 5.3 above for  $\text{CH}_2\text{BrI}$ , two-body coincident momentum imaging can be used as an efficient tool for mapping the time evolution of the internuclear separation between two dissociating fragments. In addition, for cases where the axial recoil approximation is valid, this approach can also be used to capture the spatial orientation of the molecular bond axis for quasi-diatomic or linear systems [257], [280]–[282]. However, as discussed in section 2.4, to retrieve further geometry information for polyatomic molecules using ion momentum imaging, one needs to break the molecule up into three or more ionic fragments in the probe step. To realize this approach for a time-resolved experiment, three-body coincident measurements and an advanced set of appropriate representation tools, which is discussed in detail in section 5.1, need to be extended to pump-probe experiments. In the following, we employ this approach to identify, disentangle and characterize the photodissociation pathways triggered by the UV pulse at 263 nm. First, a brief overview of the delay-dependent three-body breakup maps for the three and five-fold charge states is presented, followed by channel assignments and disentangling different dissociation pathways.

### 5.4.1 Overview of the delay-dependent data for $\text{CH}_2^+ + \text{Br}^+ + \text{I}^+$ coincident channel

Fig. 5.19 shows the measured KER distribution for the triply-charged coincident channel  $\text{CH}_2^+ + \text{Br}^+ + \text{I}^+$  as a function of the time delay between the UV and NIR pulses. For a triply charged channel, the KE of the ionic fragments mainly originates from the Coulomb repulsion between the fragments. Such time-dependent KER distribution reflects the structural changes in the molecule. The essence of this map is similar to the two-body maps presented so far. Three principal features can be identified in this time-dependent kinetic energy spectrum. First, the fragments in the broad high-energy band centered at 15 eV, which is essentially delay-independent, originate from the CE of bound molecules. This KER spectrum for this broad feature is similar to the KER distribution obtained using a single NIR pulse (see Fig. 5.5).

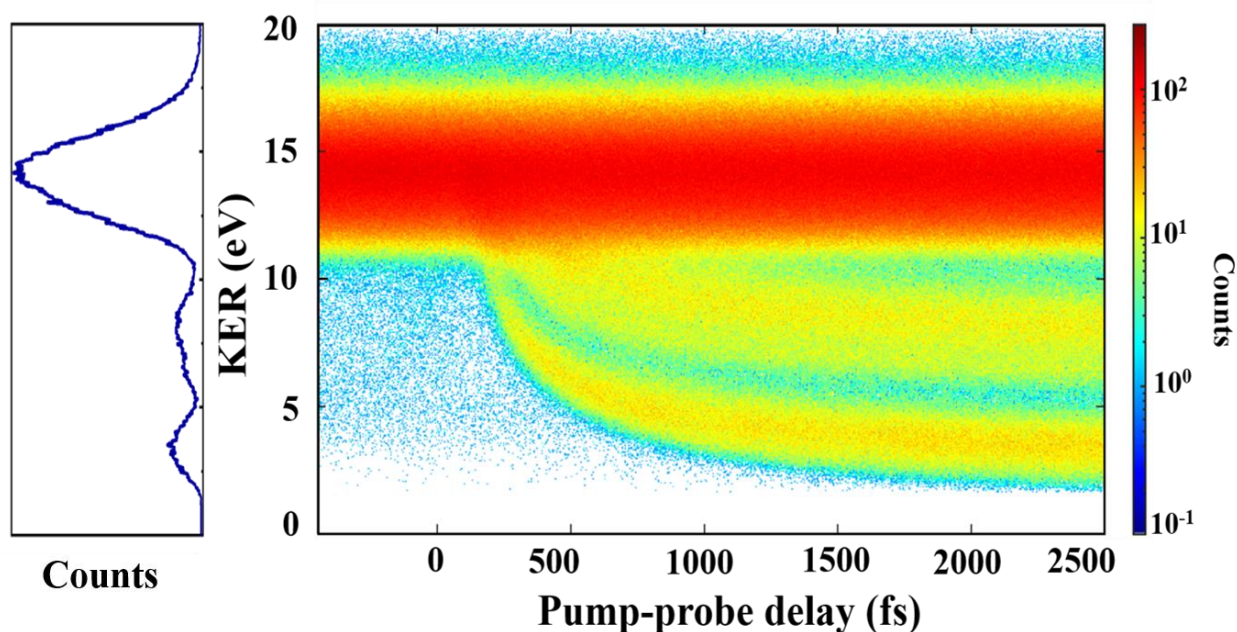


**Figure 5.19.** Delay-dependent KER distribution for  $\text{CH}_2\text{BrI}$  fragmentation into  $\text{CH}_2^+ + \text{Br}^+ + \text{I}^+$  after UV pump and NIR probe pulses. The projection of the spectrum in the delay range of 2.3–2.5 ps onto the KER axis is shown on the right. The dotted descending bands are the results of CES for  $\text{CH}_2\text{Br} + \text{I}$  (green dots),  $\text{CH}_2\text{I} + \text{Br}$  (pink dots) and  $\text{CH}_2 + \text{BrI}$  (navy blue dots) dissociation channels performed using exponential rise velocity model described in section 4.4.1. The purple dashed line marks the contribution from the three-body dissociation channel (see text).

Additionally, two broad descending bands appear at larger delays. Similar to earlier results for two-body breakup, these bands originate from Coulomb explosion of dissociating molecules.

Conceptually, these delay-dependent triple ionization events could result from probing two- and three-body dissociation in a neutral molecule, or in one of the lower charge states. Therefore, these two bands might include iodine or bromine detachment channels,  $\text{CH}_2\text{Br} + \text{I}$  and  $\text{CH}_2\text{I} + \text{Br}$ ; BrI elimination channel,  $\text{CH}_2 + \text{BrI}$ ; or three-body dissociation channel  $\text{CH}_2 + \text{Br} + \text{I}$ . These dissociation pathways might involve both neutral and charged fragments, and in all cases are probed via triply-charged final state. The projection of the 2-D map in the delay range of 2.3-2.5 ps onto KER axis shown on the right side of the plot indicates that at these delays two broad dissociating bands are already separated.

We performed a series of classical CES to track the origin of these dissociation channels. First, we simulated pump-induced two-body dissociation channels using their individual asymptotic KEs measured at large delays (20 ps) and assuming that the fragments acquire their final KEs in accordance with exponential velocity rise model described in section 4.4.1. Then, following the procedure described in section 2.4, we used the Runge Kutta algorithm to simulate three-body CE of these dissociating channels at different UV-NIR delays. The simulation results suggest that the upper of the two descending bands in Fig. 4.19 mainly reflects two different two-body dissociation channels,  $\text{CH}_2\text{Br} + \text{I}$  and  $\text{CH}_2\text{I} + \text{Br}$ . In essence, this band reflects the same dissociation dynamics that are mapped in Figs. 5.15 and 5.18(a) via the corresponding two-body CE maps, but here probed by the three-body CE into  $\text{CH}_2^+ + \text{Br}^+ + \text{I}^+$  final state. Even though direct identification of these dissociation pathways is more straightforward in the two-body data presented in the previous section, where they are naturally separated from each other and from the other dissociation processes, we will demonstrate further in this chapter, as well as in Chapter 6 that the three-body CE analysis provides valuable additional information on the dynamics of each of these channels.

The CES for  $\text{CH}_2 + \text{BrI}$  (shown by navy blue dotted line) falls into the upper edge of the lower descending band in Fig. 5.19. While this dissociation channel can indeed contribute to that band, based on the two-body data shown in Fig. 5.18 (b), we can assume that this contribution has to be rather weak and cannot be solely responsible for the whole band, which is comparable in intensity to the upper one. Based on the very low KER values observed for the maximum of this band (marked by the dashed purple line) at large delays, which lies below 3 eV, the only possible channel that can be responsible for this structure is three-body dissociation triggered by the pump pulse. While we do not have enough information to reliably simulate such three-body dissociation

process, we can verify that any other scenario, where at least one of the carbon-halogen bonds remains intact at large delays, would lead to significantly larger KER values.

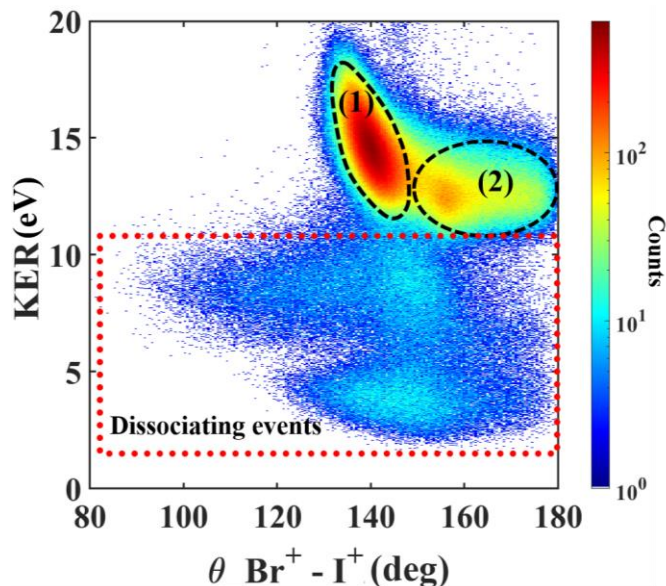


**Figure 5.20.** KER- $\theta_{23}$  plot for  $\text{CH}_2^+ + \text{Br}^+ + \text{I}^+$  coincident channel. This 2D plot is integrated over all delays from -450 fs to 2.45 ps. Dashed ovals marking regions (1) and (2) are the same as in NIR-only KER- $\theta_{23}$  map of Fig. 5.6, mainly including the events from concerted and sequential breakup of the bound molecule, respectively (see section 5.1.3). The remaining events in the dashed box at lower KERs reflect CE of dissociating molecules, which are not present in the NIR only data shown in Fig. 5.6.

To extract further information on the individual pathways contributing to the observed delay-dependent dynamics, we utilize different three-body analysis tools discussed in sections 2.4. and 5.1.3. First, in Fig. 5.20 we plot the yield of the  $\text{CH}_2^+ + \text{Br}^+ + \text{I}^+$  three-body coincident channel as a function of its KER and the angle between the iodine and bromine momentum vectors. This map is integrated over all the delay values, and thus, includes the same data as Fig. 5.19. While the upper part of this plot resembles such KER- $\theta_{23}$  map shown in Fig. 5.6 for single NIR pulse, the lower part, marked by the dashed box contains a broad distribution of events that are not present in single pulse data. Similar to the descending bands of Fig. 5.19, these events reflect the CE of the molecules dissociated by the pump pulse, where one or more internuclear separations are stretched at the time of the probe pulse arrival, resulting in smaller Coulomb repulsion of the created ions and, thus, in lower KER. The regions marked (1) and (2) in the upper part of Fig. 5.20

are chosen identical to those in Fig. 5.6 and correspond to the CE of the bound molecules in the delay-independent band in Fig. 5.19.

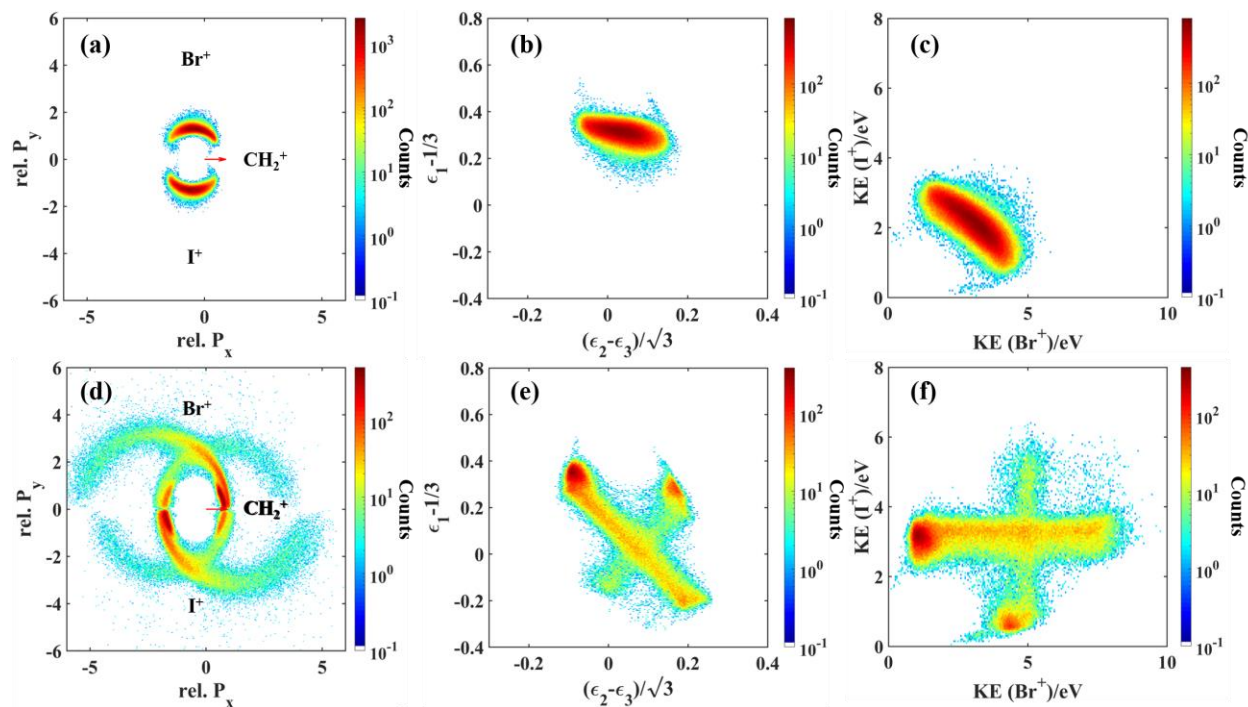


**Figure 5.21.** Different representations of the  $\text{CH}_2^+ + \text{Br}^+ + \text{I}^+$  coincident events in regions (1) (top row) and (2) (bottom row) of the KER- $\theta_{23}$  plot integrated over all delays. **(a, d)** Newton diagrams, **(b, e)** Dalitz plots, and **(c, e)** halogen energy correlation diagram.

As discussed in section 5.1.3, region (1) mainly includes the events resulting from concerted breakup of the molecule (which in this case means triple ionization and Coulomb explosion of bound  $\text{CH}_2\text{BrI}$ ), whereas region (2) is formed by sequential fragmentation pathways involving two-step breakup of the triply-charged molecule and the production of a long-lived metastable di-cationic fragment, which decays long after the probe pulse. To confirm that this assignment still holds for pump-probe data shown in Fig. 5.20, in Fig. 5.21 the Newton diagrams, Dalitz plots and halogen energy correlation diagrams are plotted separately for these two regions. The plots shown in the top row for region (1) and in the bottom row for region (2) are essentially identical to the single-pulse data for the corresponding regions shown in Figs. 5.7-5.9, confirming that these events in the pump-probe data are correctly assigned to either concerted or sequential fragmentation induced by the probe pulse.

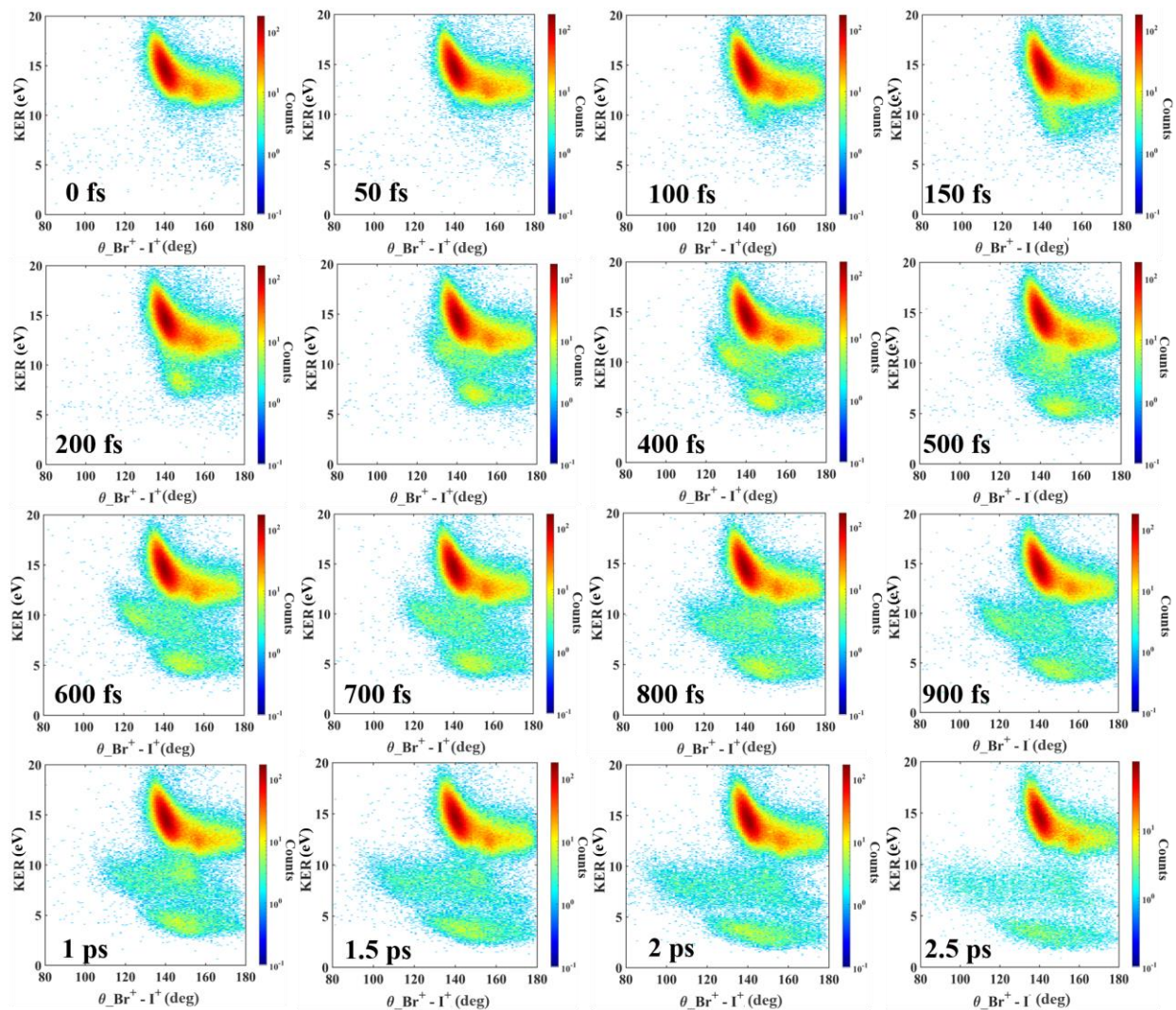


**Figure 5.22.** KER- $\theta_{23}$  snapshots for the three-body coincident  $\text{CH}_2^+ + \text{Br}^+ + \text{I}^+$  channel at different UV-NIR delays. Each snapshot corresponds to the 50 fs delay window centered at the values shown in the figure.

To obtain a time-resolved picture of the dynamics induced by the pump pulse, we consider three-body fragmentation maps at different pump-probe delays. Such multiple timed snapshots can eventually help us to make a “molecular movie” directly visualizing the evolution of the molecular system. Fig. 5.22 illustrates the time evolution of the KER- $\theta_{23}$  maps over the delay range from 0 to 2.5 ps. While the first two frames at zero and 50 fs delays still resemble single-pulse data of Fig. 5.6, highlighting that the UV pump pulse at the intensity employed in this experiment does not contribute to the triple ionization of the molecule, starting from 100 fs, the onset of dissociation

processes towards lower KER values can be observed. These events propagate to lower KER and spread in angle as the delay increases. One can trace several different features of the spectrum evolving with the delay, which split up and also spread in angle, finally ending up in two KER regions, one between 5 and 10 eV, and one below 5 eV.

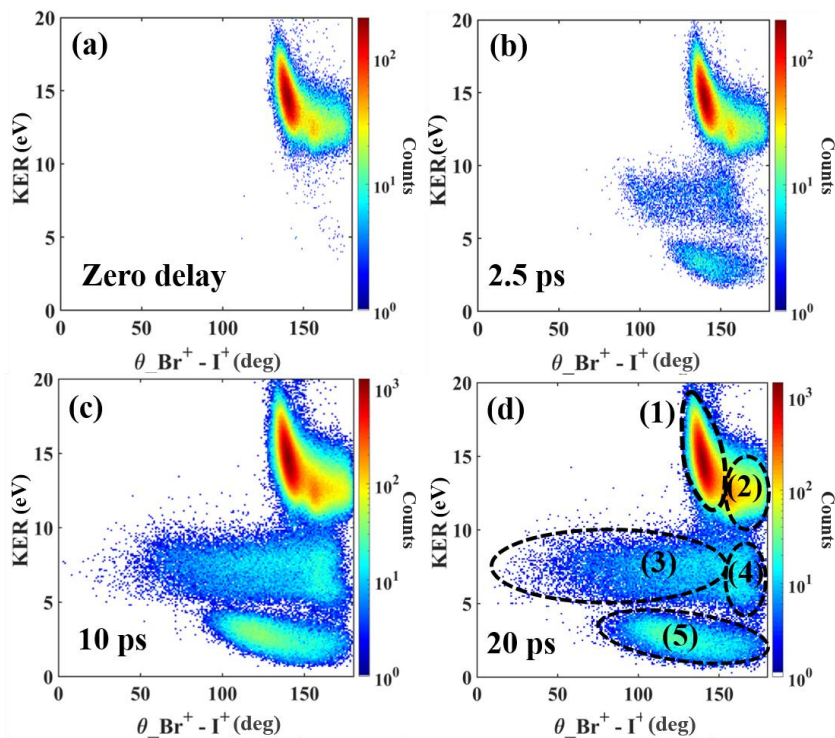


**Figure 5.23.** KER- $\theta_{23}$  snapshots for the three-body coincident  $\text{CH}_2^+ + \text{Br}^+ + \text{I}^+$  channel. (a) 0 fs, (b) 2.5 ps, (c) 10 ps, and (d) 20 ps. The regions are numbered and marked by dashed ellipses in panel (d), indicating KER- $\theta_{23}$  features corresponding to different pathways discussed in the text. Regions (1) and (2) are identical to those marked in Figs. 5.6 and 5.20.

To understand the origin of the corresponding events and to achieve better separation of different contributing reaction pathways, in Fig. 5.23 we extend these movie frames to larger delays up to 20 ps. There, different dissociation pathways have propagated long enough to separate and isolate from each other, which make tracing their signatures more straightforward and reliable.

From Fig. 5.23 it is clear that even at large delays the events at large KERs (above  $\sim 11$  eV) still resemble the first frame at zero delay, reflecting concerted and sequential breakup of the molecule by the probe pulse, again marked by dashed ovals (10 and (2) in Fig. 5.23 (d). For lower KER region, this figure illustrates how the dissociating events eventually reach their asymptotic conditions. Starting from the 2.5 ps frame in (b), different pump-induced dissociation channels

propagate towards KER, eventually forming three regions marked as (3), (4) and (5) in panel (d) at 20 ps. While region (5) is well separated from the other two at all three delays, regions (4) and (5) have rather similar KER values, and the separation between them is not very clear. Region (4) is selected to match a pronounced feature localized close to  $180^\circ$  in (c) and (d), whereas region (3) marks a broad horizontal band at the same KERs, which covers a broad angular range and spreads to smaller angles as the delay increases.

#### 5.4.2 Identification of different pump-induced dissociation channels

As a next step, we will focus on identifying different dissociation channels contributing to regions (3) and (4) marked in Fig. 5.23 (d). As previously mentioned, there are four possible dissociation pathways that can contribute to the  $\text{CH}_2^+ + \text{Br}^+ + \text{I}^+$  final state. They include  $\text{CH}_2\text{Br} + \text{I}$ ,  $\text{CH}_2\text{I} + \text{Br}$ ,  $\text{CH}_2 + \text{BrI}$  and  $\text{CH}_2 + \text{Br} + \text{I}$ , where the partners could be neutral or singly-charged, and iodine or bromine atoms can be either in spin-orbit ground or excited state. To facilitate further channel assignments, we employ CES adapted for these scenarios. The only exception is the three-body dissociation pathway  $\text{CH}_2 + \text{Br} + \text{I}$ : as mentioned in the discussion of Fig. 5.19, we did not carry out detailed CESs for this scenario. However, based on our CES for  $\text{CH}_2\text{Br}$ ,  $\text{CH}_2\text{I}$  and  $\text{BrI}$  products, we can reliably assign the three-body dissociation by the pump pulse to the events in region (5). If any of the three molecular fragments listed above was still bound at the time when the NIR probe pulse arrives, its two-body Coulomb explosion would already result in the KER larger than what we observe for region (5), leaving the three-body dissociation by the pump pulse as the only realistic possibility.

CES for all two-body dissociation channels are shown in Fig. 5.24. Fig. 5.24 (a) and (b) display simulations similar to those shown as the dotted lines in Fig. 5.19, but integrated over a broad range of delays from 0 to 20 ps. As could be expected, the simulation results move to smaller KER values for larger delays. Here, the orientation of the molecular co-fragment ( $\text{CH}_2\text{Br}$  or  $\text{CH}_2\text{I}$  for (a),  $\text{BrI}$  for (b)) is kept fixed with respect to dissociation axis at the angle corresponding to the equilibrium geometry. While for the two-body simulations discussed earlier in this and previous chapters this assumption does not make a difference since the charge is always placed in the center of mass of the molecular co-fragment, around which the rotation would take place, for three-body CE, it severely impacts the emission angles between the resulting fragments. While this might be less critical for the  $\text{BrI}$  elimination channel because at very large delays, where the  $\text{CH}_2$  group is

already far away, both fragments will always tend to fly into the opposite directions, it is a very coarse assumption for the other two pathways, where, as discussed in section 2.3.2, the  $\text{CH}_2\text{Br}$  or  $\text{CH}_2\text{I}$  co-fragment experiences significant torque upon dissociation and is expected to rotate (see Fig. 2.13). Correspondingly, while all simulations predict a reasonable set of delay-dependent KER values (as already seen in Fig. 5.19), and the simulation for  $\text{BrI}$  elimination in Fig. 5.24 (b) converges towards  $180^\circ$ , as expected, the results for  $\text{CH}_2\text{Br} + \text{I}$  or  $\text{CH}_2\text{I} + \text{Br}$  channels in Fig. 5.24 (b) clearly fail to account for a broad angular spread of the events with 5 -10 eV KER, which also clearly increases with the delay.

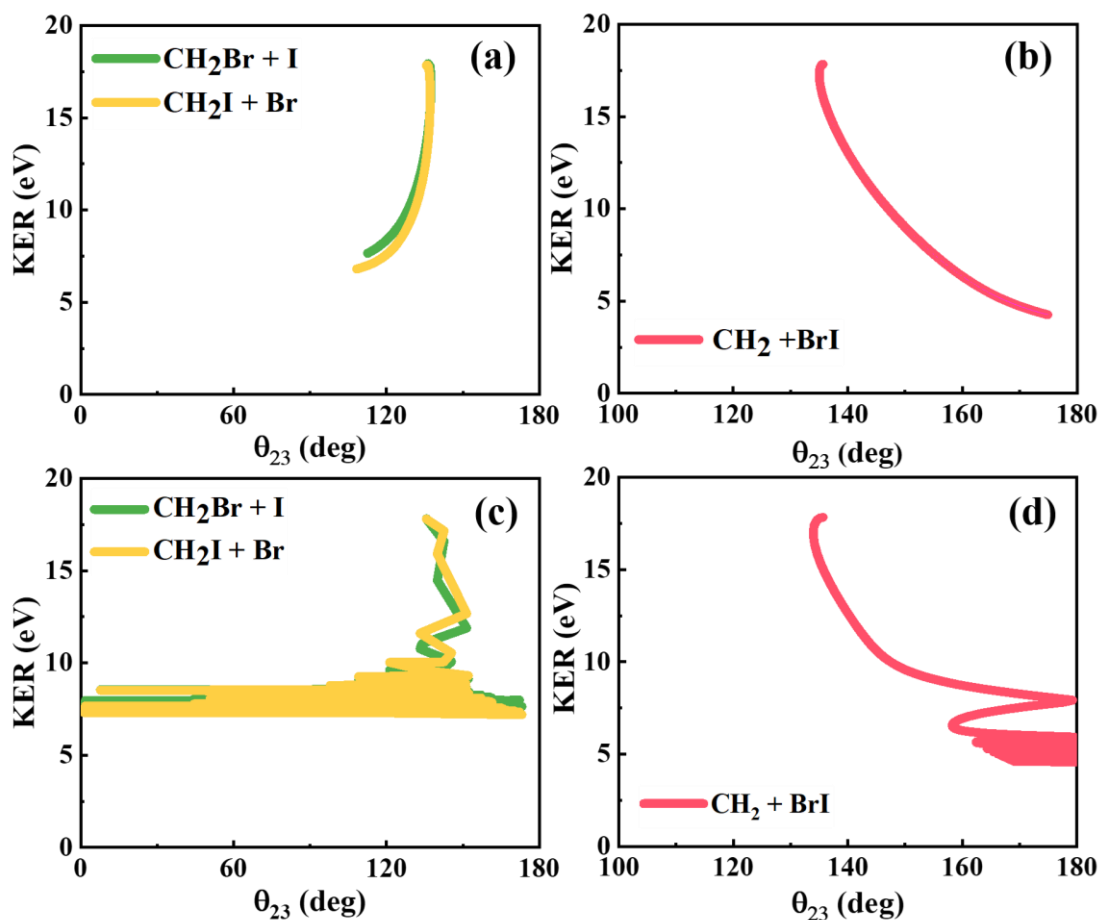


**Figure 5.24.** Simulated KER- $\theta_{23}$  for  $\text{CH}_2^+ + \text{Br}^+ + \text{I}^+$  final state assuming different dissociation pathways: (a, c)  $\text{CH}_2\text{Br} + \text{I}$  and  $\text{CH}_2\text{I} + \text{Br}$ ; (b, d)  $\text{CH}_2 + \text{BrI}$ . All results are integrated over UV-NIR delays from 0 to 20 ps. While the data in (a) and (b) are obtained from the CES for fixed orientation of  $\text{CH}_2\text{Br}$ ,  $\text{CH}_2\text{I}$  and  $\text{BrI}$  fragments, the results in (c) and (d) are calculated allowing these fragments to rotate with the periodicity of 280 fs for  $\text{CH}_2\text{Br}$ , 330 fs for  $\text{CH}_2\text{I}$  and 840 fs for  $\text{BrI}$  (see text for details).

In order to account for the observed angular spread, in Fig. 5.24 (c) we plot the results of the CES for  $\text{CH}_2\text{Br} + \text{I}$  and  $\text{CH}_2\text{I} + \text{Br}$ , where the molecular co-fragment is allowed to rotate around its center of mass. The details of this simulation will be presented in Chapter 6, which is a dedicated effort to visualize this rotational motion. Rotational periods used in the simulation for  $\text{CH}_2\text{Br}$  (280 fs) and  $\text{CH}_2\text{I}$  (330 fs) are taken from the experimental data (see section 6.1 below for details). As can be clearly seen from Fig. 5.24 (c), such rotational motion is clearly responsible for the large angular spread of the CE events in region (3) of the KER-  $\theta_{23}$  map in Fig. 4.23. We also attempted to include rotation in the CES for  $\text{CH}_2 + \text{BrI}$  channel. Since we do not have any direct input on the rotational period of potential BrI rotation in this reaction, we set it to a larger value of 840 fs, to reflect both, the heavier mass of its constituents and the smaller degree of rotational excitation, which can be expected due to dissociation geometry. As expected, the inclusion of such rotational motion has less dramatic effects on the CES results for this channel.

Based on the above discussion and the outcome of the CES simulations, we assign the events in region (3) of Fig. 4.23 (d) to two-body dissociation by the pump pulse, followed by robust rotation of molecular co-fragment. It should be noted that according to our CES, both  $\text{CH}_2\text{Br} + \text{I}$  and  $\text{CH}_2\text{I} + \text{Br}$  dissociation pathways are contributing to these events. A localized spot close to  $180^\circ$  (region (4)) can be interpreted as a signature of BrI elimination, with both iodine and bromine fragments emitted nearly back to back during the CE by the probe pulse. It should be noted that according to the simulations shown in Fig. 5.23 (c), events due to  $\text{CH}_2\text{Br} + \text{I}$  and  $\text{CH}_2\text{I} + \text{Br}$  pathways can also spread into this area, such that region (4) most likely contains the mixture of all three channels. Finally, as discussed above, the events in region (5) can be produced only by three-body dissociation of the molecule after the pump pulse. To confirm these assignments and to further disentangle overlapping channels, in the following, we examine the Newton diagrams, Dalitz plots and halogen energy correlation maps for each of these regions of Fig. 5.23 (d).

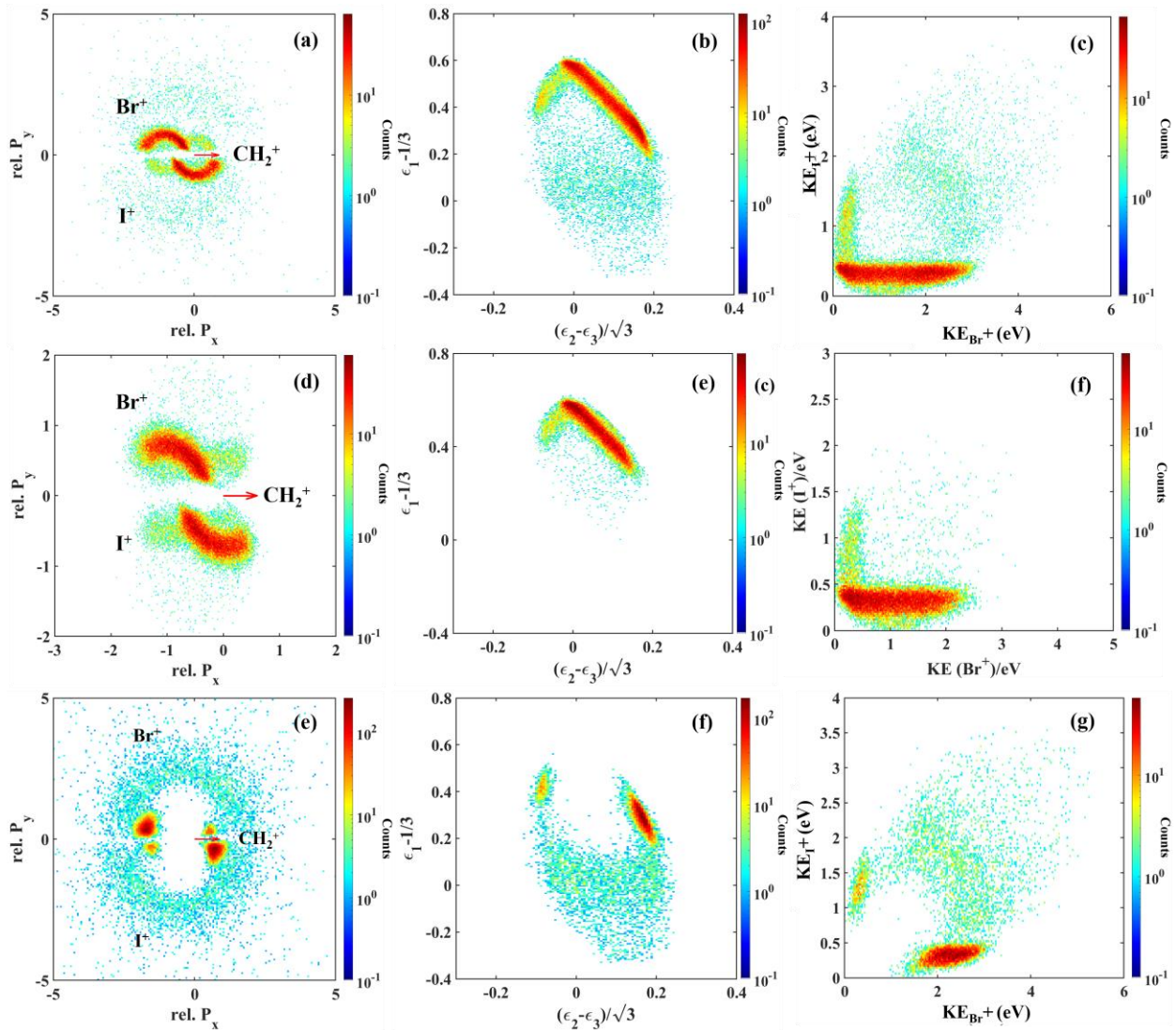


**Figure 5.25.** Different representations of the  $CH_2^+ + Br^+ + I^+$  coincident events in regions (3) and (4) of the KER- $\theta_{23}$  plot at 20 ps. Left column: Newton diagrams; middle column: Dalitz plots; right column: Br – I energy correlation map. Top row: regions (3) and (4) together; middle row: region (3) only; bottom row: region (4) only.

These three different data representations for the events in regions (3) and (4) are shown in Fig. 5.25. The top row shows the Newton diagram (a), Dalitz plot (b) and Br-I energy correlation map (c) for both regions together, whereas in the middle row these plots are shown only for region (3), and in the bottom row for region (4). The combined plots in the top row contain three different classes of features. First, they include some rather diffuse, broad distributions, which in the individual graphs are present only in the data for region (4) on the bottom. Second, there is an

intense localized structure, which appears as two offset semi-circles in the Newton diagram (a), as a diagonal band on the right in the Dalitz plot (b), and as a horizontal band at very small  $I^+$  KE in the energy correlation map in (c). Third, there is a weaker replica of this structure, which appears as a mirrored pair of offset semi-circles in (a), as a diagonal band on the left in (b), and a vertical band in (c). Although most of the events belonging to the latter two structures can be found in the middle row depicting region (3), for each of them the outer parts are cut out in the middle row, but can be traced as localized spots in the graphs for region (4) on the bottom.

This analysis confirms the assignment of region (3) to the mixture of  $CH_2Br+I$  and  $CH_2I+Br$  dissociation pathways. When the probe pulse arrives 20 ps after the pump and results in triple ionization, the detached halogen fragment is already far away from the rest of the molecule and hardly feels the effect of Coulomb repulsion. Correspondingly, its KE remains small and essentially uncorrelated with the other fragment. This can be seen in a strong horizontal band with low iodine KE in Fig. 5.25 (c, f) for  $CH_2Br + I$ , and a weaker vertical band for  $CH_2I + Br$  channels. In the Dalitz plots of Fig. 5.25 (b, e) these two channels appear as diagonal bands, and in the Newton diagrams in Fig. 5.25 (a, d) they can be seen by two pairs of offset semicircles. This semi-circular shape reflects the intermediate rotation of  $CH_2Br$  or  $CH_2I$  fragments, conceptually similar to the signatures of sequential channels in Fig. 5.7 (a, c) and Fig. 5.10(d). Some remnants of the structures due to these two channels can be found in the data for region (4) in Fig. 5.25 (g-i) because, as shown by the CES in Fig. 5.24 (c), their signatures extend to large angles up to nearly  $180^\circ$ .

To confirm the assignments of the observed features to the  $CH_2Br + I$  and  $CH_2I + Br$  dissociation channels and to better understand spectra formation mechanisms, we extended the CES presented in Fig. 5.24 (c) to the halogen energy correlation map. The results of this CES are shown in Fig. 5.26 (a). Here, the pump-probe delay is fixed at a value of 20 ps. For fixed translational energy and rotational velocity, such CES would just produce a single data point. In order to account for the observed spread of the experimental results, we performed this simulation for each channel for several translational energies (obtained from the width of asymptotic KE distributions at 20 ps) and several different rotational velocities, also extracted from the experimental data (see Chapter 6 for more details). Briefly, the simulations are performed for a kinetic energy range of 0.1-0.8 and 0.5-0.9 eV and for a rotational velocity range of 1.2-1.4 and 1.0-1.2  $^\circ/fs$  for  $CH_2Br + I$  and  $CH_2I + Br$  channels, respectively. The CES reproduces the

experimental data shown in Fig. 5.25 (c, f) very well, confirming the assignment of the horizontal band to the stronger  $\text{CH}_2\text{Br} + \text{I}$  channel, and the vertical one to the weaker  $\text{CH}_2\text{I} + \text{Br}$  pathway. Fig. 5.26 (b) shows the results of the same CES for the KER- $\theta_{23}$  map at 20 ps delay, confirming that the selected range asymptotic energies and rotation velocities can reasonably account for large angular spread of the data at a fixed delay value (compare to Fig. 5.23 (d)).

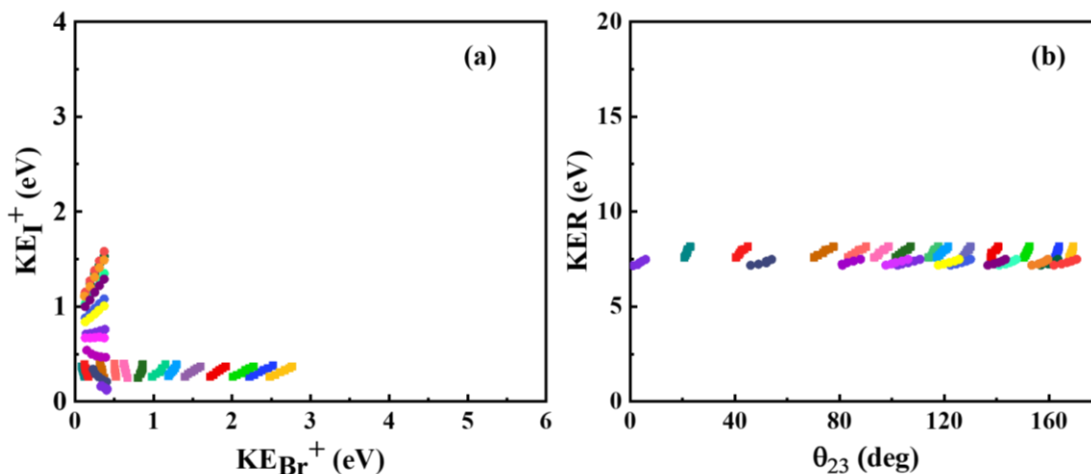


**Figure 5.26.** Simulated energy correlation map (a) and KER- $\theta_{23}$  plot (b) for  $\text{CH}_2\text{Br} + \text{I}$  (squares) and  $\text{CH}_2\text{I} + \text{Br}$  (circles) dissociating pathways probed at 20 ps delay via coincident  $\text{CH}_2^+ + \text{Br}^+ + \text{I}^+$  final state. The CES was performed using different asymptotic energies and rotation velocities. Different color corresponds to different rotation velocity and each point reflects a different asymptotic energy both within our angular velocity and asymptotic energy selection.

The CES shown in Fig. 5.24 (b, d) suggest that at least part of the events in region (4) of Fig. 5.23 (d) are due to molecular halogen elimination channel,  $\text{CH}_2 + \text{BrI}$ . This assignment is consistent with the broad diffuse features in all three-body representations shown for this region in the bottom row of Fig. 5.25. At large delays, this channel is characterized by a rather small absolute and fractional KE of the  $\text{CH}_2^+$  fragment, and by large KEs and nearly back-to-back emission of the two halogen ions. While this is, to a large extent, fulfilled for the diffuse features in Fig. 5.25 (g-i), their broad, rather delocalized appearance suggests that this reaction does not necessarily have a well-defined timing, for example, proceeding via a pre-dissociative state with non-negligible life-time. As already briefly discussed above, this is consistent with the diffuse signature of this channel in the two-body data shown in Fig. 5.18 (b).

Although it is not straightforward to disentangle signatures of such a weak channel at smaller delays, where many dissociation pathways result in overlapping signatures, in Ref. [274] it was suggested that for  $\text{CH}_2\text{I}_2$  a similar molecular halogen elimination pathway can be to a large extent separated by filtering on the sum KE of both halogen ions. According to our CES, for this channel the sum KE of  $\text{Br}^+$  and  $\text{I}^+$  is expected to be above  $\sim 4$  eV at all delays. Correspondingly, in Fig. 5.27 we plot the same delay-integrated KER- $\theta_{23}$  map as in Fig. 5.20, but with the conditions that the sum  $\text{Br}^+$  and  $\text{I}^+$  KE is above (a) and below (b) 3.8 eV value. While the data for large sum KE of both halogens include all delay-independent events at large KER, a broad descending band converging towards  $180^\circ$  angle is also clearly visible. Although this band certainly include contributions from some other channels, we argue that it predominantly consists of the events due to molecular  $\text{BrI}$  elimination, illustrating how this pathway evolves towards region (4) marked in Fig. 5.23 for large delays.

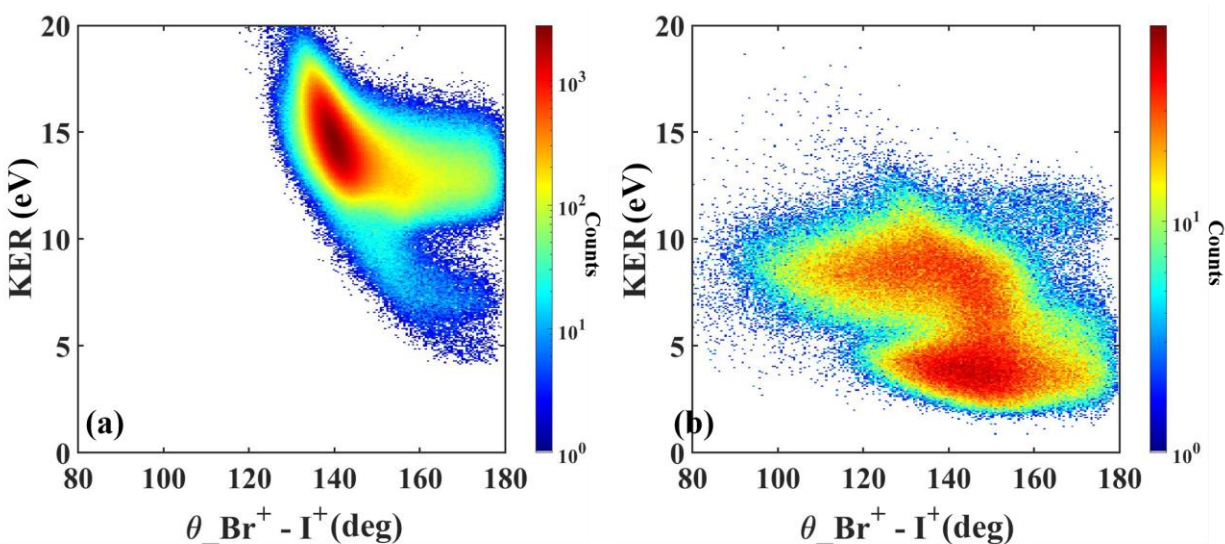


**Figure 5.27.** Delay-integrated KER- $\theta_{23}$  plots for the  $\text{CH}_2^+ + \text{Br}^+ + \text{I}^+$  coincident channel with different conditions on the sum KE of the two halogen ions. (a) The sum KE is in the range of 3.8 - 6.0 eV. (b) The sum KE is set below 3.8 eV.

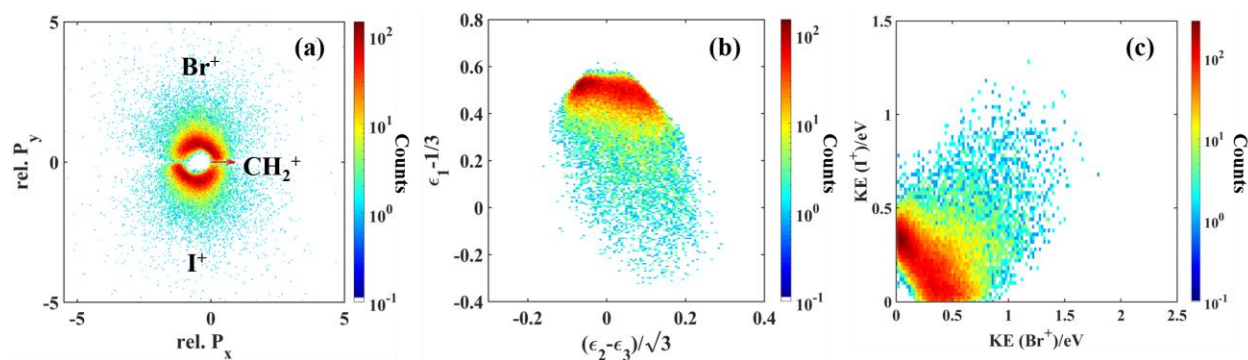


**Figure 5.28.** Different representations of the  $\text{CH}_2^+ + \text{Br}^+ + \text{I}^+$  coincident events in the region (5) of the KER-  $\theta_{23}$  plot at 20 ps: (a) Newton diagram, (b) Dalitz Plot, and (c) KE sharing of Br and I fragments.

Finally, Fig. 5.28 shows the Newton diagram (a), Dalitz plot (b) and halogen energy correlation map (c) for the events in region (5) of Fig. 5.23 (d), which we assign to the three-body dissociation of the molecule by the pump pulse. As expected, the energy correlation map displays very low  $\text{I}^+$  and  $\text{Br}^+$  energies, and the Dalitz plot indicates that the largest fraction of the total KER is carried by the  $\text{CH}_2^+$  ions, reflecting the mass ratio of the fragments. Two nearly identical semi-circles in the Newton diagram in Fig. 5.28 (a) suggest a loss of angular correlation between the halogen ions and  $\text{CH}_2^+$ , which might be a hint towards sequential nature of the three-body dissociation. However, more detailed analysis is needed to confirm this. Diffuse background in all three patterns similar to that observed for region (4) events in Fig. 5.25 (g-i) can be considered as an indication that some additional dynamics not fully accounted for by the presented analysis might contribute to these three-body CE patterns.

### 5.4.3 Analysis of $\text{CH}_2^+ + \text{Br}^{2+} + \text{I}^{2+}$ three-body coincident channel: search for transient isomerization signal

Various three-body fragmentation patterns discussed in two previous sections can be efficiently exploited for disentangling different photodissociation channels, where the molecule extends to larger internuclear separations resulting in rapidly decreasing KER of the corresponding CE channel. However, if the dynamics of interest are restricted to small internuclear distances, the corresponding CE events remain at high KER and, for triply charged final state, can be masked by the delay-independent signatures of sequential breakup channels, in particular, at large angles

between the two halogen momenta (see region (2) in Figs. 5.6, 5.20 and 5.23). As mentioned in section 5.1 and shown by the CES in section 2.4, a particular process that is expected to produce events in this region is the formation of  $\text{CH}_2\text{Br-I}$  isomer. While photoisomerization of  $\text{CH}_2\text{BrI}$  upon photoexcitation in the *A*-band was observed in solution [190], [283], to the best of our knowledge, it was not yet reported for gas-phase experiments. However, for a similar dihalomethane,  $\text{CH}_2\text{I}_2$ , transient photoisomerization in the gas phase has been predicted and observed in absorption experiments [192]. Very recently [274], signatures of short-lived states with isomer geometry have been observed in CEI measurements on  $\text{CH}_2\text{I}_2$ , technically very similar to the experiments performed in this work. Therefore, here we explore potential signatures of such transient isomerization processes in  $\text{CH}_2\text{BrI}$ .

Based on the experience and knowledge gained from previous experiments on the  $\text{CH}_2\text{I}_2$  [274], higher charged states, for which sequential pathways play lesser or negligible role, provide the opportunity to track the transient channels developing at high KER and large emission angles. In particular, as shown in Figs. 5.11 and 5.12, sequential channels do not provide a distinguishable contribution to the three-body breakup of five-fold final charge state into  $\text{CH}_2^+ + \text{Br}^{2+} + \text{I}^{2+}$  channel. Therefore, we use this channel to explore potential contributions from isomerization pathways in large KER / large angle region of our KER- $\theta_{23}$  maps. It will also serve as a complementary tool for probing photodissociation pathways discussed in the previous section.

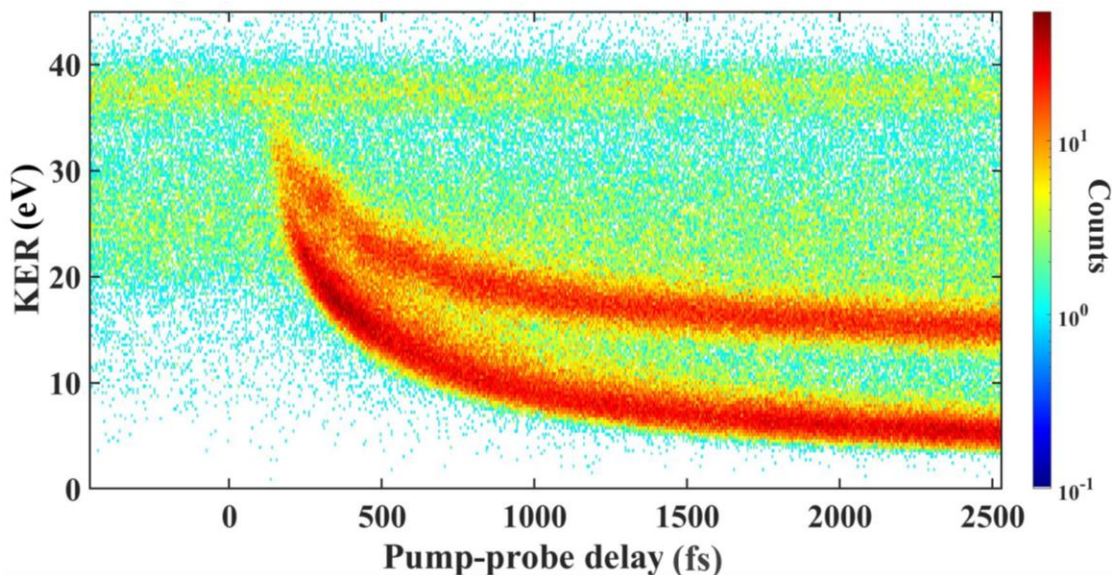


**Figure 5.29.** Delay-dependent KER distribution for  $\text{CH}_2\text{BrI}$  fragmentation into  $\text{CH}_2^+ + \text{Br}^{2+} + \text{I}^{2+}$  ions after UV pump and NIR probe pulse.

Fig. 5.29 shows the delay-dependent KER distribution for this coincident channel, which displays a relatively weak KER horizontal band at high KER due to the CE of bound molecules energy, and two sharp descending bands. Similar to the case of triply-charged final state (see Fig. 5.19), the upper descending band is due to major two-body dissociation channels,  $\text{CH}_2\text{Br} + \text{I}$  and  $\text{CH}_2\text{I} + \text{Br}$ , whereas the lower one is dominated by the three-body dissociation channel,  $\text{CH}_2 + \text{Br} + \text{I}$ .

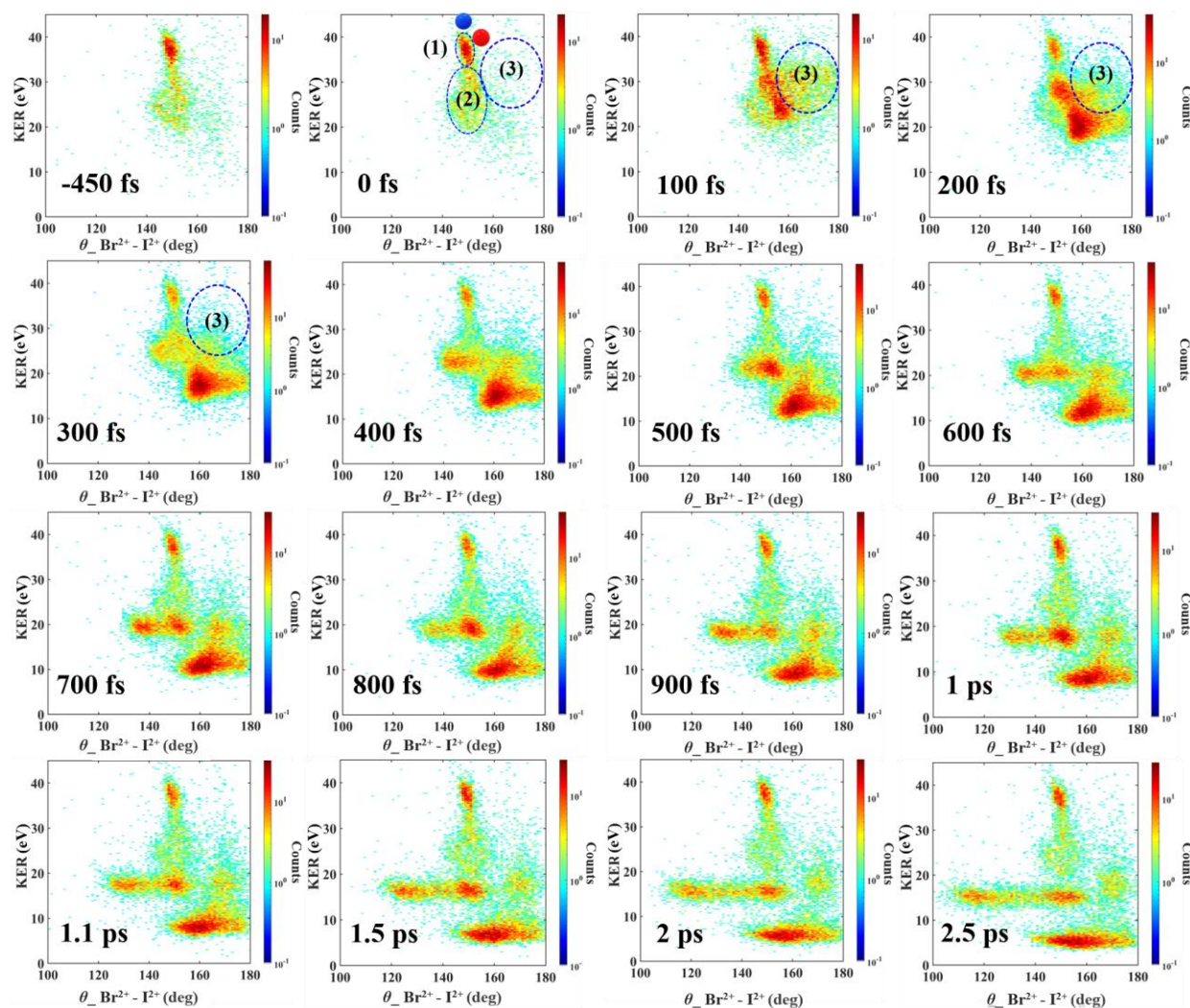


**Figure 5.30.** KER- $\theta_{23}$  snapshots for the  $\text{CH}_2^+ + \text{Br}^{2+} + \text{I}^{2+}$  three-body coincident channel at different delays from 0 to 2.5 ps. Each snapshot corresponds to the 100 fs delay window centered at the values shown in the figure. Solid dots in 0 fs panel show the results of CES for the CE of  $\text{CH}_2\text{BrI}$  at its main (blue) and isomer (red) geometry. Dashed ovals (1), (2), (3) mark the regions discussed in text.

However, as compared to the results for triply-charge final state, here we see a drastic change in the branching ratio of the horizontal and descending bands, with the latter becoming the dominant feature in Fig. 5.29. There are two possible reasons for this. First, five-fold ionization is likely to occur only in the central region of the NIR focus, where the peak intensity is the highest. If the UV and the NIR pulses perfectly overlap in space, this will result in the effective selection of the central region of the UV focus as well, corresponding to higher peak intensity of the pump. Lower charge states can stem from the outer regions of the NIR focus and, thus, sample lower pump intensities. As a consequence, we can expect less unpumped molecules and a larger contribution of non-linear effects for the events probed via higher charge states. Second, it is not unlikely that the charge state distribution with two doubly charged halogen ions favors larger internuclear separations, where the equilibration of the charge imbalance is unlikely. If the same charge state distribution is achieved in a bound molecule, it will likely deliver at least one more charge to the methylene group, which in this case will undergo further decomposition and, thus, will not contribute to the selected triple-coincidence events.

Fig. 5.30 shows the time evolution of the KER- $\theta_{23}$  maps for this coincident channel from zero to 2.5 ps, followed by a snapshot at 20 ps in Fig 5.31. The first two frames in Fig. 5.30 resemble the map obtained in the experiment with the NIR-only pulse shown in Fig. 5.11, dominated by a concerted breakup of a bound molecule, marked by ovals (1) and (2). At 100 fs, the onset of dissociation channels, which propagate towards lower KER, becomes clearly visible below 30 eV, on top of the delay-independent structure in region (2). Besides that, in the third frame, new events also appear in the right part of the map, at  $\sim 30$  eV KER and large emission angles, the region marked (3) here. Remarkably, the fragmentation patterns at larger delays show that this feature is short-lived; i.e., it rises and decays quickly such that it is distinguishable in the frames of 100 and 200 fs, with no clear evidence of the reminiscent events in the following frames. As discussed in section 2.4, qualitatively, CE of the CH<sub>2</sub>-Br-I isomer is expected to result in somewhat smaller KER and larger (Br, I) angles compared to the CE of the ground-state CH<sub>2</sub>BrI (see Fig. 2.17). Similar trend is predicted by the CES for the CH<sub>2</sub><sup>+</sup> + Br<sup>2+</sup> + I<sup>2+</sup> channel shown in Fig. 5.30. However, since simulations for both geometries still significantly overestimate the experimental results, the origin of the observed transient structure remains unclear. Before discussing it in more detail, we first consider formation mechanisms for the other parts of the KER- $\theta_{23}$  maps shown in Figs. 5.30 and 5.31.

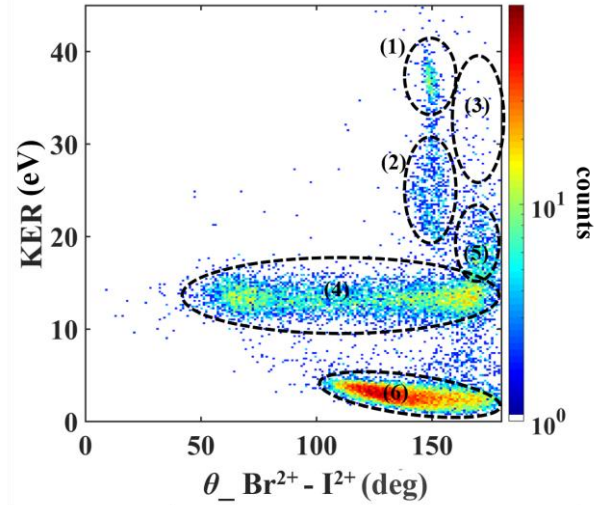


**Figure 5.31.** KER- $\theta_{23}$  plot for the three-body  $\text{CH}_2^+ + \text{Br}^{2+} + \text{I}^{2+}$  coincident channel at 20 ps. Dashed ovals (1-6) mark different regions corresponding to different fragmentation scenarios discussed in the text.

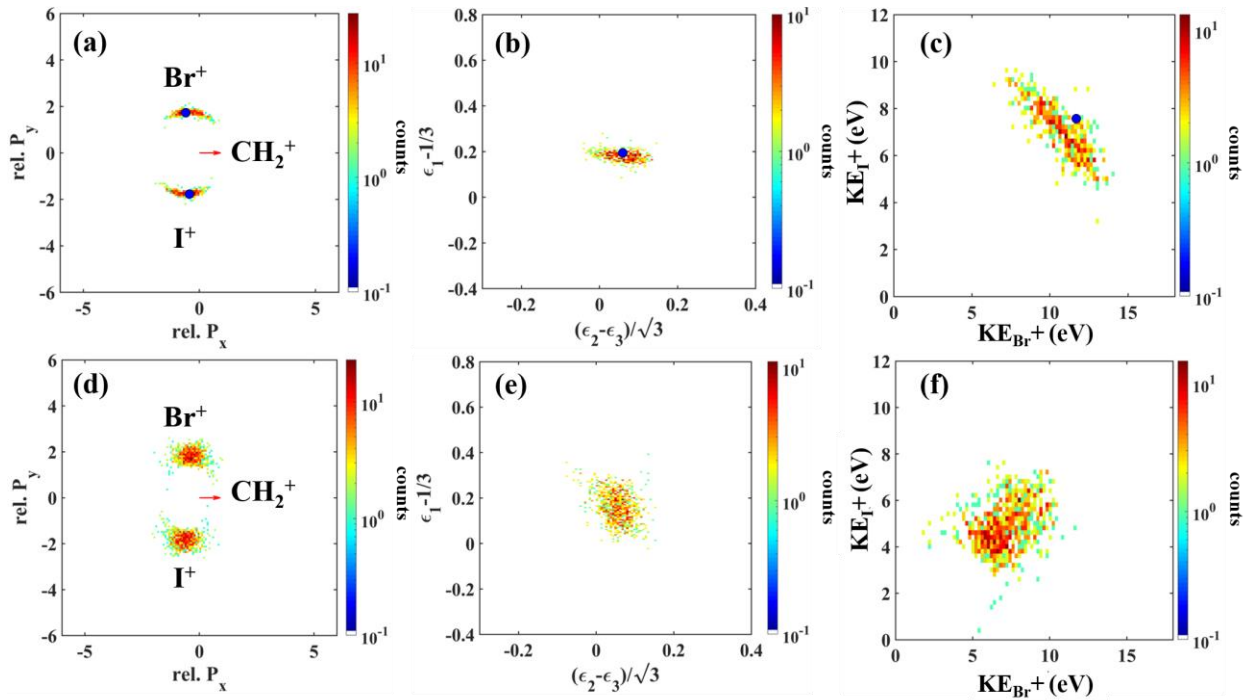


**Figure 5.32.** Different representations of the  $\text{CH}_2^+ + \text{Br}^{2+} + \text{I}^{2+}$  coincident events in regions (1) and (2) of the KER- $\theta_{23}$  plot at 20 ps. Upper row: region (1); bottom row: region (2). **(a,d)** Newton diagrams; **(b,e)** Dalitz plots; and **(c,f)** (Br, I) energy-correlation map. Blue dots represent the results of corresponding CEs for  $\text{CH}_2\text{BrI}$  equilibrium geometry.

At larger delays, the events move downward in KER and spread in angle, similar to the behaviour observed in Fig. 5.22. However, signatures of various dissociation pathways discussed in section 5.4.2 appear to be sharper and more localized when probed via the  $\text{CH}_2^+ + \text{Br}^{2+} + \text{I}^{2+}$  final state in Fig. 5.30. At large delays, these features become more isolated, finally evolving to their asymptotic shapes shown in Fig. 5.31 for 20 ps delay. Besides regions (1-3), which are the same as in Fig. 5.30, regions marked (4-6) reflect the signatures of  $\text{CH}_2\text{Br} + \text{I}$  and  $\text{CH}_2\text{I} + \text{Br}$  (4),  $\text{CH}_2 + \text{BrI}$  (5) and  $\text{CH}_2 + \text{Br} + \text{I}$  (6) dissociation channels. Note that the numbering of the respective features does not match the one used for the  $\text{CH}_2^+ + \text{Br}^+ + \text{I}^+$  analysis in the previous section, because of the addition of the region (3) in Fig. 5.30 and 5.31.

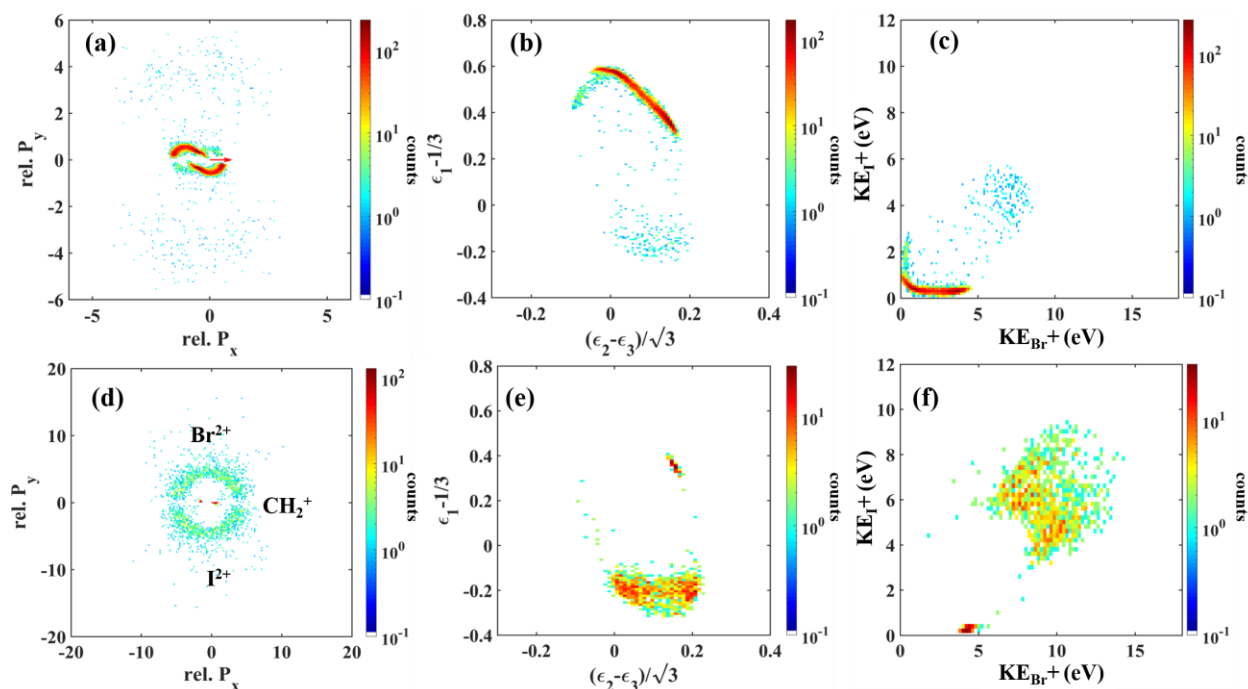


**Figure 5.33.** Different representations of the  $\text{CH}_2^+ + \text{Br}^{2+} + \text{I}^{2+}$  coincident events in regions (4) and (5) of the KER- $\theta_{23}$  plot at 20 ps (Fig. 5.31). Upper row: region (4); bottom row: region (5). (a,d) Newton diagrams; (b,e) Dalitz plots; and (c,f) (Br, I) energy-correlation map.

To confirm the assignments of various channels, we analyze Newton diagrams, Dalitz plots and halogen KE correlation maps for the individual regions marked in Fig. 5.31, following the procedure developed in section 5.4.2. We start with these three representations for regions (1) and (2) shown in Fig. 5.32. Although the graphs in Fig. 5.32 are shown for 20 ps delay, the appearance of all three plots for regions (1) and (2) is essentially the same as at zero UV-NIR delay, and is

nearly identical to the corresponding NIR-only diagrams, which are shown in Fig. 5.12 for these two regions together. This highlights once again that these two features are essentially delay-independent. However, in contrast to delay-independent contribution in region (2) for the  $\text{CH}_2^+ + \text{Br}^+ + \text{I}^+$  channel (see Figs. 5.6, 5.20 and 5.23, which originate from sequential fragmentation pathways, the graphs in the bottom row of Fig. 5.32 clearly indicate that lower-KER region (2) for  $\text{CH}_2^+ + \text{Br}^{2+} + \text{I}^{2+}$  channel is due to concerted breakup. As discussed at the end of section 5.1, a likely scenario responsible for the events in this region is the stretching of one or more molecular bonds during multiple ionization process.

Fig. 5.33 displays the same three-particle fragmentation maps for regions (4) (top row) and (5) (bottom row). The graphs for region (4) clearly indicate that the corresponding events mainly reflect  $\text{CH}_2\text{Br} + \text{I}$  (more intense bands) and  $\text{CH}_2\text{I} + \text{Br}$  (weaker bands) dissociation channels, and rotational motion of the created molecular co-fragments, similar to the results of Fig. 5.25 (d-f) for triply charged final states. The events in region (5), which manifest low  $\text{CH}_2^+$  KE, high I and Br KEs, and their nearly back-to-back emission, reflect the  $\text{CH}_2 + \text{BrI}$  pathway. Comparing the upper and the lower row in Fig. 5.33, it is clearly that the region selection in Fig. 5.31 does not ensure perfect channel separation, and some events due to  $\text{BeI}$  elimination channel appear in the upper row, and some events from the other two channels, corresponding to large ( $\text{Br}^{2+}$ ,  $\text{I}^{2+}$ ) angles, leak into the lower graphs, where they can be traced as sharp localized spots.

While the events resulting from  $\text{CH}_2\text{Br} + \text{I}$  and  $\text{CH}_2\text{I} + \text{Br}$  dissociation pathways have rather similar signatures in the three-body breakup patterns for triply- and five-fold-charged states (compare Fig. 5.33 (a-c) and Fig. 5.25 (d-f)), the situation is different for  $\text{CH}_2 + \text{BrI}$  channel (region 5). Its signatures in all three patterns shown in Fig. 5.33 (d-f) are much more localized than the corresponding features for triply-charged final state (see Fig. 5.25 (g-i)). A possible reason for this difference is the focal region selectivity of higher charge states mentioned above. Since the five-fold final states favor contributions from the central region of the probe pulse focus, they likely experience the highest pump intensity as well. Thus, potential contributions from two- or multi-photon processes driven by the pump would be enhanced in higher charge states. Since molecular halogen elimination is known to be a minor one-photon channel for the  $\text{CH}_2\text{BrI}$  A-band excitation [187], it is plausible to assume that two- or three-photon processes could be responsible for different shape of this channel for five-fold final charge state in Fig. 5.33 (d-f). We should note that three-photon DI by the pump could contribute here, since we observe some  $\text{BrI}^+$  ions in UV-

only experiments (see section 5.2). We should also note that in a similar experiment on  $\text{CH}_2\text{I}_2$  [274] a mixture of single-photon and higher-order processes has been indeed reported for 266 nm excitation.

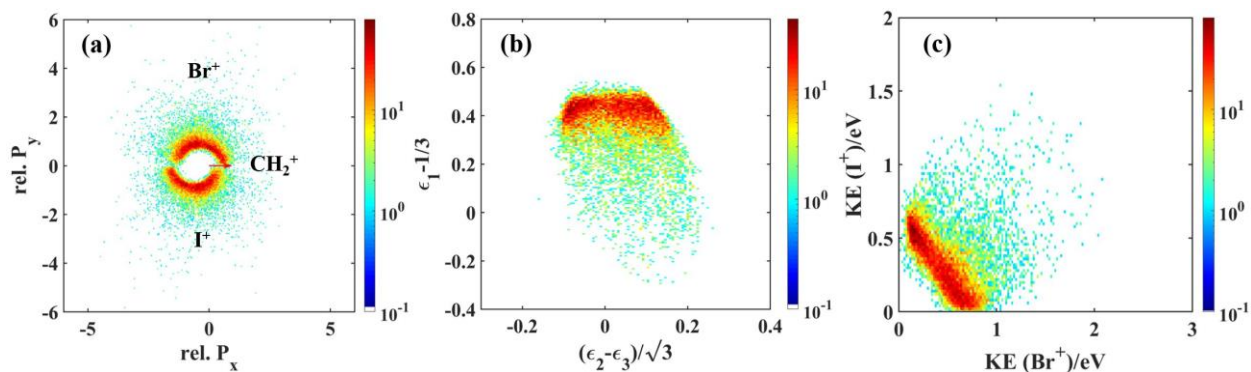


**Figure 5.34.** Newton diagram (a), Dalitz plot (b) and (Br, I) energy correlation map (c) for the events in region (6) of the KER- $\theta_{23}$  plot at 20 ps (Fig. 5.31).

Based on the same arguments as presented in section 5.4.2 for the triply charged final state, the region with the lowest KER, marked (6) in Fig. 5.31, can be unambiguously assigned to three-body dissociation of the molecule. Since the energy threshold for this channel is 5.66 eV [187], [188], single-photon absorption at 263 nm cannot trigger this reaction. Thus, it is most likely driven by two-photon absorption, consistent with stronger relative contribution of this channel observed here for five-fold final charge state. We should also note that DI of the molecule requires at least four-photon absorption to trigger three-body dissociation via cationic states and, thus, is unlikely to play a role here. The Newton diagram, Dalitz plot and halogen energy correlation map for this channel are shown in Fig. 5.34. These patterns, which are similar but somewhat sharper than the corresponding maps for the same channel probed via triply-charge final state (see Fig. 5.28), suggest that while there is clear energy correlation between the two halogen ions (evidenced by the diagonal shape of their energy correlation band in Fig. 5.34 (c)), there is much less correlation between two halogens and the  $\text{CH}_2$  fragment. This can be seen from the circular shape of the Newton diagram in Fig. 5.34 (a) and by the nearly-horizontal appearance of the dominant feature in the Dalitz plot in Fig. 5.34 (b). This behavior suggests that the three-body dissociation here proceeds via a sequential-type process, where an intermediate halogen molecule,  $\text{BrI}$ , is initially formed, which then decays at some later times well before the probe pulse arrives.

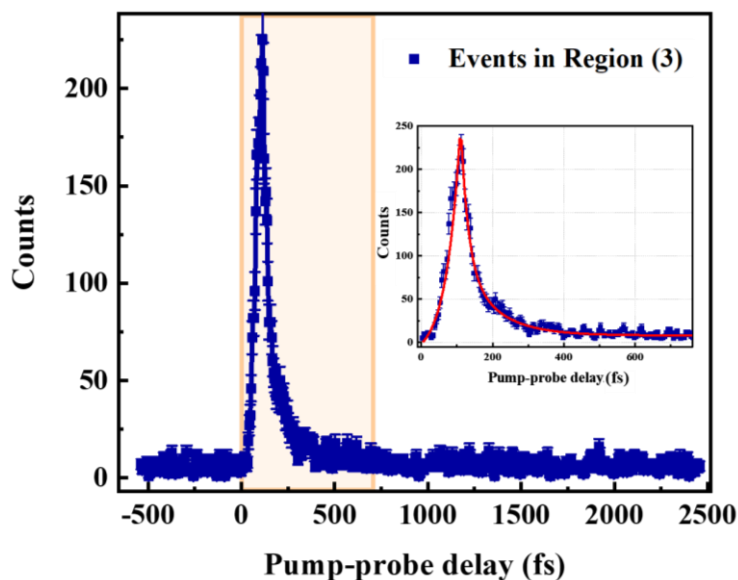


**Figure 5.35.** Delay-dependent yield of  $\text{CH}_2^+ + \text{Br}^{2+} + \text{I}^{2+}$  coincident events in region (3) of the KER- $\theta_{23}$  maps shown in Fig. 5.30. The inset shows the same curve with the enlarged view of the delay window up to 750 fs.

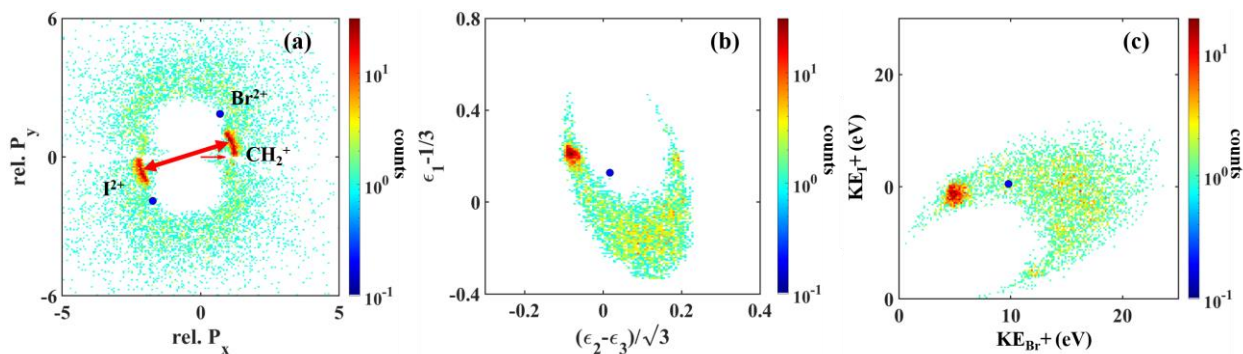


**Figure 5.36.** (a) Newton diagram, (b) Dalitz Plot, and (c) halogen energy correlation map for  $\text{CH}_2^+ + \text{Br}^{2+} + \text{I}^{2+}$  coincident events in region (3) of the KER- $\theta_{23}$  plot at 100 fs. Blue dots represent the results of the CES assuming equilibrium geometry of  $\text{CH}_2\text{Br-I}$  isomer (see section 2.4 for details).

Finally, we turn our attention back to the transient signal observed in region (3) of the KER- $\theta_{23}$  maps shown in Fig. 5.30. To quantify its transient behavior, in Fig. 5.35 we plot the yield of this channel as a function of pump-probe delay. The curve exhibits a sharp rise, peaks slightly after 100 fs, and quickly decays again, with no discernible signal beyond 300 fs. To understand in

more detail the origin of this transient feature, in Fig. 5.36 we plot the Newton diagram, Dalitz plot and halogen energy correlation map for the events in region (3) at a fixed delay of 100 fs, shortly before the maximum of this signal.

Each of the graphs in Fig. 5.36 consists of two distinct parts. First, there is an intense localized spot in the left part of the Dalitz plot (b) and energy correlation map (c), which in the Newton diagram (a) corresponds to two short lines marked by the arrow. Second, a broad, diffuse structure corresponding to large KE and momenta of Br and I fragments, and rather small momentum of  $\text{CH}_2^+$ . Neither of these feature matches the predictions of the CES for the  $\text{CH}_2\text{Br-I}$  isomer geometry, which are shown by the blue dots. Interestingly, for the localized spot in Fig. 36 (c), the KE of the iodine fragment is almost twice as high as for bromine, which is very different from what could be expected because of the mass ratio. A situation like this can be realized for a “linearized” molecular configuration, where the bromine atom is located in-between the iodine and the methylene group. In a long debate on how the halogen-halogen bond can be formed in photoexcited halomethanes [189]–[191], [283], it was, among other, suggested that this can occur via the creation of a short-lived intermediate state with nearly linear geometry, which is rather different than the geometry of a  $\text{CH}_2\text{Br-I}$  isomer sketched in Fig. 2.17. This is then followed either by the ejection of one halogen or by  $\text{BrI}$  formation. However, it should be noted that rather similar molecular configuration can be also realized early in  $\text{CH}_2\text{Br} + \text{I}$  dissociation channel, when the  $\text{CH}_2\text{Br}$  fragment rotates into alignment with the dissociation axis (see Fig. 2.13 and a discussion in Chapter 6 below).

Broad, diffuse structures in all panels of Fig. 5.36 are somewhat similar to the signatures of  $\text{BrI}$  elimination channel that can be seen in Figs. 5.25 and 5.33. In accordance with this, in the delay-dependent  $\text{KER}-\theta_{23}$  shown in Figs. 5.30 and 5.31, one can follow a trend that part of the events in region (3) move towards small KER and  $180^\circ$  angle for larger delays, converging to region (5) marked in 20 ps map on Fig. 5.31. If this channel is indeed responsible for part of the events populating region (3), one would expect that the KE of the corresponding  $\text{CH}_2^+$  ion should rapidly decrease as a function of the delay, as it separates itself from both halogens. This trend can indeed be observed in Fig. 5.37, where the KE of the  $\text{CH}_2^+$  ions from the  $\text{CH}_2^+ + \text{Br}^{2+} + \text{I}^{2+}$  coincident channel is plotted as a function of the delay for the events falling into region (3) of the  $\text{KER}-\theta_{23}$  map. Interestingly, such rapid decrease in  $\text{CH}_2^+$  energy seems to occur for nearly all events plotted in this figure, besides some diffuse background. However, this behavior is not

unique for BrI elimination channel. As will be shown in Chapter 6, rotation of molecular co-fragment in the major  $\text{CH}_2\text{Br} + \text{I}$  dissociation channel can also cause such local decrease of the  $\text{CH}_2^+$  ion KE.

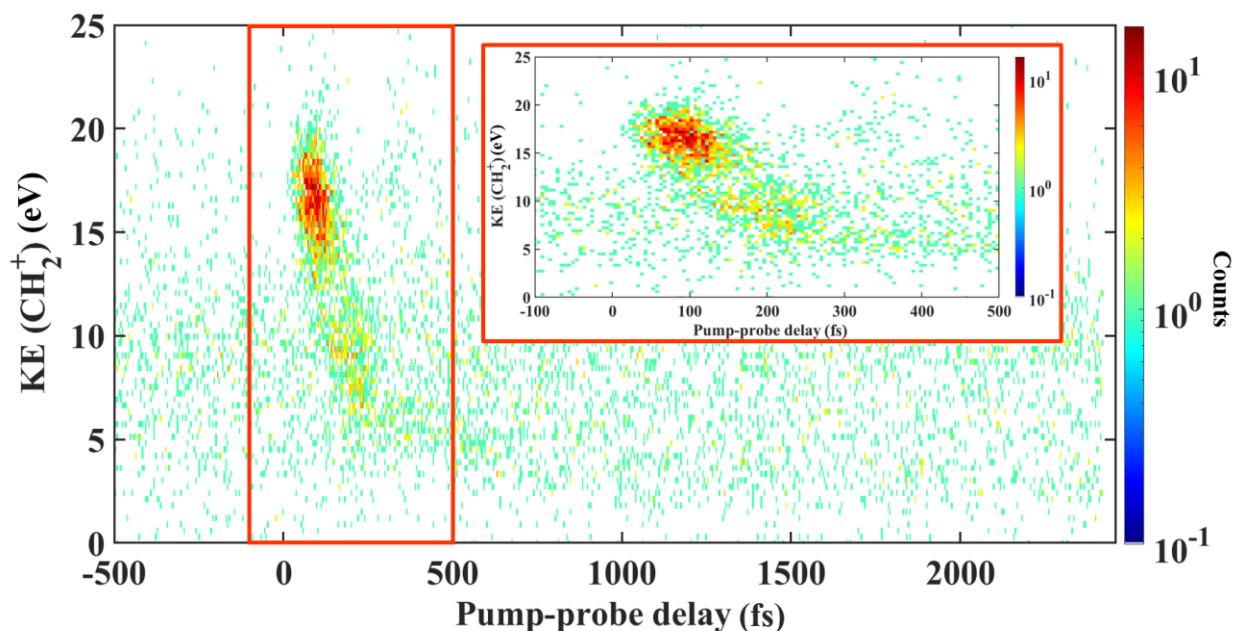


**Figure 5.37.** Delay-dependent KE of the  $\text{CH}_2^+$  ions from the  $\text{CH}_2^+ + \text{Br}^{2+} + \text{I}^{2+}$  channel in the region (3) of the KER- $\theta_{23}$  plot. The inset shows the zoomed-in view of the events within the red box.

Overall, our analysis of potential signatures of transient isomerization remains inconclusive. On one hand, we did not observe any features that can be directly associated with the  $\text{CH}_2\text{Br}-\text{I}$  isomer geometry considered in Figs. 2.17 and 2.20. On the other hand, we observe a rapidly evolving transient feature, which seem to have two components – one associated with BrI elimination reaction, and one reflecting a linearized molecular configuration. It remains open whether the latter feature can be simply a signature of a dissociating molecular co-fragment rotating itself into alignment with the dissociation axis. To achieve a more specific understanding of the dynamics behind these features, theoretical work including a detailed picture of molecular PESs, molecular dynamics simulations and explicit calculation of the experimental observables will be needed.

## 5.5 Time-resolved analysis of UV-driven photodissociation dynamics in CH<sub>2</sub>ClI probed via three-body coincident channels

The primary goal of this chapter was to investigate the photodissociation of dihalomethanes triggered by UV irradiation, focusing on the aspects that go beyond the dynamics accessible in monohalide molecules like CH<sub>3</sub>I. Correspondingly, for CH<sub>2</sub>BrI we identified the signatures of competing iodine and bromine detachment pathways, molecular halogen formation and three-body dissociation, and discussed potential contributions from transient isomerization. To examine if we can generalize our understanding of these dynamics to other dihalomethanes, in a comparative study, we repeated some of these time-resolved experiments with the CH<sub>2</sub>ClI molecule. We employed identical experimental conditions, in particular, the UV pump and NIR probe intensities of  $1 \times 10^{13}$  and  $8 \times 10^{14}$  W/cm<sup>2</sup>, respectively. The major difference between the two dihalomethanes is the mass of the second halogen, which causes different KE distributions of the fragments as well as different energy partitioning between internal and translational energies. In particular, for dissociation channels with iodine detachment the fraction of internal excitation was reported to change from 54-55% for CH<sub>2</sub>ClI [98], [147] to 64-67% for CH<sub>2</sub>BrI [187], [277]).

In a brief overview of the CH<sub>2</sub>ClI data presented below, we follow the same logic and procedures we used to identify and disentangle different UV-induced dissociation pathways in CH<sub>2</sub>BrI.

Irradiation of CH<sub>2</sub>ClI molecules with single NIR pulse results in multiple ionization, often followed by various two- and three-body fragmentation processes, similar to those discussed for CH<sub>2</sub>BrI in section 5.1. We focus on the coincident analysis of three-body CE patterns for three- and five-fold final charge states. Since chlorine has two abundant isotopes, we focused on coincident channels involving the lighter isotope, <sup>35</sup>Cl.

Fig. 5.38 shows the KER- $\theta_{23}$  maps obtained with a single NIR pulse, where  $\theta$  is the angle between the chlorine and iodine momentum vectors. The maps are plotted for (a) CH<sub>2</sub><sup>+</sup>+Cl<sup>+</sup>+I<sup>+</sup> and (b) CH<sub>2</sub><sup>+</sup>+Cl<sup>2+</sup>+I<sup>2+</sup> coincident channels. Both maps display essentially the same structures as the corresponding results for CH<sub>2</sub>BrI shown in Figs. 5.6 and 5.11, respectively. While the KER- $\theta_{23}$  map for the triply-charged state contains two main features reflecting concerted and sequential breakup of the molecule, the data for CH<sub>2</sub><sup>+</sup>+Cl<sup>2+</sup>+I<sup>2+</sup> coincident channel result from two different concerted breakup pathways, without any significant contributions from sequential channels.

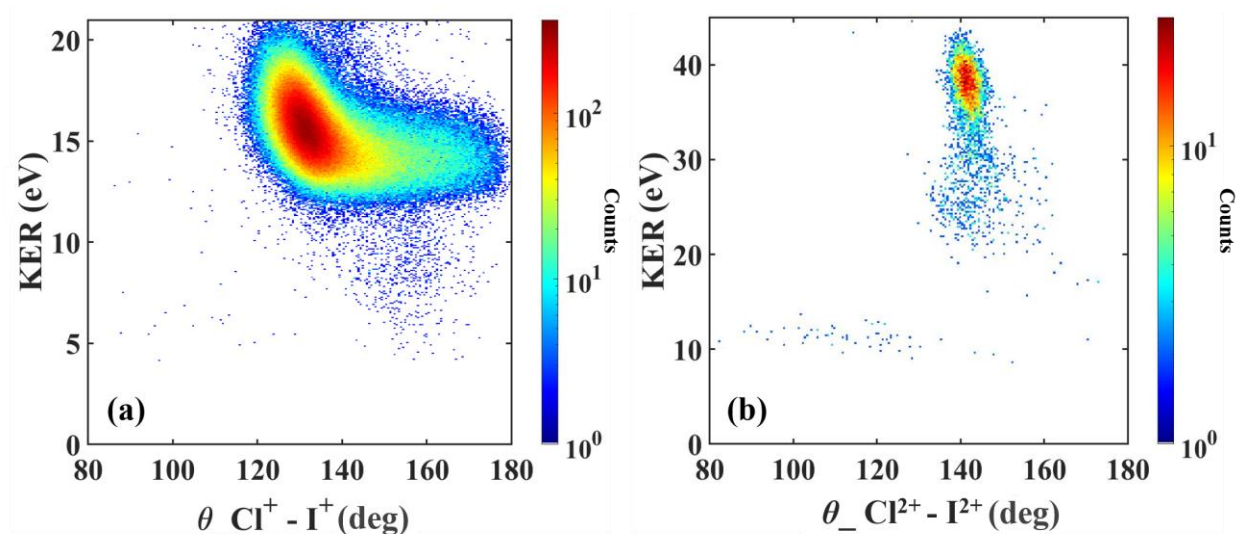


**Figure 5.38.** (a) KER- $\theta_{23}$  for the three-body fragmentation of  $\text{CH}_2\text{ClI}$  into  $\text{CH}_2^+ + \text{Cl}^+ + \text{I}^+$  and (b)  $\text{CH}_2^+ + \text{Cl}^{2+} + \text{I}^{2+}$  after a single NIR pulse with  $8 \times 10^{14} \text{ W/cm}^2$  intensity.

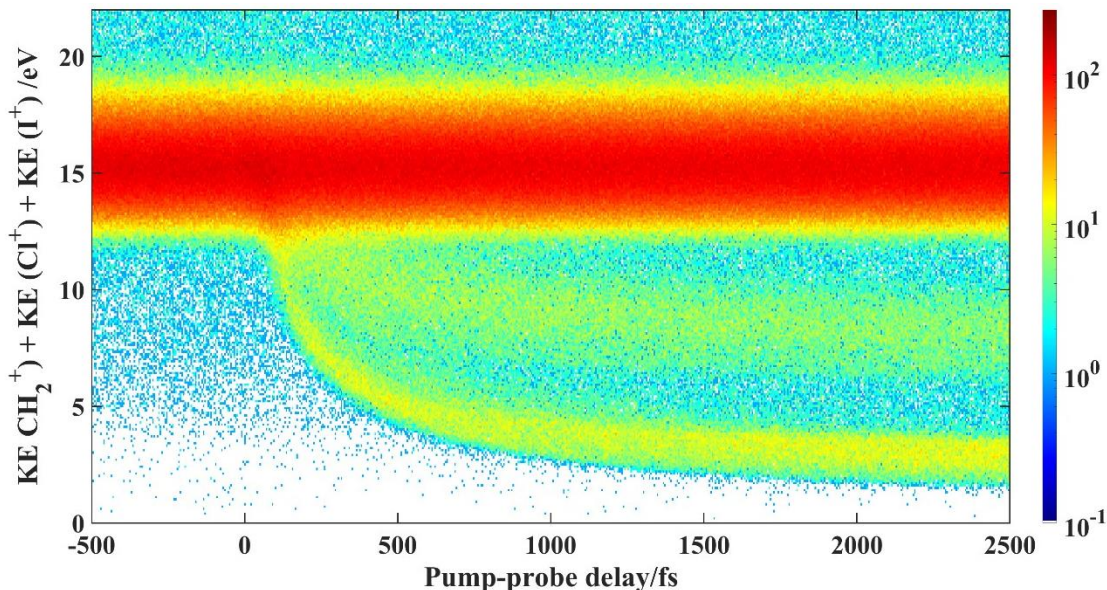


**Figure 5.39.** Delay-dependent KER distribution of  $\text{CH}_2\text{ClI}$  fragmentation into  $\text{CH}_2^+ + \text{Cl}^+ + \text{I}^+$  after UV pump and NIR probe pulses.

The results of two-body analysis of UV-pump - NIR-probe data on  $\text{CH}_2\text{ClI}$  is fully consistent with the results presented in section 5.3 for  $\text{CH}_2\text{BrI}$  and are not presented here. The dominant dissociation channel is again the C-I bond cleavage, with Cl detachment providing weaker but still significant contribution. In addition, similar to the  $\text{CH}_2\text{BrI}$  case, we observed a

weak signature of molecular halogen (CII) formation. In the following, we mainly discuss the three-body fragmentation channels, which have been shown to provide a more detailed insight into the dissociation dynamics in these polyatomic molecules.

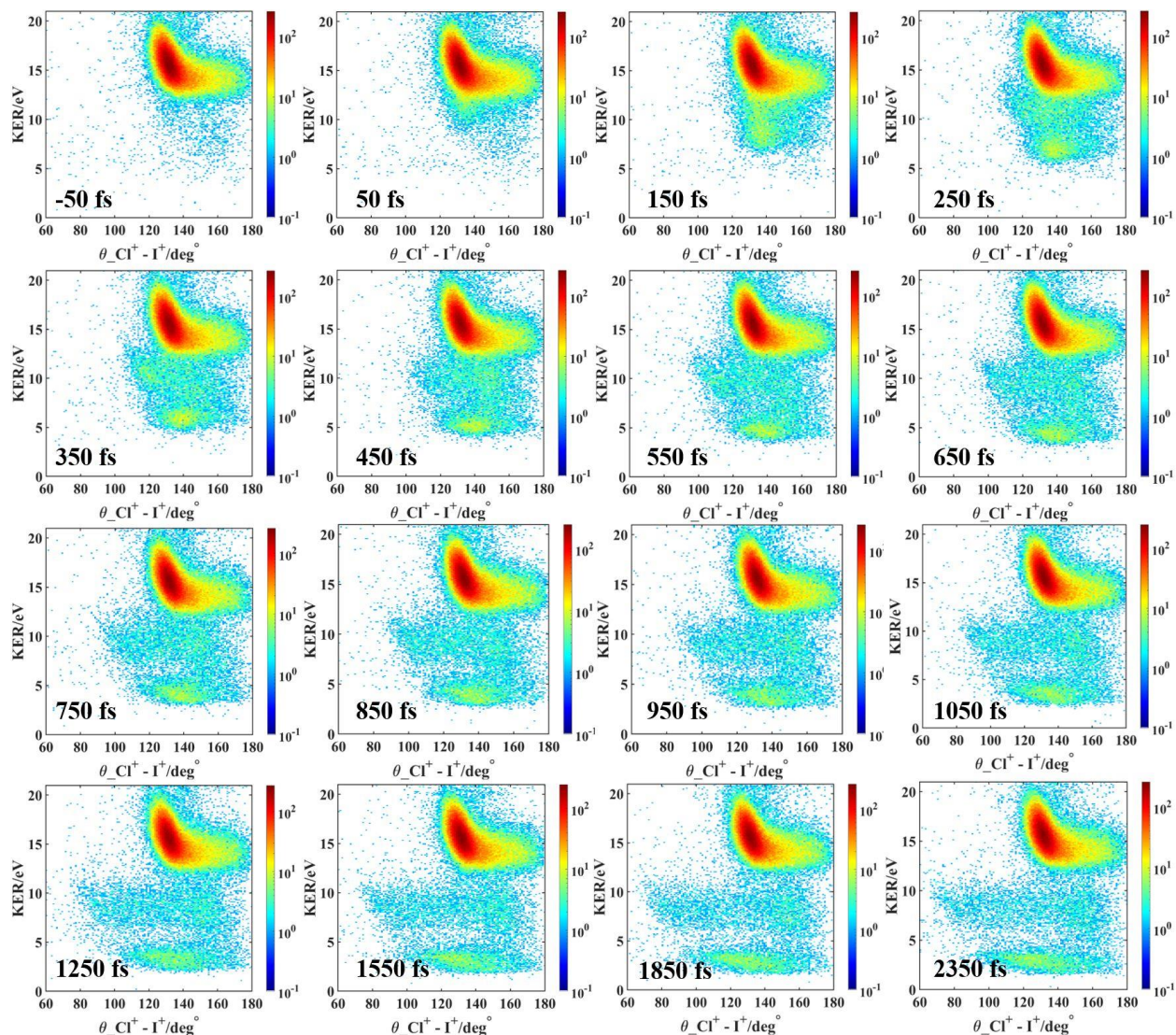


**Figure 5.40.** KER- $\theta_{23}$  maps for the three-body coincident  $\text{CH}_2^+ + \text{Cl}^+ + \text{I}^+$  channel at different delays from 0 to 2.5 ps. Each snapshot corresponds to the 50 fs delay window centered at the values shown in the figure.

Fig. 5.39 shows the measured delay-dependent KER distribution for  $\text{CH}_2^+ + \text{Cl}^+ + \text{I}^+$  three-body coincident channel. The spectrum closely resembles the analogous map for  $\text{CH}_2\text{BrI}$  molecule shown in Fig. 5.19, displaying a delay-independent high-KER band and two rather broad descending structures. The upper of these descending bands is dominated by the two-body

dissociation pathways involving the detachment of either halogen atom, whereas the lower one mainly reflects three-body dissociation.

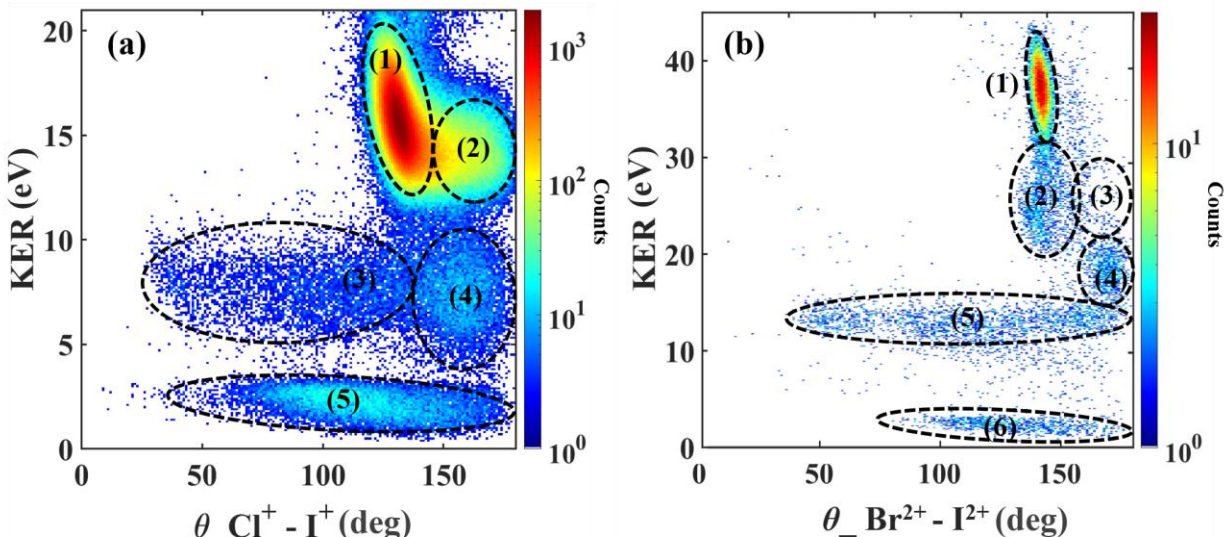


**Figure 5.41.** KER- $\theta_{23}$  snapshots for three-body coincident channels  $\text{CH}_2^+ + \text{Cl}^+ + \text{I}^+$  (a) and  $\text{CH}_2^+ + \text{Cl}^{2+} + \text{I}^{2+}$  (b) channels at 20 ps. Dashed ovals with numbers mark different regions of the spectrum discussed in text.

Fig. 5.40 shows a series of KER- $\theta_{23}$  maps for different delays, illustrating the time evolution of various dissociation channels. These frames are shown up to 2.5 ps, and are followed by the same map taken at 20 ps (Fig. 5.41). While the first frame in Fig. 5.40 closely resemble the results obtained with a single NIR pulse, already after 50 fs events due to dissociation can be traced at lower KER. At larger delays, contributions from dissociation events propagate towards lower KER, spread in angle and split into several bands.

The KER-  $\theta_{23}$  map at 20 ps (Fig. 5.41 (a)) manifest all characteristic features observed in the analogous map for  $\text{CH}_2\text{BrI}$  in Fig. 5.23 (d). They include a broad horizontal band (3) peaked at 7.5 eV and spreading to the angles below  $50^\circ$ , which is due to the  $\text{CH}_2\text{Cl} + \text{I}$  and  $\text{CH}_2\text{I} + \text{Cl}$  dissociation channels with rotation of molecular co-fragment; the pronounced spot at low KER and nearly  $180^\circ$  (4), reflecting back-to-back emission of chlorine and iodine in the CII formation channel, and the events due to three-body dissociation (5) at the lowest KER. Shape of the corresponding Newton diagrams, Dalitz plots and halogen energy correlation maps also closely resemble the results obtained for  $\text{CH}_2\text{IBr}$ . The KER- $\theta_{23}$  map for the  $\text{CH}_2^+ + \text{Cl}^{2+} + \text{I}^{2+}$  shown in Fig. 5.41 (b) is rather similar to the analogous map for  $\text{CH}_2\text{IBr}$  (Fig. 5.31) as well.

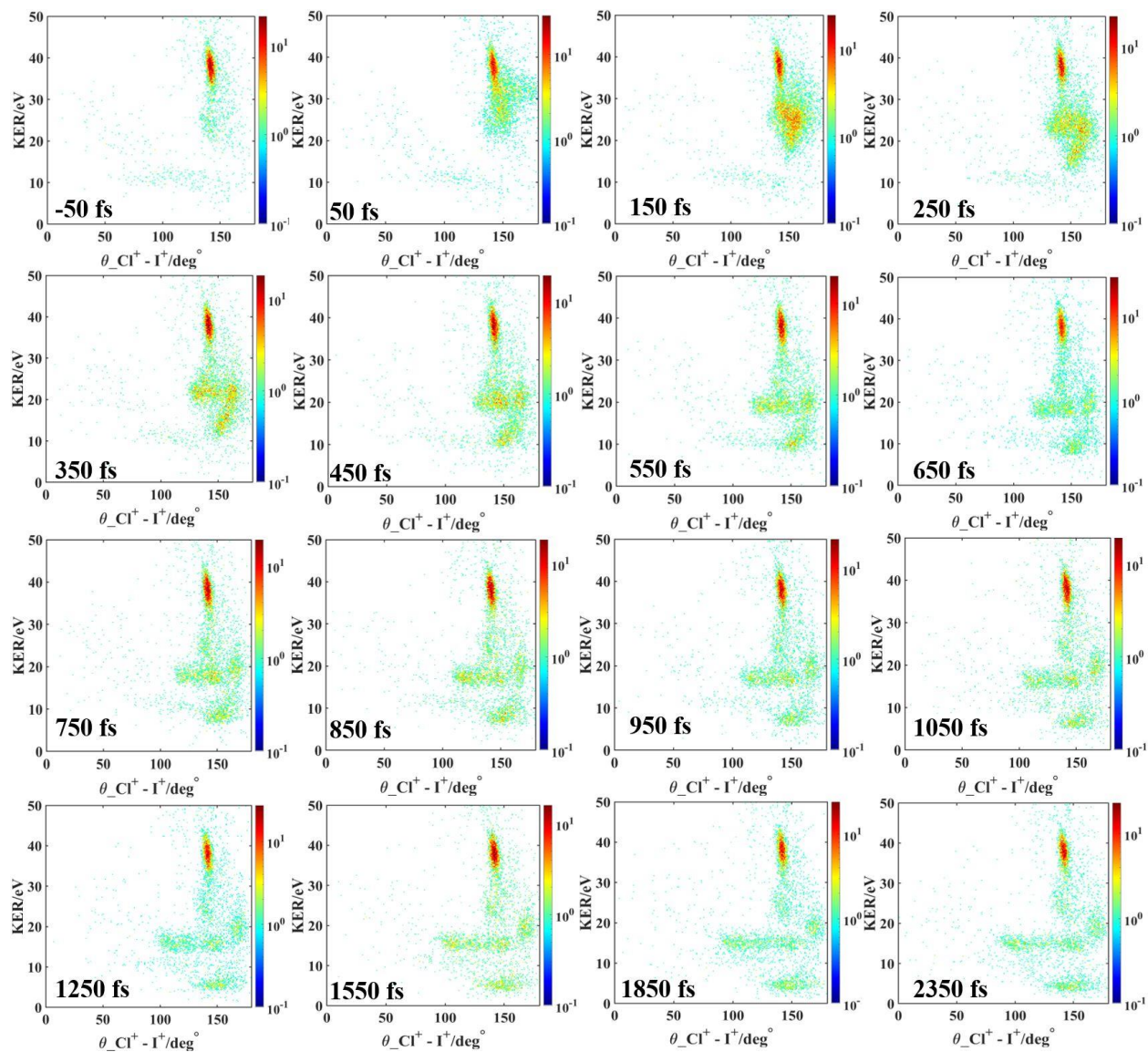


**Figure 5.42.** KER- $\theta_{23}$  snapshots for the three-body coincident  $\text{CH}_2^+ + \text{Cl}^{2+} + \text{I}^{2+}$  channel at different delays from 0 to 2.5 ps. Each snapshot corresponds to the 100 fs delay window centered at the values shown in the figure.

Finally, we take a similar approach as in previous section for  $\text{CH}_2\text{BrI}$  and look for potential signatures of transient isomerization signal, taking advantage of reaching higher-charged states and, thus, avoiding the unwanted contributions from sequential fragmentation channels. A corresponding series of consecutive KER- $\theta_{23}$  frames is shown in Fig. 5.42. One can indeed trace the appearance of a weak signal on the right from the delay-independent structure as early as 50 fs. This signal, which is somewhat weaker than for  $\text{CH}_2\text{BrI}$  in Fig. 5.30, decays very quickly

afterwards, propagating towards lower KER. Here, again, the exact origin of this very short-lived structure remains unclear.

## 5.6 Photodissociation of the CH<sub>2</sub>BrI molecule at 198 nm probed by strong-field ionization and Coulomb explosion

As discussed in Chapter 2, CH<sub>2</sub>BrI has three distinct types of electronic transitions in the UV range from 190 to 300 nm. The spectrum includes:

- 1) The excitation band that peaks at 266 nm resulting in the C-I bond cleavage, with the dissociation of the C-Br bond being a minor channel;
- 2) The excitation band that peak at 220 nm resulting in the C-Br bond cleavage;
- 3) Sharp features around 190 nm corresponding to the iodine Rydberg states.

The central wavelength of our UV pulse obtained by fourth harmonic generation is 198 nm. Hence one would expect different dissociation dynamics compared to what we observed at 263 nm dynamics. In particular, bond selectivity of the dissociation process should play a role, changing the branching ratio of C-Br to C-I bond cleavage. In this chapter, we investigate the photodissociation dynamics at this new wavelength aiming to identify important dissociation channels and compare them with the corresponding reactions discussed earlier for the longer UV wavelength.

In these time-resolved experiments, we used the same probe pulse as in our previous experiments, with a peak intensity of  $\sim 8 \times 10^{14}$  W/cm<sup>2</sup>, and employed the same data analysis and channel identification procedures as describe above for 263 nm. The UV pulse intensities we used was about  $1 \times 10^{13}$  W/cm<sup>2</sup>. The pump-probe contrast was monitored with the ratio of the signal from pumped and unpumped molecules at long asymptotic delays. We tested multiple UV intensities to identify the contributions from the higher-order (two- or multi-photon) processes, quantified by the appearance of ionic species in our TOF spectra. For the experiments described below, we have selected the lowest UV intensity where we still had a reasonable pump-probe contrast to ensure that the dissociation dynamics is predominantly driven a single UV photon absorption.

### 5.6.1 The CH<sub>2</sub>BrI molecule under single UV pulse at 198 nm

Fig. 5.43 shows the measured ion TOF spectrum obtained with the UV pulse with a peak intensity of  $5 \times 10^{12}$  W/cm<sup>2</sup>. As can be seen from the spectrum, at this intensity the ionization rate is still non-negligible. Note that the dominant contributions to the spectrum result from background contributions (scattered light or residual gas ionization). With the employed intensity, the dominant photoion from the target molecule is the singly-charged parent ion (CH<sub>2</sub>BrI<sup>+</sup>), with some contribution from the dissociative ionization products (CH<sub>2</sub>Br<sup>+</sup>, CH<sub>2</sub>I<sup>+</sup>, I<sup>+</sup>, Br<sup>+</sup>, BrI<sup>+</sup> and CH<sub>2</sub><sup>+</sup>) besides the residual gases. As highlighted by a dominant narrow central TOF peak for each of these species, the KE distributions of the ionic products peaks near zero KE.

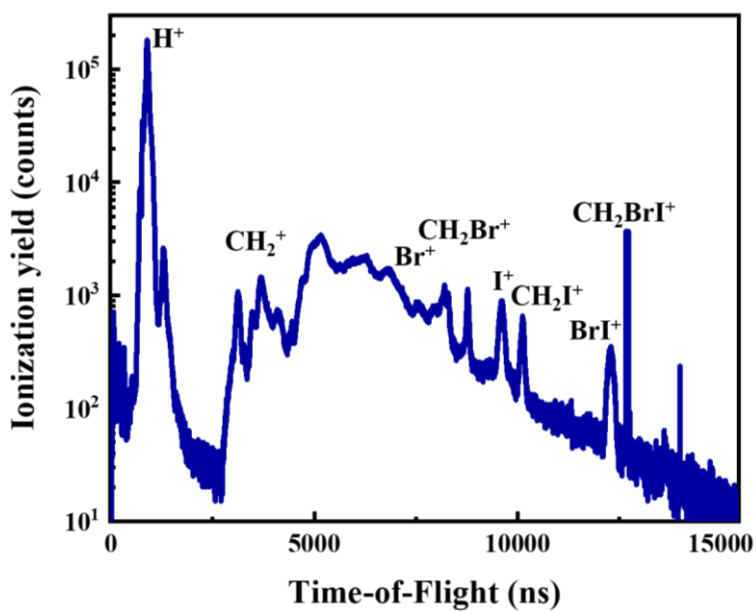


**Figure 5.43.** Time-of-Flight (TOF) of the generated ions after a single UV pulse of  $5 \times 10^{12}$  W/cm<sup>2</sup> intensity.

### 5.6.2 Pump probe results for CH<sub>2</sub>BrI at 198 nm

The delay-dependent maps for the primary two-body CE channels are shown in Fig. 5.44, where we map both the bound and dissociating molecules. Similar to the earlier data for 263 nm, each of these spectra displays two features: a delay-independent horizontal high-energy band due to the CE of bound molecules (similar to what is produced by the NIR pulse, see section 5.1), and a descending band reflecting two-body dissociation triggered by the pump pulse. The dissociating events within the descending bands were tested to scale linearly with UV intensity, confirming

that they result from the single UV-photon excitation. Comparing the spectra for two main channels,  $\text{CH}_2\text{Br} + \text{I}$  (Fig. 5.44 (a)) and  $\text{CH}_2\text{I} + \text{Br}$  (Fig. 5.44 (b)), with the corresponding results obtained with 263 nm pump (Figs. 5.15 and 5.18 (a), respectively), we conclude that the C-Br cleavage is more efficient at the 198 nm wavelength. These results reflect the sensitivity of various dissociation pathways to the electronic nature of the initial photoexcitation, and are consistent with the results of earlier photodissociation studies [187], [188].

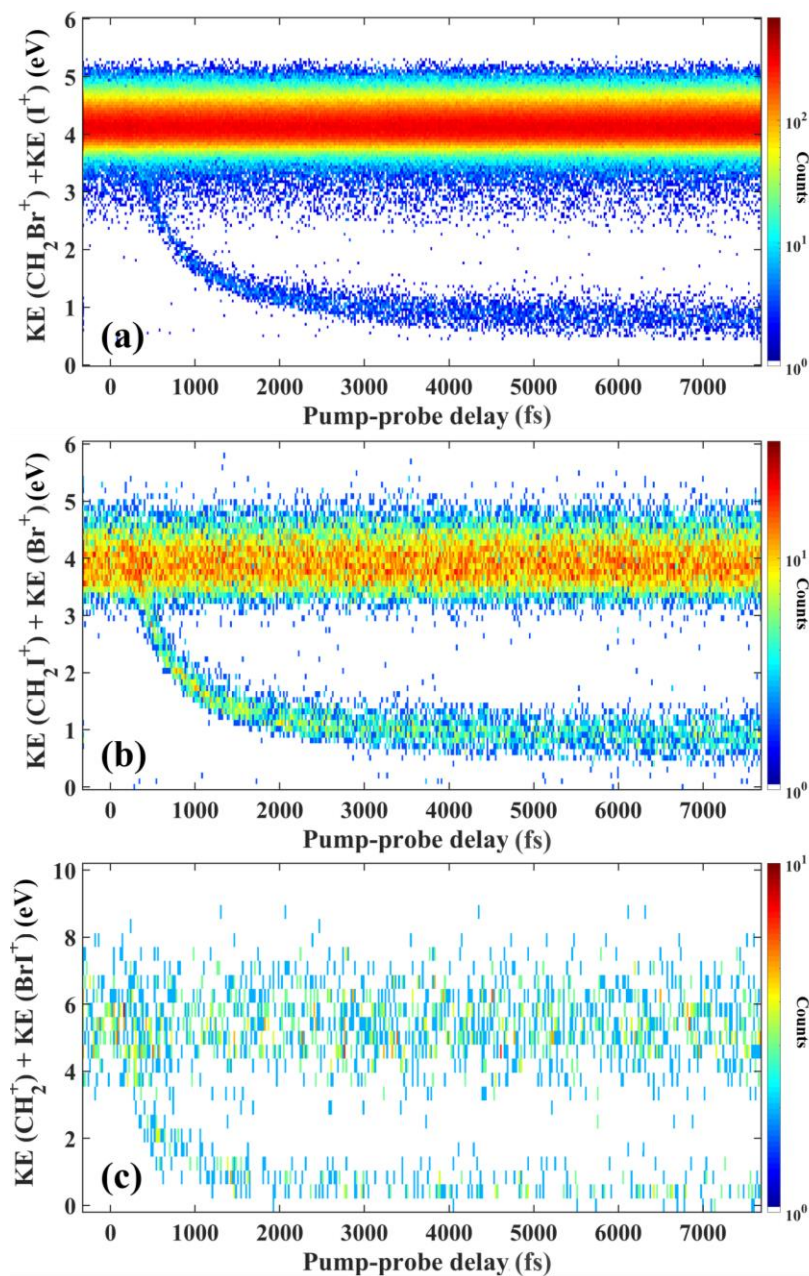


**Figure 5.44.** Delay-dependent KER distribution for the two-body (a)  $\text{CH}_2\text{Br}^+ + \text{I}^+$ , (b)  $\text{CH}_2\text{I}^+ + \text{Br}^+$  and (c)  $\text{CH}_2^+ + \text{BrI}^+$  coincident channels.

In addition, the BrI elimination is expected to become efficient below 200 nm [187]. The spectrum presented for the corresponding  $\text{CH}_2^+ + \text{BrI}^+$  two-body CE channel in Fig. 5.44 (c) shows a clear descending band in the delay-dependent KER map reflecting this channel. Although the overall event rate in this CE channel is rather low, the descending band reflecting the BrI elimination upon single-photon absorption is well-localized and comparable in strength with a delay-independent high-energy feature, very different from the corresponding 263 nm results shown in Fig. 5.18 (c).

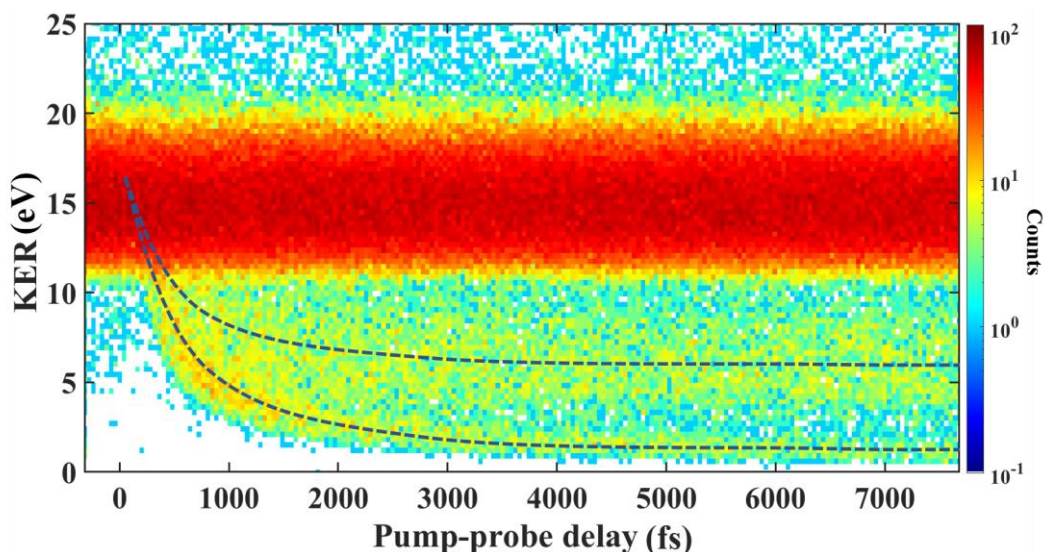


**Figure 5.45.** Delay-dependent KER distribution of fragmentation of  $\text{CH}_2\text{BrI}$  into  $\text{CH}_2^+ + \text{Br}^+ + \text{I}^+$  after UV pump at 198 nm and NIR probe pulse. The dashed lines highlight the structures due to two- (upper line) and three-body (lower line) dissociation channels.

To further elucidate the dynamics of various dissociation channels, we investigate delay-dependent three-body fragmentation patterns, following the procedures described in section 5.4 for 263 nm. Fig. 5.45 shows the delay-dependent KER for the  $\text{CH}_2^+ + \text{Br}^+ + \text{I}^+$  coincident channel. Similar to the results presented for 263 nm pump in Fig. 5.19, this spectrum includes the same delay-independent high-energy band reflecting the CE of bound molecules by the NIR probe pulse, and two descending bands due to dissociation triggered by the UV pulse. However, both of the descending bands are clearly shifted towards the lower KER values for the data obtained with 198 nm pump pulse. To reveal the nature of this shift and other dissociation details, as a next step, we explore the signatures of various contributing dissociation pathways in the  $\text{KER}-\theta_{23}$  maps for this channel, which are presented in Figs. 5.46 and 5.47 (a).

Fig. 5.46 displays the KER- $\theta_{23}$  maps for  $\text{CH}_2^+ + \text{Br}^+ + \text{I}^+$  coincident channel obtained at zero delay (a) and at 2.5 ps delay (b). Interestingly, in contrast to the results obtained with 263 nm pump pulses, already the zero delay data in Fig. 5.46 (a), besides the contribution from concerted and sequential breakup of a bound molecule, manifest the onset of dissociating events at lower KER. This can be clearly seen by comparing this figure with NIR-only data in Fig. 5.6 or the first two panels in the data with 263 nm pump (the first two panels in Fig. 5.22). The most likely reason for this is a longer duration of our 198 nm pulse compared to 263 nm. Even if at zero delay, the maxima of both UV and NIR pulses overlap, for  $>100$  fs duration of our 198 nm pulse, the events triggered by the photoabsorption in the leading edge of the pulse can propagate for more than 50 fs until the NIR probe pulse arrival, resulting in significant dissociation dynamics and, thus, lower KER.

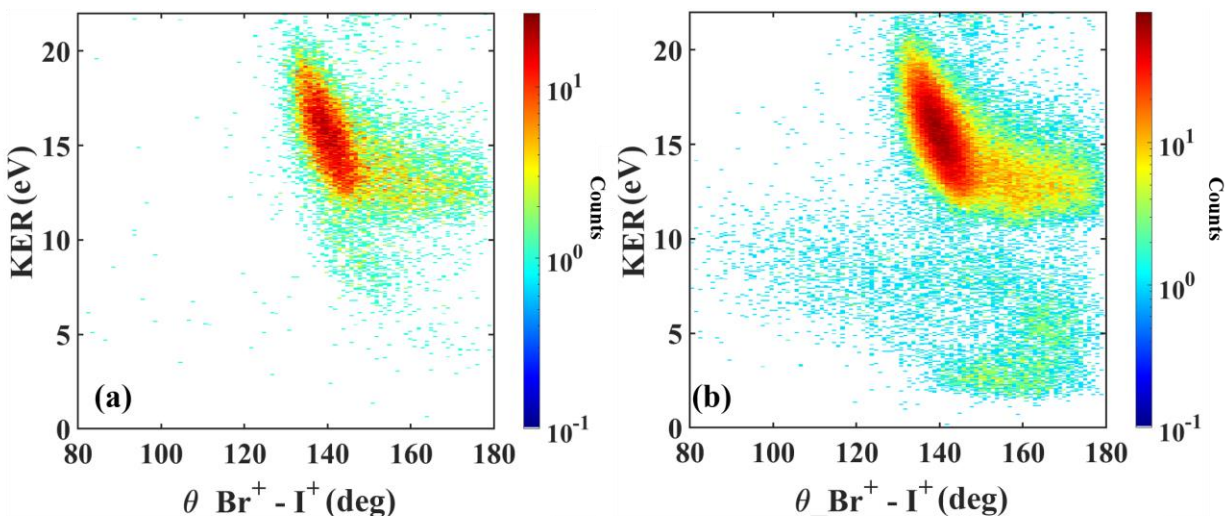


**Figure 5.46.** KER- $\theta_{23}$  snapshots for the three-body coincident  $\text{CH}_2^+ + \text{Br}^+ + \text{I}^+$  channel at (a) 0 fs, and (b) 2.5 ps.

The KER- $\theta_{23}$  map for 2.5 ps delay shown in Fig. 5.46 (b) displays a significant number of low-KER events due to various dissociation pathways. We observe a signature of three-body dissociation at very low KERs, a consolidating, somewhat localized spot above this band at large angles, and a broad, diffuse distribution of events at larger KERs and smaller angles. To assign different channels more reliably, we consider the same KER- $\theta_{23}$  map for 20 ps delay in Fig. 5.47 (a), where most of the channels are expected to reach asymptotic conditions and become well-separated. The map shows three distinct regions, marked (3-5) in the figure, where, similar to the

results presented in Fig. 5.23 (d) for 263 nm pump, regions (3) and (4) partially overlap. Considering other three-body representations (Newton diagrams, Dalitz and halogen energy correlation plots) as well as the results of our CES, we conclude that, similar to the assignments made for 263 nm data, the events in region (3) of Fig. 5.47 (a) result from halogen detachment channels ( $\text{CH}_2\text{Br}^+ + \text{I}$  and  $\text{CH}_2\text{I} + \text{Br}$ ), region (4) is predominantly due to molecular halogen elimination pathway,  $\text{CH}_2 + \text{BrI}$ , whereas the events in region (5) originate from the three-body dissociation triggered by the UV pump. However, in contrast to the 263 nm results, the latter two channels seem to provide dominant contributions to dissociation. This is even more pronounced in the results for  $\text{CH}_2^+ + \text{Br}^{2+} + \text{I}^{2+}$  channel depicted in Fig. 5.47 (b), where the signatures of BrI elimination channel in region (4) become particularly strong.

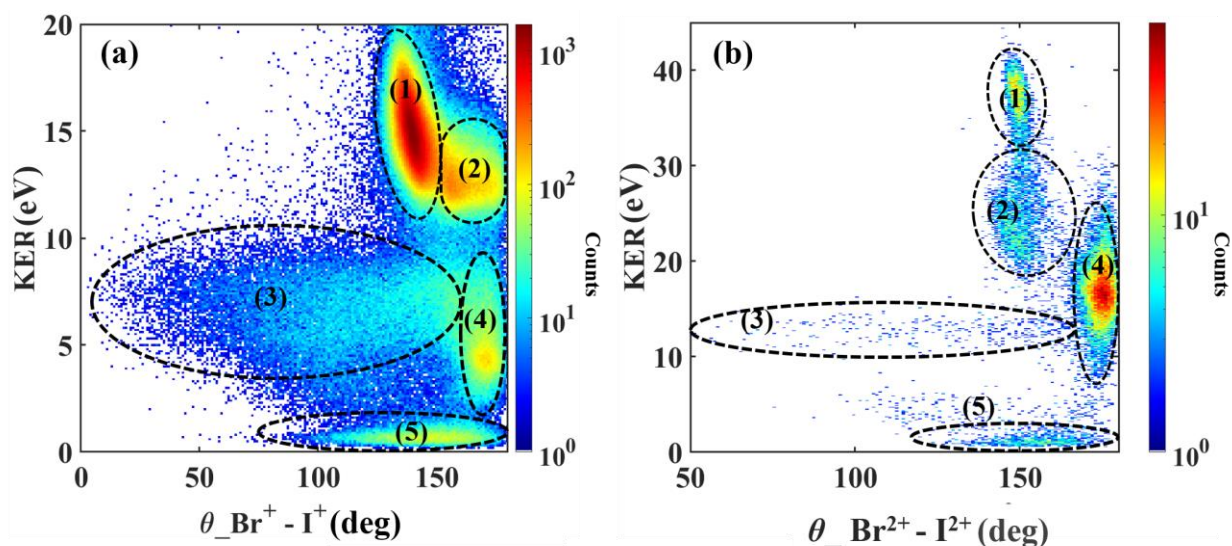


**Figure 5.47.** KER- $\theta_{23}$  snapshots for the three-body coincident (a)  $\text{CH}_2^+ + \text{Br}^+ + \text{I}^+$  and (b)  $\text{CH}_2^+ + \text{Br}^{2+} + \text{I}^{2+}$  channels at 20 ps. The regions are numbered and marked, indicating KER- $\theta_{23}$  features corresponding to different pathways discussed in the text.

The observed behavior can be rationalized based on our expectations of the energy threshold for three-body dissociation (5.66 eV) and previous knowledge about the wavelength-dependence of the branching ratio for various dissociation pathways. At 198 nm, three-body dissociation with one UV photon becomes energetically accessible, making this a prominent channel. We can also note that the access energy for this reaction triggered with one 198 nm photon is significantly smaller than for the absorption of two 263 nm, photons. Correspondingly, the asymptotic KER of the three-body dissociation process is smaller for 198 nm compared to 263 nm,

as can be clearly seen by comparing Figs. 5.45 and 5.48 (a,b) with Figs. 5.19, 5.23 (b) and 5.31, respectively. The increased branching ratio for BrI elimination channel can also be expected based on earlier spectroscopic results and on previous calculations, since this is only a minor channel upon single-photon excitation in the A-band [187], [188]. However, we should note that contributions from two-photon processes to the observed yield of this channel at 198 nm could not be excluded, given its increased branching ratio for five-fold-charged final state in Fig. 5.47 (b) and the presence of some BrI<sup>+</sup> ions in the TOF spectrum obtained with the UV pump pulse only, as shown in Fig. 5.43.

### 5.6.3 Pump probe results for CH<sub>2</sub>I<sub>2</sub> at 198 nm

In the last step, to investigate the generality of our conclusions on the dissociation dynamics triggered by the shorter UV wavelength, we repeated the same set of experiments with another molecular target, diiodomethane (CH<sub>2</sub>I<sub>2</sub>). Even though we did not consider CH<sub>2</sub>I<sub>2</sub> dynamics upon 263 nm excitation in this work, a recent PhD study [274] provides abundant reference data for comparison.

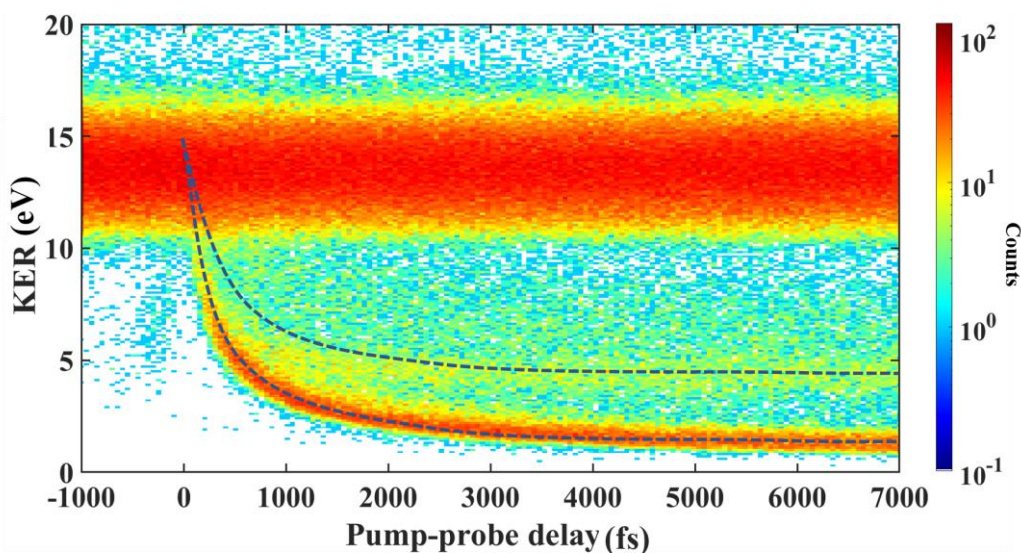


**Figure 5.48.** Delay-dependent KER distribution of fragmentation of CH<sub>2</sub>I<sub>2</sub> into CH<sub>2</sub><sup>+</sup> + I<sup>+</sup> + I<sup>+</sup> after UV pump at 198 nm and NIR probe pulse. The dashed lines highlight two- and three-body dissociation channels.

The delay-dependent KER distribution for the CE of CH<sub>2</sub>I<sub>2</sub> into CH<sub>2</sub><sup>+</sup> + I<sup>+</sup> + I<sup>+</sup> channel obtained in 198 nm pump – 790 nm probe experiment (with the same pump and probe pulse as

used for CH<sub>2</sub>BrI) is shown in Fig. 5.48, whereas the corresponding asymptotic KER- $\theta_{23}$  maps obtained at 20 ps for CH<sub>2</sub><sup>+</sup> + I<sup>+</sup> + I<sup>+</sup> and CH<sub>2</sub><sup>+</sup> + I<sup>2+</sup> + I<sup>2+</sup> channels are shown in Fig. 5.49 (a) and (b), respectively. Very similar to the CH<sub>2</sub>BrI results presented before, the results indicate a dramatic branching ratio change in single-photon processes triggered by 263 nm and 198 nm pulses, with molecular I<sub>2</sub> elimination and three-body dissociation becoming dominant reaction pathways at the shorter wavelength.

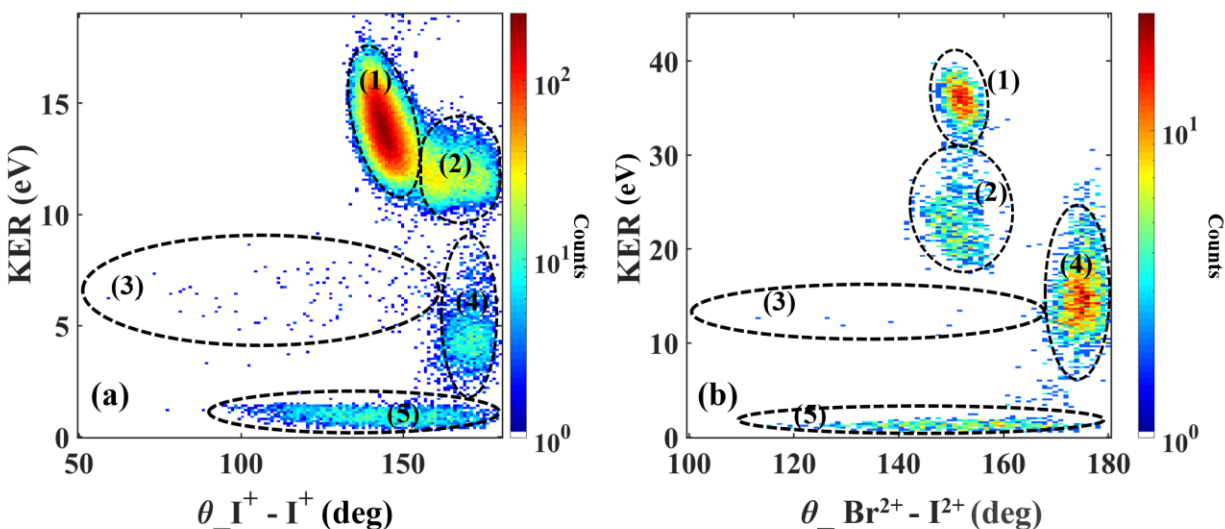


**Figure 5.49.** KER- $\theta_{23}$  snapshots for the three-body coincident (a) CH<sub>2</sub><sup>+</sup> + I<sup>+</sup> + I<sup>+</sup> and (b) CH<sub>2</sub><sup>+</sup> + I<sup>2+</sup> + I<sup>2+</sup> channels at 20 ps. The dashed ovals mark the regions of the KER- $\theta_{23}$  map corresponding to different pathways discussed in the text. The channel assignment is the same as for CH<sub>2</sub>BrI data discussed in the previous section.

## 5.7 Summary

In this chapter, we discussed photodissociation of dihalomethane molecules triggered by UV light for two different excitation wavelengths, 263 nm and 198 nm. For the longer wavelengths, dominant single-photon-induced dissociation processes result from the cleavage of one of the carbon-halogen bonds, with the contribution from C-I bond breaking being the stronger and C-Br or C-Cl bond the weaker channel for CH<sub>2</sub>BrI and CH<sub>2</sub>ClI molecules. We found that the rotational motion of a molecular co-fragment in these dissociation reactions plays a crucial role for our understanding of dissociation dynamics and of the formation of the three-body CE patterns. This rotational motion will be studied in more detail in the next chapter. We also identified pronounced contributions from three-body dissociation and molecular halogen elimination, where

the former is exclusively and the latter to a large extent driven by the absorption of two or three UV photons. Although we did not observe unambiguous signatures of UV-induced photoisomerization, we identified a set of events, where a molecule seems to pass through a transient configuration corresponding to a linearized geometry in-route towards dissociation. A deeper understanding of the dynamics behind the observed transient features will require extensive theoretical work. The observed dynamics are rather similar between the two dihalomethane molecules studied here, suggesting that most of our findings can be generalized to other systems.

For  $\text{CH}_2\text{BrI}$  photodissociation triggered by shorter excitation wavelength (198 nm), we observe a dramatic change in the branching ratios of different reaction pathways, with three-body dissociation and molecular halogen elimination becoming dominant channels. In addition, for two-body dissociation with halogen atom detachment, we observe an increased branching ratio for C-Br bond breaking with respect to C-I bond cleavage, confirming bond selectivity of UV-induced photodissociation. Finally, we obtain very similar results for excitation of  $\text{CH}_2\text{I}_2$  at 198 nm, again suggesting that our conclusions can be generalized to other molecules of halomethane family.

## Chapter 6 - Direct imaging of the UV-driven rotational motion of the radical co-fragments in the photodissociation of dihalomethanes

In the experiments described in the previous chapter, we used time-resolved coincident ion imaging to identify and disentangle signatures of different UV-induced photodissociation pathways in dihalomethane molecules. Based on these results, in this chapter we attempt to directly image the correlated motion of atomic and molecular co-fragments in some of these dissociation processes. We specifically focus on the *A*-band dissociation of CH<sub>2</sub>BrI and CH<sub>2</sub>ClI at 263 nm, apply the procedures described in Chapter 5 to select the CE events resulting from the cleavage of a particular carbon-halogen bond, and map the rotation of molecular radical co-fragment correlated with the translational motion of both reaction products.

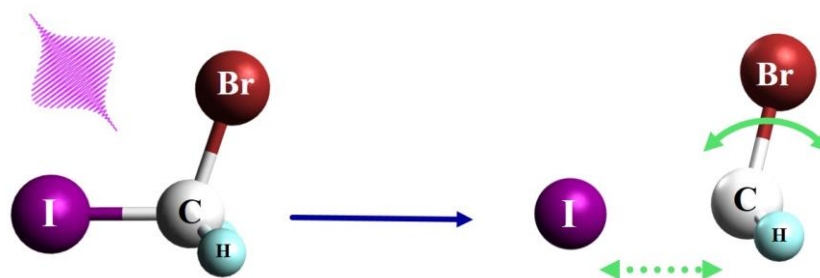


**Figure 6.1.** Mechanistic picture of CH<sub>2</sub>BrI photodissociation. Absorption of a 263 nm photon primarily breaks the C-I bond, such that the force due to dissociation is along the C-I axis. This force exerts torque on CH<sub>2</sub>Br as its center of mass lies near bromine atom.

### 6.1 Partitioning of excess energy into rotational degrees of freedom

As discussed in Chapter 2, in the dissociation of dihalomethanes in the *A*-band, a significant fraction of available energy is deposited into internal degrees of freedom of the polyatomic co-fragment. Based on the measured KE of the photodissociation products, this fraction was estimated to reach 54-55 % in CH<sub>2</sub>ClI [98], [147] and 64-67% in CH<sub>2</sub>BrI [99], [187], whereas for the linear alkyl iodides like CH<sub>3</sub>I it does not exceed a few percent level [98], [146]. Theoretical calculations predict that most of the transferred energy is channeled into rotational excitation [186], triggering robust rotational motion as illustrated in Fig. 2.13. Such energy flow into the rotational degrees of freedom can be understood in classical terms considering the “anchor” effect of the second heavy halogen atom. As illustrated in Fig. 6.1 for CH<sub>2</sub>BrI, upon photodissociation the fragment velocities

are initially directed along the C-I bond, while the CM of CH<sub>2</sub>Br lies close to Br atom. Due to this shift of the CM off the C-I bond axis, significant torque is exerted on the CH<sub>2</sub>Br co-fragment [186]. As a result, the radical fragment rotates around its CM.

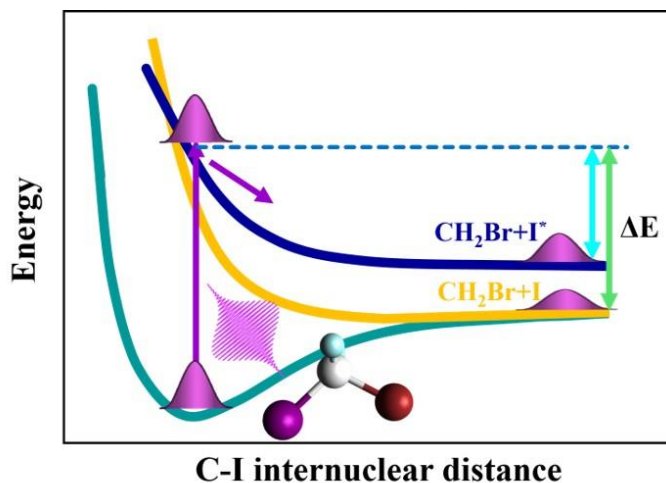


**Figure 6.2.** Schematic diagrams of the potential energy curves and cartoon snapshots of the propagating wave packet for different dissociation pathways.

To illustrate how the excess energy after photoabsorption is distributed between the KE of the photoproducts and various forms of internal energy, we consider the energetics of the photodissociation process. They are determined by the energy conservation:

$$\Delta E = h\nu - D_0 + E_{SO} \quad 6.1$$

$$\Delta E = E_{trans} + E_{int} \quad 6.2$$

where  $\Delta E$  is the excess energy following photodissociation, which partitions between the internal excitation energy ( $E_{int}$ ) and the translation energy ( $E_{trans}$ ), and  $D_0$  is the energy required for dissociation. Fig. 6.2 visualizes the excess energy using the schematic of the repulsive potential energy curves (PECs) involved in photoexcitation in the A-band.

While rotational motion of a polyatomic co-fragment for UV-driven photodissociation of dihalomethanes can be expected from the known energy partitioning [103,104], and has been also modelled theoretically [186], until very recently, no direct observations of such rotational dynamics have been reported. First signatures of such co-fragment rotation have been traced as a periodic signal in a recent UED experiment for CH<sub>2</sub>I<sub>2</sub> upon 266 nm excitation [53]. In a later CEI experiment on the same reaction, CH<sub>2</sub>I rotational motion needed to be considered in order to match the CEI data with the CES, similar to what was discussed in section

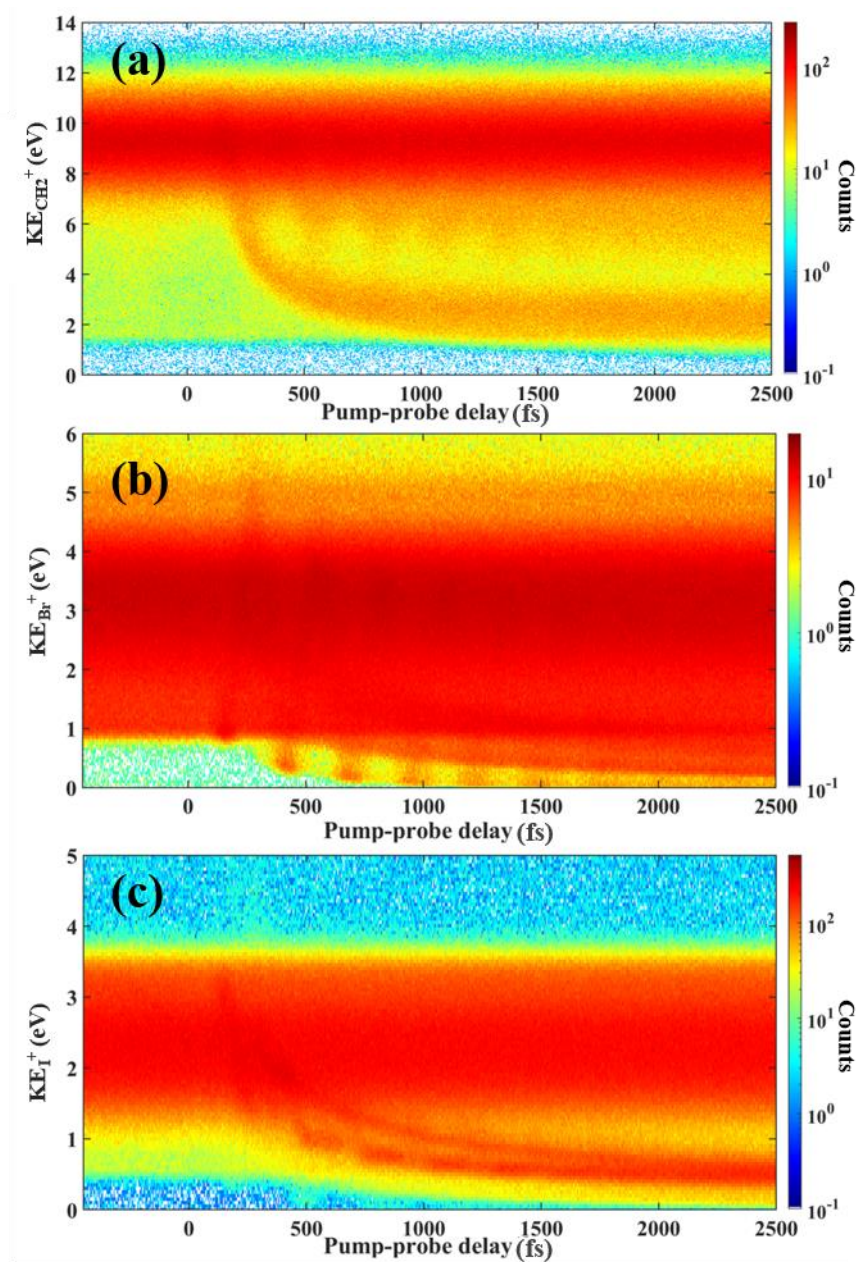
5.4.2 for CH<sub>2</sub>BrI (see also Figs. 5.24 and 5.26). Moreover, implications of such rotational motion for charge transfer in dissociating molecules have been recently discussed for several FEL experiments [284], [285]. However, all of the above-mentioned studies represent rather indirect measurements of the co-fragment rotation. The main goal of this chapter is to present a visual and intuitive picture of this rotational motion using experimental approach discussed in Chapter 5. We first present and discuss the results obtained for CH<sub>2</sub>BrI molecule, and then complement them with the data for CH<sub>2</sub>ClI, aiming to demonstrate the generality of the discussed phenomenon. To rationalize our experimental findings and underpin the correspondence between the rotational motion of interest and our experimental observables, we performed molecular dynamics simulations of the UV-induced dissociation combined with Coulomb explosion simulations. Experimentally, results presented in this chapter originate from the experiment described in section 5.4.1 for CH<sub>2</sub>BrI and in section 5.5 for CH<sub>2</sub>ClI, the intensity of 263 nm pump and 790 nm probe pulses were kept at  $1.5 \times 10^{13}$  and  $8 \times 10^{14}$  W/cm<sup>2</sup>, respectively.

## 6.2 Mapping the rotational motion of radical co-fragments

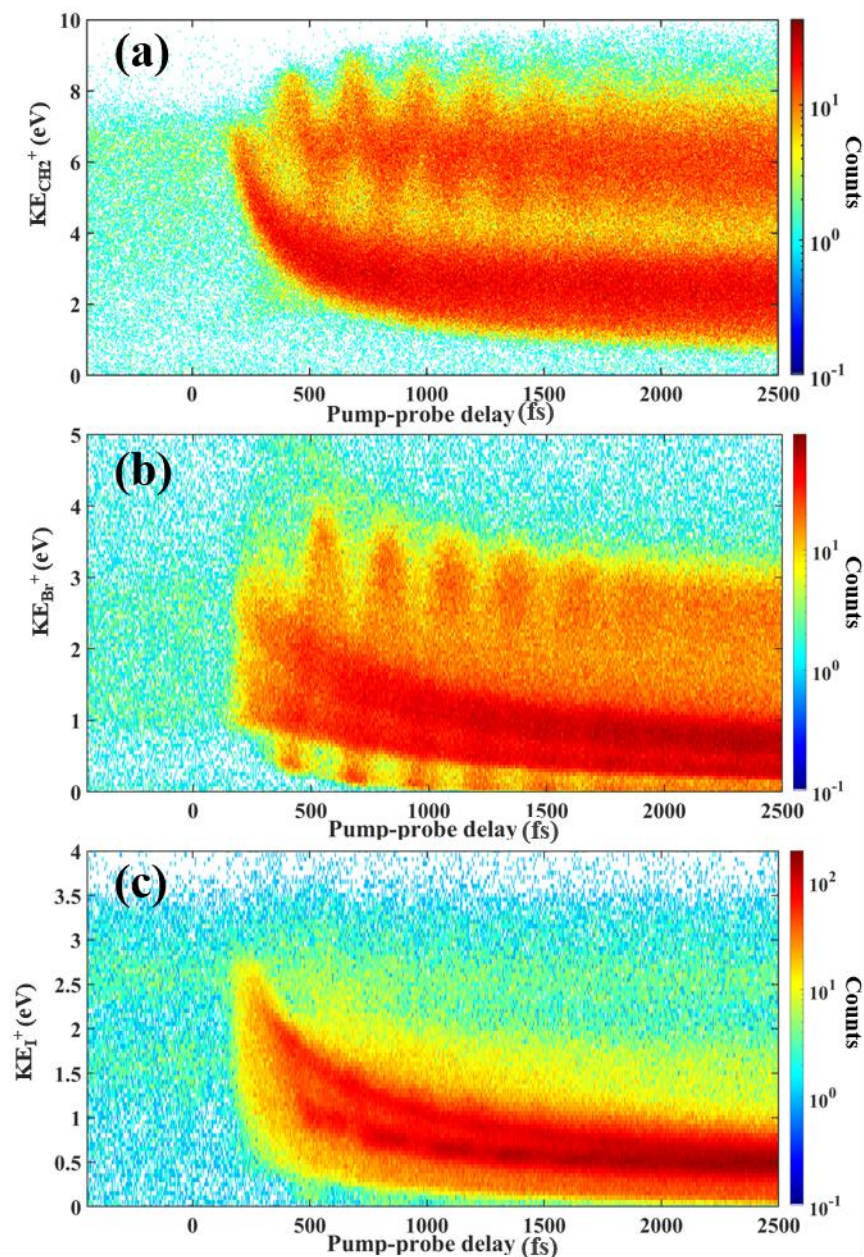
The measured KER distribution for the triply-charged coincidence channel CH<sub>2</sub><sup>+</sup> + Br<sup>+</sup> + I<sup>+</sup> as a function of the time delay between the UV and NIR pulses was shown in Fig. 5.19. In Fig. 6.3., we complement it with the delay-dependent KE distributions of the individual fragments obtained from the same event set. In addition to the characteristic horizontal and descending bands, which we observe in most of the delay-dependent KER spectra so far, some periodic oscillatory features can be seen in the lower-KE parts of the spectra. To look for the origin of these structures, we first focus on dissociating molecules only. This can be achieved by gating on the lower-KER part of the delay-dependent KER distribution shown in Fig. 5.19.

Fig. 6.4 displays the same delay-dependent KE distributions as Fig. 6.3, but with the condition that the total KER of all three particles does not exceed 11 eV. The spectra manifest a clear oscillatory structure, which is most pronounced for CH<sub>2</sub><sup>+</sup> and Br<sup>+</sup> spectra in Fig. 6.4 (a) and (b), respectively. While in the CH<sub>2</sub><sup>+</sup> data in (a) the oscillatory structure is well-separated from the broad low-KE channel, in Br<sup>+</sup> and I<sup>+</sup> it overlaps with broad descending bands.

Considering four major dissociation channels analyzed in section 5.4., we can attribute the lower descending band in Fig. 6.4 (a), which converges to rather low CH<sub>2</sub><sup>+</sup> KEs at large delays, to the mixture of three-body dissociation and CH<sub>2</sub> + BrI molecular halogen elimination pathway.



**Figure 6.3.** Delay-dependent KE distributions of the individual fragment ions (a) CH<sub>2</sub><sup>+</sup>, (b) Br<sup>+</sup>, and (c) I<sup>+</sup> from the CH<sub>2</sub><sup>+</sup> + Br<sup>+</sup> + I<sup>+</sup> coincident channel.



**Figure 6.4.** Same delay-dependent KE distributions of the individual fragment ions as in Fig. 6.4, but with the additional requirement that the total KER of the  $\text{CH}_2^+ + \text{Br}^+ + \text{I}^+$  coincident channel is below 11eV.

For both of these channels, the  $\text{CH}_2^+$  fragment is far away from its iodine and bromine partner at large delays, resulting in its low KE. In contrast, for both halogen detachment channels,  $\text{CH}_2\text{Br} + \text{I}$  and  $\text{CH}_2\text{I} + \text{Br}$ , the methylene group stays together with one of the halogens until the probe pulse arrives, leading to considerably higher KE. Based on this interpretation, in order to

clean up the oscillatory structures in  $\text{Br}^+$  and  $\text{I}^+$  data, we set an additional gate on the upper of the two  $\text{CH}_2^+$  features observed in Fig. 6.4 (a), leaving out the events with low  $\text{CH}_2^+$  KE. Delay-dependent  $\text{Br}^+$  and  $\text{I}^+$  KE distributions with this additional gate are shown in Fig. 6.5 (a) and (b), respectively. Comparing these spectra with Fig. 6.4 (b, c), we can see that the descending bands superimposed on the oscillator y structure are clearly reduced in intensity, although not completely removed.

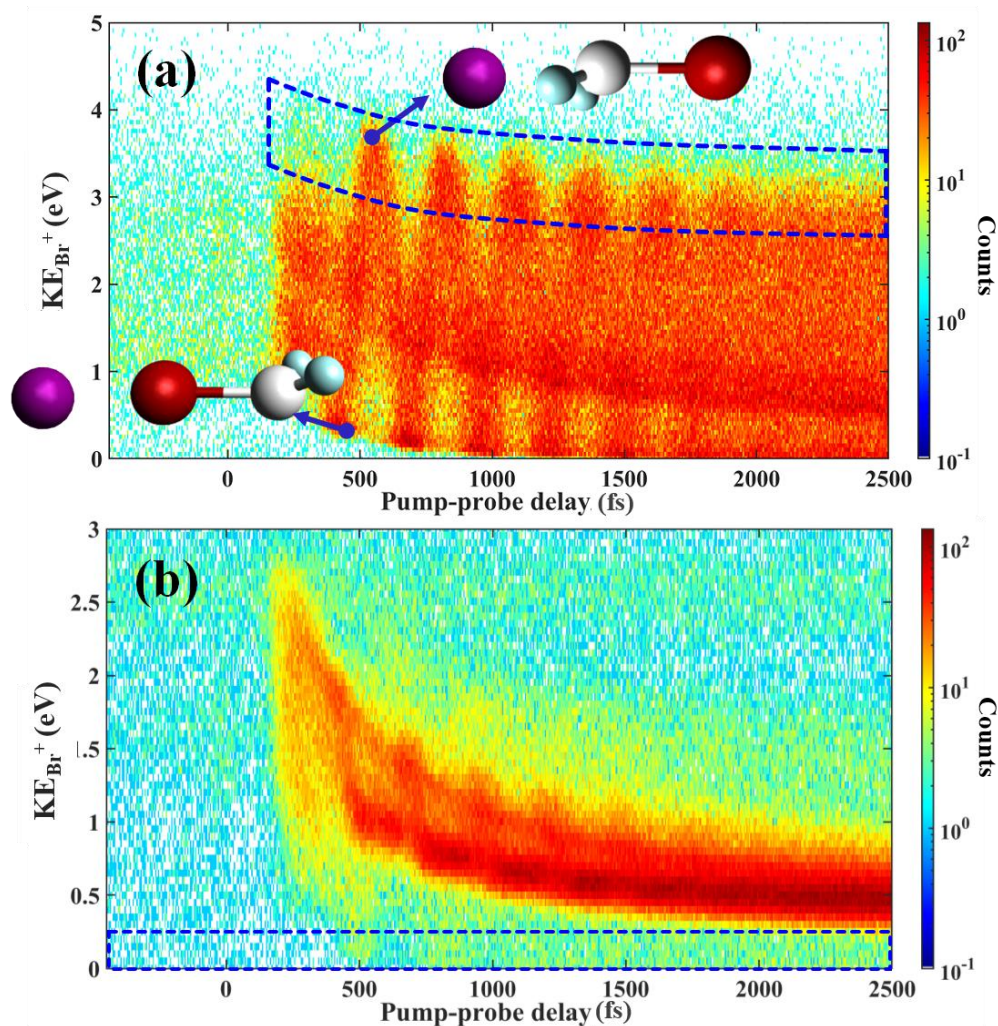


**Figure 6.5.** Delay-dependent KE distributions for (a)  $\text{Br}^+$  and (b)  $\text{I}^+$  in  $\text{CH}_2^+ + \text{Br}^+ + \text{I}^+$  coincident channel. Only the events fulfilling the conditions  $\text{KER} < 11\text{eV}$  and  $\text{KE}(\text{CH}_2^+) > 4.3\text{ eV}$  are included. The dashed contour in (a) shows the polygon gate for the projection of the  $\text{Br}^+$  map used in Fig. 6.6. The dashed rectangle in (b) highlights a signature of a weaker oscillatory structure corresponding to C-Br bond breaking (see text for details).

In these filtered spectra, the periodic structure is readily visible, in particular, in the delay-dependent KE distribution for  $\text{Br}^+$  shown in Fig. 6.5 (a). The oscillating  $\text{Br}^+$  KE covers a broad range, with its borders shifting to lower KE values with increasing delay. Remarkably, in the minima of this oscillation, the KE of  $\text{Br}^+$  reaches very small values, approaching zero at  $\sim 1000$  fs. The only scenario which can reasonably explain periodic appearances of such low KE values for fragments from triple ionization followed by CE implies that at these delay times the molecule reaches nearly linear geometry, with the bromine fragment located in-between the other two, as sketched in the lower inset in Fig/ 6.5 (a). In this configuration, mutual Coulomb repulsion from both sides after CE can bring the  $\text{Br}^+$  ion energy to nearly zero values. This scenario is consistent with rotational motion of the  $\text{CH}_2\text{Br}$  co-fragment. Correspondingly, in the maxima of the  $\text{Br}^+$  KE, the molecule approaches the opposite “linearized” geometry, with the bromine atom located on the outside as sketched in the upper inset of Fig. 6.5 (a).

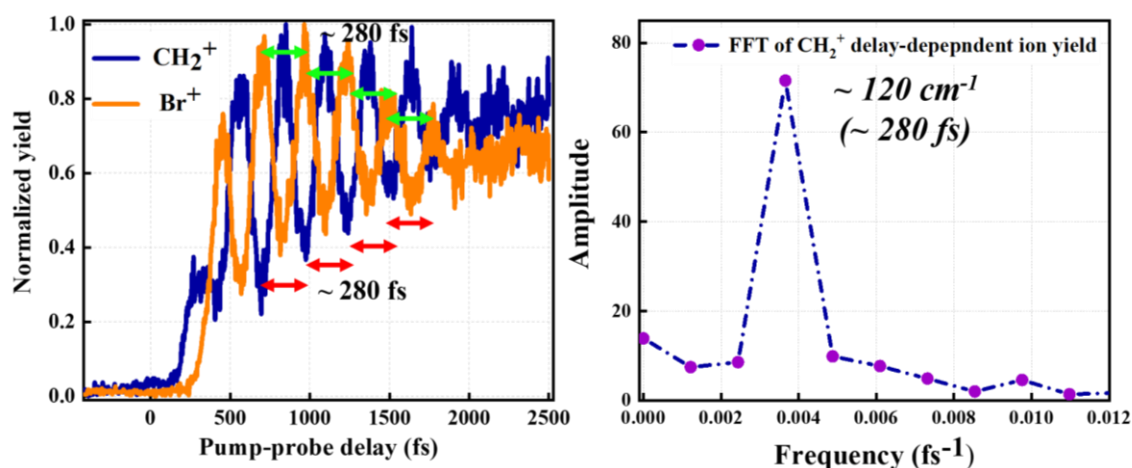


**Figure 6.6.** (a) Delay-dependence of the  $\text{CH}_2^+$  and  $\text{Br}^+$  ion yields in the regions corresponding to the maxima of the respective oscillatory structures (see dashed boxes in Figs. 6.4 (a) and 6.5 (a), respectively). (b) FFT of the  $\text{Br}^+$  signal from panel (a).

If the oscillatory structures observed in Fig. 6.3-6.5 are indeed due to  $\text{CH}_2\text{Br}$  rotation, the  $\text{CH}_2^+$  signal can be expected to be out of phase with the  $\text{Br}^+$ , as can be intuitively visualized from the two insets shown in Fig. 6.5 (a). To verify this, in Fig. 6.6, the projections of the individual two-dimensional maps of the  $\text{CH}_2^+$  and  $\text{Br}^+$  KE distributions onto the delay axis for regions selected close to their respective KE maxima, as marked by the tilted dashed boxes on the top of Fig. 6.4 (a) and 6.5 (a), are shown in Fig. 6.6 (a). The two curves display pronounced ion yield

oscillations with a 280 fs period, which are clearly out of phase with each other. Plotting a fast Fourier transform (FFT) of the corresponding  $\text{Br}^+$  signal in Fig. 6.6 (b), we observe a single peak at  $\sim 120 \text{ cm}^{-1}$ , corresponding to the periodicity observed in Fig. 6.6 (a).

In accordance with the above discussion, the behavior of the observed oscillatory signals  $\text{CH}_2^+$  and  $\text{Br}^+$  can be interpreted as a signature of the rotational motion of the  $\text{CH}_2\text{Br}$  fragment after the C-I bond cleavage. The observed rotational period (280 fs) corresponds to the classical rotation period of a state with rotational quantum number  $J \sim 48$ , fitting to the expectations of significant rotational excitation discussed above. Noticeably, the oscillations in all signals are gradually washed out at large delays. To quantify this, in Fig. 6.7 the same  $\text{Br}^+$  curve as shown in Fig. 6.6 (a) is fitted with the damping sinusoidal function, yielding the characteristic damping time of  $\sim 2.1$  ps. While a few possible reasons for such damping of the oscillatory signal due to rotations can be considered, the most straightforward explanation is a dephasing of the rotational wave packet due to different frequencies of its constituents. Such dephasing will be discussed more quantitatively in the next section, where the results of the corresponding CES will be presented. Here we should just note that the need to allow for a significant spread of angular velocities of this rotation while simulating dissociation of  $\text{CH}_2\text{BrI}$  in section 5.4.2 was already introduced in order to account for a broad KE and angular spread of the iodine and bromine fragments (see Fig. 5.26 and the discussion thereof).

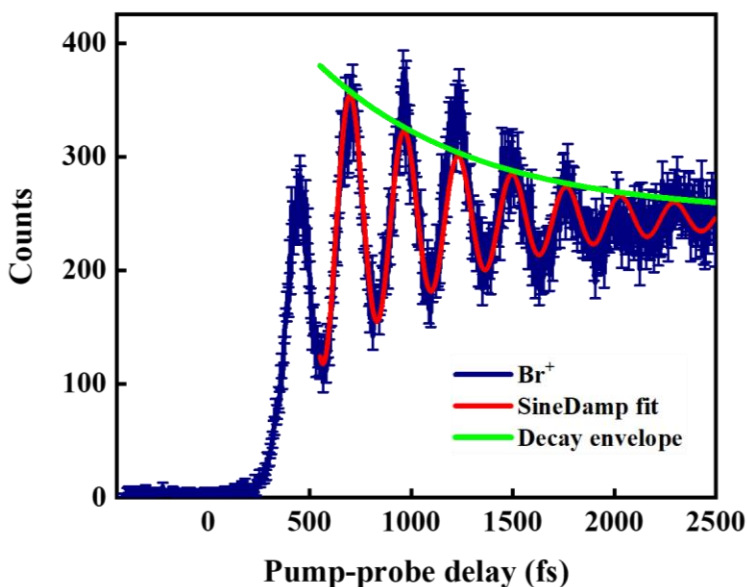


**Figure 6.7.** Delay-dependence of the  $\text{Br}^+$  ion yields and the fitting damping sinusoidal function suggesting a dephasing time of about 2 ps.

Note that the envelopes of both  $\text{CH}_2^+$  and  $\text{Br}^+$  oscillatory structures in the delay-dependent KE spectra of Figs. 6.4 (a) and 6.5 (a) move to lower KE values with increasing delay, highlighting decreasing but still non-negligible Coulomb repulsion from the detached iodine fragment at increasing internuclear separations. This reflects the correlated motion of the detached iodine atom and the rotating  $\text{CH}_2\text{Br}$  fragment, and the corresponding modulation in the descending band of the delay-dependent  $\text{I}^+$  KE map in Fig. 6.5 (c). However, in the same map, there is also a larger-scale structure, the minima of which are highlighted by the dashed rectangle on the bottom of Fig. 6.5 (c).

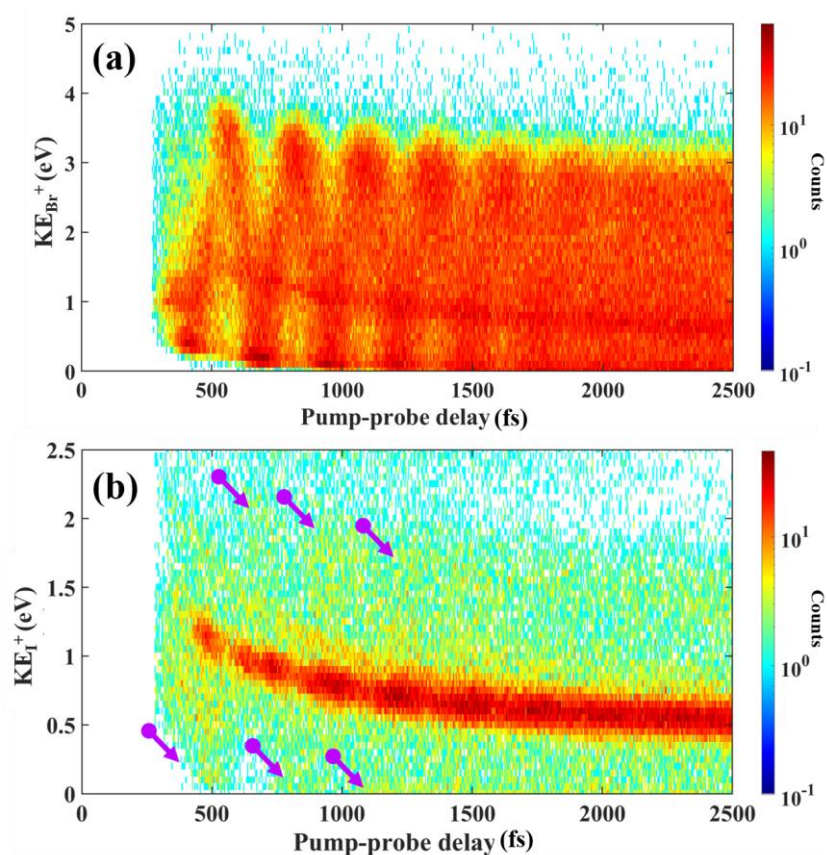


**Figure 6.8.** Gated  $\text{Br}^+$  and  $\text{I}^+$  maps. **(a)** Delay-dependent KE distribution of  $\text{Br}^+$  for the same conditions as in Fig. 6.5 ( $\text{KER} < 11\text{eV}$ ,  $\text{KE}(\text{CH}_2^+) > 4.3\text{eV}$ ), but for  $\text{KE}(\text{I}^+)$  within the descending channel shown in Fig. 6.5 (b). **(b)** Delay-dependent KE distributions of  $\text{I}^+$  for the same conditions ( $\text{KER} < 11\text{eV}$ ,  $\text{KE}(\text{CH}_2^+) > 4.3\text{eV}$ ), but for  $\text{KE}(\text{Br}^+)$  within the descending channel shown in Fig. 6.5 (a). The arrows show the maxima and minima in the weak oscillations due to  $\text{CH}_2\text{I}$  co-fragment rotation for the bromine detachment channel.

As a complementary feature, a descending band passing through the middle of the pronounced oscillation of the filtered Br KE can be also traced in Fig. 6.5 (b). Both of these features reflect the presence of a weaker dissociation channel,  $\text{CH}_2\text{I} + \text{Br}$ , which was clearly identified in the data (see the discussion in section 5.4.2). The separation of the  $\text{CH}_2\text{Br} + \text{I}$  and  $\text{CH}_2\text{I} + \text{Br}$  cannot be done based on the  $\text{CH}_2^+$  KE, since it remains rather high in both cases.

To better isolate the two competing channels, in Fig. 6.8 we present the same  $\text{Br}^+$  and  $\text{I}^+$  KE spectra as shown in Fig. 6.5, but with additional condition on the delay-dependent KE of the second halogen fragment. Specifically, in Fig. 6.8 (a) we plot  $\text{Br}^+$  data selecting the events only within the descending  $\text{I}^+$  band in Fig. 6.5 (b), whereas in Fig. 6.8 (b) for iodine, we select only the events within the descending  $\text{Br}^+$  band in Fig. 6.5 (a). The resulting spectrum for  $\text{Br}^+$  in Fig. 6.8 (a) has now even cleaner selection of events belonging to the major dissociation pathway  $\text{CH}_2\text{Br} + \text{I}$ , and only remnants of the descending band reflecting bromine detachment are visible. The selection of the  $\text{I}^+$  events in Fig. 6.8 (b) reflecting the weaker  $\text{CH}_2\text{I} + \text{Br}$  channel is less clean, containing more contamination from the dominant iodine detachment band. Nevertheless, an oscillatory structure (with maxima and minima marked by the arrows) can be now traced in this graph, reflecting the rotation of the  $\text{CH}_2\text{I}$  co-fragment in the weaker dissociation channel.

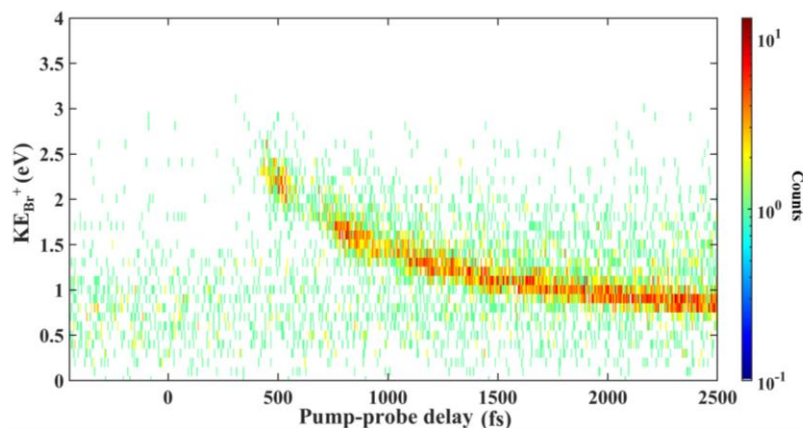


**Figure 6.9.** Delay-dependent kinetic energy distributions of  $\text{Br}^+$  with all the events satisfying the triple gates including  $\text{KER} < 11\text{eV}$ ,  $\text{KE}(\text{CH}_2^+) > 4.3\text{ eV}$  and  $\text{KE}(\text{I}^+) < 0.2\text{ eV}$ , representing the bromine detachment channel.

To visualize it, in Fig. 6.9 we plotted the corresponding  $\text{Br}^+$  events with the additional requirement that the  $\text{I}^+$  KE is below 0.2 eV (see the dashed box in Fig. 6.5 (b)), to avoid any overlap with the dominant iodine detachment band. The figure now clearly visualizes the dissociation via

the  $\text{CH}_2\text{I} + \text{Br}$  channel. Plotting the yield of the corresponding  $\text{I}^+$  events in Fig. 6.10, we observed a clear oscillation with somewhat longer period ( $\sim 330$  fs), directly reflecting the rotation of the  $\text{CH}_2\text{I}$  co-fragment.

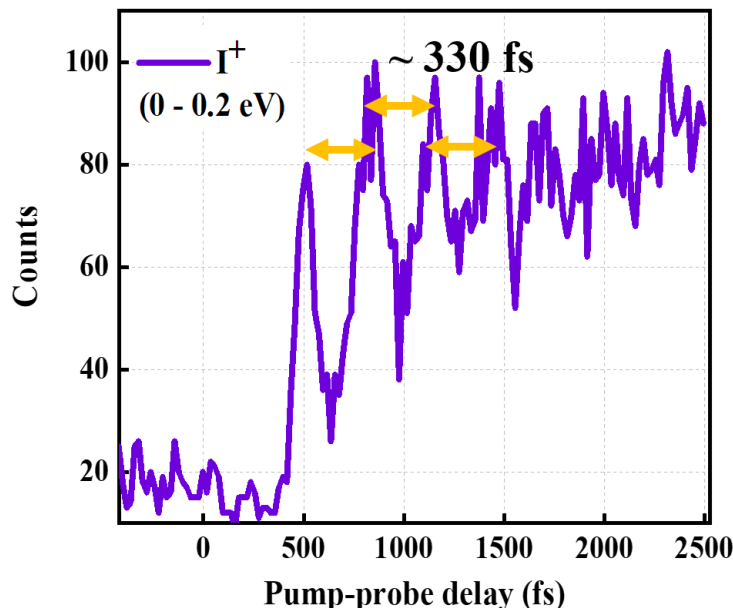


**Figure 6.10.** Delay-dependence of the  $\text{I}^+$  in the energy range of 0-0.2 eV. The oscillatory structure with a period of about 330 fs is attributed to the C-Br dissociation and the following rotational motion of the  $\text{CH}_2\text{I}$  fragment.

UV power-dependent measurements (not shown here) indicate that the observed oscillatory structures are independent of the UV pulse intensity, implying that these dynamics are not triggered by two- or three-photon excitations but mainly originate from the single UV-photon excitation.

As can be seen from the discussion of the KER- $\theta$  maps presented in Chapter 5, another useful and sometimes intuitive observable for understanding or visualizing reaction dynamics is the angle between the measured momentum vectors of the fragments. It is particularly natural to examine it in an attempt for direct visualization of rotations discussed here. Accordingly, Fig. 6.11 shows the delay-dependent momentum angles between all three pairs of the ions detected here: (a)  $\text{CH}_2^+-\text{I}^+$ , (b)  $\text{CH}_2^+-\text{Br}^+$ , and (c)  $\text{Br}^+-\text{I}^+$ . All three delay-dependent angles exhibit a clear oscillation with the same periodicity as the KE oscillations discussed earlier. When the Br atom reaches its minimum KE, the  $\text{CH}_2-\text{I}$  angle approaches nearly  $180^\circ$ , as can be expected, and the Br-I reaches its minimum. However, neither of these angular distributions cover all angles from  $0$  to  $180^\circ$ , as

one could naively expect from just the rotation of the  $\text{CH}_2\text{Br}$  molecule, and they all manifest some rather non-trivial delay dependence. This highlights once again that the measurements reported here are performed in momentum space, and the angles presented do not directly correspond to the time-dependent angles between different molecular bonds. However, this behavior can be readily rationalized based on the CESs presented in the next section.

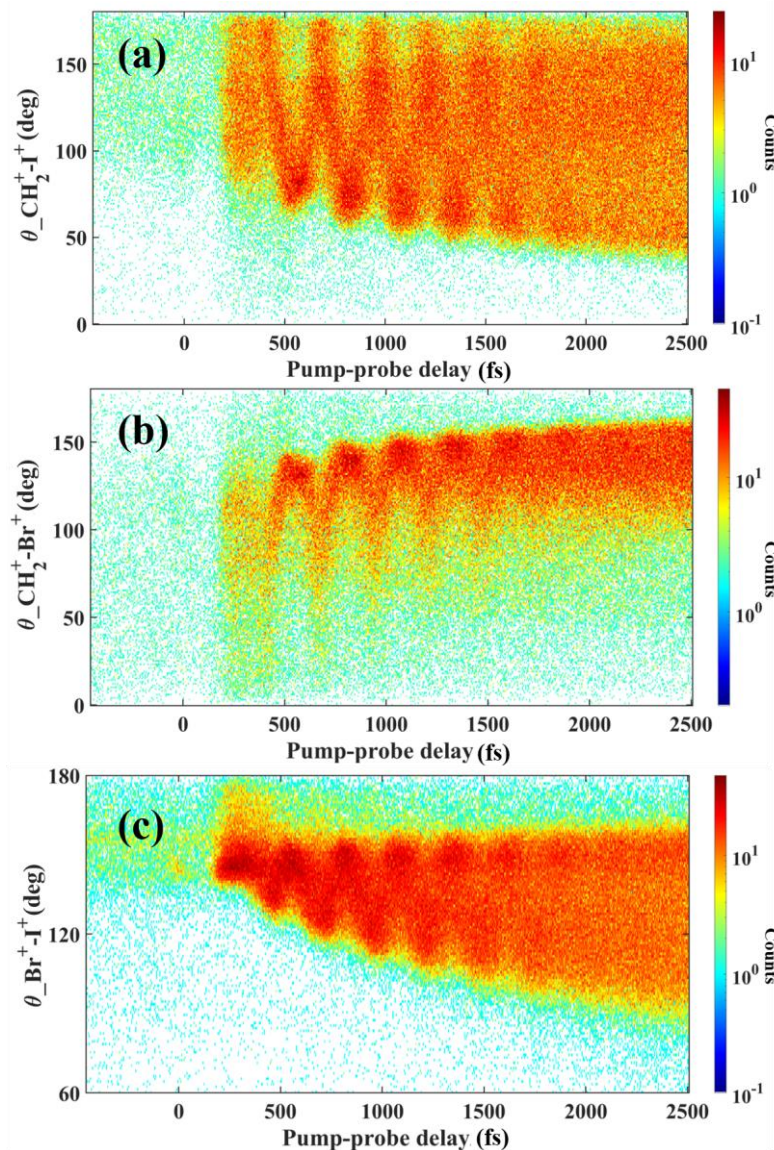


**Figure 6.11.** Delay-dependent angle between the measured momentum vectors of the two ions for (a)  $\text{CH}_2\text{-I}$ , (b)  $\text{CH}_2\text{-Br}$ , and (c)  $\text{Br-I}$ . The event selection is the same as in Fig. 6.8 (a) ( $\text{KER} < 11\text{eV}$ ,  $\text{KE}(\text{CH}_2^+) > 4.3\text{eV}$ , gated on the descending band in  $\text{I}^+$  KE distribution), ensuring that the data mainly result from  $\text{CH}_2\text{Br} + \text{I}$  dissociation channel.

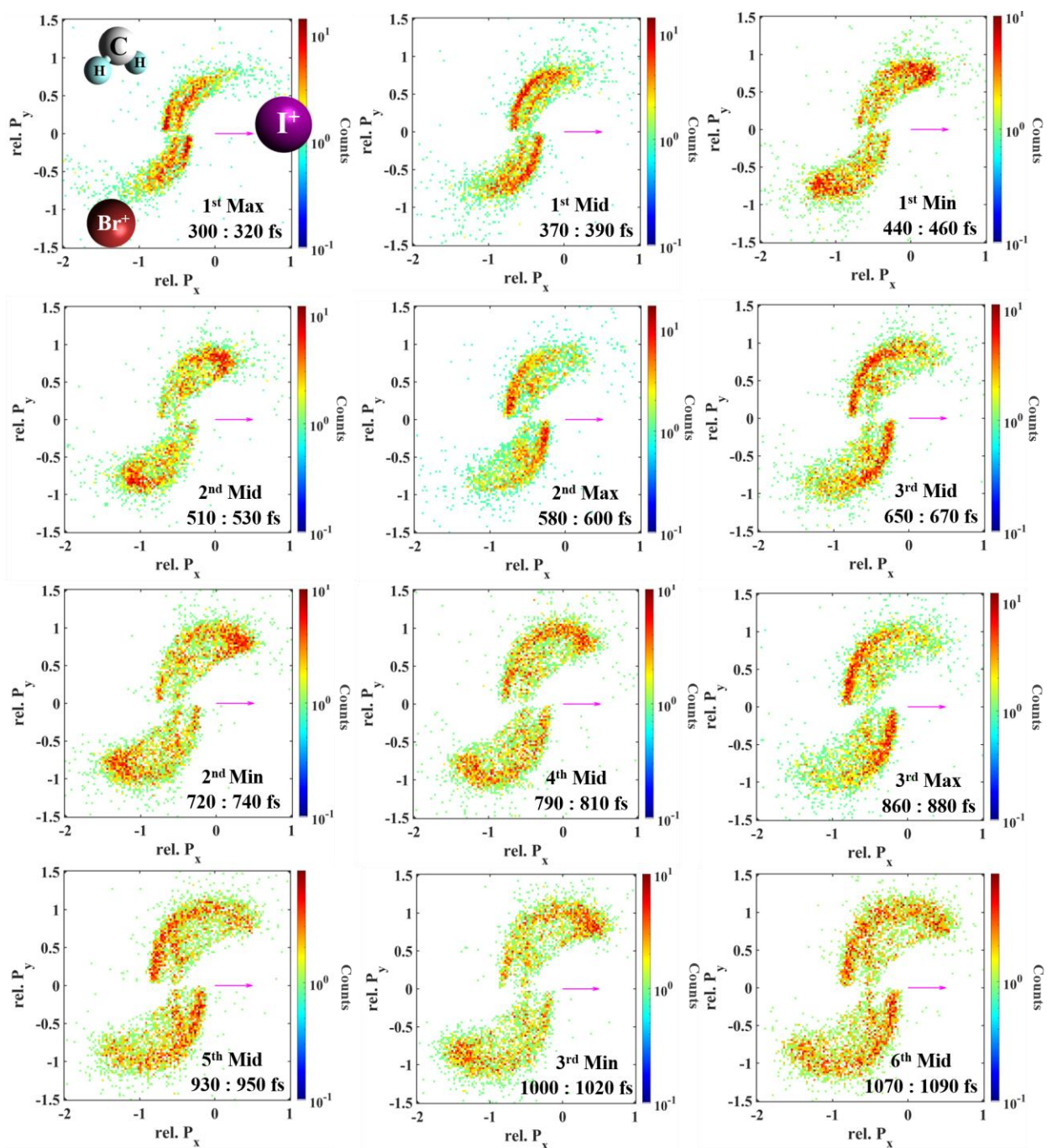


**Figure 6.12.** Time evolution of Newton diagrams with  $I^+$  momentum vector fixed along +X. Two well-separated channels are attributed to two distinct C-I and C-Br dissociation channels. A strong feature moves on the ring from the maximum to the minimum in a closed loop. The assigned fragment to each direction is indicated on the top left panel with the corresponding delay at the bottom right of each panel.

Qualitatively, there are two additional factors contributing to the non-trivial and delay-dependent changes in the angles presented in Fig. 6.11. First, the  $\text{CH}_2\text{Br}$  fragment receives an initial “momentum kick” from the dissociation, in the direction opposite to the iodine motion. Accordingly, this momentum shift is imprinted in the angles, in particular, shifting the  $\text{CH}_2^+$  and  $\text{Br}^+$  ions from the perfect back-to-back emission. Second, there is always a Coulomb repulsion between the iodine and the other two products. While the former factor can be accounted for by the “Native frames” analysis discussed in section 5.1, the latter needs to be modelled.

The ultimate goal of this work is to create a molecular movie of the dissociation reaction including the rotational motion of the polyatomic co-fragment. One possible way of doing this would be created a timed sequence of Newton diagrams, which directly visualize the relative momenta of three fragments and, thus, are sensitive to their relative positions. Such a timed sequence for the events our triple coincidence channel is plotted in Fig. 6.12 for the positions of maxima, minima and intermediate values of the  $\text{CH}_2^+$  KE oscillation shown in Fig. 6.4 (a). Here, we select the iodine momentum vector as a reference for positive X axis since this is the most natural reference frame to visualize the rotation of the  $\text{CH}_2\text{Br}$  co-fragment.

In all of the maps, there are structures reflecting the stronger C-I and the weaker C-Br dissociation channels. These two features can be also tracked in the Newton diagrams using  $\text{CH}_2^+$  fragment as a reference, shown in Fig. 6.13. We apply a gate on the more intense part of the sharp inner feature to select the most likely events for each of the selected positions, and apply this gate to the Newton maps using  $\text{I}^+$  as a reference.

The resulting set of the Newton diagrams with the iodine flying to the +X direction is shown in Fig. 6.14. This figure then directly visualizes the delay-dependent orientation of the  $\text{CH}_2\text{Br}$  axis with respect to the dissociation direction. Remarkably, the magnitude of the relative momenta also changes, highlighting the influence of the mutual orientation on the fragment energy sharing.

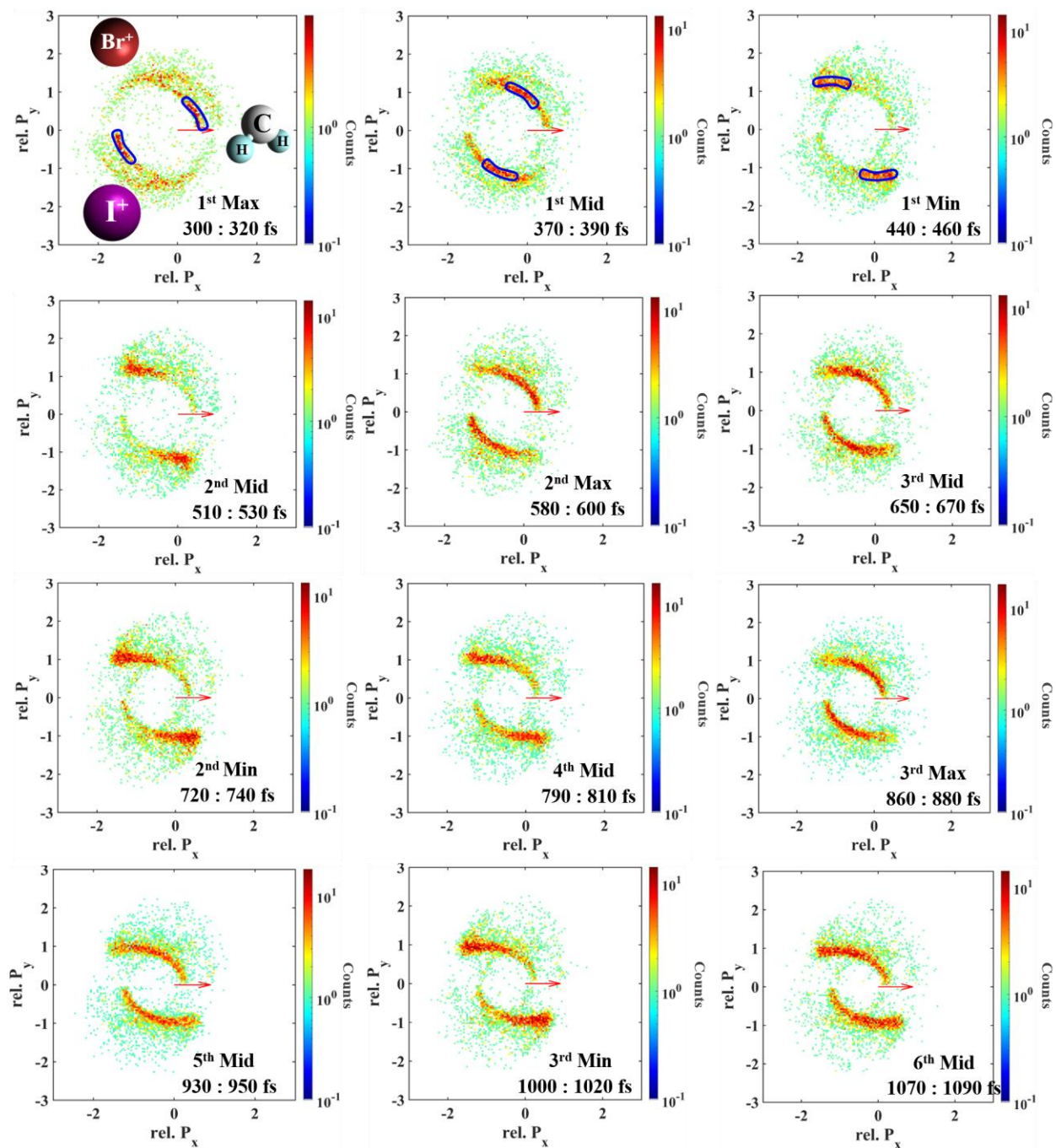


**Figure 6.13.** Time evolution of Newton diagrams with  $\text{CH}_2^+$  momentum vector fixed along  $+X$ . A pronounced feature that moves on the inner structure from “maximum” to “minimum”, marked in blue in the first three panels, is used for filtering the other set of Newton diagrams.

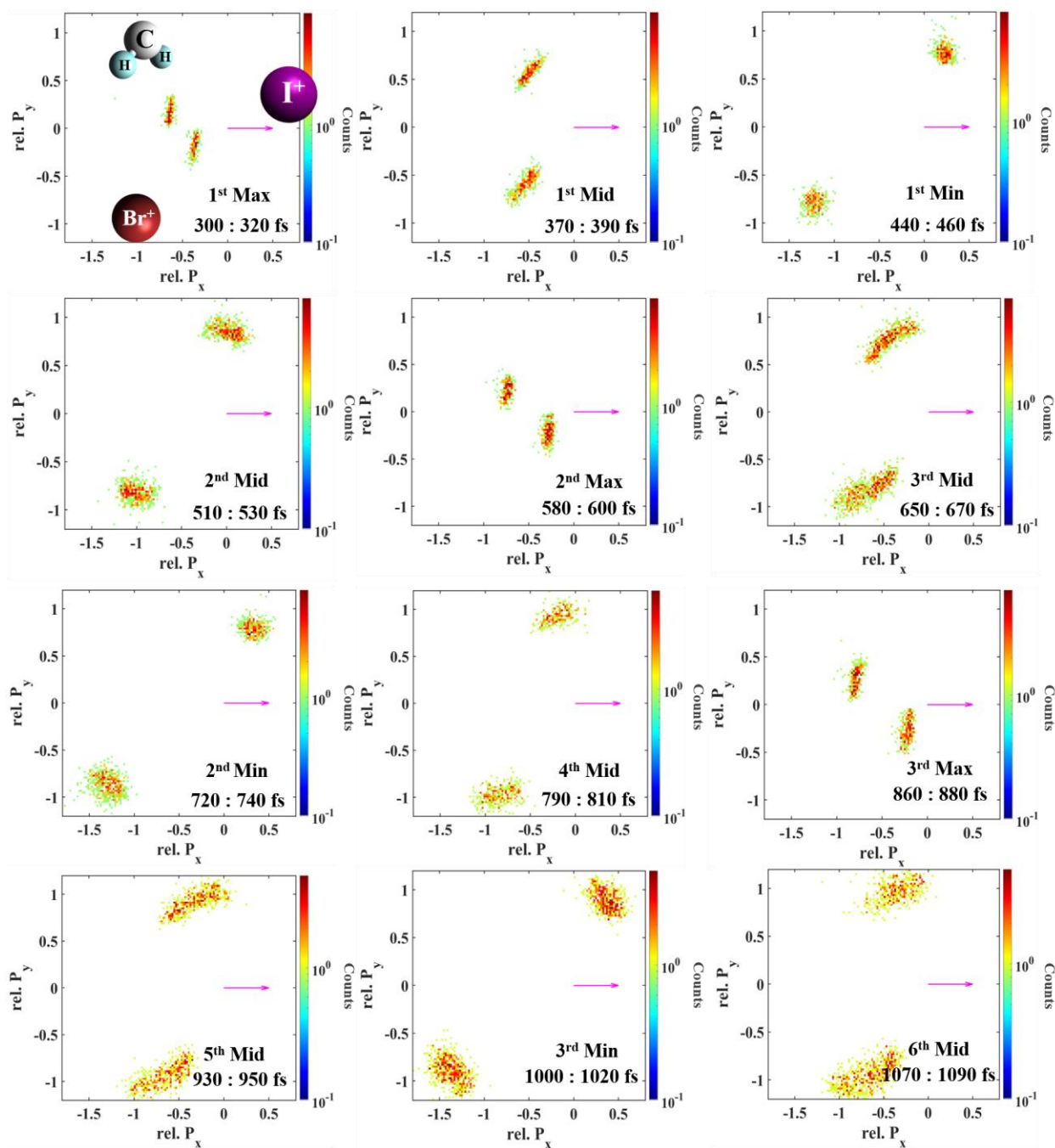


**Figure 6.14.** A set of gated Newton diagrams showing the  $\text{CH}_2^+$  and  $\text{Br}^+$  relative momenta with respect to the  $\text{I}^+$  flying to the right. At the “maximum” points (referred to  $\text{CH}_2^+$  KE), Br is in the middle close to the iodine while  $\text{CH}_2$  is on the outside. In the minimum, the  $\text{CH}_2$  is in-between, the two halogen atoms.

### 6.3 Molecular dynamics and Coulomb explosion simulations

The energy partitioning between translational and internal modes in the photodissociation process across the repulsive PES can be estimated using a rigid radical approximation of the impulsive mode. In the rigid radical limit, it is assumed that the dissociation is impulsive and the flow of energy into the vibrational degrees of freedom of the fragments is ignored. According to the rigid radical model, most of the available energy should be partitioned into translational and rotational energy. The rotational motion appears as oscillatory structure in the delay-dependent observables, e.g., kinetic energies and the relative momentum angles of the detected ions. To rationalize the experimental findings and underpin the correlation between the time-dependent oscillatory signal and the rotational motion, Dr. Enliang Wang from Dr. Rudenko's group performed molecular dynamics simulations of the UV-induced dissociation combined with Coulomb explosion simulations. We will show some related results in the following to compare with our experimental data.

The molecular dynamics on the repulsive PES prepared by the pump pulse were simulated by a classical model. We create a bunch of trajectories by increasing the C-I bond length. For each time, we extracted the position and velocity of the molecule to perform the Coulomb explosion simulation for the  $\text{CH}_2^+\text{Br}^+\text{I}^+$  final state. The initial geometry is set to be at equilibrium configuration of a neutral molecule with zero velocity. The C-I body dissociation was assumed to reach asymptotic velocities ( $v_f$ ) with an exponential rise function. The time-dependent relative velocity  $v(t)$  and internuclear distance  $R(t)$  between the two fragments are described by

$$v(t) = v_f \left[ 1 - \left( 1 - \frac{v_0}{v_f} \right) e^{-t/\tau} \right] \quad 6.3$$

$$R(t) = v_f t + (v_f - v_0) (e^{-t/\tau} - 1) \tau + R_0. \quad 6.4$$

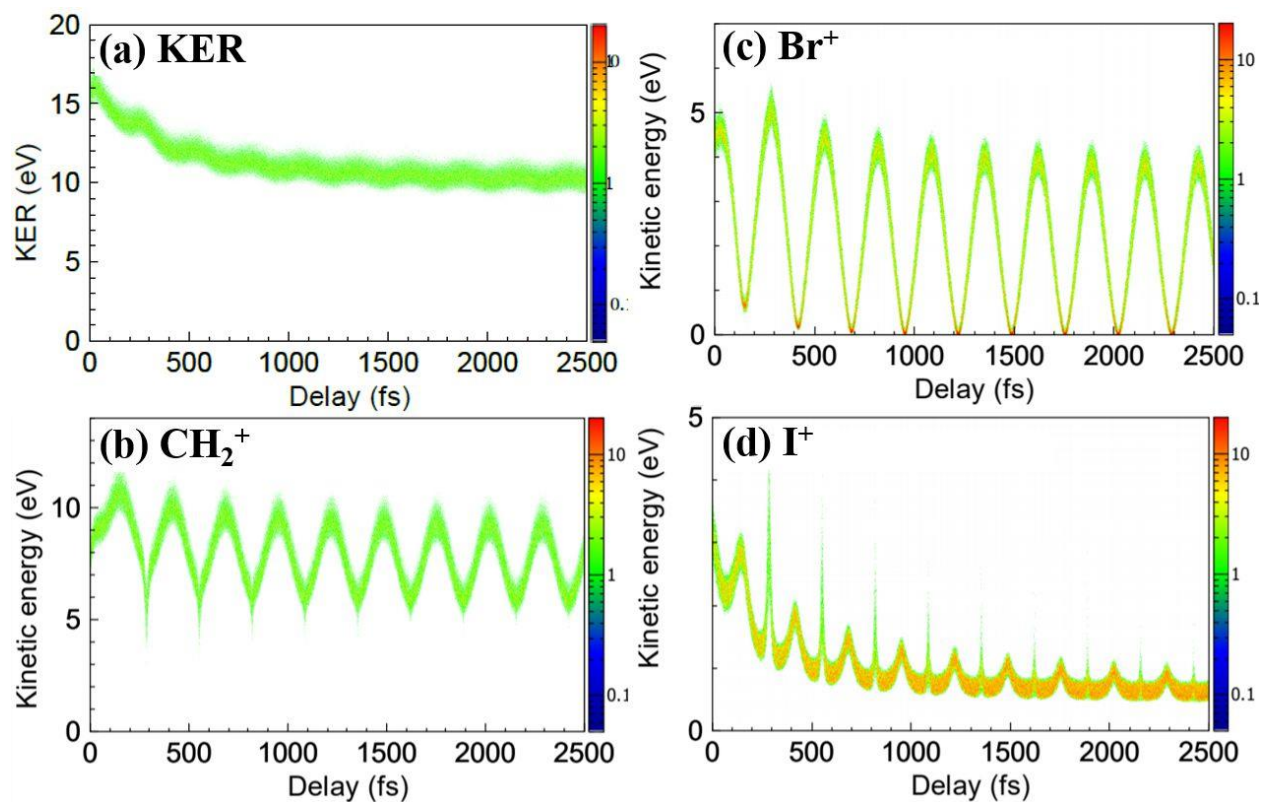
Here,  $\tau$  is the lifetime of the dissociative state, which were determined to be 50 and 115 fs for the C-I and C-Br bonds dissociations, respectively, by Attar et al. [279];  $v_0$  and  $R_0$  are the initial relative velocity and internuclear distance between the two fragments, respectively, sampled by a quantum harmonic oscillator. The asymptotic velocities ( $v_f$ ) were determined by the experimental KER of the precursor dissociation channel at 20 ps delay to subtract the Coulombic contribution from the kinetic energies. We consider the  $\text{CH}_2\text{Br}$  radicals to be rigid rotators where the exponential rise function also describes the rotational velocity with the same lifetime as the bond dissociation.

$$\omega(t) = \omega_f \left[ 1 - \left( 1 - \frac{\omega_0}{\omega_f} \right) e^{-t/\tau} \right] \quad 6.5$$

$$\theta(t) = \omega_f t + (\omega_f - \omega_0) \left( e^{-\frac{t}{\tau}} - 1 \right) \tau + \theta_0 \quad 6.6$$

where  $\omega_0$  is the initial angular velocity, and  $\omega_f$  is the asymptotic rotational velocity, which is determined by fitting the *ab initio* calculations to be  $\omega_f = 1.35^\circ/\text{fs}$ . A minor adjustment was performed on the rotational velocity to get the best fit for the experiments.

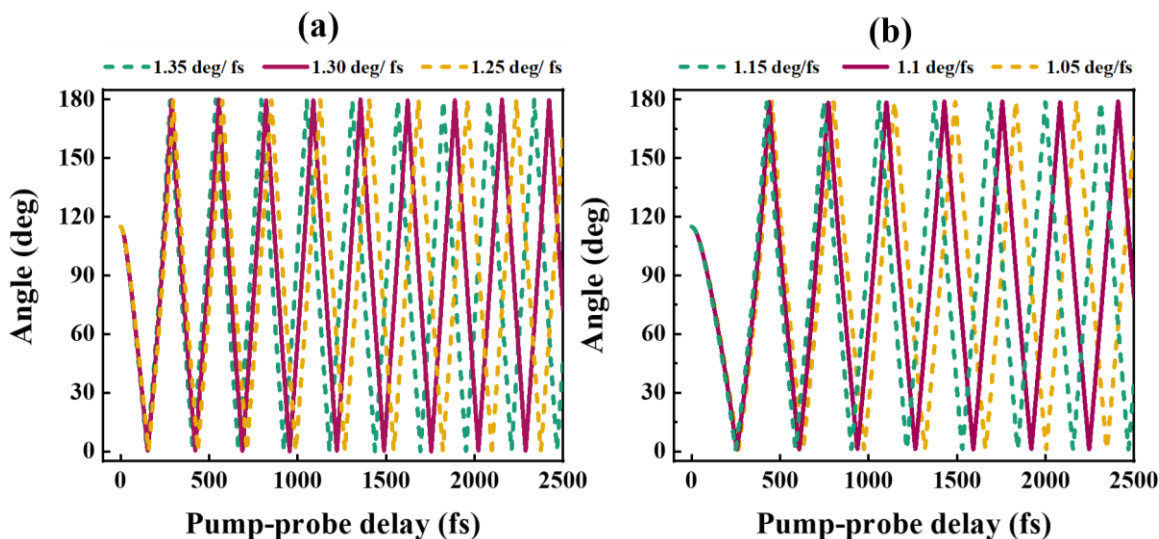
In order to authenticate the interpreted experimental results and produce a detailed picture of the structural evolution of the molecule following UV photoexcitation, we reproduced the time-dependent kinetic energy and molecular angular correlations and compared them with the experimental results. The 2D delay-dependent kinetic energy distributions are shown in Fig. 6.15. The first glimpse looks similar to the experiments having approximately the same periodicity and anti-correlation between the  $\text{Br}^+$  and  $\text{CH}_2^+$  fragments.



**Figure 6.15.** Simulated delay-dependent KER distributions of the  $\text{CH}_2^+ + \text{Br}^+ + \text{I}^+$  coincident channel and the KE distributions of the individual ions. The distributions show oscillation with the periodicity of about 280 fs and the anti-correlation between the fragments.

The double frequency of iodine KE modulation corresponds to the fact that the iodine KE is large every time the geometry approaches linear, and it is sharper if the CH<sub>2</sub> is in the middle. The CH<sub>2</sub>Br is rotating around its center of mass, which lies near the Br atom with the heavy mass. When CH<sub>2</sub> is in the middle, the distance between iodine and CH<sub>2</sub> is shorter, resulting in energy enhancement.

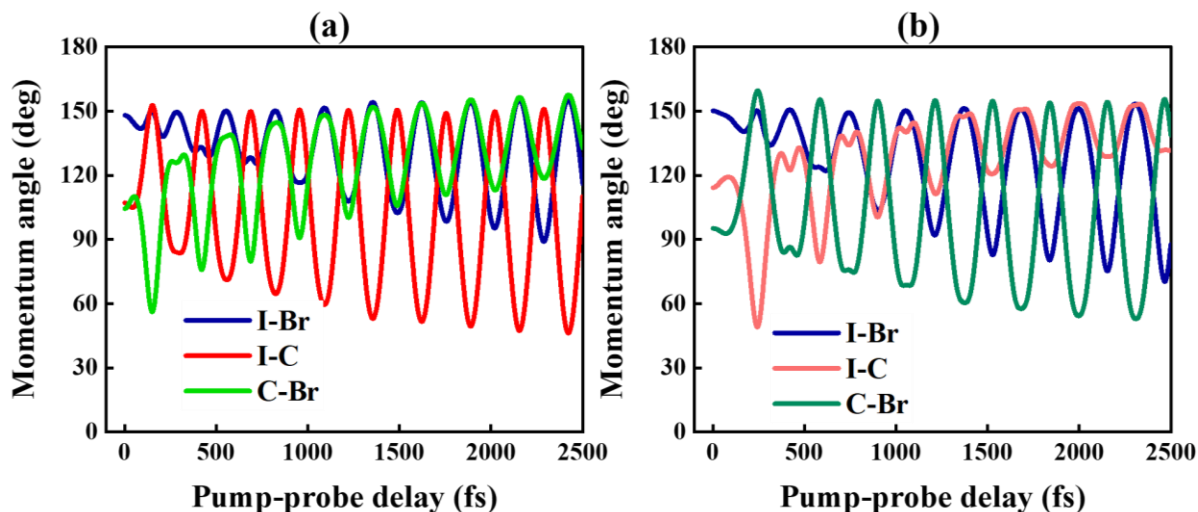
Fig. 6.16 (a) and (b) shows the I-C-Br bond angle as a function of time delay for each rotational velocity during the C-I and C-Br bond dissociation. These graphs show that analogous oscillations with identical periodic structures are observed in agreement with the experiments. Within the Frank-Condon region, the molecule dissociates starting from an area of the repulsive PES, which induces a small width of the rotational velocity. As shown by the blue, green, and magenta curves in these figures, a small difference of 0.05 °/fs of the rotational velocity exhibits dephasing at large time delays. We can resolve the rotational structure before the dephasing by taking advantage of the high temporal resolution.



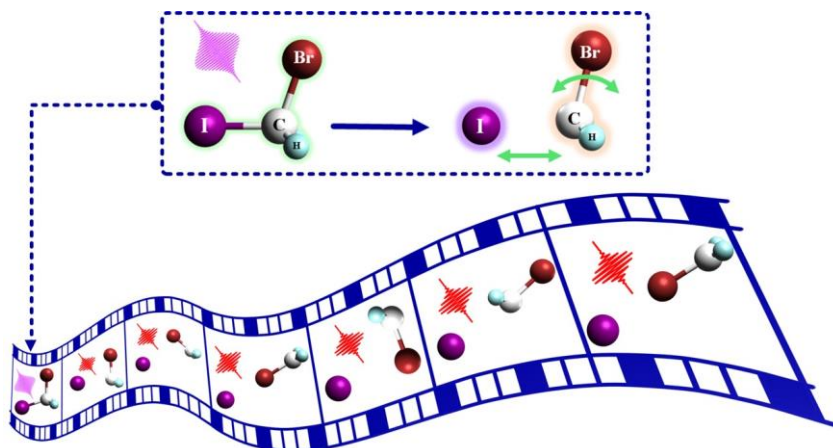
**Figure 6.16.** Time-dependent molecular bond angle, defined by C-I and C-Br bonds, in different carbon-halogen bond dissociation. **(a)** The molecular bond angle for the C-I bond dissociation for the rotation velocity of 1.35, 1.30, and 1.25°/fs are shown with the blue, green, and magenta curves. **(b)** The molecular bond angle for the C-Br bond dissociation for the rotation velocity of 1.15, 1.1, and 1.05 °/fs are shown with the blue, green, and magenta curves.

The Coulomb explosion model was introduced to describe the CE, where the atomic position and velocity were obtained by solving the equation of the motion assuming instantaneous

vertical ionization to the purely Coulombic triply-charged final state. Performing the CE simulation, every atom's three-dimensional momentum vector, the direct experimental observables, is determined. Fig. 6.17 (a) and (b) show the simulated momentum angles.



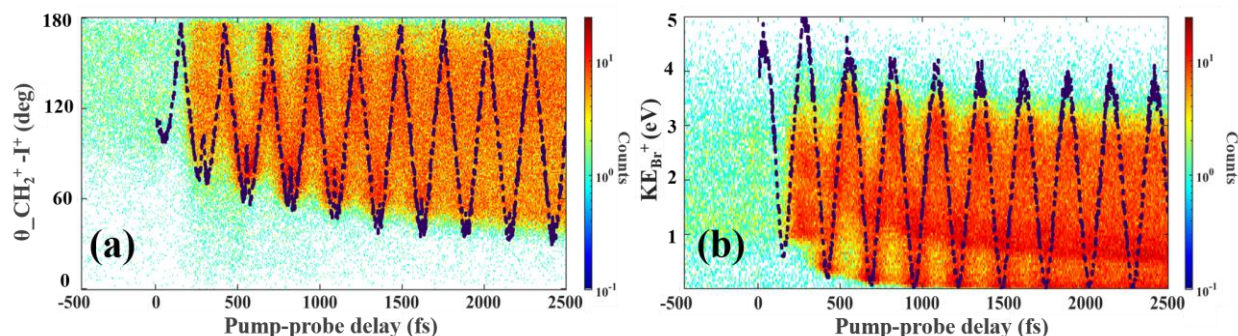
**Figure 6.17.** Simulated momentum angles for the C-I and C-Br bond dissociation. **(a)** The relative angles, defined by the momentum vectors of  $I^+$ ,  $Br^+$ , and  $CH_2^+$ , are determined by the Coulomb explosion simulation with a rotational velocity of  $1.35^\circ/\text{fs}$  for the C-I bond dissociation. **(b)** The relative angles, with a rotational velocity of  $1.1^\circ/\text{fs}$  for the C-Br bond dissociation. The blue, red and green curves correspond to the relative momentum angle defined by  $I^+ - Br^+$ ,  $I^+ - CH_2^+$ , and  $CH_2^+ - Br^+$  momentum vectors.



**Figure 6.18.** Cartoon snapshots of the molecular structure generated from simulations at different delays are stacked. At zero fs, the general motions are indicated by the green arrows. The dynamics include dissociation of the molecule and rotation of the  $CH_2Br$  co-fragment around the  $CH_2$ .

The oscillations explicitly reflect the molecular rotational motion. Fig. 6.18 shows a series of cartoon snapshots taken from molecular dynamic simulations to capture the general dynamics of the molecule following the UV-photon absorption. The two arrows shown in the first frame indicate the overall motion of the molecule displayed in the subsequent frames: dissociation of the C-I bond and the rotation of the co-fragment. These are probed by the strong-field ionization. The simulations could be improved by convolution with a Gaussian distribution with the FWHM of the experimental cross-correlation to consider the instrument response function correlated to the experimental measurements.

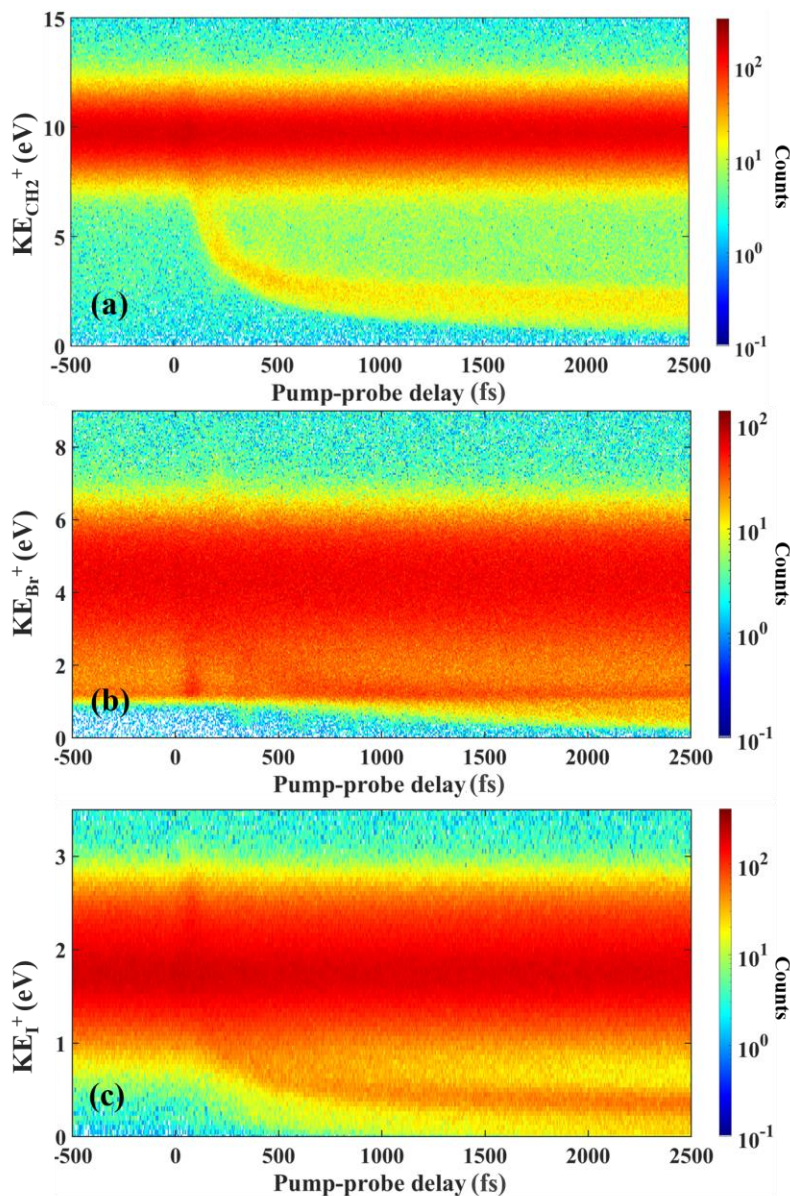
Overlaying the simulations on the experimental results highlights a good agreement between the two. The delay-dependent angle between the momenta of the  $\text{CH}_2^+$  and  $\text{I}^+$  is shown in Fig. 6.19 (a). This graph gives an intuitive picture of the photodissociation dynamics of the molecule after the UV-photon excitation. The oscillations with a period identical to the temporal modulation of the individual fragment's kinetic energy distribution shown in Fig 6.19 (b) illustrate the rotation of the  $\text{CH}_2\text{Br}$  fragment. This relative angle spans all the angles between zero degrees, representing a linear geometry where the Br atom is located in the middle of the  $\text{CH}_2$  and I, and a larger angle close to 180 degrees. This angle has not reached 180 could be explained by the influence of the iodine repulsion, which decreases as a function of delay but is nonnegligible at nearly 2.5 ps in this graph.



**Figure 6.19.** Comparison of the outcome of CES with experimental results. Delay-dependent (a) relative momentum angle of  $\text{CH}_2^+$  and  $\text{I}^+$  and (b) kinetic energy distributions of  $\text{Br}^+$  fragments overlaid with the results of a molecular dynamics simulation described in the text. The dotted lines indicate a half-period phase shift between the strong oscillatory features visible in (a) and (b).

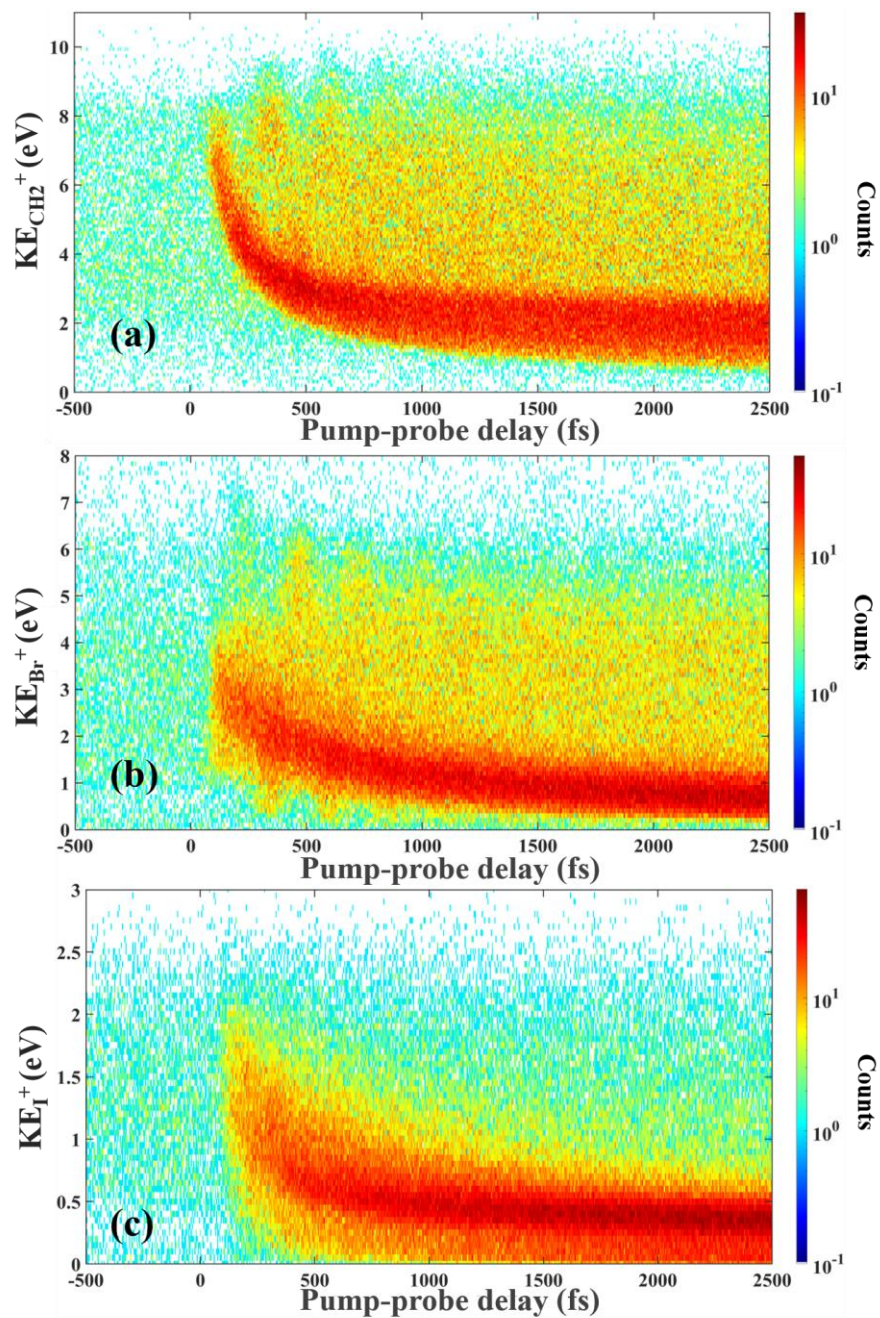
## 6.4 Imaging the rotational motion in CH<sub>2</sub>ClI triggered by ultraviolet light

In order to check whether the observations presented in the previous sections can be generalized for other dihalomethanes and look for the similarities and differences in the characteristics, we performed a similar set of experiments on the CH<sub>2</sub>ClI molecule. Below, we present a brief overview of the related results of the CH<sub>2</sub>ClI experiments.



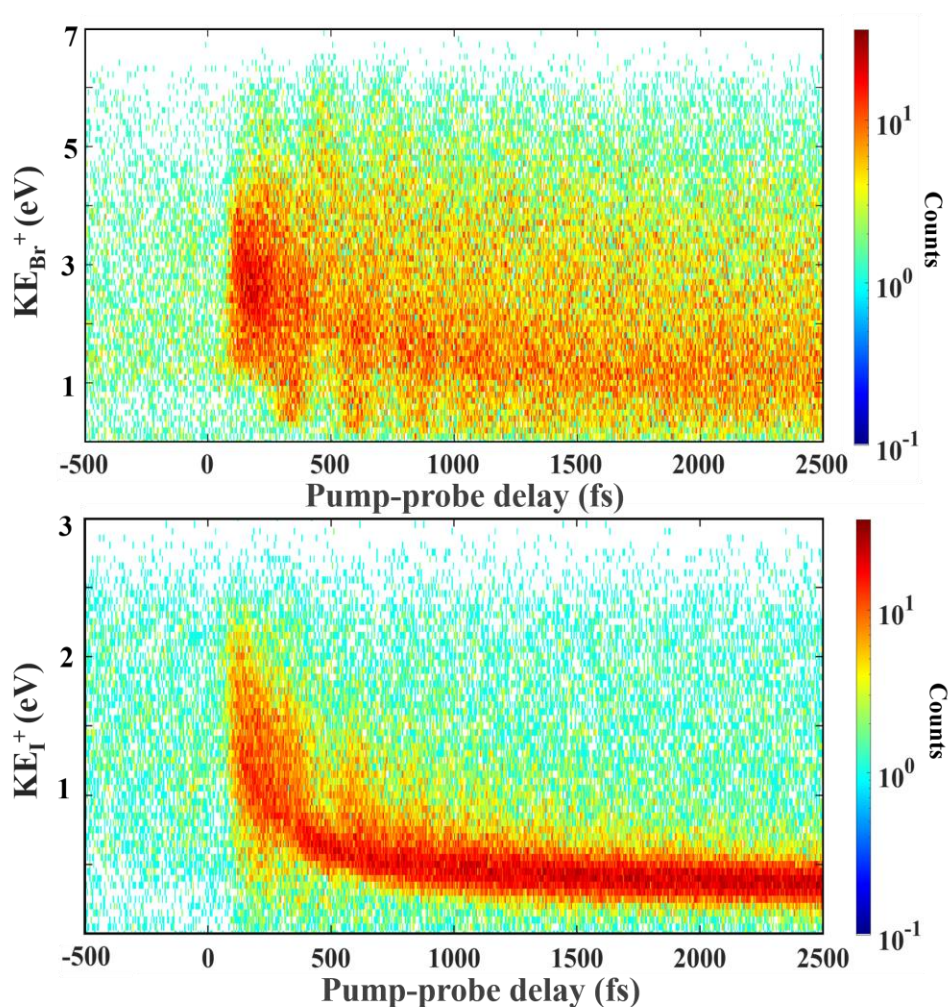
**Figure 6.20.** Delay-dependent kinetic energy distributions of the individual fragment ions. (a) CH<sub>2</sub><sup>+</sup>, (b) Cl<sup>+</sup>, and (c) I<sup>+</sup> in the three-body coincidence channel CH<sub>2</sub><sup>+</sup>+Cl<sup>+</sup>+I<sup>+</sup> show hints of periodic oscillatory features in dissociating molecules; they are much less pronounced or washed out in total KER.

Fig. 6.20 (a-c) shows the delay-dependent kinetic energy distributions of the individual ions for the  $\text{CH}_2^+ + \text{Cl}^+ + \text{I}^+$  final state. The maps contain the features discussed earlier in the  $\text{CH}_2\text{BrI}$  molecule, showing signs of periodic oscillatory features in dissociating molecules. Similar to  $\text{CH}_2\text{BrI}$ , these oscillations are nearly washed out in total KER shown in Fig. 5.44, making it challenging to track them.



**Figure 6.21.** Delay-dependent kinetic energy distributions of the individual fragment ions (a)  $\text{CH}_2^+$ , (b)  $\text{Cl}^+$ , and (c)  $\text{I}^+$  in the three-body coincidence channel  $\text{CH}_2^+ + \text{Cl}^+ + \text{I}^+$  with  $\text{KER} < 12$  eV.

We follow the same gating procedure that we described in the previous section to track and visualize the oscillations and look for the characteristics of the rotational motion associated with these oscillatory structures. In order to separate bound and dissociating molecules, we filter out all events with  $\text{KER} > 12$  eV. Fig. 6.21 (a-c) shows the individual fragments KEs after applying this condition, where the periodic oscillations are visible at least in the first two fragments—gating out the low energy three-body and CII formation events ( $\text{KE}(\text{CH}_2^+) < 4$  eV) in the  $\text{Cl}^+$  and  $\text{I}^+$  KE distributions, we get partially isolated oscillations.



**Figure 6.22.** Delay-dependent kinetic energy distributions of the individual fragment ions (a)  $\text{Br}^+$  and (b)  $\text{I}^+$  in  $\text{CH}_2^+ + \text{Cl}^+ + \text{I}^+$  coincident channel; all coincident events with  $\text{KER} < 12$  eV and  $\text{KE}(\text{CH}_2^+) > 4$  eV.

As shown in Fig. 6.22 (a), the Cl kinetic energy periodically approaches zero, which, as discussed in the previous sections, suggests that at these time the molecule approaches linear geometry. The projections of the individual two-dimensional maps of the  $\text{CH}_2^+$  and  $\text{Cl}^+$  KEs onto the delay axis and the FFT of the corresponding  $\text{CH}_2^+$  signal shown in Fig. 6.23 (a) and (b), respectively, indicate that the  $\text{CH}_2\text{Cl}$  rotation period is about 250 fs. Similar to the results discussed earlier for  $\text{CH}_2\text{BrI}$ , these oscillations can be assigned to the rotational motion of the  $\text{CH}_2\text{Cl}$  fragment resulting from the C-I bond cleavage of the molecule following UV excitation and dissociation of  $\text{CH}_2\text{CII}$ .

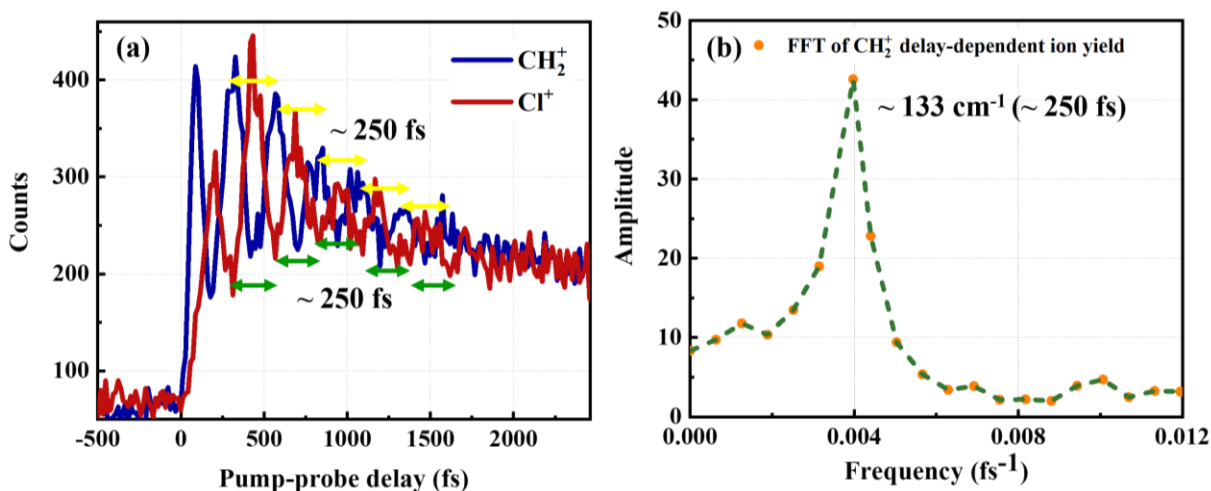


**Figure 6.23.** (a) Delay dependence of  $\text{CH}_2^+$  and  $\text{Cl}^+$  ion yields in the non-horizontal bands containing pronounced oscillations with a period of 250 fs. The oscillations are anti-correlated and washed out after several cycles in nearly 2 ps. (b) An FFT of modulating yields peaks at the frequency corresponding to a period of 250 fs.

## 6.5 Summary

In summary, we carried out time-resolved Coulomb explosion imaging of rotational motion of the polyatomic co-fragments in  $\text{CH}_2\text{BrI}$  and  $\text{CH}_2\text{CII}$  dissociation induced by the photoexcitation in the A-band. These rotations appear as oscillatory structures in the delay-dependent observables in our coincidence measurements, such as fragment's KEs and relative angles between their momenta. In  $\text{CH}_2\text{Br}$ , these oscillations show 280 and 330 fs periodicity for the C-I and C-Br bond cleavage, respectively. The two constituents of the rotating fragment exhibit KE oscillations out of phase, highlighting two different possibilities for quasi-linear orientation of the constituents of

the dissociating molecule. Varying angular velocities of the induced rotation result in rapid dephasing of the oscillations after several cycles. The results for CH<sub>2</sub>ClI show signatures of similar dynamics with somewhat shorter oscillation period (~250 fs).

We simulated the dissociation and rotational dynamics by modelling trajectories for the radical co-fragment, which is regarded as a rigid rotator, as the bond length increases. The outcome of the simulations agrees well with our experimental results, confirming the reasons for dephasing and highlighting once again how the molecule periodically approaches a nearly linear geometry, which is reflected in the anti-correlated oscillations of the CH<sub>2</sub><sup>+</sup> KE and the KE of the second halogen fragment. Thus, a combination of the experimental and simulation results provides a very detailed and visual picture of the correlated motion of molecular constituents during photodissociation.

## Chapter 7 - Pre-dissociation dynamics of CH<sub>3</sub>I in its B-band

This chapter briefly describes the preliminary experimental results on photodissociation dynamics in the B-band of CH<sub>3</sub>I excited at 198 nm. As discussed in Chapter 2, photoabsorption in the B-band results in the population of the lowest-lying Rydberg states, and their photodissociation mechanisms are different from the A-band dynamics discussed in Chapter 4. The B-band exhibits a clear bound nature with distinct vibrational structures, and the corresponding absorption spectrum is dominated by the resonance lines, which show finite lifetimes related to the pre-dissociation (see Fig. 2.10 and the corresponding discussion). As illustrated in Fig. 2.9, following excitation to the B-band, which corresponds to a perpendicular transition to the low energy <sup>3</sup>R<sub>1</sub> Rydberg state [121], CH<sub>3</sub>I mainly undergoes a pre-dissociation that involves population transfer from the excited vibrational state of a bound Rydberg state to a repulsive valence state. The dissociative state mainly involved in the cleavage of the C–I bond after photoabsorption around 200 nm is the <sup>3</sup>A<sub>1</sub> (A<sub>2</sub>) state, a component of the repulsive <sup>3</sup>Q<sub>0</sub> state belonging to the *A-band*. The time-resolved studies of these dynamics are rather scarce [162], [170]–[173], [176], and the goal of this work is an attempt to obtain additional time-domain information on the B-band dissociation dynamics taking advantage of advanced experimental schemes and tools discussed in the previous chapters of this work.

Similar to the other time-resolved experiments presented in this thesis, our study probes the photodissociated fragments by strong-field ionization to higher charged states. In particular, we monitor the time-dependent kinetic energy distributions and yields of different fragmentation channels produced via strong-field ionization by an intense NIR probe pulse.

In analogy to the previous chapters, we start the discussion with a brief overview of the ionization and fragmentation of the molecule irradiated with a single UV pulse at 198 nm. Due to the initial interest in dynamics of the lowest-lying Rydberg states triggered by the UV pulse (with about 6.25 eV), we committed ourselves to use rather low UV intensities to minimize the ionization of the molecule and, thus, avoid competing two-photon transition to ionic states. Although there are always some contributions from the higher-order processes because of our tight UV focus, the selected low intensities keep their probability rather low. Since in this experiment the molecule was probed at higher NIR intensity than in the A-band studies, we also present the results obtained with a single NIR pulse, which shows fragmentation to the higher charged states.

As shown in Chapter 3 (Fig. 3.17), the characterization measurements show a pump-probe temporal resolution of about 100 fs, suitable for following the molecule's pre-dissociation dynamics, which is expected to occur on relatively long (picosecond) timescales [172], [175], [289]. The NIR peak intensity used in this experiment was  $8 \times 10^{14}$  W/cm<sup>2</sup>. Using the beam parameters, the UV pulse intensity was estimated to be  $5 \times 10^{12}$  W/cm<sup>2</sup>.

## 7.1 Ionization by the 198-nm UV pulse

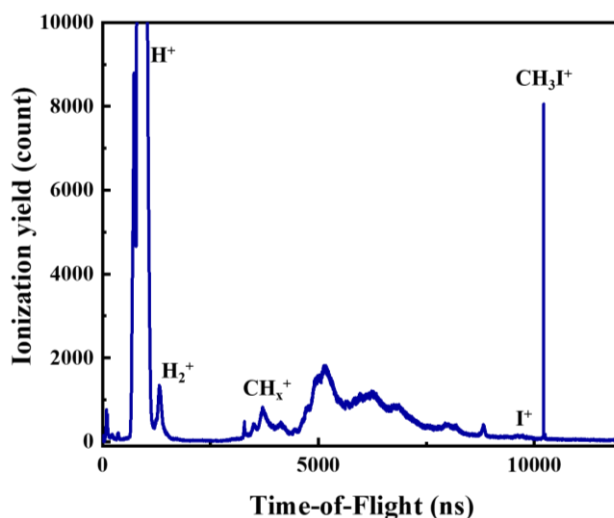


**Figure 7.1.** Time-of-Flight (TOF) spectrum of the ions generated upon irradiation of the CH<sub>3</sub>I molecule with a single UV pulse at 198 nm central wavelength and  $5 \times 10^{12}$  W/cm<sup>2</sup> intensity. The TOF peaks for ions that can potentially result from the CH<sub>3</sub>I target are labeled based on their mass-to-charge ratio. A broad unlabeled structure that peaks at 5000 ns and extends to larger TOFs is due to the background signal (most likely, resulting from some low- $I_p$  hydrocarbon contamination).

Fig. 7.1 shows the measured TOF spectrum illustrating the fragmentation and ionization pattern of the molecule after irradiation with a 198-nm UV pulse with a peak intensity of  $5 \times 10^{12}$  W/cm<sup>2</sup>. While the dominant ion is H<sup>+</sup>, much of which may stem from the ionization of contaminations present in the chamber from previous experiments, there is a significant amount of the singly charged molecular parent ion and weak signatures of the methyl and iodine ions.

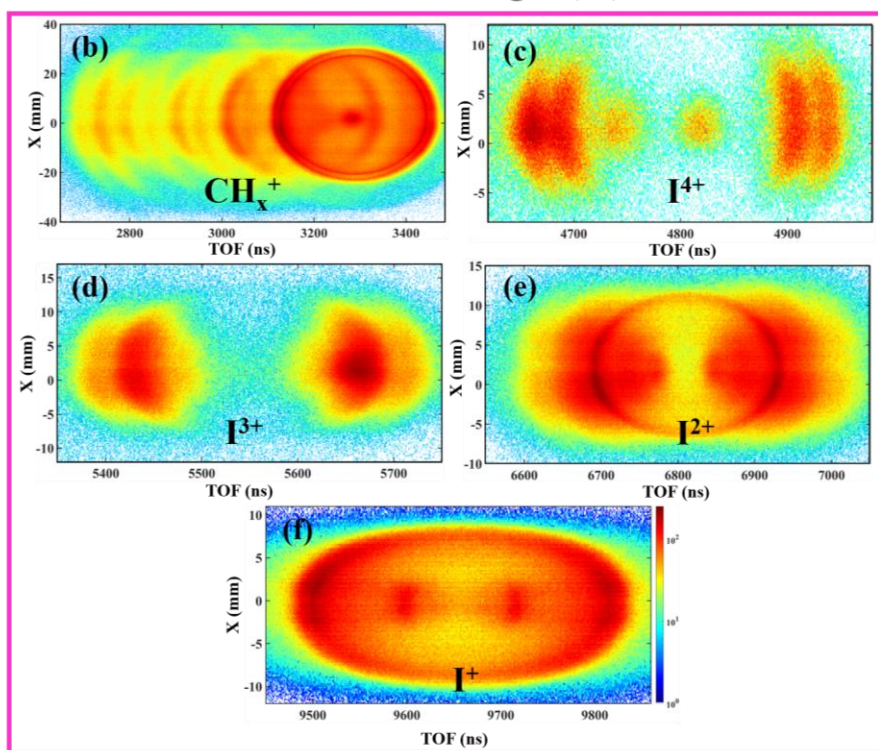
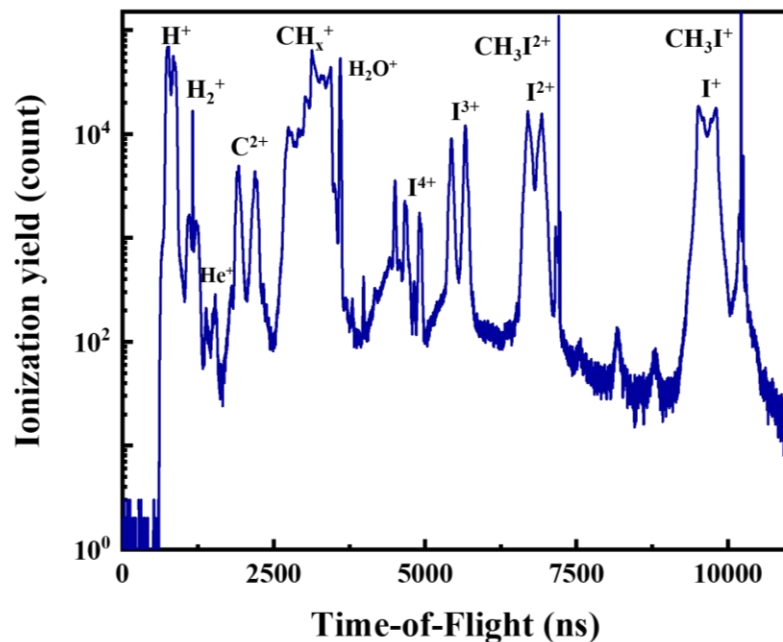


**Figure 7.2.** (a) Time-of-flight (TOF) spectrum of the ions generated upon irradiation of the  $\text{CH}_3\text{I}$  molecule with a single NIR pulse with an intensity of  $8 \times 10^{14} \text{ W/cm}^2$ . (b-f) The TOF-position maps of selected ions showing distinct contributions from various the DI and CE channels.

In addition, a broad structure between the rather sharp  $\text{CH}_x^+$  and  $\text{I}^+$  peaks originate from various residual gas contributions, in particular, due to some hydrocarbon contamination from previous experiments. The shape of the methyl and iodine TOF peaks with pronounced maxima at the zero-momentum points suggests that these fragment ions originate from dissociative ionization with a neutral partner rather than Coulomb explosion. On top of that, we did not observe any meaningful coincident events, confirming the absence of double ionization and Coulomb explosion signal.

## 7.2 Ionization and fragmentation by a single NIR pulse at relatively high intensity

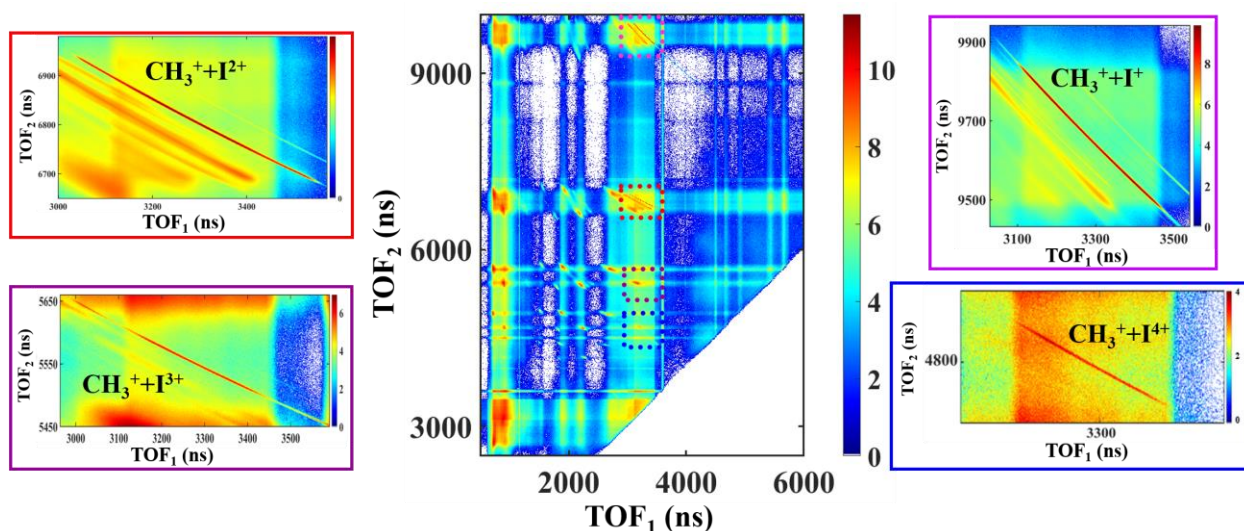


**Figure 7.3.** PIPICO map for fragmentation of  $\text{CH}_3\text{I}$  after a single NIR pulse at  $8 \times 10^{14} \text{ W/cm}^2$ . The dashed boxes indicate the complete coincident channels whose zoomed-in pictures are shown surrounding the map. We have several complete channels at the selected NIR pulse intensity, up to a total charge state of 5+.

Fig. 7.2 shows the TOF and TOF-position spectra for ionization of  $\text{CH}_3\text{I}$  by a NIR pulse with an intensity of  $8 \times 10^{14} \text{ W/cm}^2$ . Comparison of this spectrum with the TOF spectrum at lower pulse intensity ( $2.8 \times 10^{14} \text{ W/cm}^2$ ) in Fig. 4.8 showcases an increased contribution of highly-charged ions, with more pronounced peaks of doubly-charged parent ion as well as triply- and quadruply-charged iodine ions. The 2-D maps illustrate the pronounced Coulomb explosion rings

from higher-energy photofragments. The corresponding PIPICO map is shown in Fig. 7.3 with insets highlighting the dominant complete coincident channels ( $\text{CH}_3^+ + \text{I}^+$ ,  $\text{CH}_3^+ + \text{I}^{2+}$ ,  $\text{CH}_3^+ + \text{I}^{3+}$ , and  $\text{CH}_3^+ + \text{I}^{4+}$ ) for various final charge states that will be discussed in this work. As expected, we also observe several incomplete channels whose analysis is beyond the scope of this work.

### 7.3 Time-resolved dissociation dynamics observed via two-body breakup channels

Following our approach to mapping two-body dissociation dynamics, we trace the time evolution of the coincident channels discussed in the previous section. Fig. 7.4 shows the delay-dependent KER distribution for the dominant  $\text{CH}_3^+ + \text{I}^+$  channel. At a first glance, we can identify the delay-independent high-KER band, which appears to be rather similar to the ones observed in Figs. 4.14 and 4.17, as well some broad descending features at lower KER values. As in the results for 263 nm pump in Ch. 4, these delay-independent and delay-dependent bands reflect the contributions from the bound and dissociating molecules, respectively. However, the descending lower KER features are very different from the maps showing the results obtained using a 263 nm pump in Figs. 4.14 and 4.17. Contrary to the two well-defined dissociation bands with narrow distributions and asymptotic energies reflecting the direct dissociation channels upon single UV-photon absorption at 263 nm, the map for the 198 nm pump in Fig. 7.4 shows a broad, diffuse dissociation band converging to rather higher KE at long delays. The projection of this 2-D map on the KE axis in the delay range of 2.35 to 2.45 ps shown in the right panel depicts one broad peak centered at about 3 eV energy, with the low-energy tail that extends below 2 eV. This KE distribution is very different from the direct dissociation channels peaked at 1.3, and 1.97 eV energies associated with  $\text{CH}_3 + \text{I}(^2\text{P}_{1/2})$  and  $\text{CH}_3 + \text{I}(^2\text{P}_{3/2})$  channels triggered at 263 nm (see the KER projection in Fig. 4.41). These differences directly reflect different dissociation pathways involved in the A- and B-band dissociation processes.

To further track the dissociation channel(s) at longer delays, in Fig. 7.5 the KER spectra are compared for two fixed delays, 2.4 ps and 20 ps. The KE distribution of the dissociating peak are rather similar, converging to a slightly lower KE value at 20 ps. This peak is still a broad peak with a maximum at 2.90 eV. Using equation 4.1 with  $h\nu = 6.26$  eV,  $D_0 = 2.41$  eV, and  $E_{\text{so}} = 0.94$  eV, the energetics predict a KER of 2.92 eV for  $\text{CH}_3 + \text{I}(^2\text{P}_{1/2})$  and 1.96 eV for  $\text{CH}_3 + \text{I}(^2\text{P}_{3/2})$ . The figure with a pronounced peak at 2.9 eV supports the dominance of the former dissociation

channel. As discussed in Chapter 2, Alekseyev’s calculation [121] showed that the next state that could pre-dissociate the B state is the  $^1Q_1$  state correlating with  $CH_3 + I(^2P_{3/2})$ . The  $^1Q_1$  state only comes close to  $^3R_1$  and  $^3R_2$  cross at high energies ( $\sim 6.8$  eV), which means that it is not accessible by our photon energy.

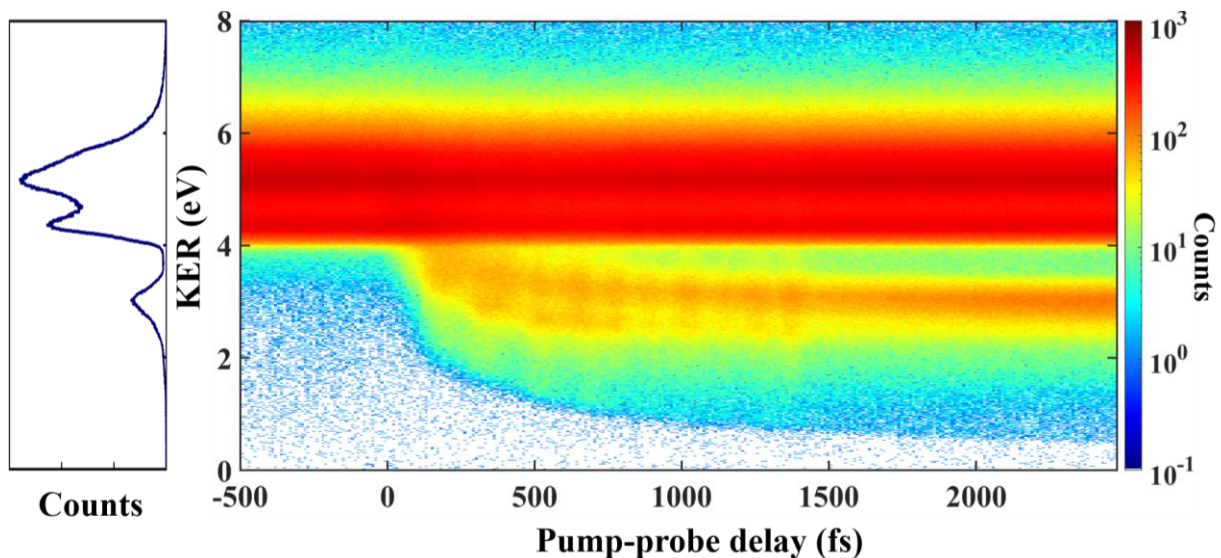


**Figure 7.4.** Delay-dependent KER distribution of the two-body coincident channel  $CH_3^+ + I^+$  after UV and NIR pulses. The peak intensity of pump and probe pulses are  $5 \times 10^{12}$  and  $8 \times 10^{14}$  W/cm $^2$ . A projection of the signal in the delay range of 2.3 – 2.4 ps onto the KER axis is shown on the right.

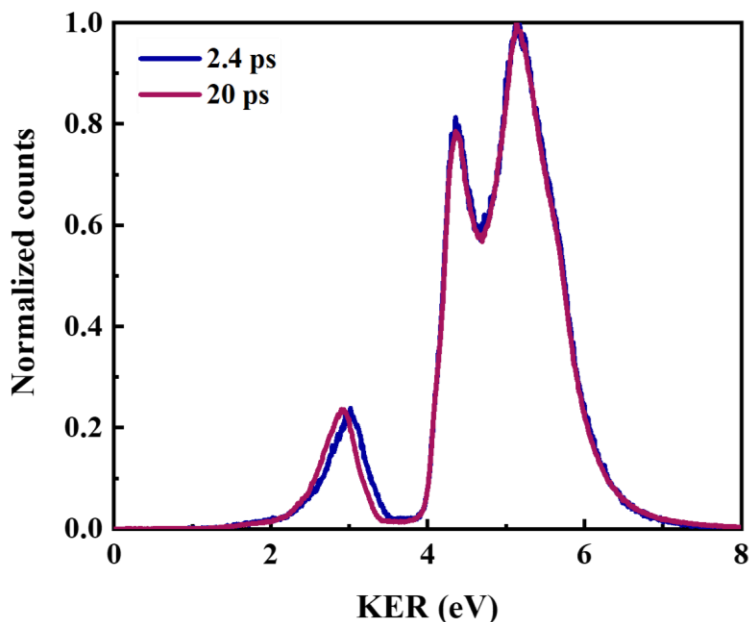


**Figure 7.5.** KE distribution of the two-body  $CH_3^+ + I^+$  coincident channel after UV pump and NIR probe pulse at 2.4 and 20 ps illustrates the dissociating molecules’ time evolution.

As discussed in section 2.3.1.2, several earlier experimental works showed a very small (a few percentage) but non-zero branching ratio of  $I(^2P_{3/2})$  and argued that the available theoretical curves might not provide the full story, either the states are shifted up or the crossing happens at lower energies. In our experimental results the broad low-energy shoulder likely contains some contribution from the  $I(^2P_{3/2})$  channel although it is clearly not as prominent as the  $I(^2P_{1/2})$  channel.

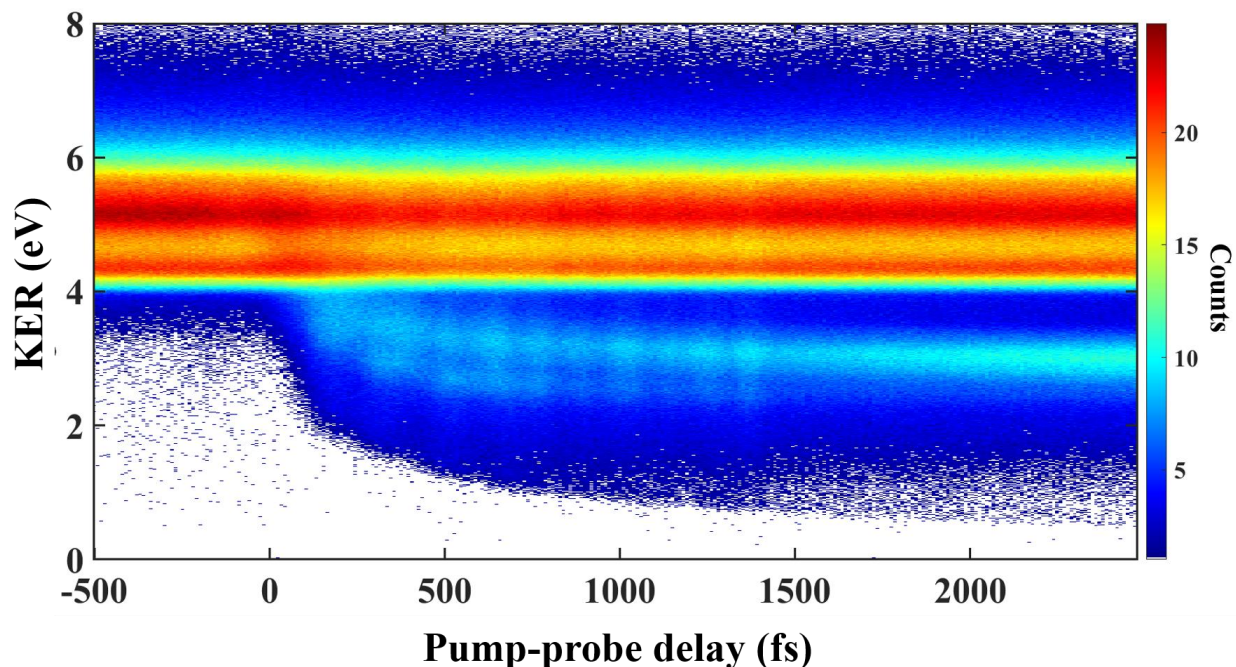


**Figure 7.6.** Delay-dependent KE distribution of the  $I^+$  originating from the doubly-charged CE channel,  $CH_3^+ + I^+$  after UV and NIR pulses. This is essentially the same spectrum as shown in Fig. 7.4 but with the color map plotted in a square-root scale of the counts in order to help make oscillations more visible while not over-suppressing the delay-independent band.

The most eye-catching feature in the delay-dependent KER distribution shown in Fig. 7.4 is a pronounced oscillatory structure in the descending band. It can be better visualized in Fig. 7.6, which shows the same delay-dependent KER distribution for the  $I^+ + CH_3^+$  coincident channel as in Fig. 7.4, but in a square-root color scale. This representation helps making the minor features (in this case, the oscillations) more visible while not over-suppressing the more dominant features.

Here, we employed a nonlinear scale for the 2-D plots to better visualize the oscillations. The color map is in a square-root scale of the counts to help make the minor features more visible while not over-suppressing the more dominant features.

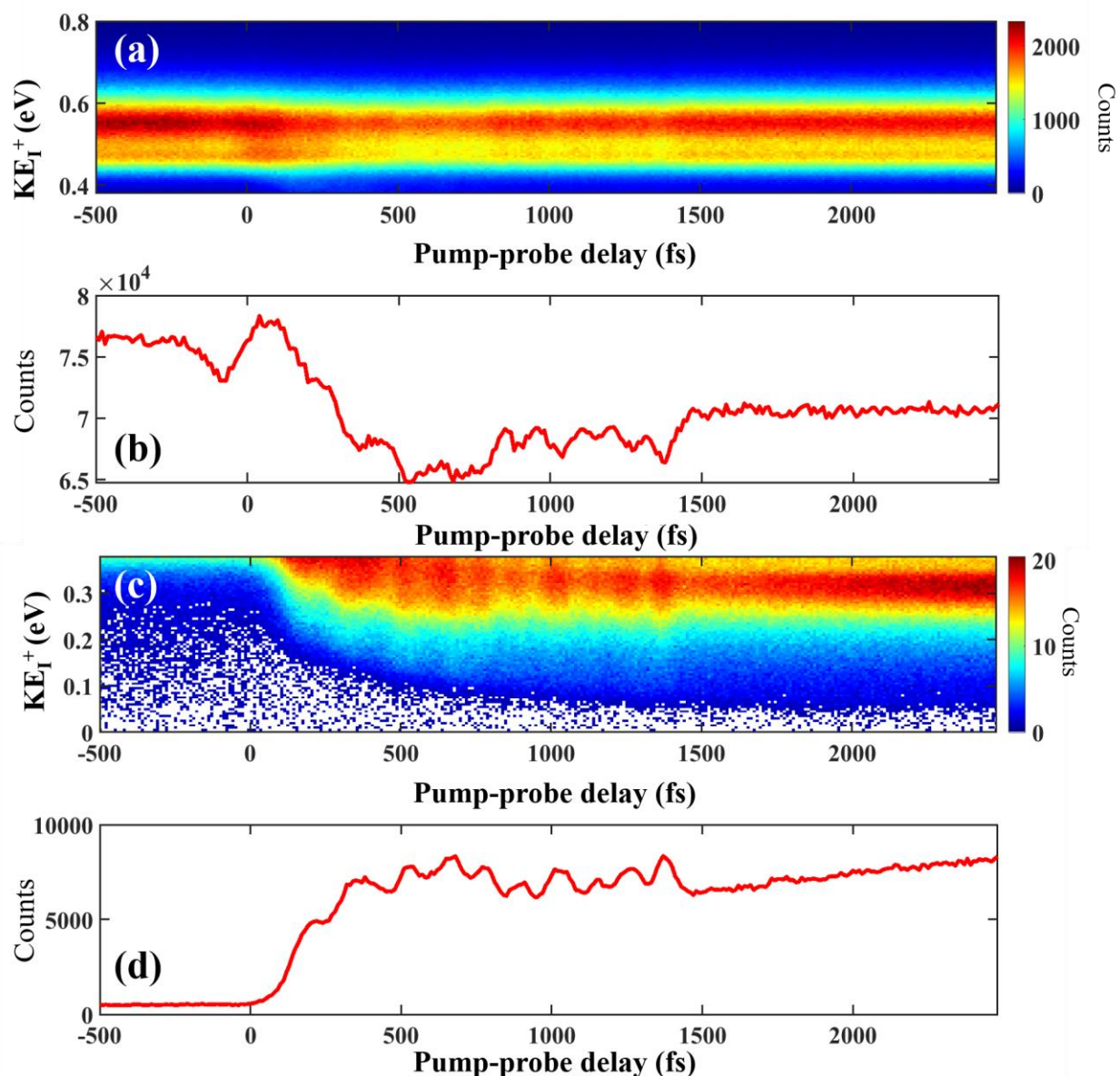


**Figure 7.7.** Delay-dependent KE distribution of the  $I^+$  originating from the doubly-charged CE channel,  $CH_3^+ + I^+$  after UV and NIR pulses in different KE ranges. **(a)** KE-delay map within the KE range of 0.38-0.8 eV and **(b)** its projection over the delay displaying the periodic depletion in the bound channel **(c)** KE-delay map within the KE range of 0 - 0.38 eV and **(d)** the projection over the delay displaying the dissociating channel with enclosed periodic oscillations.

To isolate the oscillations further, we used the individual fragments' time-dependent KE distributions in different coincident channels, as shown in Fig. 7.7. Panel (a) includes the bound channel in the energy range of 0.39 – 6.5 eV and (b) is the line out of the map showing a signal

drop at short delays followed by oscillations and recovery in 1.5 ps. Panel (c) includes the dissociating channel in the KE range of 0 – 0.39 eV, and (d) shows the projection of the map over the delay axis illustrating the appearance of the  $I^+$  signal. It rises and oscillates within 1.5 ps, and then the signal recovers to longer delays. The two projections are compared directly in Fig. 7.8, suggesting that the oscillations are out of phase. The blue arrows point out peaks and dips that illustrate this relation. The oscillations exhibit a periodicity of 130 - 140 fs and have variable amplitude across the measurement window.

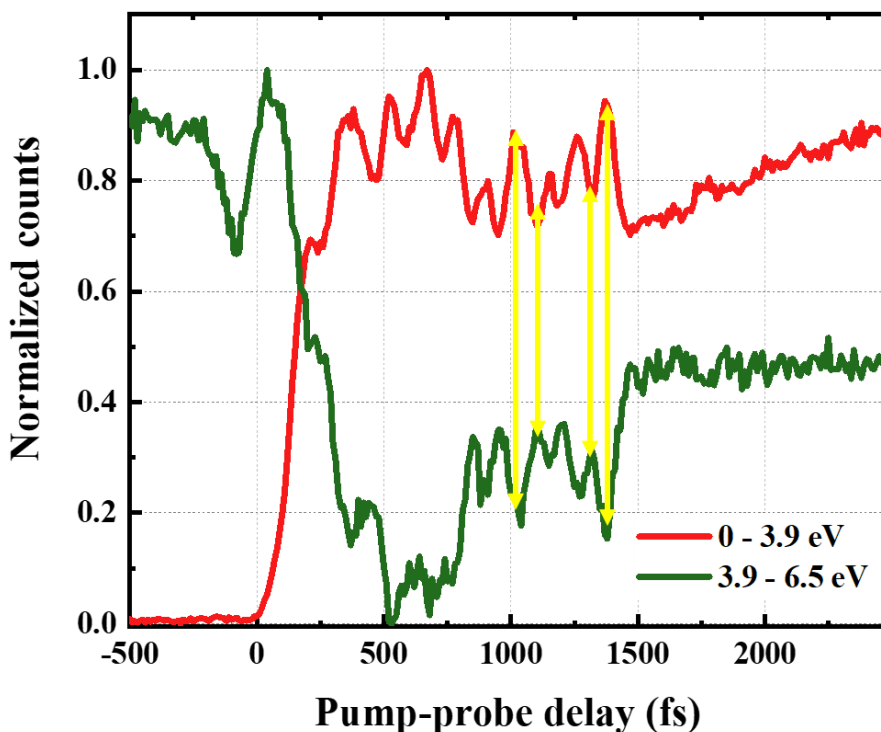


**Figure 7.8.** Projection of the bound (0.39 – 0.6.5 eV) and dissociating (0 – 0.39 eV) in the delay-dependent KE distribution of the  $I^+$  originating from the doubly-charged CE channel,  $CH_3^+ + I^+$  after UV and NIR pulses. The oscillations are out of phase with variable amplitude of the oscillations.

Many experimental results evidence the vibronic dependence of the pre-dissociation lifetime and the dissociation products [16], [287]–[291]. Using our UV pulse centered at 198 nm (FWHM  $\sim$  2 nm), we mainly excite the  $3_0^1$ ,  $6_0^1$ , and  $[1]6_0^1$  vibrational bands within the pulse. Therefore, the transitions involve vibronic levels with  $\nu = 6$  ( $CH_3$  degenerate rock) and  $\nu = 2$  ( $CH_3$  umbrella mode) and  $\nu = 3$  (C-I stretch). Using these states, the energy differences between the

states are 0.02, 0.044, and 0.064 eV, equivalent to period of 206, 94, and 64 fs. Given that our excitation includes different vibrational bands, and the period of the oscillations occur between these values, it is possible to think of the periodic motion due to the vibrational modes of the excited Rydberg states. The life time of these states are reported to be on the order of ps [286]. Therefore, although we do not precisely know the mechanism explaining this observation yet our observations suggest the oscillations most likely reflect the dynamics of the vibrational excited states, which lasts until it pre-dissociates. This explanation needs more investigation and will be a subject of further analysis and theoretical work to explain the origin of this structure.

## 7.4 Summary

In this chapter, the CH<sub>3</sub>I photodissociation is studied in the B-band at 198 nm, where the excitation of the lowest-lying Rydberg states is expected to trigger pre-dissociation dynamics. The two-body coincident channels with different charged states of iodine clearly demonstrate this pre-dissociation: The time-resolved measurement shows a broad, diffuse dissociation band, which differs from the distinct dissociation features observed for direct dissociation processes. Moreover, the data shows a pronounced periodic oscillatory structure with a periodicity of 130-140 fs, which is visible only within the pre-dissociation lifetime of the excited state (~1.5 ps) and which is most likely due to excited vibrational states, which lasts until it pre-dissociates.

## Chapter 8 - Conclusion

In this doctoral thesis, I have described several experimental studies of the photodissociation dynamics of halomethanes triggered by ultraviolet light, all of which employed the time-resolved coincident ion momentum imaging technique. As a part of my thesis work, we developed new optical setups at JRML for pump-probe experiments with individual 263 and 198 nm excitation wavelengths and a common probing scheme based on strong-field ionization and Coulomb explosion induced by intense 790 nm pulses. To achieve a high temporal resolution required for time-resolved studies presented here, we equipped the pump-probe setup with a home-built prism compressor to generate 263 nm pulses with sub-40 fs pulse duration. Currently, an identical prism compressor is being adapted for UV pulses at shorter wavelengths. Our experiments demonstrate that femtosecond pump-probe scheme coupled with ion momentum imaging is an efficient tool for studying photodissociation reactions on their natural time-scale. This approach allows us to initiate a photochemical reaction of interest and trace its evolution at each moment, thus creating a "molecular movie". The experimental results are compared to extensive Coulomb explosion simulations, which facilitate intuitive interpretation of such "movies". Although the current work is limited to studying nuclear motion and does not directly address the involved electronic dynamics, the experimental technique used here can be extended to electron dynamics studies by employing ion-electron coincidence measurements.

More specifically, we first studied direct photodissociation of the  $\text{CH}_3\text{I}$  molecule in the A-band and characterized the dissociation pathways triggered by a single-photon absorption at 263 nm. In addition, we identified signatures of two- and three-photon processes populating Rydberg and ionic states. The time-resolved coincident ion imaging helped us to track the competition between single and multi-photon processes and to illustrate how the latter contribution starts to dominate single-photon processes at increasing UV intensities. While three-photon or higher-order processes trigger the dynamics in the ionic states, with two-photon absorption, we excite the higher-lying Rydberg states, which manifest a well-defined lifetime of  $\sim 330$  fs. The contribution from these states have been characterized by tracking the time evolution of the singly-charged parent ion yield produced by the combined effect of the UV pump and NIR probe pulses. Besides that, benefiting from the improved temporal resolution and coincident measurements, we visualized the role of a bound minimum in the di-cationic potential energy curves in the formation

of the two-body CEI patterns. This effect was predicted theoretically but not yet observed experimentally. In addition, we observed rich dynamics near the overlap of the two pulses, which can be to a large extent interpreted in terms of the light-induced conical intersections (LICI).

Second, I studied the photodissociation dynamics of the  $\text{CH}_2\text{BrI}$  and  $\text{CH}_2\text{CII}$  in their A-band. Similar to  $\text{CH}_3\text{I}$ , the two-body dissociation dynamics are characterized by the dominant cleavage of the C–I bond via repulsive excited states accessed by single-photon absorption. Applying the same two-body coincidence analysis as for  $\text{CH}_3\text{I}$ , in both dihalomethanes, we also identified the minor contribution of the second carbon-halogen bond cleavage and the formation of the molecular halogen. However, for dihalomethanes, much more information beyond the “one-dimensional” dissociation picture could be obtained by the analysis of the delay-dependent three-body coincident patterns. Analyzing the time evolution of the three-body fragmentation of triply and five-fold final charged states, we identified the signatures of the two-body dissociation pathways with the detachment of the iodine or the second halogen. Here, very different from the case of  $\text{CH}_3\text{I}$ , the presence of the second halogen atom resulted in significant induced torque and, thus, rotational excitation of the molecular co-fragment upon dissociation of the molecule. The direct signature of such rotational motion could be clearly identified as pronounced oscillatory features in our three-body CEI maps. In this work, such rotational motion has been directly imaged for each carbon-halogen bond cleavage, resulting in a "molecular movie" of the dissociating and rotating molecule. To rationalize these results and underpin the correlation between the time-dependent oscillatory signal and the rotational motion, the experimental results are compared with molecular dynamics simulations of the UV-induced dissociation combined with Coulomb explosion simulations. In this modeling, the radical co-fragment rotational motion was considered as a rigid rotator with increasing C-I bond length. The simulation results agree well with our experimental results, demonstrating that the molecule periodically approaches a nearly-linear geometry with either the methylene group or the corresponding halogen atoms located in the middle and, thus, acquiring minimal kinetic energy. The experimental results provide benchmark data for theoretical modeling, which should be feasible for these prototypical molecular systems.

Analyzing the three-body fragmentation patterns for the five-fold final charge states, we also observed a signature of a short-lived transient structure resembling a linearized isomer configuration of the molecule. The temporal evolution of this transient signal showed a relatively fast rise and decay, highlighting the importance of achieving high temporal resolution for these

studies. Based on the observed dependence of the UV pump pulse power, the above-mentioned reactions are mainly driven by single-photon processes. In addition, we found clear and convincing evidence for molecular halogen formation, which seem to be dominated by the contributions from two or higher-order photon processes. We argued that the molecular halogen formation could occur either by cleaving the two carbon-halogen bonds synchronously, or through isomerization-type process and subsequent molecular halogen elimination driven by a single-photon process. Last, we identified a clear signature of the three-body dissociation pathways, which, at the 263 nm wavelength, can occur only via two-photon absorption or higher-order processes.

As the next step, to investigate the wavelength dependence of the photochemical reaction pathways, we extended these measurements to the photodissociation of  $\text{CH}_2\text{BrI}$  and  $\text{CH}_2\text{I}_2$  in the B-band at 198 nm. For  $\text{CH}_2\text{BrI}$ , we observed an increase in the branching ratio of the C-Br dissociation bond compared to the 263 nm data, in agreement with earlier spectroscopic and theoretical studies. Overall, the three-body dissociation and molecular halogen formation turned out to be the dominant photofragmentation channels for both molecules at this excitation wavelength. This observation was rationalized with the higher energy photons and transition to Rydberg excited states, ending with more excess energy.

Finally, I investigated the photodissociation of the  $\text{CH}_3\text{I}$  molecule in its B-band at 198 nm. The two-body CEI maps demonstrated the pre-dissociation of  $\text{CH}_3\text{I}$  fragmentation at this wavelength, reflected in a broad, diffuse dissociation band, which differed from the distinct dissociation features observed for direct dissociation at 263 nm. The pre-dissociation dynamics observed in the B-band led to the C-I bond's cleavage and mainly resulted in  $\text{I}^*(^2P_{1/2})$  fragments. Contrary to what we observed in the A-band dissociation, there is no clear sign of  $\text{I}(^2P_{3/2})$  fragments formation. However, the broad peak with the tail locating at the expected kinetic energy of  $\text{I}(^2P_{3/2})$  is not excluded. Furthermore, the data showed a pronounced oscillatory structure with a periodicity of 130 - 140 fs, visible only within the pre-dissociation lifetime of the excited state ( $\sim 1.5$  ps). Further data analysis, modeling and theoretical inputs are required to interpret the observed experimental results and discuss the exact origin of this structure. However, our initial hypothesis is that the observed periodic structure reflects the Rydberg-state vibrational motion, which lasts until the corresponding state pre-dissociates.

The experiments at two specific excitation wavelengths described here highlighted once again that photodissociation dynamics strongly depend on the excitation wavelength. While this

thesis addressed a few specific aspects of such wavelength dependence, in order to develop a systematic knowledge and comprehensive understanding of the wavelength-dependent photochemical reactions, it is essential to sample the excitation wavelength over the absorption spectrum of individual target molecules. This requires a tunable laser source, which would not be limited to the integer harmonic of the Ti: Sapphire laser. Recently, to address this shortcoming, a new 3 kHz laser system with a UV TOPAS tunable from visible to deep UV range has been installed at JRML and employed for pump-probe experiments. Finally, in order to combine the advantages of a tunable UV pump and a huge potential of higher repetition rates for such multi-coincidence experiments, JRML has ordered a new laser system with a broad range of accessible UV, visible and NIR wavelengths, and the 100 kHz repetition rate. With the arrival of this high repetition rate, high average power laser, the experimental schemes and tools developed in this work can be brought to the next level, enabling the creation of detailed “molecular movies” for many important photochemical reactions.

## Bibliography

- [1] A. A. Ischenko, P. M. Weber, and R. J. Dwayne Miller, "Capturing chemistry in action with electrons: realization of atomically resolved reaction dynamics," *Chem. Rev.*, vol. 117, no. 16, pp. 11066–11124, 2017, [doi: 10.1021/acs.chemrev.6b00770](https://doi.org/10.1021/acs.chemrev.6b00770).
- [2] P. Baum, "Towards ultimate temporal and spatial resolutions with ultrafast single-electron diffraction," *J. Phys. B At. Mol. Opt. Phys.*, vol. 47, no. 12, p. 124005, 2014, [doi: 10.1088/0953-4075/47/12/124005](https://doi.org/10.1088/0953-4075/47/12/124005).
- [3] R. J. D. Miller *et al.*, "Making the molecular movie: First frames," *Acta Crystallogr. Sect. A Found. Crystallogr.*, vol. 66, no. 2, pp. 137–156, 2010, [doi: 10.1107/S0108767309053926](https://doi.org/10.1107/S0108767309053926).
- [4] A. H. Zewail, "The new age of structural dynamics," *Acta Crystallogr. Sect. A Found. Crystallogr.*, vol. 66, no. 2[1], pp. 135–136, 2010, [doi: 10.1107/S0108767309047801](https://doi.org/10.1107/S0108767309047801).
- [5] J. C. Polanyi and A. H. Zewail, "Direct Observation of the Transition State," *Acc. Chem. Res.*, vol. 28, no. 3, pp. 119–132, 1995, [doi: 10.1021/ar00051a005](https://doi.org/10.1021/ar00051a005).
- [6] A. H. Zewail, "Femtochemistry: Atomic-scale dynamics of the chemical bond," *J. Phys. Chem. A*, vol. 104, no. 24, pp. 5660–5694, 2000, [doi: 10.1021/jp001460h](https://doi.org/10.1021/jp001460h).
- [7] T. Kierspel *et al.*, "X-ray diffractive imaging of controlled gas-phase molecules: Toward imaging of dynamics in the molecular frame," *J. Chem. Phys.*, vol. 152, no. 8, p. 084307, 2020, [doi: 10.1063/1.5133963](https://doi.org/10.1063/1.5133963).
- [8] G. Renger, "The light reactions of photosynthesis," *Curr. Sci.*, vol. 98, no. 10, pp. 1305–1319, 2010, [doi: stable/24107509](https://doi.org/stable/24107509).
- [9] M. Zubik *et al.*, "The negative feedback molecular mechanism which regulates excitation level in the plant photosynthetic complex LHCII: Towards identification of the energy dissipative state," *Biochim. Biophys. Acta - Bioenerg.*, vol. 1827, no. 3, pp. 355–364, 2013, [doi: 10.1016/j.bbabi.2012.11.013](https://doi.org/10.1016/j.bbabi.2012.11.013).
- [10] C. E. Crespo-Hernández, B. Cohen, P. M. Hare, and B. Kohler, "Ultrafast excited-state dynamics in nucleic acids," *Chem. Rev.*, vol. 104, no. 4, pp. 1977–2019, 2004, [doi: 10.1021/cr0206770](https://doi.org/10.1021/cr0206770).
- [11] J. M. L. Pecourt, J. Peon, and B. Kohler, "Ultrafast internal conversion of electronically excited RNA and DNA nucleosides in water," *J. Am. Chem. Soc.*, vol. 122, no. 38, pp.

- 9348–9349, Sep. 2000, [doi: 10.1021/ja0021520](https://doi.org/10.1021/ja0021520).
- [12] R. P. Sinha and D. P. Häder, “UV-induced DNA damage and repair: A review,” *Photochem. Photobiol. Sci.*, vol. 1, no. 4, pp. 225–236, 2002, [doi: 10.1039/b201230h](https://doi.org/10.1039/b201230h).
- [13] C. Canuel, M. Mons, F. Piuze, B. Tardivel, I. Dimicoli, and M. Elhanine, “Excited states dynamics of DNA and RNA bases: Characterization of a stepwise deactivation pathway in the gas phase,” *J. Chem. Phys.*, vol. 122, no. 7, p. 074316, 2005, [doi: 10.1063/1.1850469](https://doi.org/10.1063/1.1850469).
- [14] D. Polli *et al.*, “Conical intersection dynamics of the primary photoisomerization event in vision,” *Nature*, vol. 467, no. 7314, pp. 440–443, 2010, [doi: 10.1038/nature09346](https://doi.org/10.1038/nature09346).
- [15] L. A. Peteanu, R. W. Schoenlein, Q. Wang, R. A. Mathies, and C. V. Shank, “The first step in vision occurs in femtoseconds: Complete blue and red spectral studies,” *Proc. Natl. Acad. Sci. U. S. A.*, vol. 90, no. 24, pp. 11762–11766, 1993, [doi: 10.1073/pnas.90.24.11762](https://doi.org/10.1073/pnas.90.24.11762).
- [16] Q. Wang, R. W. Schoenlein, L. A. Peteanu, R. A. Mathies, and C. V. Shank, “Vibrationally coherent photochemistry in the femtosecond primary event of vision,” *Science (80-. )*, vol. 266, no. 5184, pp. 422–424, 1994, [doi: 10.1126/science.7939680](https://doi.org/10.1126/science.7939680).
- [17] T. Gustavsson, R. Improta, and D. Markovitsi, “DNA/RNA: Building blocks of life under UV irradiation,” *Journal of Physical Chemistry Letters*, vol. 1, no. 13, pp. 2025–2030, 2010, [doi: 10.1021/jz1004973](https://doi.org/10.1021/jz1004973).
- [18] R. W. Schoenlein, L. A. Peteanu, R. A. Mathies, and C. V. Shank, “The first step in vision: Femtosecond isomerization of rhodopsin,” *Science (80-. )*, vol. 254, no. 5030, pp. 412–415, 1991, [doi: 10.1126/science.1925597](https://doi.org/10.1126/science.1925597).
- [19] M. F. Holick, “Skin: Site of the Synthesis of Vitamin D and a Target Tissue for the Active Form, 1,25-Dihydroxy vitamin D<sub>3</sub>,” *Ann. N. Y. Acad. Sci.*, vol. 548, no. 1, pp. 14–26, Dec. 1988, [doi: 10.1111/j.1749-6632.1988.tb18789.x](https://doi.org/10.1111/j.1749-6632.1988.tb18789.x).
- [20] M. F. Perutz and Kendrew John, “Nobel Lectures, Chemistry 1962, X-Ray Analysis of Haemoglobin, December 11, 1962,” *Nobel Lect.*, 1962, [Online]. Available: <https://www.nobelprize.org/prizes/chemistry/1962/perutz/lecture/>.
- [21] W. Jou and O. F. P. Information, “A Horse’s Motion Scientifically Determined,” *Sci. Am.*, vol. 39, no. 16, pp. 241–241, 1878, [doi: 10.1038/scientificamerican10191878-241b](https://doi.org/10.1038/scientificamerican10191878-241b).
- [22] J. S. Lim and S. K. Kim, “Experimental probing of conical intersection dynamics in the photodissociation of thioanisole,” *Nat. Chem.*, vol. 2, no. 8, pp. 627–632, 2010, [doi: 10.1038/nchem.702](https://doi.org/10.1038/nchem.702).

- [23] W. G. Roeterdink and M. H. M. Janssen, “Femtosecond velocity map imaging of dissociative ionization dynamics in CF<sub>3</sub>I,” in *Physical Chemistry Chemical Physics*, 2002, vol. 4, no. 4, pp. 601–612, [doi: 10.1039/b107897f](https://doi.org/10.1039/b107897f).
- [24] S. L. Horton *et al.*, “Excited state dynamics of CH<sub>2</sub>I<sub>2</sub> and CH<sub>2</sub>BrI studied with UV pump VUV probe photoelectron spectroscopy,” *J. Chem. Phys.*, vol. 150, no. 17, p. 174201, May 2019, [doi: 10.1063/1.5086665](https://doi.org/10.1063/1.5086665).
- [25] E. G. Champenois *et al.*, “Ultrafast photodissociation dynamics and nonadiabatic coupling between excited electronic states of methanol probed by time-resolved photoelectron spectroscopy,” *J. Chem. Phys.*, vol. 150, no. 11, p. 114301, Mar. 2019, [doi: 10.1063/1.5079549](https://doi.org/10.1063/1.5079549).
- [26] Y. Zhao *et al.*, “Rotational and nuclear-spin level dependent photodissociation dynamics of H<sub>2</sub>S,” *Nat. Commun.*, vol. 12, no. 1, p. 4459, 2021, [doi: 10.1038/s41467-021-24782-6](https://doi.org/10.1038/s41467-021-24782-6).
- [27] M. Staniforth and V. G. Stavros, “Recent advances in experimental techniques to probe fast excited-state dynamics in biological molecules in the gas phase: Dynamics in nucleotides, amino acids and beyond,” *Proceedings of the Royal Society A: Mathematical, Physical and Engineering Sciences*, vol. 469, no. 2159, p. 20130458, 2013, [doi: 10.1098/rspa.2013.0458](https://doi.org/10.1098/rspa.2013.0458).
- [28] C. Dugave and L. Demange, “Cis-trans isomerization of organic molecules and biomolecules: Implications and applications,” *Chemical Reviews*, vol. 103, no. 7, pp. 2475–2532, 2003, [doi: 10.1021/cr0104375](https://doi.org/10.1021/cr0104375).
- [29] Y. H. Jiang *et al.*, “Ultrafast extreme ultraviolet induced isomerization of acetylene cations,” *Phys. Rev. Lett.*, vol. 105, no. 26, p. 263002, 2010, [doi: 10.1103/PhysRevLett.105.263002](https://doi.org/10.1103/PhysRevLett.105.263002).
- [30] T. J. Martínez, “Insights for light-driven molecular devices from ab initio multiple spawning excited-state dynamics of organic and biological chromophores,” *Acc. Chem. Res.*, vol. 39, no. 2, pp. 119–126, 2006, [doi: 10.1021/ar040202q](https://doi.org/10.1021/ar040202q).
- [31] C. E. Liekhus-Schmaltz *et al.*, “Ultrafast isomerization initiated by X-ray core ionization,” *Nat. Commun.*, vol. 6, p. 8199, 2015, [doi: 10.1038/ncomms9199](https://doi.org/10.1038/ncomms9199).
- [32] B. G. Levine and T. J. Martínez, “Isomerization through conical intersections,” *Annu. Rev. Phys. Chem.*, vol. 58, pp. 613–634, 2007, [doi: 10.1146/annurev.physchem.57.032905.104612](https://doi.org/10.1146/annurev.physchem.57.032905.104612).
- [33] A. C. Florean, D. Cardoza, J. L. White, J. K. Lanyi, R. J. Sension, and P. H. Bucksbaum, “Control of retinal isomerization in bacteriorhodopsin in the high-intensity regime,” *Proc.*

- Natl. Acad. Sci. U. S. A.*, vol. 106, no. 27, pp. 10896–10900, 2009, [doi: 10.1073/pnas.0904589106](https://doi.org/10.1073/pnas.0904589106).
- [34] S. Deb and P. M. Weber, “The ultrafast pathway of photon-induced electrocyclic ring-opening reactions: The case of 1,3-cyclohexadiene,” *Annu. Rev. Phys. Chem.*, vol. 62, no. 1, pp. 19–39, Mar. 2011, [doi: 10.1146/annurev.physchem.012809.103350](https://doi.org/10.1146/annurev.physchem.012809.103350).
- [35] M. S. Schuurman and A. Stolow, “Dynamics at Conical Intersections,” *Annu. Rev. Phys. Chem.*, vol. 69, pp. 427–450, 2018, [doi: 10.1146/annurev-physchem-052516-050721](https://doi.org/10.1146/annurev-physchem-052516-050721).
- [36] G. A. Worth and L. S. Cederbaum, “Beyond born-oppenheimer: Molecular dynamics through a conical intersection,” *Annual Review of Physical Chemistry*, vol. 55, pp. 127–158, 2004, [doi: 10.1146/annurev.physchem.55.091602.094335](https://doi.org/10.1146/annurev.physchem.55.091602.094335).
- [37] G. Käb, C. Schröder, and D. Schwarzer, “Intramolecular vibrational redistribution and energy relaxation in solution: A molecular dynamics approach,” *Phys. Chem. Chem. Phys.*, vol. 4, no. 2, pp. 271–278, 2002, [doi: 10.1039/B107256K](https://doi.org/10.1039/B107256K).
- [38] A. Tramer, C. Jungen, and F. Lahmani, *Energy dissipation in molecular systems*. 2005, [doi: 10.1007/b137820](https://doi.org/10.1007/b137820)
- [39] M. H. Farag, A. Bastida, M. F. Ruiz-López, G. Monard, and F. Ingrosso, “Vibrational energy relaxation of the amide I mode of N-methylacetamide in D2O studied through born-oppenheimer molecular dynamics,” *J. Phys. Chem. B*, vol. 118, no. 23, pp. 6186–6197, 2014, [doi: 10.1021/jp500304z](https://doi.org/10.1021/jp500304z).
- [40] M. Seel and W. Domcke, “Femtosecond time-resolved ionization spectroscopy of ultrafast internal-conversion dynamics in polyatomic molecules: Theory and computational studies,” *J. Chem. Phys.*, vol. 95, no. 11, pp. 7808–7822, 1991, [doi: 10.1063/1.461816](https://doi.org/10.1063/1.461816).
- [41] S. Ullrich, T. Schultz, M. Z. Zgierski, and A. Stolow, “Direct Observation of Electronic Relaxation Dynamics in Adenine via Time-Resolved Photoelectron Spectroscopy,” *J. Am. Chem. Soc.*, vol. 126, no. 8, pp. 2262–2263, 2004, [doi: 10.1021/ja030532q](https://doi.org/10.1021/ja030532q).
- [42] H. Tao *et al.*, “Ultrafast internal conversion in ethylene. I. the excited state lifetime,” *J. Chem. Phys.*, vol. 134, no. 24, p. 244306, 2011, [doi: 10.1063/1.3604007](https://doi.org/10.1063/1.3604007).
- [43] T. K. Allison *et al.*, “Ultrafast internal conversion in ethylene. II. Mechanisms and pathways for quenching and hydrogen elimination,” *J. Chem. Phys.*, vol. 136, no. 12, p. 124317, 2012, [doi: 10.1063/1.3697760](https://doi.org/10.1063/1.3697760).
- [44] B. Kim, C. P. Schick, and P. M. Weber, “Time-delayed two-color photoelectron spectra of

- aniline, 2-aminopyridine, and 3-aminopyridine: Snapshots of the nonadiabatic curve crossings,” *J. Chem. Phys.*, vol. 103, no. 16, pp. 6903–6913, 1995, [doi: 10.1063/1.470368](https://doi.org/10.1063/1.470368).
- [45] R. S. Minns, D. S. N. Parker, T. J. Penfold, G. A. Worth, and H. H. Fielding, “Competing ultrafast intersystem crossing and internal conversion in the “channel 3” region of benzene,” *Phys. Chem. Chem. Phys.*, vol. 12, no. 48, pp. 15607–15615, 2010, [doi: 10.1039/c001671c](https://doi.org/10.1039/c001671c).
- [46] D. R. Yarkony, “Conical intersections: The new conventional wisdom,” *Journal of Physical Chemistry A*, vol. 105, no. 26, pp. 6277–6293, 2001, [doi: 10.1021/jp003731u](https://doi.org/10.1021/jp003731u).
- [47] T. Suzuki and B. J. Whitaker, “Non-adiabatic effects in chemistry revealed by time-resolved charged-particle imaging,” *International Reviews in Physical Chemistry*, vol. 20, no. 3, pp. 313–356, 2001, [doi: 10.1080/01442350110045046](https://doi.org/10.1080/01442350110045046).
- [48] A. Stolow, “Femtosecond Time-Resolved Photoelectron Spectroscopy of Polyatomic Molecules,” *Annual Review of Physical Chemistry*, vol. 54, pp. 89–119, 2003, [doi: 10.1146/annurev.physchem.54.011002.103809](https://doi.org/10.1146/annurev.physchem.54.011002.103809).
- [49] A. Stolow, “Time-resolved photoelectron spectroscopy: Non-adiabatic dynamics in polyatomic molecules,” *International Reviews in Physical Chemistry*, vol. 22, no. 2, pp. 377–405, 2003, [doi: 10.1080/0144235031000092448](https://doi.org/10.1080/0144235031000092448).
- [50] Z. H. Loh, M. Khalil, R. E. Correa, R. Santra, C. Buth, and S. R. Leone, “Quantum state-resolved probing of strong-field-ionized Xenon atoms using femtosecond high-order harmonic transient absorption spectroscopy,” *Phys. Rev. Lett.*, vol. 98, no. 14, p. 143601, 2007, [doi: 10.1103/PhysRevLett.98.143601](https://doi.org/10.1103/PhysRevLett.98.143601).
- [51] L. R. Baker *et al.*, “Charge carrier dynamics of photoexcited Co<sub>3</sub>O<sub>4</sub> in methanol: Extending high harmonic transient absorption spectroscopy to liquid environments,” *Nano Lett.*, vol. 14, no. 10, pp. 5883–5890, 2014, [doi: 10.1021/nl502817a](https://doi.org/10.1021/nl502817a).
- [52] R. Geneaux, H. J. B. Marroux, A. Guggenmos, D. M. Neumark, and S. R. Leone, “Transient absorption spectroscopy using high harmonic generation: A review of ultrafast X-ray dynamics in molecules and solids,” *Philosophical Transactions of the Royal Society A: Mathematical, Physical and Engineering Sciences*, vol. 377, no. 2145, p. 20170463, 2019, [doi: 10.1098/rsta.2017.0463](https://doi.org/10.1098/rsta.2017.0463).
- [53] Y. Liu *et al.*, “Spectroscopic and Structural Probing of Excited-State Molecular Dynamics with Time-Resolved Photoelectron Spectroscopy and Ultrafast Electron Diffraction,” *Phys. Rev. X*, vol. 10, no. 2, p. 021016, 2020, [doi: 10.1103/PhysRevX.10.021016](https://doi.org/10.1103/PhysRevX.10.021016).

- [54] J. Yang *et al.*, “Imaging CF<sub>3</sub>I conical intersection and photodissociation dynamics with ultrafast electron diffraction,” *Science* (80-. ), vol. 361, no. 6397, pp. 64–67, 2018, [doi: 10.1126/science.aat0049](https://doi.org/10.1126/science.aat0049).
- [55] J. Yang *et al.*, “Direct observation of ultrafast hydrogen bond strengthening in liquid water,” *Nature*, vol. 596, no. 7873, pp. 531–535, 2021, [doi: 10.1038/s41586-021-03793-9](https://doi.org/10.1038/s41586-021-03793-9).
- [56] Y. Xiong, K. J. Wilkin, and M. Centurion, “High-resolution movies of molecular rotational dynamics captured with ultrafast electron diffraction,” *Phys. Rev. Res.*, vol. 2, no. 4, p. 043064, 2020, [doi: 10.1103/PhysRevResearch.2.043064](https://doi.org/10.1103/PhysRevResearch.2.043064).
- [57] J. Yang *et al.*, “Simultaneous observation of nuclear and electronic dynamics by ultrafast electron diffraction,” *Science* (80-. ), vol. 368, no. 6493, pp. 885–889, 2020, [doi: 10.1126/science.abb2235](https://doi.org/10.1126/science.abb2235).
- [58] S. P. Weathersby *et al.*, “Mega-electron-volt ultrafast electron diffraction at SLAC National Accelerator Laboratory,” *Rev. Sci. Instrum.*, vol. 86, no. 7, p. 073702, 2015, [doi: 10.1063/1.4926994](https://doi.org/10.1063/1.4926994).
- [59] J. B. Hastings *et al.*, “Ultrafast time-resolved electron diffraction with megavolt electron beams,” *Appl. Phys. Lett.*, vol. 89, no. 18, p. 184109, 2006, [doi: 10.1063/1.2372697](https://doi.org/10.1063/1.2372697).
- [60] J. Yang, J. Beck, C. J. Uiterwaal, and M. Centurion, “Imaging of alignment and structural changes of carbon disulfide molecules using ultrafast electron diffraction,” *Nat. Commun.*, vol. 6, p. 8172, 2015, [doi: 10.1038/ncomms9172](https://doi.org/10.1038/ncomms9172).
- [61] G. Sciaini and R. J. D. Miller, “Femtosecond electron diffraction: Heralding the era of atomically resolved dynamics,” *Reports on Progress in Physics*, vol. 74, no. 9, p. 096101, 2011, [doi: 10.1088/0034-4885/74/9/096101](https://doi.org/10.1088/0034-4885/74/9/096101).
- [62] J. Cao, H. Ihee, and A. H. Zewail, “Ultrafast electron diffraction and direct observation of transient structures in a chemical reaction,” *Proc. Natl. Acad. Sci. U. S. A.*, vol. 96, no. 2, pp. 338–342, Jan. 1999, [doi: 10.1073/pnas.96.2.338](https://doi.org/10.1073/pnas.96.2.338).
- [63] J. R. Dwyer *et al.*, “Femtosecond electron diffraction: ‘Making the molecular movie,’” *Philos. Trans. R. Soc. A Math. Phys. Eng. Sci.*, vol. 364, no. 1840, pp. 741–778, Mar. 2006, [doi: 10.1098/rsta.2005.1735](https://doi.org/10.1098/rsta.2005.1735).
- [64] D. Shorokhov and A. H. Zewail, “4D electron imaging: Principles and perspectives,” *Phys. Chem. Chem. Phys.*, vol. 10, no. 20, pp. 2879–2893, 2008, [doi: 10.1039/b801626g](https://doi.org/10.1039/b801626g).
- [65] M. P. Minitti *et al.*, “Imaging Molecular Motion: Femtosecond X-Ray Scattering of an

- Electrocyclic Chemical Reaction,” *Phys. Rev. Lett.*, vol. 114, no. 25, p. 255501, 2015, [doi: 10.1103/PhysRevLett.114.255501](https://doi.org/10.1103/PhysRevLett.114.255501).
- [66] M. M. Seibert *et al.*, “Single mimivirus particles intercepted and imaged with an X-ray laser,” *Nature*, vol. 470, no. 7332, pp. 78–82, 2011, [doi: 10.1038/nature09748](https://doi.org/10.1038/nature09748).
- [67] J. Küpper *et al.*, “X-ray diffraction from isolated and strongly aligned gas-phase molecules with a free-electron laser,” *Phys. Rev. Lett.*, vol. 112, no. 8, p. 083002, 2014, [doi: 10.1103/PhysRevLett.112.083002](https://doi.org/10.1103/PhysRevLett.112.083002).
- [68] L. Young *et al.*, “Roadmap of ultrafast x-ray atomic and molecular physics,” *Journal of Physics B: Atomic, Molecular and Optical Physics*, vol. 51, no. 3, p. 032003, 2018, [doi: 10.1088/1361-6455/aa9735](https://doi.org/10.1088/1361-6455/aa9735).
- [69] A. Rudenko and D. Rolles, “Time-resolved studies with FELs,” *J. Electron Spectros. Relat. Phenomena*, vol. 204, pp. 228–236, 2015, [doi: 10.1016/j.elspec.2015.07.010](https://doi.org/10.1016/j.elspec.2015.07.010).
- [70] J. C. H. Spence, U. Weierstall, and H. N. Chapman, “X-ray lasers for structural and dynamic biology,” *Reports Prog. Phys.*, vol. 75, no. 10, p. 102601, Oct. 2012, [doi: 10.1088/0034-4885/75/10/102601](https://doi.org/10.1088/0034-4885/75/10/102601).
- [71] F. Carbone, P. Musumeci, O. J. Luiten, and C. Hebert, “A perspective on novel sources of ultrashort electron and X-ray pulses,” *Chem. Phys.*, vol. 392, no. 1, pp. 1–9, 2012, [doi: 10.1016/j.chemphys.2011.10.010](https://doi.org/10.1016/j.chemphys.2011.10.010).
- [72] A. Rousse, C. Rischel, and J. C. Gauthier, “Colloquium: Femtosecond x-ray crystallography,” *Rev. Mod. Phys.*, vol. 73, no. 1, pp. 17–31, Jan. 2001, [doi: 10.1103/RevModPhys.73.17](https://doi.org/10.1103/RevModPhys.73.17).
- [73] J. Kim, K. H. Kim, J. H. Lee, and H. Ihee, “Ultrafast X-ray diffraction in liquid, solution and gas: Present status and future prospects,” *Acta Crystallogr. Sect. A Found. Crystallogr.*, vol. 66, no. 2, pp. 270–280, Mar. 2010, [doi: 10.1107/S0108767309052052](https://doi.org/10.1107/S0108767309052052).
- [74] M. G. Pullen *et al.*, “Imaging an aligned polyatomic molecule with laser-induced electron diffraction,” *Nat. Commun.*, vol. 6, p. 7262, 2015, [doi: 10.1038/ncomms8262](https://doi.org/10.1038/ncomms8262).
- [75] N. Suárez, A. Chacón, M. F. Ciappina, B. Wolter, J. Biegert, and M. Lewenstein, “Above-threshold ionization and laser-induced electron diffraction in diatomic molecules,” *Phys. Rev. A*, vol. 94, no. 4, p. 043423, 2016, [doi: 10.1103/PhysRevA.94.043423](https://doi.org/10.1103/PhysRevA.94.043423).
- [76] K. Amini *et al.*, “Imaging the Renner–Teller effect using laser-induced electron diffraction,” *Proc. Natl. Acad. Sci. U. S. A.*, vol. 116, no. 17, pp. 8173–8177, 2019, [doi: 10.1073/pnas.1811111116](https://doi.org/10.1073/pnas.1811111116).

[10.1073/pnas.1817465116](https://doi.org/10.1073/pnas.1817465116).

- [77] S. J. Wang, J. Daněk, C. I. Blaga, L. F. Dimauro, J. Biegert, and C. D. Lin, “Two-dimensional retrieval methods for ultrafast imaging of molecular structure using laser-induced electron diffraction,” *J. Chem. Phys.*, vol. 155, no. 16, p. 164104, 2021, [doi: 10.1063/5.0064761](https://doi.org/10.1063/5.0064761).
- [78] A. Sanchez *et al.*, “Molecular structure retrieval directly from laboratory-frame photoelectron spectra in laser-induced electron diffraction,” *Nat. Commun.*, vol. 12, no. 1, p. 1520, 2021, [doi: 10.1038/s41467-021-21855-4](https://doi.org/10.1038/s41467-021-21855-4).
- [79] C. I. Blaga *et al.*, “Imaging ultrafast molecular dynamics with laser-induced electron diffraction,” *Nature*, vol. 483, no. 7388, pp. 194–197, 2012, [doi: 10.1038/nature10820](https://doi.org/10.1038/nature10820).
- [80] J. Xu *et al.*, “Laser-induced electron diffraction for probing rare gas atoms,” *Phys. Rev. Lett.*, vol. 109, no. 23, p. 233002, 2012, [doi: 10.1103/PhysRevLett.109.233002](https://doi.org/10.1103/PhysRevLett.109.233002).
- [81] R. Boll *et al.*, “Femtosecond photoelectron diffraction on laser-aligned molecules: Towards time-resolved imaging of molecular structure,” *Phys. Rev. A - At. Mol. Opt. Phys.*, vol. 88, no. 6, p. 061402, 2013, [doi: 10.1103/PhysRevA.88.061402](https://doi.org/10.1103/PhysRevA.88.061402).
- [82] G. Kastirke *et al.*, “Double Core-Hole Generation in O<sub>2</sub> Molecules Using an X-Ray Free-Electron Laser: Molecular-Frame Photoelectron Angular Distributions,” *Phys. Rev. Lett.*, vol. 125, no. 16, p. 163201, 2020, [doi: 10.1103/PhysRevLett.125.163201](https://doi.org/10.1103/PhysRevLett.125.163201).
- [83] H. Stapelfeldt, E. Constant, H. Sakai, and P. B. Corkum, “Time-resolved Coulomb explosion imaging: A method to measure structure and dynamics of molecular nuclear wave packets,” *Phys. Rev. A - At. Mol. Opt. Phys.*, vol. 58, no. 1, pp. 426–433, 1998, [doi: 10.1103/PhysRevA.58.426](https://doi.org/10.1103/PhysRevA.58.426).
- [84] M. Pitzer *et al.*, “Direct determination of absolute molecular stereochemistry in gas phase by coulomb explosion imaging,” *Science (80-. )*, vol. 341, no. 6150, pp. 1096–1100, 2013, [doi: 10.1126/science.1240362](https://doi.org/10.1126/science.1240362).
- [85] R. N. Zare, “Dissociation of H<sub>2</sub><sup>+</sup> by electron impact: Calculated angular distribution,” *J. Chem. Phys.*, vol. 47, no. 1, pp. 204–215, 1967, [doi: 10.1063/1.1711847](https://doi.org/10.1063/1.1711847).
- [86] H. Hasegawa, A. Hishikawa, and K. Yamanouchi, “Coincidence imaging of Coulomb explosion of CS<sub>2</sub> in intense laser fields,” *Chem. Phys. Lett.*, vol. 349, no. 1–2, pp. 57–63, 2001, [doi: 10.1016/S0009-2614\(01\)01087-9](https://doi.org/10.1016/S0009-2614(01)01087-9).
- [87] L. Christensen, L. Christiansen, B. Shepperson, and H. Stapelfeldt, “Deconvoluting

- nonaxial recoil in Coulomb explosion measurements of molecular axis alignment,” *Phys. Rev. A*, vol. 94, no. 2, p. 023410, 2016, [doi: 10.1103/PhysRevA.94.023410](https://doi.org/10.1103/PhysRevA.94.023410).
- [88] E. P. Kanter *et al.*, “Role of excited electronic states in the interactions of fast (MeV) molecular ions with solids and gases,” *Phys. Rev. A*, vol. 20, no. 3, pp. 834–854, 1979, [doi: 10.1103/PhysRevA.20.834](https://doi.org/10.1103/PhysRevA.20.834).
- [89] N. Neumann *et al.*, “Fragmentation dynamics of  $\text{CO}_2^{3+}$  investigated by multiple electron capture in collisions with slow highly charged ions,” *Phys. Rev. Lett.*, vol. 104, no. 10, 2010, [doi: 10.1103/PhysRevLett.104.103201](https://doi.org/10.1103/PhysRevLett.104.103201).
- [90] K. Amini, “Studies of Ultrafast Molecular Photofragmentation and Dynamics Using Fast Imaging Sensors,” PhD thesis, University of Oxford, 2017.
- [91] R. Karimi, W. K. Liu, and J. Sanderson, “Femtosecond laser-induced coulomb explosion imaging,” in *Advances in Multi-Photon Processes and Spectroscopy*, vol. 23, 2016, pp. 97–153. [doi: 10.1063/1.5049555](https://doi.org/10.1063/1.5049555)
- [92] J. Gagnon, K. F. Lee, D. M. Rayner, P. B. Corkum, and V. R. Bhardwaj, “Coincidence imaging of polyatomic molecules via laser-induced Coulomb explosion,” *J. Phys. B At. Mol. Opt. Phys.*, vol. 41, no. 21, p. 215104, 2008, [doi: 10.1088/0953-4075/41/21/215104](https://doi.org/10.1088/0953-4075/41/21/215104).
- [93] J. D. Pickering, B. Shepperson, L. Christiansen, and H. Stapelfeldt, “Femtosecond laser induced Coulomb explosion imaging of aligned OCS oligomers inside helium nanodroplets,” *J. Chem. Phys.*, vol. 149, no. 15, p. 154306, 2018, [doi: 10.1063/1.5049555](https://doi.org/10.1063/1.5049555).
- [94] F. Légaré *et al.*, “Laser Coulomb-explosion imaging of small molecules,” *Phys. Rev. A - At. Mol. Opt. Phys.*, vol. 71, no. 1, p. 013415, 2005, [doi: 10.1103/PhysRevA.71.013415](https://doi.org/10.1103/PhysRevA.71.013415).
- [95] I. A. Bocharova *et al.*, “Direct Coulomb-explosion imaging of coherent nuclear dynamics induced by few-cycle laser pulses in light and heavy hydrogen,” *Phys. Rev. A - At. Mol. Opt. Phys.*, vol. 77, no. 5, p. 053407, 2008, [doi: 10.1103/PhysRevA.77.053407](https://doi.org/10.1103/PhysRevA.77.053407).
- [96] I. Bocharova *et al.*, “Charge resonance enhanced ionization of  $\text{CO}_2$  probed by laser coulomb explosion imaging,” *Phys. Rev. Lett.*, vol. 107, no. 6, p. 063201, 2011, [doi: 10.1103/PhysRevLett.107.063201](https://doi.org/10.1103/PhysRevLett.107.063201).
- [97] J. W. L. Lee *et al.*, “Three-dimensional covariance-map imaging of molecular structure and dynamics on the ultrafast timescale,” *Commun. Chem.*, vol. 3, no. 1, p. 72, 2020, [doi: 10.1038/s42004-020-0320-3](https://doi.org/10.1038/s42004-020-0320-3).
- [98] F. Allum *et al.*, “Coulomb explosion imaging of  $\text{CH}_3\text{I}$  and  $\text{CH}_2\text{ClI}$  photodissociation

- dynamics,” *J. Chem. Phys.*, vol. 149, no. 20, p. 204313, 2018, [doi: 10.1063/1.5041381](https://doi.org/10.1063/1.5041381).
- [99] M. Burt *et al.*, “Coulomb-explosion imaging of concurrent CH<sub>2</sub>BrI photodissociation dynamics,” *Phys. Rev. A*, vol. 96, no. 4, p. 043415, 2017, [doi: 10.1103/PhysRevA.96.043415](https://doi.org/10.1103/PhysRevA.96.043415).
- [100] K. Amini *et al.*, “Photodissociation of aligned CH<sub>3</sub>I and C<sub>6</sub>H<sub>3</sub>F<sub>2</sub>I molecules probed with time-resolved Coulomb explosion imaging by site-selective extreme ultraviolet ionization,” *Struct. Dyn.*, vol. 5, no. 1, p. 014301, 2018, [doi: 10.1063/1.4998648](https://doi.org/10.1063/1.4998648).
- [101] L. Christensen *et al.*, “Dynamic stark control of torsional motion by a pair of laser pulses,” *Phys. Rev. Lett.*, vol. 113, no. 7, p. 073005, 2014, [doi: 10.1103/PhysRevLett.113.073005](https://doi.org/10.1103/PhysRevLett.113.073005).
- [102] C. S. Slater *et al.*, “Coulomb-explosion imaging using a pixel-imaging mass-spectrometry camera,” *Phys. Rev. A - At. Mol. Opt. Phys.*, vol. 91, no. 5, p. 053424, 2015, [doi: 10.1103/PhysRevA.91.053424](https://doi.org/10.1103/PhysRevA.91.053424).
- [103] X. Zhao *et al.*, “Tracking the nuclear movement of the carbonyl sulfide cation after strong-field ionization by time-resolved Coulomb-explosion imaging,” *Phys. Rev. A*, vol. 103, no. 5, p. 053103, 2021, [doi: 10.1103/PhysRevA.103.053103](https://doi.org/10.1103/PhysRevA.103.053103).
- [104] L. Christensen, J. H. Nielsen, C. S. Slater, A. Lauer, M. Brouard, and H. Stapelfeldt, “Using laser-induced Coulomb explosion of aligned chiral molecules to determine their absolute configuration,” *Phys. Rev. A - At. Mol. Opt. Phys.*, vol. 92, no. 3, p. 033411, 2015, [doi: 10.1103/PhysRevA.92.033411](https://doi.org/10.1103/PhysRevA.92.033411).
- [105] X. Li *et al.*, “Coulomb explosion imaging of small polyatomic molecules with ultrashort x-ray pulses,” *Phys. Rev. Res.*, vol. 4, no. 1, p. 13029, Jan. 2022, [doi: 10.1103/PhysRevResearch.4.013029](https://doi.org/10.1103/PhysRevResearch.4.013029).
- [106] M. Ueyama, H. Hasegawa, A. Hishikawa, and K. Yamanouchi, “Concerted and sequential Coulomb explosion processes of N<sub>2</sub>O in intense laser fields by coincidence momentum imaging,” *J. Chem. Phys.*, vol. 123, no. 15, p. 154305, Oct. 2005, [doi: 10.1063/1.2032988](https://doi.org/10.1063/1.2032988).
- [107] T. Endo, H. Fujise, A. Matsuda, M. Fushitani, H. Kono, and A. Hishikawa, “Coincidence momentum imaging of asymmetric Coulomb explosion of CO<sub>2</sub> in phase-locked two-color intense laser fields,” *J. Electron Spectros. Relat. Phenomena*, vol. 207, pp. 50–54, 2016, [doi: 10.1016/j.elspec.2015.12.010](https://doi.org/10.1016/j.elspec.2015.12.010).
- [108] A. Hishikawa, A. Matsuda, M. Fushitani, and E. J. Takahashi, “Visualizing recurrently migrating hydrogen in acetylene dication by intense ultrashort laser pulses,” *Phys. Rev.*

- Lett.*, vol. 99, no. 25, p. 258302, 2007, [doi: 10.1103/PhysRevLett.99.258302](https://doi.org/10.1103/PhysRevLett.99.258302).
- [109] R. Boll *et al.*, “X-ray multiphoton-induced Coulomb explosion images complex single molecules,” *Nat. Phys.*, 2022, [doi: 10.1038/s41567-022-01507-0](https://doi.org/10.1038/s41567-022-01507-0).
- [110] J. Rajput *et al.*, “Native Frames: Disentangling Sequential from Concerted Three-Body Fragmentation,” *Phys. Rev. Lett.*, vol. 120, no. 10, p. 103001, 2018, [doi: 10.1103/PhysRevLett.120.103001](https://doi.org/10.1103/PhysRevLett.120.103001).
- [111] T. Severt, “Imaging light-induced molecular fragmentation dynamics,” PhD thesis, Kansas State University, 2021, <https://hdl.handle.net/2097/41547>
- [112] T. Severt *et al.*, “Native frames : A new approach for separating sequential and concerted three-body fragmentation,” *Unpublished*, vol. 1, pp. 1–23, 2022.
- [113] H. Ibrahim *et al.*, “Tabletop imaging of structural evolutions in chemical reactions demonstrated for the acetylene cation,” *Nat. Commun.*, vol. 5, p. 4422, 2014, [doi: 10.1038/ncomms5422](https://doi.org/10.1038/ncomms5422).
- [114] M. McDonnell *et al.*, “Ultrafast Laser-Induced Isomerization Dynamics in Acetonitrile,” *J. Phys. Chem. Lett.*, vol. 11, no. 16, pp. 6724–6729, 2020, [doi: 10.1021/acs.jpcllett.0c01344](https://doi.org/10.1021/acs.jpcllett.0c01344).
- [115] J. J. Larsen, K. Hald, N. Bjerre, H. Stapelfeldt, and T. Seideman, “Three dimensional alignment of molecules using elliptically polarized laser fields,” *Phys. Rev. Lett.*, vol. 85, no. 12, p. 2470, 2000, [doi: 10.1103/PhysRevLett.85.2470](https://doi.org/10.1103/PhysRevLett.85.2470).
- [116] T. Ergler *et al.*, “Quantum-phase resolved mapping of ground-state vibrational D2 wave packets via selective depletion in intense laser pulses,” *Phys. Rev. Lett.*, vol. 97, no. 10, p. 103004, 2006, [doi: 10.1103/PhysRevLett.97.103004](https://doi.org/10.1103/PhysRevLett.97.103004).
- [117] Y. Malakar *et al.*, “Time-resolved imaging of bound and dissociating nuclear wave packets in strong-field ionized iodomethane,” *Phys. Chem. Chem. Phys.*, vol. 21, no. 26, pp. 14090–14102, 2019, [doi: 10.1039/c8cp07032f](https://doi.org/10.1039/c8cp07032f).
- [118] S. Eden, P. Limão-Vieira, S. V. Hoffmann, and N. J. Mason, “VUV spectroscopy of CH<sub>3</sub>Cl and CH<sub>3</sub>I,” *Chem. Phys.*, vol. 331, no. 2–3, pp. 232–244, 2007, [doi: 10.1016/j.chemphys.2006.10.021](https://doi.org/10.1016/j.chemphys.2006.10.021).
- [119] A. B. Alekseyev, H.-P. Liebermann, R. J. Buenker, and S. N. Yurchenko, “An ab initio study of the CH<sub>3</sub>I photodissociation. I. Potential energy surfaces,” *J. Chem. Phys.*, vol. 126, no. 23, p. 234102, Jun. 2007, [doi: 10.1063/1.2736695](https://doi.org/10.1063/1.2736695).
- [120] A. B. Alekseyev, H. P. Liebermann, and R. J. Buenker, “An ab initio study of the CH<sub>3</sub>I

- photodissociation. II. Transition moments and vibrational state control of the I\* quantum yields,” *J. Chem. Phys.*, vol. 126, no. 23, p. 234103, 2007, [doi: 10.1063/1.2736696](https://doi.org/10.1063/1.2736696).
- [121] A. B. Alekseyev, H. P. Liebermann, and R. J. Buenker, “Ab initio configuration interaction study of the B- and C-band photodissociation of methyl iodide,” *J. Chem. Phys.*, vol. 134, no. 4, p. 044303, 2011, [doi: 10.1063/1.3532926](https://doi.org/10.1063/1.3532926).
- [122] A. Tokmakoff, “Introduction to Light-Matter Interactions,” 2020. <https://chem.libretexts.org/@go/page/107251>.
- [123] “Essentials of molecular photochemistry,” *Choice Rev. Online*, vol. 29, no. 01, 1991, [doi: 10.5860/choice.29-0309](https://doi.org/10.5860/choice.29-0309).
- [124] K. Scherzer, “Photodissoziation Dynamics, Spectroscopy and Fragmentation of Small Polyatomic Molecules,” *Zeitschrift für Phys. Chemie*, vol. 194, no. 1, 1996, [doi: 10.1524/zpch.1996.194.part\\_1.132b](https://doi.org/10.1524/zpch.1996.194.part_1.132b).
- [125] Hugh Burrows, “Principles of Molecular Photochemistry - An Introduction,” *Bol. da Soc. Port. Química*, 2010, [doi: 10.52590/m3.p649.a30001592](https://doi.org/10.52590/m3.p649.a30001592).
- [126] “Springer handbook of atomic, molecular, and optical physics,” *Choice Rev. Online*, vol. 43, no. 10, 2006, [doi: 10.5860/choice.43-5953](https://doi.org/10.5860/choice.43-5953).
- [127] N. J. Turro, *Principles of molecular photochemistry: an introduction*. 2009.
- [128] M. L. M. Sánchez, “Ultrafast studies on time-resolved structural dynamics of photodissociating molecules,” 2021.
- [129] R. N. Zare, *Photoejection Dynamics*, vol. 4, no. 1. 1972, <https://apps.dtic.mil/sti/citations/ADA540204>.
- [130] “Selection rules and transition moment integral,” 2020. <https://chem.libretexts.org/@go/page/1784>.
- [131] E. Teller, “The crossing of potential surfaces,” *J. Phys. Chem.*, vol. 41, no. 1, pp. 109–116, 1937, [doi: 10.1021/j150379a010](https://doi.org/10.1021/j150379a010).
- [132] M. Boggio-Pasqua, “Computational mechanistic photochemistry: The central role of conical intersections,” 2015, <https://tel.archives-ouvertes.fr/tel-01184241>.
- [133] K. Ammosov, Delone, *Multiphoton processes in atoms*. Springer, 2000, [doi: 10.1007/978-3-642-57208-1](https://doi.org/10.1007/978-3-642-57208-1).
- [134] M. J. Molina and F. S. Rowland, “Stratospheric sink for chlorofluoromethanes: chlorine atom-catalysed destruction of ozone,” *Nature*, vol. 249, no. 5460, pp. 810–812, 1974, [doi: 10.1038/249810a0](https://doi.org/10.1038/249810a0).

[10.1038/249810a0](https://doi.org/10.1038/249810a0).

- [135] L. J. Carpenter, D. J. Wevill, C. J. Palmer, and J. Michels, “Depth profiles of volatile iodine and bromine-containing halocarbons in coastal Antarctic waters,” *Mar. Chem.*, vol. 103, no. 3–4, pp. 227–236, 2007, [doi: 10.1016/j.marchem.2006.08.003](https://doi.org/10.1016/j.marchem.2006.08.003).
- [136] M. E. Corrales, G. Gitzinger, J. González-Vázquez, V. Loriot, R. De Nalda, and L. Bañares, “Velocity map imaging and theoretical study of the Coulomb explosion of CH<sub>3</sub>I under intense femtosecond IR pulses,” *J. Phys. Chem. A*, vol. 116, no. 11, pp. 2669–2677, 2012, [doi: 10.1021/jp207367a](https://doi.org/10.1021/jp207367a).
- [137] M. E. Corrales, J. González-Vázquez, G. Balerdi, I. R. Solá, R. De Nalda, and L. Bañares, “Control of ultrafast molecular photodissociation by laser-field-induced potentials,” *Nat. Chem.*, vol. 6, no. 9, pp. 785–790, 2014, [doi: 10.1038/nchem.2006](https://doi.org/10.1038/nchem.2006).
- [138] M. E. Corrales, J. González-Vázquez, R. De Nalda, and L. Bañares, “Coulomb Explosion Imaging for the Visualization of a Conical Intersection,” *J. Phys. Chem. Lett.*, vol. 10, no. 2, pp. 138–143, 2019, [doi: 10.1021/acs.jpcclett.8b03726](https://doi.org/10.1021/acs.jpcclett.8b03726).
- [139] M. E. Corrales, P. S. Shternin, L. Rubio-Lago, R. De Nalda, O. S. Vasyutinskii, and L. Bañares, “Femtosecond Time-Resolved Photofragment Rotational Angular Momentum Alignment in Electronic Predissociation Dynamics,” *J. Phys. Chem. Lett.*, vol. 7, no. 22, pp. 4458–4463, 2016, [doi: 10.1021/acs.jpcclett.6b01874](https://doi.org/10.1021/acs.jpcclett.6b01874).
- [140] F. G. Godwin, P. A. Gorry, P. M. Hughes, D. Raybone, T. M. Watkinson, and J. C. Whitehead, “Two-photon VUV laser-induced fluorescence detection of I\*(<sup>2</sup>P<sub>1/2</sub>) and I(<sup>2</sup>P<sub>1/2</sub>) from alkyl iodide photodissociation at 248 nm,” *Chem. Phys. Lett.*, vol. 135, no. 1–2, p. 163, 1987, [doi: 10.1016/0009-2614\(87\)87237-8](https://doi.org/10.1016/0009-2614(87)87237-8).
- [141] E. M. Warne *et al.*, “Photodissociation dynamics of methyl iodide probed using femtosecond extreme ultraviolet photoelectron spectroscopy,” *Phys. Chem. Chem. Phys.*, vol. 22, no. 44, pp. 25695–25703, 2020, [doi: 10.1039/d0cp03478a](https://doi.org/10.1039/d0cp03478a).
- [142] B. Downes-Ward *et al.*, “Photodissociation dynamics of methyl iodide across the A-band probed by femtosecond extreme ultraviolet photoelectron spectroscopy,” *J. Phys. B At. Mol. Opt. Phys.*, vol. 54, no. 13, p. 134003, 2021, [doi: 10.1088/1361-6455/ac08f3](https://doi.org/10.1088/1361-6455/ac08f3).
- [143] E. M. Warne *et al.*, “Photodissociation dynamics of CH<sub>3</sub>I probed via multiphoton ionisation photoelectron spectroscopy,” *Phys. Chem. Chem. Phys.*, vol. 21, no. 21, pp. 11142–11149, 2019, [doi: 10.1039/c9cp01477b](https://doi.org/10.1039/c9cp01477b).

- [144] A. R. Attar, A. Bhattacharjee, and S. R. Leone, “Direct Observation of the Transition-State Region in the Photodissociation of CH<sub>3</sub>I by Femtosecond Extreme Ultraviolet Transient Absorption Spectroscopy,” *J. Phys. Chem. Lett.*, vol. 6, no. 24, pp. 5072–5077, 2015, [doi: 10.1021/acs.jpcllett.5b02489](https://doi.org/10.1021/acs.jpcllett.5b02489).
- [145] A. T. J. B. Eppink and D. H. Parker, “Methyl iodide A-band decomposition study by photofragment velocity imaging,” *J. Chem. Phys.*, vol. 109, no. 12, p. 4758, 1998, [doi: 10.1063/1.477087](https://doi.org/10.1063/1.477087).
- [146] A. T. J. B. Eppink and D. H. Parker, “Energy partitioning following photodissociation of methyl iodide in the A band: A velocity mapping study,” *J. Chem. Phys.*, vol. 110, no. 2, p. 832, 1999, [doi: 10.1063/1.478051](https://doi.org/10.1063/1.478051).
- [147] M. L. Murillo-Sánchez, S. Marggi Poullain, J. González-Vázquez, M. E. Corrales, G. Balardi, and L. Bañares, “Femtosecond photodissociation dynamics of chloriodomethane in the first absorption band,” *Chem. Phys. Lett.*, vol. 683, pp. 22–28, 2017, [doi: 10.1016/j.cplett.2017.02.037](https://doi.org/10.1016/j.cplett.2017.02.037).
- [148] R. De Nalda, J. G. Izquierdo, J. Durá, and L. Bañares, “Femtosecond multichannel photodissociation dynamics of CH<sub>3</sub>I from the A band by velocity map imaging,” *J. Chem. Phys.*, vol. 126, no. 2, p. 021101, 2007, [doi: 10.1063/1.2426332](https://doi.org/10.1063/1.2426332).
- [149] K. F. Chang, H. Wang, S. M. Poullain, D. Prendergast, D. M. Neumark, and S. R. Leone, “Mapping wave packet bifurcation at a conical intersection in CH<sub>3</sub>I by attosecond XUV transient absorption spectroscopy,” *J. Chem. Phys.*, vol. 154, no. 23, p. 234301, 2021, [doi: 10.1063/5.0056299](https://doi.org/10.1063/5.0056299).
- [150] K. Walter, R. Weinkauff, U. Boesl, and E. W. Schlag, “Molecular ion spectroscopy: Mass selected, resonant two-photon dissociation spectra of CH<sub>3</sub>I<sup>+</sup> and CD<sub>3</sub>I<sup>+</sup>,” *J. Chem. Phys.*, vol. 89, no. 4, p. 1914, 1988, [doi: 10.1063/1.455088](https://doi.org/10.1063/1.455088).
- [151] A. Tehlar and H. J. Wörner, “Time-resolved high-harmonic spectroscopy of the photodissociation of CH<sub>3</sub>I and CF<sub>3</sub>I,” *Mol. Phys.*, vol. 111, no. 14–15, pp. 2057–2067, 2013, [doi: 10.1080/00268976.2013.782439](https://doi.org/10.1080/00268976.2013.782439).
- [152] K. Matthíasson, G. Koumariou, M. X. Jiang, P. Glodic, P. C. Samartzis, and Á. Kvaran, “Formation of highly excited iodine atoms from multiphoton excitation of CH<sub>3</sub>I,” *Phys. Chem. Chem. Phys.*, vol. 22, no. 9, pp. 4984–4992 BibTex, 2020, [doi: 10.1039/c9cp06242d](https://doi.org/10.1039/c9cp06242d).
- [153] H. Liu, Z. Yang, Z. Gao, and Z. Tang, “Ionization and dissociation of CH<sub>3</sub>I in intense laser

- field,” *J. Chem. Phys.*, vol. 126, no. 4, p. 044316, 2007, [doi: 10.1063/1.2424703](https://doi.org/10.1063/1.2424703).
- [154] M. H. M. Janssen, M. Dantus, H. Guo, and A. H. Zewail, “Femtosecond reaction dynamics of Rydberg states. Methyl iodide,” *Chem. Phys. Lett.*, vol. 214, no. 3–4, pp. 281–289, 1993, [doi: 10.1016/0009-2614\(93\)85635-2](https://doi.org/10.1016/0009-2614(93)85635-2).
- [155] B. Erk *et al.*, “Imaging charge transfer in iodomethane upon x-ray photoabsorption,” *Science (80-. )*, vol. 345, no. 6194, pp. 288–291, 2014, [doi: 10.1126/science.1253607](https://doi.org/10.1126/science.1253607).
- [156] J. H. D. Eland, R. Frey, A. Kuestler, H. Schulte, and B. Brehm, “Unimolecular dissociations and internal conversions of methyl halide ions,” *Int. J. Mass Spectrom. Ion Phys.*, vol. 22, no. 1–2, pp. 155–170, 1976, [doi: 10.1016/0020-7381\(76\)80116-7](https://doi.org/10.1016/0020-7381(76)80116-7).
- [157] A. Baumann, D. Rompotis, O. Schepp, M. Wieland, and M. Drescher, “Time-Resolved Dissociation Dynamics of Iodomethane Resulting from Rydberg and Valence Excitation,” *J. Phys. Chem. A*, vol. 122, no. 21, pp. 4779–4784, 2018, [doi: 10.1021/acs.jpca.8b01248](https://doi.org/10.1021/acs.jpca.8b01248).
- [158] D. H. Parker, R. Pandolfi, P. R. Stannard, and M. A. El-Sayed, “Two-photon MPI spectroscopy of alkyl iodides,” *Chem. Phys.*, vol. 45, no. 1, pp. 27–37, 1980, [doi: 10.1016/0301-0104\(80\)85165-2](https://doi.org/10.1016/0301-0104(80)85165-2).
- [159] J. A. Syage, “Predissociation lifetimes of the  $\tilde{B}$  and  $\tilde{C}$  Rydberg states of  $\text{CH}_3\text{I}$ ,” *Chem. Phys. Lett.*, vol. 212, no. 1, pp. 124–128, 1993, [doi: 10.1016/0009-2614\(93\)87119-N](https://doi.org/10.1016/0009-2614(93)87119-N).
- [160] R. S. Mulliken, “Intensities in molecular electronic spectra: X. Calculations on mixed-halogen, hydrogen halide, alkyl halide, and hydroxyl spectra,” *J. Chem. Phys.*, vol. 8, no. 5, p. 382, 1940, [doi: 10.1063/1.1750671](https://doi.org/10.1063/1.1750671).
- [161] L. Rubio-Lago, A. García-Vela, A. Arregui, G. A. Amaral, and L. Bañares, “The photodissociation of  $\text{CH}_3\text{I}$  in the red edge of the A -band: Comparison between slice imaging experiments and multisurface wave packet calculations,” *J. Chem. Phys.*, vol. 131, no. 17, p. 174309, 2009, [doi: 10.1063/1.3257692](https://doi.org/10.1063/1.3257692).
- [162] M. G. González, J. D. Rodríguez, L. Rubio-Lago, A. García-Vela, and L. Bañares, “Slice imaging and wave packet study of the photodissociation of  $\text{CH}_3\text{I}$  in the blue edge of the A-band: Evidence of reverse  $^3\text{Q}_0 \leftarrow ^1\text{Q}_1$  non-adiabatic dynamics,” *Phys. Chem. Chem. Phys.*, vol. 13, no. 36, pp. 16404–16415, 2011, [doi: 10.1039/c1cp21378d](https://doi.org/10.1039/c1cp21378d).
- [163] D. Imre, J. L. Kinsey, A. Sinha, and J. Krenos, “Chemical dynamics studied by emission spectroscopy of dissociating molecules,” *Journal of Physical Chemistry*, vol. 88, no. 18, pp. 3956–3964, 1984, [doi: 10.1021/j150662a017](https://doi.org/10.1021/j150662a017).

- [164] S. M. Poullain, D. V. Chicharro, L. Rubio-Lago, A. García-Vela, and L. Bañares, “A velocity-map imaging study of methyl non-resonant multiphoton ionization from the photodissociation of CH<sub>3</sub>I in the A-band,” *Philos. Trans. R. Soc. A Math. Phys. Eng. Sci.*, vol. 375, no. 2092, p. 20160205, 2017, [doi: 10.1098/rsta.2016.0205](https://doi.org/10.1098/rsta.2016.0205).
- [165] A. Gedanken and M. D. Rowe, “Magnetic circular dichroism spectra of the methyl halides. Resolution of the  $n \rightarrow \sigma^*$  continuum,” *Chem. Phys. Lett.*, vol. 34, no. 1, pp. 39–43, 1975, [doi: 10.1016/0009-2614\(75\)80196-5](https://doi.org/10.1016/0009-2614(75)80196-5).
- [166] R. De Nalda, J. Durá, A. García-Vela, J. G. Izquierdo, J. González-Vázquez, and L. Bañares, “A detailed experimental and theoretical study of the femtosecond A -band photodissociation of C H<sub>3</sub>I,” *J. Chem. Phys.*, vol. 128, no. 24, p. 244309, 2008, [doi: 10.1063/1.2943198](https://doi.org/10.1063/1.2943198).
- [167] R. S. Mulliken and E. Teller, “Interpretation of the methyl iodide absorption bands near 2000,” *Phys. Rev.*, vol. 61, no. 5–6, p. 283, 1942, [doi: 10.1103/PhysRev.61.283](https://doi.org/10.1103/PhysRev.61.283).
- [168] M. R. Dobber, W. J. Buma, and C. A. De Lange, “Resonance enhanced multiphoton ionization photoelectron spectroscopy on nanosecond and picosecond time scales of Rydberg states of methyl iodide,” *J. Chem. Phys.*, vol. 99, no. 2, p. 836, 1993, [doi: 10.1063/1.465347](https://doi.org/10.1063/1.465347).
- [169] K. Tsukiyama, B. Katz, and R. Bersohn, “Competition between photodissociation and photoionization in methyl iodide,” *Chem. Phys. Lett.*, vol. 124, no. 4, pp. 309–312, 1986, [doi: 10.1016/0009-2614\(86\)85023-0](https://doi.org/10.1016/0009-2614(86)85023-0).
- [170] N. Thiré, R. Cireasa, D. Staedter, V. Blanchet, and S. T. Pratt, “Time-resolved predissociation of the vibrationless level of the B state of CH<sub>3</sub>I,” *Phys. Chem. Chem. Phys.*, vol. 13, no. 41, pp. 18485–18496, 2011, [doi: 10.1039/c1cp22057h](https://doi.org/10.1039/c1cp22057h).
- [171] N. Thiré, R. Cireasa, V. Blanchet, and S. T. Pratt, “Time-resolved photoelectron spectroscopy of the CH<sub>3</sub>I B<sup>1</sup>E 6s [2] state,” *Phys. Chem. Chem. Phys.*, vol. 12, no. 48, pp. 15644–15652, 2010, [doi: 10.1039/c004220j](https://doi.org/10.1039/c004220j).
- [172] G. Gitzinger, M. E. Corrales, V. Lorient, G. A. Amaral, R. de Nalda, and L. Bañares, “A femtosecond velocity map imaging study on B-band predissociation in CH<sub>3</sub>I. I. The band origin,” *J. Chem. Phys.*, vol. 132, no. 23, p. 234313, Jun. 2010, [doi: 10.1063/1.3455207](https://doi.org/10.1063/1.3455207).
- [173] G. Gitzinger, M. E. Corrales, V. Lorient, R. De Nalda, and L. Bañares, “A femtosecond velocity map imaging study on B-band predissociation in CH<sub>3</sub>I. II. the 2<sup>0</sup><sub>1</sub> and 3<sup>0</sup><sub>1</sub> vibronic

- levels,” *J. Chem. Phys.*, vol. 136, no. 7, p. 074303, 2012, [doi: 10.1063/1.3683252](https://doi.org/10.1063/1.3683252).
- [174] H. Xu and S. T. Pratt, “A new look at the photodissociation of methyl iodide at 193 nm,” *J. Chem. Phys.*, vol. 139, no. 21, p. 214310, 2013, [doi: 10.1063/1.4829747](https://doi.org/10.1063/1.4829747).
- [175] A. P. Baronavski and J. C. Owrutsky, “Vibronic dependence of the  $\tilde{B}$  state lifetimes of  $\text{CH}_3\text{I}$  and  $\text{CD}_3\text{I}$  using femtosecond photoionization spectroscopy,” *J. Chem. Phys.*, vol. 108, no. 9, pp. 3445–3452, Mar. 1998, [doi: 10.1063/1.475744](https://doi.org/10.1063/1.475744).
- [176] Y. Wang, H. Shen, L. Hua, C. Hu, and B. Zhang, “Predissociation dynamics of the B state of  $\text{CH}_3\text{I}$  by femtosecond pump-probe technique,” *Opt. Express*, vol. 17, no. 13, pp. 10506–10513, Jun. 2009, [doi: 10.1364/OE.17.010506](https://doi.org/10.1364/OE.17.010506).
- [177] R. Forbes *et al.*, “Time-resolved site-selective imaging of predissociation and charge transfer dynamics: The  $\text{CH}_3\text{I}$  B-band,” *J. Phys. B At. Mol. Opt. Phys.*, vol. 53, no. 22, p. 224001, 2020, [doi: 10.1088/1361-6455/abb1fd](https://doi.org/10.1088/1361-6455/abb1fd).
- [178] H. Guo and A. H. Zewail, “Femtosecond real-time probing of reactions. XIV. Rydberg states of methyl iodide,” *Can. J. Chem.*, vol. 72, no. 3, p. 947, 1994, [doi: 10.1139/v94-123](https://doi.org/10.1139/v94-123).
- [179] D. J. Donaldson, M. S. Child, and V. Vaida, “Surface crossings and predissociation dynamics of methyl iodide Rydberg states,” *J. Chem. Phys.*, vol. 88, no. 12, p. 7410, 1988, [doi: 10.1063/1.454304](https://doi.org/10.1063/1.454304).
- [180] M. Tadjeddine, J. P. Flament, and C. Teichteil, “Non-empirical spin-orbit calculation of the  $\text{CH}_3\text{I}$  ground state,” *Chem. Phys.*, vol. 118, no. 1, pp. 45–55, 1987, [doi: 10.1016/0301-0104\(87\)85035-8](https://doi.org/10.1016/0301-0104(87)85035-8).
- [181] W. P. Hess, R. Naaman, and S. R. Leone, “Nonunity quantum yield of excited iodine atoms in the 193 nm photodissociation of methyl iodide,” *J. Phys. Chem.*, vol. 91, no. 24, pp. 6085–6087, Nov. 1987, [doi: 10.1021/j100308a004](https://doi.org/10.1021/j100308a004).
- [182] A. Gilchrist, G. Hancock, R. Peverall, G. Richmond, G. A. D. Ritchie, and S. Taylor, “Methyl iodide photodissociation at 193 nm: The  $\text{I}(^2\text{P}_{1/2})$  quantum yield,” *J. Phys. Chem. A*, vol. 112, no. 20, pp. 4531–4536, 2008, [doi: 10.1021/jp710799k](https://doi.org/10.1021/jp710799k).
- [183] M. Brouard *et al.*, “The application of the fast, multi-hit, pixel imaging mass spectrometry sensor to spatial imaging mass spectrometry,” *Rev. Sci. Instrum.*, vol. 83, no. 11, p. 114101, 2012, [doi: 10.1063/1.4766938](https://doi.org/10.1063/1.4766938).
- [184] H. Keller-Rudek, G. K. Moortgat, R. Sander, and R. Sørensen, “The MPI-Mainz UV/VIS spectral atlas of gaseous molecules of atmospheric interest,” *Earth System Science Data*,

- 2013.
- [185] S. Marggi Poullain, D. V. Chicharro, E. Navarro, L. Rubio-Lago, J. González-Vázquez, and L. Bañares, “Photodissociation dynamics of bromiodomethane from the first and second absorption bands. A combined velocity map and slice imaging study,” *Phys. Chem. Chem. Phys.*, vol. 20, no. 5, pp. 3490–3503, 2018, [doi: 10.1039/c7cp07077b](https://doi.org/10.1039/c7cp07077b).
- [186] M. L. Murillo-Sánchez *et al.*, “Halogen-atom effect on the ultrafast photodissociation dynamics of the dihalomethanes CH<sub>2</sub>ICl and CH<sub>2</sub>BrI,” *Phys. Chem. Chem. Phys.*, vol. 20, no. 32, pp. 20766–20778, 2018, [doi: 10.1039/c8cp03600d](https://doi.org/10.1039/c8cp03600d).
- [187] L. J. Butler, E. J. Hints, S. F. Shane, and Y. T. Lee, “The electronic state-selective photodissociation of CH<sub>2</sub>BrI at 248, 210, and 193 nm,” *J. Chem. Phys.*, vol. 86, no. 4, pp. 2051–2074, Feb. 1987, [doi: 10.1063/1.452155](https://doi.org/10.1063/1.452155).
- [188] S. J. Lee and R. Bersohn, “ChemInform Abstract: Photodissociation of a molecule with two chromophores. bromiodomethane,” *Chem. Informationsd.*, vol. 13, no. 24, pp. 728–730, 1982, [doi: 10.1002/chin.198224130](https://doi.org/10.1002/chin.198224130).
- [189] Y.-J. Liu, D. Ajitha, J. W. Krogh, A. N. Tarnovsky, and R. Lindh, “Spin–Orbit Ab Initio Investigation of the Photolysis of Bromiodomethane,” *ChemPhysChem*, vol. 7, no. 4, pp. 955–963, Apr. 2006, [doi: 10.1002/cphc.200500654](https://doi.org/10.1002/cphc.200500654).
- [190] X. Zheng and D. L. Phillips, “Photoisomerization reaction of CH<sub>2</sub>BrI following A -band and B -band photoexcitation in the solution phase: Transient resonance Raman observation of the iso-CH<sub>2</sub>I–Br photoproduct,” *J. Chem. Phys.*, vol. 113, no. 8, p. 3194, 2000, [doi: 10.1063/1.1286920](https://doi.org/10.1063/1.1286920).
- [191] V. A. Borin, S. M. Matveev, D. S. Budkina, P. Z. El-Khoury, and A. N. Tarnovsky, “Direct photoisomerization of CH<sub>2</sub>I<sub>2</sub>: Vs. CHBr<sub>3</sub> in the gas phase: A joint 50 fs experimental and multireference resonance-theoretical study,” *Phys. Chem. Chem. Phys.*, vol. 18, no. 41, pp. 28883–28892, 2016, [doi: 10.1039/c6cp05129d](https://doi.org/10.1039/c6cp05129d).
- [192] A. S. Mereshchenko, E. V Butaeva, V. A. Borin, A. Eyzips, and A. N. Tarnovsky, “Roaming-mediated ultrafast isomerization of geminal tri-bromides in the gas and liquid phases,” *Nat. Chem.*, vol. 7, no. 7, pp. 562–568, 2015, [doi: 10.1038/nchem.2278](https://doi.org/10.1038/nchem.2278).
- [193] A. N. Tarnovsky, J.-L. Alvarez, A. P. Yartsev, V. Sundström, and E. Åkesson, “Photodissociation dynamics of diiodomethane in solution,” *Chem. Phys. Lett.*, vol. 312, no. 2, pp. 121–130, 1999, [doi: 10.1016/S0009-2614\(99\)00916-1](https://doi.org/10.1016/S0009-2614(99)00916-1).

- [194] P. Martin *et al.*, “Direct Determination of Absolute Molecular Stereochemistry in Gas Phase by Coulomb Explosion Imaging,” *Science* (80-. ), vol. 341, no. 6150, pp. 1096–1100, Sep. 2013, [doi: 10.1126/science.1240362](https://doi.org/10.1126/science.1240362).
- [195] E. Tomoyuki *et al.*, “Capturing roaming molecular fragments in real time,” *Science* (80-. ), vol. 370, no. 6520, pp. 1072–1077, Nov. 2020, [doi: 10.1126/science.abc2960](https://doi.org/10.1126/science.abc2960).
- [196] X. Ren *et al.*, “Single-shot carrier-envelope-phase tagging using an f-2f interferometer and a phase meter: A comparison,” *J. Opt. (United Kingdom)*, vol. 19, no. 12, p. 124017, 2017, [doi: 10.1088/2040-8986/aa9865](https://doi.org/10.1088/2040-8986/aa9865).
- [197] J. H. Posthumus, “The dynamics of small molecules in intense laser fields,” *Reports Prog. Phys.*, vol. 67, no. 5, p. 623, 2004, [doi: 10.1088/0034-4885/67/5/R01](https://doi.org/10.1088/0034-4885/67/5/R01).
- [198] T. Brabec and F. Krausz, “Intense few-cycle laser fields: Frontiers of nonlinear optics,” *Rev. Mod. Phys.*, vol. 72, no. 2, p. 545, 2000, [doi: 10.1103/RevModPhys.72.545](https://doi.org/10.1103/RevModPhys.72.545).
- [199] J. C. Diels and W. Rudolph, *Ultrashort Laser Pulse Phenomena*. 2006.
- [200] D. E. Spence, P. N. Kean, and W. Sibbett, “60-fsec pulse generation from a self-mode-locked Ti:sapphire laser,” *Opt. Lett.*, vol. 16, no. 1, pp. 42–44, 1991, [doi: 10.1364/OL.16.000042](https://doi.org/10.1364/OL.16.000042).
- [201] M. Piché, “Beam reshaping and self-mode-locking in nonlinear laser resonators,” *Opt. Commun.*, vol. 86, no. 2, pp. 156–160, 1991, [doi: 10.1016/0030-4018\(91\)90552-O](https://doi.org/10.1016/0030-4018(91)90552-O).
- [202] Z. Chang, *Fundamentals of Attosecond Optics*. 2016.
- [203] M. Zohrabi, “Quantum control of molecular fragmentation in strong laser fields,” PhD thesis, Kansas State University 2014, <http://hdl.handle.net/2097/18401>.
- [204] E. Hecht and A. Zajac, “Optics,” *Am. J. Phys.*, vol. 42, no. 10, pp. 921–922, Oct. 1974, [doi: 10.1119/1.1987895](https://doi.org/10.1119/1.1987895).
- [205] R. Goldstein, “Pockels Cell Primer,” *Laser Focus*, vol. 34, no. 1. 1968.
- [206] R. Trebino, *Frequency-Resolved Optical Gating: The Measurement of Ultrashort Laser Pulses*. 2000, [doi: 10.1007/978-1-4615-1181-6](https://doi.org/10.1007/978-1-4615-1181-6).
- [207] T. C. Wong and R. Trebino, “Single-frame measurement of complex laser pulses tens of picoseconds long using pulse-front tilt in cross-correlation frequency-resolved optical gating,” *J. Opt. Soc. Am. B*, vol. 30, no. 11, pp. 2781–2786, 2013, [doi: 10.1364/josab.30.002781](https://doi.org/10.1364/josab.30.002781).
- [208] R. J. Lanzafame and J.-C. D. and W. Rudolph, *Ultrashort Laser Pulse Phenomena*:

- Fundamentals, Techniques, and Applications on a Femtosecond Time Scale*, vol. 25, no. 1. 2007, [doi: 10.1016/B978-0-12-215493-5.X5000-9](https://doi.org/10.1016/B978-0-12-215493-5.X5000-9).
- [209] K. W. DeLong, B. Kohler, K. Wilson, D. N. Fittinghoff, and R. Trebino, “Pulse retrieval in frequency-resolved optical gating based on the method of generalized projections,” *Opt. Lett.*, vol. 19, no. 24, pp. 2152–2154, 1994, [doi: 10.1364/ol.19.002152](https://doi.org/10.1364/ol.19.002152).
- [210] R. Trebino and D. J. Kane, “Using phase retrieval to measure the intensity and phase of ultrashort pulses: frequency-resolved optical gating,” *J. Opt. Soc. Am. A*, vol. 10, no. 5, pp. 1101–1111, 1993, [doi: 10.1364/josaa.10.001101](https://doi.org/10.1364/josaa.10.001101).
- [211] D. J. Kane and R. Trebino, “Characterization of Arbitrary Femtosecond Pulses Using Frequency-Resolved Optical Gating,” *IEEE J. Quantum Electron.*, vol. 29, no. 2, pp. 571–579, 1993, [doi: 10.1109/3.199311](https://doi.org/10.1109/3.199311).
- [212] J. N. Sweetser, D. N. Fittinghoff, and R. Trebino, “Transient-grating frequency-resolved optical gating,” *Opt. Lett.*, vol. 22, no. 8, pp. 519–521, 1997, [doi: 10.1364/ol.22.000519](https://doi.org/10.1364/ol.22.000519).
- [213] K. W. DeLong, R. Trebino, J. Hunter, and W. E. White, “Frequency-resolved optical gating with the use of second-harmonic generation,” *J. Opt. Soc. Am. B*, vol. 11, no. 11, pp. 2206–2215, 1994, [doi: 10.1364/josab.11.002206](https://doi.org/10.1364/josab.11.002206).
- [214] D. J. Kane, “Real-time measurement of ultrashort laser pulses using principal component generalized projections,” *IEEE J. Sel. Top. Quantum Electron.*, vol. 4, no. 2, pp. 278–284, 1998, [doi: 10.1109/2944.686733](https://doi.org/10.1109/2944.686733).
- [215] S. Linden, H. Giessen, and J. Kuhl, “XFROG - A new method for amplitude and phase characterization of weak ultrashort pulses,” *Phys. Status Solidi Basic Res.*, vol. 206, no. 1, pp. 119–124, 1998, [doi: 10.1002/\(SICI\)1521-3951\(199803\)206:1<119::AID-PSSB119>3.0.CO;2-X](https://doi.org/10.1002/(SICI)1521-3951(199803)206:1<119::AID-PSSB119>3.0.CO;2-X).
- [216] G. New, *Introduction to nonlinear optics*, vol. 9780521877015. 2011, [doi: 10.1017/CBO9780511975851](https://doi.org/10.1017/CBO9780511975851).
- [217] R. Boyd, *Nonlinear Optics*. Academic Press, 2003.
- [218] K. Nassau, “Handbook of non-linear optical crystals,” *Mater. Res. Bull.*, vol. 27, no. 11, 1992, [doi: 10.1016/0025-5408\(92\)90102-6](https://doi.org/10.1016/0025-5408(92)90102-6).
- [219] A. V Smith, *Crystal Nonlinear Optics: With SNLO Examples*. AS-Photonics, 2018.
- [220] J. Lekner, “Reflection and refraction by uniaxial crystals,” *J. Phys. Condens. Matter*, vol. 3, no. 32, pp. 6121–6133, Aug. 1991, [doi: 10.1088/0953-8984/3/32/017](https://doi.org/10.1088/0953-8984/3/32/017).

- [221] S. Y. Chen *et al.*, “I<sub>2</sub> molecular elimination in single-photon dissociation of CH<sub>2</sub>I<sub>2</sub> at 248 nm by using cavity ring-down absorption spectroscopy,” *J. Chem. Phys.*, vol. 134, no. 3, p. 034315, 2011, [doi: 10.1063/1.3523571](https://doi.org/10.1063/1.3523571).
- [222] T. Kobayashi, H. Yao, K. Amano, Y. Fukushima, A. Morimoto, and T. Sueta, “Optical pulse compression using high-frequency electrooptic phase modulation,” *IEEE J. Quantum Electron.*, vol. 24, no. 2, pp. 382–387, 1988, [doi: 10.1109/3.135](https://doi.org/10.1109/3.135).
- [223] M. R. Panman *et al.*, “Observing the Structural Evolution in the Photodissociation of Diiodomethane with Femtosecond Solution X-Ray Scattering,” *Phys. Rev. Lett.*, vol. 125, no. 22, p. 226001, 2020, [doi: 10.1103/PhysRevLett.125.226001](https://doi.org/10.1103/PhysRevLett.125.226001).
- [224] P. Dombi, V. S. Yakovlev, K. O’Keeffe, T. Fuji, M. Lezius, and G. Tempea, “Pulse compression with time-domain optimized chirped mirrors,” *Opt. Express*, vol. 13, no. 26, pp. 10888–10894, 2005, [doi: 10.1364/OPEX.13.010888](https://doi.org/10.1364/OPEX.13.010888).
- [225] A. M. Weiner, *Ultrafast Optics*. 2009, [doi: 10.1002/9780470473467](https://doi.org/10.1002/9780470473467).
- [226] E. B. Treacy, “Optical Pulse Compression with Diffraction Gratings,” *IEEE J. Quantum Electron.*, vol. 5, no. 9, pp. 454–458, 1969, [doi: 10.1109/JQE.1969.1076303](https://doi.org/10.1109/JQE.1969.1076303).
- [227] P. J. Collings, “The Fast Fourier Transform by E. Oran Brigham. Reviewed,” *Am. J. Phys.*, vol. 43, no. 2, p. 200, 1975, [doi: 10.1119/1.9909](https://doi.org/10.1119/1.9909).
- [228] R. E. Sherriff, “Analytic expressions for group-delay dispersion and cubic dispersion in arbitrary prism sequences,” *J. Opt. Soc. Am. B*, vol. 15, no. 3, pp. 1224–1230, 1998, [doi: 10.1364/JOSAB.15.001224](https://doi.org/10.1364/JOSAB.15.001224).
- [229] S. Kane and J. Squier, “Grism-pair stretcher–compressor system for simultaneous second- and third-order dispersion compensation in chirped-pulse amplification,” *J. Opt. Soc. Am. B*, vol. 14, no. 3, pp. 661–665, 1997, [doi: 10.1364/JOSAB.14.000661](https://doi.org/10.1364/JOSAB.14.000661).
- [230] “Grating Pulse Compressor,” [https://ibsen.com/wp-content/uploads/PCG\\_Calculator\\_V1.html](https://ibsen.com/wp-content/uploads/PCG_Calculator_V1.html).
- [231] R. L. Fork, O. E. Martinez, and J. P. Gordon, “Negative dispersion using pairs of prisms,” *Opt. Lett.*, vol. 9, no. 5, pp. 150–152, 1984, [doi: 10.1364/ol.9.000150](https://doi.org/10.1364/ol.9.000150).
- [232] C. Froehly, B. Colombeau, and M. Vampouille, “II Shaping and Analysis of Picosecond Light Pulses,” *Prog. Opt.*, vol. 20, no. C, pp. 63–153, 1983, [doi: 10.1016/S0079-6638\(08\)70277-4](https://doi.org/10.1016/S0079-6638(08)70277-4).
- [233] S. Akturk, X. Gu, P. Gabolde, and R. Trebino, “The general theory of first-order spatio-

- temporal distortions of Gaussian pulses and beams,” *Opt. Express*, vol. 13, no. 21, pp. 8642–8661, 2005, [doi: 10.1364/opex.13.008642](https://doi.org/10.1364/opex.13.008642).
- [234] V. K. Chauhan, J. Cohen, P. M. Vaughan, P. Bowlan, and R. Trebino, “Distortion-free single-prism/grating ultrashort laser pulse compressor,” *IEEE J. Quantum Electron.*, vol. 46, no. 12, pp. 1726–1731, 2010, [doi: 10.1109/JQE.2010.2063017](https://doi.org/10.1109/JQE.2010.2063017).
- [235] O. E. Martinez, J. P. Gordon, and R. L. Fork, “Negative group-velocity dispersion using refraction,” *J. Opt. Soc. Am. A*, vol. 1, no. 10, pp. 1003–1006, 1984, [doi: 10.1364/josaa.1.001003](https://doi.org/10.1364/josaa.1.001003).
- [236] J. P. Gordon and R. L. Fork, “Optical resonator with negative dispersion,” *Opt. Lett.*, vol. 9, no. 5, pp. 153–155, 1984, [doi: 10.1364/ol.9.000153](https://doi.org/10.1364/ol.9.000153).
- [237] F. Ziaee *et al.*, “Probing ultrafast molecular dynamics by time-resolved coincident ion momentum imaging,” in *Optics InfoBase Conference Papers*, 2019, vol. Part F144-FiO 2019, [doi: 10.1364/FIO.2019.FM1F.3.pdf](https://doi.org/10.1364/FIO.2019.FM1F.3.pdf).
- [238] H. Dachraoui, C. Oberer, M. Michelswirth, and U. Heinzmann, “Direct time-domain observation of laser pulse filaments in transparent media,” *Phys. Rev. A - At. Mol. Opt. Phys.*, vol. 82, no. 4, p. 043820, 2010, [doi: 10.1103/PhysRevA.82.043820](https://doi.org/10.1103/PhysRevA.82.043820).
- [239] J. K. Wahlstrand, Y. H. Chen, Y. H. Cheng, S. R. Varma, and H. M. Milchberg, “Measurements of the high field optical nonlinearity and electron density in gases: Application to filamentation experiments,” *IEEE J. Quantum Electron.*, vol. 48, no. 6, pp. 760–767, 2012, [doi: 10.1109/JQE.2012.2187881](https://doi.org/10.1109/JQE.2012.2187881).
- [240] B. Berry *et al.*, “Note: Determining the detection efficiency of excited neutral atoms by a microchannel plate detector,” *Rev. Sci. Instrum.*, vol. 86, no. 4, p. 46103, Apr. 2015, [doi: 10.1063/1.4916953](https://doi.org/10.1063/1.4916953).
- [241] I. Ben-Itzhak *et al.*, “Dissociation and Ionization of  $H_2^+$  by Ultrashort Intense Laser Pulses Probed by Coincidence 3D Momentum Imaging,” *Phys. Rev. Lett.*, vol. 95, no. 7, p. 73002, Aug. 2005, [doi: 10.1103/PhysRevLett.95.073002](https://doi.org/10.1103/PhysRevLett.95.073002).
- [242] I. Ben-Itzhak, “Fragmentation of molecular-ion beams in intense ultrashort laser pulses,” in *Fragmentation Processes: Topics in Atomic and Molecular Physics*, C. T. Whelan, Ed. Cambridge: Cambridge University Press, 2012, pp. 72–97, [doi: 10.1017/CBO9781139017572.004](https://doi.org/10.1017/CBO9781139017572.004).
- [243] J. Ullrich, R. Moshhammer, A. Dorn, R. Dörner, L. P. H. Schmidt, and H. Schmidt-Böcking,

- “Recoil-ion and electron momentum spectroscopy: Reaction-microscopes,” *Reports Prog. Phys.*, vol. 66, no. 9, p. 1463, 2003, [doi: 10.1088/0034-4885/66/9/203](https://doi.org/10.1088/0034-4885/66/9/203).
- [244] R. Dörner *et al.*, “Cold Target Recoil Ion Momentum Spectroscopy: A ‘momentum microscope’ to view atomic collision dynamics,” *Phys. Rep.*, vol. 330, no. 2–3, pp. 95–192, 2000, [doi: 10.1016/S0370-1573\(99\)00109-X](https://doi.org/10.1016/S0370-1573(99)00109-X).
- [245] C. L. Cocke and R. E. Olson, “Recoil ions,” *Phys. Rep.*, vol. 205, no. 4, pp. 153–219, 1991, [doi: 10.1016/0370-1573\(91\)90072-T](https://doi.org/10.1016/0370-1573(91)90072-T).
- [246] G. Scoles *et al.*, *Atomic and Molecular Beam Methods: Vol. 1*. 1998, [doi: 10.1007/978-3-642-56800-8](https://doi.org/10.1007/978-3-642-56800-8)
- [247] [http://www.dmphotronics.com/MCP\\_MCPIImageIntensifiers/microchannel\\_plates.htm](http://www.dmphotronics.com/MCP_MCPIImageIntensifiers/microchannel_plates.htm).
- [248] “RoentDek,” <https://roentdek.com/products/detectors>.
- [249] A. Rudenko *et al.*, “Fragmentation dynamics of molecular hydrogen in strong ultrashort laser pulses,” *J. Phys. B At. Mol. Opt. Phys.*, vol. 38, no. 5, p. 487, 2005, [doi: 10.1088/0953-4075/38/5/002](https://doi.org/10.1088/0953-4075/38/5/002).
- [250] “SpecTcl Home page,” <http://docs.nscl.msu.edu/daq/spectcl>.
- [251] A. M. Sayler, “Laser-induced fragmentation; Molecular ion; Ion beam; Ultrashort; Intense,” PhD thesis, Kansas State University, 2008, <http://hdl.handle.net/2097/2611>.
- [252] G. G. Paulus, W. Nicklich, H. Xu, P. Lambropoulos, and H. Walther, “Plateau in above threshold ionization spectra,” *Phys. Rev. Lett.*, vol. 72, no. 18, pp. 2851–2854, May 1994, [doi: 10.1103/PhysRevLett.72.2851](https://doi.org/10.1103/PhysRevLett.72.2851).
- [253] P. B. Corkum, “Plasma perspective on strong field multiphoton ionization,” *Phys. Rev. Lett.*, vol. 71, no. 13, pp. 1994–1997, Sep. 1993, [doi: 10.1103/PhysRevLett.71.1994](https://doi.org/10.1103/PhysRevLett.71.1994).
- [254] T. Osipov, “Experimental Study of Photo-Electron Diraction from Two-Center Molecules by Means of the COLTRIMS Technique,” PhD thesis, Kansas State University, 2003.
- [255] B. Jochim *et al.*, “Three-dimensional momentum imaging of dissociation in flight of metastable molecules,” *New J. Phys.*, vol. 19, no. 10, p. 103006, 2017, [doi: 10.1088/1367-2630/aa81ab](https://doi.org/10.1088/1367-2630/aa81ab).
- [256] J. Durá, R. De Nalda, G. A. Amaral, and L. Baares, “Imaging transient species in the femtosecond A -band photodissociation of CH<sub>3</sub>I,” *J. Chem. Phys.*, vol. 131, no. 13, p. 134311, 2009, [doi: 10.1063/1.3236808](https://doi.org/10.1063/1.3236808).
- [257] J. Laksman, D. Céolin, E. P. Månsson, S. L. Sorensen, and M. Gisselbrecht, “Development

- and characterization of a multiple-coincidence ion-momentum imaging spectrometer,” *Rev. Sci. Instrum.*, vol. 84, no. 12, p. 123113, Dec. 2013, [doi: 10.1063/1.4853435](https://doi.org/10.1063/1.4853435).
- [258] C. L. Cocke, “Momentum Imaging in Atomic Collisions,” *Phys. Scr.*, vol. 110, p. 9, 2004, [doi: 10.1238/physica.topical.110a00009](https://doi.org/10.1238/physica.topical.110a00009).
- [259] R. Boll *et al.*, “Charge transfer in dissociating iodomethane and fluoromethane molecules ionized by intense femtosecond X-ray pulses,” *Struct. Dyn.*, vol. 3, no. 4, p. 043207, 2016, [doi: 10.1063/1.4944344](https://doi.org/10.1063/1.4944344).
- [260] H. Sabzyan and M. Vafaei, “Intensity dependence of the  $H_2^+$  ionization rates in Ti:sapphire laser fields above the Coulomb-explosion threshold,” *Phys. Rev. A*, vol. 71, no. 6, p. 63404, Jun. 2005, [doi: 10.1103/PhysRevA.71.063404](https://doi.org/10.1103/PhysRevA.71.063404).
- [261] S. Erattupuzha *et al.*, “Enhanced ionisation of polyatomic molecules in intense laser pulses is due to energy upshift and field coupling of multiple orbitals,” *J. Phys. B At. Mol. Opt. Phys.*, vol. 50, no. 12, p. 125601, 2017, [doi: 10.1088/1361-6455/aa7098](https://doi.org/10.1088/1361-6455/aa7098).
- [262] E. Constant, H. Stapelfeldt, and P. B. Corkum, “Observation of Enhanced Ionization of Molecular Ions in Intense Laser Fields,” *Phys. Rev. Lett.*, vol. 76, no. 22, pp. 4140–4143, May 1996, [doi: 10.1103/PhysRevLett.76.4140](https://doi.org/10.1103/PhysRevLett.76.4140).
- [263] K. Codling, L. J. Frasinski, and P. A. Hatherly, “On the field ionisation of diatomic molecules by intense laser fields,” *J. Phys. B At. Mol. Opt. Phys.*, vol. 22, no. 12, pp. L321–L327, 1989, [doi: 10.1088/0953-4075/22/12/004](https://doi.org/10.1088/0953-4075/22/12/004).
- [264] C. Burger *et al.*, “Time-resolved nuclear dynamics in bound and dissociating acetylene,” *Struct. Dyn.*, vol. 5, no. 4, p. 44302, Jul. 2018, [doi: 10.1063/1.5037686](https://doi.org/10.1063/1.5037686).
- [265] E. Lötstedt, T. Kato, and K. Yamanouchi, “Enhanced ionization of acetylene in intense laser fields,” *Phys. Rev. A*, vol. 85, no. 4, p. 41402, Apr. 2012, [doi: 10.1103/PhysRevA.85.041402](https://doi.org/10.1103/PhysRevA.85.041402).
- [266] S. Yazdian Kashani, A. Afzalian, F. Shirinichi, and M. Keshavarz Moraveji, “Microfluidics for core–shell drug carrier particles – a review,” *RSC Adv.*, vol. 11, no. 1, pp. 229–249, 2021, [doi: 10.1039/D0RA08607J](https://doi.org/10.1039/D0RA08607J).
- [267] E. Lötstedt, T. Kato, and K. Yamanouchi, “Intramolecular electron dynamics in the ionization of acetylene by an intense laser pulse,” *J. Chem. Phys.*, vol. 138, no. 10, p. 104304, Mar. 2013, [doi: 10.1063/1.4794130](https://doi.org/10.1063/1.4794130).
- [268] T. Seideman, M. Y. Ivanov, and P. B. Corkum, “Role of Electron Localization in Intense-

- Field Molecular Ionization,” *Phys. Rev. Lett.*, vol. 75, no. 15, pp. 2819–2822, Oct. 1995, doi: 10.1103/PhysRevLett.75.2819.
- [269] A. H. Zewail, “Femtosecond real time probing of reactions XXII Kinetic description of probe absorption fluorescence depletion and mass spectrometry,” *Mol. Phys.*, vol. 89, no. 5, pp. 1455–1502, Dec. 1996, doi: [10.1080/002689796173291](https://doi.org/10.1080/002689796173291).
- [270] D. Krajnovich, L. J. Butler, and Y. T. Lee, “UV photodissociation of C<sub>2</sub>F<sub>5</sub>Br, C<sub>2</sub>F<sub>5</sub>I, and 1,2-C<sub>2</sub>F<sub>4</sub>BrI,” *J. Chem. Phys.*, vol. 81, no. 7, pp. 4561–4566, 1984, doi: [10.1063/1.448056](https://doi.org/10.1063/1.448056).
- [271] K. Liu, H. Zhao, C. Wang, A. Zhang, S. Ma, and Z. Li, “A theoretical study of bond selective photochemistry in CH<sub>2</sub>BrI,” *J. Chem. Phys.*, vol. 122, no. 4, 2005, doi: [10.1063/1.1835955](https://doi.org/10.1063/1.1835955).
- [272] D. G. Abrashkevich, M. Shapiro, and P. Brumer, “Coherent control of the CH<sub>2</sub>Br+I←CH<sub>2</sub>BrI→CH<sub>2</sub>I+Br branching photodissociation reaction,” *J. Chem. Phys.*, vol. 116, no. 13, pp. 5584–5592, Mar. 2002, doi: [10.1063/1.1457440](https://doi.org/10.1063/1.1457440).
- [273] K. M. Kapnas, B. W. Toulson, E. S. Foreman, S. A. Block, J. G. Hill, and C. Murray, “UV photodissociation dynamics of CH<sub>2</sub>Cl and its role as a photolytic precursor for a chlorinated Criegee intermediate,” *Phys. Chem. Chem. Phys.*, vol. 19, no. 46, 2017, doi: [10.1039/c7cp06532a](https://doi.org/10.1039/c7cp06532a).
- [274] Balram Kaderiya, “Imaging photo-induced dynamics in halomethane molecules with coincident ion momentum spectroscopy,” PhD thesis, Kansas State University, 2021, <https://hdl.handle.net/2097/41294>.
- [275] A. Hishikawa, H. Hasegawa, and K. Yamanouchi, “Sequential three-body Coulomb explosion of CS<sub>2</sub> in intense laser fields appearing in momentum correlation map,” *Chem. Phys. Lett.*, vol. 361, no. 3, pp. 245–250, 2002, doi: [10.1016/S0009-2614\(02\)00880-1](https://doi.org/10.1016/S0009-2614(02)00880-1).
- [276] A. F. Lago *et al.*, “Dissociative photoionization and thermochemistry of dihalomethane compounds studied by threshold photoelectron photoion coincidence spectroscopy,” *J. Phys. Chem. A*, vol. 109, no. 9, pp. 1802–1809, 2005, doi: [10.1021/jp045337s](https://doi.org/10.1021/jp045337s).
- [277] D. Senapati and P. K. Das, “Cl\*(<sup>2</sup>P<sub>1/2</sub>) production dynamics from chloriodomethane (CH<sub>2</sub>ICl) in the ultraviolet,” *Chem. Phys. Lett.*, vol. 393, no. 4–6, pp. 535–538, 2004, doi: [10.1016/j.cplett.2004.06.095](https://doi.org/10.1016/j.cplett.2004.06.095).
- [278] D. Senapati, K. Kavita, and P. K. Das, “Photodissociation dynamics of CH<sub>2</sub>ICl at 222, 236, 266, 280, and ~304 nm,” *J. Phys. Chem. A*, vol. 106, no. 36, pp. 8479–8482, 2002, doi: [10.1021/jp026021s](https://doi.org/10.1021/jp026021s).

- [279] A. R. Attar, L. Piticco, and S. R. Leone, “Core-to-valence spectroscopic detection of the CH<sub>2</sub>Br radical and element-specific femtosecond photodissociation dynamics of CH<sub>2</sub>I-Br,” *J. Chem. Phys.*, vol. 141, no. 16, p. 164308, 2014, [doi: 10.1063/1.4898375](https://doi.org/10.1063/1.4898375).
- [280] S. V. Levchenko *et al.*, “Photodissociation dynamics of the NO dimer. I. Theoretical overview of the ultraviolet singlet excited states,” *J. Chem. Phys.*, vol. 125, no. 8, p. 84301, Aug. 2006, [doi: 10.1063/1.2222355](https://doi.org/10.1063/1.2222355).
- [281] P. Hockett, C. Z. Bisgaard, O. J. Clarkin, and A. Stolow, “Time-resolved imaging of purely valence-electron dynamics during a chemical reaction,” *Nat. Phys.*, vol. 7, no. 8, pp. 612–615, 2011, [doi: 10.1038/nphys1980](https://doi.org/10.1038/nphys1980).
- [282] H. V. S. Lam *et al.*, “Angle-dependent strong-field ionization and fragmentation of carbon dioxide measured using rotational wave packets,” *Phys. Rev. A*, vol. 102, no. 4, p. 43119, Oct. 2020, [doi: 10.1103/PhysRevA.102.043119](https://doi.org/10.1103/PhysRevA.102.043119).
- [283] K.-C. Tang, J. Peng, K. G. Spears, and R. J. Sension, “Communications: Photoinitiated bond dissociation of bromiodomethane in solution: Comparison of one-photon and two-photon excitations and the formation of iso-CH<sub>2</sub>Br-I and iso-CH<sub>2</sub>I-Br,” *J. Chem. Phys.*, vol. 132, no. 14, p. 141102, Apr. 2010, [doi: 10.1063/1.3374680](https://doi.org/10.1063/1.3374680).
- [284] H. Köckert *et al.*, “UV-induced dissociation of CH<sub>2</sub>BrI probed by intense femtosecond XUV pulses,” *J. Phys. B At. Mol. Opt. Phys.*, vol. 55, no. 1, p. 14001, 2022, [doi: 10.1088/1361-6455/ac489d](https://doi.org/10.1088/1361-6455/ac489d).
- [285] H. Köckert, “Multi-mass imaging in chemical reaction dynamics,” 2019.
- [286] H. Xu and S. T. Pratt, “Photodissociation of Methyl Iodide via Selected Vibrational Levels of the  $\tilde{B}$  (<sup>2</sup>E<sub>3/2</sub>)6s Rydberg State,” *J. Phys. Chem. A*, vol. 119, no. 28, pp. 7548–7558, Jul. 2015, [doi: 10.1021/acs.jpca.5b00860](https://doi.org/10.1021/acs.jpca.5b00860).
- [287] P. G. Wang and L. D. Ziegler, “Mode-specific subpicosecond photodissociation dynamics of the methyl iodide B state,” *J. Chem. Phys.*, vol. 95, no. 1, pp. 288–296, Jul. 1991, [doi: 10.1063/1.461485](https://doi.org/10.1063/1.461485).
- [288] D. J. Campbell and L. D. Ziegler, “Resonance hyper-Raman scattering polarization. A measure of methyl iodide B-state subpicosecond lifetimes,” *J. Chem. Phys.*, vol. 98, no. 1, pp. 150–157, Jan. 1993, [doi: 10.1063/1.464665](https://doi.org/10.1063/1.464665).
- [289] P. G. Wang, Y. P. Zhang, C. J. Ruggles, and L. D. Ziegler, “The spontaneous resonance Raman scattering of CH<sub>3</sub>I in a supersonic jet,” *J. Chem. Phys.*, vol. 92, no. 5, pp. 2806–

- 2817, Mar. 1990, [doi: 10.1063/1.457927](https://doi.org/10.1063/1.457927).
- [290] P. G. Wang and L. D. Ziegler, “Rovibrational Raman scattering of CH<sub>3</sub>I vapor: Resonance with a perpendicularly polarized electronic transition,” *J. Chem. Phys.*, vol. 90, no. 8, pp. 4115–4124, Apr. 1989, [doi: 10.1063/1.455770](https://doi.org/10.1063/1.455770).
- [291] X. Zhang *et al.*, “Formation of surface nanodroplets under controlled flow conditions,” *Proc. Natl. Acad. Sci.*, vol. 112, no. 30, pp. 9253 LP – 9257, Jul. 2015, [doi: 10.1073/pnas.1506071112](https://doi.org/10.1073/pnas.1506071112).

## Appendix A - Native-frame analysis

In this appendix, we describe the native-frame analysis we employed to separate the sequential and concerted fragmentation channel of  $\text{CH}_2\text{Br}^{2+}$  discussed in chapter 5.1.3. The native-frame analysis method was introduced in Refs. [110]–[112], and we follow the same approach here. This method takes advantage of the expected uniform angular distribution after the intermediate molecular fragment rotation in its CM frame if its lifetime is significantly long. Here, we take advantage of the two-step nature of the sequential process. We analyze the first step in the CM frame of the parent ion,  $\text{CH}_2\text{IBr}^{3+}$  and the second step in the CM frame of the intermediate  $\text{CH}_2\text{Br}^{2+}$  di-cation using the relative momenta. The sequential fragmentation proceeding through the  $\text{CH}_2\text{Br}^{2+}$  intermediate is characterized with a uniform distribution of the angle between momentum vectors of the detached iodine and the remaining molecular intermediate  $\text{CH}_2\text{Br}^{2+}$ , due to the rotation of the latter [110]–[112]. In this method, we first define the Jacobi coordinates, as shown schematically in Fig. A.1 (a), in which the relative position vector associated with the first step of the sequential fragmentation is

$$\vec{\rho}_{\text{CH}_2\text{Br},\text{I}} = \vec{r}_{\text{I}} - \vec{X}_{\text{CH}_2\text{Br}}$$

where  $X_{\text{CH}_2\text{Br}}$  is the center of mass of the intermediate  $\text{CH}_2\text{Br}^{2+}$  di-cation in the lab frame:

$$\vec{\rho}_{\text{CH}_2\text{Br},\text{I}} = \vec{r}_{\text{I}} - \frac{1}{m_{\text{CH}_2} + m_{\text{Br}}} (m_{\text{CH}_2} \vec{r}_{\text{CH}_2} + m_{\text{Br}} \vec{r}_{\text{Br}})$$

The relative position vector associated with the 2<sup>nd</sup> step is defined as

$$\vec{\rho}_{\text{CH}_2\text{Br}} = \vec{r}_{\text{Br}} - \vec{r}_{\text{CH}_2}$$

with the center of mass of the parent molecule in the lab frame as below:

$$\vec{X}_{\text{CH}_2\text{BrI}} = \frac{m_{\text{CH}_2} \vec{r}_{\text{CH}_2} + m_{\text{Br}} \vec{r}_{\text{Br}} + m_{\text{I}} \vec{r}_{\text{I}}}{m_{\text{CH}_2} + m_{\text{Br}} + m_{\text{I}}}$$

As shown in Fig. A.1 (b), the relative momentum vector associated with the first step is obtained as:

$$\vec{p}_{\text{CH}_2\text{Br},\text{I}} = \mu_{\text{CH}_2\text{Br},\text{I}} \vec{\rho}_{\text{CH}_2\text{Br},\text{I}}$$

$$\vec{p}_{\text{CH}_2\text{Br},\text{I}} = \mu_{\text{CH}_2\text{Br},\text{I}} \left( \frac{\vec{P}_{\text{I}}}{m_{\text{I}}} - \frac{1}{m_{\text{CH}_2} + m_{\text{Br}}} (\vec{P}_{\text{CH}_2} + \vec{P}_{\text{Br}}) \right) = \frac{m_{\text{CH}_2\text{Br}}}{M} \vec{P}_{\text{I}} - \frac{m_{\text{I}}}{M} (\vec{P}_{\text{CH}_2} + \vec{P}_{\text{Br}})$$

Due to momentum conservation,  $\vec{P}_{\text{CH}_2} + \vec{P}_{\text{Br}} = -\vec{P}_{\text{I}}$  resulting in

$$\vec{p}_{\text{CH}_2\text{Br},\text{I}} = \frac{m_{\text{CH}_2\text{Br}}}{M} \vec{P}_{\text{I}} + \frac{m_{\text{I}}}{M} \vec{P}_{\text{I}} \vec{p}_{\text{CH}_2\text{Br},\text{I}} = \vec{P}_{\text{I}}$$

The relative momentum vector associated with the second step is defined as:

$$\vec{p}_{\text{CH}_2\text{Br}} = \mu_{\text{CH}_2\text{Br}} \vec{\rho}_{\text{CH}_2\text{Br}}$$

As shown in Fig. A.1 (c),  $\theta_{\text{CH}_2\text{Br},\text{I}}$  is defined as the angle between the relative momenta of the first and the second step of the fragmentation

$$\theta_{\text{CH}_2\text{Br},\text{I}} = \text{Cos}^{-1} \left( \frac{\vec{P}_{\text{I}} \cdot \vec{p}_{\text{CH}_2\text{Br}}}{|\vec{P}_{\text{I}}| |\vec{p}_{\text{CH}_2\text{Br}}|} \right)$$

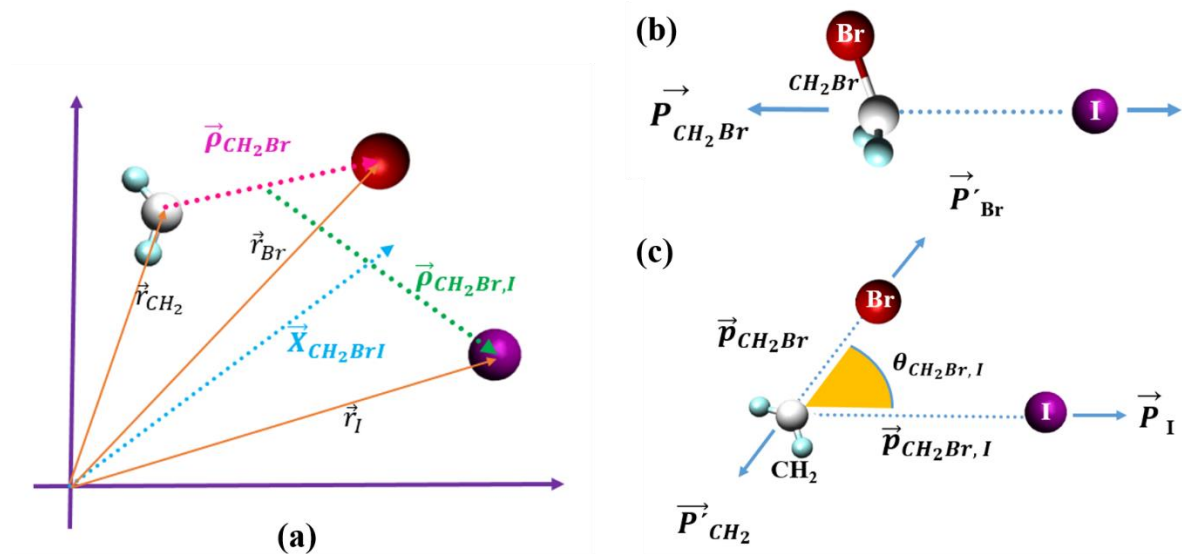


**Figure 8.1.** (a) Schematic definition of the Jacobi coordinates;  $\rho_{\text{CH}_2\text{Br},\text{I}}$ ,  $\rho_{\text{CH}_2\text{Br}}$ ,  $X_{\text{CH}_2\text{Br},\text{I}}$ . (b) Schematic illustrating the two-step sequential fragmentation through  $\text{CH}_2\text{Br}^{2+}$ . (c) The definition of the  $\theta_{\text{CH}_2\text{Br},\text{I}}$  angle.

In Fig. A.2 (a), the KER of the second step defined as  $\text{KER}_{\text{CH}_2\text{Br}} = \frac{p_{\text{CH}_2\text{Br}}^2}{2\mu_{\text{CH}_2\text{Br}}}$ , is plotted versus the angle  $\theta_{\text{CH}_2\text{Br},\text{I}}$ . Here, the sequential fragmentation through the  $\text{CH}_2\text{Br}^{2+}$  intermediate manifests itself as a uniform angular distribution in the energy range of 4 to 5 eV and angle range between 0 to 180 degrees.

Performing this analysis, we identified the corresponding three-body events and found that these sequential fragmentation events correspond to the events in the so-called region 2 in  $\text{KER}_{\text{BrI}}$  map shown in Fig. 5.6, at about 12 eV covering the angular range up to  $180^\circ$ . These identified events are shown in Fig. A.2 (b). Similarly, these events show up as one of the line pairs of X-shaped feature in Dalitz plot shown in Fig. A2 (c) and one of the semi-circles in the Newton diagram shown in Fig. A.2 (d). In Fig. A.2 (a), the dominant localized spot centered at 10 eV

originates from the concerted breakup, and the dashed “tangent-shaped” feature is related to the other intermediate di-cation ( $\text{CH}_2\text{I}^{2+}$ ), which corresponds to the weaker line and semi-circle features in the Dalitz and Newton diagrams.

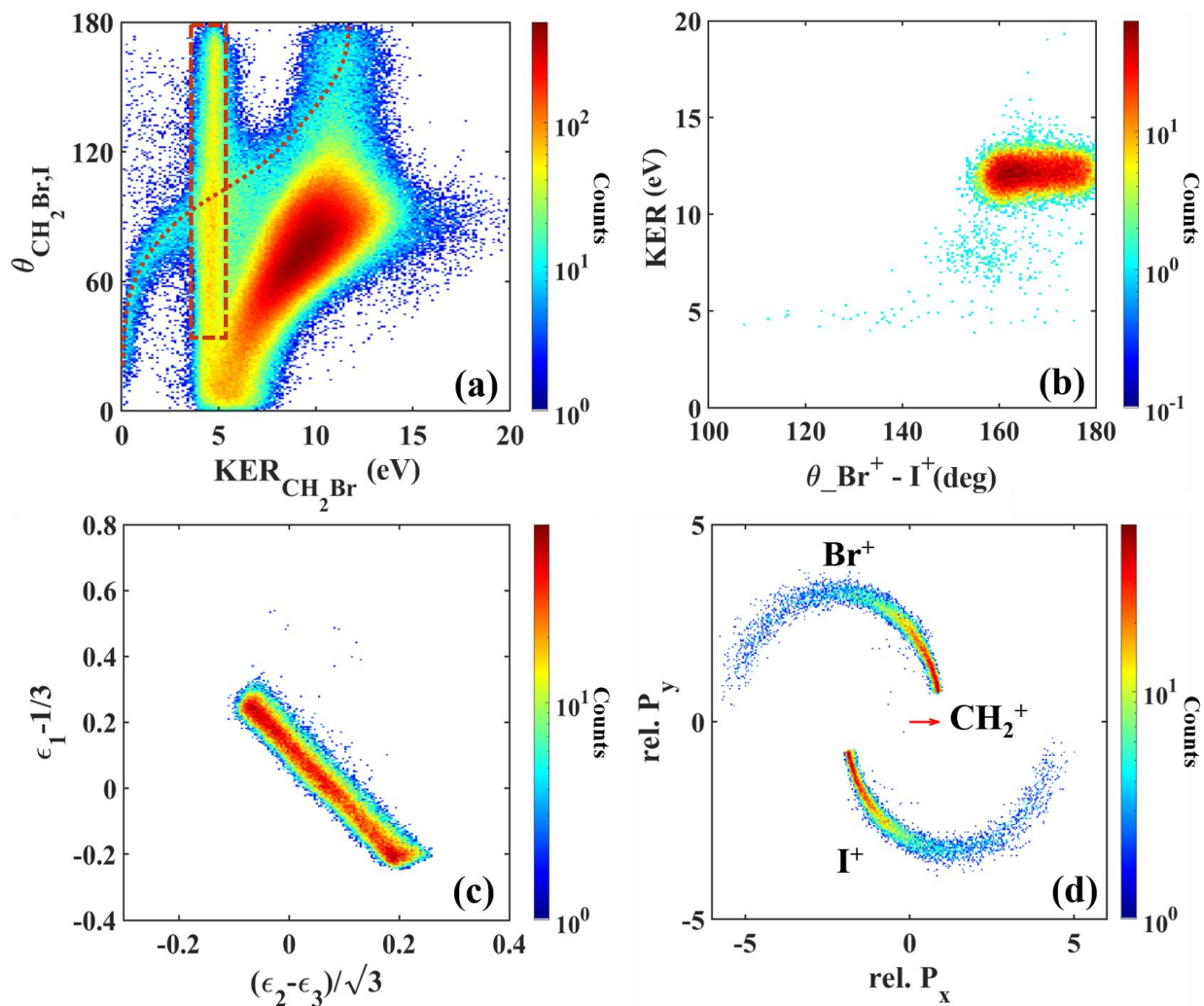


**Figure 8.2.** (a) Yield of the  $\text{CH}_2^{++} \text{Br}^+ + \text{I}^+$  coincidence channel as a function of the  $\text{KER}_{\text{CH}_2\text{Br}}$  and  $\theta_{\text{CH}_2\text{Br}, \text{I}}$ . (b) KER- $\theta_{\text{BrI}}$  map; (c) Dalitz plot; and (d) Newton diagram for the events confined to the rectangular box in panel (a). Dotted curve in (a) reflects the location of events corresponding to sequential channel (2) involving metastable  $\text{CH}_2\text{I}^{2+}$  di-cation.